# Macquarie University PhD Thesis

# An Investigation of Quantization Effects in OFDM at Digital IF in High Capacity Digital Wireless Systems

Thesis by

Boyd Murray

In Partial Fulfillment of the Requirements
for the Degree of
Doctor of Philosophy in Engineering

Macquarie University
New South Wales, Australia

2012
(Submitted March 27, 2013)

I dedicate this thesis to:

My beloved wife Robyn whose constant love and support allowed me to start and complete this work,

My mother Melva whose tenacity is an inspiration to me,

and

to the many friends who encouraged me to continue to completion.

# Acknowledgements

Thank you to my supervisor, Associate Professor Sam Reisenfeld who provided consistent technical and moral help and support throughout the creation of this thesis. Thanks also are due to Colin Jacka (CSIRO) and Robin Braun (UTS) for encouraging me to take on the the challenge of a PhD.

# Abstract

OFDM (Orthogonal Frequency Division Multiplexing) modulation has been widely implemented in existing WLAN (Wireless Local Area Network) systems as well as being the modulation of choice for the emerging 4G LTE (Long Term Evolution) mobile phone data system. Quantization is a very important part of the design of such systems since much of the required complex signal processing is done in the digital domain. Quantization implemented by ADCs (analogue to digital converters) and DACs (digital to analogue converters) is a significant contributor to power consumption in battery-powered hand-held terminals and optimization of the quantization yields power savings and extended battery-life. Until now, the quantization process for OFDM systems has been poorly understood and the models used have been inadequate. This thesis introduces new methods to illuminate the OFDM quantization process and to optimize it for use in the target high capacity digital wireless systems.

# List of Symbols

| | |
|---|---|
| $\forall$ | For all. |
| $\in$ | 'Is in' or 'is an entry of'. Usually refers to a variable being being taken from a set of constants. |
| $\cup$ | The union of two sets. |
| $\star$ | The convolution operator. |
| $\circ$ | The Schur product (a.k.a. "Hadamard product" or "entry-wise product") operator. Used with vectors and matrices. |
| $\{\}$ | The empty set. A set with no elements. |
| $\{\cdot\}$ | An operation on some unnamed variable represented by the dot. |
| $\{\cdot\}^*$ | The complex conjugate. |
| $\{\cdot\}^{\mathrm{H}}$ | The complex conjugate of the transpose of a vector or matrix. Also known as the 'Hermitian'. |
| $\{\cdot\}^{\mathrm{T}}$ | The transpose of a vector or matrix. |
| $\lvert\cdot\rvert$ | The magnitude of a scalar or magnitude of a vector. |
| $(x_{l,m})$ | The matrix whose $(l,m)^{\mathrm{th}}$ entry is $x_{l,m}$. |
| $[\boldsymbol{x}]_l, x_l$ | The $l^{\mathrm{th}}$ entry of a vector $\boldsymbol{x}$. |
| $[\boldsymbol{X}]_{l,m}, x_{l,m}$ | The $(l,m)^{\mathrm{th}}$ entry of a matrix $\boldsymbol{X}$. |
| $\{x_l\}_{l=1}^{Nx}$ | The set $\{x_1, x_2, \cdots, x_{N_x}\}$. |
| $\mathcal{A}_x$ | The alphabet of a variable $x$. |
| $\beta$ | The amplitude scaling factor caused by the quantization operation. At the quantizer output, the required signal has been scaled by $\beta$ and quantization noise has been added. Set by making the quantizer error zero-mean. |
| $b$ | The number of quantizer bits. |

| | |
|---|---|
| $\mathbf{CORR}(\boldsymbol{x})$ | The correlation matrix of a vector $\boldsymbol{x}$. Also written as $\mathbf{CORR}(\boldsymbol{x},\boldsymbol{x})$. |
| $\mathrm{corr}(x,y)$ | The Pearson's correlation factor of two scalars $x$ and $y$. |
| $\mathbf{CORR}(\boldsymbol{x},\boldsymbol{y})$ | The correlation matrix of a vector $\boldsymbol{x}$ and a vector $\boldsymbol{y}$. Each matrix entry is a Pearson's correlation factor of an entry of $\boldsymbol{x}$ with an entry of $\boldsymbol{y}$. |
| $\mathrm{cov}(x)$ | The covariance of a scalar $x$. Also written as $\mathrm{cov}(x,x)$. Also known as the variance $\mathrm{var}(x)$ or $\sigma_x^2$. |
| $\mathbf{COV}(\boldsymbol{x})$ | The covariance matrix of a vector $\boldsymbol{x}$. Also written as $\mathbf{COV}(\boldsymbol{x},\boldsymbol{x})$. Also known as the variance matrix $\mathbf{VAR}(\boldsymbol{x})$. |
| $\mathrm{cov}(x,y)$ | The covariance of two scalars $x$ and $y$. |
| $\mathbf{COV}(\boldsymbol{x},\boldsymbol{y})$ | The covariance matrix of a two vectors $\boldsymbol{x}$ and $\boldsymbol{y}$. Each matrix entry is the covariance of an entry of $\boldsymbol{x}$ with an entry of $\boldsymbol{y}$. |
| $\delta(x)$ | The Dirac delta function of a variable $x$. |
| $\mathbf{DIAG}(\boldsymbol{x})$ | The square matrix whose diagonal entries going from top-left to bottom-right correspond to the entries of a vector $\boldsymbol{x}$ going from first to last; and whose other entries are zero. |
| $\mathbf{DIAG}(\boldsymbol{X})$ | The square matrix whose diagonal entries correspond to the diagonal entries of another matrix $\boldsymbol{X}$; and whose other entries are zero. |
| $\mathrm{E}[x]$ | The expected value of a variable $x$. Also known as the statistical expectation. |
| $\mathrm{E_s}$ | Energy per symbol. |
| $f$ | Frequency. |
| $\boldsymbol{F}$ | The normalized DFT or FFT matrix. Multiplying a time-domain vector by this matrix converts it into a frequency-domain vector. 'Normalized' refers to the property that the frequency-domain vector has the same total energy as the time-domain vector. |
| $\boldsymbol{F}^{-1}$ | The normalized IDFT or IFFT matrix. Multiplying a frequency-domain vector by this matrix converts it into a time-domain vector. 'Normalized' refers to the property that the time-domain vector has the same total energy as the frequency-domain vector. |
| $f_s'$ | Sampling frequency at baseband. |
| $f_s$ | Sampling frequency at digital IF. |
| $f_x(x')$ | The probability distribution function (PDF) of a variable $x$ as a function of the dummy-variable $x'$. |

| | |
|---|---|
| $F_x(x')$ | The cumulative distribution function (CDF) of a variable $x$ as a function of the dummy-variable $x'$. |
| $\mathrm{H}(x)$ | The entropy of a random variable $x$. |
| $\Im\{x\}$ | The imaginary-part of a variable $x$. Also written $\mathrm{Im}(x)$ or $x_{\Im}$. |
| $\boldsymbol{I}, \boldsymbol{I}_N$ | The identity matrix. A square matrix whose diagonal entries are all unity and whose other entries are all zero. Any subscript, say $N$, indicates the dimensions of the square matrix. |
| $\mathrm{I}(x;y)$ | The mutual information between two random variables $x$ and $y$. |
| $M$ | The size variable of a modulation alphabet. Used individually and as a prefix before the modulation type (e.g. $M$QAM, $M$PSK). |
| $N'$ | The size of an IDFT or DFT being used at baseband. |
| $N$ | The size of an IDFT or DFT being used at digital IF. |
| $\mathrm{N}_0$ | Noise power spectral density. |
| $N_\delta$ | Number of diracs in a PDF. |
| $\sim \mathcal{O}(N)$ | Having the order of some variable N. Indicates the approximate size. |
| $\mathrm{P_b}$ | The probability of a bit error. |
| $\mathrm{P_s}$ | The probability of a symbol error. |
| $\mathrm{P}_x$ | The probability of an event $x$. |
| $\mathrm{P}_{x\|y}(x'\|y')$ | Conditional probability. The probability of a random variable $x$ being equal to $x'$ conditioned on another random variable $y$ being equal to $y'$. Sometimes shorthanded to $\mathrm{P}(x\|y)$. |
| $\mathrm{Q}(x)$ | The normalized Gaussian complementary cumulative distribution function $\frac{1}{\sqrt{2\pi}} \int_x^\infty e^{\frac{-t^2}{2}} dt$. |
| $\Re\{x\}$ | The real-part of a variable $x$. Also written as $\mathrm{Re}(x)$ or $x_{\Re}$. |
| $R_0$ | The cutoff rate. Used for practical finite length block codes in discrete memoryless channels to upper-bound codeword error rates after maximum likelihood decoding. |
| $\mathrm{S}_x(f)$ | The power spectral density (a.k.a. PSD or spectrum) of a variable $x$ as a function of frequency $f$. |
| $\mathbb{Z}$ | The infinite set of all integers. |
| $\mathbb{Z}_N$ | The finite set of integers: $\{0, 1, \cdots N-1\}$. |

# List of Acronyms

| | |
|---|---|
| ADC | Analogue to Digital Converter. |
| AGC | Automatic Gain Control. A receiver gain block whose gain is automatically set for optimal demodulation. |
| a.k.a | Also known as. |
| BER | Bit Error Ratio or Bit Error Rate. The ratio of errored received bits to total received bits. |
| BPSK | Binary Phase Shift Keying. A type of modulation. The same as 2QAM and 2PSK. |
| CCDF | Complimentary Cumulative Distribution Function. |
| CDF | Cumulative Distribution Function. |
| CSI | Channel State Information. The gains and phases of all the paths in a channel. |
| DAC | Digital to Analogue Converter. |
| DFT | Discrete Fourier Transform. |
| DIF | Digital Intermediate Frequency. An intermediate frequency generated directly in the digital domain. |
| FFT | Fast Fourier Transform. A fast algorithm to perform a DFT operation. |
| I | The In-phase (or real) component of a modulated signal. |
| IDFT | Inverse Discrete Fourier Transform. |
| IEEE | Institute of Electrical and Electronics Engineers. |
| IF | Intermediate Frequency. A frequency between baseband and RF. |
| IFFT | Inverse Fast Fourier Transform. A fast algorithm to perform an IDFT operation. |

| | |
|---|---|
| LNA | Low Noise Amplifier. Usually, the first amplifier in a receiver. |
| LTE | Long Term Evolution. A wireless access communications standard. |
| MIMO | Multiple Input Multiple Output. Describes a communications system with multiple transmitters and multiple receivers. |
| MISO | Multiple Input Single Output. Describes a communications system with multiple transmitters and a single receiver. |
| $M$PSK | Phase Shift Keying modulation with an alphabet of $M$ symbols. |
| $M$QAM | Quadrature Amplitude Modulation with an alphabet of $M$ symbols. |
| NCO | Numerically Controlled Oscillator. A digital-domain oscillator whose frequency is controlled by a number in a register. Often used as a local oscillator input into a digital-domain mixer. |
| OFDM | Orthogonal Frequency Division Multiplexing. A modulation where multiple sub-carriers are each modulated with data, then added (or 'multiplexed') together. |
| PDF | Probability Density Function. |
| PSD | Power Spectral Density. Usually versus frequency. Also known as 'spectrum'. |
| PSK | Phase Shift Keying modulation. |
| Q | The Quadrature (or imaginary) component of a modulated signal. |
| QAM | Quadrature Amplitude Modulation. |
| QPSK | Quadrature Phase Shift Keying. A type of modulation. The same as 4QAM and 4PSK. |
| RF | Radio Frequency. The frequency which gets transmitted to air. |
| RMS | Root Mean Square. |
| RX, Rx | Receiver. |
| SIMO | Single Input Multiple Output. Describes a communications system with a single transmitter and multiple receivers. |
| SISO | Multiple Input Single Output. Describes a communications system with a single transmitter and a single receiver. |
| SNR | Signal to Noise Ratio. |

SQNR — Signal to Quantization Noise Ratio. SQNR measures the ratio of the average power of the desired signal the average power of any quantization noise. It does not include other noise sources (e.g. LNA noise).

TX, Tx — Transmitter.

VCO — Voltage Controlled Oscillator. An analogue-domain oscillator whose frequency is controlled by a voltage (which is usually controlled by a phase locked loop). Often used as a local oscillator input into a analogue-domain mixer.

Wi-Fi — Shorthand for ‘Wireless-Fidelity’. The popular name given by the Wi-Fi Alliance to the IEEE 802.11 WLAN standards.

WiMAX — Worldwide Interoperability for Microwave Access. A wireless access communications standard.

WLAN — Wireless Local Area Network.

ZF — Zero-Forcing. A technique to force unwanted cross-channel interfering components to zero, whilst leaving the wanted components remaining. One form of MIMO detection.

# List of Definitions

| | |
|---|---|
| 802.11 | A series of IEEE WLAN standards (including 802.11a, 802.11b, and 802.11n). Also known as Wi-Fi. |
| Alphabet | The set of all unique values (or 'letters') which can be taken on by a variable or signal. The variable can be a scalar, vector, matrix, or something else. |
| Constellation | The pattern formed by the full alphabet of a signal. For QAM or PSK modulations, it is represented in 2-dimensional space with real and imaginary dimensions. |
| Downconvert | To move the spectrum of a signal down in frequency. |
| Frequency-sample | A sample occurring in the frequency-domain. Usually at the input of an IDFT or IFFT, or after the output of a DFT or FFT. |
| Gaussian | Description of a bell-shaped probability distribution. Same as 'normal'. |
| Letter | A unique value which can be taken on by a variable. When a variable has multiple letters, the set of letters forms the alphabet for that variable. |
| Pre-code | To adjust a signal before transmission. |
| Quantize | To map continuous or discrete numbers from one domain into discrete numbers in another domain. |
| Time-sample | A sample occurring in the time-domain. Usually after the output of an IDFT or IFFT or at the input to a DFT or FFT. |
| Upconvert | To move the spectrum of a signal up in frequency. |

# Notation

| Item | Example | Font |
|---|---|---|
| Matrix constant | $\mathbf{X}$ | Upper-case, bold, regular |
| Matrix variable | $\boldsymbol{X}$ | Upper-case, bold, italic |
| Scalar constant | $\mathrm{x}$ | Lower-case, non-bold, regular |
| Scalar variable | $x$ | Lower-case, non-bold, italic |
| Vector constant | $\mathbf{x}$ | Lower-case, bold, regular |
| Vector variable | $\boldsymbol{x}$ | Lower-case, bold, italic |
| Set | $\mathcal{X}$ | Upper case, regular, calligraphic |

# Contents

# List of Figures

# List of Tables

# Chapter 1

# Introduction

Many modern wireless telecommunication systems are now adopting OFDM (Orthogonal Frequency Division Multiplexing) and its variants as the modulation of choice. OFDM wireless systems, like other wireless systems, require the use of quantization as an essential ingredient.

Quantization is the gateway between the real-world 'analogue' domain and the 'digital' domain where the vast majority of signal-processing is done in the modern wireless technology. It is the key enabler which allows a vast arsenal of digital processing algorithms to process data obtained from the external analogue domain.

Modern wireless telecommunication systems are significant exemplars of digital signal processing (DSP) systems and are capable of transmitting Gbit/s data-rates over ranges from several metres up to tens of kilometres wirelessly.

Quantization of OFDM systems is currently not generally well understood and is often either ignored in the literature or simplified with the use of various, often unjustified, assumptions.

This thesis addresses these short-comings. It provides significant insights into OFDM quantization as well as much reference data. It also shows some of the assumptions in the literature to be either untrue or limited in their applicability and, in some cases, provides new exact analytical results.

It is hoped that this thesis will add substantially to the state-of-the-art for OFDM quantization.

## 1.1 Research Context

Despite being such an important topic, the literature regarding quantization of OFDM systems is sparse. An extensive literature search on the 'OFDM quantization' results in only a few tens of hits and many of those are not directly relevant to the interests of this thesis. The literature which has been deemed to be directly relevant to our topis is discussed below.

Bussgang's 1952 paper 'Crosscorrelation functions of amplitude-distorted gaussian signals' [7] addresses Gaussian signals being passed through any general non-linearity (such as a quantizer). It models such non-linearities as a gain factor plus uncorrelated noise. Many subsequent quantization papers refer to this paper and adopt its model (as this thesis also does). This thesis shows that, even though ODFM signals are not truly Gaussian, the model of a gain factor is valid. However, for OFDM, the quantization noise is correlated under some circumstances. Also, it is very worthwhile to note at this point that 'uncorrelated' is not the same as independent since the averaging process used in determining the correlation can average out the dependencies.

Widrow's 1996 paper 'Statistical theory of quantization' [43] adopts the Bussgang [7] quantization model comprising a gain factor plus additive quantization noise, which is the same as that used in this thesis. The paper makes the very salient statement that the quantization noise added by the quantizer is deterministically related to the input. Also, it differentiates between independence and correlation with regards to additive quantization noise in its statement 'although the quantization noise and the quantizer input are deterministically related, it is a curious fact that under certain circumstances, the input and noise are uncorrelated'. In the majority of the literature, the non-use of these two ideas mistakenly leads to incorrect assumptions and conclusions . However, this thesis does address the dependence of the quantizer noise on the quantizer input. The main shortcoming of this Widrow paper is that it does not address clipping, which is addressed in this thesis. Also, the assumption of a Gaussian signal cannot be blindly applied to OFDM systems.

Moschitta's 2002 paper 'Wideband communication system sensitivity to quantization noise' [34] considers a specific OFDM system with the large number of 2048 sub-carriers and invokes the Central Limit Theorem to support many of its conclusions. The paper states that the granular noise model (i.e. quantization with no clipping) has been generalized to an 'extended model' by assuming that a limited amount of clipping does not affect the statistical properties of the noise at the output of the FFT (i.e. in the frequency-domain where symbol decisions are ultimately made). However, normally, optimization of the quantizer performance is achieved by balancing the effects of both granular quantization noise and clipping noise, so when an optimal clipping-level is found, we would expect that the noise contributions from granular quantization and clipping to be roughly the same. This tends to negate the idea of a 'limited [negligible] amount of clipping' making the basis of the paper somewhat doubtful.

Dardari's 2003 paper 'Exact analysis of joint clipping and quantization effects in high speed WLAN receivers' [12] addresses both clipping and quantization of OFDM systems. It states that proper characterization of quantized receiver performance needs to be characterized in both the spectral (frequency) and statistical domains, but then only addresses the spectral domain. Without addressing the statistical domain, no conclusions are drawn regarding the effect of the quantization on performance metrics such as the bit error ratio BER and capacity. The paper refers to the PQN (Pseudo Quantization Noise) model of Widrow and Liu [43] and then uses the unjustified assumption that OFDM signals can be treated as Gaussian so that the PQN model applies. The PQN model assumes that quantization noise (for Gaussian signal) is additive, uncorrelated and independent of the input signal, and uniform and which leads to the adoption of a quantization model comprising a gain factor plus additive quantization noise which is the same as that used in this thesis. The assumptions of uncorrelated and independent additive noise are disputed in this thesis. Also, the PQN model does not address clipping and this thesis reveals that clipping is a major source of correlated quantization noise.

Dardari's 2006 paper 'Joint clip and quantization effects characterization in OFDM receivers' [13] appears to be a rewrite and update of Dardari's earlier 2003 paper [12] already discussed above. The main assumptions of the earlier 2003 paper [12] remain in this paper.

Ehm's 2006 paper 'Analytic quantization modeling of OFDM signals using normal Gaussian distribution' [16] only attempts to find a clipping-level which optimizes the quantizer output's SNR. It doesn't address the PDF of the quantizer noise and therefore any performance predictions are based on the assumption that the noise PDF is Gaussian. As the title indicates, the paper assumes that the OFDM signal is Gaussian which does not take into account the hidden structure of OFDM. Also, the paper doesn't address correlation effects and and doesn't look at the quantization noise in the frequency-domain where data symbol decisions are ultimately made.

Araujo and Dinis's 2007 paper 'Performance Evaluation of Quantization Effects on Multicarrier Modulated Signals' [3] adopts the Bussgang [7] quantization model comprising a gain factor plus additive quantization noise which is the same as that used in this thesis. However, the paper only evaluates the effective SNR (ESNR) due to quantization noise, but does not address the PDF of the noise so that no conclusions can be drawn regarding the effect of the quantization on performance metrics such as the bit error ratio BER and capacity. Also, correlation of the quantization noise with the required signal is addressed but there appears to be no differentiation between non-correlation and independence thus leading to the unjustified assertion that BER can be calculated from the ESNR.

Widrow and Kollar's 2008 book 'Quantization Noise: Round Off Error in Digital Computation, Signal Processing, Control and Communications' [42] addresses quantization of continuous Gaussian sinusoidal signals and includes much of the material presented in his earlier 1996 paper [43] already discussed above. Newer additional material includes covariance, correlations, and cross-correlations relating to the quantizer input, quantizer output, and quantizer error. These quantities are also addressed in this thesis. Unfortunately, all of Widrow and Kollar's analyses assume either a Gaussian or sinusoidal input into the quantizer. This thesis addresses the quantization of time-domain OFDM signals which are shown to diverge from true Gaussian distributions. Whereas Widrow and Kollar's analyses give insight, their restriction to ideal Gaussian and sinusoidal signals mean that they cannot be blindly applied to real-world OFDM signals. This thesis addresses that short-coming.

Liyanage's 2010 paper 'Statistical Analysis of Quantization Noise in an End-to-End OFDM Link' [31] correctly says, that quantization noise is not always independently additive. It also addresses clipping noise. However, the paper assumes that the OFDM signal PDF is Gaussian (due to the Central Limit Theorem) which this thesis shows to be not entirely true. The paper also states that all of the individual OFDM time-samples emanating from the output of an IDFT have the same variance which this thesis categorically shows to be untrue. The analysis in the paper also states that the covariance matrix of the ODFM time-samples before an after the quantizer is diagonal. Again, this thesis shows that to be untrue in the cases of severe clipping and large quantizer step-size.

Ramakrishnan 2010 paper 'Exploiting signal and noise statistics for fixed point FFT design optimization in OFDM systems' states 'for reasonably large N, the time-domain samples $x(n)$ are Gaussian distributed due to the Central Limit Theorem'. It then uses this assumption to obtain the SQNR (Signal to Quantization Noise Ratio). However, there is no mention of the PDF of the SQNR and the SQNR is not related to any meaningful performance metric like BER.

As can be seen from the above literature review, quantization of OFDM is still an inexact science with many of the published results based on ultimately unjustified assumptions.

## 1.2 Motivation for This Research

### 1.2.1 Reduced Energy Consumption Through Reducing the Number of Quantizer Bits

Handheld wireless technology terminals now abound in the general community. A key performance metric of handheld terminals is battery-life and the literature shows that battery-life is related to both the number of quantizer bits and the quantizer sample rate. The need to minimizing the number of quantizer bits to reduce power-consumption whilst still achieving various target system performance metrics is therefore a compelling motivator for this thesis.

The relationship between minimal theoretical ADC power dissipation $P_{\text{min}}$, sampling rate $f_s$, and number of bits $b$ is [24]

$$P_{\text{min}} = k \cdot T \cdot f_s \cdot 10^{(b+1.76)/10}, \tag{1.1}$$

from which we can see that the power dissipation $P_{\text{min}}$ is linearly related to the sampling frequency and exponentially related to the number of ADC bits $b$. Practical power dissipations are sometimes many orders of magnitude higher than the minimal power stated in (1.1) but the above relationships generally hold [28].

Also, Liyanage [31] states very recently in 2010 that 'an IEEE 802.11a transceiver operating at 54Mbps uses about 21% of the [its total power consumption] on the DAC circuitry, while the the ADC consumes 47% of the power'.

Given these alarming statistics, we reiterate that reduction of the DAC and ADC power consumptions through reduction of the number of bits used is a compelling motivation for this thesis.

## 1.3 Research Objectives

### 1.3.1 Challenging of the Unjustified Assumptions Often Made in OFDM Quantization Analyses

In the literature review of §1.1 above, we found that many assumptions often made in the literature regarding OFDM quantization analyses are unjustified and can lead to incorrect conclusions. Exposing and correcting such incorrect assumptions in order to advance the state of knowledge in this important topic is a key research objective for this thesis.

The key assumptions challenged in this thesis are

- that the PDF of OFDM signals is Gaussian,
- that the quantization noise is Gaussian, and
- that the quantization noise is independent from the quantizer input signal.

### 1.3.2 The Inclusion of Clipping in OFDM Quantization Analysis

As already discussed in §1.1, the inclusion of clipping is only evident in a few publications in the literature. This thesis includes clipping in its analysis and, in some cases, separates out the effects of clipping and quantization.

### 1.3.3 The Generation of Exact Correlation, PDF, and CDF Results, Where Possible

A large majority of the relevant literature relies on simplifying assumptions to obtain results pertaining to OFDM quantization. This thesis aims to provide as much exact analysis as possible. This includes

- exact PDFs and CDFs for the OFDM signals before and after the quantizer for low complexity OFDM systems,
- exact PDFs and CDFs for the OFDM signals before quantizer (at the IDFT output for arbitrary-complexity OFDM systems,
- exact covariance and correlation matrices after quantizer for low-complexity OFDM systems, and
- exact covariance and correlation matrices before and after the IDFT for arbitrary-complexity OFDM systems.

### 1.3.4 The Provision of Reference Data for OFDM Quantization Optimization

Much of the literature does not pertain to real-world OFDM systems. This thesis aims to provide a prodigious amount of reference data for PDFs, CDFs, covariance matrices, and correlation matrices for both small-complexity systems and larger-scale real-world OFDM systems such as IEEE 802.11a. The first goal of this reference data is to provide a benchmark against which the various claims in the literature can be tested. The second goal is to provide data from which OFDM system performance metrics (such as BER) can be derived.

## 1.4 Thesis Structure

This thesis is structured as follows.

Chapter 1 provides an introduction which includes the research context, motivation for the thesis, research objectives, original contributions to the field, and author's publications.

Chapter 2 provides a review of OFDM and digital IF. Firstly, a brief background of OFDM is presented. Then, a description of a novel 'Digital IF' signal processing scheme is discussed. This 'Digital IF' scheme bypasses the typically-used direction modulation schemes, which require two DACs/ADCs and analogue mixers and adders (with their accompanying signal impairments), to produce the OFDM signal directly at the target digital IF frequency with the use of a single DAC/ADC and no analogue components. This is an original contribution to the state-of-the-art. Also, this new scheme simplifies the quantizer analysis to only one quantizer and is used throughout this thesis.

Chapter 3 commences the technical analysis by presenting a numerical Monte Carlo simulation study of the new digital IF scheme implemented in an IEEE 802.11n WLAN OFDM system. Results are presented for the quantization clipping-factor optimization, in terms of contribution to the BER from quantization, for various numbers of quantizer bits; and design tables presented for choosing the quantization suitable for various design targets.

Chapter 4 then introduces a detailed model of the digital IF system used for the rest of the thesis (except for the MIMO chapter).

Chapter 5 addresses numerical approaches for obtaining OFDM quantization results. The first approach is the 'Exhaustive' method which exhaustively applies every possible data input into the system, then processes the system outputs to obtain PDFs, CDF, covariance matrices, and correlation matrices. The second approach is the 'Monte Carlo' method which applies a randomly chosen subset of all possible data inputs, then processes the results in the same way as for the 'Exhaustive Method'. This 'Monte Carlo' method is used for large-complexity systems for which the simulation times would be impossibly large for the 'Exhaustive' method. 'Monte Carlo' results are presented for the real-world IEEE 802.11a WLAN OFDM system showing the PDFs and CDFs of the frequency-domain quantization errors. These results reveal significant departures from the expected Gaussian PDFs resulting from various unjustified assumptions in the literature.

Chapter 6 addresses various analytical approaches to obtaining results for a quantized OFDM system. The 'Matrix Transformation' method produces exact results for the covariance and correlation matrices at the input and output of the IDFT which produces the digital IF OFDM signal. This is an original contribution. The 'Convolution Method' produces exact PDFs and CDFs of an arbitrary-complexity unquantized digital IF OFDM signal. This, too, is an original contribution. Exact PDF and CDF results are presented for the IEEE 802.11a WLAN system. Finally, the 'Combinatorics' method is discussed as a possible solution for obtaining exact PDFs and CDFs for arbitrary-complexity OFDM systems. This commences a new contribution to the field.

Chapter 7 is a slight diversion from the main thrust of this thesis. It considers quantization of baseband (not OFDM) signals in a MIMO (not SISO) system. A 2 x 2 baseband MIMO is subjected to receiver quantization and the multiple receiver quantizers used are optimized in terms of the so-called 'cutoff' rate which provides a measure of the coded BER performance of any arbitrary coding system.

Finally, Chapter 8 provides conclusions and recommendations for future research.

## 1.5 Original Contributions to the Field

This thesis present several new contributions to the field of OFDM and OFDM quantization as follows.

Firstly, a new 'Digital IF' scheme to is presented. The scheme bypasses the typically-used direction modulation schemes, which require two DACs/ADCs and analogue mixers and adders (with their accompanying signal impairments). Instead it produces the OFDM signal directly at the target digital IF frequency with the use of a single DAC/ADC and no analogue components. This is an original contribution to the state-of-the-art.

Secondly, the 'Matrix Transformation' method is presented. It produces exact results for the covariance and correlation matrices at the input and output of the IDFT which produces the digital IF OFDM signal. This is an original contribution.

Thirdly, the 'Convolution Method' method is presented. This method produces exact PDFs and CDFs of an arbitrary-complexity unquantized digital IF OFDM signal. This, too, is an original contribution. Exact PDF and CDF results are presented for the IEEE 802.11a WLAN system.

Finally, the 'Combinatorics' method is presented as a possible solution for obtaining exact PDFs and CDFs for arbitrary-complexity OFDM systems. This commences a new contribution to the field. A final solution is beyond the scope of this thesis, but this thesis has laid some ground-work for continuance in a possible future study.

## 1.6 Author's Publications

Publications related to the field of this thesis for which the author is the primary author are as follows.

[36] B. M. Murray and S. Reisenfeld. Maximizing the cutoff rate in a quantized MIMO wireless system with AGC. In *1'st Australian Conference on Wireless Broadband and Ultra Wideband Communications (AusWireless'06)*, Mar. 2006

[35] B. M. Murray and I. B. Collings. AGC and Quantization Effects in a Zero-Forcing MIMO Wireless System. In *Vehicular Technology Conference, 2006. VTC 2006-Spring. IEEE 63rd*, volume 4, pages 1802 -1806, May. 2006.

[37] B. M. Murray, H. Suzuki, and S. Reisenfeld. Optimal quantization of OFDM at digital IF. In *TENCON 2008 - 2008 IEEE Region 10 Conference*, pages 1 - 5, Nov. 2008.

Publications related to the field of this thesis for which the author is the secondary author are as follows.

[40] H. Suzuki, B. Murray, B., A. Grancea, A., R. Shaw, R., J. Pathikulangara, and I. B. Collings. Real-time wideband MIMO demonstrator. In *Communications and Information Technologies, 2007. ISCIT '07. International Symposium on*, Pages 284 - 289, Oct. 2007.

# Chapter 2

# A Review of OFDM and the New Digital IF Scheme

In this short chapter, we will do brief reviews of the two main topics of this thesis - OFDM and Digital IF.

## 2.1 OFDM

OFDM (Orthogonal Frequency Division Multiplexing) is a modulation scheme used widely in today's advanced wireless communication systems such as WLANs [15], WiMAX [19], and LTE [17] because it allows relatively simple adaptive equalization of frequency selective fading in multi-path channel environments.

OFDM is a DTM (Discrete Multi Tone) modulation. Symbols for transmission (typically QAM or PSK) are split into parallel streams each of which are then simultaneously modulated by a unique discrete sub-carrier frequency. The modulated symbols are then all added together to form the signal to be transmitted. A detailed description of OFDM is considered outside of the scope of this thesis, but such detailed descriptions can easily be found in the literature [5, 39].

Transmitted signals for such systems are created in the digital domain before crossing over to the analog domain with the use of a DAC (Digital to Analog Converter) which necessarily introduces quantization artifacts due to its finite number of bits and finite signal range. Reduction of the number of DAC (quantizer) bits contributes to many system improvements including reduced DAC die size, complexity, cost, power dissipation, heat dissipation, and settling time; increased DAC speed, and reduced signal processing bus-widths [10, 25]. All of these system improvements are particularly important for low-cost, battery-powered, hand-held wireless terminals which are becoming increasingly popular. This thesis gives insights into how the number of quantizer bits can be minimized whilst maintaining other system performance metrics such as capacity, uncoded BER, coded BER, and cutoff rate

## 2.2 New OFDM Digital IF Scheme

In this thesis, we use a novel and very simple, but effective, OFDM digital IF (Intermediate frequency) topology whose upconversion and downconversion processes are achieved entirely by an IDFT (or IFFT) and DFT (or FFT) respectively. Having done an extensive literature search which could not find such a topology elsewhere, we believe this topology to be an entirely original contribution to the state-of-the-art.

A comparison of this new digital IF topology against a traditional direct-conversion analogue IF topology and a traditional digital IF topology is shown in Figure 2.1.

Comparing Figure 2.1(a) to (c), we see that the new digital IF scheme does not require the use of analogue mixers, filters, and an analogue adder and uses only one DAC / ADC compared to the two DACs / ADCs required for the direct-conversion analogue scheme. Additionally, it is not subject to the analogue impairments such as gain and phase imbalances between the I and Q arms of the direct-conversion analogue IF scheme. However, it does require a double-sized IDFT and DFT running at twice the speed compared to the direct-conversion analogue IF scheme

Also, comparing Figure 2.1(a) to (c), we see that the upsampler, interpolation filter, image filter, and downsampler of the traditional digital IF scheme have been entirely eliminated in the new digital IF scheme. However, the size of the IDFT / DFT has been doubled.

A significant benefit of using the new digital IF topology is that its analysis is greatly simplified because only a single quantizer appears in the transmitter signal processing chain and a single quantizer in the receiver processing chain. Also, the absence of the NCOs and mixers of the traditional digital IF scheme allows the use of the new ‘Matrix Transformation’ method introduced in §6.1.

The traditional digital IF scheme is used in §3 and is described in more detail there.

The new digital IF scheme is used throughout §4 to §6 and is described and analysed in much more detail in §4.1.

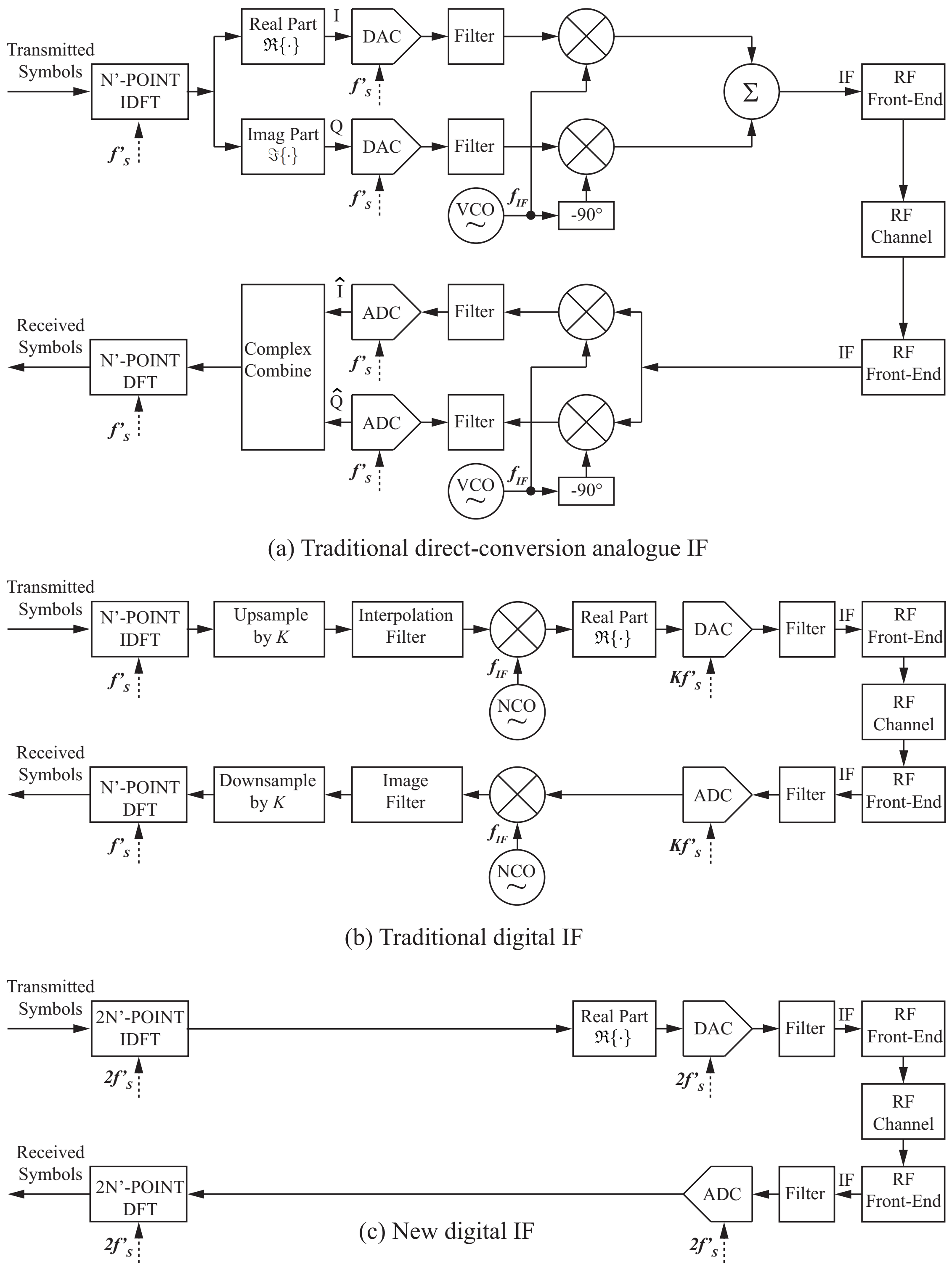


(a) Traditional direct-conversion analogue IF

(b) Traditional digital IF

(c) New digital IF

Figure 2.1: Comparison of the new OFDM digital IF scheme against traditional IF schemes.

# Chapter 3

# Starters: A Monte Carlo Simulation Case Study

In order to acquire some preliminary insight, we commence with a Monte Carlo simulation case-study of digital to analog conversion of OFDM signals which have been digitally upconverted to a digital IF (Intermediate Frequency) at a transmitter using the traditional digital IF topology already discussed in §2.2. Numerical simulation is simpler to perform than an analytical approach; so, we start with it.

We examine the effect of clipping and quantization on the received constellations and the uncoded bit error rate (BER) and find that, in many (but not all) of the cases examined, the clipping and quantization can be characterized as a gain and the addition of noise which is uncorrelated to the quantizer input and which has a Gaussian distribution. Extensive simulations support this result for BPSK, QPSK, 16QAM, and 64QAM with 2 to 14 quantization bits. We also present results showing the optimal quantizer clipping-factor and resultant optimal signal-to-noise ratio for the above modulations and numbers of bits. Finally, we present design curves allowing the selection of the minimum number of bits required to achieve target uncoded BERs in systems which do include channel noise (e.g. LNA noise). For example, to achieve a target uncoded BER of $< 10^{-8}$, only 6 quantization bits are required for all of the above modulations.

Most analyses and implementations of OFDM systems apply quantization at the transmitter to both the real (in-phase or I) and imaginary (quadrature or Q) components of the baseband OFDM signal before upconversion to IF (Intermediate Frequency) with an analogue complex modulator (e.g. [13]). Such schemes are susceptible to signal impairments due to gain and phase imbalances in the I and Q arms of the complex modulator [29].

Here, we take a different approach by performing the upconversion in the digital domain, using the traditional digital IF topology already discussed in in §2.2, and then applying the quantization to the digital IF signal which does not have the aforementioned impairments [38]. We then perform an ideal downconversion and OFDM demodulation to evaluate solely the effect of the quantization of the transmitted OFDM digital IF signal. We intentionally do not include the effects of any channel noise (e.g. LNA noise). Using a simulation approach, we determine the optimal clipping-factor in terms of maximal signal-to-quantization-noise ratio (SQNR) of the received constellation. At each clipping-factor, we also determine the constellation gain factor, quantization noise PDF, and correlation factor (between the required signal and the quantization noise) of the required of the received signal in order to validate a model of the quantization process consisting of a gain plus additive uncorrelated Gaussian noise. The author is not aware of this type of analysis of OFDM digital IF quantization appearing anywhere else in the literature.

## 3.1 System Description

The OFDM system under consideration in this numerical simulation case-study has been selected to match a typical IEEE 802.11n (draft standard) WLAN [2] with a digital IF and is depicted in Figure 7.1.

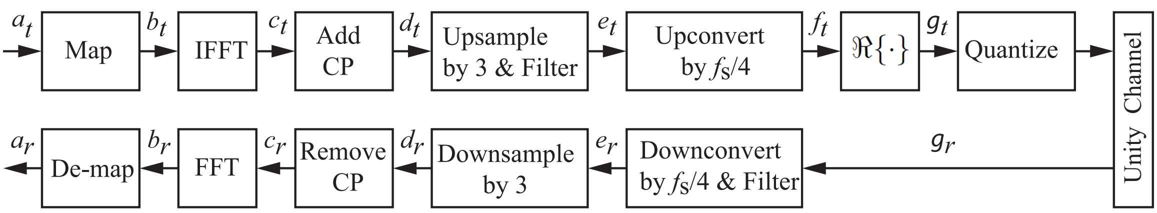


Figure 3.1: System model.

The transmitter passes source integers $a_t$ through a mapper to get complex baseband BPSK or MQAM symbols $b_t$ which are passed through a 128-point IFFT to get the time-domain signal $c_t$. Fourteen of the sub-carriers are nulled per the IEEE 802.11n WLAN draft standard [2] so that the OFDM signal resembles IEEE 802.11n except for the BPSK pilots. A 32-sample cyclic prefix (CP) is added to get signal $d_t$ which is then upsampled by a factor of 3 and passed through an interpolation filter to get signal $e_t$. This upsampling and filtering creates gaps in the spectra of $e_t$ and thence $f_t$ so that information is not overwritten during the subsequent real-part operation $\Re\{\cdot\}$. A complex upconversion by one quarter of the sampling frequency $f_s$ is then performed on signal $e_t$ to get signal $f_t$ whose real part is taken to get signal $g_t$ which is then passed through the quantizer and an ideal unity gain channel to get the real received signal $g_r$. The receiver then downconverts signal $g_r$ by $f_s/4$ and filters it to get the complex baseband signal $e_r$ which is then downsampled by a factor of 3 to get signal $d_r$. The cyclic prefix is removed to get signal $c_r$ which is passed through a 128-point FFT to get the received complex baseband BPSK or MQAM symbols $b_r$ which are then de-mapped to the received integers $a_r$.

## 3.2 Quantizer Description

The quantizer shown in Figure 7.1 is a uniform symmetric mid-riser quantizer [18]. The quantizer input thresholds are given by

$$u_\ell = \begin{cases} -\infty\ , & \ell = 1 \\ (\frac{-L}{2} - 1 + \ell)\Delta\ , & \ell \in \{2, 3, \cdots, L\} \\ +\infty\ , & \ell = L + 1 \end{cases} \tag{3.1}$$

where $\Delta$ is the quantizer step-size and $L = 2^b$ is the number of quantizer levels for $b$ quantizer bits. The quantizer output levels are given by

$$v_\ell = \left(\frac{-L}{2} - \frac{1}{2} + \ell\right)\Delta\ ,\ \ell \in \{1, 2, \cdots, L\}. \tag{3.2}$$

The quantizer function is given by

$$g_r = v_\ell,\ u_\ell \le g_t < u_{\ell+1},\ \ell \in \{1, 2, \cdots, L\}, \tag{3.3}$$

which is depicted in Figure 3.2. The quantizer input clip level is given by

$$k = -v_1 = v_L = \left(\frac{L}{2} - \frac{1}{2}\right)\Delta, \tag{3.4}$$

and the quantizer clipping-factor is defined as

$$\kappa = \frac{k}{\sigma}, \tag{3.5}$$

where $\sigma = \sqrt{\mathrm{E}[|g_t|^2]}$ is the RMS signal level into the quantizer.

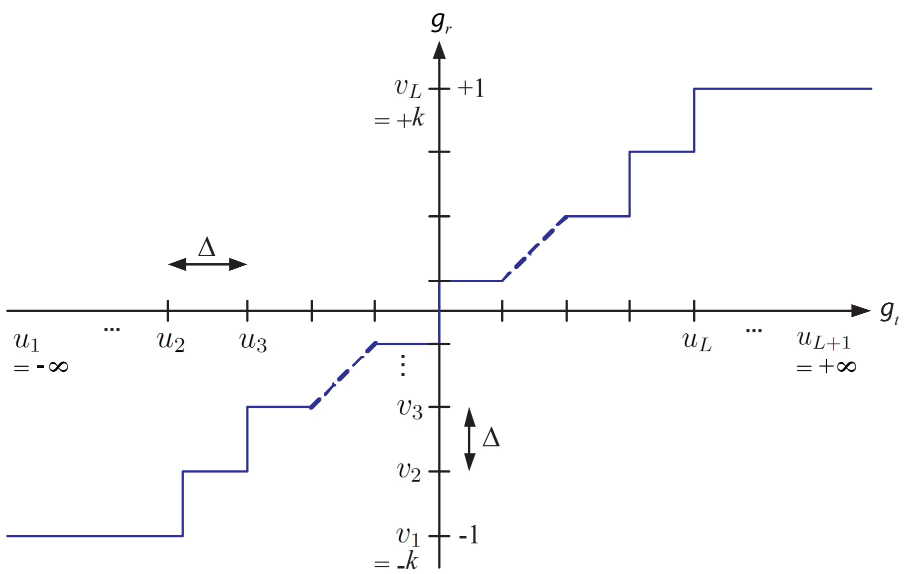


Figure 3.2: Quantizer function.

## 3.3 Characterization of Noise Due to Quantization

### 3.3.1 Noise Distribution

We begin our investigation of the quantized system performance by considering an example system with $b = 2$ quantizer bits and QPSK modulation. Figure 3.3a shows time-domain constellations of the quantizer input $g_t$ and output $g_r$. Note that the quantizer input, output, and error are all real signals, so that the constellations show no imaginary component. The four points of the $g_r$ constellation correspond to the four output levels of the quantizer. The constellation of the quantizer error $g_e = g_t - g_r$ is shown in Figure 3.3b. The corresponding empirical PDF $f^{\mathrm{E}}_{g_e}(g'_e)$ shown in Figure 3.3c has an approximately flat main lobe whose width corresponds to the quantizer step-size $\Delta$ and whose upper and lower tails are caused by quantizer clipping.

Next, we observe in Figure 3.4 the effect of the quantization on the complex frequency-domain signals. Figure 3.4a shows the constellations (including all the subcarriers of all of the OFDM symbols) of the transmitted signal $b_t$, scaled transmitted signal $b_s$, and received signal $b_r$. The received signal may be modeled by

$$b_r = \beta b_t + b_e = b_s + b_e, \tag{3.6}$$

where $b_s$ is a scaled version of the transmitted signal $b_t$, $b_e$ is the quantizer error signal (additive noise), and $\beta$ is the scaling factor chosen to make $b_e$ zero-mean. This signal model is shown graphically in Figure 3.5. The constellation of the quantizer error signal $b_e$ shown in Figure 3.4b is circularly symmetric and zero-mean. The empirical PDF $f^{\mathrm{E}}_{b_{e,\Re}}(b'_{e,\Re})$ of the real part $b_{e,\Re}$ of $b_e$ is shown in Figure 3.4c. Also in Figure 3.4c, we see $f^{\mathrm{E}}_{b_{e,\Re}}(b'_{e,\Re})$ closely matches the Gaussian PDF $f^{\mathrm{G}}_{b_{e,\Re}}(b'_{e,\Re})$ which is zero-mean and has the same variance as $b_{e,\Re}$. We therefore conclude that $b_{e,\Re}$ is closely approximated by a zero-mean Gaussian variable. Likewise, the simulations confirm that the imaginary part $b_{e,\Im}$ of $b_e$ closely approximates a zero-mean Gaussian variable.

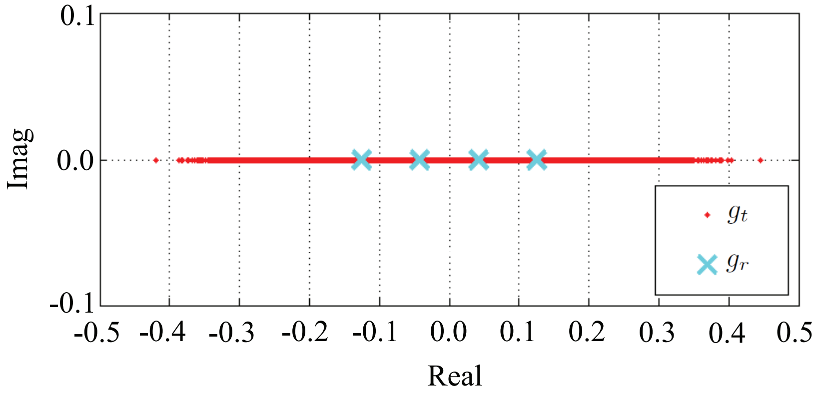


(a) Constellations of quantizer input $g_t$ and output $g_r$.

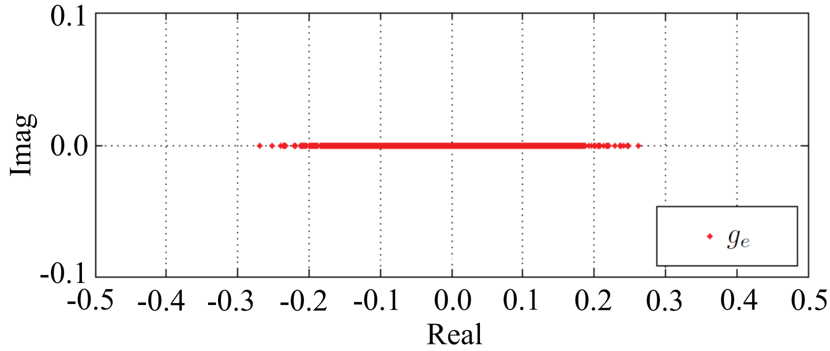


(b) Constellation of quantizer error $g_e$.

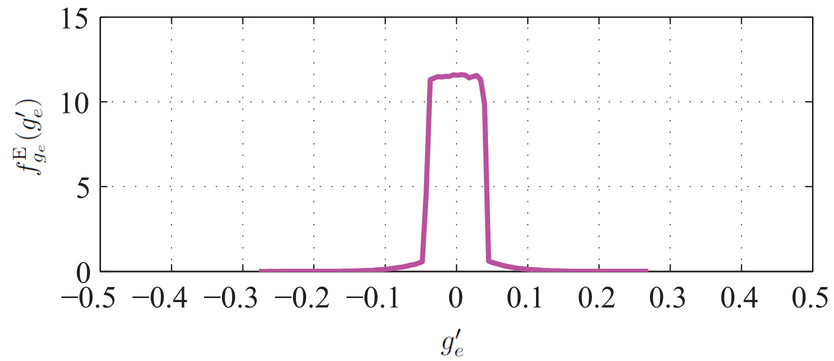


(c) Empirical PDF $f_{g_e}^{\mathrm{E}}(g_e')$ of quantizer error $g_e$.

Figure 3.3: Time-domain real constellations and PDF of quantizer signals, $b = 2$ bits, clipping-factor $\kappa = 1$, QPSK.

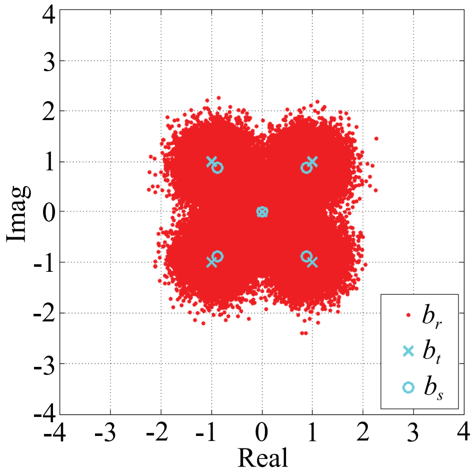


(a) Constellations of transmitted signal $b_t$, scaled transmitted signal $b_s$, and received signal $b_r$.

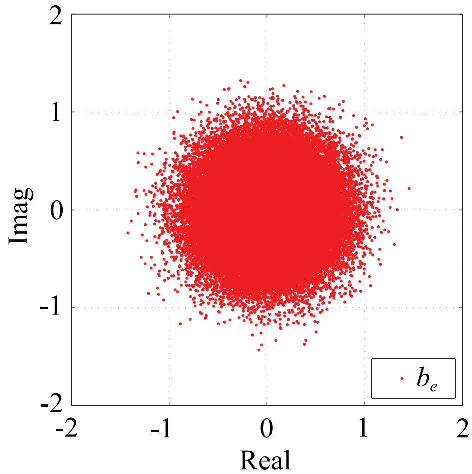


(b) Constellation of error (noise) signal $b_e$.

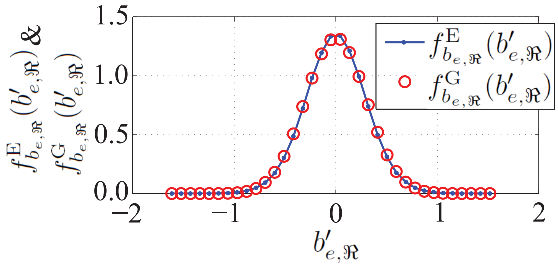


(c) Empirical PDF $f^{\mathrm{E}}_{b_{e,\Re}}(b'_{e,\Re})$ and equivalent Gaussian PDF $f^{\mathrm{G}}_{b_{e,\Re}}(b'_{e,\Re})$ of real part $b_{e,\Re}$ of error $b_e$ between scaled transmitted signal $b_s$ and received signal $b_r$.

Figure 3.4: Frequency-domain signal plots, $b = 2$ bits, clipping-factor $\kappa = 1$, QPSK.

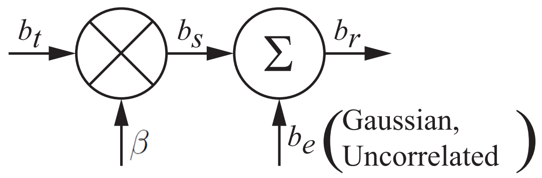


Figure 3.5: Model of signal chain from transmitted signal $b_t$, to received signal $b_r$.

### 3.3.2 Noise Correlation

We now consider the correlation coefficient between $b_s$ and $b_e$ given by

$$\rho_{se} = \frac{\mathrm{E}[b_s b_e^*]}{\sigma_{b_s} \sigma_{b_e}}, \tag{3.7}$$

where E[·] is the expectation operator, $\{\cdot\}^*$ is the complex conjugate, $\sigma_{b_s}$ and $\sigma_{b_e}$ are standard deviations of $b_s$ and $b_e$ respectively. Signal $b_s$ is zero-mean because it is a symmetric, unquantized OFDM signal. Signal $b_e$ is almost zero-mean because the quantizer characteristic is almost symmetric - the notable exception to perfect symmetry being that a value of exactly zero at the quantizer input (possible for OFDM signals) will yield a value of half the quantizer step size $+\Delta/2$ at the quantizer output. Figure 3.6 shows the magnitude $|\rho_{se}|$ of the correlation factor between the scaled transmitted signal $b_s$ and the error signal $b_e$ versus the clipping-factor $\kappa$ for the aforementioned example system. We see that $|\rho_{se}|$ is very small ($< 5 \times 10^{-3}$) over the range of clipping-factors $\kappa$ considered. The variation in $|\rho_{se}|$ for significant clipping when $\kappa < 3$ may be due to an unsufficiently large number of OFDM input symbols being used in the numerical simulation. Nevertheless, as already stated, $|\rho_{se}|$ is very small. For $\kappa > 3$, there is little variation in $|\rho_{se}|$ because of the absence of significant clipping. Our results so far show that, for the example system, the error signal $b_e$ is approximately both Gaussian and uncorrelated with the scaled transmitted signal $b_s$ and we may use the model of the signal chain from transmitted signal $b_t$ to received signal $b_r$ described in (3.6) and shown in Figure 3.5.

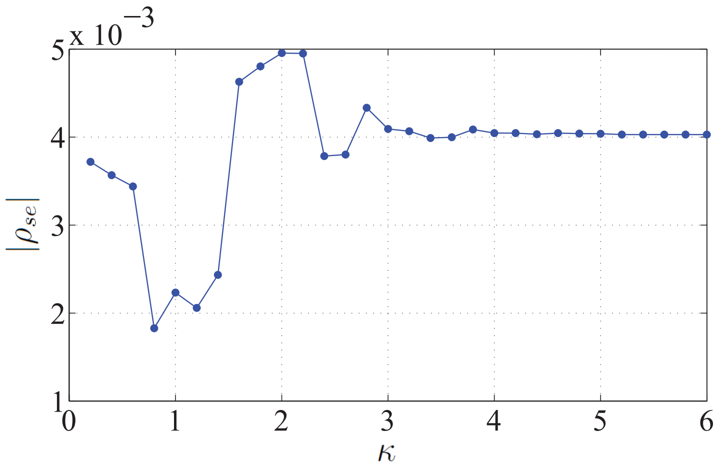


Figure 3.6: Magnitude $|\rho_{se}|$ of correlation factor between scaled transmitted signal $b_s$ and error signal $b_e$ versus clipping-factor $\kappa$, $b = 2$ bits, QPSK.

At this point, we note, as we do on numerous other occasions throughout this thesis, that two variables being uncorrelated is not the same as those same variables being independent. Referring to the model in Figure 3.5, independence (not uncorrelated-ness) is what is required to allow convolution of the PDF of the scaled desired signal $b_s$ with the PDF of the additive quantization noise $b_e$ to obtain the PDF of the received signal $b_r$ from which symbol error rates are determined. Determining the correlation is useful in that if we find any significant correlation between two variables, we can definitely say that the two variables are not independent. On the other hand, if we find zero or very small correlations between the two variables, we cannot say that the variables are independent. As already discussed in §1.1, the confusion of uncorrelated-ness with independence is quite prevalent in the literature and often leads to conclusions which may not be correct. In our immediate case here, we can only determine whether the quantizer noise $b_e$ is independent from the desired signal $b_s$ by observing whether the observed symbol error rate supports that.

The results presented in Figure 3.7 show a reasonably close match between the empirical symbol error rate $\mathrm{P_s^E}$ obtained by Monte Carlo simulation and the symbol error rate $\mathrm{P_s^G}$ calculated assuming a Gaussian noise model and using the measured

SQNR given by

$$\gamma = \frac{S}{N} = \frac{\mathrm{E}[|b_s|^2]}{\mathrm{E}[|b_e|^2]}, \tag{3.8}$$

where $S = \mathrm{E}[|b_s|^2]$ is the signal power and $N = \mathrm{E}[|b_e|^2]$ is the quantization noise power [6]. The results (not shown here) of numerous other simulations in this study confirm that the model of Figure 3.5 is valid for most (but not all) cases of $b \in \{2, \cdots, 12\}$, $\kappa \in (0.2, 6.0)$, and BPSK, QPSK, 16QAM, and 64QAM. Curiously, at a relatively small number of combinations of the number of bits $b$ and the clipping factor $\kappa$, the empirical results diverged from the Gaussian approximation results. This divergence is the motivation for more detailed study into this phenomenom in subsequent chapters of this thesis.

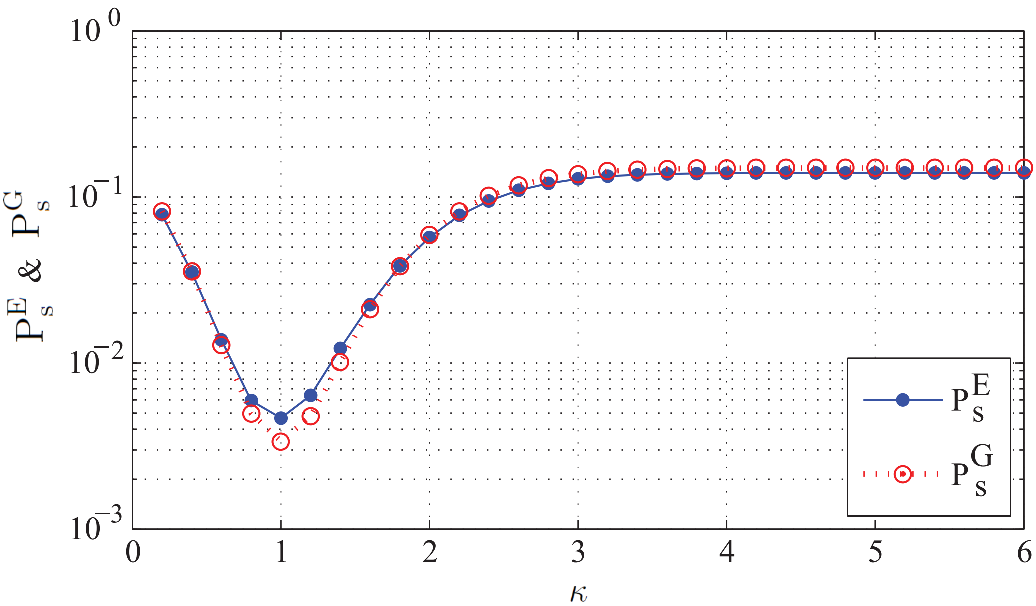


Figure 3.7: Empirical determined symbol error rate $\mathrm{P_s^E}$ (due to quantization noise only) and symbol error rate assuming the quantization noise is Gaussian $\mathrm{P_s^G}$ versus clipping-factor $\kappa$, $b = 2$ bits, QPSK.

## 3.4 Optimization of Quantization Parameters

We now optimize the SQNR $\gamma$ of the received constellation $b_r$ which also optimizes the symbol error rate $\mathrm{P_s}$ and uncoded bit error rate $\mathrm{P_b}$. Figure 3.8 demonstrates the effect of varying the clipping-factor $\kappa$ on signal power $S$, noise power $N$, SNR $\gamma$, and scale factor $\beta$ for $b \in \{2,3\}$ bits. In Figure 3.8a, we see a clear peak in the SNR $\gamma$ at $\kappa = 1$ (coinciding with the minimal symbol error rate shown in Figure 3.7). As expected, when $\kappa \leq 1$, the scaling factor $\beta$ is less than 0 dB (unity) due to significant clipping. This can also be seen as a small reduction in the size of the $b_s$ constellation relative to the $b_t$ constellation in Figure 3.4a. Interestingly, $\beta$ begins increasing beyond 0 dB for $\kappa > 2$ as the quantizer step size $\Delta$ increases and the quantizer "pulls" the time-domain data $g_r$ to larger quantizer output levels. This phenomenom exists for all numbers of quantizer bits $b$; but as $b$ increases, so does the value of $\kappa$ at which it begins to occur. Figure 3.8b verifies that it does not occur for $\kappa < 6$ for $b = 3$ bits.

Figure 3.9 shows the dependence of the SQNR $\gamma$ on the clipping-factor $\kappa$ for BPSK obtained by extensive simulations. Curves for QPSK, 16QAM, and 64QAM constellations are very similar. For each number of quantization bits $b$, an optimal (maximal) SQNR $\gamma^*$ is achieved at a clipping ratio denoted $\kappa^*$. For $\kappa < \kappa^*$, clipping noise dominates $\gamma$ and for $\kappa > \kappa^*$, granular quantization noise dominates $\gamma$.

Figure 3.10 and Figure 3.11 show the dependence of $\kappa^*$ and $\gamma^*$, respectively, on $b$ for various OFDM modulations. The curves for each modulation are very close to each other and $\gamma^*$ (in dB) is almost linearly related to $b$ making for a very simple model for optimal performance.

Figure 3.12 shows what the optimal bit error rate $\mathrm{P}_\mathrm{b}^*$ would be for each of the optimal signal-to-quantization-noise ratios $\gamma^*$ for various modulations if we assume that the quantization noise is additive, uncorrelated, independent Gaussian and no other noise is present.

We note here that the assumption of truly Gaussian quantization noise is unrealistic, since the PDF of such Gaussian noise has probability tails extending to $\pm\infty$. The frequency-domain PDF of real-world quantization noise is limited in extent (i.e. does not extend to $\infty$) as we shall see in later chapters of this thesis. In fact, as the number of bits $b$ increases, the probability of a symbol error at the optimal clipping-factor $\kappa^*$ becomes zero since, the PDF of the quantization error (refer Figure 3.4) does not cross an intersymbol boundary.

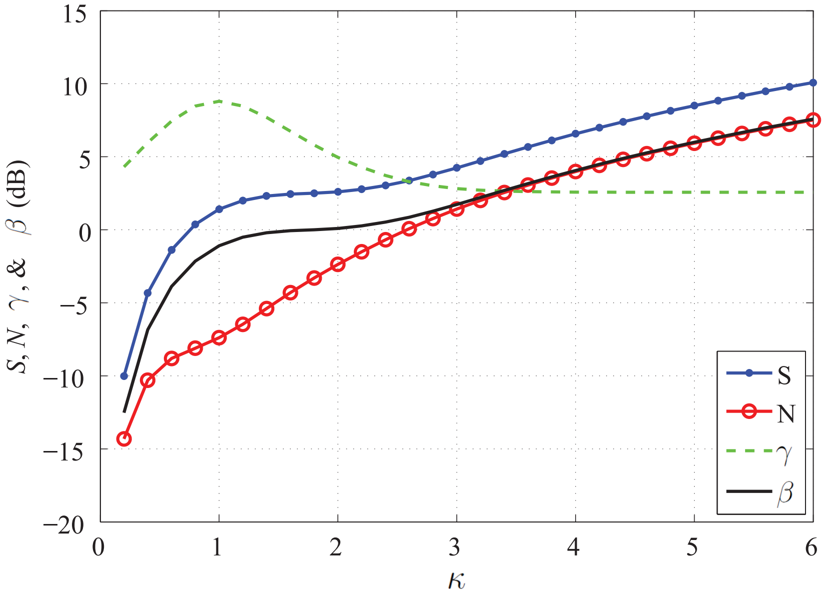


(a) $b = 2$ quantizer bits.

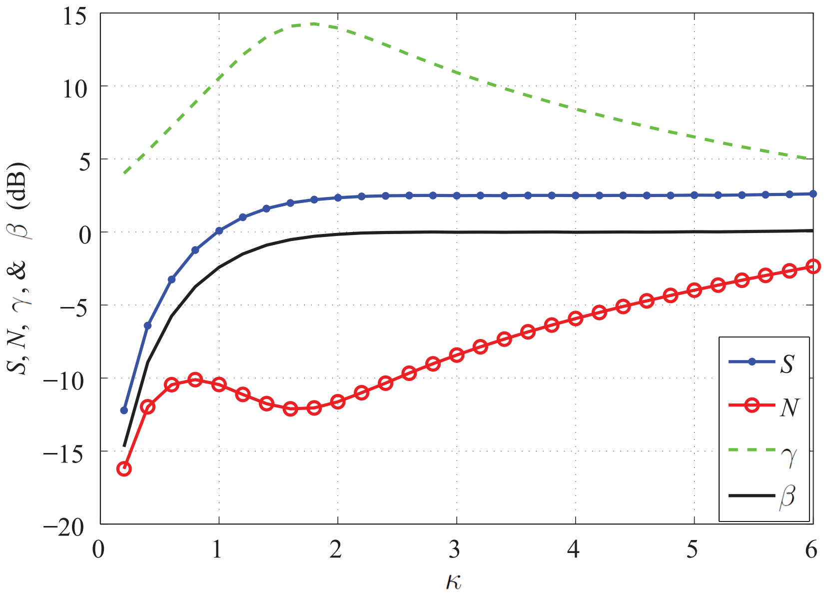


(b) $b = 3$ quantizer bits.

Figure 3.8: Signal power $S$, noise power $N$, SQNR $\gamma$, and scale factor $\beta$ of received signal $b_r$ versus quantizer clipping-factor $\kappa$ for QPSK modulation.

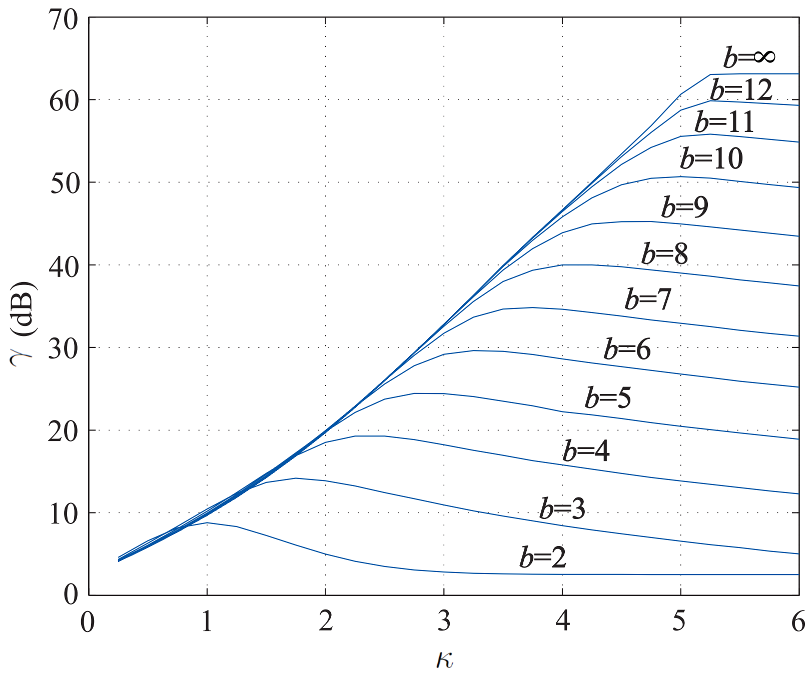


Figure 3.9: SQNR $\gamma$ of received BPSK constellation $b_r$ versus quantizer clipping-factor $\kappa$ for various numbers of quantizer bits $b$.

Nevertheless, Figure 3.12 can be used as an approximate starting-point design tool to establish the minimum number of bits required to achieve a target BER for an high channel SNR (i.e. no channel noise). For example, a target BER of $\mathrm{P_b} < 10^{-4}$ can be achieved at a high channel SNR for BPSK, QPSK, and 16QAM using only $b \geq 4$ quantizer bits, and for 64QAM using only $b \geq 5$ quantizer bits.

## 3.5 Conclusions

The simulations have demonstrated that, in most (but not all) cases, quantization of a real time-domain OFDM signal at a digital intermediate frequency can be modeled as a scaling of the frequency-domain transmitted BPSK or MQAM source symbol constellations plus the addition of uncorrelated noise which is Gaussian. Also, we have provided curves to set the quantizer clipping ratio to obtain the optimal SQNR (and uncoded bit error rate) for numbers of quantizer bits ranging from 2 to 12 and

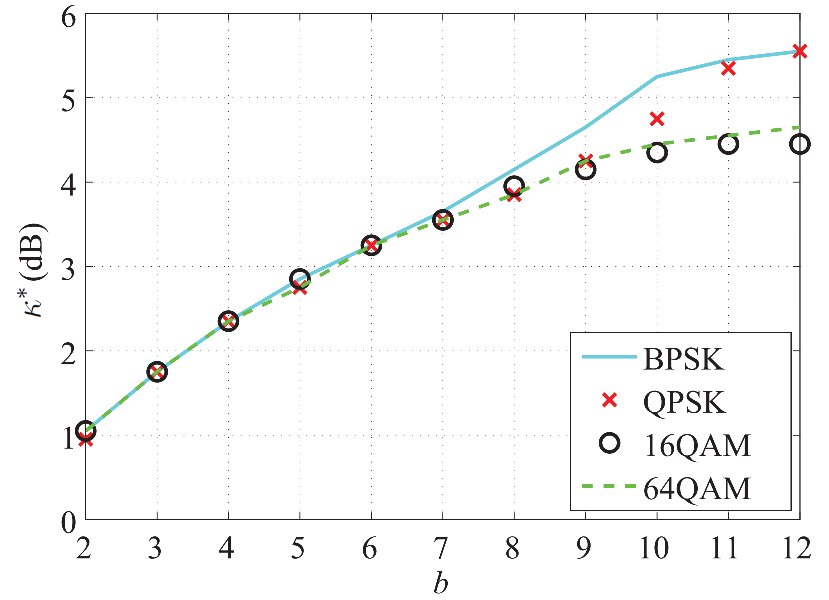


Figure 3.10: Optimal clipping-factor $\kappa^*$ versus number of quantizer bits $b$ for various modulations.

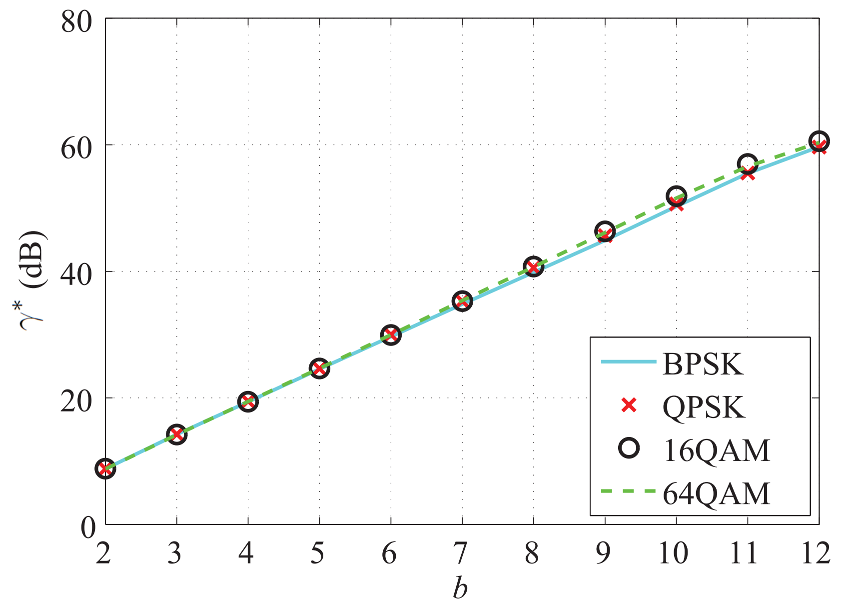


Figure 3.11: Optimal SQNR $\gamma^*$ versus number of quantizer bits $b$ for various modulations.

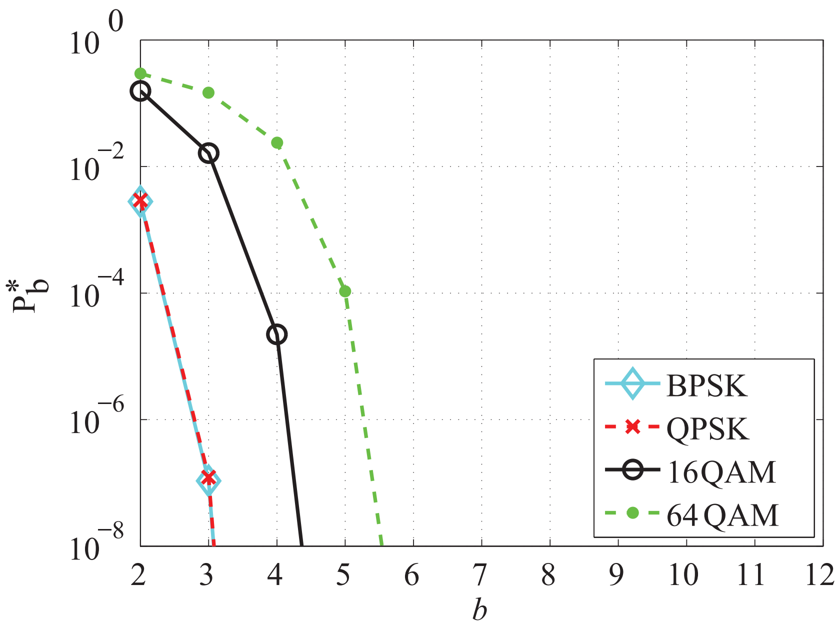


Figure 3.12: Optimal bit error rate $P_b^*$ (assuming an uncorrelated, additive Gaussian quantization noise model with no other noise present) versus number of quantizer bits $b$ for various modulations.

for BPSK, QPSK, 16QAM, and 64QAM OFDM modulations. Another set of curves allows the selection of the number of bits to achieve a target uncoded bit error rate for the above modulations. Those curves show that 6 quantizer bits is sufficient to achieve uncoded bit error rates of $P_b < 10^{-8}$ for the above modulations on an high SNR channel.

During the course of the simulations, at a relatively small number of combinations of the number of bits $b$ and the clipping factor $\kappa$, the empirical results diverged from those expected from the uncorrelated, independent, additive Gaussian noise model of Figure 3.5.

An example of this divergence can be seen in Figure 3.7 for the case of $\kappa = 1, b = 2$ where the uncorrelated, independent, additive Gaussian noise model predicts a symbol error rate of $P_s^G = 3.6 \times 10^{-3}$, compared to the empirically determined value of $P_s^E = 4.8 \times 10^{-3}$. Divergences such as in this example are the motivation for more detailed study into this phenomenon in subsequent chapters of this thesis.

# Chapter 4

# System Description

## 4.1 Full System Model

For the remainder of this thesis, we use a slightly different system model from that in §3 for an OFDM communications system employing a digital IF. The full system model, which includes discrete, continuous, bit, frequency, and time-domains is shown in Figure 4.1. For the sake of limiting the analysis complexity, none of the non-linear characteristics of the analogue system elements (DACs, mixers, amplifiers, etc.) have been included - resulting in a purely linear model. We will now describe step-by-step all of the operations in the transmitter and receiver signal processing chains.

At the transmitter, the transmitter data vector $\boldsymbol{a}$ (usually bits) is mapped through a process of coding, interleaving, and modulation (generally to BPSK, MQAM, MPSK, or MPAM) to a complex vector $\boldsymbol{b}$ of baseband OFDM sub-carriers. These sub-carriers are then upconverted in frequency to a complex vector $\boldsymbol{c}$ of digital IF OFDM sub-carriers by another mapping process, designated "UPCONVERT #1" in Figure 4.1 and described mathematically later in (4.3), consisting of sub-carrier re-indexing and insertion of extra Zero sub-carriers. The vector $\boldsymbol{c}$ of digital IF OFDM sub-carriers is then passed through the diagonal pre-coding matrix $\boldsymbol{X}$ which typically is used to adjust the amplitude and phase of each modulated sub-carrier to pre-compensate the frequency-response of the filters, mixers, amplifiers, etc. in the following transmitter chain so that the transmitted spectrum is the required shape. The resulting signal vector $\boldsymbol{y}$ is then passed though an IDFT to get a complex vector

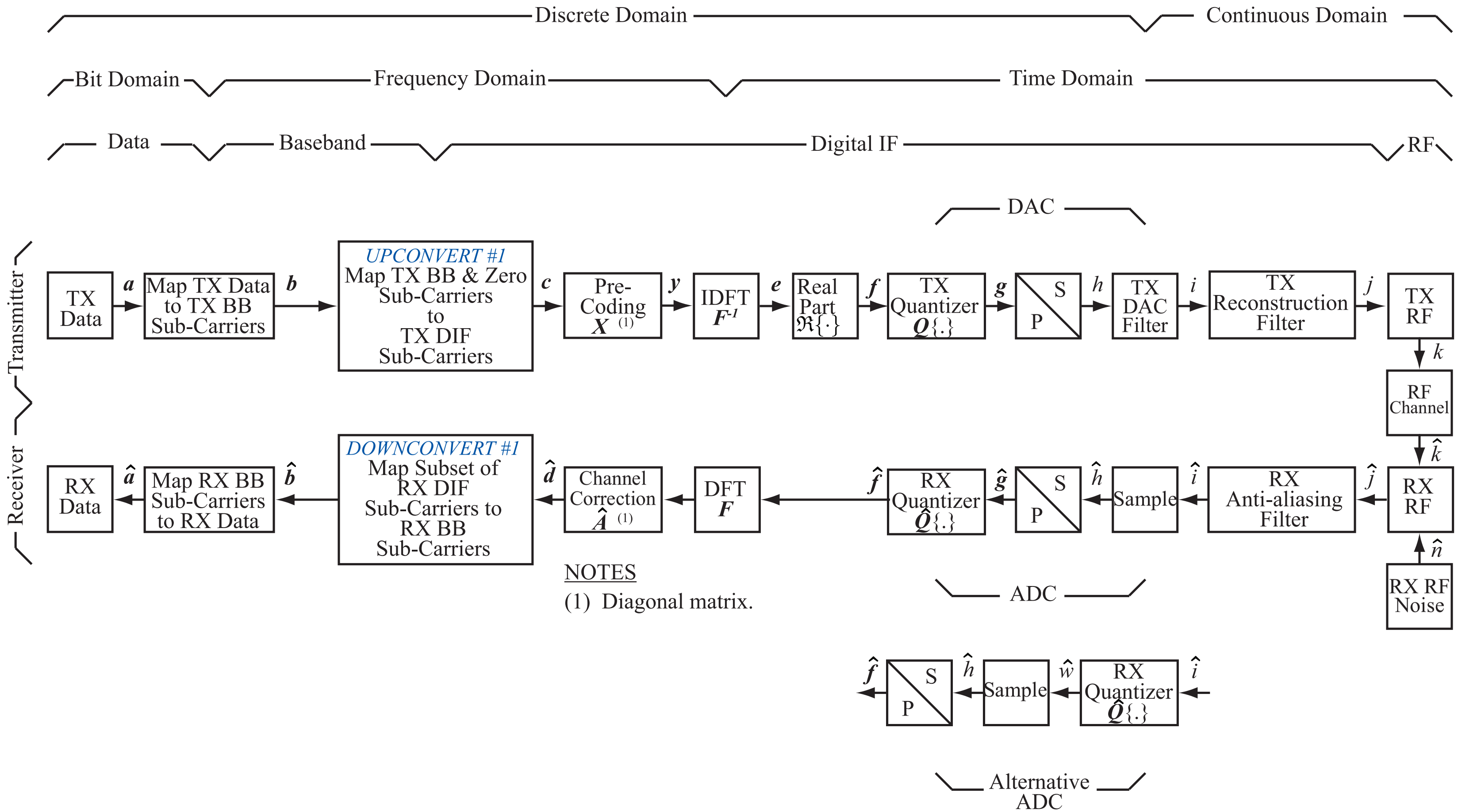


Figure 4.1: Full system model for the OFDM communication system employing digital IF.

$\boldsymbol{e}$ of digital IF time-samples whose real part is taken to get a real vector $\boldsymbol{f}$ of digital IF time-samples. The vector $\boldsymbol{f}$ of digital IF time-samples is then passed from the digital domain to the analogue domain via a DAC (digital to analogue converter) which quantizes it to get vector $\boldsymbol{g}$ which is then time-serialized by a parallel to serial converter to form analogue pulse-stream $h$ which is then shaped by a DAC filter (e.g. sample & hold / NRZ, RTZ, or complimentary interpolation filters) to get the continuous-time analogue IF signal $i$ (which still contains many Nyquist frequency images of the digital IF signal). Signal $i$ is then passed through a so-called "reconstruction filter" (a low-pass or band-pass filter which selects out the Nyquist frequency zone for the required digital IF frequency) to get signal $j$ which is then processed by the transmitter RF front end (IF to RF upconverter, filter, power amplifier, diplexer, antenna, etc.) and sent to air as the transmitter RF signal $k$ which then passes through the air RF channel.

At the receiver, all of the transmitter processes already described above are reversed. At the output of the air RF channel, the real received RF signal $\hat{k}$ is processed by the receiver RF front end (antenna, LNA, AGC, filters, RF to IF downconverter, filters, etc.) where it also has noise $\hat{n}$ added to it (mainly by the receiver LNA) to form the receiver analogue IF signal $\hat{j}$. Signal $\hat{j}$ is then passed through an anti-aliasing filter (to remove unwanted frequency components which could alias to the primary Nyquist zone during sampling) to form the filtered analogue IF signal $\hat{i}$. Signal $\hat{i}$ is then passed into the digital domain via an ADC (analogue to digital converter) which samples it to form the pulse-train signal $\hat{h}$, which is then parallelized to form the vector $\hat{\boldsymbol{g}}$ which is then quantized to form the real vector $\hat{\boldsymbol{f}}$ of digital IF time-samples. Vector $\hat{\boldsymbol{f}}$ is then converted from the time-domain to the frequency-domain via a DFT to form a vector of complex frequency-domain samples each of which is gain and phase adjusted by the diagonal complex channel correction matrix $\hat{\boldsymbol{A}}$ to bring all of the modulated sub-carrier signals in the complex entries of vector $\hat{\boldsymbol{d}}$ to their nominal amplitudes and phases. Complex vector $\hat{\boldsymbol{d}}$ is then downconverted in frequency to a complex vector $\hat{\boldsymbol{b}}$ of baseband OFDM sub-carriers by a process of sub-carrier re-indexing and removal of un-needed sub-carriers in the "DOWNCONVERT #1" block which is described mathematically later in (4.48). Complex vector $\hat{\boldsymbol{b}}$ of baseband OFDM sub-carriers is then mapped through a process of demodulation (usually from BPSK, QAM, or PAM), de-interleaving, and decoding to the receiver data vector $\hat{\boldsymbol{a}}$ which should estimate the transmitter data vector $\boldsymbol{a}$ as closely as possible (although errors may have been introduced by noise added in the transmitter and receiver signal processing chains).

## 4.2 Equivalent Discrete Domain System Model

The equivalent discrete domain model for the system of Figure 4.1 is shown in Figure 4.2 in which all of the continuous time and frequency-domain blocks have been moved into the discrete time and frequency-domains.

The transmitter quantizer has been modeled as a gain factor $\beta$ with the addition of a transmitter quantization noise (or error) vector $\boldsymbol{q}$. The reason for this may be determined by referring back to Figure 3.4b where it can be seen that the effect of the quantizer has been to reduce the size of the constellation and add quantization noise. As discussed in §3.3.1, the gain factor $\beta$ is chosen to make the PDF of the quantizer error zero-mean and uni-modal. Bussgang [7] uses a similar model for the case of Gaussian signals being passed through any general non-linearity (such as a quantizer).

The transmitter DAC filter, transmitter RF front-end, RF channel, receiver RF front-end, and receiver anti-aliasing filter have been modeled by convolution with the channel impulse response vector $\boldsymbol{t}$ and the addition of an RF noise vector $\hat{\boldsymbol{n}}$. Finally, the receiver quantizer has been modeled as a gain factor $\hat{\beta}$ with the addition of a receiver quantization noise (or error) vector $\hat{\boldsymbol{q}}$.

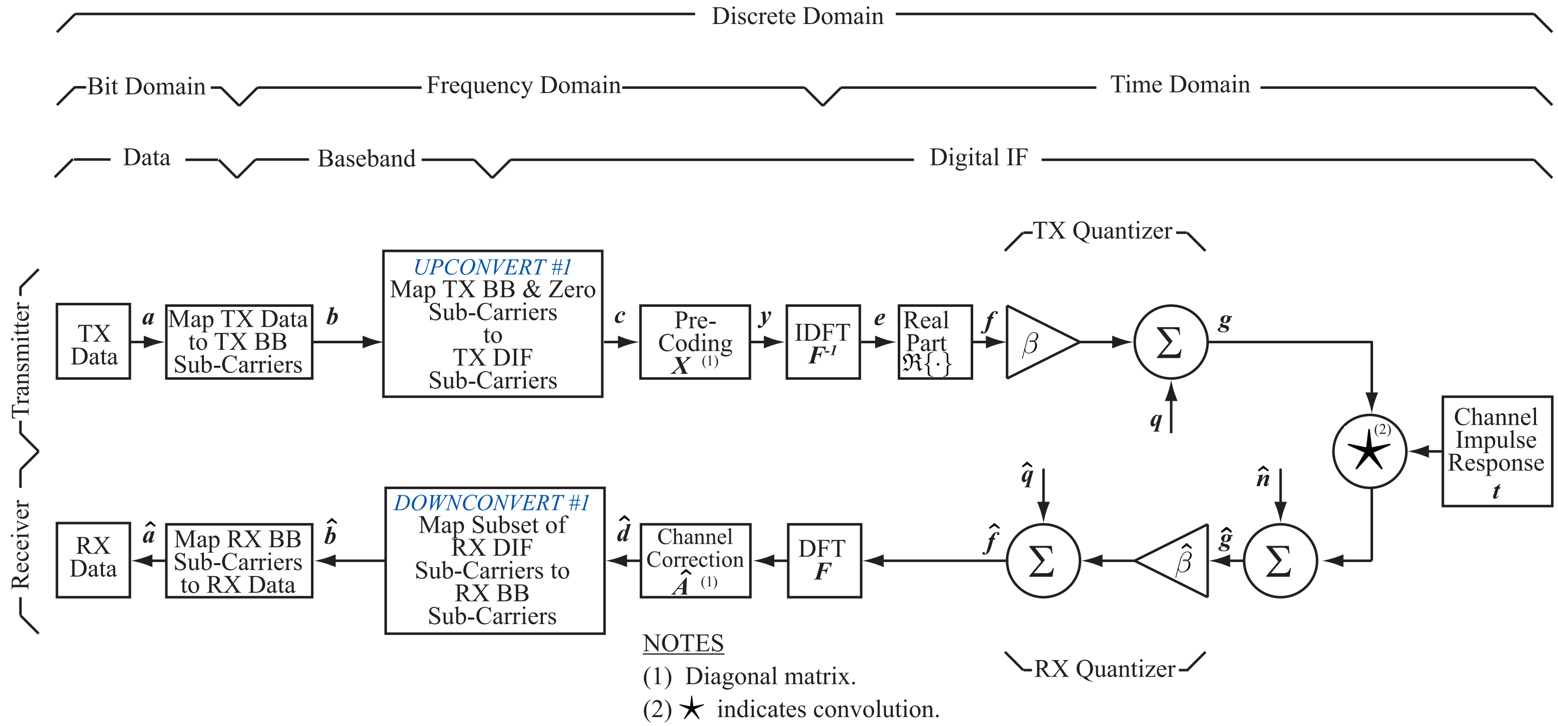


Figure 4.2: Equivalent discrete domain system model for the OFDM communication system employing digital IF.

## 4.3 Equivalent Discrete Frequency-Domain System Model

The equivalent discrete frequency-domain model for the system of Figure 4.2 is shown in Figure 4.4 which has had all time-domain blocks moved into the frequency-domain.

A useful conceptualization of this domain-changing process is achieved by referring to Figure 4.2 and imagining each block after the IDFT being "pulled" through the IDFT from the time-domain into the frequency-domain. Eventually, the IDFT block appears directly adjacent to the DFT block, and the IDFT and DFT blocks then cancel leaving all signals in the frequency-domain as shown in Figure 4.4.

We commence this domain-changing process with the time-domain "Real Part" block of Figure 4.2 being "pulled" through the IDFT block into the frequency-domain and then further "pulled" through the pre-coding block to yield the modified configuration in Figure 4.3. As shown in Figure 4.3, this is achieved by the addition of the conjugate block $\{\cdot\}^*$, the replacement of the pre-coding matrix $\boldsymbol{X}$ with a modified pre-coding matrix $\boldsymbol{P}$, and the replacement of the "UPCONVERT #1" mapping block with the modified "UPCONVERT #2" mapping block whose mapping function is described mathematically later in (4.23).

Next, the gain blocks of Figure 4.3 are "pulled" into the frequency-domain in Figure 4.4 with no change.

Then, the summation blocks of Figure 4.3 are "pulled" into the frequency-domain in Figure 4.4 with the term being summed-in subjected to a DFT operation.

Lastly, the time-domain convolution with the channel impulse-response vector $\boldsymbol{t}$ of Figure 4.3 is "pulled" into the frequency-domain in Figure 4.4 by replacing it by a matrix multiplication with the diagonal channel frequency response matrix $\boldsymbol{H}$.

It should be noted that, although the blocks of Figure 4.4 are all in the frequency-domain, the frequency-domain quantizer noises $\boldsymbol{r}$ and $\hat{\boldsymbol{r}}$ are calculated from the DFTs of the corresponding time-domain quantizer noises $\boldsymbol{q}$ and $\hat{\boldsymbol{q}}$ respectively.

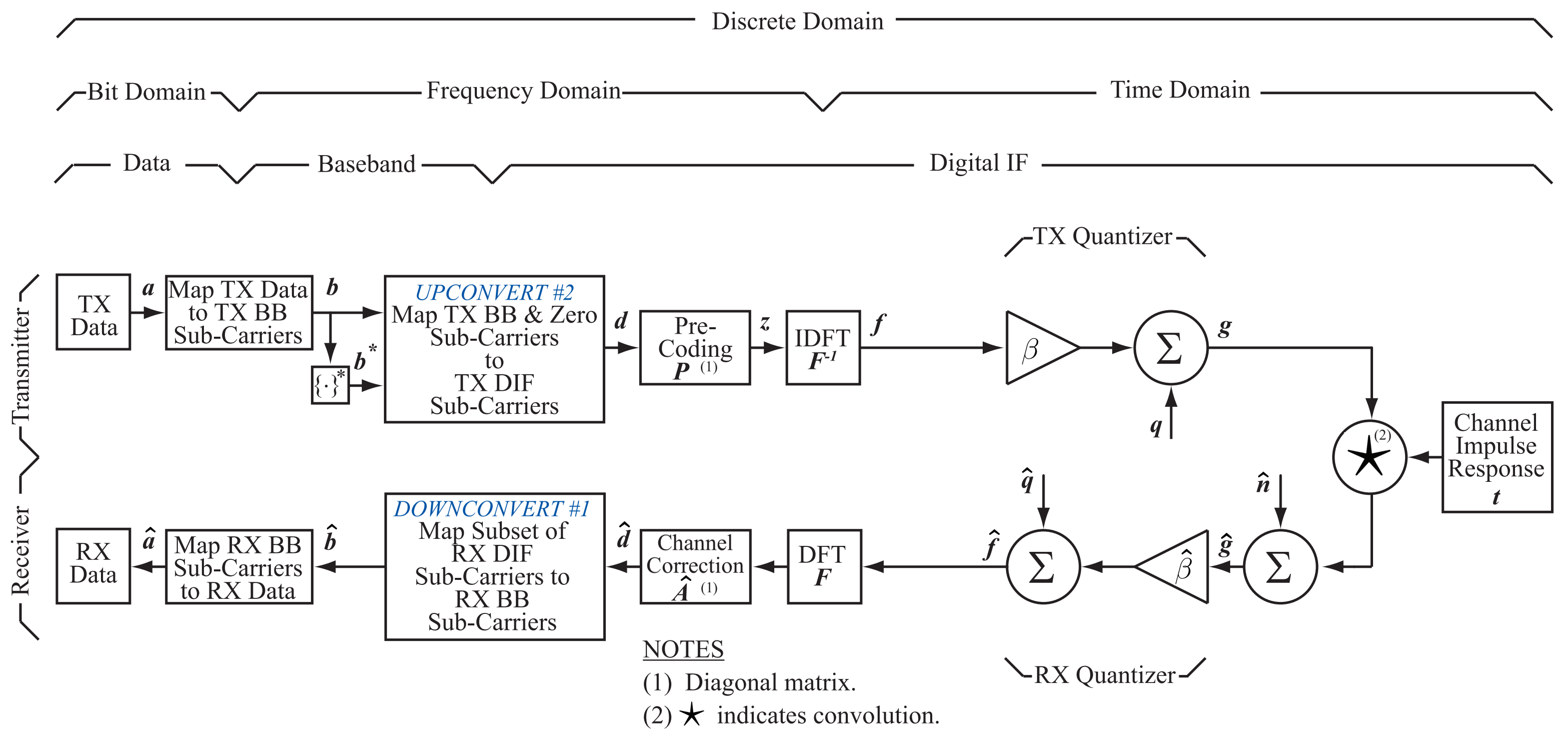


Figure 4.3: Equivalent discrete domain system model, with real-part block incorporated into frequency-domain, for the OFDM communication system employing digital IF.

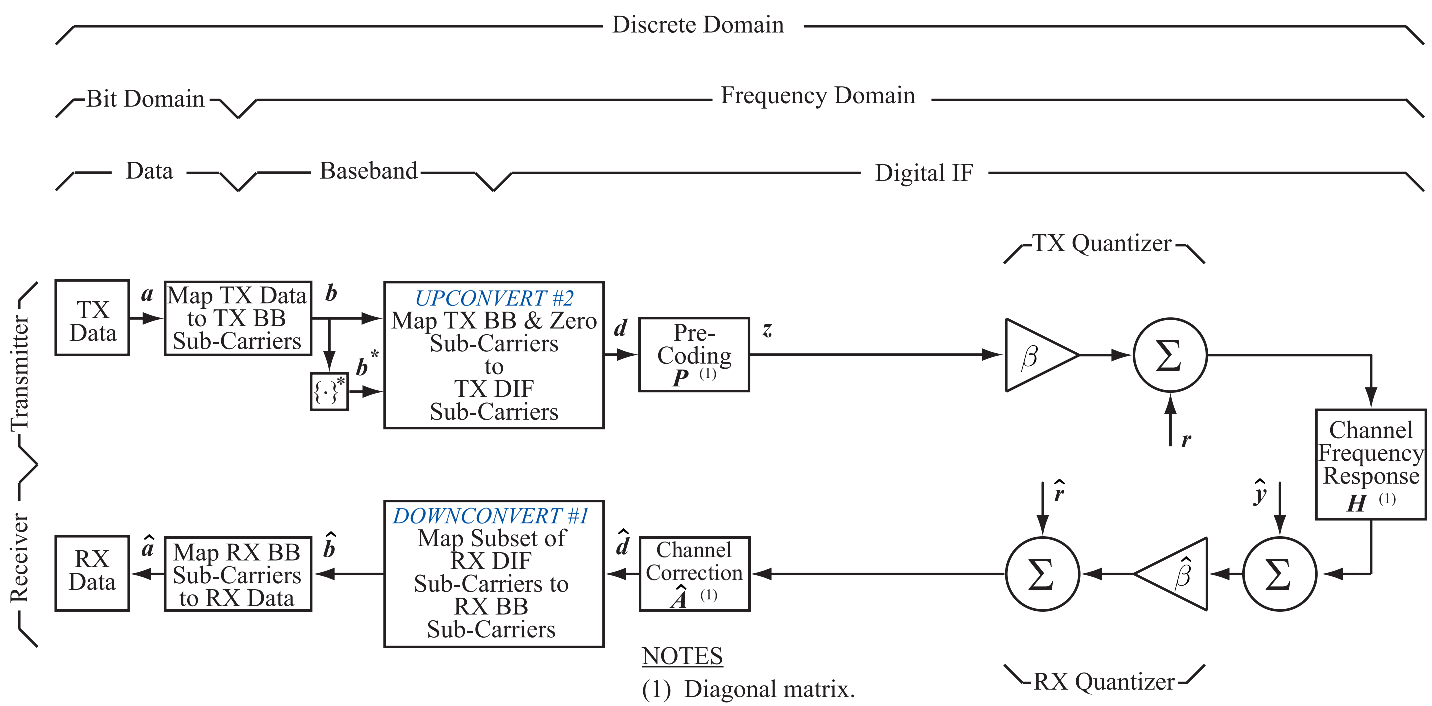


Figure 4.4: Equivalent discrete frequency-domain system model for the OFDM communication system employing digital IF.

## 4.4 Transmitter Frequency Spectra

The frequency spectra (power spectral densities) for various signals on the transmitter side of the OFDM digital IF system of Figure 4.1 are shown in Figure 4.5. In general, $S_x(f)$ indicates power spectral density of a signal $x$ as a function of frequency $f$.

In Figure 4.5(a), we see the transmitter baseband OFDM spectrum as it would appear if the sub-carriers of complex vector $\boldsymbol{b}$ were applied to an $N'$-point IDFT with baseband sample-rate $f_s'$ (although such a baseband $N'$-point IDFT is not actually used since a digital IF is created directly). The spectrum in the primary Nyquist zone $-f_s'/2 \leq f < +f_s'/2$ is replicated at frequency intervals of $f_s'$ out to $f = -\infty$ and $f = +\infty$ . Also, each spectral image is depicted as being asymmetric so that spectral inversions may be clearly seen in later spectral plots.

In the upconvert block, the complex modulated transmitter baseband sub-carriers represented by the entries of vector $\boldsymbol{b}$ are upconverted by a frequency-shift of $+f_s'/2$ simply by modulo-$N'$ adding $N'/2$ to each sub-carrier index, doubling the number of sub-carriers from $N'$ to $N = 2N'$, doubling the IDFT sampling rate from $f_s'$ to $f_s = 2f_s'$, and inserting zero-values into the $n = 0$ sub-carrier the upper-half sub-carriers with indeces $n \in \{N/2, \cdots, N - 1\}$. The doubling of the number of sub-carriers and the sampling rate is known as 'oversampling' and an integer oversampling factor larger than 2 (as we have used here) could also have been used. Simultaneously increasing the IDFT size and the sampling rate by the same oversampling factor keeps the resulting digital IF sub-carrier frequency spacing the same as that at baseband. The $n = 0$ sub-carrier is zeroed since it can't carry imaginary data anyway because of the following real-part operation (see below). The insertion of zero-valued upper-half sub-carriers allows a spectral gap which will be used in the following real-part operation (see below). The spectrum of the resulting complex digital IF signal $\boldsymbol{c}$ is shown in Figure 4.5(b).

The spectrum of frequency-domain signal vector $\boldsymbol{c}$ is then reshaped by the pre-coding matrix $\boldsymbol{X}$ to obtain signal vector $\boldsymbol{y}$ whose spectrum is shown in Figure 4.5(c). The purpose of this pre-coding is to pre-compensate the frequency responses of ana-

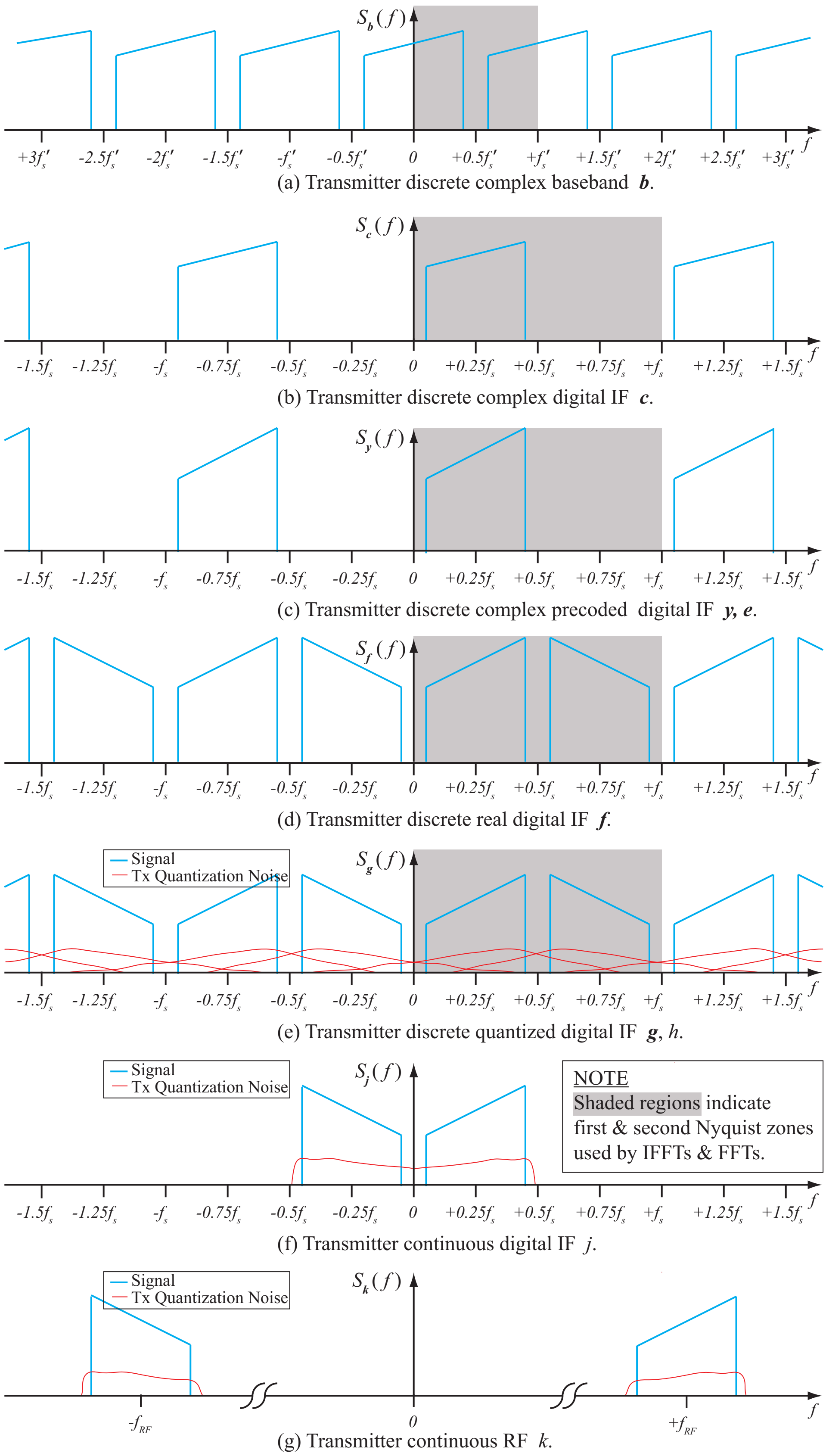


Figure 4.5: Transmitter frequency spectra.

logue elements later in the transmitter chain so as to achieve the desired transmitter RF signal spectrum shape (which is often regulated by a spectrum management authority). Referring back to Figure 4.1, we can see the transmitter chain elements which can affect the spectrum from the transmitter DAC output.

The first element is the transmitter DAC filter which converts the discrete domain sample impulses into continuous domain waveforms. The most common DAC filter type is 'NRZ' (non return to zero) a.k.a 'S & H' (sample and hold) or 'zero-order hold'. In the time domain, it extends the sample impulse to a constant value over the entire sample period. In the frequency domain, its transfer function is a sinc function with a peak at 0 Hz and zeros at positive and negative multiples of the sampling frequency $f_s$. Another common DAC filter type is the 'RTZ' (return to zero). In the time domain, it extends the sample impulse to a constant value over the first half of the sample period, then 'returns to zero' over the second half of the sample period. In the frequency domain, its transfer function is a sinc function with a peak at 0 Hz and zeros at positive and negative multiples of twice the sampling frequency $f_s$. 'Complimentary interpolation' (CI) DAC filters are sometimes used. In the time domain, this filter extends the sample impulse to a constant value over the first half of the sample period, then outputs the 'compliment' (negative) of this value over the second half of the sample period. In the frequency domain, its transfer function has a zero at 0 Hz, a peak at the sampling frequency $f_s$, and zeros at positive and negative multiples of twice the sampling frequency $f_s$.

The transmitter chain element following the transmitter DAC filter is the transmitter reconstruction filter. In the time domain, this filter 'smoothes out' the steps introduced by the transmitter DAC filter. In the frequency domain, this filter eliminates unwanted residual images of the required signal spectrum. Non-idealities in this filter lead to gain and phase perturbations in the passband signal spectrum.

Following the transmitter reconstruction filter is the transmitter transmitter RF block which upconverts the digital IF signal to the RF frequency. This block consists of various amplifiers, mixers, and filters each of which contribute to an overall frequency-domain transfer function for this block.

The frequency-dependent gain and phase deviations of each of the transmitter DAC filter, transmitter reconstruction filter, and transmitter RF block transmitter chain elements are all concatenated to appear at the transmitter RF output. Some or all components of the resulting overall frequency-dependent transfer function slope can be compensated by the pre-coding block which achieves this by introducing an appropriate gain and phase adjustment at each sub-carrier frequency.

Now we return to Figure 4.5. Following the pre-coding block, the transmitter complex pre-coded digital IF signal vector $\boldsymbol{y}$ is then passed from the frequency-domain into the time-domain through an IDFT to obtain the transmitter complex digital IF signal vector $\boldsymbol{e}$.

Next, the real part of the transmitter complex digital IF signal vector $\boldsymbol{e}$ is taken to obtain the transmitter real digital IF signal vector $\boldsymbol{f}$. This real part operation is equivalent to the addition of the complex conjugate of $\boldsymbol{e}$ to $\boldsymbol{e}$ and a halving. In the spectral domain, this results in the addition of spectral mirror-images of all spectral components as shown in Figure 4.5(d) (where the amplitude halving is not shown). Comparing Figure 4.5(c) to Figure 4.5(d), we can see that all of the spectral mirror-images fit into the spectral gaps introduced by the zero-valued sub-carriers previously introduced. This means that none of the spectral information of the complex transmitter digital IF signal vector $\boldsymbol{e}$ has been lost by overwriting with a spectral mirror-image whilst taking it's real part.

Passage of the the real transmitter digital IF signal vector $\boldsymbol{f}$ through the transmitter quantizer produces the real quantized digital IF signal vector $\boldsymbol{g}$ whose spectrum is shown in Figure 4.5(e). The quantization operation has reduced the amplitude of the spectrum as well as added transmitter quantization noise. The amount of amplitude-reduction and quantization noise addition is strongly related to the quantizer function. Just as multiple images and mirror-images of the signal spectrum exist due to the sampling and real-part operations, multiple images and mirror-images of the quantization noise spectrum also exist for the same reasons and will very probably overlap between the various spectral Nyquist regions. This then adds to the in-band noise (which can't be filtered out) which, in turn, reduces the overall signal-to-noise ratio which worsens the information data error performance. It is worth noting that the amount of quantization noise spectral overlap could be reduced compared to our 2-times oversampling case here by increasing the oversampling factor and also the digital IF centre frequency in order to spread the spectral images further apart.

After the transmitter quantized real digital IF signal vector $\boldsymbol{g}$ is serialized and filtered by the TX DAC and TX reconstruction filters to get the continuous time-domain digital IF signal $j$ whose spectrum is shown in Figure 4.5(f). The important thing to note is that the unwanted spectral images have been filtered out. For simplicity, effects of the non-flat frequency responses of the two filters have not been included in the spectral shape since these can easily be counteracted where required by the earlier frequency pre-equalization. Also, the multiple overlapping contributions of the transmitter quantization noise have aggregated.

Finally, after upconversion, filtering, and power amplification by the transmitter RF front end, we obtain transmitter RF signal $k$ whose spectrum is shown in Figure 4.5(g). The centre frequency of the signal and noise spectra has been shifted from the digital IF frequency $f_s/4$ to the RF frequency $f_{\mathrm{RF}}$. Elimination of nearby unwanted signal images in the upconversion process may require sharp filtering which may not be easily achieved. This can be overcome with the use of a single sideband mixer (which eliminates the unwanted sideband image), or with a double conversion topology which upconverts from the digital IF to a second IF frequency before upconverting again to the final RF frequency.

## 4.5 Receiver Frequency Spectra

The frequency spectra (power spectral densities) for various signals on the receiver side of the OFDM digital IF system of Figure 4.1 are shown in Figure 4.6. The spectrum of the receiver continuous RF signal $\hat{k}$ is shown in Figure 4.6(a). For simplicity, any path-loss or frequency-selective fading due to the signal-processing blocks and RF channel has not been shown making the spectrum appear identical to the spectrum of the transmitted RF signal $k$.

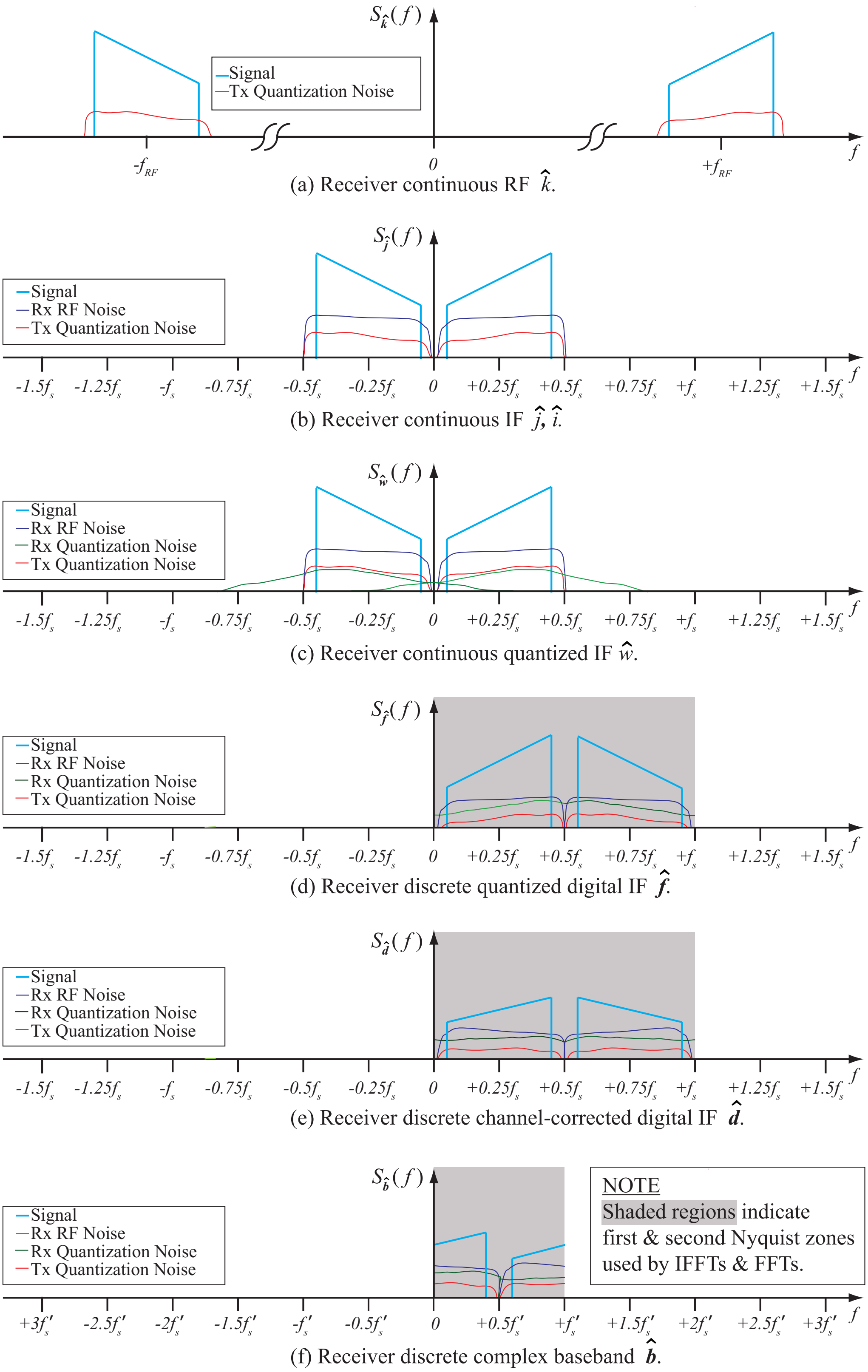


Figure 4.6: Receiver frequency spectra.

The receiver RF signal is then passed through the receiver RF front-end (LNA, AGC, downconverter, filters) to obtain the receiver analogue IF signal $\hat{j}$ which has had the receiver RF front-end noise $\hat{n}$ (mainly from the LNA) added to it as shown in Figure 4.6(b). The actual level of the receiver front-end RF noise relative to the transmitter quantization noise depends upon the channel path-loss.

The receiver continuous digital IF signal $\hat{j}$ is then filtered, sampled, parallelized, and quantized to obtain the receiver quantized digital IF signal vector $\hat{\boldsymbol{f}}$ whose spectrum is shown in Figure 4.6(d) where, we note, the now discrete domain spectrum is shown in the first and second Nyquist zones $0 \leq f \leq f_s$ (depicted in the figure by shading) to match the sub-carrier frequencies used in the IDFTs and DFTs.

We now note that, for the purposes of spectral analysis, and because we are dealing with a linear system, the position of the quantizer can be moved to *before* the sampler as shown in the alternative ADC model of Figure 4.1. Using this model, the quantization process adds the receiver quantization noise $\hat{n}_Q$ whose spectrum exceeds the first Nyquist zone $-f_s/2 \leq f < +f_s/2$ as shown in Figure 4.6(c). This receiver quantization noise spectrum is then aliased between the first and second Nyquist zones as shown in Figure 4.6 (c) and (d) by the sampling process as shown in Figure 4.6(d). We note that a higher sampling rate (not used here) would reduce the effect of the receiver quantization noise spectrum aliasing.

The receiver real quantized digital IF signal vector $\hat{\boldsymbol{f}}$ is then converted from the discrete time-domain to the discrete frequency-domain by passing it through a DFT.

The resulting signal vector is then further passed through the receiver frequency-domain channel-correction matrix $\hat{\boldsymbol{A}}$ which compensates the overall channel frequency-response (including the effect of the transmitter precoder) so as to obtain nominal-sized PAM/QAM symbols on the modulated sub-carriers of the complex digital IF signal vector $\boldsymbol{d}$ whose spectrum is shown in Figure 4.6 (e).

In the following "DOWNCONVERT #1" block, the modulated digital IF sub-carriers of complex digital IF vector $\hat{\boldsymbol{d}}$ are downconverted by a frequency-shift of $-f_s/4$ simply by selecting the half of all sub-carriers with indeces $n \in \{0, \cdots, N/2-1\}$, then modulo-$N/2$ subtracting $N/4$ from each sub-carrier index, and finally halving the DFT sampling rate from $f_s$ to $f_s^{'} = f_s/2$. This is described mathematically later in (4.46). Simultaneously decreasing the DFT size from $N$ to $N^{'} = N/2$ and the sampling rate from $f_s$ to $f_s^{'} = f_s/2$ (i.e. by the same undersampling factor) keeps the resulting baseband sub-carrier frequency spacing the same as that at digital IF. In Figure 4.6(e), we see the receiver baseband OFDM spectrum as it would appear if the sub-carriers of complex vector $\hat{\boldsymbol{b}}$ were applied to an $N^{'}$-point IDFT with baseband sample-rate $f_s^{'}$ (although such a baseband $N^{'}$-point IDFT is not actually used since the baseband sub-carriers are obtained directly from a mapping of the digital IF sub-carriers). The main components of this spectrum are the required signal and three noise components from the transmitter quantizer, the receiver RF, and the receiver quantizer. One of the main goals of this thesis is balancing the relative amplitudes of these three noise sources to achieve a required target information error rate whilst optimally reducing the complexity of the transmitter and receiver quantizers.

## 4.6 Mathematical Analysis

Having already described the OFDM digital IF system under consideration in terms of its block diagrams in §4.1 and §4.3, and its spectra in §4.4, we now proceed to a mathematical description of the equivalent digital domain model depicted in Figure 4.2.

We commence by defining all of the symbols which will be used as follows.

As previously described, in the transmitter upconvert block, the sub-carriers corresponding to each entry of the transmitter complex baseband signal vector

$$\boldsymbol{b} = [b_0, \cdots, b_{N'-1}]^{\mathrm{T}}, \tag{4.1}$$

(with $b_{N'/2}$ unused and set to zero) are upconverted by a frequency-shift of $+f_s^{'}/2$ simply by modulo-$N'$ adding $N'/2$ to each sub-carrier index, doubling the number of sub-carriers from $N^{'}$ to $N = 2N^{'}$, doubling the IDFT sampling rate from $f_s^{'}$ to $f_s = 2f_s^{'}$, and inserting zero-values into the upper-half sub-carriers with indeces

$k \in \{N/2, \cdots, N-1\}$ so that the resulting transmitter complex frequency-domain digital IF signal vector is given by

$$\boldsymbol{c} = [c_0, \cdots, c_{N-1}]^{\mathrm{T}}, \tag{4.2}$$

where

$$c_k = \begin{cases} 0 & , k = 0 \\ b_{(k-N/4) \bmod N/2} & , k \in \{1, \cdots, N/2-1\} \\ 0 & , k = N/2 \\ 0 & , k \in \{N/2+1, \cdots, N-1\}. \end{cases} \tag{4.3}$$

Note that the mapping function described by (4.3) corresponds to the "UPCONVERT #1" blocks in Figs. 4.1 and 4.2.

The transmitter complex frequency-domain digital IF signal vector $\boldsymbol{c}$ is then passed through the diagonal transmitter pre-coding matrix

$$\boldsymbol{X} = \mathbf{DIAG}(\boldsymbol{x}), \tag{4.4}$$

where

$$\boldsymbol{x} = [x_0, \cdots, x_{N-1}]^{\mathrm{T}}, \tag{4.5}$$

to yield the transmitter complex pre-coded digital IF signal vector

$$\boldsymbol{y} = [y_0, \cdots, y_{N-1}]^{\mathrm{T}} = \boldsymbol{X}\boldsymbol{c}, \tag{4.6}$$

whose entries have had their amplitudes and phases modified from those of $\boldsymbol{c}$ so as to pre-compensate the frequency response of the transmitter analogue front end.

The transmitter complex pre-coded frequency-domain digital IF signal vector $\boldsymbol{y}$ is then passed through a normalized IDFT matrix

$$\boldsymbol{F}^{-1} = ([\boldsymbol{F}^{-1}]_{n,k}), \quad n, k \in \{0, \cdots, N-1\}, \tag{4.7}$$

where the $(n,k)^{\text{th}}$ entry of $\boldsymbol{F}^{-1}$ is

$$[\boldsymbol{F}^{-1}]_{n,k} = \frac{1}{\sqrt{N}} \cdot e^{j\frac{2\pi kn}{N}}, \tag{4.8}$$

to produce the transmitter complex time-domain digital IF signal vector

$$\boldsymbol{e} = [e_0, \cdots, e_{N-1}]^{\mathrm{T}} = \boldsymbol{F}^{-1}\boldsymbol{y}. \tag{4.9}$$

We will now proceed to obtain a frequency-domain equivalent model of the time-domain "real-part" block of Figure 4.1.

The real part of the transmitter complex time-domain digital IF signal vector $\boldsymbol{e}$ is taken to obtain the transmitter real time-domain digital IF vector

$$\begin{aligned}
\boldsymbol{f} &= [f_0, \cdots, f_{N-1}]^{\mathrm{T}} \\
&= \Re\{\boldsymbol{e}\} \\
&= \Re\{\boldsymbol{F}^{-1}\boldsymbol{y}\} \\
&= 1/2 \cdot (\boldsymbol{F}^{-1}\boldsymbol{y} + (\boldsymbol{F}^{-1}\boldsymbol{y})^*) \\
&= 1/2 \cdot \big(\boldsymbol{F}^{-1}\boldsymbol{y} + (\boldsymbol{F}^{-1})^*\boldsymbol{y}^*\big) \\
&= 1/2 \cdot \big(\boldsymbol{F}^{-1}\boldsymbol{y} + (\boldsymbol{F}^*)^*\boldsymbol{y}^*\big) \\
&= 1/2 \cdot \big(\boldsymbol{F}^{-1}\boldsymbol{y} + \boldsymbol{F}\boldsymbol{y}^*\big) \\
&= 1/2 \cdot \big(\boldsymbol{F}^{-1}\boldsymbol{y} + \boldsymbol{F}^{-1}\boldsymbol{F}^2\boldsymbol{y}^*\big) \\
&= \boldsymbol{F}^{-1}\big(1/2 \cdot \big(\boldsymbol{y} + \boldsymbol{F}^2\boldsymbol{y}^*\big)\big) \\
&= \boldsymbol{F}^{-1}\boldsymbol{z},
\end{aligned} \tag{4.10}$$

where

$$\boldsymbol{z} = [z_0, \cdots, z_{N-1}]^{\mathrm{T}} \quad \triangleq \quad 1/2 \cdot \big(\boldsymbol{y} + \boldsymbol{F}^2\boldsymbol{y}^*\big), \tag{4.11}$$

and the normalized DFT matrix is given by

$$\boldsymbol{F} = ([\boldsymbol{F}]_{k,n}), \quad k, n \in \{0, \cdots, N-1\}, \tag{4.12}$$

where the $(k,n)^{\text{th}}$ entry of $\boldsymbol{F}$ is

$$[\boldsymbol{F}]_{k,n} = \frac{1}{\sqrt{N}} \cdot e^{-j\frac{2\pi kn}{N}}. \tag{4.13}$$

As an aside, a notable result of (4.10) is that an equivalent frequency-domain model of the time-domain real-part of IDFT operation is given by

$$\Re\{\boldsymbol{F}^{-1}\boldsymbol{y}\} = \boldsymbol{F}^{-1}\boldsymbol{z}, \tag{4.14}$$

where $\boldsymbol{z}$ is already defined in 4.11.

Next, in order to expand the expression in the right-hand side of (4.11), we commence by evaluating $\boldsymbol{F}^2$. Using the expression for the $(k,n)^{\text{th}}$ entry of the normalized DFT matrix $\boldsymbol{F}$ given in (4.13), we determine that the $(l,m)^{\text{th}}$ entry of $\boldsymbol{F}^2$ is

$$\begin{aligned}
[\boldsymbol{F}^2]_{l,m} &= [\boldsymbol{F}\boldsymbol{F}]_{l,m} \\
&= \sum_{p=0}^{N-1} \boldsymbol{F}_{l,p}[\boldsymbol{F}]_{p,m} \\
&= \frac{1}{N}\sum_{p=0}^{N-1} e^{-j\frac{2\pi lp}{N}} \cdot e^{-j\frac{2\pi pm}{N}} \\
&= \frac{1}{N}\sum_{p=0}^{N-1} e^{-j\frac{2\pi(l+m)p}{N}} \\
&= \begin{cases} 1, & m = l = 0 \\ 1, & m = N-l \\ 0, & \text{otherwise.} \end{cases}
\end{aligned} \tag{4.15}$$

Using (4.15) and (4.11), we now evaluate the $k^{\text{th}}$ entry of $\boldsymbol{z}$ as

$$z_k = [1/2 \cdot (\boldsymbol{y} + \boldsymbol{F}^2\boldsymbol{y}^*)]_k = 1/2 \cdot (y_k + y^*_{N-k}). \tag{4.16}$$

Now, from Figure 4.1, we see that

$$\boldsymbol{y} = \boldsymbol{X}\boldsymbol{c}. \tag{4.17}$$

So, remembering from (4.4) and (4.25) that the precoding matrix $\boldsymbol{X}$ is diagonal with its $k^{\text{th}}$ diagonal element designated $x_k$ , we obtain the $k^{\text{th}}$ entry of $\boldsymbol{y}$ as

$$y_k = x_k \cdot c_k. \tag{4.18}$$

Substituting (4.18) into (4.16), we then obtain

$$z_k = 1/2 \cdot (x_k \cdot c_k + x^*_{\substack{(N-k)\\ \text{mod N}}} \cdot c^*_{\substack{(N-k)\\ \text{mod N}}}). \tag{4.19}$$

$c_k$ is already given in (4.3) and some minor manipulation of (4.3) also yields

$$c^*_{\substack{(N-k)\\ \text{mod N}}} = \begin{cases} 0 & , k = 0 \\ 0 & , k \in \{1, \cdots, N/2-1\} \\ 0 & , k = N/2 \\ b^*_{\substack{(3N/4-k)\\ \text{mod N/2}}} & , k \in \{N/2+1, \cdots, N-1\}. \end{cases} \tag{4.20}$$

So, substituting (4.3) and (4.20) into (4.19), we re-evaluate the $k^{\text{th}}$ entry of $\boldsymbol{z}$ in (4.14), this time in terms of the entries $b_k$ of the transmitter baseband complex source symbol vector $\boldsymbol{b}$, as

$$z_k = \begin{cases} 0 & , k = 0 \\ \frac{1}{2} x_k \cdot b_{\substack{(k-N/4)\\ \text{mod N/2}}} & , k \in \{1, \cdots, N/2-1\} \\ 0 & , k = N/2 \\ \frac{1}{2} x^*_{N-k} \cdot b^*_{\substack{(3N/4-k)\\ \text{mod N/2}}} & , k \in \{N/2+1, \cdots, N-1\}. \end{cases} \tag{4.21}$$

We now wish to further decompose the mapping function from $\boldsymbol{b}$ to $\boldsymbol{z}$ described in (4.21) above, into a mapping function from $\boldsymbol{b}$ to a signal vector $\boldsymbol{d}$ followed by a multiplication by a modified diagonal pre-coding matrix $\boldsymbol{P}$ to obtain $\boldsymbol{z}$, so that

$$\boldsymbol{z} = \boldsymbol{P}\boldsymbol{d}, \tag{4.22}$$

as shown in the system frequency-domain model of Figure 4.4. This is achieved with the "UPCONVERT #2" mapping function

$$d_k = \begin{cases} 0 & , k = 0 \\ b_{\substack{(k-N/4) \\ \text{mod N/2}}} & , k \in \{1, \cdots, N/2-1\} \\ 0 & , k = N/2 \\ b^*_{\substack{(3N/4-k) \\ \text{mod N/2}}} & , k \in \{N/2+1, \cdots, N-1\}, \end{cases} \tag{4.23}$$

and the modified pre-coding matrix

$$\boldsymbol{P} = \mathbf{DIAG}(\boldsymbol{p}), \tag{4.24}$$

where

$$\boldsymbol{p} = [p_0, \cdots, p_{N-1}]^{\mathrm{T}}, \tag{4.25}$$

and

$$p_k = \begin{cases} 0 & , k = 0 \\ \frac{1}{2} \cdot x_k & , k \in \{1, \cdots, N/2-1\} \\ 0 & , k = N/2 \\ \frac{1}{2} \cdot x^*_{N-k} & , k \in \{N/2+1, \cdots, N-1\}. \end{cases} \tag{4.26}$$

Our goal of obtaining a frequency-domain equivalent model of the time-domain "real-part" block of Figure 4.1 has now been achieved by the modified "UPCONVERT #2" mapping function block described by (4.23) and the modified pre-coding matrix $\boldsymbol{P}$ described by (4.24), (4.25), and (4.26). These blocks are shown in the frequency-domain system model of Figure 4.4.

Next, referring again to Figure 4.2, the transmitter real time-domain digital IF vector $\boldsymbol{f}$ is further passed through the transmitter front-end blocks, the channel, and the receiver front-end blocks to eventually obtain the receiver real time-domain digital IF vector

$$\hat{\boldsymbol{f}} = \hat{\beta}(\boldsymbol{t} \star (\beta \boldsymbol{f} + \boldsymbol{q}) + \hat{\boldsymbol{n}}) + \hat{\boldsymbol{q}}, \tag{4.27}$$

where

| | | | |
|---|---|---|---|
| $\hat{\beta}$ | | is the receiver quantizer gain factor, | |
| $\boldsymbol{t} =$ | $[t_0, \cdots, t_{N-1}]^{\mathrm{T}}$ | is the channel time-domain impulse response vector, | (4.28) |
| $\star$ | | indicates the vector-convolution operation, | |
| $\beta$ | | is the transmitter quantizer gain factor, | |
| $\boldsymbol{f} =$ | $[f_0, \cdots, f_{N-1}]^{\mathrm{T}}$ | is the transmitter real time-domain digital IF vector, | (4.29) |
| $\boldsymbol{q} =$ | $[q_0, \cdots, q_{N-1}]^{\mathrm{T}}$ | is the transmitter time-domain quantizer noise vector, | (4.30) |
| $\hat{\boldsymbol{n}} =$ | $[\hat{n}_0, \cdots, \hat{n}_{N-1}]^{\mathrm{T}}$ | is the receiver time-domain RF noise vector, and | (4.31) |
| $\hat{\boldsymbol{q}} =$ | $[\hat{q}_0, \cdots, \hat{q}_{N-1}]^{\mathrm{T}}$ | is the receiver time-domain quantizer noise vector. | (4.32) |

The receiver real time-domain digital IF vector $\hat{\boldsymbol{f}}$ is then converted from the time-domain to the frequency-domain via a DFT, and then further amplitude and phase-corrected by the diagonal channel correction matrix

$$\hat{\boldsymbol{A}} = \mathbf{DIAG}(\hat{\boldsymbol{a}}), \tag{4.33}$$

where

$$\hat{\boldsymbol{a}} = [\hat{a}_0, \cdots, \hat{a}_{N-1}]^{\mathrm{T}}, \tag{4.34}$$

to obtain the receiver complex frequency-domain digital IF signal vector

$$\begin{aligned}
\hat{\boldsymbol{d}} &= [\hat{d}_0, \cdots, \hat{d}_{N-1}]^{\mathrm{T}} \\
&= \hat{\boldsymbol{A}}\boldsymbol{F}\hat{\boldsymbol{f}} \\
&= \hat{\boldsymbol{A}}\boldsymbol{F}\left(\hat{\beta}(\boldsymbol{t} \star (\beta\boldsymbol{f} + \boldsymbol{q}) + \hat{\boldsymbol{n}}) + \hat{\boldsymbol{q}}\right) \\
&= \hat{\boldsymbol{A}}(\boldsymbol{F}\hat{\beta}\boldsymbol{t} \star \beta\boldsymbol{f} + \boldsymbol{F}\hat{\beta}\boldsymbol{t} \star \boldsymbol{q} + \boldsymbol{F}\hat{\beta}\hat{\boldsymbol{n}} + \boldsymbol{F}\hat{\boldsymbol{q}}) \\
&= \hat{\boldsymbol{A}}(\beta\hat{\beta}\boldsymbol{F}(\boldsymbol{t} \star \boldsymbol{f}) + \hat{\beta}\boldsymbol{F}(\boldsymbol{t} \star \boldsymbol{q}) + \hat{\beta}\boldsymbol{F}\hat{\boldsymbol{n}} + \boldsymbol{F}\hat{\boldsymbol{q}}).
\end{aligned} \tag{4.35}$$

Now, applying the general result that the DFT of the vector-convolution of two vectors is equal to the Schur-product (a.k.a. "Hadamard product" or "entry-wise product") of the DFTs of the two vectors, we obtain

$$\begin{aligned}
\boldsymbol{F}(\boldsymbol{t} \star \boldsymbol{f}) &= (\boldsymbol{F}\boldsymbol{t}) \circ (\boldsymbol{F}\boldsymbol{f}) \\
&= \boldsymbol{h} \circ (\boldsymbol{F}\boldsymbol{f}) \\
&= \boldsymbol{H}\boldsymbol{F}\boldsymbol{f},
\end{aligned} \tag{4.36}$$

and, similarly,

$$\boldsymbol{F}(\boldsymbol{t} \star \boldsymbol{q}) = \boldsymbol{H}\boldsymbol{F}\boldsymbol{q}, \tag{4.37}$$

where $\circ$ is the Schur-product operator,

$$\boldsymbol{h} = [h_0, \cdots, h_{N-1}]^{\mathrm{T}} \quad \triangleq \quad \boldsymbol{F}\boldsymbol{t} \tag{4.38}$$

is the the channel frequency response vector, and

$$\boldsymbol{H} \triangleq \mathbf{DIAG}(\boldsymbol{h}) \tag{4.39}$$

is the diagonal channel frequency response matrix which is used so as to replace the Schur-product operator in the second line of (4.36) with the standard matrix product operator in the third line of (4.36).

We now define the transmitter frequency-domain quantization noise

$$\boldsymbol{R} = [r_0, \cdots, r_{N-1}]^{\mathrm{T}} \quad \triangleq \quad \boldsymbol{F}\boldsymbol{q}, \tag{4.40}$$

and the receiver frequency-domain quantization noise

$$\hat{\boldsymbol{r}} = [\hat{r}_0, \cdots, \hat{r}_{N-1}]^{\mathrm{T}} \quad \triangleq \quad \boldsymbol{F}\hat{\boldsymbol{q}}. \tag{4.41}$$

Substituting (4.22), (4.36), (4.37), (4.40), and (4.41) into (4.35), we then obtain the expression for the receiver frequency-domain digital IF vector as

$$\begin{aligned} \hat{\boldsymbol{d}} &= \hat{\boldsymbol{A}}(\beta\hat{\beta}\boldsymbol{H}\boldsymbol{P}\boldsymbol{d} + \hat{\beta}\boldsymbol{H}\boldsymbol{R} + \hat{\beta}\hat{\boldsymbol{y}} + \hat{\boldsymbol{r}}) \\ &= \hat{\boldsymbol{A}}(\hat{\beta}(\boldsymbol{H}(\beta\boldsymbol{P}\boldsymbol{d} + \boldsymbol{R}) + \hat{\boldsymbol{y}}) + \hat{\boldsymbol{r}}), \end{aligned} \tag{4.42}$$

from which is derived a substantial portion of the equivalent discrete frequency-domain system model of Figure 4.4.

Now, from (4.42) and (4.23), remembering that matrices $\hat{\boldsymbol{A}}$ and $\boldsymbol{H}$ are both diagonal, we obtain the $k^{\text{th}}$ entry of the received digital IF vector $\hat{\boldsymbol{d}}$ as

$$\hat{d}_k = \begin{cases} \hat{a}_k\hat{\beta}h_k r_k + \hat{a}_k\hat{\beta}\hat{y}_k + \hat{a}_k\hat{r}_k & , k = 0 \\ \frac{1}{2}\hat{a}_k\beta\hat{\beta}h_k p_k \cdot b_{\substack{(k-N/4) \\ \text{mod N/2}}} + \hat{a}_k\hat{\beta}h_k r_k + \hat{a}_k\hat{\beta}\hat{y}_k + \hat{a}_k\hat{r}_k & , k \in \{1, \cdots, N/2-1\} \\ \hat{a}_k\hat{\beta}h_k r_k + \hat{a}_k\hat{\beta}\hat{y}_k + \hat{a}_k\hat{r}_k & , k = N/2 \\ \frac{1}{2}\hat{a}_k\beta\hat{\beta}h_k p_k \cdot b^*_{\substack{(3N/4-k) \\ \text{mod N/2}}} + \hat{a}_k\hat{\beta}h_k r_k + \hat{a}_k\hat{\beta}\hat{y}_k + \hat{a}_k\hat{r}_k & , k \in \{N/2+1, \cdots, N-1\}. \end{cases} \tag{4.43}$$

The function of $k^{\text{th}}$ channel correction entry $\hat{a}_k$ is to return the $k^{\text{th}}$ sub-carrier $\hat{d}_k$ of the receiver digital IF vector $\hat{\boldsymbol{d}}$ back to the original amplitude and phase of the $k^{\text{th}}$ sub-carrier $d_k$ of the transmitter digital IF vector $\boldsymbol{d}$ as formulated in (4.23). So, comparing the first terms of the second and forth lines of (4.23) with those of (4.43), we assign the $k^{\text{th}}$ channel correction entry as

$$\hat{a}_k = \frac{1}{\beta\hat{\beta}h_k p_k}, \tag{4.44}$$

which, when substituted into (4.43), yields the $k^{\text{th}}$ entry of the receiver digital IF vector $\hat{\boldsymbol{d}}$ as

$$\hat{d}_k = \begin{cases} \frac{1}{\beta p_k} \cdot r_k + \frac{1}{\beta h_k p_k} \cdot \hat{y}_k + \frac{1}{\beta\hat{\beta}h_k p_k} \cdot \hat{r}_k & , k = 0 \\ \frac{1}{2} \cdot b_{\substack{(k-N/4) \\ \text{mod N/2}}} + \frac{1}{\beta p_k} \cdot r_k + \frac{1}{\beta h_k p_k} \cdot \hat{y}_k + \frac{1}{\beta\hat{\beta}h_k p_k} \cdot \hat{r}_k & , k \in \{1, \cdots, N/2-1\} \\ \frac{1}{\beta p_k} \cdot r_k + \frac{1}{\beta h_k p_k} \cdot \hat{y}_k + \frac{1}{\beta\hat{\beta}h_k p_k} \cdot \hat{r}_k & , k = N/2 \\ \frac{1}{2} \cdot b^*_{\substack{(3N/4-k) \\ \text{mod N/2}}} + \frac{1}{\beta p_k} \cdot r_k + \frac{1}{\beta h_k p_k} \cdot \hat{y}_k + \frac{1}{\beta\hat{\beta}h_k p_k} \cdot \hat{r}_k & , k \in \{N/2+1, \cdots, N-1\}. \end{cases} \tag{4.45}$$

As previously described, the receiver complex frequency-domain digital IF signal vector $\hat{\boldsymbol{d}}$ is next downconverted in frequency to a complex vector $\hat{\boldsymbol{b}}$ of receiver frequency-domain baseband OFDM modulated sub-carriers by a process of sub-carrier re-indexing and removal of un-needed sub-carriers. This is implemented in the "DOWN-CONVERT #1" mapping function:

$$\hat{b}_k = 2\hat{d}_{\substack{(k+N/4) \\ \text{mod N/2}}} \quad , k \in \{0, \cdots, N/4-1, N/4+1, \cdots, N/2-1\}, \tag{4.46}$$

which is also depicted as a processing block in the system models shown Figs. 4.1, 4.2, and 4.4. We note that the $N/4^{\text{th}}$ sub-carrier $\hat{b}_{N/4}$ of the receiver baseband vector

$$\hat{\boldsymbol{b}} = [\hat{b}_0, \cdots, \hat{b}_{N-1}]^{\text{T}} \tag{4.47}$$

is not used since it corresponds to the $0^{\text{th}}$ sub-carrier $\hat{d}_0$ of the receiver channel-corrected digital IF vector $\hat{\boldsymbol{d}}$ which is not used because the real part operation (refer to Figure 4.1) causes the imaginary part of $d_0$ (and therefore $\hat{d}_0$) to be permanently lost.

Now, substituting (4.46) into 4.45, we obtain the expression for all of the entries (modulated sub-carriers) of the recovered receiver baseband vector $\hat{\boldsymbol{b}}$ as

$$\begin{aligned}
\hat{b}_k = & \quad b_k \\
& + \frac{2}{\beta p_{\substack{(k+N/4) \\ \text{mod N/2}}}} \cdot r_{\substack{(k+N/4) \\ \text{mod N/2}}} \\
& + \frac{2}{\beta h_{\substack{(k+N/4) \\ \text{mod N/2}}} \cdot p_{\substack{(k+N/4) \\ \text{mod N/2}}}} \cdot \hat{y}_{\substack{(k+N/4) \\ \text{mod N/2}}} \\
& + \frac{2}{\beta \hat{\beta} h_{\substack{(k+N/4) \\ \text{mod N/2}}} \cdot p_{\substack{(k+N/4) \\ \text{mod N/2}}}} \cdot \hat{r}_{\substack{(k+N/4) \\ \text{mod N/2}}} \\
& , k \in \{0, \cdots, N/4-1, N/4+1, \cdots N/2-1\}. \qquad (4.48)
\end{aligned}$$

Examining (4.48), we see that the $k^{\text{th}}$ received sub-carrier $\hat{b}_k$ consists of the required $k^{\text{th}}$ originally transmitted sub-carrier $b_k$ (1'st term) plus a transmitter quantization noise component (2'nd term) plus an receiver RF noise component (3'rd term) plus a receiver quantization noise component ($4^{\text{th}}$ term). This can also be seen graphically in the frequency spectrum in Figure 4.6(f).

At this stage, we have achieved our goal of obtaining, at the receiver, estimates of the originally transmitted BPSK or QAM symbols (albeit with some noise corruption).

## 4.7 Conclusions

In this chapter, we commenced by defining the system under consideration in the discrete and continuous domains which included the frequency and time domains. We then transformed all of the continuous-domain system blocks into the discrete domain to produce an all-discrete-domain model which contained both frequency-domain and time-domain elements. Next, the time-domain elements were transformed into the frequency-domain to obtain an all-frequency-domain discrete-domain model. This model was then further elucidated by graphical depictions of the transmitter frequency spectra and receiver frequency spectra showing the effects of each of the elements of the system model. Finally, a rigorous mathematical model was developed which fully describes the effects of all of the system blocks including, in particular, the transmitter and receiver quantization. This system model is used in subsequent chapters for the analysis of quantization effects in OFDM systems.

# Chapter 5

# Numerical Approaches

## 5.1 OFDM Types and Results Schedule

In §5 and §6, various different OFDM types are used to generate results for the various methods described and used in this thesis. These OFDM types are enumerated in Table 5.1 where

$N'$ is the total number of baseband sub-carriers,

$N'_{SZ}$ is the number of baseband Zero sub-carriers,

$N'_{SP}$ is the number of baseband Pilot sub-carriers,

$N'_{SP}$ is the number of baseband Data sub-carriers,

$M_{SP}$ is the modulation type for all Pilot sub-carriers , and

$M_{SD}$ is the modulation type for all Data sub-carriers.

Referring to Table 5.1, we see that OFDM types with relatively small numbers of sub-carriers are used for the 'Exhaustive' method (which has a size limitation) whereas OFDM types with relatively large numbers of sub-carriers are used for the other methods. Also, the results of the other methods are all independently verified by the 'Exhaustive' method - thus proving the validity of these methods.

| OFDM Type | $N'$ | $N'_{SZ}$ | $N'_{SP}$ | $N'_{SD}$ | $M_{SP}$ | $M_{SD}$ | 'Exhaustive' Method | 'Monte Carlo' Method | 'Matrix Transformation' Method | 'Convolution' Method | Standard | Description |
|---|---|---|---|---|---|---|---|---|---|---|---|---|
| 1.2 | 8 | 0 | 0 | 8 | - | 2 | ✓ | | | | - | Small number of sub-carriers, no zeros, no pilots, BPSK data |
| 1.4 | 8 | 0 | 0 | 8 | - | 2 | ✓ | | | | - | Small number of sub-carriers, no zeros, no pilots, QPSK data |
| 2.2 | 8 | 2 | 3 | 3 | 2 | 2 | ✓ | | ✓ | | - | Small number of sub-carriers, some zeros, BPSK pilots, BPSK data |
| 2.4 | 8 | 2 | 3 | 3 | 2 | 4 | ✓ | | ✓ | | - | Small number of sub-carriers, some zeros, BPSK pilots, QPSK data |
| 3.2 | 16 | 0 | 0 | 16 | - | 2 | ✓ | ✓ | | ✓ | - | Medium number of sub-carriers, no zeros, no pilots, BPSK data |
| 4.2 | 16 | 2 | 4 | 10 | 2 | 2 | ✓ | | | ✓ | - | Medium number of sub-carriers, some zeros, BPSK pilots, BPSK data |
| 5.2 | 64 | 12 | 4 | 48 | 2 | 2 | | ✓ | ✓ | ✓ | IEEE 802.11a | Large number of sub-carriers, some zeros, BPSK pilots, BPSK data |
| 5.4 | 64 | 12 | 4 | 48 | 2 | 4 | | ✓ | ✓ | ✓ | IEEE 802.11a | Large number of sub-carriers, some zeros, BPSK pilots, QPSK data |
| 5.16 | 64 | 12 | 4 | 48 | 2 | 16 | | ✓ | ✓ | ✓ | IEEE 802.11a | Large number of sub-carriers, some zeros, BPSK pilots, 16QAM data |
| 5.64 | 64 | 12 | 4 | 48 | 2 | 64 | | ✓ | ✓ | ✓ | IEEE 802.11a | Large number of sub-carriers, some zeros, BPSK pilots, 64QAM data |

Table 5.1: OFDM types - descriptions and results schedule.

## 5.2 Some Symbol Definitions

Before proceeding further, we introduce definitions of key symbols which shall be used in this and subsequent chapters.

$\mathcal{A}_{\mathrm{SZ}} = \{0\}$ is the alphabet of the Zero sub-carrier symbols,

$\mathcal{A}_{\mathrm{SP}}$ is the complex alphabet of the Pilot sub-carrier symbols,

$\mathcal{A}_{\mathrm{SD}}$ is the complex alphabet of the Data sub-carrier symbols,

$\mathcal{K}_{\mathrm{SZ}}$ is the set of sub-carrier indeces corresponding to the Zero digital IF sub-carrier symbols,

$\mathcal{K}_{\mathrm{SP}}$ is the set of sub-carrier indeces corresponding to the Pilot digital IF sub-carrier symbols,

$\mathcal{K}_{\mathrm{SD}}$ is the set of sub-carrier indeces corresponding to the Data digital IF sub-carrier symbols,

$\mathcal{A}_{\mathrm{BPSK}} \equiv \mathcal{A}_{\mathrm{2QAM}} \equiv \mathcal{A}_{\mathrm{2PSK}}$ is the unity average energy per symbol BPSK symbol alphabet,

$\mathcal{A}_{\mathrm{MQAM}} \triangleq \{\mathcal{A}_{\mathrm{2QAM}}, \mathcal{A}_{\mathrm{4QAM}}, \mathcal{A}_{\mathrm{16QAM}}, \cdots\}$ is the alphabet of all unity average energy per symbol MQAM symbol alphabets,

$\mathcal{A}_{\mathrm{MPSK}} \triangleq \{\mathcal{A}_{\mathrm{2PSK}}, \mathcal{A}_{\mathrm{8PSK}}, \mathcal{A}_{\mathrm{16QAM}}, \cdots\}$ is the alphabet of all unity average energy per symbol MPSK symbol alphabets,

$\mathcal{K}_{\mathrm{S}} \triangleq \mathcal{K}_{\mathrm{SZ}} \cup \mathcal{K}_{\mathrm{SP}} \cup \mathcal{K}_{\mathrm{SD}}$ is the set of all sub-carrier indeces,

$\mathcal{K}_{\mathrm{SPD}} \triangleq \mathcal{K}_{\mathrm{SP}} \cup \mathcal{K}_{\mathrm{SD}}$ is the set of digital IF sub-carrier indeces corresponding to the Pilot and Data symbols combined,

$N_{\mathrm{SZ}} \triangleq |\mathcal{K}_{\mathrm{SZ}}|$ is the number of Zero digital IF sub-carrier symbols,

$N_{\mathrm{SP}} \triangleq |\mathcal{K}_{\mathrm{SP}}|$ is the number of Pilot digital IF sub-carrier symbols,

$N_{\mathrm{SD}} \triangleq |\mathcal{K}_{\mathrm{SD}}|$ is the number of Data digital IF sub-carrier symbols,

$N_{\mathrm{SPD}} \triangleq |\mathcal{K}_{\mathrm{SPD}}|$ is the number of Pilot and Data digital IF sub-carrier symbols combined, and

$N \triangleq N_{\mathrm{SZ}} + N_{\mathrm{SP}} + N_{\mathrm{SD}}$ is the total number of digital IF sub-carriers.

## 5.3 The Exact 'Exhaustive' Method

We start by employing a simple method to obtain exact PDFs of various signals in the transmitter chain of the equivalent digital domain model depicted in Figure 4.2. This method is described as 'exhaustive' since it requires the use of *all* possible alphabet letters (or distinct instances) of the IDFT input vector $\boldsymbol{d}$ and 'exact' since it produces exact results (PDFs, CDFs, etc). We note here that the number of alphabet letters can become impossibly large for practical OFDM systems.

### 5.3.1 'Exhaustive' PDF of the OFDM Frequency-Sample Vector at the IDFT Input

We begin with the complex IDFT input vector $\boldsymbol{d} = [d_0, d_1, \cdots d_{N-1}]$. Each entry $d_k$ of $\boldsymbol{d}$ is drawn from an alphabet of possible symbols $\mathcal{A}_{d_k}$ (e.g. ZERO, BPSK, QPSK, etc), so that

$$d_k \in \mathcal{A}_{d_k}, k \in \mathbb{Z}_n. \tag{5.1}$$

The alphabet of the complex IDFT input vector $\boldsymbol{d}$ is therefore the Cartesian product of the alphabets for each $d_k$ and is given by

$$\mathcal{A}_{\boldsymbol{d}} = \mathcal{A}_{d_0} \times \mathcal{A}_{d_1} \times \cdots \times \mathcal{A}_{d_{N-1}}. \tag{5.2}$$

We note that $\boldsymbol{d}$ can take on many different distinct letters (instances) so that

$$\boldsymbol{d} \in \mathcal{A}_{\boldsymbol{d}} = \{\boldsymbol{d}_j\}_{j=1}^{N_{\boldsymbol{d}}}, \tag{5.3}$$

where $\mathcal{A}_{\boldsymbol{d}}$ is the alphabet of all possible letters (or distinct instances) of $\boldsymbol{d}$, $\boldsymbol{d}_j$ is the $j^{\text{th}}$ letter of $\mathcal{A}_{\boldsymbol{d}}$, and $N_{\boldsymbol{d}}$ is the total number of letters in $\mathcal{A}_{\boldsymbol{d}}$. We also note that the number of occurrences of each $\boldsymbol{d}_j$ is one; so that the probability of occurrence of each $\boldsymbol{d}_j$ is

$$\mathrm{P}_{\boldsymbol{d}_j} = \frac{1}{N_{\boldsymbol{d}}}, \forall j. \tag{5.4}$$

The multi-dimensional complex PDF of the IDFT complex input vector $\boldsymbol{d}$ is then given by

$$
\begin{aligned}
f_{\boldsymbol{d}}(\boldsymbol{d}') &= \sum_{\boldsymbol{d}\in\mathcal{A}_{\boldsymbol{d}}} \mathrm{P}_{\boldsymbol{d}}\, \delta\left(\boldsymbol{d}' - \boldsymbol{d}\right) \\
&= \sum_{j=1}^{N_{\boldsymbol{d}}} \mathrm{P}_{\boldsymbol{d}_j} \delta\left(\boldsymbol{d}' - \boldsymbol{d}_j\right) \\
&= \frac{1}{N_{\boldsymbol{d}}} \sum_{j=1}^{N_{\boldsymbol{d}}} \delta\left(\boldsymbol{d}' - \boldsymbol{d}_j\right), \qquad (5.5)
\end{aligned}
$$

where $\delta(\cdot)$ is the Dirac delta operator.

### 5.3.2 'Exhaustive' PDF of the IDFT Output Time-Sample Vector

The IDFT complex output vector $\boldsymbol{e}$ is given by

$$
\boldsymbol{e} = \boldsymbol{F}^{-1}\boldsymbol{d}, \qquad (5.6)
$$

where $\boldsymbol{F}^{-1}$ is the normalized IDFT matrix; and the particular instance of $\boldsymbol{e}$ which corresponds to the $j^{\text{th}}$ letter $\boldsymbol{d}_j$ of the IDFT input vector alphabet $\mathcal{A}_{\boldsymbol{d}}$ is therefore given by

$$
\boldsymbol{e}_j = \boldsymbol{F}^{-1}\boldsymbol{d}_j. \qquad (5.7)
$$

The multi-dimensional complex PDF of $\boldsymbol{e}$ is therefore

$$
f_{\boldsymbol{e}}(\boldsymbol{e}') = \frac{1}{N_{\boldsymbol{d}}} \sum_{j=1}^{N_{\boldsymbol{d}}} \delta\left(\boldsymbol{e}' - \boldsymbol{e}_j\right). \qquad (5.8)
$$

### 5.3.3 'Exhaustive' PDF of the IDFT Output Time-Sample Real-Part Vector

The real part $\boldsymbol{f}$ of the IDFT output vector $\boldsymbol{e}$ is given by

$$\boldsymbol{f} = \Re\{\boldsymbol{e}\} = \Re\left\{\boldsymbol{F}^{-1}\boldsymbol{d}\right\}, \tag{5.9}$$

and the particular instance of $\boldsymbol{f}$ which corresponds to the $j^{\text{th}}$ letter $\boldsymbol{d}_j$ of the IDFT input vector alphabet $\mathcal{A}_{\boldsymbol{d}}$ is therefore given by

$$\boldsymbol{f}_j = \Re\left\{\boldsymbol{F}^{-1}\boldsymbol{d}_j\right\}. \tag{5.10}$$

The multi-dimensional real PDF of $\boldsymbol{f}$ is therefore

$$f_{\boldsymbol{f}}(\boldsymbol{f}') = \frac{1}{N_{\boldsymbol{d}}} \sum_{j=1}^{N_{\boldsymbol{d}}} \delta\left(\boldsymbol{f}' - \boldsymbol{f}_j\right). \tag{5.11}$$

### 5.3.4 'Exhaustive' Covariance Matrix of the IDFT Output Time-Sample Real-Part Vector

In general, the covariance matrix (also known as the variance matrix or the dispersion matrix) of a single random vector is a matrix whose $(l, m)^{\text{th}}$ entry is the covariance between the $l^{\text{th}}$ and $m^{\text{th}}$ entries of the random vector.

The $(l, m)^{\text{th}}$ entry of the covariance matrix $\mathbf{COV}(\boldsymbol{f})$ of the IDFT output time-sample real-part vector $\boldsymbol{f}$ is therefore given by

$$\begin{aligned} [\mathbf{COV}(\boldsymbol{f})]_{l,m} &= \operatorname{cov}(f_l, f_m) \\ &= \mathrm{E}\Big[\big(f_l - \mathrm{E}[f_l]\big) \cdot \big(f_m - \mathrm{E}[f_m]\big)\Big] \\ &= \mathrm{E}[f_l f_m] - \mathrm{E}[f_l]\mathrm{E}[f_m]. \end{aligned} \tag{5.12}$$

The matrix formulation of the covariance matrix of the IDFT output time-sample real-part vector $\boldsymbol{f}$ is

$$\begin{aligned}
\mathbf{COV}(\boldsymbol{f}) &\equiv \mathbf{COV}(\boldsymbol{f},\boldsymbol{f}) \equiv \mathbf{VAR}(\boldsymbol{f}) \\
&= \mathrm{E}\left[\big(\boldsymbol{f}-\mathrm{E}[\boldsymbol{f}]\big)\big(\boldsymbol{f}-\mathrm{E}[\boldsymbol{f}]\big)^{\mathrm{T}}\right] \\
&= \mathrm{E}\left[\boldsymbol{f}\boldsymbol{f}^{\mathrm{T}}\right] - \mathrm{E}\left[\boldsymbol{f}\right]\mathrm{E}\left[\boldsymbol{f}^{\mathrm{T}}\right]. \qquad (5.13)
\end{aligned}$$

which, using (5.10), is expanded to

$$\begin{aligned}
\mathbf{COV}(\boldsymbol{f}) = \; & \frac{1}{N_{\boldsymbol{d}}}\sum_{j=1}^{N_{\boldsymbol{d}}}\Big(\Re\left\{\boldsymbol{F}^{-1}\boldsymbol{d}_j\right\}\Big)\;\Big(\Re\left\{\boldsymbol{F}^{-1}\boldsymbol{d}_j\right\}\Big)^{\mathrm{T}} \\
& - \frac{1}{N_{\boldsymbol{d}}^2}\sum_{j=1}^{N_{\boldsymbol{d}}}\Big(\Re\left\{\boldsymbol{F}^{-1}\boldsymbol{d}_j\right\}\Big)\;\sum_{j=1}^{N_{\boldsymbol{d}}}\Big(\Re\left\{\boldsymbol{F}^{-1}\boldsymbol{d}_j\right\}\Big)^{\mathrm{T}}. \qquad (5.14)
\end{aligned}$$

#### 5.3.4.1 Case: OFDM Type 2.2, Zero, Pilot, and Data Sub-Carriers, No Pre-Coding, BPSK Data

For an example case of Zero, Pilot, and BPSK Data sub-carriers all present, $N = 16$ digital IF sub-carriers and no pre-coding, using (5.14), the numerical result for the covariance matrix $\mathbf{COV}(\boldsymbol{f})$ of the real digital IF time-sample vector $\boldsymbol{f}$ at the the IDFT output is shown in Figure 5.1.

We note in Figure 5.1, and in subsequent similar figures, that $N$ is the total number sub-carriers, $\mathcal{K}_{\mathrm{SZ}}$ is the set of Zero sub-carrier indeces, $\mathcal{K}_{\mathrm{SP}}$ is the set of Pilot sub-carrier indeces, $\mathcal{K}_{\mathrm{SD}}$ is the set of Data sub-carrier indeces, $\mathcal{D}_{\mathrm{SP}}$ is the set of Pilot sub-carrier values matching the indices in $\mathcal{K}_{\mathrm{SP}}$, $\mathcal{A}_{\mathrm{SP}}$ is the symbol alphabet of the Pilot sub-carriers, and $\mathcal{A}_{\mathrm{SD}}$ is the symbol alphabet of the Data sub-carriers; all for the digital IF.

$$
\begin{bmatrix}
1.000 & -0.123 & -0.427 & 0.449 & 0.250 & 0.258 & -0.073 & -0.585 & -0.500 & -0.585 & -0.073 & 0.258 & 0.250 & 0.449 & -0.427 & -0.123 \\
-0.123 & 0.787 & 0.517 & -0.588 & -0.354 & -0.412 & 0.190 & 0.213 & -0.585 & 0.213 & 0.190 & -0.412 & -0.354 & -0.588 & 0.517 & 0.787 \\
-0.427 & 0.517 & 0.625 & -0.286 & -0.250 & -0.421 & -0.125 & 0.190 & -0.073 & 0.190 & -0.125 & -0.421 & -0.250 & -0.286 & 0.625 & 0.517 \\
0.449 & -0.588 & -0.286 & 0.963 & 0.354 & 0.037 & -0.421 & -0.412 & 0.258 & -0.412 & -0.421 & 0.037 & 0.354 & 0.963 & -0.286 & -0.588 \\
0.250 & -0.354 & -0.250 & 0.354 & 0.250 & 0.354 & -0.250 & -0.354 & 0.250 & -0.354 & -0.250 & 0.354 & 0.250 & 0.354 & -0.250 & -0.354 \\
0.258 & -0.412 & -0.421 & 0.037 & 0.354 & 0.963 & -0.286 & -0.588 & 0.449 & -0.588 & -0.286 & 0.963 & 0.354 & 0.037 & -0.421 & -0.412 \\
-0.073 & 0.190 & -0.125 & -0.421 & -0.250 & -0.286 & 0.625 & 0.517 & -0.427 & 0.517 & 0.625 & -0.286 & -0.250 & -0.421 & -0.125 & 0.190 \\
-0.585 & 0.213 & 0.190 & -0.412 & -0.354 & -0.588 & 0.517 & 0.787 & -0.123 & 0.787 & 0.517 & -0.588 & -0.354 & -0.412 & 0.190 & 0.213 \\
-0.500 & -0.585 & -0.073 & 0.258 & 0.250 & 0.449 & -0.427 & -0.123 & 1.000 & -0.123 & -0.427 & 0.449 & 0.250 & 0.258 & -0.073 & -0.585 \\
-0.585 & 0.213 & 0.190 & -0.412 & -0.354 & -0.588 & 0.517 & 0.787 & -0.123 & 0.787 & 0.517 & -0.588 & -0.354 & -0.412 & 0.190 & 0.213 \\
-0.073 & 0.190 & -0.125 & -0.421 & -0.250 & -0.286 & 0.625 & 0.517 & -0.427 & 0.517 & 0.625 & -0.286 & -0.250 & -0.421 & -0.125 & 0.190 \\
0.258 & -0.412 & -0.421 & 0.037 & 0.354 & 0.963 & -0.286 & -0.588 & 0.449 & -0.588 & -0.286 & 0.963 & 0.354 & 0.037 & -0.421 & -0.412 \\
0.250 & -0.354 & -0.250 & 0.354 & 0.250 & 0.354 & -0.250 & -0.354 & 0.250 & -0.354 & -0.250 & 0.354 & 0.250 & 0.354 & -0.250 & -0.354 \\
0.449 & -0.588 & -0.286 & 0.963 & 0.354 & 0.037 & -0.421 & -0.412 & 0.258 & -0.412 & -0.421 & 0.037 & 0.354 & 0.963 & -0.286 & -0.588 \\
-0.427 & 0.517 & 0.625 & -0.286 & -0.250 & -0.421 & -0.125 & 0.190 & -0.073 & 0.190 & -0.125 & -0.421 & -0.250 & -0.286 & 0.625 & 0.517 \\
-0.123 & 0.787 & 0.517 & -0.588 & -0.354 & -0.412 & 0.190 & 0.213 & -0.585 & 0.213 & 0.190 & -0.412 & -0.354 & -0.588 & 0.517 & 0.787
\end{bmatrix}
$$

| | |
|---|---|
| OFDM Type 2.2: | $N = 16, \mathcal{K}_{\mathrm{SZ}} = \{0, 7, 8, 9\}, \mathcal{K}_{\mathrm{SP}} = \{2, 4, 6, 10, 12, 14\}$, $\mathcal{K}_{\mathrm{SD}} = \{1, 3, 5, 11, 13, 15\}, \mathcal{D}_{\mathrm{SP}} = \{+1, -1, -1, -1, -1, +1\}$, $\mathcal{A}_{\mathrm{SD}} = \mathcal{A}_{\mathrm{BPSK}}$. |

Figure 5.1: 'Exhaustive' covariance matrix $\mathbf{COV}(\boldsymbol{f})$ of the real digital IF time-sample vector $\boldsymbol{f}$ at the the IDFT output, OFDM Type = 2.2.

Referring to Figure 5.1, we note that all of the non-diagonal entries of the the covariance matrix $\mathbf{COV}(\boldsymbol{f})$ of the real digital IF time-sample vector $\boldsymbol{f}$ at the IDFT output are non-zero; and therefore, in this case, all of the digital IF time-samples $f_n, n \in \mathbb{Z}_N$ are correlated (and dependent). This is not unexpected since every one of the time-sample entries $f_n, n \in \mathbb{Z}_N$ of the IDFT output vector $\boldsymbol{f}$ is comprised of a weighted sum (the IDFT equation) of the frequency-sample entries $d_k, k \in \mathbb{Z}_N$ of the IDFT input vector $\boldsymbol{d}$. Accordingly, any two IDFT output time-samples, say $f_n$ and $f'_n$ will be comprised of common terms which in most cases will lead to a correlation between the two IDFT output time-samples.

#### 5.3.4.2 Case: OFDM Type 2.4, Zero, Pilot, and Data Sub-Carriers, No Pre-Coding, 4QAM Data

For an example case of Zero, Pilot, and MQAM or MPSK (excluding BPSK) Data sub-carriers all present, $N = 16$ digital IF sub-carriers and no pre-coding, using (5.14), the numerical result for the covariance matrix $\mathbf{COV}(\boldsymbol{f})$ of the real digital IF time-sample vector $\boldsymbol{f}$ at the the IDFT output is shown in Figure 5.2.

Referring to Figure 5.2, we note that all of the non-diagonal entries of the covariance matrix $\mathbf{COV}(\boldsymbol{f})$ of the real digital IF time-sample vector $\boldsymbol{f}$ at the the IDFT output are non-zero; and therefore, in this case, as for the previously discussed BPSK Data sub-carrier case, all of the digital IF time-samples $f_n, n \in \mathbb{Z}_N$ are correlated (and dependent).

$$
\begin{bmatrix}
0.625 & -0.238 & -0.338 & 0.401 & 0.250 & 0.306 & -0.162 & -0.469 & -0.125 & -0.469 & -0.162 & 0.306 & 0.250 & 0.401 & -0.338 & -0.238 \\
-0.238 & 0.875 & 0.469 & -0.588 & -0.306 & -0.500 & 0.306 & 0.588 & -0.469 & 0.125 & 0.238 & -0.412 & -0.401 & -0.500 & 0.401 & 0.412 \\
-0.338 & 0.469 & 0.625 & -0.238 & -0.338 & -0.306 & 0.250 & 0.306 & -0.162 & 0.238 & -0.125 & -0.469 & -0.162 & -0.401 & 0.250 & 0.401 \\
0.401 & -0.588 & -0.238 & 0.875 & 0.469 & 0.412 & -0.306 & -0.500 & 0.306 & -0.412 & -0.469 & 0.125 & 0.238 & 0.588 & -0.401 & -0.500 \\
0.250 & -0.306 & -0.338 & 0.469 & 0.625 & 0.469 & -0.338 & -0.306 & 0.250 & -0.401 & -0.162 & 0.238 & -0.125 & 0.238 & -0.162 & -0.401 \\
0.306 & -0.500 & -0.306 & 0.412 & 0.469 & 0.875 & -0.238 & -0.588 & 0.401 & -0.500 & -0.401 & 0.588 & 0.238 & 0.125 & -0.469 & -0.412 \\
-0.162 & 0.306 & 0.250 & -0.306 & -0.338 & -0.238 & 0.625 & 0.469 & -0.338 & 0.401 & 0.250 & -0.401 & -0.162 & -0.469 & -0.125 & 0.238 \\
-0.469 & 0.588 & 0.306 & -0.500 & -0.306 & -0.588 & 0.469 & 0.875 & -0.238 & 0.412 & 0.401 & -0.500 & -0.401 & -0.412 & 0.238 & 0.125 \\
-0.125 & -0.469 & -0.162 & 0.306 & 0.250 & 0.401 & -0.338 & -0.238 & 0.625 & -0.238 & -0.338 & 0.401 & 0.250 & 0.306 & -0.162 & -0.469 \\
-0.469 & 0.125 & 0.238 & -0.412 & -0.401 & -0.500 & 0.401 & 0.412 & -0.238 & 0.875 & 0.469 & -0.588 & -0.306 & -0.500 & 0.306 & 0.588 \\
-0.162 & 0.238 & -0.125 & -0.469 & -0.162 & -0.401 & 0.250 & 0.401 & -0.338 & 0.469 & 0.625 & -0.238 & -0.338 & -0.306 & 0.250 & 0.306 \\
0.306 & -0.412 & -0.469 & 0.125 & 0.238 & 0.588 & -0.401 & -0.500 & 0.401 & -0.588 & -0.238 & 0.875 & 0.469 & 0.412 & -0.306 & -0.500 \\
0.250 & -0.401 & -0.162 & 0.238 & -0.125 & 0.238 & -0.162 & -0.401 & 0.250 & -0.306 & -0.338 & 0.469 & 0.625 & 0.469 & -0.338 & -0.306 \\
0.401 & -0.500 & -0.401 & 0.588 & 0.238 & 0.125 & -0.469 & -0.412 & 0.306 & -0.500 & -0.306 & 0.412 & 0.469 & 0.875 & -0.238 & -0.588 \\
-0.338 & 0.401 & 0.250 & -0.401 & -0.162 & -0.469 & -0.125 & 0.238 & -0.162 & 0.306 & 0.250 & -0.306 & -0.338 & -0.238 & 0.625 & 0.469 \\
-0.238 & 0.412 & 0.401 & -0.500 & -0.401 & -0.412 & 0.238 & 0.125 & -0.469 & 0.588 & 0.306 & -0.500 & -0.306 & -0.588 & 0.469 & 0.875
\end{bmatrix}
$$

OFDM Type 2.4: $N = 16, \mathcal{K}_{\text{SZ}} = \{0, 7, 8, 9\}, \mathcal{K}_{\text{SP}} = \{2, 4, 6, 10, 12, 14\}$,
$\mathcal{K}_{\text{SD}} = \{1, 3, 5, 11, 13, 15\}, \mathcal{D}_{\text{SP}} = \{+1, -1, -1, -1, -1, +1\}$,
$\mathcal{A}_{\text{SD}} \in \mathcal{A}_{\text{4QAM}}$, $\text{E}[f^2] = 1$.

Figure 5.2: ‘Exhaustive’ covariance matrix $\mathbf{COV}(\boldsymbol{f})$ of the real digital IF time-sample vector $\boldsymbol{f}$ at the IDFT output, OFDM Type = 2.4.

### 5.3.5 'Exhaustive' Correlation Matrix of the IDFT Output Time-Sample Real-Part Vector

In general, the correlation matrix of a random vector is a matrix whose $(l, m)$ $^{\text{th}}$ entry is the Pearson's correlation coefficient between the $l^{\text{th}}$ and $m^{\text{th}}$ entries of the random vector.

The $(l, m)$ $^{\text{th}}$ entry of the correlation matrix of the IDFT output time-sample real-part vector $\boldsymbol{f}$, in terms of the entries of its covariance matrix $\mathbf{COV}(\boldsymbol{f})$ already obtained in (5.14) above, is therefore

$$\begin{aligned}[\mathbf{CORR}(\boldsymbol{f})]_{l,m} &= \frac{\operatorname{cov}(f_l, f_m)}{\sqrt{\operatorname{cov}(f_l, f_l)} \cdot \sqrt{\operatorname{cov}(f_m, f_m)}} \\ &= \frac{[\mathbf{COV}(\boldsymbol{f})]_{l,m}}{\sqrt{[\mathbf{COV}(\boldsymbol{f})]_{l,l}} \cdot \sqrt{[\mathbf{COV}(\boldsymbol{f})]_{m,m}}}. \end{aligned} \tag{5.15}$$

The matrix formulation of the correlation matrix of the IDFT output time-sample real-part vector $\boldsymbol{f}$, in terms of its covariance matrix $\mathbf{COV}(\boldsymbol{f})$ already obtained in (5.14) above, is then neatly given by

$$\mathbf{CORR}(\boldsymbol{f}) = \left(\mathbf{DIAG}[\mathbf{COV}(\boldsymbol{f})]\right)^{-1/2} \ \mathbf{COV}(\boldsymbol{f}) \ \left(\mathbf{DIAG}[\mathbf{COV}(\boldsymbol{f})]\right)^{-1/2}. \tag{5.16}$$

#### 5.3.5.1 Case: OFDM Type 2.2, Zero, Pilot, and Data Sub-Carriers, No Pre-Coding, BPSK Data

For the example case, already used for the determination of $\mathbf{COV}(\boldsymbol{f})$ in §5.3.4.1, of Zero, Pilot, and BPSK Data sub-carriers all present, $N = 16$ digital IF sub-carriers and no pre-coding, using (5.14) and (5.16), the numerical result for the correlation matrix $\mathbf{CORR}(\boldsymbol{f})$ of the real digital IF time-sample vector $\boldsymbol{f}$ at the the IDFT output is shown in Figure 5.3.

Referring to Figure 5.3, we note that all of the entries of the correlation matrix $\mathbf{CORR}(\boldsymbol{f})$ of the real digital IF time-sample vector $\boldsymbol{f}$ at the the IDFT output are non-zero; and therefore, in this case, all of the digital IF time-samples $f_n, n \in \mathbb{Z}_N$ are correlated (and dependent).

$$
\begin{bmatrix}
1.000 & -0.138 & -0.540 & 0.458 & 0.500 & 0.263 & -0.093 & -0.659 & -0.500 & -0.659 & -0.093 & 0.263 & 0.500 & 0.458 & -0.540 & -0.138 \\
-0.138 & 1.000 & 0.737 & -0.676 & -0.797 & -0.473 & 0.271 & 0.271 & -0.659 & 0.271 & 0.271 & -0.473 & -0.797 & -0.676 & 0.737 & 1.000 \\
-0.540 & 0.737 & 1.000 & -0.368 & -0.632 & -0.543 & -0.200 & 0.271 & -0.093 & 0.271 & -0.200 & -0.543 & -0.632 & -0.368 & 1.000 & 0.737 \\
0.458 & -0.676 & -0.368 & 1.000 & 0.720 & 0.038 & -0.543 & -0.473 & 0.263 & -0.473 & -0.543 & 0.038 & 0.720 & 1.000 & -0.368 & -0.676 \\
0.500 & -0.797 & -0.632 & 0.720 & 1.000 & 0.720 & -0.632 & -0.797 & 0.500 & -0.797 & -0.632 & 0.720 & 1.000 & 0.720 & -0.632 & -0.797 \\
0.263 & -0.473 & -0.543 & 0.038 & 0.720 & 1.000 & -0.368 & -0.676 & 0.458 & -0.676 & -0.368 & 1.000 & 0.720 & 0.038 & -0.543 & -0.473 \\
-0.093 & 0.271 & -0.200 & -0.543 & -0.632 & -0.368 & 1.000 & 0.737 & -0.540 & 0.737 & 1.000 & -0.368 & -0.632 & -0.543 & -0.200 & 0.271 \\
-0.659 & 0.271 & 0.271 & -0.473 & -0.797 & -0.676 & 0.737 & 1.000 & -0.138 & 1.000 & 0.737 & -0.676 & -0.797 & -0.473 & 0.271 & 0.271 \\
-0.500 & -0.659 & -0.093 & 0.263 & 0.500 & 0.458 & -0.540 & -0.138 & 1.000 & -0.138 & -0.540 & 0.458 & 0.500 & 0.263 & -0.093 & -0.659 \\
-0.659 & 0.271 & 0.271 & -0.473 & -0.797 & -0.676 & 0.737 & 1.000 & -0.138 & 1.000 & 0.737 & -0.676 & -0.797 & -0.473 & 0.271 & 0.271 \\
-0.093 & 0.271 & -0.200 & -0.543 & -0.632 & -0.368 & 1.000 & 0.737 & -0.540 & 0.737 & 1.000 & -0.368 & -0.632 & -0.543 & -0.200 & 0.271 \\
0.263 & -0.473 & -0.543 & 0.038 & 0.720 & 1.000 & -0.368 & -0.676 & 0.458 & -0.676 & -0.368 & 1.000 & 0.720 & 0.038 & -0.543 & -0.473 \\
0.500 & -0.797 & -0.632 & 0.720 & 1.000 & 0.720 & -0.632 & -0.797 & 0.500 & -0.797 & -0.632 & 0.720 & 1.000 & 0.720 & -0.632 & -0.797 \\
0.458 & -0.676 & -0.368 & 1.000 & 0.720 & 0.038 & -0.543 & -0.473 & 0.263 & -0.473 & -0.543 & 0.038 & 0.720 & 1.000 & -0.368 & -0.676 \\
-0.540 & 0.737 & 1.000 & -0.368 & -0.632 & -0.543 & -0.200 & 0.271 & -0.093 & 0.271 & -0.200 & -0.543 & -0.632 & -0.368 & 1.000 & 0.737 \\
-0.138 & 1.000 & 0.737 & -0.676 & -0.797 & -0.473 & 0.271 & 0.271 & -0.659 & 0.271 & 0.271 & -0.473 & -0.797 & -0.676 & 0.737 & 1.000
\end{bmatrix}
$$

OFDM Type 2.2: $N = 16, \mathcal{K}_{\mathrm{SZ}} = \{0, 7, 8, 9\}, \mathcal{K}_{\mathrm{SP}} = \{2, 4, 6, 10, 12, 14\}$,
$\mathcal{K}_{\mathrm{SD}} = \{1, 3, 5, 11, 13, 15\}, \mathcal{D}_{\mathrm{SP}} = \{+1, -1, -1, -1, -1, +1\}$,
$\mathcal{A}_{\mathrm{SD}} = \mathcal{A}_{\mathrm{BPSK}}$.

Figure 5.3: ‘Exhaustive’ correlation matrix $\mathbf{CORR}(\boldsymbol{f})$ of the real digital IF time-sample vector $\boldsymbol{f}$ at the the IDFT output, OFDM Type = 2.2.

We note also that many of the correlation magnitudes are quite large with the maximal non-diagonal and non-offset-anti-diagonal correlation magnitude being $|\,[\mathbf{CORR}(\boldsymbol{f})]_{4,7}| = 0.797$.

Of particular interest are the offset-anti-diagonal correlation magnitudes all being unity for this BPSK case. The 'Exhaustive' method yields this result but cannot explain why it occurs. However, the 'Matrix Transformation' method gives insight into the special BPSK case in §6.1.2 and more specifically in (6.21).

#### 5.3.5.2 Case: OFDM Type 2.4, Zero, Pilot, and Data Sub-Carriers, No Pre-Coding, 4QAM Data

For the example case, already used for the determination of $\mathbf{COV}(\boldsymbol{f})$ in §5.3.4.2 , of Zero, Pilot, and 4QAM Data sub-carriers all present, $N = 16$ digital IF sub-carriers and no pre-coding, using (5.14) and (5.16), the numerical result for the correlation matrix $\mathbf{CORR}(\boldsymbol{f})$ of the real digital IF time-sample vector $\boldsymbol{f}$ at the the IDFT output is shown in Figure 5.4.

Referring to Figure 5.4, we note that all of the entries of the the correlation matrix $\mathbf{CORR}(\boldsymbol{f})$ of the real digital IF time-sample vector $\boldsymbol{f}$ at the the IDFT output are non-zero; and therefore, in this case, all of the digital IF time-samples $f_n, n \in \mathbb{Z}_N$ are correlated (and therefore dependent).

Like the BPSK case already discussed in §5.3.5.1, we note for this case that many of the correlation magnitudes are quite large with the maximal non-diagonal and non-offset-anti-diagonal correlation magnitude being $|\,[\mathbf{CORR}(\boldsymbol{f})]_{3,13}| = 0.672$.

$$
\begin{bmatrix}
1.000 & -0.322 & -0.541 & 0.543 & 0.400 & 0.413 & -0.259 & -0.634 & -0.200 & -0.634 & -0.259 & 0.413 & 0.400 & 0.543 & -0.541 & -0.322 \\
-0.322 & 1.000 & 0.634 & -0.672 & -0.413 & -0.571 & 0.413 & 0.672 & -0.634 & 0.143 & 0.322 & -0.470 & -0.543 & -0.571 & 0.543 & 0.470 \\
-0.541 & 0.634 & 1.000 & -0.322 & -0.541 & -0.413 & 0.400 & 0.413 & -0.259 & 0.322 & -0.200 & -0.634 & -0.259 & -0.543 & 0.400 & 0.543 \\
0.543 & -0.672 & -0.322 & 1.000 & 0.634 & 0.470 & -0.413 & -0.571 & 0.413 & -0.470 & -0.634 & 0.143 & 0.322 & 0.672 & -0.543 & -0.571 \\
0.400 & -0.413 & -0.541 & 0.634 & 1.000 & 0.634 & -0.541 & -0.413 & 0.400 & -0.543 & -0.259 & 0.322 & -0.200 & 0.322 & -0.259 & -0.543 \\
0.413 & -0.571 & -0.413 & 0.470 & 0.634 & 1.000 & -0.322 & -0.672 & 0.543 & -0.571 & -0.543 & 0.672 & 0.322 & 0.143 & -0.634 & -0.470 \\
-0.259 & 0.413 & 0.400 & -0.413 & -0.541 & -0.322 & 1.000 & 0.634 & -0.541 & 0.543 & 0.400 & -0.543 & -0.259 & -0.634 & -0.200 & 0.322 \\
-0.634 & 0.672 & 0.413 & -0.571 & -0.413 & -0.672 & 0.634 & 1.000 & -0.322 & 0.470 & 0.543 & -0.571 & -0.543 & -0.470 & 0.322 & 0.143 \\
-0.200 & -0.634 & -0.259 & 0.413 & 0.400 & 0.543 & -0.541 & -0.322 & 1.000 & -0.322 & -0.541 & 0.543 & 0.400 & 0.413 & -0.259 & -0.634 \\
-0.634 & 0.143 & 0.322 & -0.470 & -0.543 & -0.571 & 0.543 & 0.470 & -0.322 & 1.000 & 0.634 & -0.672 & -0.413 & -0.571 & 0.413 & 0.672 \\
-0.259 & 0.322 & -0.200 & -0.634 & -0.259 & -0.543 & 0.400 & 0.543 & -0.541 & 0.634 & 1.000 & -0.322 & -0.541 & -0.413 & 0.400 & 0.413 \\
0.413 & -0.470 & -0.634 & 0.143 & 0.322 & 0.672 & -0.543 & -0.571 & 0.543 & -0.672 & -0.322 & 1.000 & 0.634 & 0.470 & -0.413 & -0.571 \\
0.400 & -0.543 & -0.259 & 0.322 & -0.200 & 0.322 & -0.259 & -0.543 & 0.400 & -0.413 & -0.541 & 0.634 & 1.000 & 0.634 & -0.541 & -0.413 \\
0.543 & -0.571 & -0.543 & 0.672 & 0.322 & 0.143 & -0.634 & -0.470 & 0.413 & -0.571 & -0.413 & 0.470 & 0.634 & 1.000 & -0.322 & -0.672 \\
-0.541 & 0.543 & 0.400 & -0.543 & -0.259 & -0.634 & -0.200 & 0.322 & -0.259 & 0.413 & 0.400 & -0.413 & -0.541 & -0.322 & 1.000 & 0.634 \\
-0.322 & 0.470 & 0.543 & -0.571 & -0.543 & -0.470 & 0.322 & 0.143 & -0.634 & 0.672 & 0.413 & -0.571 & -0.413 & -0.672 & 0.634 & 1.000
\end{bmatrix}
$$

OFDM Type 2.4: $N = 16, \mathcal{K}_{\mathrm{SZ}} = \{0, 7, 8, 9\}, \mathcal{K}_{\mathrm{SP}} = \{2, 4, 6, 10, 12, 14\},$
$\mathcal{K}_{\mathrm{SD}} = \{1, 3, 5, 11, 13, 15\}, \mathcal{D}_{\mathrm{SP}} = \{+1, -1, -1, -1, -1, +1\},$
$\mathcal{A}_{\mathrm{SD}} \in \mathcal{A}_{\mathrm{4QAM}}, \mathrm{E}[f^2] = 1.$

Figure 5.4: 'Exhaustive' correlation matrix $\mathbf{CORR}(\boldsymbol{f})$ of the real digital IF time-sample vector $\boldsymbol{f}$ at the IDFT output, OFDM Type = 2.4.

### 5.3.6 'Exhaustive' PDF and CDF of Individual IDFT Output Time-Sample Real-Parts

The $n^{\text{th}}$ time-sample $f_n$ of the IDFT output real-part vector $\boldsymbol{f}$ is given by

$$f_n = [\boldsymbol{f}]_n = \left[\Re\left\{\boldsymbol{F}^{-1}\boldsymbol{d}\right\}\right]_n, \tag{5.17}$$

and the particular instance of $f_n$ which corresponds to the $j^{\text{th}}$ letter $\boldsymbol{d}_j$ of the IDFT input vector alphabet $\mathcal{A}_{\boldsymbol{d}}$ is therefore given by

$$f_{j,n} = \left[\Re\left\{\boldsymbol{F}^{-1}\boldsymbol{d}_j\right\}\right]_n. \tag{5.18}$$

The one-dimensional real PDF of $f_n$ is therefore

$$f_{f_n}(f'_n) = \frac{1}{N_{\boldsymbol{d}}}\sum_{j=1}^{N_{\boldsymbol{d}}}\delta\left(f'_n - f_{j,n}\right). \tag{5.19}$$

Next, the CDF of the $n^{\text{th}}$ time-sample $f_n$ of the real part $\boldsymbol{f}$ of the IDFT output vector is given by

$$\begin{aligned} F_{f_n}(f''_n) &= \int_{-\infty}^{f''_n} f_{f_n}(f'_n)\ \mathrm{d}f'_n \\ &= \int_{-\infty}^{f''_n} \frac{1}{N_{\boldsymbol{d}}}\sum_{j=1}^{N_{\boldsymbol{d}}}\delta\left(f'_n - f_{j,n}\right)\ \mathrm{d}f'_n \\ &= \frac{1}{N_{\boldsymbol{d}}}\sum_{f_{j,n}\le f''} 1. \end{aligned} \tag{5.20}$$

Note that the PDF and CDF results shown throughout this thesis are obtained by first normalizing the the power of some closely associated variable to unity. For the particular case of the PDFs and CDFs of the individual IDFT output time-sample real parts $f_n$, the average power of all of IDFT output time-sample real parts $f$ is set to unity so that $E[f^2] = 1$ (remembering that $f$ is zero-mean). This is shown as a condition in the 'OFDM Type 1.4' box at the bottom of Figure 5.5.

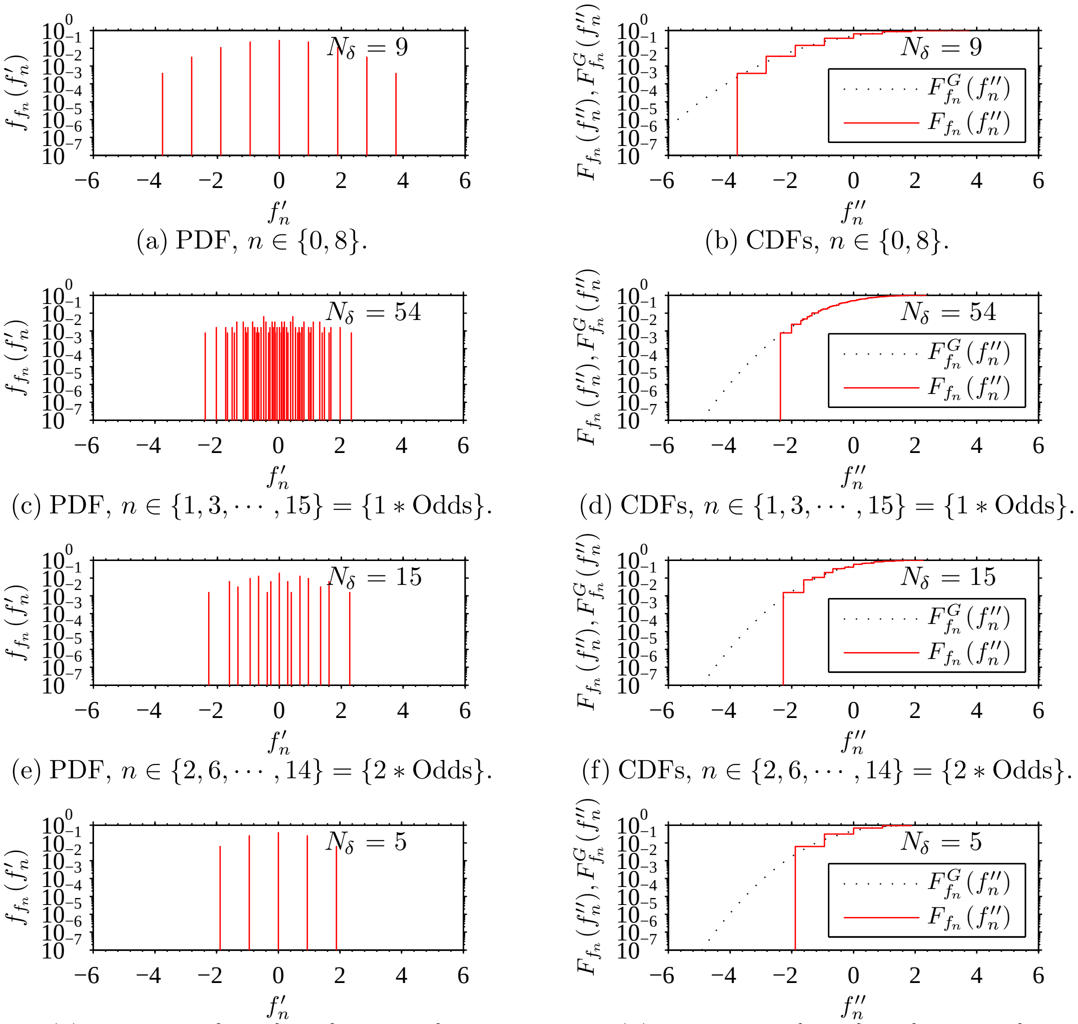

(a) PDF, $n \in \{0, 8\}$.

(b) CDFs, $n \in \{0, 8\}$.

(c) PDF, $n \in \{1, 3, \cdots, 15\} = \{1 * \text{Odds}\}$.

(d) CDFs, $n \in \{1, 3, \cdots, 15\} = \{1 * \text{Odds}\}$.

(e) PDF, $n \in \{2, 6, \cdots, 14\} = \{2 * \text{Odds}\}$.

(f) CDFs, $n \in \{2, 6, \cdots, 14\} = \{2 * \text{Odds}\}$.

(g) PDF, $n \in \{4, 12\} = \{4 * \text{Odds}\}$.

(h) CDFs, $n \in \{4, 12\} = \{4 * \text{Odds}\}$.

OFDM Type 1.2: $N = 16, \mathcal{K}_{\text{SZ}} = \{\}, \mathcal{K}_{\text{SP}} = \{\}, \mathcal{K}_{\text{SD}} = \mathbb{Z}_N, \mathcal{A}_{\text{SD}} = \mathcal{A}_{\text{BPSK}}, \text{E}[f^2] = 1.$

Figure 5.5: 'Exhaustive' PDFs $f_{f_n}(f'_n)$, CDFs $F_{f_n}(f''_n)$, and Gaussian approximation CDFs $F^G_{f_n}(f''_n)$ of individual IDFT output time-sample real-parts, OFDM Type $= 1.2$, for each time-sample index $n$.

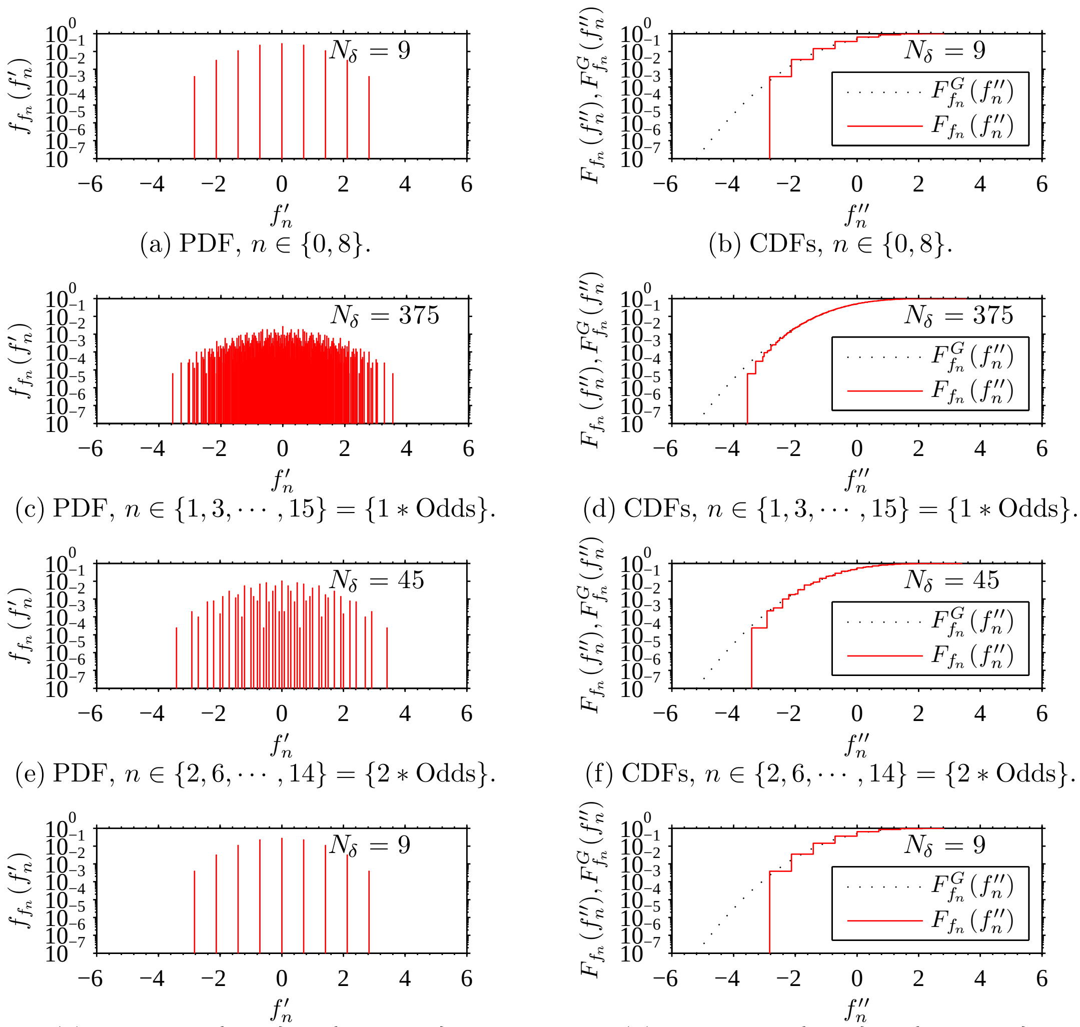


(a) PDF, $n \in \{0, 8\}$.

(b) CDFs, $n \in \{0, 8\}$.

(c) PDF, $n \in \{1, 3, \cdots, 15\} = \{1 * \text{Odds}\}$.

(d) CDFs, $n \in \{1, 3, \cdots, 15\} = \{1 * \text{Odds}\}$.

(e) PDF, $n \in \{2, 6, \cdots, 14\} = \{2 * \text{Odds}\}$.

(f) CDFs, $n \in \{2, 6, \cdots, 14\} = \{2 * \text{Odds}\}$.

(g) PDF, $n \in \{4, 12\} = \{4 * \text{Odds}\}$.

(h) CDFs, $n \in \{4, 12\} = \{4 * \text{Odds}\}$.

OFDM Type 1.4: $N = 16, \mathcal{K}_{\text{SZ}} = \{\}, \mathcal{K}_{\text{SP}} = \{\}, \mathcal{K}_{\text{SD}} = \mathbb{Z}_N$, $\mathcal{A}_{\text{SD}} = \mathcal{A}_{\text{QPSK}}$, $\text{E}[f^2] = 1$.

Figure 5.6: 'Exhaustive' PDFs $f_{f_n}(f'_n)$, CDFs $F_{f_n}(f''_n)$, and Gaussian approximation CDFs $F^G_{f_n}(f''_n)$ of individual IDFT output time-sample real-parts, OFDM Type = 1.4, for each time-sample index $n$.

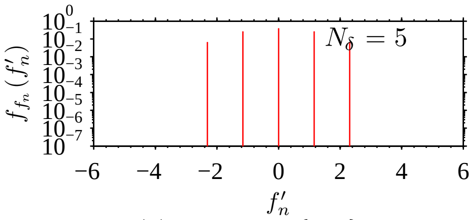


(a) PDF, $n \in \{0, 8\}$.

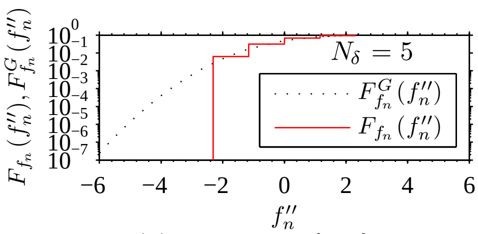


(b) CDFs, $n \in \{0, 8\}$.

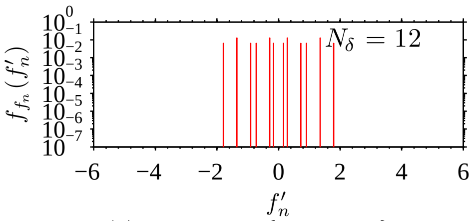


(c) PDF, $n \in \{1, 7, 9, 15\}$.

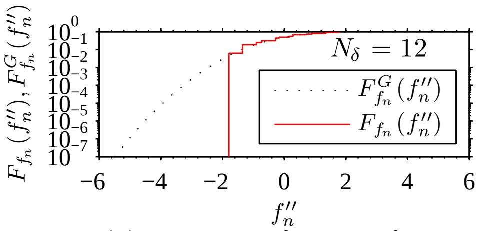


(d) CDFs, $n \in \{1, 7, 9, 15\}$.

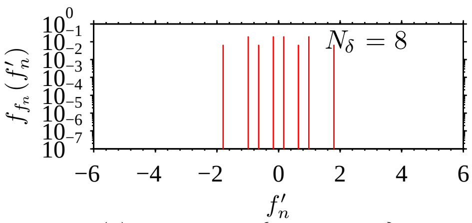


(e) PDF, $n \in \{2, 6, 10, 14\}$.

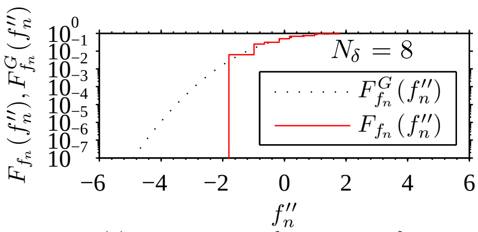


(f) CDFs, $n \in \{2, 6, 10, 14\}$.

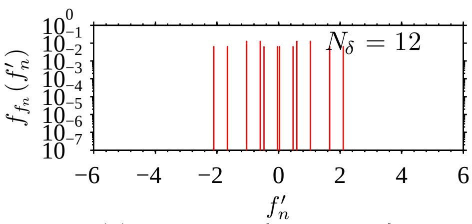


(g) PDF, $n \in \{3, 5, 11, 13\}$.

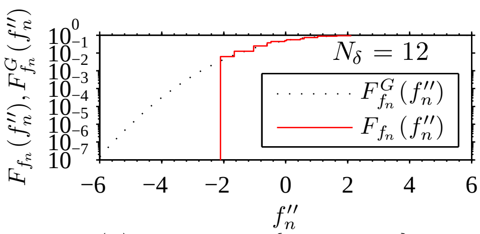


(h) CDFs, $n \in \{3, 5, 11, 13\}$.

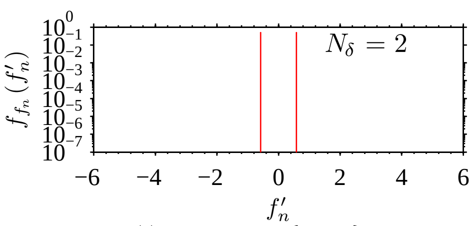


(i) PDF, $n \in \{4, 12\}$.

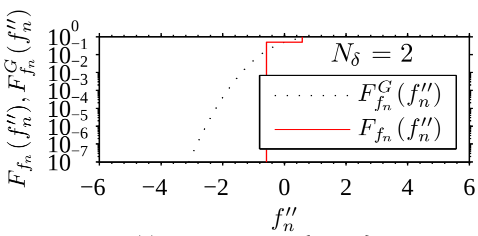


(j) CDFs, $n \in \{4, 12\}$.

OFDM Type 2.2: $N = 16$, $\mathcal{K}_{\text{SZ}} = \{0, 7, 8, 9\}, \mathcal{K}_{\text{SP}} = \{2, 4, 6, 10, 12, 14\}, \mathcal{A}_{\text{SP}} = \mathcal{A}_{\text{BPSK}}$,
$\mathcal{K}_{\text{SD}} = \{1, 3, 5, 11, 13, 15\}$, $\mathcal{A}_{\text{SD}} = \mathcal{A}_{\text{BPSK}}$,
$\mathcal{D}_{\text{SP}} = \{+1, -1, -1, -1, -1, +1\}$, $\mathrm{E}[f^2] = 1$.

Figure 5.7: 'Exhaustive' PDFs $f_{f_n}(f'_n)$, CDFs $F_{f_n}(f''_n)$, and Gaussian approximation CDFs $F^G_{f_n}(f''_n)$ of individual IDFT output time-sample real-parts, OFDM Type 2.2, for each time-sample index $n$.

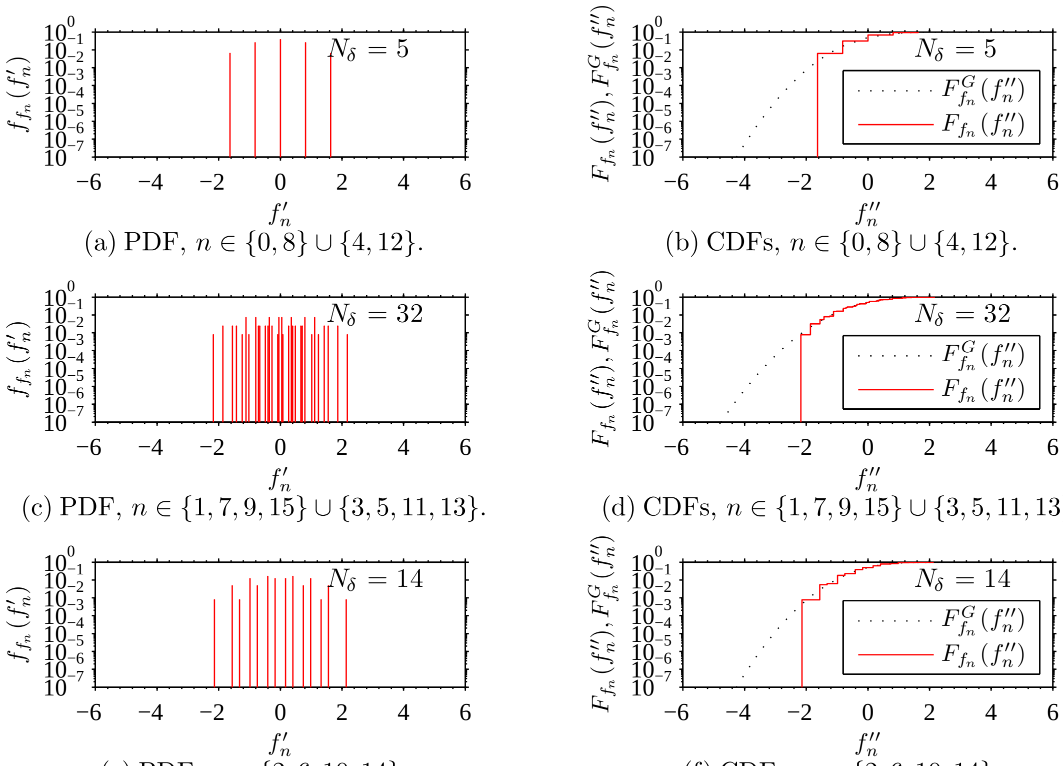


(a) PDF, $n \in \{0, 8\} \cup \{4, 12\}$. (b) CDFs, $n \in \{0, 8\} \cup \{4, 12\}$.

(c) PDF, $n \in \{1, 7, 9, 15\} \cup \{3, 5, 11, 13\}$. (d) CDFs, $n \in \{1, 7, 9, 15\} \cup \{3, 5, 11, 13\}$.

(e) PDF, $n \in \{2, 6, 10, 14\}$. (f) CDFs, $n \in \{2, 6, 10, 14\}$.

OFDM Type 2.4: $N = 16, \mathcal{K}_{\mathrm{SZ}} = \{0, 7, 8, 9\}, \mathcal{K}_{\mathrm{SP}} = \{2, 4, 6, 10, 12, 14\}$, $\mathcal{A}_{\mathrm{SP}} = \mathcal{A}_{\mathrm{QPSK}}$,
$\mathcal{K}_{\mathrm{SD}} = \{1, 3, 5, 11, 13, 15\}, \mathcal{A}_{\mathrm{SD}} = \mathcal{A}_{\mathrm{BPSK}}$,
$\mathcal{D}_{\mathrm{SP}} = \{+1, -1, -1, -1, -1, +1\}, \mathrm{E}[f^2] = 1$.

Figure 5.8: 'Exhaustive' PDFs $f_{f_n}(f'_n)$, CDFs $F_{f_n}(f''_n)$, and Gaussian approximation CDFs $F^G_{f_n}(f''_n)$ of individual IDFT output time-sample real-parts, OFDM Type 2.4, for each time-sample index $n$.

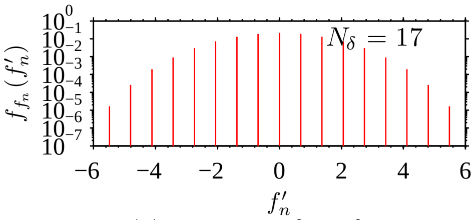


(a) PDF, $n \in \{0, 16\}$.

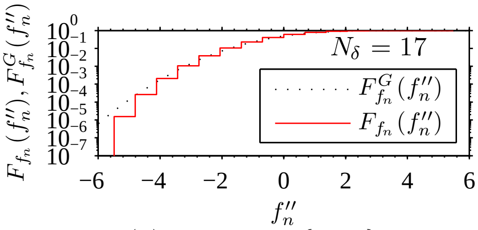


(b) CDFs, $n \in \{0, 16\}$.

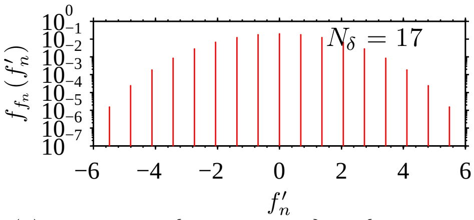


(c) PDF, $n \in \{1, 3, \cdots, 31\} = \{1 * \text{Odds}\}$.

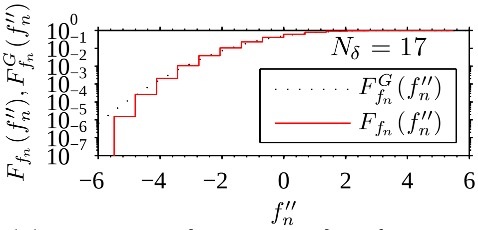


(d) CDFs, $n \in \{1, 3, \cdots, 31\} = \{1 * \text{Odds}\}$.

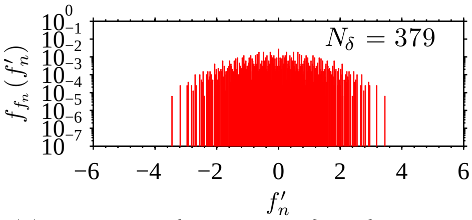


(e) PDF, $n \in \{2, 6, \cdots, 30\} = \{2 * \text{Odds}\}$.

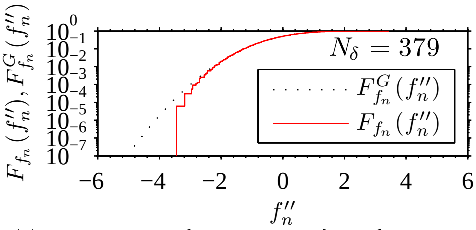


(f) CDFs, $n \in \{2, 6, \cdots, 30\} = \{2 * \text{Odds}\}$.

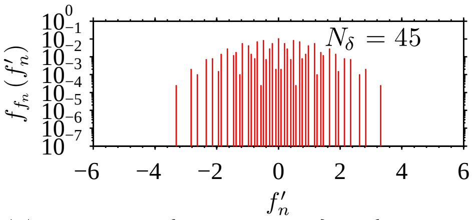


(g) PDF, $n \in \{4, 12, \cdots, 28\} = \{4 * \text{Odds}\}$.

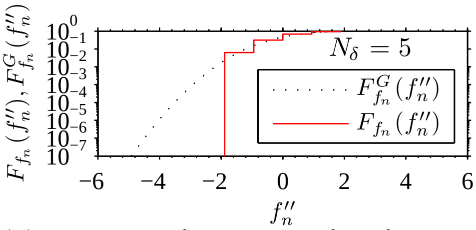


(h) CDFs, $n \in \{4, 12, \cdots, 28\} = \{4 * \text{Odds}\}$.

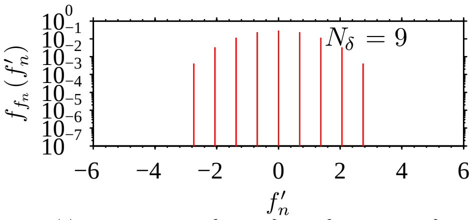


(i) PDF, $n \in \{8, 24\} = \{8 * \text{Odds}\}$.

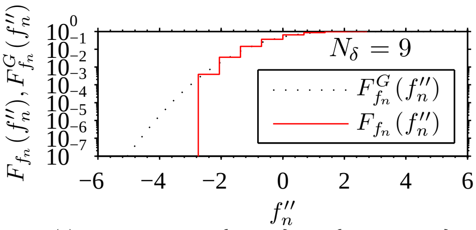


(j) CDFs, $n \in \{8, 24\} = \{8 * \text{Odds}\}$.

OFDM Type 3.2: $N = 32$, $\mathcal{K}_{\text{SZ}} = \{\}, \mathcal{K}_{\text{SP}} = \{\}, \mathcal{K}_{\text{SD}} = \mathbb{Z}_N, \mathcal{A}_{\text{SD}} = \mathcal{A}_{\text{BPSK}}, \text{E}[f^2] = 1.$

Figure 5.9: 'Exhaustive' PDFs $f_{f_n}(f'_n)$, CDFs $F_{f_n}(f''_n)$, and Gaussian approximation CDFs $F^G_{f_n}(f''_n)$ of individual IDFT output time-sample real-parts, OFDM Type = 3.2, for each time-sample index $n$.

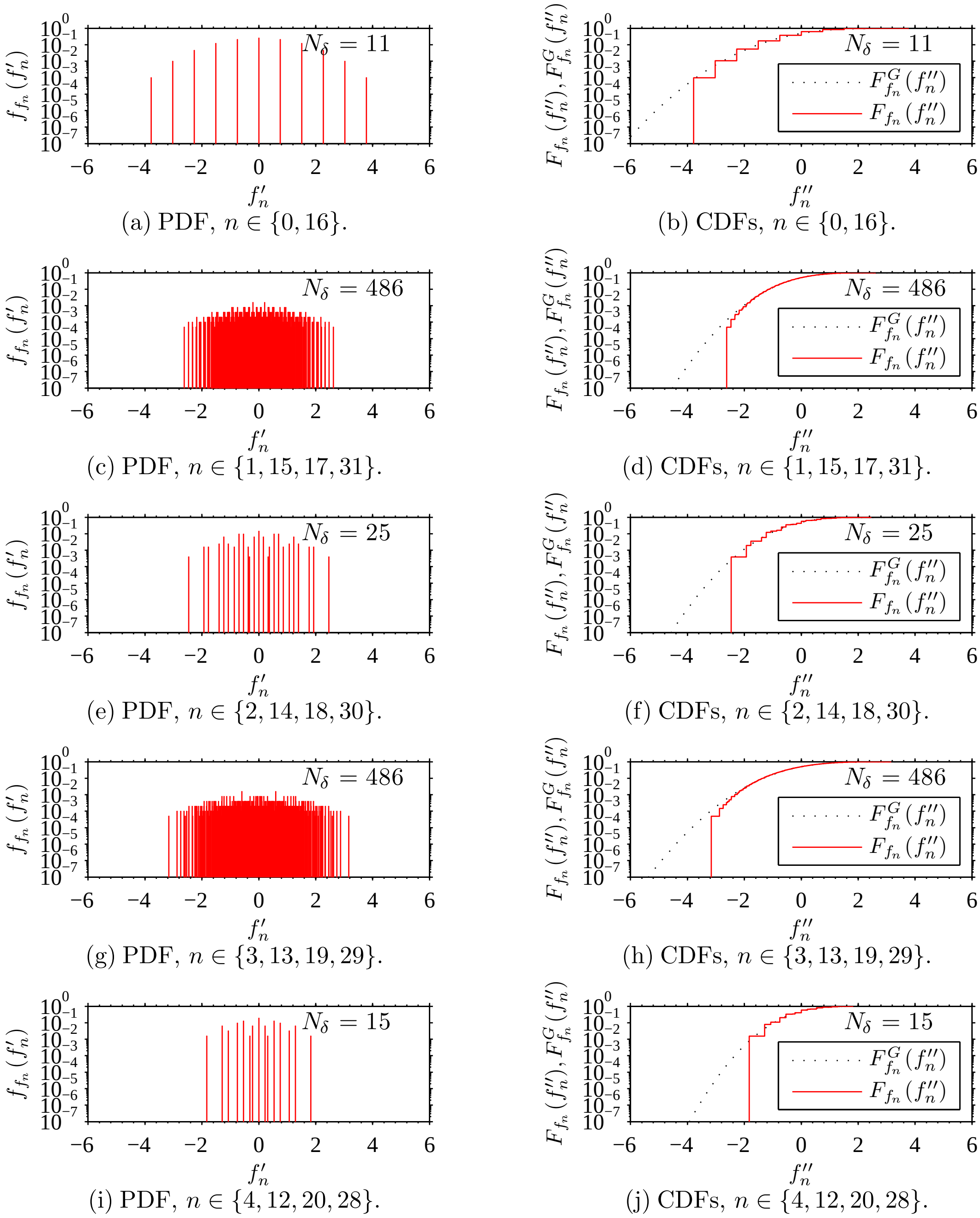


OFDM Type 4.2: $N = 32$, $\mathcal{K}_{\mathrm{SZ}} = \{0, 8, 16, 24\}$, $\mathcal{K}_{\mathrm{SP}} = \{3, 5, 11, 13, 19, 21, 27, 29\}$, $\mathcal{A}_{\mathrm{SP}} = \mathcal{A}_{\mathrm{BPSK}}$, $\mathcal{K}_{\mathrm{SD}} = \{1, 2, 4, 6, 7, 9, 10, 12, 14, 15, 17, 18, 20, 22, 23, 25, 28, 30, 31\}$, $\mathcal{A}_{\mathrm{SD}} = \mathcal{A}_{\mathrm{BPSK}}$, $\mathcal{D}_{\mathrm{SP}} = \{-1, +1, -1, +1, +1, -1, +1, -1\}$, $\mathrm{E}[f^2] = 1$.

Figure 5.10: 'Exhaustive' PDFs $f_{f_n}(f'_n)$, CDFs $F_{f_n}(f''_n)$, and Gaussian approximation CDFs $F^G_{f_n}(f''_n)$ of individual IDFT output time-sample real-parts, OFDM Type 4.2, for each time-sample index $n$.

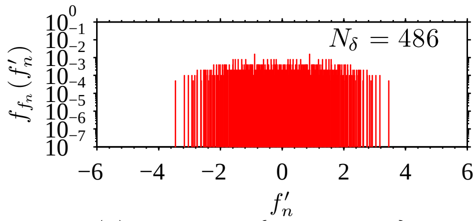


(k) PDF, $n \in \{5, 11, 21, 27\}$.

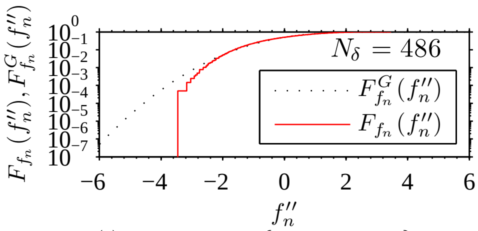


(l) CDFs, $n \in \{5, 11, 21, 27\}$.

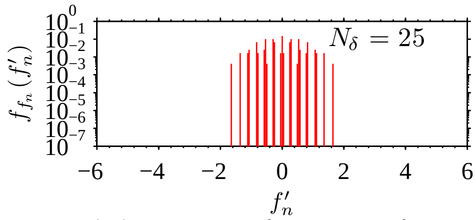


(m) PDF, $n \in \{6, 10, 22, 26\}$.

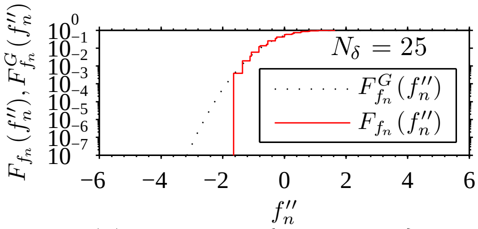


(n) CDFs, $n \in \{6, 10, 22, 26\}$.

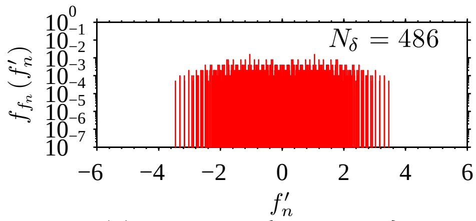


(o) PDF, $n \in \{7, 9, 23, 25\}$.

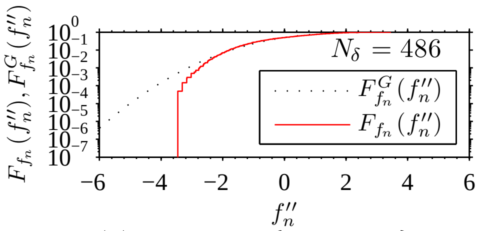


(p) CDFs, $n \in \{7, 9, 23, 25\}$.

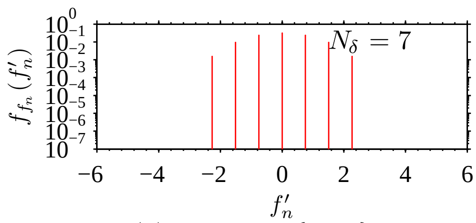


(q) PDF, $n \in \{8, 24\}$.

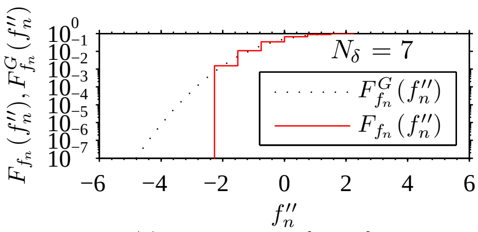


(r) CDFs, $n \in \{8, 24\}$.

OFDM Type 4.2: $N = 32, \mathcal{K}_{\mathrm{SZ}} = \{0, 8, 16, 24\}, \mathcal{K}_{\mathrm{SP}} = \{3, 5, 11, 13, 19, 21, 27, 29\}, \mathcal{A}_{\mathrm{SP}} = \mathcal{A}_{\mathrm{BPSK}},$
$\mathcal{K}_{\mathrm{SD}} = \{1, 2, 4, 6, 7, 9, 10, 12, 14, 15, 17, 18, 20, 22, 23, 25, 28, 30, 31\}, \mathcal{A}_{\mathrm{SD}} = \mathcal{A}_{\mathrm{BPSK}},$
$\mathcal{D}_{\mathrm{SP}} = \{-1, +1, -1, +1, +1, -1, +1, -1\}, \mathrm{E}[f^2] = 1.$

Figure 5.10: (Cont'd) 'Exhaustive' PDFs $f_{f_n}(f'_n)$, CDFs $F_{f_n}(f''_n)$, and Gaussian approximation CDFs $F^G_{f_n}(f''_n)$ of individual IDFT output time-sample real-parts, OFDM Type 4.2, for each time-sample index $n$.

#### 5.3.6.1 Example Results

Some example results for the PDF $f_{f_n}(f_n')$ and the CDF $F_{f_n}(f_n'')$ of the individual IDFT output time-sample real-parts for OFDM types 1.2, 1.4, 2.2, 2.4, 3.2, and 4.2, are shown in Figures 5.5 to 5.10 respectively.

For the case of OFDM type 1.2 with a total of only $N = 16$ digital IF sub-carriers all used as Data sub-carriers in Figure 5.5, we see firstly that the PDFs are discrete each with a small number $N_\delta$ of diracs compared to the IDFT input alphabet size $|\mathcal{A}_{\boldsymbol{d}}| = 2^8 = 256$. This leads us to the conclusion that many different IDFT input symbol vectors $\boldsymbol{d}_j$ map to the same level at each of the IDFT output time-samples $f_n$. This is elucidated in the later section on the 'Combinatorics' method. Another noteworthy feature is that not all of the time-samples $f_n$ have the same PDF. On the other hand, some time-samples $f_n$ do have exactly the same PDF as some other time-samples. The groups of time-samples with the same PDF have curious properties - namely: $n \in \{0, 8\}, n \in \{1 * \text{Odds}\}, n \in \{2 * \text{Odds}\}, n \in \{4 * \text{Odds}\}$. The 'Exhaustive' method gives no insight into why this is so. Again, the 'Combinatorics' method in a later chapter does give the desired insight. Our final comment on this figure is that the CDFs diverge from Gaussian in that they are stepped (due to the discrete PDFs) and that they have finite ranges.

Comparing Figures 5.5 and 5.6, we see the effect of changing from BPSK to QPSK modulation on all of the Data sub-carriers. The number of PDF diracs $N_\delta$ for each IDFT output time-sample $f_n$ has increased in some cases but is still very small compared to the IDFT input alphabet size which, in this case, is $|\mathcal{A}_{\boldsymbol{d}}| = 4^8 = 65,536$. For most of the $f_n$, the PDF/CDF range has increased.

Comparing Figures 5.5 and 5.7, we see the effect of reducing the number of Data sub-carriers and adding Zero and Pilot sub-carriers. In Figure 5.7, we see that the number of PDF diracs $N_\delta$ has been reduced because the IDFT input alphabet size has been reduced to $|\mathcal{A}_{\boldsymbol{d}}| = 2^3 \times 2 = 16$. Also, the groups of time-samples with the same PDF/CDF have changed. Again this will be elucidated by the 'Combinatorics' method in a later section.

The effect of changing from BPSK to QPSK modulation on the Data sub-carriers can be seen by comparing Figure 5.7 to Figure 5.8 where the number of PDF diracs has increased.

Comparing Figures 5.5 and 5.9 , we see the effect of increasing the total number of digital IF sub-carriers $N$ from 16 to 32 whilst using all sub-carriers for BPSK data. The effect is an increase in the number of diracs $N_\delta$ in the PDFs. However, for all of the time-samples $f_n$ in Figure 5.9, $N_\delta$ is very small compared to the IDFT input vector alphabet size $|\mathcal{A}_{\boldsymbol{d}}| = 2^{16} = 65,536$.

Lastly, the effect of using some of the sub-carriers for Zeros and Pilots in the $N = 32$ case can be seen by comparing Figures 5.9 and 5.10. In Figure 5.10, the number of PDF diracs has been reduced and the groupings of time-samples $f_n$ with the same PDF have changed.

### 5.3.7 'Exhaustive' PDF and CDF of All IDFT Output Time-Sample Real-Parts

By taking the expected value of *all* of the PDFs $f_{f_n},\ n \in \mathbb{Z}_N$, of the IDFT output time-sample real-parts $f_n$, we find that the PDF of *all* IDFT output time-sample real-parts is

$$\begin{aligned} f_f(f') &= \mathrm{E}\left[f_{f_n}(f')\right] \\ &= \frac{1}{N}\sum_{n=0}^{N-1} f_{f_n}(f') \\ &= \frac{1}{N}\sum_{n=0}^{N-1}\frac{1}{N_{\boldsymbol{d}}}\sum_{j=1}^{N_{\boldsymbol{d}}}\delta\left(f' - f_{j,n}\right). \end{aligned} \tag{5.21}$$

Next, the CDF of *all* IDFT output time-sample real-parts $f_n$ is equal to the expected value of *all* of the CDFs $F_{f_n}, n \in \mathbb{Z}_N$ of *all* of the IDFT output time-samples real-parts and is given by

$$
\begin{aligned}
F_f(f'') &= \mathrm{E}\left[F_{f_n}(f'')\right] \\
&= \frac{1}{N}\sum_{n=0}^{N-1} F_{f_n}(f'') \\
&= \frac{1}{N \cdot N_{\boldsymbol{d}}}\sum_{n=0}^{N-1}\sum_{f_{j,n} \le f''} 1.
\end{aligned} \tag{5.22}
$$

#### 5.3.7.1 Example Results

Some example results for the PDF $f_f(f')$ and the CDF $F_f(f'')$ are shown in Figure 5.11.

Analysing these results, we first note that the number of PDF diracs $N_\delta$ is small compared to the alphabet size for each OFDM type. For example, the expected IDFT input alphabet size for OFDM Type 1.2 shown in Figure 5.11(a,b) is $|\mathcal{A}_{\boldsymbol{d}}| = 2^8 = 256$ compared to the number of PDF diracs $N_\delta = 75$. Also, the expected alphabet size for OFDM Type 1.4 shown in Figure 5.11(c,d) is $|\mathcal{A}_{\boldsymbol{d}}| = 4^8 = 65,536$ compared to the number of PDF diracs $N_\delta = 409$. Clearly, many different input symbols $\boldsymbol{d}_j, j \in \{1, \cdots, |\mathcal{A}_{\boldsymbol{d}}|\}$ can map to the same PDF dirac. This observation leads to the 'Convolution' method investigated later in this thesis.

Next, comparing Figure 5.11(a,b) to Figure 5.11(c,d), we see that changing from BPSK data to QPSK data increases the number of PDF diracs $N_\delta$ but slightly decreases the PDF range. The increase in $N_\delta$ is due to the IDFT input alphabet size increasing from $|\mathcal{A}_{\boldsymbol{d}}| = 2^8 = 256$ to $|\mathcal{A}_{\boldsymbol{d}}| = 4^8 = 65,536$. The PDF range decrease is attributed to the presence of smaller-sized symbols in the QPSK alphabet $\mathcal{A}_{\mathrm{QPSK}}$ used by each of IDFT input symbol vector entries $d_k$ after the power normalization $\mathrm{E}[f^2] = 1$ has been applied. We also see the same PDF range decrease when from BPSK to QPSK Data sub-carrier modulation for lower numbers of Data sub-carriers when comparing Figure 5.11(e,f) to Figure 5.11(g,h).

Comparing Figure 5.11(a,b) to Figure 5.11(e,f), we see the effect of reducing the number of Data sub-carriers whilst adding Zero and Pilot sub-carriers. Firstly, the number of PDF diracs $N_\delta$ has been reduced due to the reduction of IDFT input alphabet size $|\mathcal{A}_{\boldsymbol{d}}|$. Secondly, the PDF range has been reduced.

Comparing Figure 5.11(a,b) to Figure 5.11(i,j), we see the effect of increasing the total number of digital IF sub-carriers from $N = 16$ to $N = 32$. Firstly, the number of PDF diracs $N_\delta$ has been increased due to the increase of IDFT input alphabet size from $|\mathcal{A}_{\boldsymbol{d}}| = 2^8 = 256$ to $|\mathcal{A}_{\boldsymbol{d}}| = 2^{16} = 65.536$. Nevertheless, it is striking that the number of PDF diracs in Figure 5.11(i,j) is only $N_\delta = 4849$ compared to the IDFT input alphabet sized of $|\mathcal{A}_{\boldsymbol{d}}| = 65,536$.

Comparing Figure 5.11(i,j) to Figure 5.11(k,l), we see the effect of reducing the number of Data sub-carriers whilst adding Zero and Pilot sub-carriers. As expected, the number of PDF diracs $N_\delta$ has been reduced due to the reduction of IDFT input alphabet size $|\mathcal{A}_{\boldsymbol{d}}|$. Secondly, the PDF range has been reduced. However, curiously, some of the large PDF diracs in Figure 5.11(i,j) have disappeared or been reduced in Figure 5.11(k,l). The 'Convolution' method investigated later in this thesis gives insight into this phenomenom.

Lastly, looking at the various CDFs in Figure 5.11, we see that they are fairly close to Gaussian until the the PDF/CDF range is reached; after which they drop to zero. However, a noticeable exception to this exists in Figure 5.11(j) where the CDF value deviates from Gaussian by approximately an order of magnitude for some values of the dummy variable $f''$.

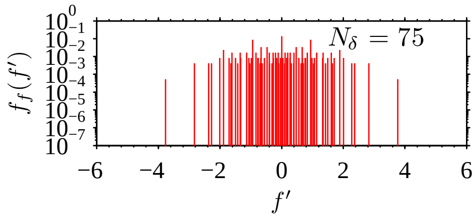


(a) PDF, OFDM Type 1.2.

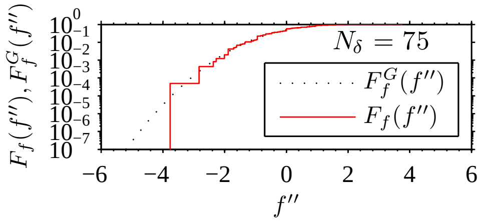


(b) CDFs, OFDM Type 1.2.

OFDM Type 1.2: $N = 16, \mathcal{K}_{\mathrm{SZ}} = \{\}, \mathcal{K}_{\mathrm{SP}} = \{\}, \mathcal{K}_{\mathrm{SD}} = \mathbb{Z}_N, \mathcal{A}_{\mathrm{SD}} = \mathcal{A}_{\mathrm{BPSK}}, \mathrm{E}[f^2] = 1.$

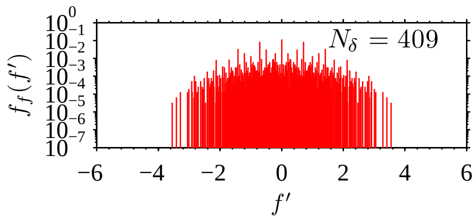


(c) PDF, OFDM Type 1.4.

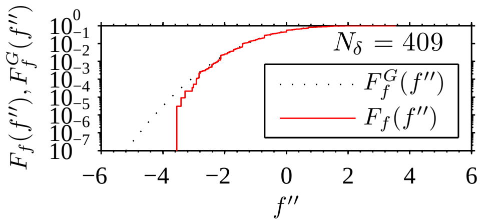


(d) CDFs, OFDM Type 1.4.

OFDM Type 1.4: $N = 16, \mathcal{K}_{\mathrm{SZ}} = \{\}, \mathcal{K}_{\mathrm{SP}} = \{\}, \mathcal{K}_{\mathrm{SD}} = \mathbb{Z}_N, \mathcal{A}_{\mathrm{SD}} = \mathcal{A}_{\mathrm{QPSK}}, \mathrm{E}[f^2] = 1.$

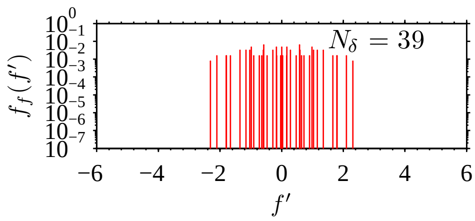


(e) PDF, OFDM Type 2.2.

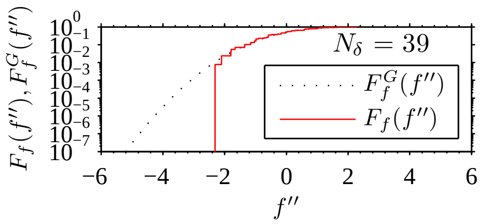


(f) CDFs, OFDM Type 2.2.

OFDM Type 2.2: $N = 16, \mathcal{K}_{\mathrm{SZ}} = \{0, 7, 8, 9\}, \mathcal{K}_{\mathrm{SP}} = \{2, 4, 6, 10, 12, 14\}, \mathcal{A}_{\mathrm{SP}} = \mathcal{A}_{\mathrm{BPSK}},$
$\mathcal{K}_{\mathrm{SD}} = \{1, 3, 5, 11, 13, 15\}, \mathcal{A}_{\mathrm{SD}} = \mathcal{A}_{\mathrm{BPSK}},$
$\mathcal{D}_{\mathrm{SP}} = \{+1, -1, -1, -1, -1, +1\}, \mathrm{E}[f^2] = 1.$

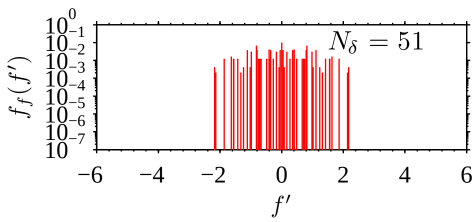


(g) PDF, OFDM Type 2.4.

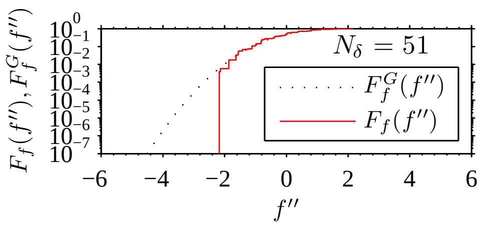


(h) CDFs, OFDM Type 2.4.

OFDM Type 2.4: $N = 16, \mathcal{K}_{\mathrm{SZ}} = \{0, 7, 8, 9\}, \mathcal{K}_{\mathrm{SP}} = \{2, 4, 6, 10, 12, 14\}, \mathcal{A}_{\mathrm{SP}} = \mathcal{A}_{\mathrm{BPSK}},$
$\mathcal{K}_{\mathrm{SD}} = \{1, 3, 5, 11, 13, 15\}, \mathcal{A}_{\mathrm{SD}} = \mathcal{A}_{\mathrm{QPSK}},$
$\mathcal{D}_{\mathrm{SP}} = \{+1, -1, -1, -1, -1, +1\}, \mathrm{E}[f^2] = 1.$

Figure 5.11: 'Exhaustive' PDFs $f_f(f')$, CDFs $F_f(f'')$, and Gaussian approximation CDFs $F_f^G(f'')$ of all IDFT output time-sample real-parts, for various OFDM types.

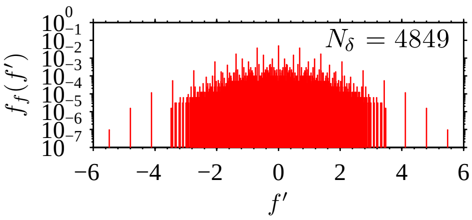


(i) PDF, OFDM Type 3.2.

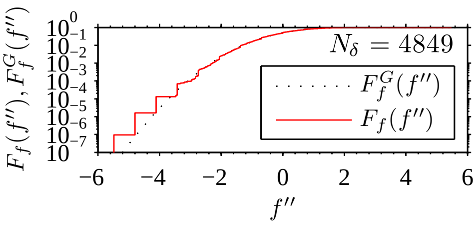


(j) CDFs, OFDM Type 3.2.

OFDM Type 3.2: $N = 32, \mathcal{K}_{\mathrm{SZ}} = \{\}, \mathcal{K}_{\mathrm{SP}} = \{\}, \mathcal{K}_{\mathrm{SD}} = \mathbb{Z}_N, \mathcal{A}_{\mathrm{SD}} = \mathcal{A}_{\mathrm{BPSK}}$, $\mathrm{E}[f^2] = 1$.

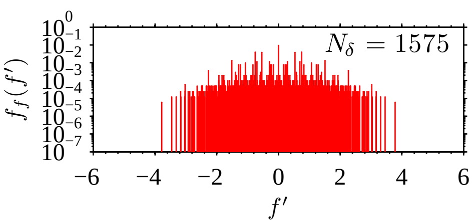


(k) PDF, OFDM Type 4.2.

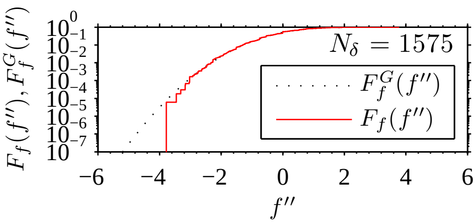


(l) CDFs, OFDM Type 4.2.

OFDM Type 4.2: $N = 32$, $\mathcal{K}_{\mathrm{SZ}} = \{0, 8, 16, 24\}, \mathcal{K}_{\mathrm{SP}} = \{3, 5, 11, 13, 19, 21, 27, 29\}$, $\mathcal{A}_{\mathrm{SP}} = \mathcal{A}_{\mathrm{BPSK}}$,
$\mathcal{K}_{\mathrm{SD}} = \{1, 2, 4, 6, 7, 9, 10, 12, 14, 15, 17, 18, 20, 22, 23, 25, 28, 30, 31\}$, $\mathcal{A}_{\mathrm{SD}} = \mathcal{A}_{\mathrm{BPSK}}$,
$\mathcal{D}_{\mathrm{SP}} = \{-1, +1, -1, +1, +1, -1, +1, -1\}$, $\mathrm{E}[f^2] = 1$.

Figure 5.11: (Cont'd) 'Exhaustive' PDFs $f_f(f')$, CDFs $F_f(f'')$, and Gaussian approximation CDFs $F_f^G(f'')$ of all IDFT output time-sample real-parts, for various OFDM types.

### 5.3.8 'Exhaustive' PDF of the Quantizer Output Time-Sample Vector

The quantized real part $\boldsymbol{g}$ of the IDFT output vector is given by

$$\boldsymbol{g} = \mathrm{Q}\left\{\Re\{\boldsymbol{e}\}\right\} = \mathrm{Q}\left\{\Re\left\{\boldsymbol{F}^{-1}\boldsymbol{d}\right\}\right\}, \tag{5.23}$$

where $\mathrm{Q}\{\cdot\}$ indicates the quantization operation; and the particular instance of $\boldsymbol{g}$ which corresponds to the $j^{\mathrm{th}}$ letter $\boldsymbol{d}_j$ of the IDFT input vector alphabet $\mathcal{A}_{\boldsymbol{d}}$ is therefore given by

$$\boldsymbol{g}_j = \mathrm{Q}\left\{\Re\{\boldsymbol{F}^{-1}\boldsymbol{d}_j\}\right\}. \tag{5.24}$$

The multi-dimensional real PDF of $\boldsymbol{g}$ is therefore

$$f_{\boldsymbol{g}}(\boldsymbol{g}') = \frac{1}{N_{\boldsymbol{d}}}\sum_{j=1}^{N_{\boldsymbol{d}}} \delta\left(\boldsymbol{g}' - \boldsymbol{g}_j\right), \tag{5.25}$$

### 5.3.9 'Exhaustive' Covariance Matrix of the Quantizer Output Time-Sample Vector

The covariance matrix of the quantizer output time-sample vector $\boldsymbol{g}$ is given by

$$\begin{aligned} \mathbf{COV}(\boldsymbol{g}) &= \mathrm{E}\left[\big(\boldsymbol{g} - \mathrm{E}[\boldsymbol{g}]\big)\big(\boldsymbol{g} - \mathrm{E}[\boldsymbol{g}]\big)^{\mathrm{T}}\right] \\ &= \mathrm{E}\left[\boldsymbol{g}\boldsymbol{g}^{\mathrm{T}}\right] - \mathrm{E}\left[\boldsymbol{g}\right]\mathrm{E}\left[\boldsymbol{g}^{\mathrm{T}}\right], \end{aligned} \tag{5.26}$$

which, using (5.24), is expanded to

$$\begin{aligned} \mathbf{COV}(\boldsymbol{g}) = {} & \frac{1}{N_{\boldsymbol{d}}}\sum_{j=1}^{N_{\boldsymbol{d}}}\Big(\mathrm{Q}\left\{\Re\{\boldsymbol{F}^{-1}\boldsymbol{d}_j\}\right\}\Big)\Big(\mathrm{Q}\left\{\Re\{\boldsymbol{F}^{-1}\boldsymbol{d}_j\}\right\}\Big)^{\mathrm{T}} \\ & - \frac{1}{N_{\boldsymbol{d}}^2}\sum_{j=1}^{N_{\boldsymbol{d}}}\Big(\mathrm{Q}\left\{\Re\{\boldsymbol{F}^{-1}\boldsymbol{d}_j\}\right\}\Big)\sum_{j=1}^{N_{\boldsymbol{d}}}\Big(\mathrm{Q}\left\{\Re\{\boldsymbol{F}^{-1}\boldsymbol{d}_j\}\right\}\Big)^{\mathrm{T}}. \end{aligned} \tag{5.27}$$

### 5.3.10 'Exhaustive' Correlation Matrix of the Quantizer Output Time-Sample Vector

The correlation matrix of the quantizer output time-sample vector $\boldsymbol{g}$, in terms of its covariance matrix $\mathbf{COV}(\boldsymbol{g})$ already obtained in (5.27) above, is given by

$$\mathbf{CORR}(\boldsymbol{g}) = \Big(\mathbf{DIAG}[\mathbf{COV}(\boldsymbol{g})]\Big)^{-1/2}\ \mathbf{COV}(\boldsymbol{g})\ \Big(\mathbf{DIAG}[\mathbf{COV}(\boldsymbol{g})]\Big)^{-1/2}. \quad (5.28)$$

### 5.3.11 'Exhaustive' PDF and CDF of Individual Quantizer Output Time-Samples

The $n^{\text{th}}$ time-sample $g_n$ of the quantized real part $\boldsymbol{g}$ of the IDFT output vector is given by

$$g_n = [\boldsymbol{g}]_n = \left[\mathrm{Q}\left\{\Re\left\{\boldsymbol{F}^{-1}\boldsymbol{d}\right\}\right\}\right]_n, \quad (5.29)$$

and the particular instance of $g_n$ which corresponds to the $j^{\text{th}}$ letter $\boldsymbol{d}_j$ of the IDFT input vector alphabet $\mathcal{A}_{\boldsymbol{d}}$ is therefore given by

$$g_{j,n} = \left[\mathrm{Q}\left\{\Re\left\{\boldsymbol{F}^{-1}\boldsymbol{d}_j\right\}\right\}\right]_n. \quad (5.30)$$

The one-dimensional real PDF of $g_n$ is therefore

$$f_{g_n}(g'_n) = \frac{1}{N_{\boldsymbol{d}}}\sum_{j=1}^{N_{\boldsymbol{d}}}\delta\left(g'_n - g_{j,n}\right). \quad (5.31)$$

Next, the CDF of the $n^{\text{th}}$ time-sample $g_n$ of the quantized real part $\boldsymbol{g}$ of the IDFT output is given by

$$\begin{aligned} F_{g_n}(g''_n) &= \int_{-\infty}^{g''_n} f_{g_n}(g'_n)\ \mathrm{d}g'_n \\ &= \int_{-\infty}^{g''_n} \frac{1}{N_{\boldsymbol{d}}}\sum_{j=1}^{N_{\boldsymbol{d}}}\delta\left(g'_n - g_{j,n}\right)\ \mathrm{d}g'_n \\ &= \frac{1}{N_{\boldsymbol{d}}}\sum_{g_{j,n}\le g''_n} 1. \end{aligned} \quad (5.32)$$

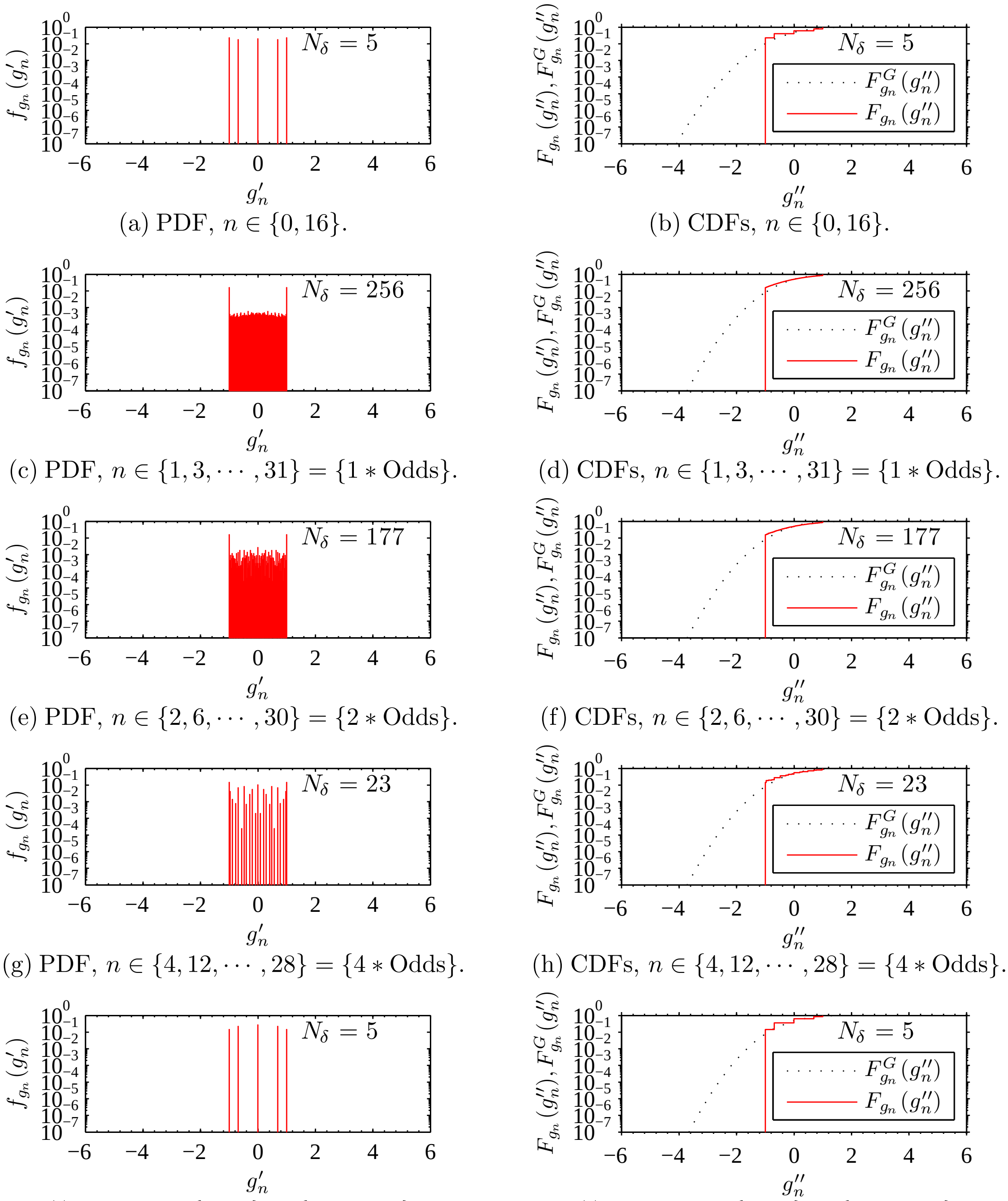

(a) PDF, $n \in \{0, 16\}$. (b) CDFs, $n \in \{0, 16\}$.

(c) PDF, $n \in \{1, 3, \cdots, 31\} = \{1 * \text{Odds}\}$. (d) CDFs, $n \in \{1, 3, \cdots, 31\} = \{1 * \text{Odds}\}$.

(e) PDF, $n \in \{2, 6, \cdots, 30\} = \{2 * \text{Odds}\}$. (f) CDFs, $n \in \{2, 6, \cdots, 30\} = \{2 * \text{Odds}\}$.

(g) PDF, $n \in \{4, 12, \cdots, 28\} = \{4 * \text{Odds}\}$. (h) CDFs, $n \in \{4, 12, \cdots, 28\} = \{4 * \text{Odds}\}$.

(i) PDF, $n \in \{8, 24\} = \{8 * \text{Odds}\}$. (j) CDFs, $n \in \{8, 24\} = \{8 * \text{Odds}\}$.

OFDM Type 3.2: $N = 32, \mathcal{K}_{\text{SZ}} = \{\}, \mathcal{K}_{\text{SP}} = \{\}, \mathcal{K}_{\text{SD}} = \mathbb{Z}_N, \mathcal{A}_{\text{SD}} = \mathcal{A}_{\text{BPSK}}, \text{E}[f^2] = 1.$

Figure 5.12: 'Exhaustive' PDFs $f_{g_n}(g_n')$, CDFs $F_{g_n}(g_n'')$, and Gaussian approximation CDFs $F_{g_n}^G(g_n'')$ of individual quantizer output time-samples, OFDM Type = 3.2, $b = 8, \kappa = 1$ (severe clipping), for various time-sample indeces $n$.

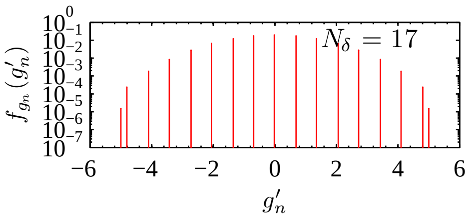


(a) PDF, $n \in \{0, 16\}$.

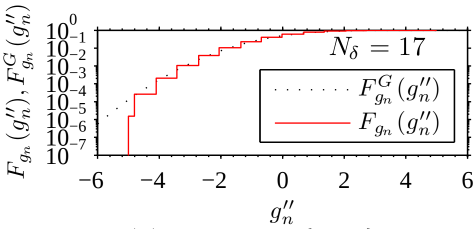


(b) CDFs, $n \in \{0, 16\}$.

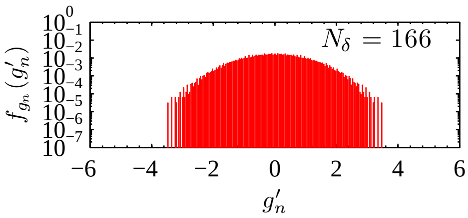


(c) PDF, $n \in \{1, 3, \cdots, 31\} = \{1 * \text{Odds}\}$.

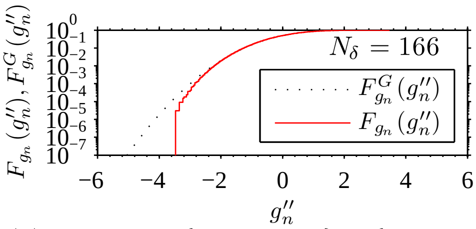


(d) CDFs, $n \in \{1, 3, \cdots, 31\} = \{1 * \text{Odds}\}$.

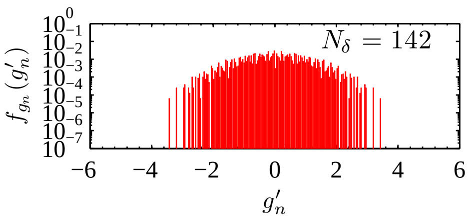


(e) PDF, $n \in \{2, 6, \cdots, 30\} = \{2 * \text{Odds}\}$.

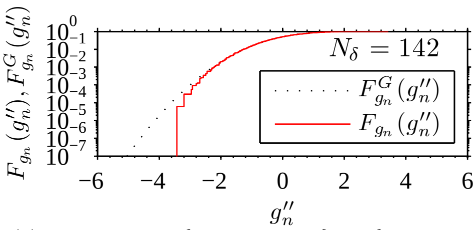


(f) CDFs, $n \in \{2, 6, \cdots, 30\} = \{2 * \text{Odds}\}$.

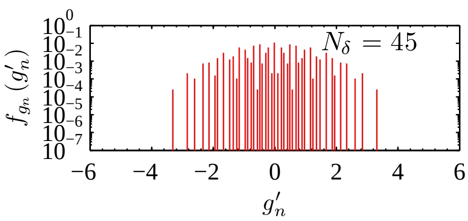


(g) PDF, $n \in \{4, 12, \cdots, 28\} = \{4 * \text{Odds}\}$.

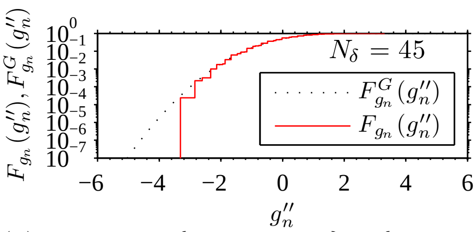


(h) CDFs, $n \in \{4, 12, \cdots, 28\} = \{4 * \text{Odds}\}$.

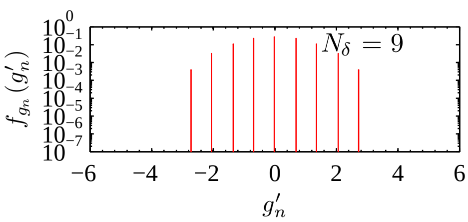


(i) PDF, $n \in \{8, 24\} = \{8 * \text{Odds}\}$.

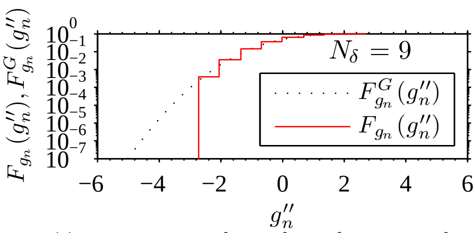


(j) CDFs, $n \in \{8, 24\} = \{8 * \text{Odds}\}$.

OFDM Type 3.2: $N = 32, \mathcal{K}_{\text{SZ}} = \{\}, \mathcal{K}_{\text{SP}} = \{\}, \mathcal{K}_{\text{SD}} = \mathbb{Z}_N, \mathcal{A}_{\text{SD}} = \mathcal{A}_{\text{BPSK}}, \text{E}[f^2] = 1.$

Figure 5.13: 'Exhaustive' PDFs $f_{g_n}(g'_n)$, CDFs $F_{g_n}(g''_n)$, and Gaussian approximation CDFs $F^G_{g_n}(g''_n)$ of individual quantizer output time-samples, OFDM Type $= 3.2$, $b = 8$, $\kappa = 5$ (no clipping), for various time-sample indeces $n$.

#### 5.3.11.1 Example Results

Example results are shown in Figures 5.12 and 5.13.

Beginning with the no clipping case of $\kappa = 5$ in Figure 5.13, we first make the observation that not all of the time samples have exactly the same PDF. In fact, there is quite a wide variation in the number of PDF diracs and the PDF ranges between various groups of time samples.

Next, we note that many of the time samples have exactly the same PDF/CDF as other time samples thus forming groups of time samples each with the same PDF/CDF. These PDF/CDF repetitions are particularly apparent for cases such as ODFM 3.X where all the sub-carriers are used as Data sub-carriers. Insight is given into the reasons for this in section on the 'Combinatorics' method later in this thesis.

The next noticeable feature is that the PDFs for some time samples have small numbers of diracs $N_\delta$ compared to the size of the IDFT input alphabet $|\mathcal{A}_{\boldsymbol{d}}| = 2^{16} = 65,536$ for this case of OFDM Type 3.2. For example in Figure 5.13(a), $N_\delta = 17$ compared to $|\mathcal{A}_{\boldsymbol{d}}| = 65,536$ for samples $n \in \{0, 16\}$. In all other cases $N_\delta \ll |\mathcal{A}_{\boldsymbol{d}}|$. Again, insight is given into this in the later section on the 'Combinatorics' method.

Comparing the above-discussed no clipping case of $\kappa = 5$ in Figure 5.13 with the severe clipping case of $\kappa = 1$ in Figure 5.12, we can see (particularly in Figure 5.12(e)) that the tails of the PDFs for the unclipped case have been aggregated into the extreme negative and positive PDF diracs (representing the clip level) for the severe clipped case.

### 5.3.12 'Exhaustive' PDF and CDF of All Quantizer Output Time-Samples

By taking the expected value of *all* of the PDFs $f_{g_n}$, $n \in \mathbb{Z}_N$, of *all* of the quantized real parts $g_n$, $n \in \mathbb{Z}_N$ of the IDFT output time-samples, we find that the overall PDF of *all* of the quantized real parts $g_n, n \in \mathbb{Z}_N$, of the IDFT output time-samples is

$$f_g(g') = \mathrm{E}\left[f_{g_n}(g')\right] = \frac{1}{N}\sum_{n=0}^{N-1} f_{g_n}(g'). \tag{5.33}$$

Next, the CDF of *all* of the quantized real parts $g_n,\ n \in \mathbb{Z}_N$ of the IDFT output time-samples, is equal to the expected value of *all* of the CDFs $F_{g_n}, n \in \mathbb{Z}_N$ of the quantized real parts $g_n,\ n \in \mathbb{Z}_N$ of *all* of the IDFT output time-samples and is given by

$$\begin{aligned} F_g(g'') &= \mathrm{E}\left[F_{g_n}(g'')\right] \\ &= \frac{1}{N}\sum_{n=0}^{N-1} F_{g_n}(g'') \\ &= \frac{1}{N \cdot N_{\boldsymbol{d}}}\sum_{n=0}^{N-1}\sum_{g_{j,n}\le g''} 1. \end{aligned} \tag{5.34}$$

#### 5.3.12.1 Example Results

Example results are shown in Figures 5.14 and 5.15.

Figure 5.15 shows the effect of the normalized clipping level $\kappa$ on the PDF/CDF of all of the IDFT output time-samples when clipping only (no granular quantization) is applied. For the severe clipping case of $\kappa = 1$ shown in Figures 5.15(a,b), the probability of clipping is aggregated into the diracs at the positive and negative extremes of the PDF. As the clipping becomes less severe, the normalized clipping level $\kappa$ transits from 1 (severe clipping) to 5 (no clipping) in Figures 5.15 (a,c,e,g,i) resulting in increased PDF ranges and reduced probabilities of clipping in the positive and negative dirac extremes.

Figure 5.14 shows the same effect of the normalized clipping level $\kappa$ on the PDF/CDF of all of the IDFT output time-samples when 8-bit granular quantization is applied. The main difference between Figures 5.14 and 5.15 is the much smaller number of PDF diracs in Figure 5.15 due to the finite number of quantizer output levels ($2^8 = 256$) for 8-bit granular quantization.

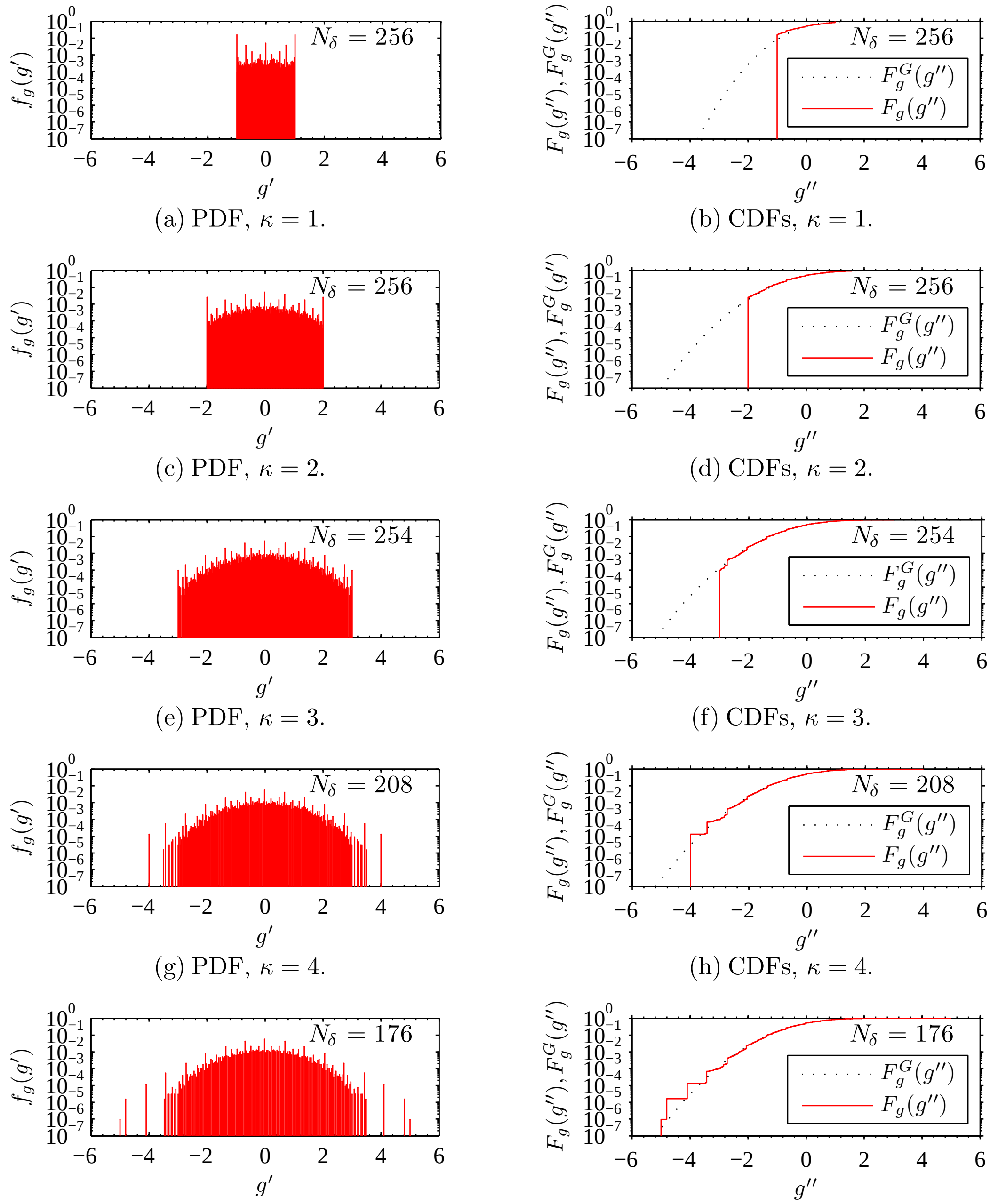


(a) PDF, $\kappa = 1$. (b) CDFs, $\kappa = 1$.

(c) PDF, $\kappa = 2$. (d) CDFs, $\kappa = 2$.

(e) PDF, $\kappa = 3$. (f) CDFs, $\kappa = 3$.

(g) PDF, $\kappa = 4$. (h) CDFs, $\kappa = 4$.

(i) PDF, $\kappa = 5$. (j) CDFs, $\kappa = 5$.

OFDM Type 3.2: $N = 32, \mathcal{K}_{\mathrm{SZ}} = \{\}, \mathcal{K}_{\mathrm{SP}} = \{\}, \mathcal{K}_{\mathrm{SD}} = \mathbb{Z}_N, \mathcal{A}_{\mathrm{SD}} = \mathcal{A}_{\mathrm{BPSK}}, \mathrm{E}[f^2] = 1.$

Figure 5.14: ‘Exhaustive’ $f_g(g')$, CDFs $F_g(g'')$, and Gaussian approximation CDFs $F_g^G(g'')$ of all quantizer output time-samples, OFDM Type = 3.2, $b = 8$, for various clipping-factors $\kappa$.

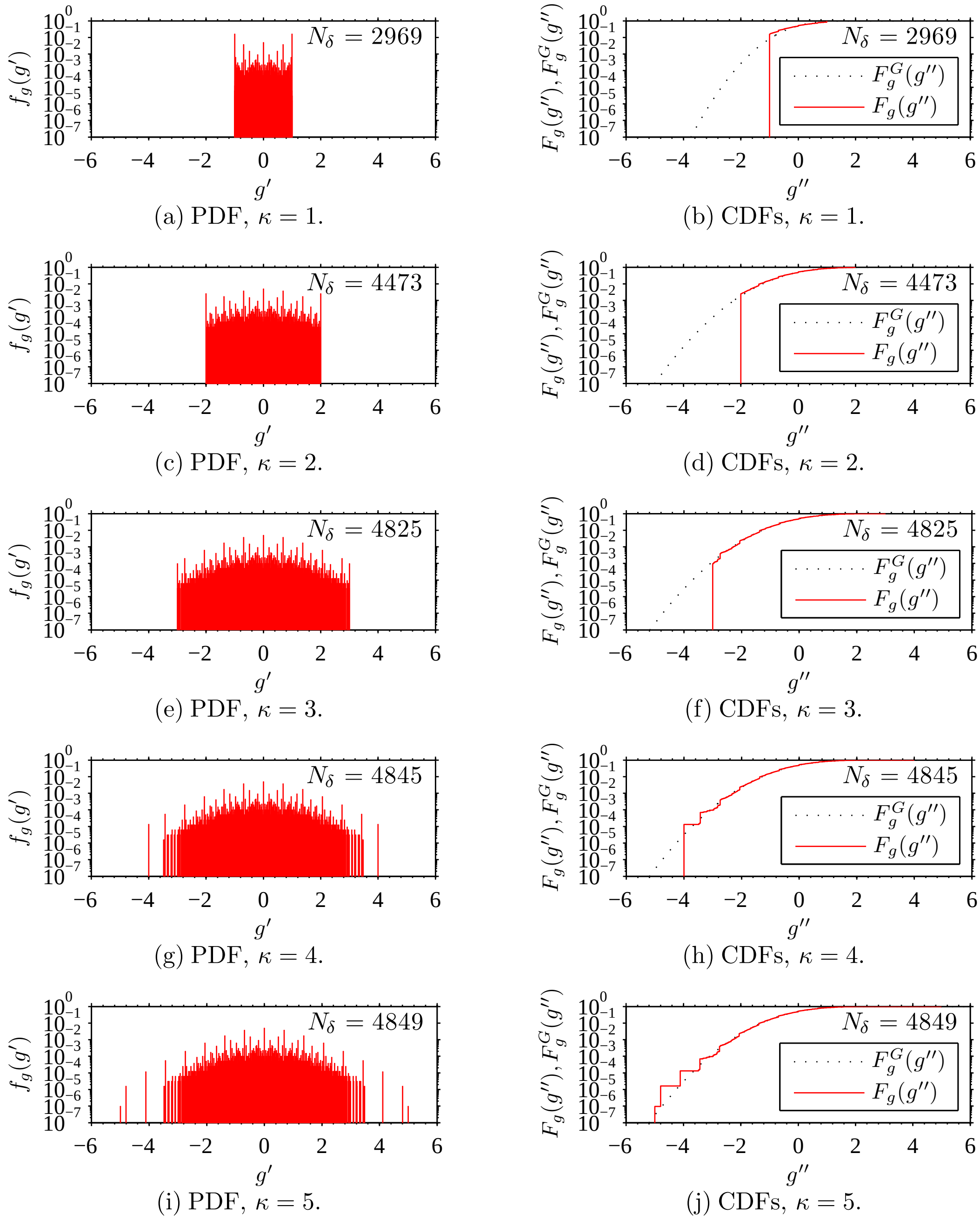


(a) PDF, $\kappa = 1$. (b) CDFs, $\kappa = 1$.

(c) PDF, $\kappa = 2$. (d) CDFs, $\kappa = 2$.

(e) PDF, $\kappa = 3$. (f) CDFs, $\kappa = 3$.

(g) PDF, $\kappa = 4$. (h) CDFs, $\kappa = 4$.

(i) PDF, $\kappa = 5$. (j) CDFs, $\kappa = 5$.

OFDM Type 3.2: $N = 32, \mathcal{K}_{\mathrm{SZ}} = \{\}, \mathcal{K}_{\mathrm{SP}} = \{\}, \mathcal{K}_{\mathrm{SD}} = \mathbb{Z}_N, \mathcal{A}_{\mathrm{SD}} = \mathcal{A}_{\mathrm{BPSK}}, \mathrm{E}[f^2] = 1$.

Figure 5.15: 'Exhaustive' $f_g(g')$, CDFs $F_g(g'')$, and Gaussian approximation CDFs $F_g^G(g'')$ of all quantizer output time-samples, OFDM Type = 3.2, $b = \infty$ (clipping only), for various clipping-factors $\kappa$.

### 5.3.13 'Exhaustive' PDF of the Quantizer Error Time-Sample Vector

The quantizer error time-sample vector $\boldsymbol{q}$ is given by

$$\begin{aligned}\boldsymbol{q} &= \boldsymbol{g} - \beta\boldsymbol{f} \\ &= \mathrm{Q}\{\boldsymbol{f}\} - \beta\boldsymbol{f} \\ &= \mathrm{Q}\left\{\Re\left\{\boldsymbol{F}^{-1}\boldsymbol{d}\right\}\right\} - \beta\Re\left\{\boldsymbol{F}^{-1}\boldsymbol{d}\right\},\end{aligned} \tag{5.35}$$

and the particular instance of $\boldsymbol{q}$ which corresponds to the $j^{\mathrm{th}}$ letter $\boldsymbol{d}_j$ of the IDFT input vector alphabet $\mathcal{A}_{\boldsymbol{d}}$ is therefore given by

$$\boldsymbol{q}_j = \mathrm{Q}\left\{\Re\left\{\boldsymbol{F}^{-1}\boldsymbol{d}_j\right\}\right\} - \beta\Re\left\{\boldsymbol{F}^{-1}\boldsymbol{d}_j\right\}. \tag{5.36}$$

The multi-dimensional real PDF of $\boldsymbol{q}$ is therefore

$$f_{\boldsymbol{q}}(\boldsymbol{q}') = \frac{1}{N_{\boldsymbol{d}}}\sum_{j=1}^{N_{\boldsymbol{d}}}\delta\left(\boldsymbol{q}' - \boldsymbol{q}_j\right). \tag{5.37}$$

### 5.3.14 'Exhaustive' Covariance Matrix of the Quantizer Error Time-Sample Vector

The covariance matrix of the quantizer error time-sample vector $\boldsymbol{q}$ is given by

$$\begin{aligned}\mathbf{COV}(\boldsymbol{q}) &= \mathrm{E}\left[\left(\boldsymbol{q} - \mathrm{E}[\boldsymbol{q}]\right)\left(\boldsymbol{q} - \mathrm{E}[\boldsymbol{q}]\right)^{\mathrm{T}}\right] \\ &= \mathrm{E}\left[\boldsymbol{q}\boldsymbol{q}^{\mathrm{T}}\right] - \mathrm{E}\left[\boldsymbol{q}\right]\mathrm{E}\left[\boldsymbol{q}^{\mathrm{T}}\right],\end{aligned} \tag{5.38}$$

which, using (5.36), is expanded to

$$\begin{aligned}\mathbf{COV}(\boldsymbol{q}) \;=\;& \frac{1}{N_{\boldsymbol{d}}}\sum_{j=1}^{N_{\boldsymbol{d}}}\Big(\mathrm{Q}\left\{\Re\left\{\boldsymbol{F}^{-1}\boldsymbol{d}_j\right\}\right\}-\beta\Re\left\{\boldsymbol{F}^{-1}\boldsymbol{d}_j\right\}\Big)\;\Big(\mathrm{Q}\left\{\Re\left\{\boldsymbol{F}^{-1}\boldsymbol{d}_j\right\}\right\}-\beta\Re\left\{\boldsymbol{F}^{-1}\boldsymbol{d}_j\right\}\Big)^{\mathrm{T}}\\ &-\frac{1}{N_{\boldsymbol{d}}^2}\sum_{j=1}^{N_{\boldsymbol{d}}}\Big(\mathrm{Q}\left\{\Re\left\{\boldsymbol{F}^{-1}\boldsymbol{d}_j\right\}\right\}-\beta\Re\left\{\boldsymbol{F}^{-1}\boldsymbol{d}_j\right\}\Big)\;\sum_{j=1}^{N_{\boldsymbol{d}}}\Big(\mathrm{Q}\left\{\Re\left\{\boldsymbol{F}^{-1}\boldsymbol{d}_j\right\}\right\}-\beta\Re\left\{\boldsymbol{F}^{-1}\boldsymbol{d}_j\right\}\Big)^{\mathrm{T}}.\end{aligned} \tag{5.39}$$

### 5.3.15 'Exhaustive' Correlation Matrix of the Quantizer Error Time-Sample Vector

The correlation matrix of the quantizer output time-sample vector $\boldsymbol{q}$, in terms of its covariance matrix $\mathbf{COV}(\boldsymbol{q})$ already obtained in (5.39) above, is given by

$$\mathbf{CORR}(\boldsymbol{q})=\Big(\mathbf{DIAG}[\mathbf{COV}(\boldsymbol{q})]\Big)^{-1/2}\;\mathbf{COV}(\boldsymbol{q})\;\Big(\mathbf{DIAG}[\mathbf{COV}(\boldsymbol{q})]\Big)^{-1/2}. \tag{5.40}$$

### 5.3.16 'Exhaustive' PDF and CDF of Individual Quantizer Error Time-Samples

The $n^{\text{th}}$ time-sample of the quantizer error is given by

$$q_n=[\boldsymbol{q}]_n=\left[\mathrm{Q}\left\{\Re\left\{\boldsymbol{F}^{-1}\boldsymbol{d}\right\}\right\}-\beta\Re\left\{\boldsymbol{F}^{-1}\boldsymbol{d}\right\}\right]_n, \tag{5.41}$$

and the particular instance of $q_n$ which corresponds to the $j^{\text{th}}$ letter $\boldsymbol{d}_j$ of the IDFT input vector alphabet $\mathcal{A}_{\boldsymbol{d}}$ is therefore given by

$$q_{j,n}=\left[\boldsymbol{q}_j\right]_n=\left[\mathrm{Q}\left\{\Re\left\{\boldsymbol{F}^{-1}\boldsymbol{d}_j\right\}\right\}-\beta\Re\left\{\boldsymbol{F}^{-1}\boldsymbol{d}_j\right\}\right]_n. \tag{5.42}$$

The one-dimensional real PDF of $q_n$ therefore

$$f_{q_n}(q_n')=\frac{1}{N_{\boldsymbol{d}}}\sum_{j=1}^{N_{\boldsymbol{d}}}\delta\left(q_n'-q_{j,n}\right). \tag{5.43}$$

Next, the CDF of the $n^{\text{th}}$ time-sample $q_n$ of the quantizer error vector $\boldsymbol{q}$ is given by

$$\begin{aligned} F_{q_n}(q_n'') &= \int_{-\infty}^{q_n''} f_{q_n}(q_n') \ \mathrm{d}q_n' \\ &= \int_{-\infty}^{q_n''} \frac{1}{N_{\boldsymbol{d}}} \sum_{j=1}^{N_{\boldsymbol{d}}} \delta\left(q_n' - q_{j,n}\right) \ \mathrm{d}q_n' \\ &= \frac{1}{N_{\boldsymbol{d}}} \sum_{q_{j,n} \leq q_n''} 1. \end{aligned} \tag{5.44}$$

#### 5.3.16.1 Example Results

Example results are shown in Figures 5.16 and 5.17.

We first note that the black vertical dotted lines appearing in Figures 5.16 and subsequent similar figures represent the quantizer step boundaries at $\pm\Delta/2$. For clarity, $\Delta/2$ is also displayed numerically on each of the plots.

Now, beginning with the $\kappa = 6$ (no clipping) case in Figure 5.17, we note that the quantizer error PDFs are not continuous, but are discrete as indicated by the presence of the PDF diracs. This is caused by the fact that quantizer input (IDFT output) and quantizer output PDFs are both discrete themselves. Secondly, we note that the number of PDF diracs is very small in some cases compared to the IDFT input alphabet size $\mathcal{A}_{\boldsymbol{f}} = 2^8 = 256$. Next, we note that not all of the PDFs/CDFs for each time sample $n$ are the same. However, curiously, sub-groups of time samples $n$ have the same PDF. Moving on, we note that the error PDF range is confined to within half of the quantizer step-size $\Delta/2$. This is because there is no clipping. Lastly, we note that the large steps in some of the CDFs indicate a significant divergence from a uniform distribution which would manifest itself as a straight-line CDF.

Referring to Figure 5.16, we see the effect of severe clipping with $\kappa = 1$. Most noticeably, we observe that the PDF range now significantly exceeds half of the quantizer step-size $\Delta/2$ due to the clipping.

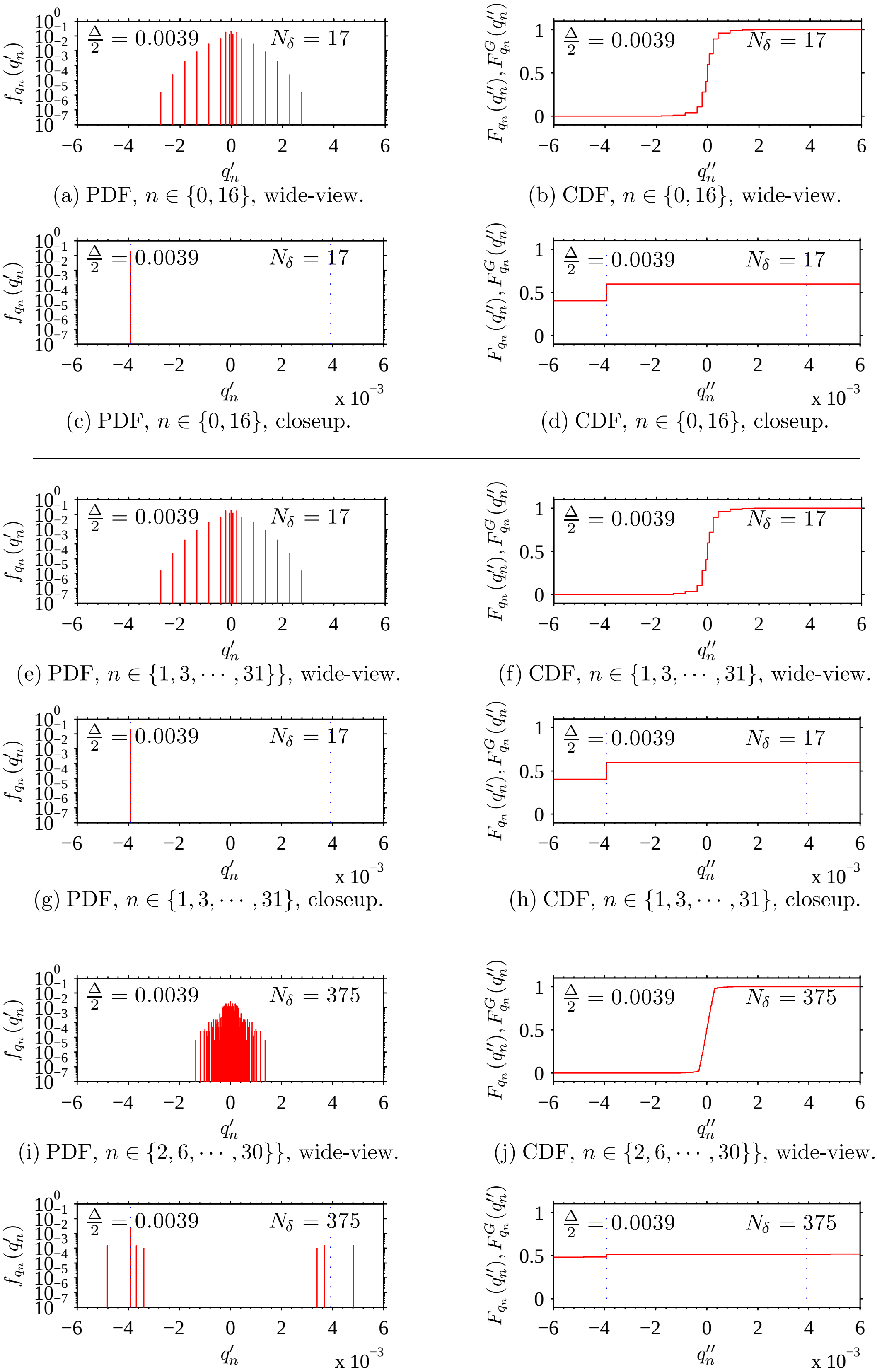


(a) PDF, $n \in \{0, 16\}$, wide-view.

(b) CDF, $n \in \{0, 16\}$, wide-view.

(c) PDF, $n \in \{0, 16\}$, closeup.

(d) CDF, $n \in \{0, 16\}$, closeup.

(e) PDF, $n \in \{1, 3, \cdots, 31\}\}$, wide-view.

(f) CDF, $n \in \{1, 3, \cdots, 31\}$, wide-view.

(g) PDF, $n \in \{1, 3, \cdots, 31\}$, closeup.

(h) CDF, $n \in \{1, 3, \cdots, 31\}$, closeup.

(i) PDF, $n \in \{2, 6, \cdots, 30\}\}$, wide-view.

(j) CDF, $n \in \{2, 6, \cdots, 30\}\}$, wide-view.

(k) PDF, $n \in \{2, 6, \cdots, 30\}$, closeup.

(l) CDF, $n \in \{2, 6, \cdots, 30\}$, closeup.

OFDM Type 3.2: $N = 32, \mathcal{K}_{\text{SZ}} = \{\}, \mathcal{K}_{\text{SP}} = \{\}, \mathcal{K}_{\text{SD}} = \mathbb{Z}_N, \mathcal{A}_{\text{SD}} = \mathcal{A}_{\text{BPSK}}, \text{E}[f^2] = 1.$

Figure 5.16: 'Exhaustive' PDFs $f_{q_n}(q'_n)$ and CDFs $F_{q_n}(q''_n)$ of individual quantizer error time-samples, OFDM Type $= 3.2$, $b = 8, \kappa = 1$, (severe clipping), for various time-sample indeces $n$.

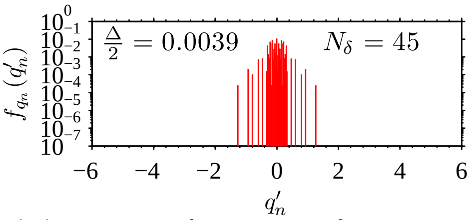

(m) PDF, $n \in \{4, 12, \cdots, 28\}$, wide-view.

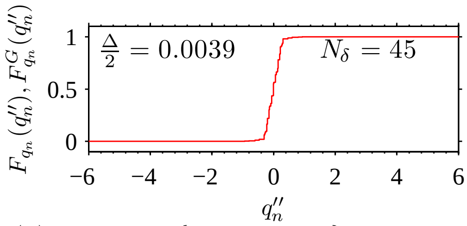

(n) CDF, $n \in \{4, 12, \cdots, 28\}$, wide-view.

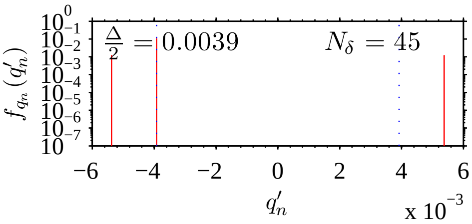

(o) PDF, $n \in \{4, 12, \cdots, 28\}$, closeup.

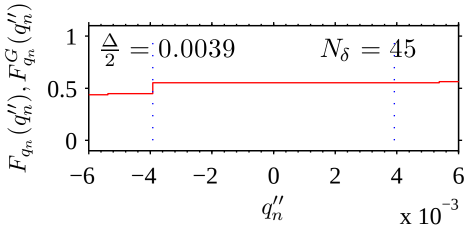

(p) CDF, $n \in \{4, 12, \cdots, 28\}$, closeup.

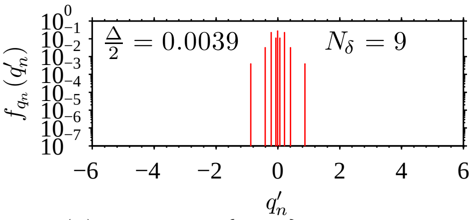

(q) PDF, $n \in \{8, 24\}$, wide-view.

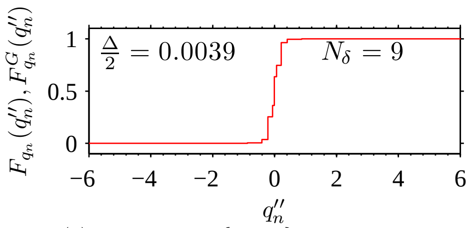

(r) CDF, $n \in \{8, 24\}$, wide-view.

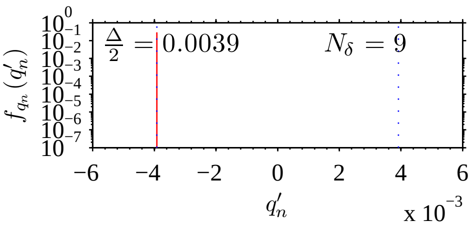

(s) PDF, $n \in \{8, 24\}$, closeup.

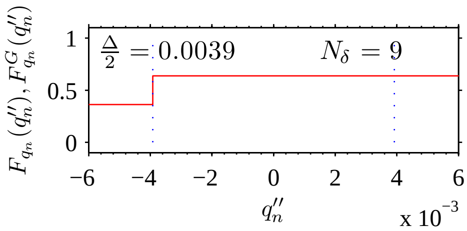

(t) CDF, $n \in \{8, 24\}$, closeup.

OFDM Type 3.2: $N = 32, \mathcal{K}_{\rm SZ} = \{\}, \mathcal{K}_{\rm SP} = \{\}, \mathcal{K}_{\rm SD} = \mathbb{Z}_N, \mathcal{A}_{\rm SD} = \mathcal{A}_{\rm BPSK}, {\rm E}[f^2] = 1.$

Figure 5.16: (Cont'd) 'Exhaustive' PDFs $f_{q_n}(q'_n)$ and CDFs $F_{q_n}(q''_n)$ of individual quantizer error time-samples, OFDM Type = 3.2, $b = 8, \kappa = 1$ (severe clipping), for various time-sample indeces $n$.

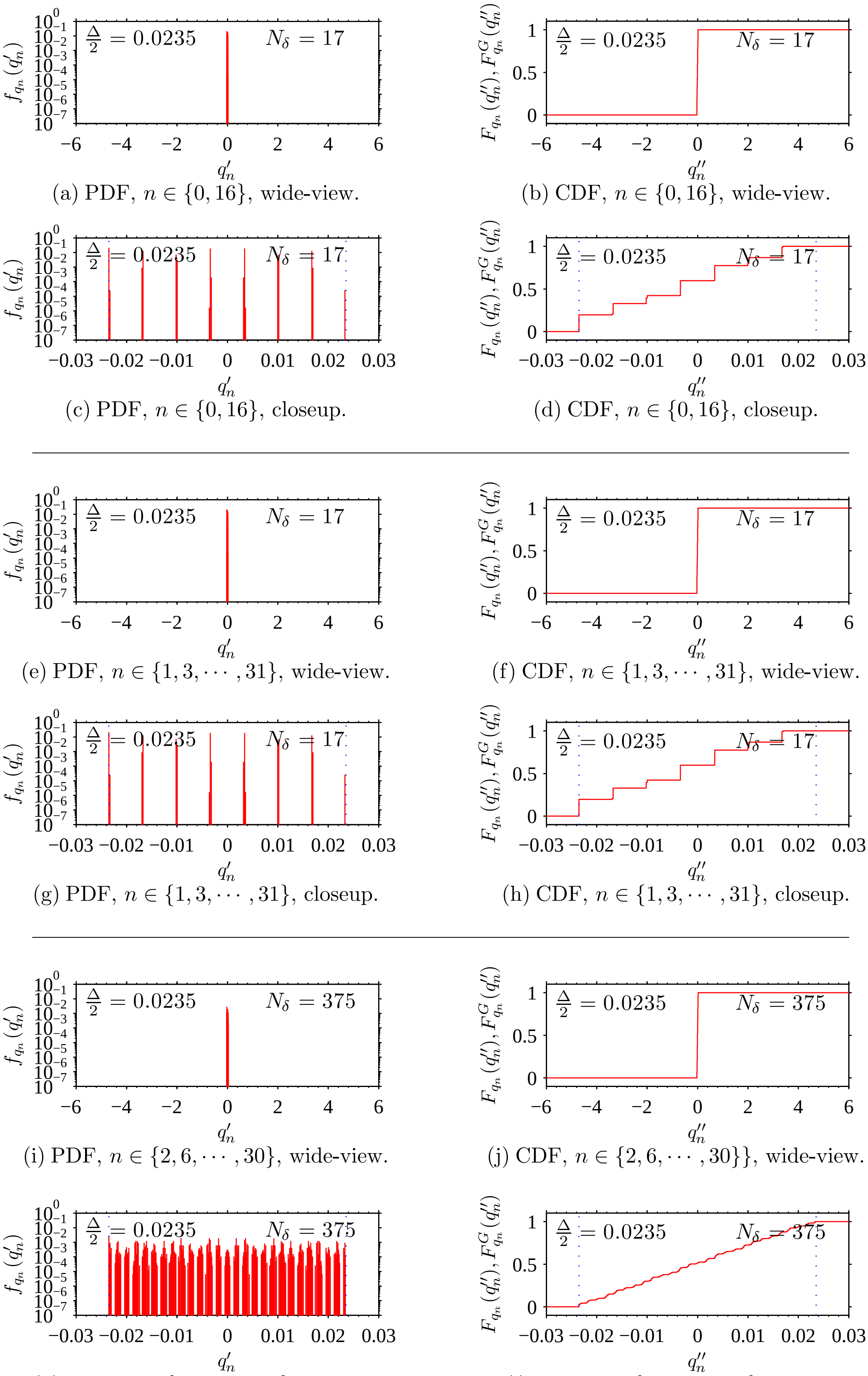


(a) PDF, $n \in \{0, 16\}$, wide-view.

(b) CDF, $n \in \{0, 16\}$, wide-view.

(c) PDF, $n \in \{0, 16\}$, closeup.

(d) CDF, $n \in \{0, 16\}$, closeup.

(e) PDF, $n \in \{1, 3, \cdots, 31\}$, wide-view.

(f) CDF, $n \in \{1, 3, \cdots, 31\}$, wide-view.

(g) PDF, $n \in \{1, 3, \cdots, 31\}$, closeup.

(h) CDF, $n \in \{1, 3, \cdots, 31\}$, closeup.

(i) PDF, $n \in \{2, 6, \cdots, 30\}$, wide-view.

(j) CDF, $n \in \{2, 6, \cdots, 30\}\}$, wide-view.

(k) PDF, $n \in \{2, 6, \cdots, 30\}$, closeup.

(l) CDF, $n \in \{2, 6, \cdots, 30\}$, closeup.

OFDM Type 3.2: $N = 32, \mathcal{K}_{\text{SZ}} = \{\}, \mathcal{K}_{\text{SP}} = \{\}, \mathcal{K}_{\text{SD}} = \mathbb{Z}_N, \mathcal{A}_{\text{SD}} = \mathcal{A}_{\text{BPSK}}, \text{E}[f^2] = 1.$

Figure 5.17: 'Exhaustive' $f_{q_n}(q'_n)$ and CDFs $F_{q_n}(q''_n)$ of individual quantizer error time-samples, OFDM Type $= 3.2$, $b = 8$, $\kappa = 6$ (no clipping), for various time-sample indeces $n$.

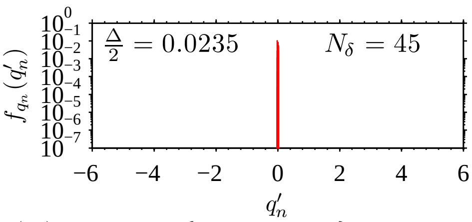


(m) PDF, $n \in \{4, 12, \cdots, 28\}$, wide-view.

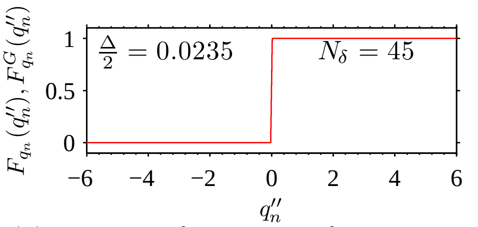


(n) CDF, $n \in \{4, 12, \cdots, 28\}$, wide-view.

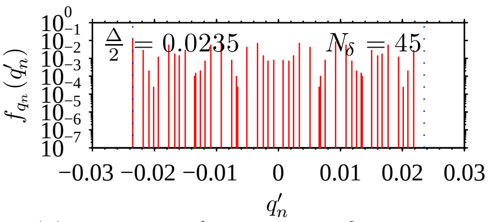


(o) PDF, $n \in \{4, 12, \cdots, 28\}$, closeup.

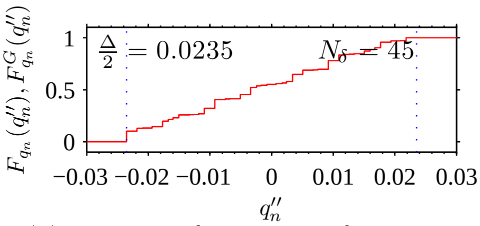


(p) CDF, $n \in \{4, 12, \cdots, 28\}$, closeup.

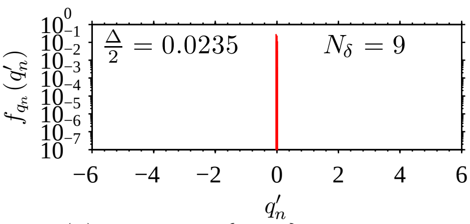


(q) PDF, $n \in \{8, 24\}$, wide-view.

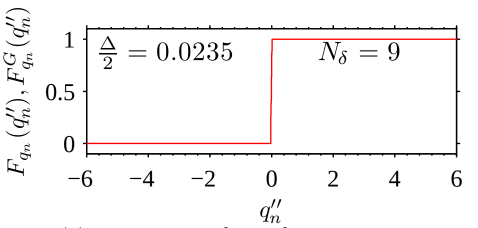


(r) CDF, $n \in \{8, 24\}$, wide-view.

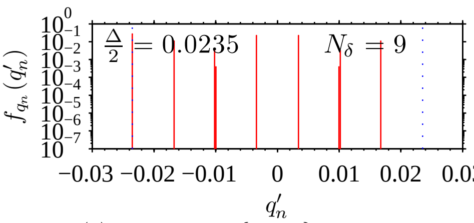


(s) PDF, $n \in \{8, 24\}$, closeup.

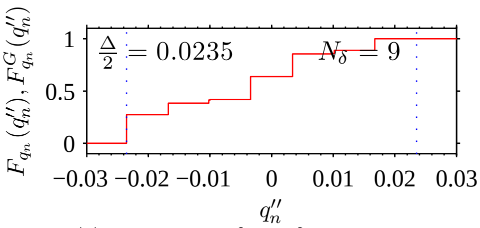


(t) CDF, $n \in \{8, 24\}$, closeup.

OFDM Type 3.2: $N = 32, \mathcal{K}_{\text{SZ}} = \{\}, \mathcal{K}_{\text{SP}} = \{\}, \mathcal{K}_{\text{SD}} = \mathbb{Z}_N, \mathcal{A}_{\text{SD}} = \mathcal{A}_{\text{BPSK}}, \text{E}[f^2] = 1.$

Figure 5.17: (Cont'd) 'Exhaustive' PDFs $f_{q_n}(q'_n)$ and CDFs $F_{q_n}(q''_n)$ of individual quantizer error time-samples, OFDM Type = 3.2, $b = 8, \kappa = 6$ (no clipping), for various time-sample indeces $n$.

### 5.3.17 'Exhaustive' PDF and CDF of All Quantizer Error Time-Samples

By taking the expected value of *all* of the PDFs $f_{q_n},\ n \in \mathbb{Z}_N$, of *all* of the quantizer error time-samples $q_n,\ n \in \mathbb{Z}_N$, we find that the overall PDF of *all* of the quantizer error time-samples $q_n, n \in \mathbb{Z}_N$, is

$$f_q(q') = \mathrm{E}\left[f_{q_n}(q')\right] = \frac{1}{N}\sum_{n=0}^{N-1} f_{q_n}(q'). \tag{5.45}$$

Next, the CDF of *all* of the quantizer error time-samples $q_n, n \in \mathbb{Z}_N$, is equal to the expected value of *all* of the CDFs $F_{q_n},\ n \in \mathbb{Z}_N$ of *all* of the individual time-samples $q_n, n \in \mathbb{Z}_N$ and is given by

$$\begin{aligned} F_q(q'') &= \mathrm{E}\left[F_{q_n}(q'')\right] \\ &= \frac{1}{N}\sum_{n=0}^{N-1} F_{q_n}(q'') \\ &= \frac{1}{N \cdot N_{\boldsymbol{d}}}\sum_{n=0}^{N-1}\sum_{q_{j,n} \leq q''} 1. \end{aligned} \tag{5.46}$$

#### 5.3.17.1 Example Results

Example results are shown in Figures 5.18 and 5.19.

Beginning with the $b = \infty$ (clipping only, no granular quantization) case in Figure 5.19, we first note that for no clipping as shown in Figure 5.19(s,t) the quantizer error is zero with probability unity. Transiting backwards from Figure 5.19(u,v,w,x) to (a,b,c,d), we observe the effect of increased clipping only (without granular quantization) as the normalized clipping factor decreases from $\kappa = 6$ (no clipping) to $\kappa = 1$ (severe clipping). Clearly, the PDF/CDF range increases as the clipping becomes more severe.

Now, referring to Figure 5.18, we see the added effect of quantization with 8 bits for the same normalized clipping levels as in Figure 5.19. Comparing the no clipping, 8-bit quantization case in Figure 5.18(u,v,w,x) to the no clipping, no granular quantization case in 5.19(u,v,w,x), we clearly see that the granular quantization noise dominates when there is no clipping. However, comparing the severe clipping, 8-bit quantization case in Figure 5.18(a,b,c,d) to the severe clipping, no granular quantization case in 5.19(a,b,c,d), we clearly see that the clipping noise dominates when there is severe clipping. This illustrates the trade-off between clipping noise and granular quantization noise which must be optimized by setting the normalized clipping factor $\kappa$ to achieve the maximal signal to quantization and clipping noise ratio.

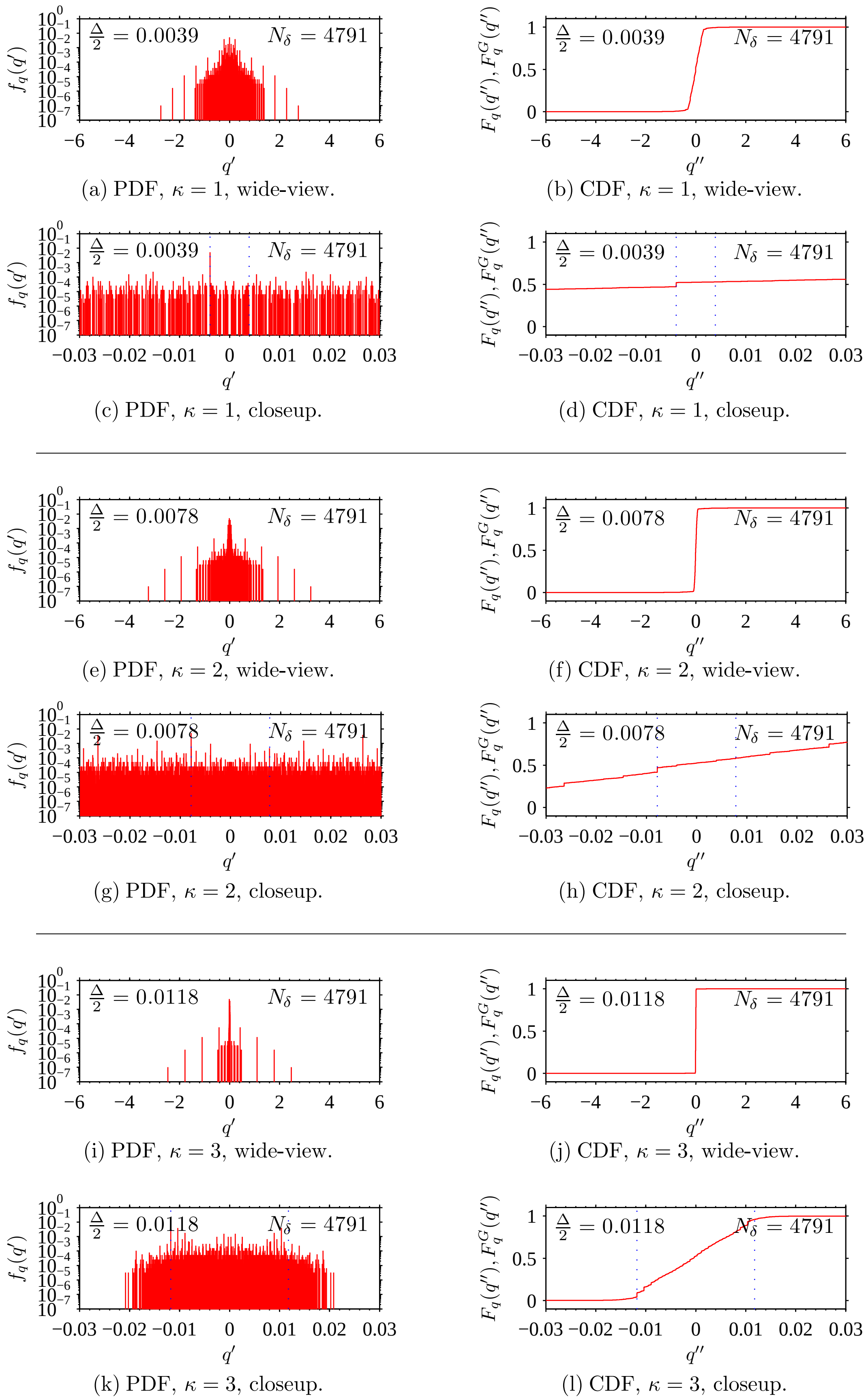

(a) PDF, $\kappa = 1$, wide-view. (b) CDF, $\kappa = 1$, wide-view.

(c) PDF, $\kappa = 1$, closeup. (d) CDF, $\kappa = 1$, closeup.

(e) PDF, $\kappa = 2$, wide-view. (f) CDF, $\kappa = 2$, wide-view.

(g) PDF, $\kappa = 2$, closeup. (h) CDF, $\kappa = 2$, closeup.

(i) PDF, $\kappa = 3$, wide-view. (j) CDF, $\kappa = 3$, wide-view.

(k) PDF, $\kappa = 3$, closeup. (l) CDF, $\kappa = 3$, closeup.

OFDM Type 3.2: $N = 32, \mathcal{K}_{\rm SZ} = \{\}, \mathcal{K}_{\rm SP} = \{\}, \mathcal{K}_{\rm SD} = \mathbb{Z}_N, \mathcal{A}_{\rm SD} = \mathcal{A}_{\rm BPSK}, \mathrm{E}[f^2] = 1.$

Figure 5.18: 'Exhaustive' PDFs $f_q(q')$ and CDFs $F_q(q'')$ of all quantizer error time-samples, OFDM Type $= 3.2$, $b = 8$, for various clipping-factors $\kappa$.

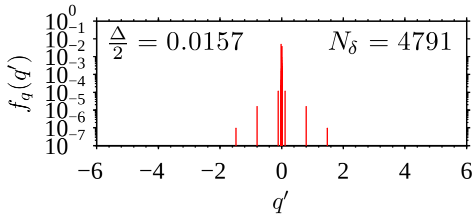


(m) PDF, $\kappa = 4$, wide-view.

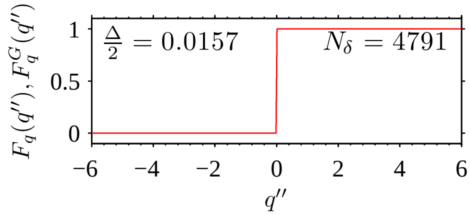


(n) CDF, $\kappa = 4$, wide-view.

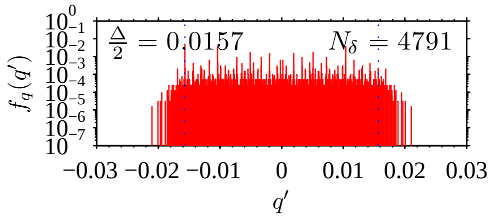


(o) PDF, $\kappa = 4$, closeup.

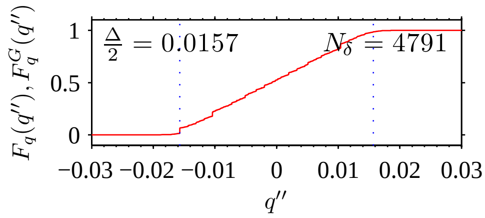


(p) CDF, $\kappa = 4$, closeup.

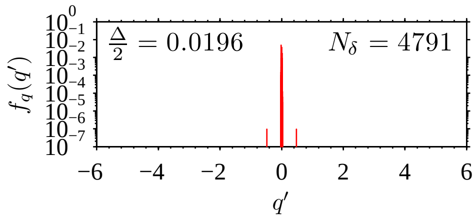


(q) PDF, $\kappa = 5$, wide-view.

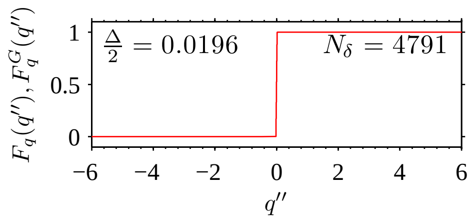


(r) CDF, $\kappa = 5$, wide-view.

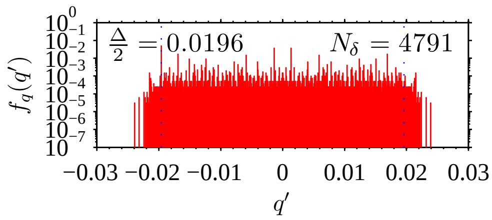


(s) PDF, $\kappa = 5$, closeup.

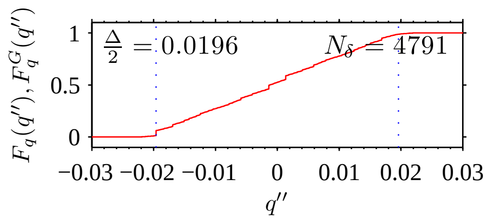


(t) CDF, $\kappa = 5$, closeup.

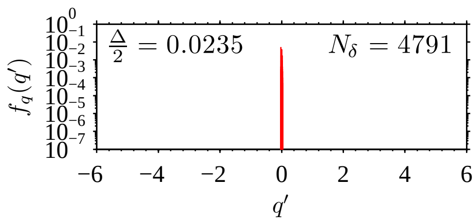


(u) PDF, $\kappa = 6$ (no clipping), wide-view.

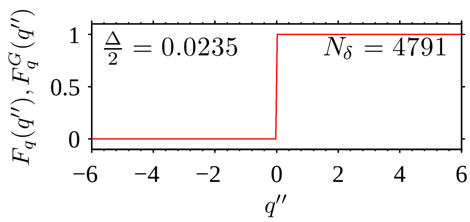


(v) CDF, $\kappa = 6$ (no clipping), wide-view.

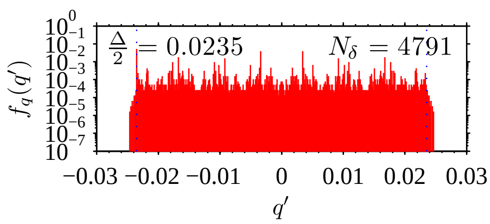


(w) PDF, $\kappa = 6$ (no clipping), closeup.

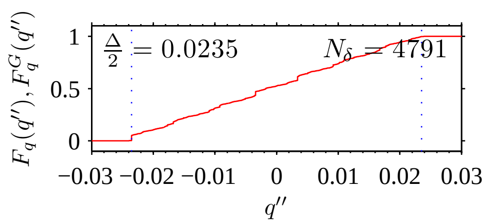


(x) CDF, $\kappa = 6$ (no clipping), closeup.

OFDM Type 3.2: $N = 32, \mathcal{K}_{\mathrm{SZ}} = \{\}, \mathcal{K}_{\mathrm{SP}} = \{\}, \mathcal{K}_{\mathrm{SD}} = \mathbb{Z}_N, \mathcal{A}_{\mathrm{SD}} = \mathcal{A}_{\mathrm{BPSK}}, \mathrm{E}[f^2] = 1.$

Figure 5.18: (Cont'd) 'Exhaustive' PDFs $f_q(q')$ and CDFs $F_q(q'')$ of all quantizer error time-samples, OFDM Type = 3.2, $b = 8$, for various clipping-factors $\kappa$.

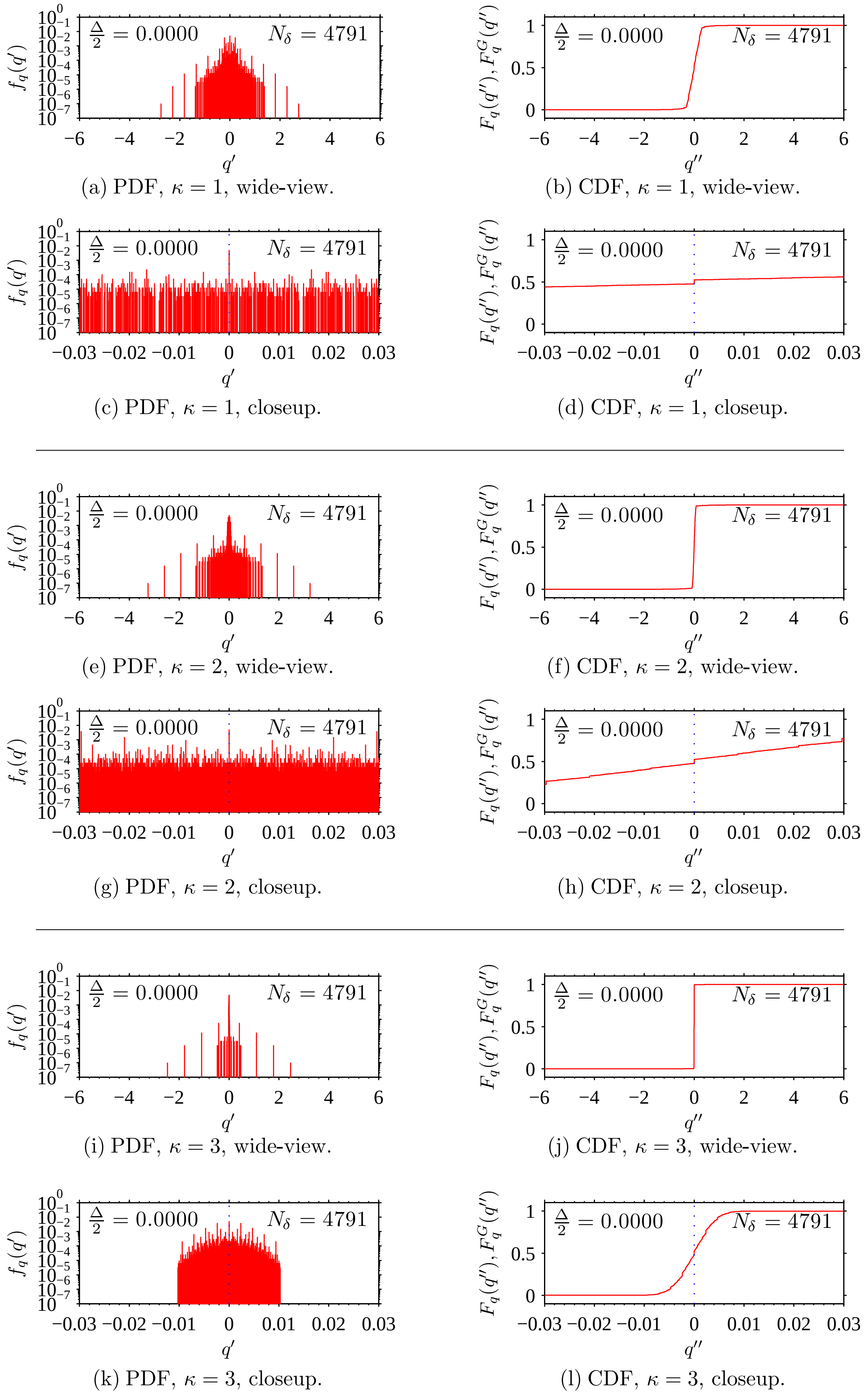

(a) PDF, $\kappa = 1$, wide-view.
(b) CDF, $\kappa = 1$, wide-view.
(c) PDF, $\kappa = 1$, closeup.
(d) CDF, $\kappa = 1$, closeup.
(e) PDF, $\kappa = 2$, wide-view.
(f) CDF, $\kappa = 2$, wide-view.
(g) PDF, $\kappa = 2$, closeup.
(h) CDF, $\kappa = 2$, closeup.
(i) PDF, $\kappa = 3$, wide-view.
(j) CDF, $\kappa = 3$, wide-view.
(k) PDF, $\kappa = 3$, closeup.
(l) CDF, $\kappa = 3$, closeup.

OFDM Type 3.2: $N = 32, \mathcal{K}_{\text{SZ}} = \{\}, \mathcal{K}_{\text{SP}} = \{\}, \mathcal{K}_{\text{SD}} = \mathbb{Z}_N, \mathcal{A}_{\text{SD}} = \mathcal{A}_{\text{BPSK}}, \text{E}[f^2] = 1.$

Figure 5.19: 'Exhaustive' PDFs $f_q(q')$ and CDFs $F_q(q'')$ of all quantizer error time-samples, OFDM Type = 3.2, $b = \infty$ (clipping only), for various clipping-factors $\kappa$.

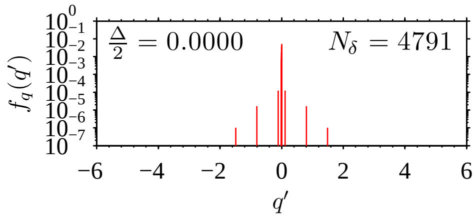


(m) PDF, $\kappa = 4$, wide-view.

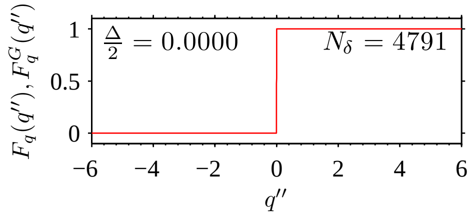


(n) CDF, $\kappa = 4$, wide-view.

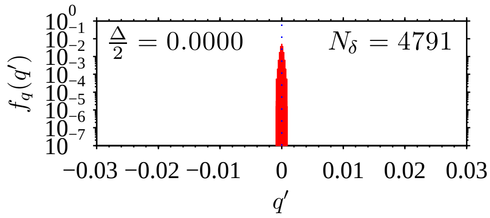


(o) PDF, $\kappa = 4$, closeup.

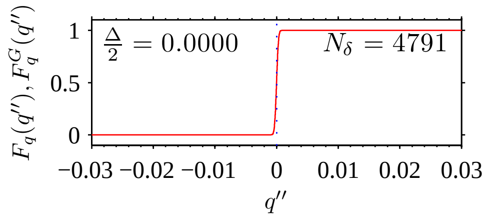


(p) CDF, $\kappa = 4$, closeup.

---

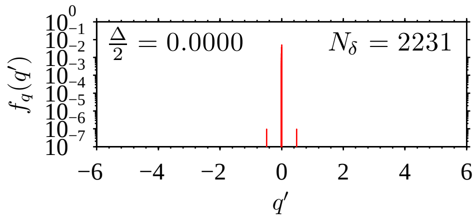


(q) PDF, $\kappa = 5$, wide-view.

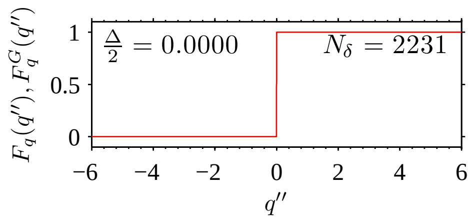


(r) CDF, $\kappa = 5$, wide-view.

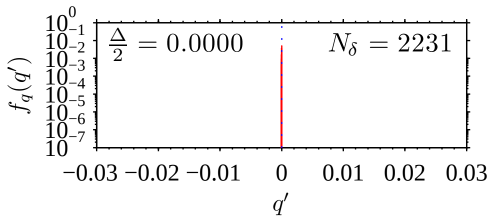


(s) PDF, $\kappa = 5$, closeup.

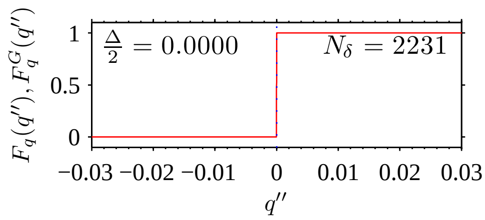


(t) CDF, $\kappa = 5$, closeup.

---

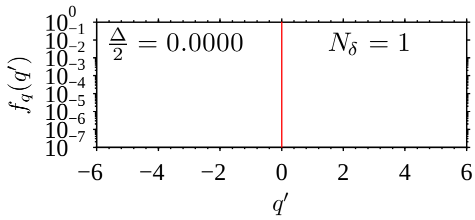


(u) PDF, $\kappa = 6$ (no clipping), wide-view.

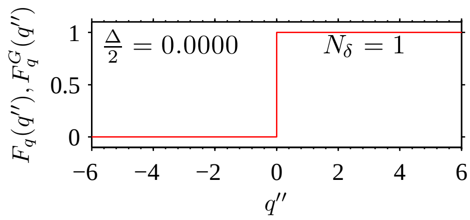


(v) CDF, $\kappa = 6$ (no clipping), wide-view.

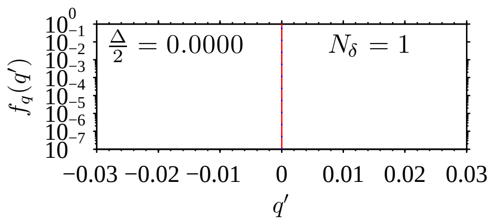


(w) PDF, $\kappa = 6$ (no clipping), closeup.

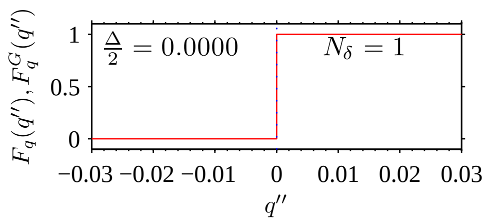


(x) CDF, $\kappa = 6$ (no clipping), closeup.

OFDM Type 3.2: $N = 32, \mathcal{K}_{\mathrm{SZ}} = \{\}, \mathcal{K}_{\mathrm{SP}} = \{\}, \mathcal{K}_{\mathrm{SD}} = \mathbb{Z}_N, \mathcal{A}_{\mathrm{SD}} = \mathcal{A}_{\mathrm{BPSK}}, \mathrm{E}[f^2] = 1.$

Figure 5.19: (Cont'd) 'Exhaustive' PDFs $f_q(q')$ and CDFs $F_q(q'')$ of all quantizer error time-samples, OFDM Type = 3.2, $b = \infty$ (clipping only), for various clipping-factors $\kappa$.

### 5.3.18 'Exhaustive' PDF of the Quantizer Error Frequency-Sample Vector

The quantizer error complex frequency-sample vector $\hat{\boldsymbol{r}}$ is obtained by taking the DFT of the quantizer error time-sample vector $\boldsymbol{q}$ and is given by

$$\begin{aligned}
\hat{\boldsymbol{r}} &= \boldsymbol{F}\boldsymbol{q} \\
&= \boldsymbol{F}\left(\boldsymbol{g} - \beta \boldsymbol{f}\right) \\
&= \boldsymbol{F}\left(\mathrm{Q}\left\{\boldsymbol{f}\right\} - \beta \boldsymbol{f}\right) \\
&= \boldsymbol{F}\left(\mathrm{Q}\left\{\Re\left\{\boldsymbol{F}^{-1}\boldsymbol{d}\right\}\right\} - \beta \Re\left\{\boldsymbol{F}^{-1}\boldsymbol{d}\right\}\right),
\end{aligned} \tag{5.47}$$

and the particular instance of $\hat{\boldsymbol{r}}$ which corresponds to the $j^{\text{th}}$ letter $\boldsymbol{d}_j$ of the IDFT input vector alphabet $\mathcal{A}_{\boldsymbol{d}}$ is therefore given by

$$\hat{\boldsymbol{r}}_j = \boldsymbol{F}\left(\mathrm{Q}\left\{\Re\left\{\boldsymbol{F}^{-1}\boldsymbol{d}_j\right\}\right\} - \beta \Re\left\{\boldsymbol{F}^{-1}\boldsymbol{d}_j\right\}\right). \tag{5.48}$$

The multi-dimensional complex PDF of $\hat{\boldsymbol{r}}$ is therefore

$$f_{\hat{\boldsymbol{r}}}(\hat{\boldsymbol{r}}') = \frac{1}{N_{\boldsymbol{d}}} \sum_{j=1}^{N_{\boldsymbol{d}}} \delta\left(\hat{\boldsymbol{r}}' - \hat{\boldsymbol{r}}_j\right). \tag{5.49}$$

The frequency domain quantization error will now be split into its real and imaginary parts which will be considered separately in §5.3.19 to §5.3.23 and §5.3.24 to §5.3.25 respectively'.

### 5.3.19 'Exhaustive' PDF of the Quantizer Error Frequency-Sample Real-Part Vector

The real part $\hat{\boldsymbol{u}}$ of the complex quantizer error frequency-sample vector $\hat{\boldsymbol{r}}$ is given by

$$\begin{aligned}
\hat{\boldsymbol{u}} &= \Re\{\hat{\boldsymbol{r}}\} \\
&= \Re\left\{\boldsymbol{F}\Big(Q\{\ \Re\left\{\boldsymbol{F}^{-1}\boldsymbol{d}\right\}\ \}\ \ - \beta \Re\left\{\boldsymbol{F}^{-1}\boldsymbol{d}\right\}\ \Big)\right\}\ ,
\end{aligned} \tag{5.50}$$

and the particular instance of $\hat{\boldsymbol{u}}$ which corresponds to the $j^{\text{th}}$ letter $\boldsymbol{d}_j$ of the IDFT input vector alphabet $\mathcal{A}_{\boldsymbol{d}}$ is therefore given by

$$\hat{\boldsymbol{u}}_j = \Re\left\{\boldsymbol{F}\Big(Q\big\{\,\Re\{\boldsymbol{F}^{-1}\boldsymbol{d}_j\}\big\} \;-\beta\Re\{\boldsymbol{F}^{-1}\boldsymbol{d}_j\}\Big)\right\} \;. \tag{5.51}$$

The multi-dimensional real PDF of $\hat{\boldsymbol{u}}$ is therefore

$$f_{\hat{\boldsymbol{u}}}(\hat{\boldsymbol{u}}') = \frac{1}{N_{\boldsymbol{d}}}\sum_{j=1}^{N_{\boldsymbol{d}}} \delta\left(\hat{\boldsymbol{u}}' - \hat{\boldsymbol{u}}_j\right). \tag{5.52}$$

### 5.3.20 'Exhaustive' Covariance Matrix of the Real Part of the Quantizer Error Frequency-Sample Real-Part Vector

The covariance matrix of the quantizer error frequency-sample real-part vector $\hat{\boldsymbol{u}}$ is given by

$$\begin{aligned}\mathbf{COV}(\hat{\boldsymbol{u}}) &= \mathrm{E}\left[\big(\hat{\boldsymbol{u}} - \mathrm{E}[\hat{\boldsymbol{u}}]\big)\big(\hat{\boldsymbol{u}} - \mathrm{E}[\hat{\boldsymbol{u}}]\big)^{\mathrm{T}}\right] \\ &= \mathrm{E}\left[\hat{\boldsymbol{u}}\hat{\boldsymbol{u}}^{\mathrm{T}}\right] - \mathrm{E}\left[\hat{\boldsymbol{u}}\right]\mathrm{E}\left[\hat{\boldsymbol{u}}^{\mathrm{T}}\right],\end{aligned} \tag{5.53}$$

which, using (5.51), is expanded to

$$\begin{aligned}\mathbf{COV}(\hat{\boldsymbol{u}}) = {} & \frac{1}{N_{\boldsymbol{d}}}\sum_{j=1}^{N_{\boldsymbol{d}}} \left(\Re\left\{\boldsymbol{F}\Big(Q\big\{\,\Re\{\boldsymbol{F}^{-1}\boldsymbol{d}_j\}\big\} \;-\beta\Re\{\boldsymbol{F}^{-1}\boldsymbol{d}_j\}\Big)\right\}\right) \\ & \qquad \left(\Re\left\{\boldsymbol{F}\Big(Q\big\{\,\Re\{\boldsymbol{F}^{-1}\boldsymbol{d}_j\}\big\} \;-\beta\Re\{\boldsymbol{F}^{-1}\boldsymbol{d}_j\}\Big)\right\}\right)^{\mathrm{T}} \\ & - \frac{1}{N_{\boldsymbol{d}}^2}\sum_{j=1}^{N_{\boldsymbol{d}}} \left(\Re\left\{\boldsymbol{F}\Big(Q\big\{\,\Re\{\boldsymbol{F}^{-1}\boldsymbol{d}_j\}\big\} \;-\beta\Re\{\boldsymbol{F}^{-1}\boldsymbol{d}_j\}\Big)\right\}\right) \\ & \qquad \sum_{j=1}^{N_{\boldsymbol{d}}} \left(\Re\left\{\boldsymbol{F}\Big(Q\big\{\,\Re\{\boldsymbol{F}^{-1}\boldsymbol{d}_j\}\big\} \;-\beta\Re\{\boldsymbol{F}^{-1}\boldsymbol{d}_j\}\Big)\right\}\right)^{\mathrm{T}}.\end{aligned} \tag{5.54}$$

### 5.3.21 'Exhaustive' Correlation Matrix of the Quantizer Error Frequency-Sample Real-Part Vector

The correlation matrix of the quantizer error frequency-sample real-part vector $\hat{\boldsymbol{u}}$, in terms of its covariance matrix $\mathbf{COV}(\hat{\boldsymbol{u}})$ already obtained in (5.54) above, is given by

$$\mathbf{CORR}(\hat{\boldsymbol{u}}) = \Big(\mathbf{DIAG}[\mathbf{COV}(\hat{\boldsymbol{u}})]\Big)^{-1/2} \; \mathbf{COV}(\hat{\boldsymbol{u}}) \; \Big(\mathbf{DIAG}[\mathbf{COV}(\hat{\boldsymbol{u}})]\Big)^{-1/2}. \quad (5.55)$$

### 5.3.22 'Exhaustive' PDF and CDF of the Individual Quantizer Error Frequency-Sample Real-Parts

The $k^{\text{th}}$ quantizer error frequency-sample real-part $\hat{u}_k$ is given by

$$\hat{u}_k = [\boldsymbol{u}]_k = \Big[\Re\,\Big\{\boldsymbol{F}\Big(Q\{\,\Re\{\boldsymbol{F}^{-1}\boldsymbol{d}\}\,\} \;-\beta\Re\{\boldsymbol{F}^{-1}\boldsymbol{d}\}\Big)\Big\}\;\Big]_k, \quad (5.56)$$

and the particular instance of $\hat{u}_k$ which corresponds to the $j^{\text{th}}$ letter $\boldsymbol{d}_j$ of the IDFT input vector alphabet $\mathcal{A}_{\boldsymbol{d}}$ is therefore given by

$$\hat{u}_{j,k} = \Big[\Re\,\Big\{\boldsymbol{F}\Big(Q\{\,\Re\{\boldsymbol{F}^{-1}\boldsymbol{d}_j\}\,\} \;-\beta\Re\{\boldsymbol{F}^{-1}\boldsymbol{d}_j\}\Big)\Big\}\;\Big]_k. \quad (5.57)$$

The one-dimensional real PDF of $\hat{u}_k$ is therefore

$$f_{\hat{u}_k}(\hat{u}'_k) = \frac{1}{N_{\boldsymbol{d}}}\sum_{j=1}^{N_{\boldsymbol{d}}} \delta\left(\hat{u}'_k - \hat{u}_{j,k}\right). \quad (5.58)$$

Next, the CDF of the $k^{\text{th}}$ quantizer error frequency-sample real-part $\hat{u}_k$ is given by

$$\begin{aligned} F_{\hat{u}_k}(\hat{u}_k'') &= \int_{-\infty}^{\hat{u}_k''} f_{\hat{u}_k}(\hat{u}_k') \ \mathrm{d}\hat{u}_k' \\ &= \int_{-\infty}^{\hat{u}_k''} \frac{1}{N_{\boldsymbol{d}}} \sum_{j=1}^{N_{\boldsymbol{d}}} \delta\left(\hat{u}_k' - \hat{u}_{j,k}\right) \ \mathrm{d}\hat{u}_k' \\ &= \frac{1}{N_{\boldsymbol{d}}} \sum_{\hat{u}_{j,k} \leq \hat{u}_k''} 1. \end{aligned} \tag{5.59}$$

#### 5.3.22.1 Example Results

Example results are shown in Figures 5.20 and 5.21.

Beginning with the no clipping $\kappa = 6$ case in Figure 5.21, we immediately observe the discrete nature of the PDFs for individual frequency samples $\hat{u}_k$. The number of PDF diracs $N_\delta$ for each of the frequency-samples groups is remarkably small compared to the IDFT input alphabet size $|A_{\boldsymbol{d}}| = 2^{16} = 65,536$ leading to the conclusion that, even through the IDFT, the quantizer, and the DFT, multiple IDFT input alphabet letters map to the same quantizer error. We also observe the variation of the frequency-sample PDFs/CDFs - i.e. not all of the frequency samples have the same PDF/CDF. Following on from this observation, we also note that multiple frequency-samples $\hat{u}_k$ have exactly the same PDF. Insight is given into this in the later section on the 'Convolution' method. Looking at the CDFs, we see that they are reasonably close to Gaussian except for some small 'lumpy' deviations due to the PDF diracs and the drop-off to zero at the PDF range limit.

Next, we look at the effect of major clipping in the $\kappa = 2$ case shown in Figure 5.20. Here, the clipping has greatly increased the number of PDF diracs $N_\delta$. Also, we observe in the CDFs large deviations from the equivalent Gaussian CDF. This is one of the major findings in this thesis. This $\kappa = 2$ example case is chosen because it clearly demonstrates the deviation from Gaussian of the quantization noise PDF in the received signal decision domain (the receiver frequency domain). However, very curiously, other values of the normalized clipping level $\kappa$ (not shown here) do not result in this deviation from Gaussian.

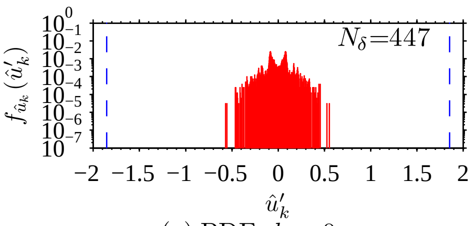


(a) PDF, $k = 0$.

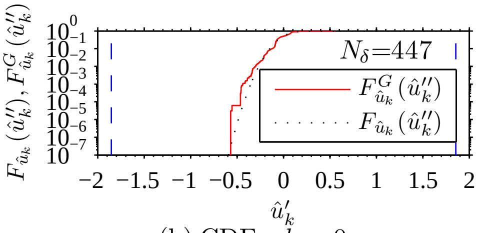


(b) CDFs, $k = 0$.

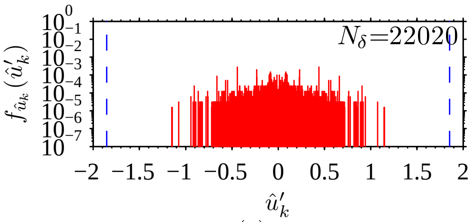


(c)

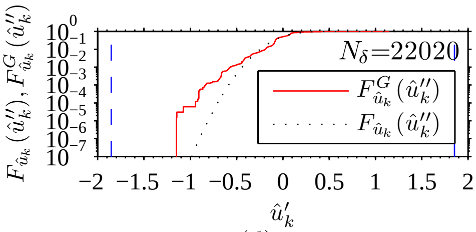


(d)

PDF,$k \in \{1, 3, 5, 7, 9, 11, 13, 15\} = \{1 * \text{Odds}\}$. CDFs,$k \in \{1, 3, 5, 7, 9, 11, 13, 15\} = \{1 * \text{Odds}\}$.

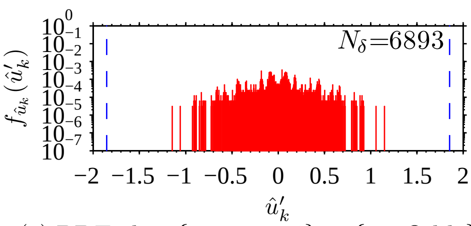


(e) PDF, $k \in \{2, 6, 10, 14\} = \{2 * \text{Odds}\}$.

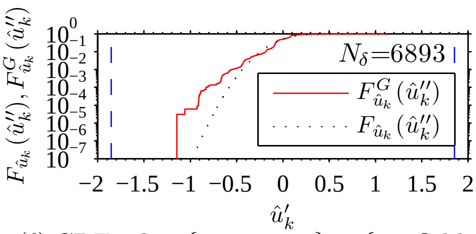


(f) CDFs, $k \in \{2, 6, 10, 14\} = \{2 * \text{Odds}\}$.

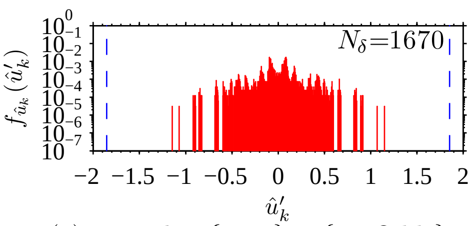


(g) PDF, $k \in \{4, 12\} = \{4 * \text{Odds}\}$.

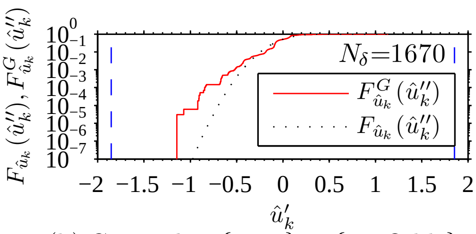


(h) CDFs, $k \in \{4, 12\} = \{4 * \text{Odds}\}$.

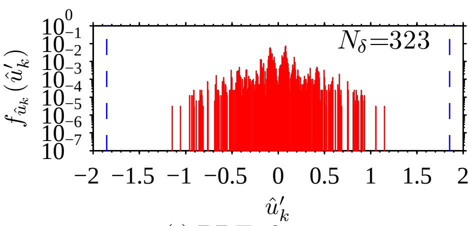


(i) PDF, $k = 8$.

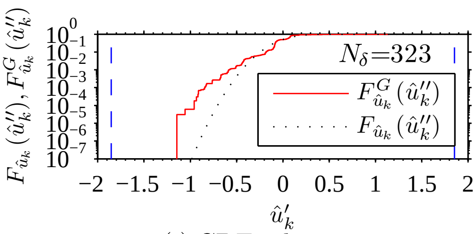


(j) CDFs, $k = 8$.

OFDM Type 3.2: $N = 32, \mathcal{K}_{\text{SZ}} = \{\}, \mathcal{K}_{\text{SP}} = \{\}, \mathcal{K}_{\text{SD}} = \mathbb{Z}_N, \mathcal{A}_{\text{SD}} = \mathcal{A}_{\text{BPSK}}, \text{E}[f^2] = 1.$

Figure 5.20: 'Exhaustive' PDFs $f_{\hat{u}_k}(\hat{u}'_k)$, CDFs $F_{\hat{u}_k}(\hat{u}''_k)$, and Gaussian approximation CDFs $F^G_{\hat{u}_k}(\hat{u}''_k)$ for individual quantizer error frequency-sample real-parts $\hat{u}_k$, OFDM Type $= 3.2$, $b = 8, \kappa = 2$ (major clipping), for various frequency-sample indeces $k$.

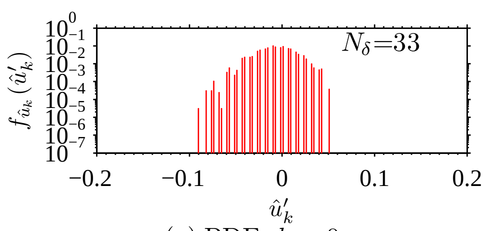


(a) PDF, $k = 0$.

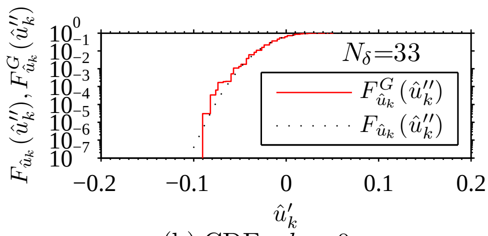


(b) CDFs, $k = 0$.

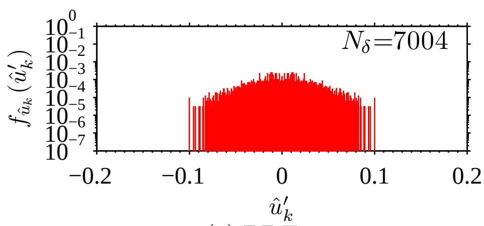


(c) PDF,

$k \in \{1, 3, 5, 7, 9, 11, 13, 15\} = \{1 * \text{Odds}\}$.

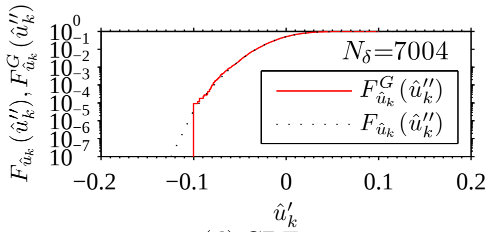


(d) CDFs,

$k \in \{1, 3, 5, 7, 9, 11, 13, 15\} = \{1 * \text{Odds}\}$.

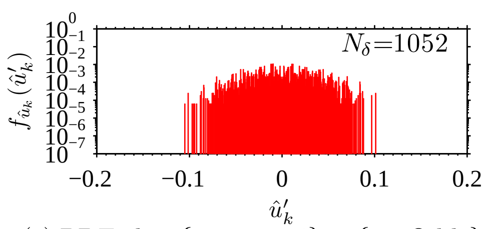


(e) PDF, $k \in \{2, 6, 10, 14\} = \{2 * \text{Odds}\}$.

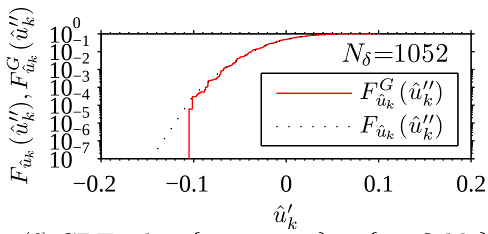


(f) CDFs, $k \in \{2, 6, 10, 14\} = \{2 * \text{Odds}\}$.

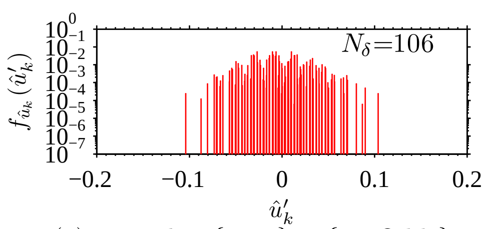


(g) PDF, $k \in \{4, 12\} = \{4 * \text{Odds}\}$.

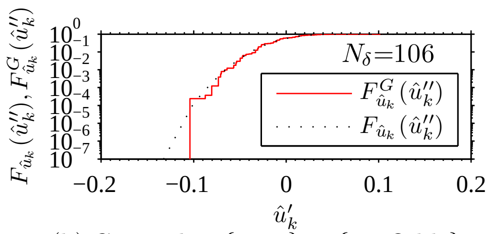


(h) CDFs, $k \in \{4, 12\} = \{4 * \text{Odds}\}$.

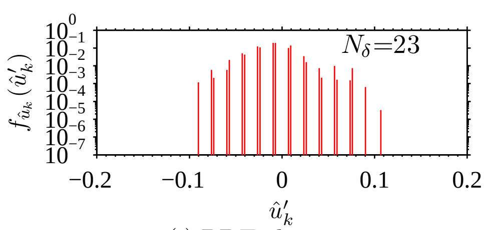


(i) PDF, $k = 8$.

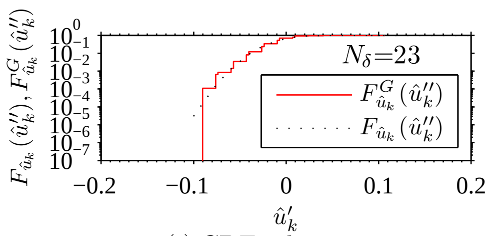


(j) CDFs, $k = 8$.

OFDM Type 3.2: $N = 32, \mathcal{K}_{\text{SZ}} = \{\}, \mathcal{K}_{\text{SP}} = \{\}, \mathcal{K}_{\text{SD}} = \mathbb{Z}_N, \mathcal{A}_{\text{SD}} = \mathcal{A}_{\text{BPSK}}, \text{E}[f^2] = 1.$

Figure 5.21: 'Exhaustive' PDFs $f_{\hat{u}_k}(\hat{u}'_k)$, CDFs $F_{\hat{u}_k}(\hat{u}''_k)$, and Gaussian approximation CDFs $F^G_{\hat{u}_k}(\hat{u}''_k)$ for individual quantizer error frequency-sample real-parts $\hat{u}_k$, OFDM Type $= 3.2$, $b = 8$, $\kappa = 6$ (no clipping), for various frequency-sample indeces $k$.

### 5.3.23 'Exhaustive' PDF and CDF of All Quantizer Error Frequency-Sample Real-Parts

By taking the expected value of *all* of the PDFs $f_{\hat{u}_k},\ k \in \mathbb{Z}_N$, of the quantizer error frequency-sample real-parts $\hat{u}_k$, we find that the overall PDF of *all* of the quantizer error frequency-sample real-parts, is

$$f_{\hat{u}}(\hat{u}') = \mathrm{E}\left[f_{\hat{u}_k}(\hat{u}')\right] = \frac{1}{N}\sum_{k=0}^{N-1} f_{\hat{u}_k}(\hat{u}'). \tag{5.60}$$

Next, the CDF of *all* of the quantizer error frequency-sample real-parts $\hat{u}_k, k \in \mathbb{Z}_N$ is equal to the expected value of *all* of the CDFs $F_{\hat{u}_k},\ k \in \mathbb{Z}_N$, and is given by

$$\begin{aligned} F_{\hat{u}}(\hat{u}'') &= \mathrm{E}\left[F_{\hat{u}_k}(\hat{u}'')\right] \\ &= \frac{1}{N}\sum_{n=0}^{N-1} F_{\hat{u}_k}(\hat{u}'') \\ &= \frac{1}{N \cdot N_{\boldsymbol{d}}}\sum_{n=0}^{N-1}\sum_{\hat{u}_{j,k} \leq \hat{u}''} 1. \end{aligned} \tag{5.61}$$

#### 5.3.23.1 Example Results

Example results are shown in Figures 5.22, 5.23, 5.24, and 5.25.

Before starting our analysis of the results, we note that $\beta$ is the gain factor caused by the transmitter quantization process, $D_{\mathrm{S}}$ is half the distance between the BPSK Data symbols before transmitter quantization, and $\beta D_{\mathrm{S}}/2$ is the distance between the BPSK DATA symbols after transmitter quantization. Significantly, when the quantizer error frequency-sample real or imaginary parts exceed $\beta D_{\mathrm{S}}/2$, a BPSK bit error occurs.

Beginning with the clipping only (no granular quantization) $b = \infty$ case in Figure 5.25, we observe the effect of varying the normalized clipping factor $\kappa$ on the PDFs/CDFs of all of the frequency samples $u$. Looking at the CDFs, we see large variations from the equivalent Gaussian CDF for normalized clipping factor values of $\kappa \in \{2, 3, 4\}$. This is one of the major results of this thesis. From this, we deduce that clipping alone contributes to the sometimes non-Gaussian nature of the PDFs/CDFs. Nevertheless, curiously, the $\kappa = 1$ severe clipping case yields a CDF which is quite close to Gaussian.

Figures 5.22, 5.23, and 5.24 show results for 4-bit, 6-bit, and 8-bit quantization respectively.

The CDFs for 4-bit quantization in Figure 5.22 all appear to be close to Gaussian except for the $\kappa = 2$ case. This leads to the conclusion that, in most cases, large-ish granular quantization noise will 'pull' the CDF back to being close to Gaussian.

The CDFs for the 6-bit case in Figure 5.23 show large deviations from Gaussian. This is noteworthy since the optimal signal to quantization noise ratio, indicated by $\gamma_{\hat{u}}$ in the PDF plots, occurs for $\kappa \in \{3, 4\}$ when the CDFs deviate greatly from Gaussian. Here, BER predictions based on a Gaussian PDF assumption would yield incorrect results - a major assertion of this thesis.

Finally, we note that the CDFs for the 8-bit case in Figure 5.24 also show large deviations from Gaussian.

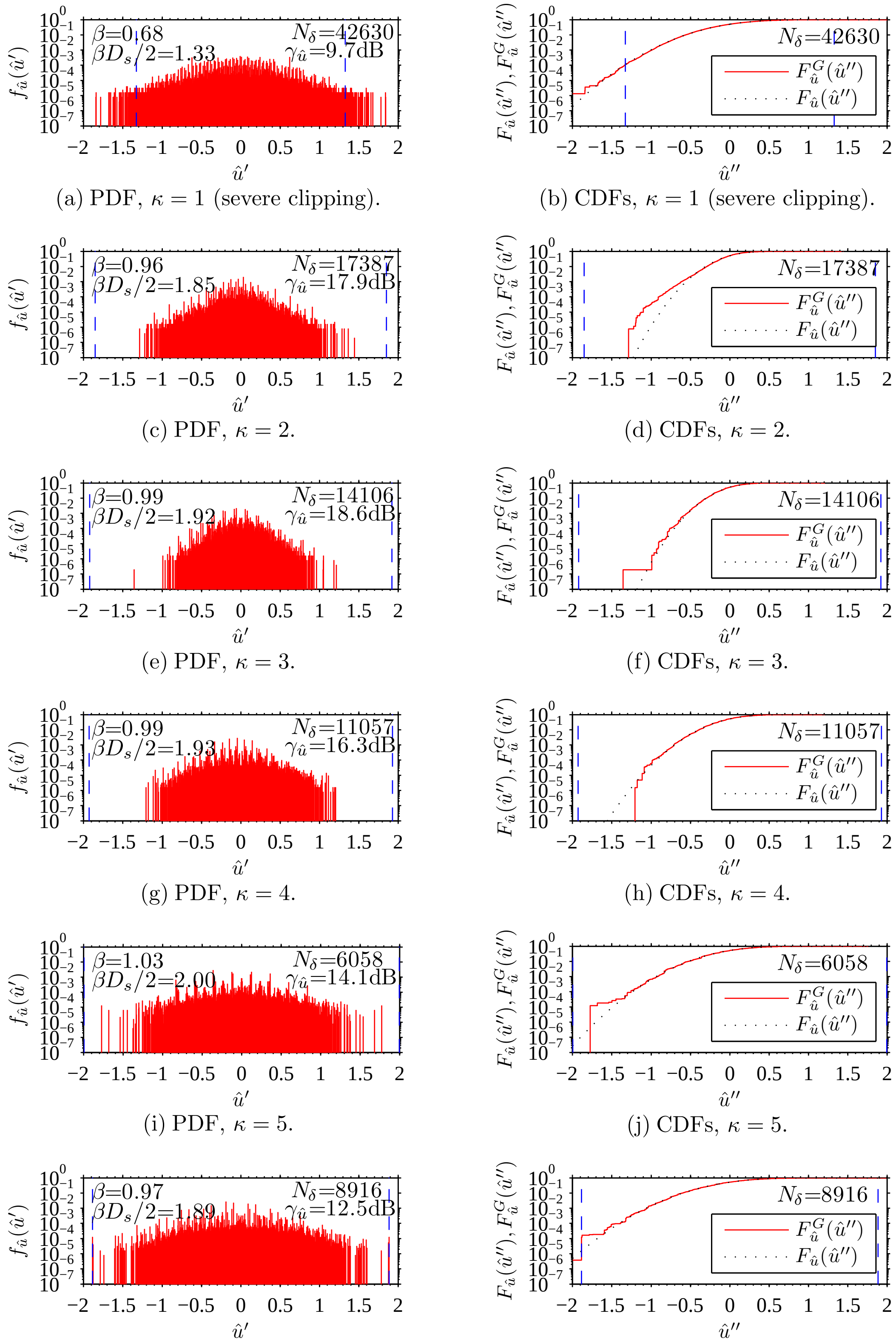


(a) PDF, $\kappa = 1$ (severe clipping).

(b) CDFs, $\kappa = 1$ (severe clipping).

(c) PDF, $\kappa = 2$.

(d) CDFs, $\kappa = 2$.

(e) PDF, $\kappa = 3$.

(f) CDFs, $\kappa = 3$.

(g) PDF, $\kappa = 4$.

(h) CDFs, $\kappa = 4$.

(i) PDF, $\kappa = 5$.

(j) CDFs, $\kappa = 5$.

(k) PDF, $\kappa = 6$ (no clipping).

(l) CDFs, $\kappa = 6$ (no clipping).

OFDM Type 3.2: $N = 32, \mathcal{K}_{\text{SZ}} = \{\}, \mathcal{K}_{\text{SP}} = \{\}, \mathcal{K}_{\text{SD}} = \mathbb{Z}_N, \mathcal{A}_{\text{SD}} = \mathcal{A}_{\text{BPSK}}, \text{E}[f^2] = 1.$

Figure 5.22: 'Exhaustive' PDFs $f_{\hat{u}}(\hat{u}')$, CDFs $F_{\hat{u}}(\hat{u}'')$, and Gaussian approximation CDFs $F^G_{\hat{u}}(u'')$ of all quantizer error frequency-sample real-parts, OFDM Type = 3.2, $\text{E}[f^2] = 1$, $b = 4$ bits , for various normalized clipping levels $\kappa$.

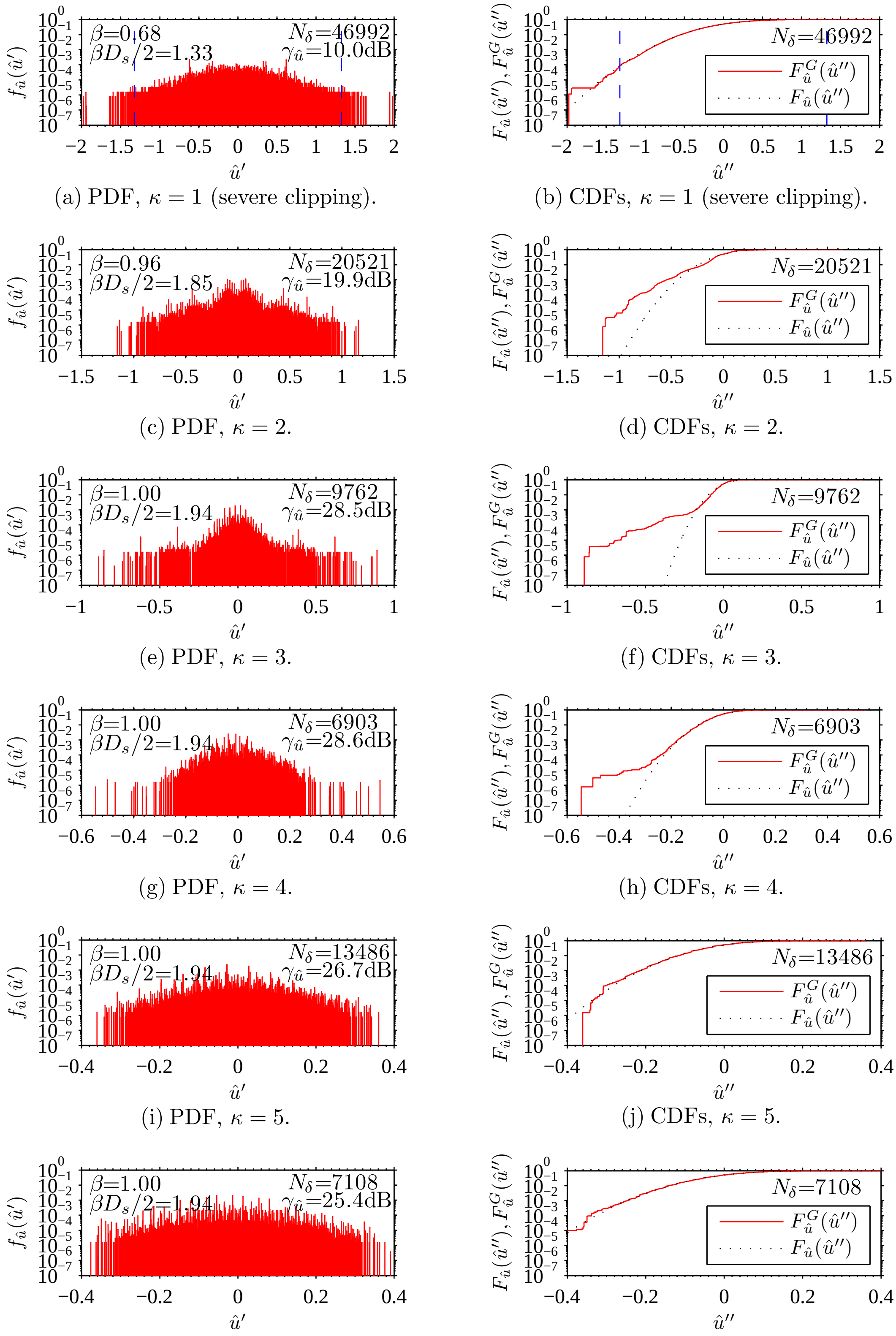


(a) PDF, $\kappa = 1$ (severe clipping).

(b) CDFs, $\kappa = 1$ (severe clipping).

(c) PDF, $\kappa = 2$.

(d) CDFs, $\kappa = 2$.

(e) PDF, $\kappa = 3$.

(f) CDFs, $\kappa = 3$.

(g) PDF, $\kappa = 4$.

(h) CDFs, $\kappa = 4$.

(i) PDF, $\kappa = 5$.

(j) CDFs, $\kappa = 5$.

(k) PDF, $\kappa = 6$ (no clipping).

(l) CDFs, $\kappa = 6$ (no clipping).

OFDM Type 3.2: $N = 32, \mathcal{K}_{\text{SZ}} = \{\}, \mathcal{K}_{\text{SP}} = \{\}, \mathcal{K}_{\text{SD}} = \mathbb{Z}_N, \mathcal{A}_{\text{SD}} = \mathcal{A}_{\text{BPSK}}, \text{E}[f^2] = 1.$

Figure 5.23: 'Exhaustive' PDFs $f_{\hat{u}}(\hat{u}')$, CDFs $F_{\hat{u}}(\hat{u}'')$, and Gaussian approximation CDFs $F_{\hat{u}}^{G}(u'')$ of all quantizer error frequency-sample real-parts, OFDM Type = 3.2, $\text{E}[f^2] = 1$, $b = 6$ bits , for various normalized clipping levels $\kappa$.

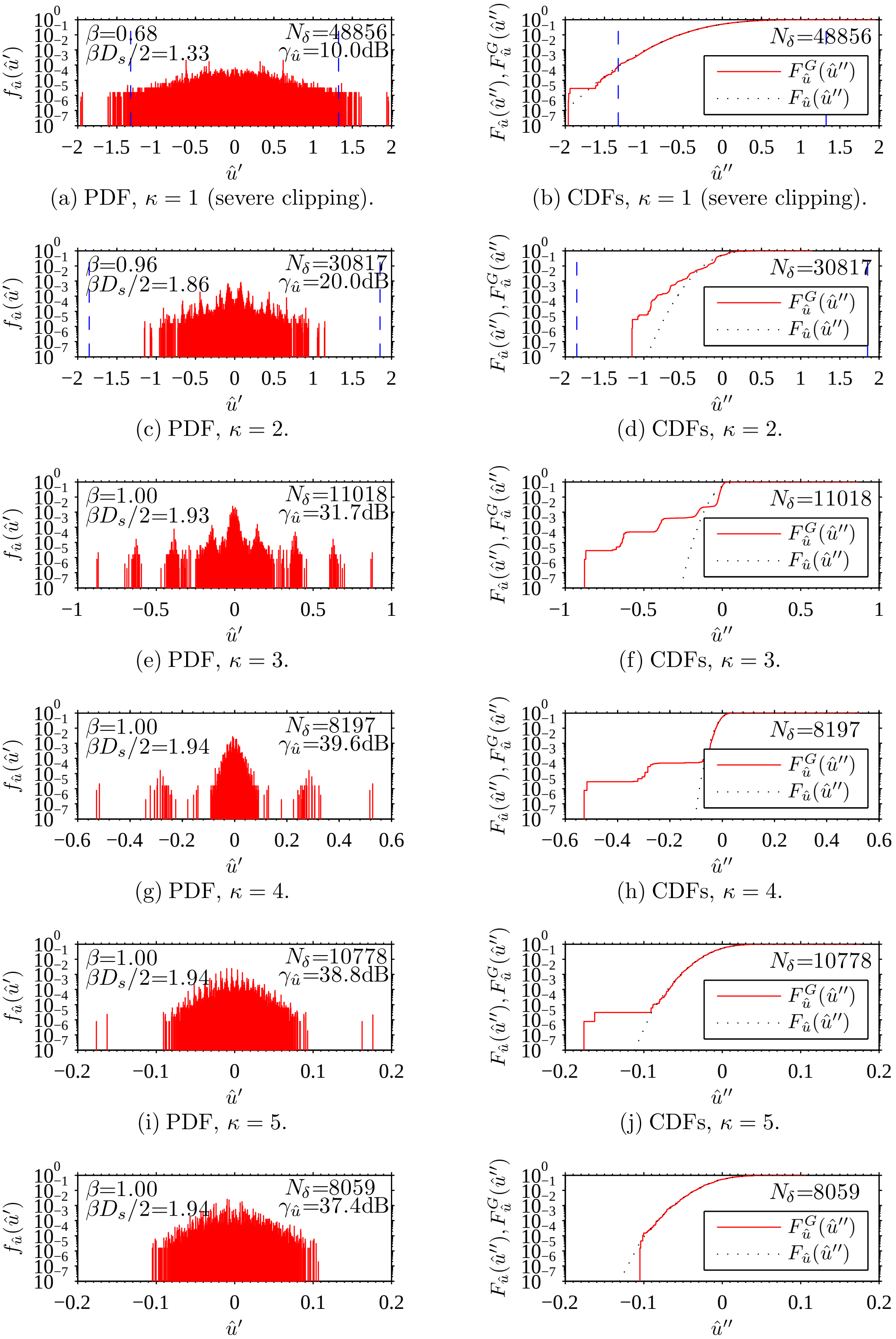


(a) PDF, $\kappa = 1$ (severe clipping). (b) CDFs, $\kappa = 1$ (severe clipping).

(c) PDF, $\kappa = 2$. (d) CDFs, $\kappa = 2$.

(e) PDF, $\kappa = 3$. (f) CDFs, $\kappa = 3$.

(g) PDF, $\kappa = 4$. (h) CDFs, $\kappa = 4$.

(i) PDF, $\kappa = 5$. (j) CDFs, $\kappa = 5$.

(k) PDF, $\kappa = 6$ (no clipping). (l) CDFs, $\kappa = 6$ (no clipping).

OFDM Type 3.2: $N = 32, \mathcal{K}_{\text{SZ}} = \{\}, \mathcal{K}_{\text{SP}} = \{\}, \mathcal{K}_{\text{SD}} = \mathbb{Z}_N, \mathcal{A}_{\text{SD}} = \mathcal{A}_{\text{BPSK}}, \text{E}[f^2] = 1.$

Figure 5.24: 'Exhaustive' PDFs $f_{\hat{u}}(\hat{u}')$, CDFs $F_{\hat{u}}(\hat{u}'')$, and Gaussian approximation CDFs $F_{\hat{u}}^G(\hat{u}'')$ of all quantizer error frequency-sample real-parts, OFDM Type = 3.2, $\text{E}[f^2] = 1$, $b = 8$ bits, for various normalized clipping levels $\kappa$.

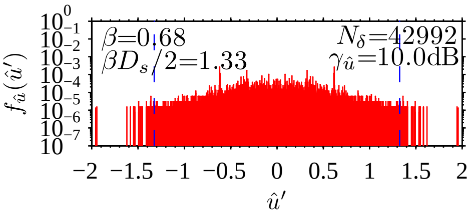


(a) PDF, $\kappa = 1$ (severe clipping).

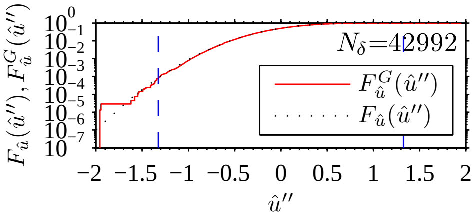


(b) CDFs, $\kappa = 1$ (severe clipping).

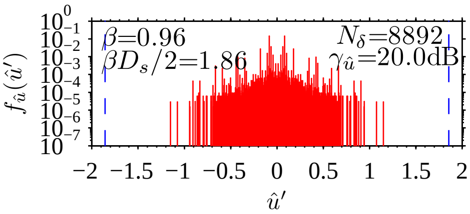


(c) PDF, $\kappa = 2$.

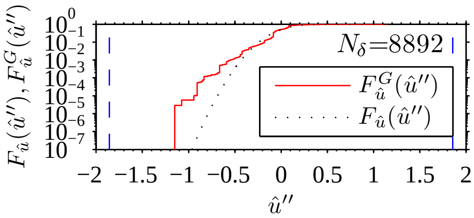


(d) CDFs, $\kappa = 2$.

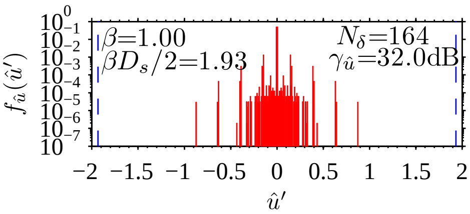


(e) PDF, $\kappa = 3$.

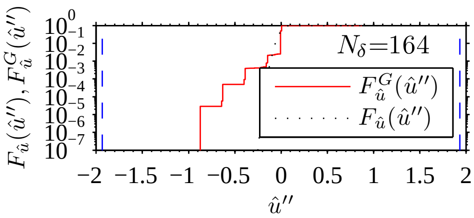


(f) CDFs, $\kappa = 3$.

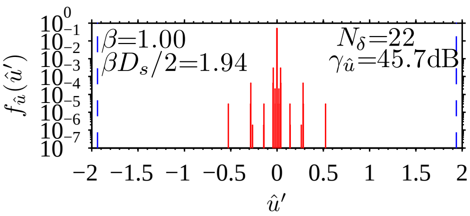


(g) PDF, $\kappa = 4$.

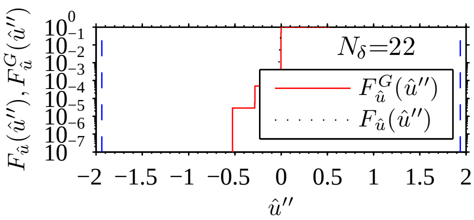


(h) CDFs, $\kappa = 4$.

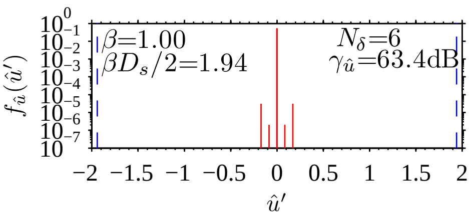


(i) PDF, $\kappa = 5$.

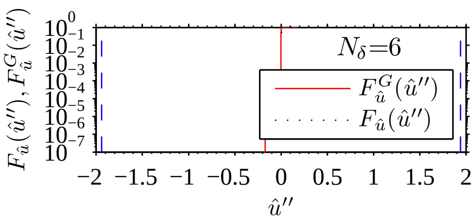


(j) CDFs, $\kappa = 5$.

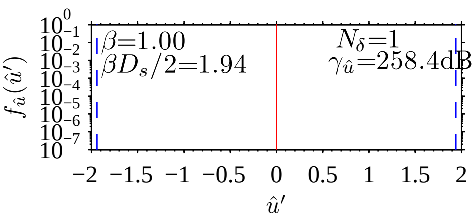


(k) PDF, $\kappa = 6$ (no clipping).

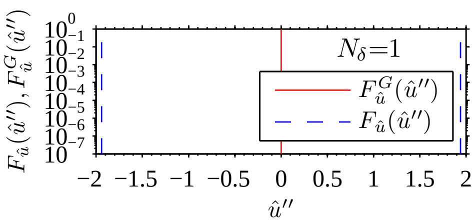


(l) CDFs, $\kappa = 6$ (no clipping).

OFDM Type 3.2: $N = 32, \mathcal{K}_{\text{SZ}} = \{\}, \mathcal{K}_{\text{SP}} = \{\}, \mathcal{K}_{\text{SD}} = \mathbb{Z}_N, \mathcal{A}_{\text{SD}} = \mathcal{A}_{\text{BPSK}}, \mathrm{E}[f^2] = 1.$

Figure 5.25: 'Exhaustive' PDFs $f_{\hat{u}}(\hat{u}')$, CDFs $F_{\hat{u}}(\hat{u}'')$, and Gaussian approximation CDFs $F^G_{\hat{u}}(\hat{u}'')$ of all quantizer error frequency-sample real-parts, OFDM Type = 3.2, $\mathrm{E}[f^2] = 1$, $b = \infty$ bits (clipping only), for various normalized clipping levels $\kappa$.

### 5.3.24 'Exhaustive' PDF of the Quantizer Error Frequency-Sample Imaginary-Part Vector

The imaginary part $\hat{\boldsymbol{v}}$ of the complex quantizer frequency-sample vector $\hat{\boldsymbol{r}}$ is given by

$$\begin{aligned}\hat{\boldsymbol{v}} &= \Im\{\hat{\boldsymbol{r}}\} \\ &= \Im\left\{\boldsymbol{F}\left(\mathrm{Q}\left\{\Re\left\{\boldsymbol{F}^{-1}\boldsymbol{d}\right\}\right\} - \beta\Re\left\{\boldsymbol{F}^{-1}\boldsymbol{d}\right\}\right)\right\}, \end{aligned} \tag{5.62}$$

and the particular instance of $\hat{\boldsymbol{v}}$ which corresponds to the $j^{\text{th}}$ letter $\boldsymbol{d}_j$ of the IDFT input vector alphabet $\mathcal{A}_{\boldsymbol{d}}$ is therefore given by

$$\hat{\boldsymbol{v}}_j = \Im\left\{\boldsymbol{F}\left(\mathrm{Q}\left\{\Re\left\{\boldsymbol{F}^{-1}\boldsymbol{d}_j\right\}\right\} - \beta\Re\left\{\boldsymbol{F}^{-1}\boldsymbol{d}_j\right\}\right)\right\}. \tag{5.63}$$

The multi-dimensional imaginary PDF of $\hat{\boldsymbol{v}}$ is therefore

$$f_{\hat{\boldsymbol{v}}}(\hat{\boldsymbol{v}}') = \frac{1}{N_{\boldsymbol{d}}}\sum_{j=1}^{N_{\boldsymbol{d}}}\delta\left(\hat{\boldsymbol{v}}' - \hat{\boldsymbol{v}}_j\right). \tag{5.64}$$

### 5.3.25 'Exhaustive' Covariance Matrix of the Quantizer Error Frequency-Sample Imaginary-Part Vector

The covariance matrix of the quantizer error frequency-sample imaginary-part vector $\hat{\boldsymbol{v}}$ is given by

$$\begin{aligned}\mathbf{COV}(\hat{\boldsymbol{v}}) &= \mathrm{E}\left[\left(\hat{\boldsymbol{v}} - \mathrm{E}[\hat{\boldsymbol{v}}]\right)\left(\hat{\boldsymbol{v}} - \mathrm{E}[\hat{\boldsymbol{v}}]\right)^{\mathrm{T}}\right] \\ &= \mathrm{E}\left[\hat{\boldsymbol{v}}\hat{\boldsymbol{v}}^{\mathrm{T}}\right] - \mathrm{E}\left[\hat{\boldsymbol{v}}\right]\mathrm{E}\left[\hat{\boldsymbol{v}}^{\mathrm{T}}\right]. \end{aligned} \tag{5.65}$$

which, using (5.63), is expanded to

$$\begin{aligned}\mathbf{COV}(\hat{\boldsymbol{v}}) \quad = \quad & \frac{1}{N_{\boldsymbol{d}}}\sum_{j=1}^{N_{\boldsymbol{d}}} \left(\Im\left\{\boldsymbol{F}\big(Q\{\ \Re\{\boldsymbol{F}^{-1}\boldsymbol{d}_j\}\}\ -\beta\Re\{\boldsymbol{F}^{-1}\boldsymbol{d}_j\}\big)\right\}\ \right) \\ & \qquad \left(\Im\left\{\boldsymbol{F}\big(Q\{\ \Re\{\boldsymbol{F}^{-1}\boldsymbol{d}_j\}\}\ -\beta\Re\{\boldsymbol{F}^{-1}\boldsymbol{d}_j\}\big)\right\}\ \right)^{\mathrm{T}} \\ & - \frac{1}{N_{\boldsymbol{d}}^2}\sum_{j=1}^{N_{\boldsymbol{d}}} \left(\Im\left\{\boldsymbol{F}\big(Q\{\ \Re\{\boldsymbol{F}^{-1}\boldsymbol{d}_j\}\}\ -\beta\Re\{\boldsymbol{F}^{-1}\boldsymbol{d}_j\}\big)\right\}\ \right) \\ & \qquad \sum_{j=1}^{N_{\boldsymbol{d}}} \left(\Im\left\{\boldsymbol{F}\big(Q\{\ \Re\{\boldsymbol{F}^{-1}\boldsymbol{d}_j\}\}\ -\beta\Re\{\boldsymbol{F}^{-1}\boldsymbol{d}_j\}\big)\right\}\ \right)^{\mathrm{T}}. \end{aligned} \tag{5.66}$$

### 5.3.26 'Exhaustive' Correlation Matrix of the Quantizer Error Frequency-Sample Imaginary-Part Vector

The correlation matrix of the quantizer error frequency-sample imaginary-part vector $\hat{\boldsymbol{v}}$, in terms of its covariance matrix $\mathbf{COV}(\hat{\boldsymbol{v}})$ already obtained in (5.66) above, is given by

$$\mathbf{CORR}(\hat{\boldsymbol{u}}) = \big(\mathbf{DIAG}[\mathbf{COV}(\hat{\boldsymbol{u}})]\big)^{-1/2}\ \mathbf{COV}(\hat{\boldsymbol{u}})\ \big(\mathbf{DIAG}[\mathbf{COV}(\hat{\boldsymbol{u}})]\big)^{-1/2}. \tag{5.67}$$

### 5.3.27 'Exhaustive' PDF and CDF of Individual Quantizer Error Frequency-Sample Imaginary-Parts

The $k^{\text{th}}$ quantizer error frequency-sample imaginary-part $\hat{v}_k$ is given by

$$\hat{v}_k = [\boldsymbol{v}]_k = \left[\Im\left\{\boldsymbol{F}\left(\mathrm{Q}\left\{\Re\left\{\boldsymbol{F}^{-1}\boldsymbol{d}\right\}\right\} - \beta\Re\left\{\boldsymbol{F}^{-1}\boldsymbol{d}\right\}\right)\right\}\right]_k, \tag{5.68}$$

and the particular instance of $\hat{v}_k$ which corresponds to the $j^{\text{th}}$ letter $\boldsymbol{d}_j$ of the IDFT input vector alphabet $\mathcal{A}_{\boldsymbol{d}}$ is therefore given by

$$\hat{v}_{j,k} = [\hat{\boldsymbol{v}}_j]_k = \left[\Im\left\{\boldsymbol{F}\left(\mathrm{Q}\left\{\Re\left\{\boldsymbol{F}^{-1}\boldsymbol{d}_j\right\}\right\} - \beta\Re\left\{\boldsymbol{F}^{-1}\boldsymbol{d}_j\right\}\right)\right\}\right]_k. \tag{5.69}$$

The one-dimensional imaginary PDF of $\hat{v}_k$ is therefore

$$f_{\hat{v}_k}(\hat{v}'_k) = \frac{1}{N_{\boldsymbol{d}}} \sum_{j=1}^{N_{\boldsymbol{d}}} \delta\left(\hat{v}'_k - \hat{v}_{j,k}\right). \tag{5.70}$$

Next, the CDF of the $k^{\text{th}}$ quantizer error frequency-sample imaginary-part $\hat{v}_k$ is given by

$$\begin{aligned} F_{\hat{v}_k}(\hat{v}''_k) &= \int_{-\infty}^{\hat{v}''_k} f_{\hat{v}_k}(\hat{v}'_k)\ \mathrm{d}\hat{v}'_k \\ &= \int_{-\infty}^{\hat{v}''_k} \frac{1}{N_{\boldsymbol{d}}} \sum_{j=1}^{N_{\boldsymbol{d}}} \delta\left(\hat{v}'_k - \hat{v}_{j,k}\right)\ \mathrm{d}v'_k \\ &= \frac{1}{N_{\boldsymbol{d}}} \sum_{\hat{v}_{j,k} \leq \hat{v}''_k} 1. \end{aligned} \tag{5.71}$$

### 5.3.28 'Exhaustive' PDF and CDF of All Quantizer Error Frequency-Sample Imaginary-Parts

By taking the expected value of *all* of the PDFs $f_{\hat{v}_k},\ k \in \mathbb{Z}_N$, of the quantizer error frequency-sample imaginary-parts $\hat{v}_k$, we find that the overall PDF of *all* of the imaginary parts $\hat{v}_k, k \in \mathbb{Z}_N$ of the quantizer error frequency-sample imaginary-parts is

$$f_{\hat{v}}(\hat{v}') = \mathrm{E}\left[f_{\hat{v}_k}(\hat{v}')\right] = \frac{1}{N} \sum_{k=0}^{N-1} f_{\hat{v}_k}(\hat{v}'). \tag{5.72}$$

Next, the CDF of *all* of the quantizer error frequency-sample imaginary-parts $\hat{v}_k, k \in \mathbb{Z}_N$, is equal to the expected value of *all* of the CDFs $F_{\hat{v}_k},\ k \in \mathbb{Z}_N$, of *all* of the quantizer error frequency-sample imaginary-parts $\hat{v}_k,\ k \in \mathbb{Z}_N$, and is given by

$$\begin{aligned} F_{\hat{v}}(\hat{v}'') &= \mathrm{E}\left[F_{\hat{v}_k}\left(\hat{v}''\right)\right] \\ &= \frac{1}{N} \sum_{k=0}^{N-1} F_{\hat{v}_k}(\hat{v}'') \\ &= \frac{1}{N \cdot N_{\boldsymbol{d}}} \sum_{k=0}^{N-1} \sum_{\hat{v}_{j,k} \leq \hat{v}''} 1. \end{aligned} \tag{5.73}$$

### 5.3.29 'Exhaustive' Covariance Matrix of the IDFT Output Time-Sample Real-Part Vector and the Quantizer Output Time-Sample Vector

Now §5.3.29 to §5.3.32 will consider the cross correlation between the transmitter quantizer input and output signals.

In general, the covariance matrix of two random vectors is a matrix whose $(l, m)$ $^{\text{th}}$ entry is the covariance between the $l^{\text{th}}$ entry of the first random vector and the $m^{\text{th}}$ entry of the second random vector.

The $(l, m)$ $^{\text{th}}$ entry of the covariance matrix $\mathbf{COV}(\boldsymbol{f}, \boldsymbol{g})$ of the IDFT output time-sample real-part vector $\boldsymbol{f}$ and the quantizer output time-sample vector $\boldsymbol{g}$ is therefore given by

$$\begin{aligned}
[\mathbf{COV}(\boldsymbol{f}, \boldsymbol{g})]_{l,m} &= \operatorname{cov}(f_l, g_m) \\
&= E\Big[\big(f_l - \mathrm{E}[f_l]\big)\,\big(g_m - \mathrm{E}[g_m]\big)\Big] \\
&= \mathrm{E}[f_l g_m] - \mathrm{E}[f_l]\mathrm{E}[g_m]. \qquad (5.74)
\end{aligned}$$

The matrix formulation of $\mathbf{COV}(\boldsymbol{f}, \boldsymbol{g})$ is

$$\begin{aligned}
\mathbf{COV}(\boldsymbol{f}, \boldsymbol{g}) &= \mathrm{E}\left[\big(\boldsymbol{f} - \mathrm{E}[\boldsymbol{f}]\big)\big(\boldsymbol{g} - \mathrm{E}[\boldsymbol{g}]\big)^{\mathrm{T}}\right] \\
&= \mathrm{E}\left[\boldsymbol{f}\boldsymbol{g}^{\mathrm{T}}\right] - \mathrm{E}\left[\boldsymbol{f}\right]\mathrm{E}\left[\boldsymbol{g}^{\mathrm{T}}\right], \qquad (5.75)
\end{aligned}$$

which, using (5.10) and (5.24), is expanded to

$$\begin{aligned}
\mathbf{COV}(\boldsymbol{f}, \boldsymbol{g}) = \quad & \frac{1}{N_{\boldsymbol{d}}} \sum_{j=1}^{N_{\boldsymbol{d}}} \Big(\Re\left\{\boldsymbol{F}^{-1}\boldsymbol{d}_j\right\}\Big)\ \Big(\mathrm{Q}\left\{\Re\{\boldsymbol{F}^{-1}\boldsymbol{d}_j\}\right\}\Big)^{\mathrm{T}} \\
- \quad & \frac{1}{N_{\boldsymbol{d}}^2} \sum_{j=1}^{N_{\boldsymbol{d}}} \Big(\Re\left\{\boldsymbol{F}^{-1}\boldsymbol{d}_j\right\}\Big)\ \sum_{j=1}^{N_{\boldsymbol{d}}} \Big(\mathrm{Q}\left\{\Re\{\boldsymbol{F}^{-1}\boldsymbol{d}_j\}\right\}\Big)^{\mathrm{T}}. \qquad (5.76)
\end{aligned}$$

### 5.3.30 'Exhaustive' Correlation Matrix of the IDFT Output Time-Sample Real-Part Vector and the Quantizer Output Time-Sample Vector

In general, the correlation matrix of two random vectors is a matrix whose $(l,m)^{\text{th}}$ entry is the Pearson's correlation coefficient between the $l^{\text{th}}$ entry of the first random vector and the $m^{\text{th}}$ entry of the second random vector.

The $(l,m)^{\text{th}}$ entry of the correlation matrix $\mathbf{CORR}(\boldsymbol{f},\boldsymbol{g})$ of the IDFT output time-sample real-part vector $\boldsymbol{f}$ and the quantizer output time-sample vector $\boldsymbol{g}$ is therefore

$$\begin{aligned}
[\mathbf{CORR}(\boldsymbol{f},\boldsymbol{g})]_{l,m} &= \frac{\operatorname{cov}(f_l, g_m)}{\sqrt{\operatorname{cov}(f_l, f_l)} \cdot \sqrt{\operatorname{cov}(g_m, g_m)}} \\
&= \frac{[\mathbf{COV}(\boldsymbol{f},\boldsymbol{g})]_{l,m}}{\sqrt{[\mathbf{COV}(\boldsymbol{f})]_{l,l}} \cdot \sqrt{[\mathbf{COV}(\boldsymbol{g})]_{m,m}}}. \qquad (5.77)
\end{aligned}$$

The matrix formulation of $\mathbf{CORR}(\boldsymbol{f},\boldsymbol{g})$ , in terms of the entries of the covariance matrix $\mathbf{COV}(\boldsymbol{f},\boldsymbol{g})$ of $\boldsymbol{f}$ and $\boldsymbol{g}$ in (5.76), the covariance matrix $\mathbf{COV}(\boldsymbol{f})$ of $\boldsymbol{f}$ in (5.27), and the covariance matrix $\mathbf{COV}(\boldsymbol{g})$ of $\boldsymbol{g}$ in (5.14), is then neatly given by

$$\mathbf{CORR}(\boldsymbol{f},\boldsymbol{g}) = \Big(\mathbf{DIAG}[\mathbf{COV}(\boldsymbol{f})]\Big)^{-1/2} \; \mathbf{COV}(\boldsymbol{f},\boldsymbol{g}) \; \Big(\mathbf{DIAG}[\mathbf{COV}(\boldsymbol{g})]\Big)^{-1/2}. \qquad (5.78)$$

### 5.3.31 'Exhaustive' Covariance Matrix of the IDFT Output Time-Sample Real-Part Vector and the Quantizer Error Time-Sample Vector

We now consider how the quantization error is related to the quantizer input signal.

The matrix formulation of the covariance matrix of the IDFT output time-sample real-part vector $\boldsymbol{f}$ and the quantizer error time-sample vector $\boldsymbol{q}$ is

$$\begin{aligned}\mathbf{COV}(\boldsymbol{f},\boldsymbol{q}) &= \mathbf{COV}(\boldsymbol{f},\boldsymbol{q}) \\ &= \mathbf{COV}(\boldsymbol{f},\boldsymbol{g}-\beta\boldsymbol{f}) \\ &= \mathbf{COV}(\boldsymbol{f},\boldsymbol{g})-\beta\,\mathbf{COV}(\boldsymbol{f},\boldsymbol{f}) \\ &= \mathbf{COV}(\boldsymbol{f},\boldsymbol{g})-\beta\mathbf{COV}(\boldsymbol{f}),\end{aligned} \tag{5.79}$$

where $\mathbf{COV}(\boldsymbol{f},\boldsymbol{g})$ is given in (5.76) and $\mathbf{COV}(\boldsymbol{f})$ is given in (5.14).

### 5.3.32 'Exhaustive' Correlation Matrix of the IDFT Output Time-Sample Real-Part Vector and the Quantizer Error Time-Sample Vector

The matrix formulation of the correlation matrix of the IDFT output time-sample real-part vector $\boldsymbol{f}$ and the quantizer error time-sample vector $\boldsymbol{q}$, in terms of the covariance matrix $\mathbf{COV}(\boldsymbol{f},\boldsymbol{q})$ of $\boldsymbol{f}$ and $\boldsymbol{q}$ given in (5.79), the covariance matrix $\mathbf{COV}(\boldsymbol{f})$ of $\boldsymbol{f}$ given in (5.27), and the covariance matrix $\mathbf{COV}(\boldsymbol{q})$ of $\boldsymbol{q}$ given in (5.39), is

$$\mathbf{CORR}(\boldsymbol{f},\boldsymbol{q}) = \Big(\mathbf{DIAG}[\mathbf{COV}(\boldsymbol{f})]\Big)^{-1/2}\ \mathbf{COV}(\boldsymbol{f},\boldsymbol{q})\ \Big(\mathbf{DIAG}[\mathbf{COV}(\boldsymbol{q})]\Big)^{-1/2}. \tag{5.80}$$

### 5.3.33 Applicability of the Exact 'Exhaustive' Method

In §5.3, we have seen that the exact 'exhaustive' method is capable of obtaining exact PDFs, CDFs, covariance matrices, and correlation matrices. The number of calculations required to obtain results for the 'exhaustive' method is $\sim \mathcal{O}(N_{\boldsymbol{d}})$, where $N_{\boldsymbol{d}}$ is the size of the exhaustive alphabet $\mathcal{A}_{\boldsymbol{d}}$ of all possible IDFT input symbol vectors $\boldsymbol{d}$.

For a system having $N'_{\mathrm{SD}}$ baseband random Data sub-carriers each modulated with the same $M$QAM/$M$PSK symbol alphabet $\mathcal{A}_{\mathrm{SD}}$ of size $|\mathcal{A}_{\mathrm{SD}}| = M$, the IDFT input alphabet is given by

$$\mathcal{A}_{\boldsymbol{d}} = \begin{cases} \mathcal{A}_{\mathrm{SD}}^{N'_{\mathrm{SD}}} & \text{, Pilot sub-carriers not present} \\ \mathcal{A}_{\mathrm{SP}} \times \mathcal{A}_{\mathrm{SD}}^{N'_{\mathrm{SD}}} & \text{, Pilot sub-carriers present.} \end{cases} \tag{5.81}$$

where $\mathcal{A}_{\mathrm{SP}}$ indicates the Pilot sub-carrier sequence alphabet (when Pilots are present), $\times$ indicates Cartesian-product, and $\mathcal{A}_{\mathrm{SD}}^{N'_{\mathrm{SD}}}$ indicates the $N'_{\mathrm{SD}}$-fold Cartesian-product of $\mathcal{A}_{\mathrm{SD}}$ with itself.

We assume that, when Pilots sub-carriers are present, there are two Pilot sequences (a single Pilot sequence multiplied pseudo-randomly either by +1 or -1) per normal practice (e.g. [2]); so that the alphabet size of any Pilot sub-carrier sequence is $|\mathcal{A}_{\mathrm{SP}}| = 2$. The size of the the exhaustive alphabet $\mathcal{A}_{\boldsymbol{d}}$ of all possible IDFT input symbol vectors $\boldsymbol{d}$ is therefore

$$N_{\boldsymbol{d}} = \begin{cases} M^{N'_{\mathrm{SD}}} & \text{, Pilot sub-carriers not present} \\ 2M^{N'_{\mathrm{SD}}} & \text{, Pilot sub-carriers present.} \end{cases} \tag{5.82}$$

Applying (5.82) for the various OFDM types used in this thesis, we obtain exhaustive alphabet sizes for each OFDM Type as shown in Table 5.2.

| OFDM Type | $M$ | $N'_{SD}$ | Pilots? | $N_{\boldsymbol{d}}$ | 'Exhaustive' Possible? | Comment |
|---|---|---|---|---|---|---|
| 1.2 | 2 | 3 | Yes | 16 | Yes | |
| 1.4 | 4 | 3 | Yes | 128 | Yes | |
| 2.2 | 2 | 8 | No | 256 | Yes | |
| 2.4 | 4 | 8 | No | 65,536 | Yes | |
| 3.2 | 2 | 16 | No | 65,536 | Yes | |
| 4.2 | 2 | 10 | Yes | 2,048 | Yes | |
| 5.2 | 2 | 48 | Yes | $5.6\text{x}10^{14}$ | No | IEEE 802.11a, BPSK |
| 5.4 | 4 | 48 | Yes | $1.6\text{x}10^{29}$ | No | IEEE 802.11a, QPSK |
| 5.16 | 16 | 48 | Yes | $1.3\text{x}10^{58}$ | No | IEEE 802.11a, 16QAM |
| 5.64 | 64 | 48 | Yes | $9.9\text{x}10^{86}$ | No | IEEE 802.11a, 64QAM |

Table 5.2: Size $N_{\boldsymbol{d}}$ of the exhaustive alphabet $\mathcal{A}_{\boldsymbol{d}}$ of all possible IDFT input symbol vectors $\boldsymbol{d}$, for various OFDM Types.

Clearly, from Table 5.2, we see that, due to the prohibitively large number of calculations required, the 'exhaustive' method cannot be used for medium-sized practical OFDM systems such as IEEE 802.11a [1]. We must therefore resort to other methods to analyse such systems.

### 5.3.34 Results Summary

In §5.3, many results have been obtained using the 'Exhaustive' method for small-scale quantized OFDM systems. In particular, we have obtained exact results for the PDFs, CDFs, covariance matrices, and correlation matrices relating to the IDFT input frequency-samples, the unquantized IDFT output time-samples, the quantized IDFT output time-samples, the quantizer error time-samples, and the quantizer error frequency-samples.

Regarding the PDF results, the small number of PDF diracs relative to the IDFT alphabet size at all points in the processing chain is notable leading to a questioning of whether there is some hidden structure in the OFDM signal. This question is explored in the later section on the 'Convolution' method. Also, a divergence from Gaussian is discovered in both the time-domain and frequency-domain PDFs which is contrary to the assumptions of most of the extant literature on this topic. In particular, the divergence from Gaussian of the quantization error in the receiver decision domain (frequency-domain) means that a Gaussian assumption will lead to incorrect BER predictions. This is a major finding of this thesis.

Regarding the correlation matrices results, significant correlations found between the quantizer input and the quantizer output mean that that the additive quantizer noise cannot be considered to be independent. This is contrary to most of the extant literature and is another major finding of this thesis.

## 5.4 The Approximate 'Monte Carlo' Method

In §5.3.33, we found that the exact 'exhaustive' method cannot be used for medium-sized OFDM systems such as IEEE 802.11a due to the prohibitively large number of calculations required to include every possible letter of the IDFT input alphabet $\mathcal{A}_{\boldsymbol{d}}$ in the calculations.

As a sub-optimal and non-exact alternative, we can use the Monte Carlo method which randomly selects a smaller sub-set of the exhaustive alphabet for our calculations. All of the equations of §5.3 still apply except, now, a smaller, randomly chosen alphabet $\mathcal{A}_{\boldsymbol{d}}$ is used.

The Monte Carlo method has the advantage of limiting the number of calculations (and the associated simulation time) to acceptable levels.

The Monte Carlo method also has several disadvantages. Firstly, any simulation results are no longer exact but are only approximations. Secondly, low probability 'tail events' may not be chosen in the random selection process and, therefore, any calculated tail-probabilities may not be accurate. Thirdly, 'infuential' events may not be chosen in the random selection process leading to misleading results.

As a rule-of-thumb, the Monte Carlo method should be chosen only as a last resort when other exact or bounded numerical or analytical methods are not practicable.

The Monte Carlo results become more accurate as the IDFT input alphabet size $|\mathcal{A}_{\boldsymbol{d}}|$ approaches that for the 'exhaustive' method. Accordingly, for Monte Carlo simulations, the IDFT input alphabet size $|\mathcal{A}_{\boldsymbol{d}}|$ should be chosen as large as practicable. Note that each result has the IDFT input alphabet size $|\mathcal{A}_{\boldsymbol{d}}|$ used for the Monte Carlo simulation clearly displayed.

See the following sub-sections for results for the IEEE 802.11a WLAN system [1] obtained using the Monte Carlo method.

### 5.4.1 'Monte Carlo' Correlation Matrix of the IDFT Output Time-Sample Real-Part Vector

We begin with Monte Carlo results for the correlation matrix $\mathbf{CORR}(\boldsymbol{f})$ of the IDFT output time-sample real-part vector $\boldsymbol{f}$. We do this primarily because Monte Carlo results for $\mathbf{CORR}(\boldsymbol{f})$ can be verified against results obtained independently by the 'Matrix Transformation' method later in §6.1. With these Monte Carlo results associated with the IDFT output vector $\boldsymbol{f}$ thus verified, we will have built confidence in the various Monte Carlo results associated with the quantizer output vector $\boldsymbol{g}$ (occurring downstream from $\boldsymbol{f}$ in the processing chain) which cannot be independently verified.

#### 5.4.1.1 Case: OFDM Type 5.2, IEEE 802.11a WLAN, BPSK Data

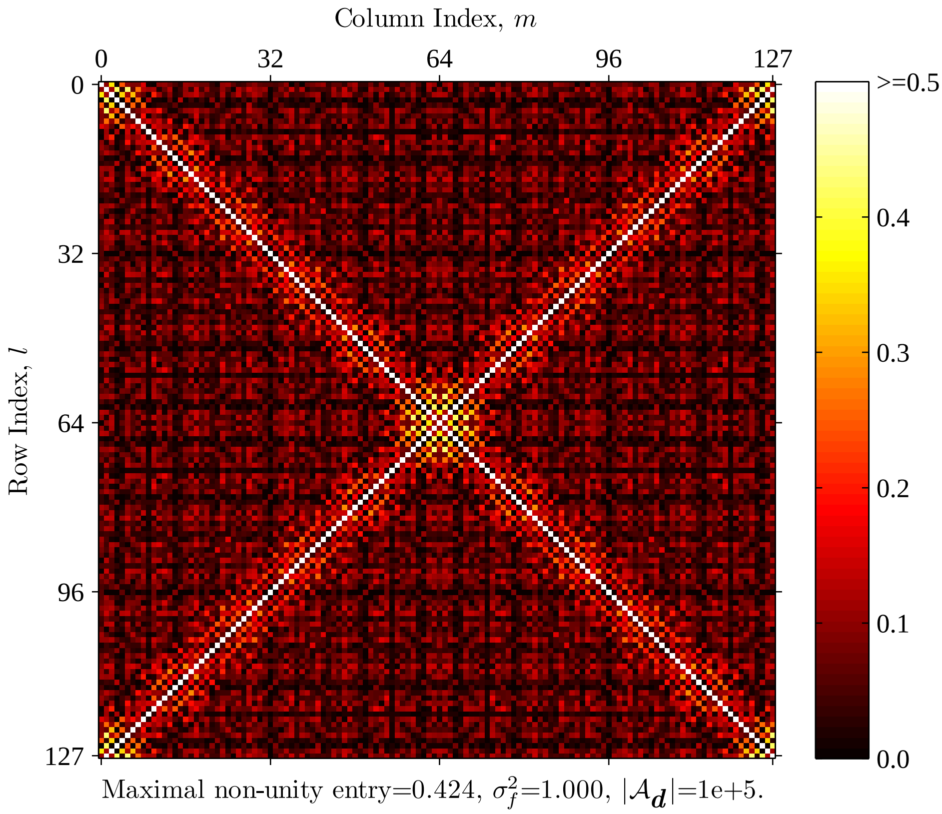


| | |
|---|---|
| OFDM Type 5.2: | IEEE 802.11a, $N = 128, \mathcal{K}_{\mathrm{SZ}} = \{0{:}5,32,59{:}69,96,123{:}127\}$,<br>$\mathcal{K}_{\mathrm{SP}} = \{11, 25, 39, 53, 75, 89, 103, 117\}, \mathcal{A}_{\mathrm{SP}} = \mathcal{A}_{\mathrm{BPSK}}$,<br>$\mathcal{K}_{\mathrm{SD}} = \{6{:}10,12{:}24,26{:}31,33{:}38,40{:}52,54{:}58,70{:}74,76{:}88,90{:}95,97{:}102,104{:}116,118{:}122\}$,<br>$\mathcal{A}_{\mathrm{SD}} = \mathcal{A}_{\mathrm{BPSK}}, \mathcal{D}_{\mathrm{SP}} = \{+1, +1, +1, -1, -1, +1, +1, +1\}$. |

Figure 5.26: 'Monte Carlo' magnitude $|\mathbf{CORR}(\boldsymbol{f})|$ of the correlation matrix of the real digital IF time-sample vector $\boldsymbol{f}$ at the IDFT output, OFDM Type = 5.2 (IEEE 802.11a, BPSK).

#### 5.4.1.2 Case: OFDM Type 5.4, IEEE 802.11a WLAN, QPSK Data

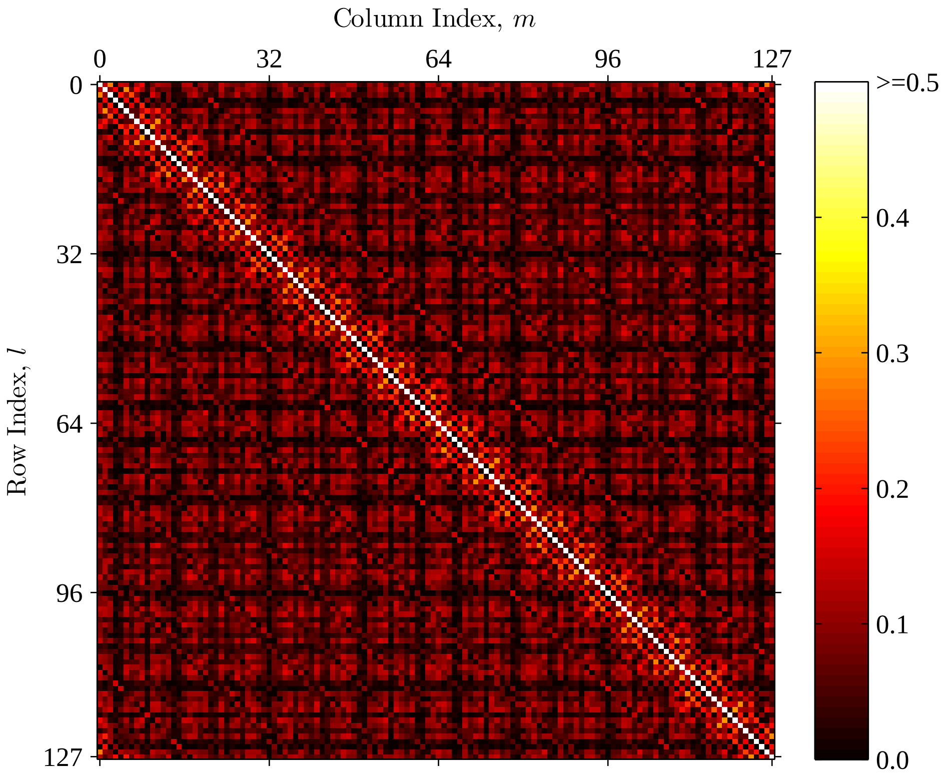


Maximal non-unity entry=0.293, $\sigma_f^2$=1.000, $|\mathcal{A}_{\boldsymbol{d}}|$=1e+5.

OFDM Type 5.4: IEEE 802.11a, $N = 128, \mathcal{K}_{\mathrm{SZ}} = \{0{:}5,32,59{:}69,96,123{:}127\}$,
$\mathcal{K}_{\mathrm{SP}} = \{11, 25, 39, 53, 75, 89, 103, 117\}, \mathcal{A}_{\mathrm{SP}} = \mathcal{A}_{\mathrm{BPSK}}$,
$\mathcal{K}_{\mathrm{SD}} = \{6{:}10,12{:}24,26{:}31,33{:}38,40{:}52,54{:}58,70{:}74,76{:}88,90{:}95,97{:}102,104{:}116,118{:}122\}$,
$\mathcal{A}_{\mathrm{SD}} = \mathcal{A}_{\mathrm{QPSK}}, \mathcal{D}_{\mathrm{SP}} = \{+1, +1, +1, -1, -1, +1, +1, +1\}$.

Figure 5.27: 'Monte Carlo' magnitude $|\mathbf{CORR}(\boldsymbol{f})|$ of the correlation matrix of the real digital IF time-sample vector $\boldsymbol{f}$ at the IDFT output, OFDM Type = 5.4 (IEEE 802.11a, QPSK).

The unity-valued offset-anti-diagonal entries of $\mathbf{CORR}(\boldsymbol{f})$ which appear for the BPSK case in Figure 5.26 have disappeared for this QPSK case.

Also, we note that the results for this QPSK case strongly match the results for the 16QAM case in Figure 5.28 and the 64QAM case in Figure 5.29.

#### 5.4.1.3 Case: OFDM Type 5.16, IEEE 802.11a WLAN, 16QAM Data

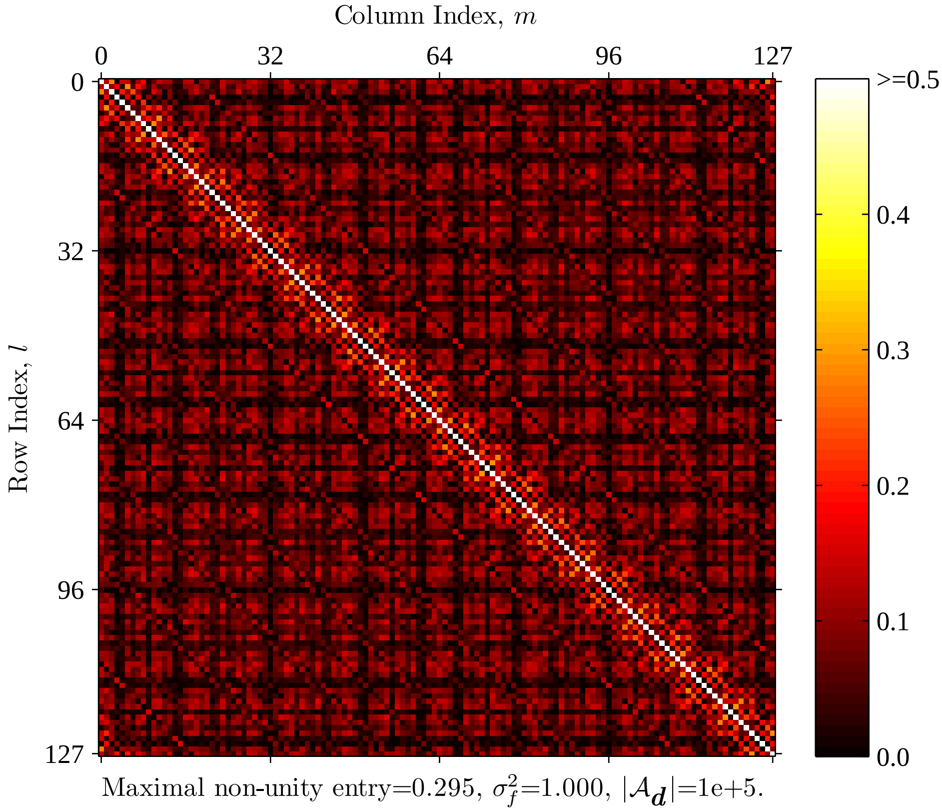


| | |
|---|---|
| OFDM Type 5.16: | IEEE 802.11a, $N = 128, \mathcal{K}_{\text{SZ}} = \{0{:}5{,}32{,}59{:}69{,}96{,}123{:}127\}$, $\mathcal{K}_{\text{SP}} = \{11, 25, 39, 53, 75, 89, 103, 117\}, \mathcal{A}_{\text{SP}} = \mathcal{A}_{\text{BPSK}}$, $\mathcal{K}_{\text{SD}} = \{6{:}10{,}12{:}24{,}26{:}31{,}33{:}38{,}40{:}52{,}54{:}58{,}70{:}74{,}76{:}88{,}90{:}95{,}97{:}102{,}104{:}116{,}118{:}122\}$, $\mathcal{A}_{\text{SD}} = \mathcal{A}_{\text{16QAM}}, \mathcal{D}_{\text{SP}} = \{+1, +1, +1, -1, -1, +1, +1, +1\}$. |

Figure 5.28: 'Monte Carlo' magnitude $|\mathbf{CORR}(\boldsymbol{f})|$ of the correlation matrix of the real digital IF time-sample vector $\boldsymbol{f}$ at the IDFT output, OFDM Type = 5.16 (IEEE 802.11a, 16QAM).

#### 5.4.1.4 Case: OFDM Type 5.64, IEEE 802.11a WLAN, 64QAM Data

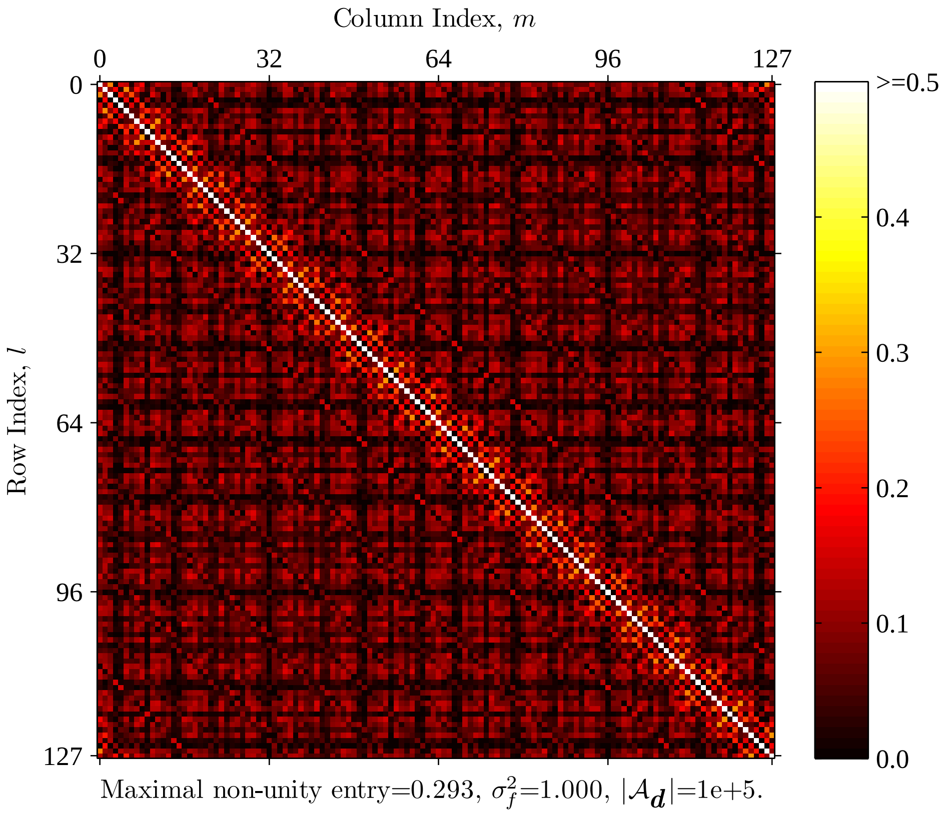


| | |
|---|---|
| OFDM Type 5.64: | IEEE 802.11a, $N = 128, \mathcal{K}_{\mathrm{SZ}} = \{0{:}5,32,59{:}69,96,123{:}127\}$,<br>$\mathcal{K}_{\mathrm{SP}} = \{11, 25, 39, 53, 75, 89, 103, 117\}, \mathcal{A}_{\mathrm{SP}} = \mathcal{A}_{\mathrm{BPSK}}$,<br>$\mathcal{K}_{\mathrm{SD}} = \{6{:}10,12{:}24,26{:}31,33{:}38,40{:}52,54{:}58,70{:}74,76{:}88,90{:}95,97{:}102,104{:}116,118{:}122\}$,<br>$\mathcal{A}_{\mathrm{SD}} = \mathcal{A}_{\mathrm{64QAM}}, \mathcal{D}_{\mathrm{SP}} = \{+1, +1, +1, -1, -1, +1, +1, +1\}$. |

Figure 5.29: 'Monte Carlo' magnitude $|\mathbf{CORR}(\boldsymbol{f})|$ of the correlation matrix of the real digital IF time-sample vector $\boldsymbol{f}$ at the IDFT output, OFDM Type = 5.64 (IEEE 802.11a, 64QAM).

#### 5.4.1.5 Summary of Results

The above IEEE 802.11a Monte Carlo results for the correlation matrix $\mathbf{CORR}(\boldsymbol{f})$ of the IDFT output $\boldsymbol{f}$ show significant correlations between the IDFT output time samples $f_n, n \in \mathbb{Z}_N$. This is not unexpected since any such band-limited system should show correlations between the time-samples.

For the BPSK case in Figure 6.1.3.3, there are unity correlations in the offset-anti-diagonal entries of $\mathbf{CORR}(\boldsymbol{f})$. However, for the QPSK, 16QAM, and 64QAM cases, these offset-anti-diagonal entries disappear. This curious phenomenom will be explained later in the 'Matrix Transformation' section §6.1.

There is a strong match between the $\mathbf{CORR}(\boldsymbol{f})$ results for the QPSK, 16QAM, and 64QAM (i.e. the non-BPSK) cases. This phenomenom is explained later in the 'Matrix Transformation' section §6.1.

The above Monte Carlo results for $\mathbf{CORR}(\boldsymbol{f})$ have been independently verified against the equivalent 'Matrix Transformation' results in §6.1 thus lending confidence to other later Monte Carlo results.

### 5.4.2 'Monte Carlo' Correlation Matrix of the Quantizer Output Time-Sample Vector

Next, we examine the correlation matrix $\mathbf{CORR}(\boldsymbol{g})$ of the quantizer output time sample vector $\boldsymbol{g}$ for the cases shown in Table 5.3.

| Figure | OFDM Type | $b$ | Quantization | Clipping | $\kappa \in$ | $\Delta \in$ |
|---|---|---|---|---|---|---|
| 5.30 | 5.2 | 3 | Yes | Yes | {0.4,0.6,1,2,3,10} | {1.1e-1,1.7e-1,2.9e-1,5.7e-1,8.6e-1,2.9e+0} |
| 5.31 | 5.2 | - | No | Yes | {0.4,0.6,1,2,3,10} | {0} |
| 5.32 | 5.2 | - | Yes | No | - | {1.1e-1,1.7e-1,2.9e-1,5.7e-1,8.6e-1,2.9e+0} |
| 5.33 | 5.2 | 6 | Yes | Yes | {0.4,0.6,1,2,3,10} | {1.3e-2,1.9e-2,3.9e-2,6.3e-2,9.5e-2,3.2e-1} |
| 5.34 | 5.2 | - | No | Yes | {0.4,0.6,1,2,3,10} | {0} |
| 5.35 | 5.2 | - | Yes | No | - | {1.3e-2,1.9e-2,3.9e-2,6.3e-2,9.5e-2,3.2e-1} |

Table 5.3: Schedule for Monte Carlo $\mathbf{CORR}(\boldsymbol{g})$ results.

These particular cases are selected as exemplars to demonstrate the effects of combined quantization and clipping, clipping only, quantization only, and the number of quantizer bits on the magnitude $|\mathbf{CORR}(\boldsymbol{g})|$ of the correlation matrix of the quantizer output time-sample vector $\boldsymbol{g}$ of a typical OFDM system - IEEE 802.11a WLAN [1] with BPSK data.

#### 5.4.2.1 Summary of Results

For the 3-bit, combined quantization and clipping case in Figure 5.30, we observe that the variance (average energy per sample) $\sigma_g^2$ of the quantizer output samples decreases with decreasing clipping-factor $\kappa$. This is expected since the clipping 'clips off' some of the energy per sample. In the same way, the scaling factor $\beta = \sqrt{\sigma_g^2/\sigma_f^2}$ decreases with decreasing clipping-factor $\kappa$. This also expected since the variance $\sigma_f^2$ (average energy per sample) of the IDFT output (quantizer input) is held constant at unity as recorded in Figure 5.26. We observe also that the quantizer step-size $\Delta$ decreases with decreasing clipping factor since, for combined quantization and clipping, $\Delta$ is a fixed constant times the clipping level.

Looking through all of the results of Figures 5.30 to 5.35, we note that the magnitudes of the correlations between quantizer output time-samples $[|\mathbf{CORR}(\boldsymbol{g})|]_{l,m}$ as indicated by the colours in the two-dimensional plots, do not appear to be significantly affected by the clipping-factor $\kappa$, the quantizer step-size $\Delta$, or the number of quantizer bits $b$. In all cases, there is a strong resemblance to the results of the unquantized case $[|\mathbf{CORR}(\boldsymbol{f})|]_{l,m}$ shown in Figure 5.26.

Summing up, the magnitude $|\mathbf{CORR}(\boldsymbol{g})|$ of the correlation matrix of the quantizer output time-sample vector $\boldsymbol{g}$ is not a good indicator of the effects of quantization. However, these results are included here for completeness.

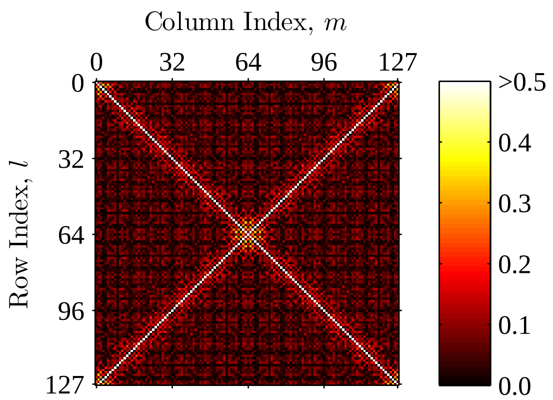


Maximal non-unity entry=0.335, $\sigma_g^2$=0.128,
$|\mathcal{A}_{\boldsymbol{d}}|$=1e+5, $\Delta$=1.1e-1, $\beta$=0.357.
(a) $\kappa = 0.4$ (severe clipping).

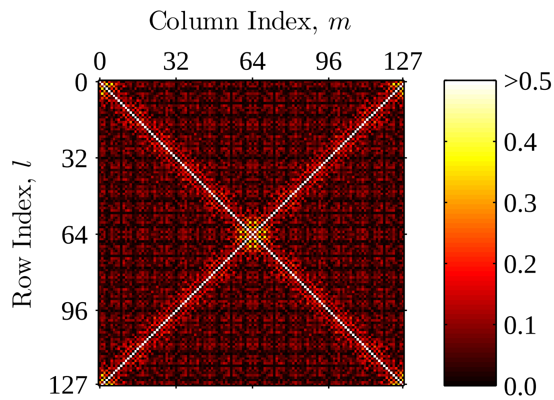


Maximal non-unity entry=0.360, $\sigma_g^2$=0.252,
$|\mathcal{A}_{\boldsymbol{d}}|$=1e+5, $\Delta$=1.7e-1, $\beta$=0.502.
(b) $\kappa = 0.6$.

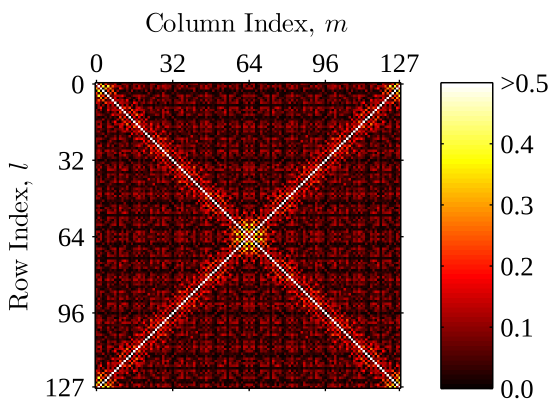


Maximal non-unity entry=0.392, $\sigma_g^2$=0.524,
$|\mathcal{A}_{\boldsymbol{d}}|$=1e+5, $\Delta$=2.9e-1, $\beta$=0.724.
(c) $\kappa = 1$.

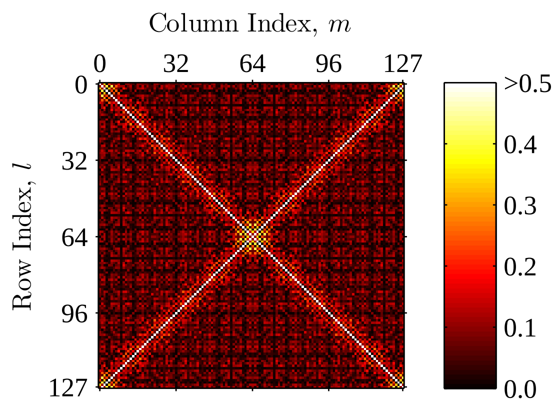


Maximal non-unity entry=0.412, $\sigma_g^2$=0.955,
$|\mathcal{A}_{\boldsymbol{d}}|$=1e+5, $\Delta$=5.7e-1, $\beta$=0.977.
(d) $\kappa = 2$.

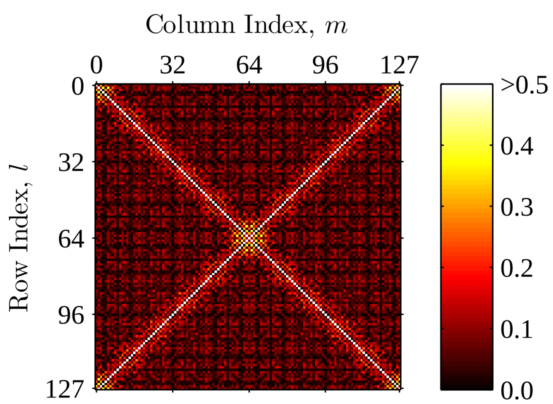


Maximal non-unity entry=0.397, $\sigma_g^2$=1.053,
$|\mathcal{A}_{\boldsymbol{d}}|$=1e+5, $\Delta$=8.6e-1, $\beta$=1.026.
(e) $\kappa = 3$.

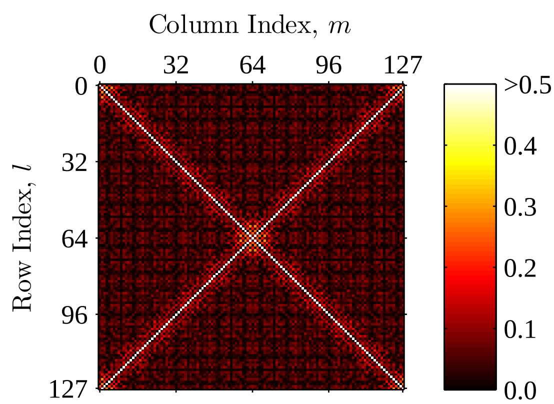


Maximal non-unity entry=0.283, $\sigma_g^2$=2.106,
$|\mathcal{A}_{\boldsymbol{d}}|$=1e+5, $\Delta$=2.9e+0, $\beta$=1.451.
(f) $\kappa = 10$ (no clipping).

OFDM Type 5.2: IEEE 802.11a, $N = 128, \mathcal{K}_{\mathrm{SZ}} = \{0{:}5,32,59{:}69,96,123{:}127\}$,
$\mathcal{K}_{\mathrm{SP}} = \{11, 25, 39, 53, 75, 89, 103, 117\}, \mathcal{A}_{\mathrm{SP}} = \mathcal{A}_{\mathrm{BPSK}}$,
$\mathcal{K}_{\mathrm{SD}} = \{6{:}10,12{:}24,26{:}31,33{:}38,40{:}52,54{:}58,70{:}74,76{:}88,90{:}95,97{:}102,104{:}116,118{:}122\}$,
$\mathcal{A}_{\mathrm{SD}} = \mathcal{A}_{\mathrm{BPSK}}, \mathcal{D}_{\mathrm{SP}} = \{+1, +1, +1, -1, -1, +1, +1, +1\}$.

Figure 5.30: 'Monte Carlo' magnitude $|\mathbf{CORR}(\boldsymbol{g})|$ of the correlation matrix of the quantizer output time-sample vector $\boldsymbol{g}$, OFDM Type = 5.2 (IEEE 802.11a, BPSK), $b = 3$ bits, for various clipping-factors $\kappa$.

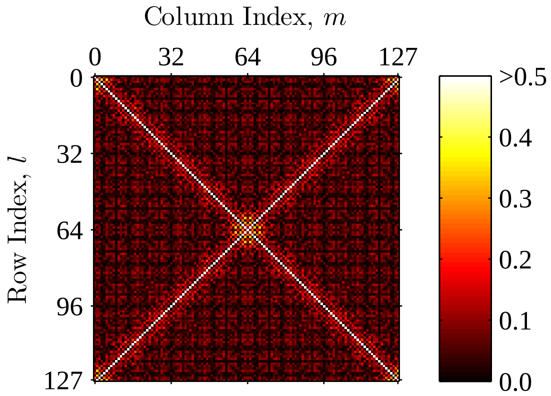


Maximal non-unity entry=0.337, $\sigma_g^2$=0.127, $|\mathcal{A}_{\boldsymbol{d}}|$=1e+5, $\Delta$=0.0e+0, $\beta$=0.356.

(a) $\kappa = 0.4$ (severe clipping).

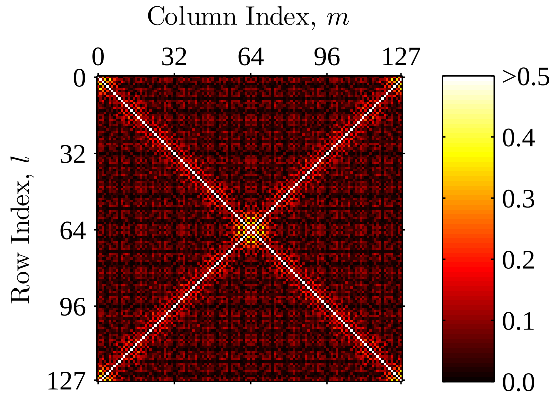


Maximal non-unity entry=0.362, $\sigma_g^2$=0.249, $|\mathcal{A}_{\boldsymbol{d}}|$=1e+5, $\Delta$=0.0e+0, $\beta$=0.499.

(b) $\kappa = 0.6$.

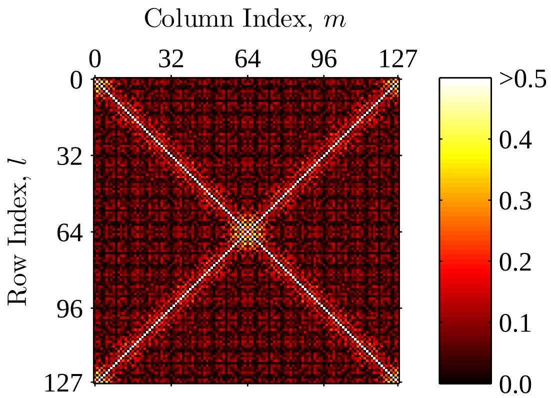


Maximal non-unity entry=0.396, $\sigma_g^2$=0.517, $|\mathcal{A}_{\boldsymbol{d}}|$=1e+5, $\Delta$=0.0e+0, $\beta$=0.719.

(c) $\kappa = 1$.

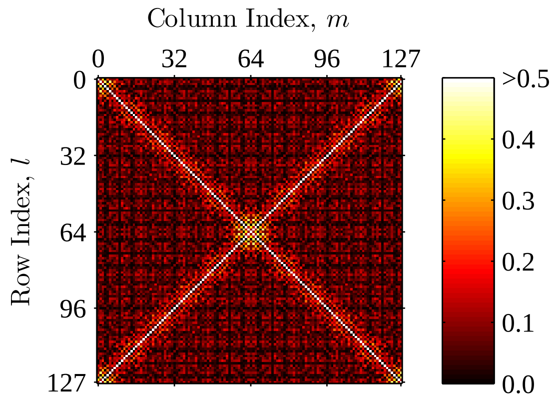


Maximal non-unity entry=0.423, $\sigma_g^2$=0.922, $|\mathcal{A}_{\boldsymbol{d}}|$=1e+5, $\Delta$=0.0e+0, $\beta$=0.960.

(d) $\kappa = 2$.

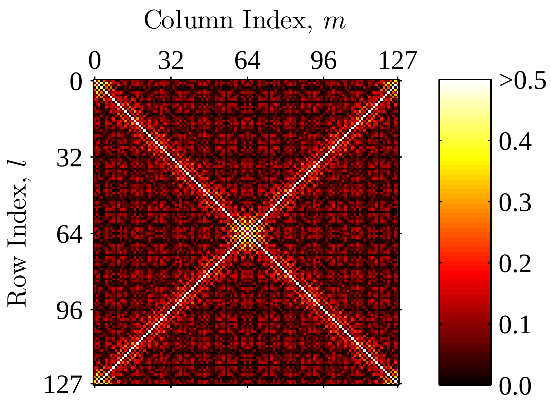


Maximal non-unity entry=0.424, $\sigma_g^2$=0.995, $|\mathcal{A}_{\boldsymbol{d}}|$=1e+5, $\Delta$=0.0e+0, $\beta$=0.997.

(e) $\kappa = 3$.

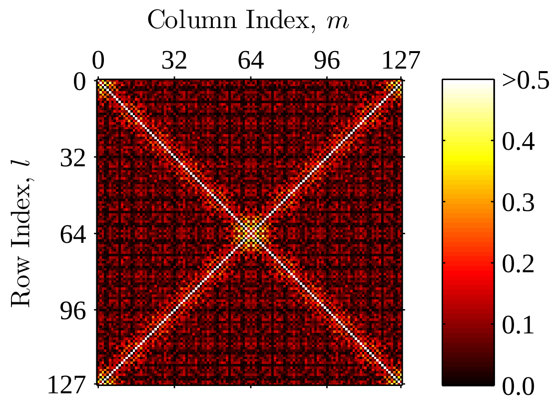


Maximal non-unity entry=0.424, $\sigma_q^2$=1.000 $|\mathcal{A}_{\boldsymbol{d}}|$=1e+5, $\Delta$=0.0e+0, $\beta$=1.000.

(f) $\kappa = 10$ (no clipping).

OFDM Type 5.2: IEEE 802.11a, $N = 128, \mathcal{K}_{\text{SZ}} = \{0{:}5,32,59{:}69,96,123{:}127\}$,
$\mathcal{K}_{\text{SP}} = \{11, 25, 39, 53, 75, 89, 103, 117\}, \mathcal{A}_{\text{SP}} = \mathcal{A}_{\text{BPSK}}$,
$\mathcal{K}_{\text{SD}} = \{6{:}10,12{:}24,26{:}31,33{:}38,40{:}52,54{:}58,70{:}74,76{:}88,90{:}95,97{:}102,104{:}116,118{:}122\}$,
$\mathcal{A}_{\text{SD}} = \mathcal{A}_{\text{BPSK}}, \mathcal{D}_{\text{SP}} = \{+1, +1, +1, -1, -1, +1, +1, +1\}$.

Figure 5.31: 'Monte Carlo' magnitude $|\mathbf{CORR}(\boldsymbol{g})|$ of the correlation matrix of the quantizer output time-sample vector $\boldsymbol{g}$, OFDM Type = 5.2 (IEEE 802.11a, BPSK), no quantization, clipping only, for various clipping-factors $\kappa$ matching the $b = 3$ case in Figure 5.30.

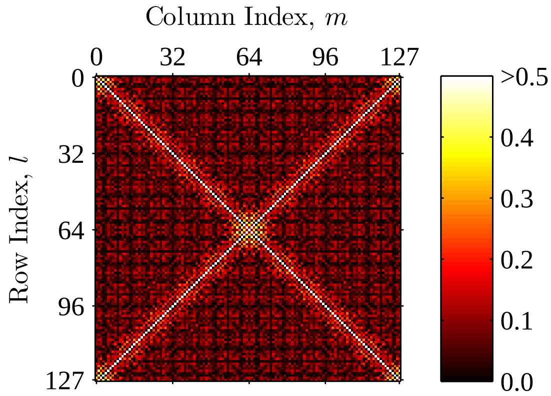


Maximal non-unity entry=0.424, $\sigma_g^2$=1.001, $|\mathcal{A}_{\boldsymbol{d}}|$=1e+5, $\Delta$=1.1e-1, $\beta$=1.001.

(a) $\Delta$=1.1e-1.

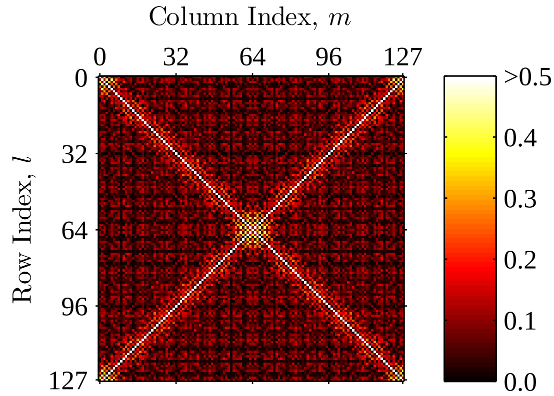


Maximal non-unity entry=0.423, $\sigma_g^2$=1.003, $|\mathcal{A}_{\boldsymbol{d}}|$=1e+5, $\Delta$=1.7e-1, $\beta$=1.001.

(b) $\Delta$=1.7e-1.

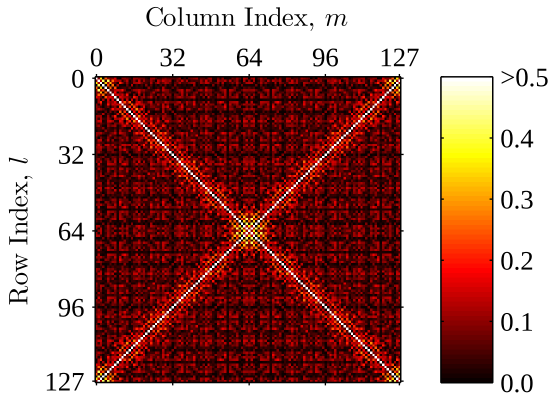


Maximal non-unity entry=0.421, $\sigma_g^2$=1.007, $|\mathcal{A}_{\boldsymbol{d}}|$=1e+5, $\Delta$=2.9e-1, $\beta$=1.003.

(c) $\Delta$=2.9e-1.

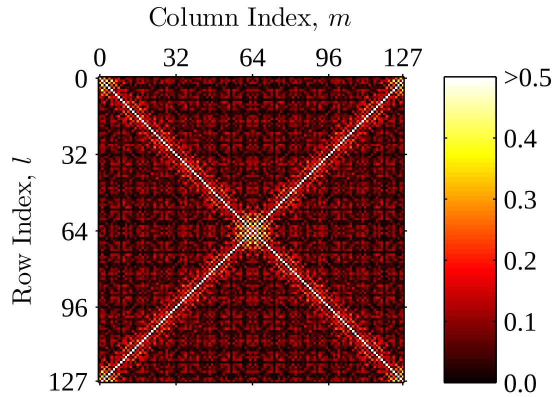


Maximal non-unity entry=0.414, $\sigma_g^2$=1.030, $|\mathcal{A}_{\boldsymbol{d}}|$=1e+5, $\Delta$=5.7e-1, $\beta$=1.015.

(d) $\Delta$=5.7e-1.

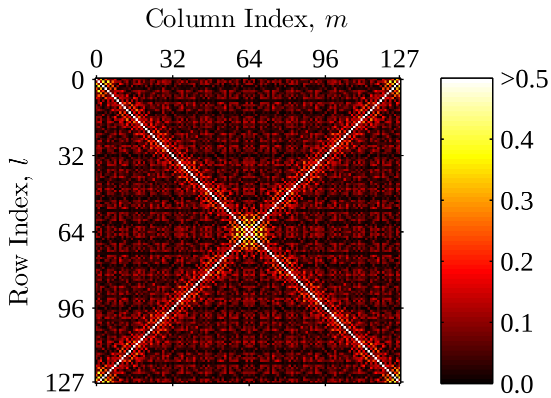


Maximal non-unity entry=0.397, $\sigma_g^2$=1.057, $|\mathcal{A}_{\boldsymbol{d}}|$=1e+5, $\Delta$=8.6e-1, $\beta$=1.028.

(e) $\Delta$=8.6e-1.

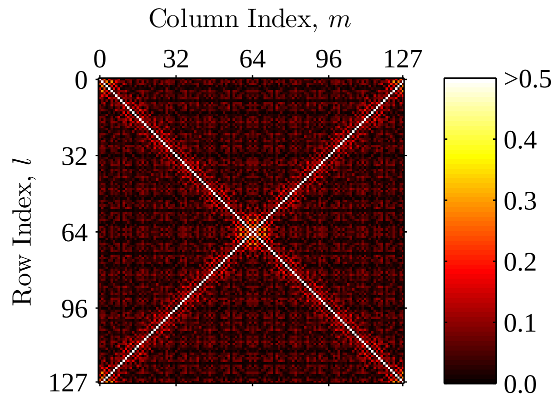


Maximal non-unity entry=0.283, $\sigma_g^2$=2.106, $|\mathcal{A}_{\boldsymbol{d}}|$=1e+5, $\Delta$=2.9e+0, $\beta$=1.451.

(f) $\Delta$=2.9e+0.

OFDM Type 5.2: IEEE 802.11a, $N = 128, \mathcal{K}_{\text{SZ}} = \{0{:}5,32,59{:}69,96,123{:}127\}$,
$\mathcal{K}_{\text{SP}} = \{11, 25, 39, 53, 75, 89, 103, 117\}, \mathcal{A}_{\text{SP}} = \mathcal{A}_{\text{BPSK}}$,
$\mathcal{K}_{\text{SD}} = \{6{:}10,12{:}24,26{:}31,33{:}38,40{:}52,54{:}58,70{:}74,76{:}88,90{:}95,97{:}102,104{:}116,118{:}122\}$,
$\mathcal{A}_{\text{SD}} = \mathcal{A}_{\text{BPSK}}, \mathcal{D}_{\text{SP}} = \{+1, +1, +1, -1, -1, +1, +1, +1\}$.

Figure 5.32: 'Monte Carlo' magnitude $|\mathbf{CORR}(\boldsymbol{g})|$ of the correlation matrix of the quantizer output time-sample vector $\boldsymbol{g}$, OFDM Type = 5.2 (IEEE 802.11a, BPSK), quantization only, no clipping, for various quantizer step sizes $\Delta$ matching the $b = 3$ case in Figure 5.30.

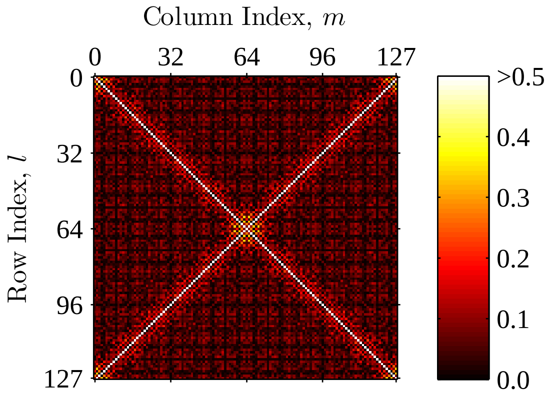


Maximal non-unity entry=0.337, $\sigma_g^2$=0.127,
$|\mathcal{A}_{\boldsymbol{d}}|$=1e+5, $\Delta$=1.3e-2, $\beta$=0.356.
(a) $\kappa = 0.4$ (severe clipping).

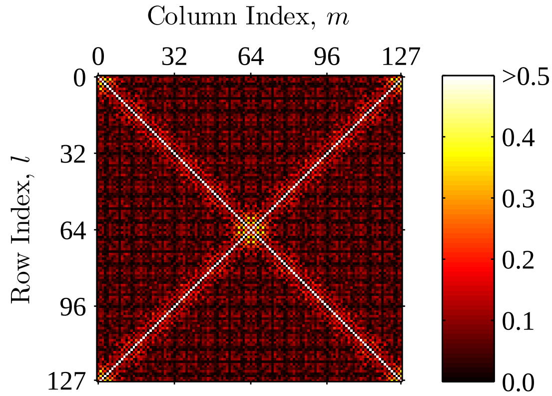


Maximal non-unity entry=0.362, $\sigma_g^2$=0.249,
$|\mathcal{A}_{\boldsymbol{d}}|$=1e+5, $\Delta$=1.9e-2, $\beta$=0.499.
(b) $\kappa = 0.6$.

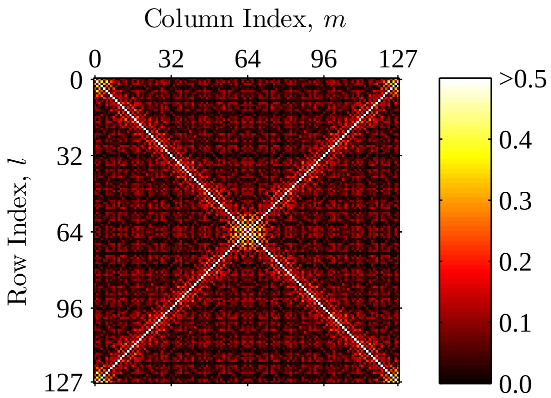


Maximal non-unity entry=0.396, $\sigma_g^2$=0.517,
$|\mathcal{A}_{\boldsymbol{d}}|$=1e+5, $\Delta$=3.2e-2, $\beta$=0.719.
(c) $\kappa = 1$.

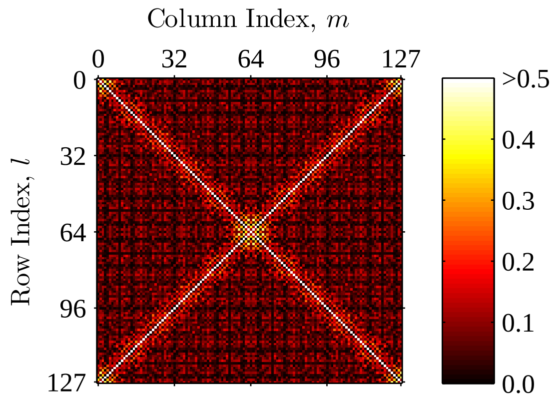


Maximal non-unity entry=0.423, $\sigma_g^2$=0.922,
$|\mathcal{A}_{\boldsymbol{d}}|$=1e+5, $\Delta$=6.3e-2, $\beta$=0.960.
(d) $\kappa = 2$.

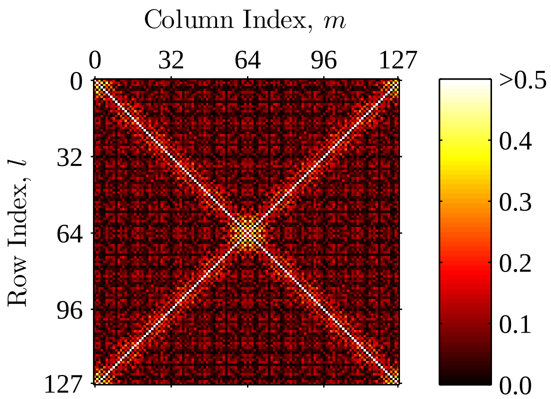


Maximal non-unity entry=0.424, $\sigma_g^2$=0.996,
$|\mathcal{A}_{\boldsymbol{d}}|$=1e+5, $\Delta$=9.5e-2, $\beta$=0.998.
(e) $\kappa = 3$.

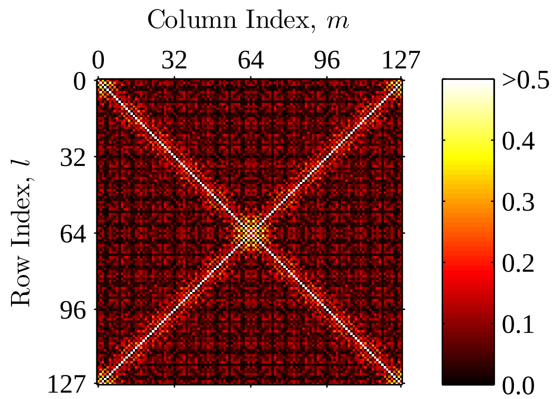


Maximal non-unity entry=0.421, $\sigma_g^2$=1.007,
$|\mathcal{A}_{\boldsymbol{d}}|$=1e+5, $\Delta$=3.2e-1, $\beta$=1.003.
(f) $\kappa = 10$ (no clipping).

OFDM Type 5.2: IEEE 802.11a, $N = 128, \mathcal{K}_{\mathrm{SZ}} = \{0{:}5{,}32{,}59{:}69{,}96{,}123{:}127\}$,
$\mathcal{K}_{\mathrm{SP}} = \{11, 25, 39, 53, 75, 89, 103, 117\}, \mathcal{A}_{\mathrm{SP}} = \mathcal{A}_{\mathrm{BPSK}}$,
$\mathcal{K}_{\mathrm{SD}} = \{6{:}10{,}12{:}24{,}26{:}31{,}33{:}38{,}40{:}52{,}54{:}58{,}70{:}74{,}76{:}88{,}90{:}95{,}97{:}102{,}104{:}116{,}118{:}122\}$,
$\mathcal{A}_{\mathrm{SD}} = \mathcal{A}_{\mathrm{BPSK}}, \mathcal{D}_{\mathrm{SP}} = \{+1, +1, +1, -1, -1, +1, +1, +1\}$.

Figure 5.33: ‘Monte Carlo’ magnitude $|\mathbf{CORR}(\boldsymbol{g})|$ of the correlation matrix of the quantizer output time-sample vector $\boldsymbol{g}$, OFDM Type = 5.2 (IEEE 802.11a, BPSK), $b = 6$ bits, for various clipping-factors $\kappa$.

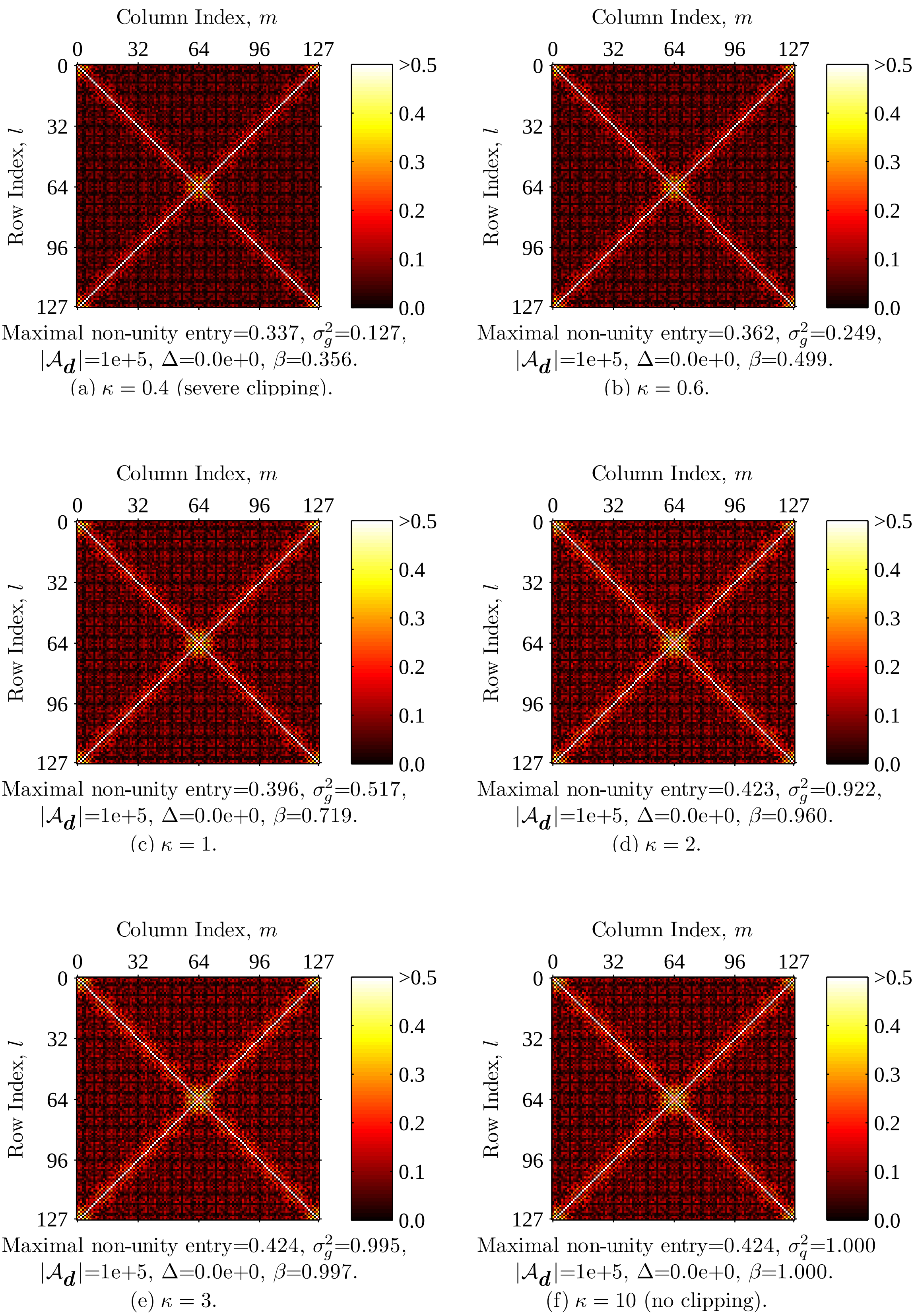


Maximal non-unity entry=0.337, $\sigma_g^2$=0.127, $|\mathcal{A}_{\boldsymbol{d}}|$=1e+5, $\Delta$=0.0e+0, $\beta$=0.356.
(a) $\kappa = 0.4$ (severe clipping).

Maximal non-unity entry=0.362, $\sigma_g^2$=0.249, $|\mathcal{A}_{\boldsymbol{d}}|$=1e+5, $\Delta$=0.0e+0, $\beta$=0.499.
(b) $\kappa = 0.6$.

Maximal non-unity entry=0.396, $\sigma_g^2$=0.517, $|\mathcal{A}_{\boldsymbol{d}}|$=1e+5, $\Delta$=0.0e+0, $\beta$=0.719.
(c) $\kappa = 1$.

Maximal non-unity entry=0.423, $\sigma_g^2$=0.922, $|\mathcal{A}_{\boldsymbol{d}}|$=1e+5, $\Delta$=0.0e+0, $\beta$=0.960.
(d) $\kappa = 2$.

Maximal non-unity entry=0.424, $\sigma_g^2$=0.995, $|\mathcal{A}_{\boldsymbol{d}}|$=1e+5, $\Delta$=0.0e+0, $\beta$=0.997.
(e) $\kappa = 3$.

Maximal non-unity entry=0.424, $\sigma_q^2$=1.000 $|\mathcal{A}_{\boldsymbol{d}}|$=1e+5, $\Delta$=0.0e+0, $\beta$=1.000.
(f) $\kappa = 10$ (no clipping).

OFDM Type 5.2: IEEE 802.11a, $N = 128, \mathcal{K}_{\mathrm{SZ}} = \{0{:}5,32,59{:}69,96,123{:}127\}$,
$\mathcal{K}_{\mathrm{SP}} = \{11, 25, 39, 53, 75, 89, 103, 117\}, \mathcal{A}_{\mathrm{SP}} = \mathcal{A}_{\mathrm{BPSK}}$,
$\mathcal{K}_{\mathrm{SD}} = \{6{:}10,12{:}24,26{:}31,33{:}38,40{:}52,54{:}58,70{:}74,76{:}88,90{:}95,97{:}102,104{:}116,118{:}122\}$,
$\mathcal{A}_{\mathrm{SD}} = \mathcal{A}_{\mathrm{BPSK}}, \mathcal{D}_{\mathrm{SP}} = \{+1, +1, +1, -1, -1, +1, +1, +1\}$.

Figure 5.34: 'Monte Carlo' magnitude $|\mathbf{CORR}(\boldsymbol{g})|$ of the correlation matrix of the quantizer output time-sample vector $\boldsymbol{g}$, OFDM Type = 5.2 (IEEE 802.11a, BPSK), no quantization, clipping only, for various clipping-factors $\kappa$ matching the $b = 6$ case in Figure 5.33.

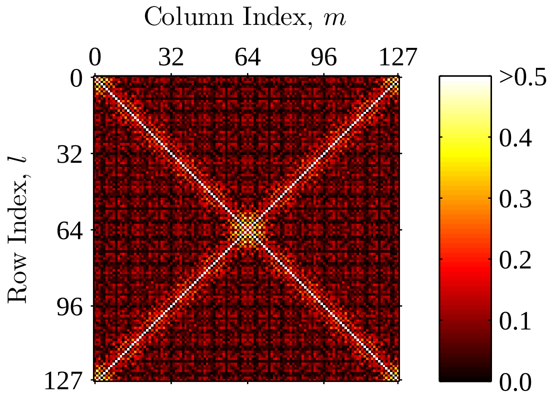


Maximal non-unity entry=0.424, $\sigma_g^2$=1.000,
$|\mathcal{A}_{\boldsymbol{d}}|$=1e+5, $\Delta$=1.3e-2, $\beta$=1.000.

(a) $\Delta$=1.3e-2.

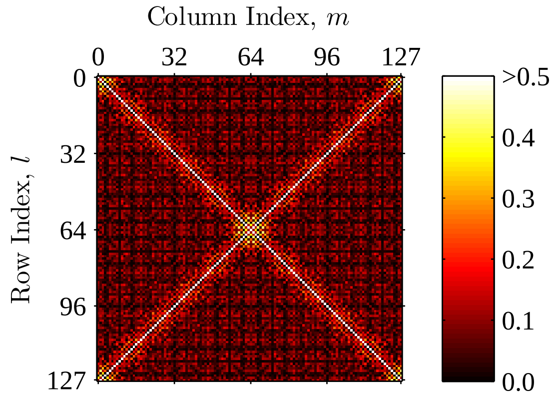


Maximal non-unity entry=0.424, $\sigma_g^2$=1.000,
$|\mathcal{A}_{\boldsymbol{d}}|$=1e+5, $\Delta$=1.9e-2, $\beta$=1.000.

(b) $\Delta$=1.9e-2.

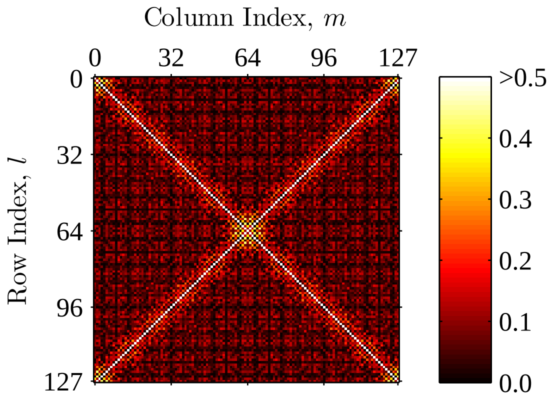


Maximal non-unity entry=0.425, $\sigma_g^2$=1.000,
$|\mathcal{A}_{\boldsymbol{d}}|$=1e+5, $\Delta$=3.2e-2, $\beta$=1.000.

(c) $\Delta$=3.2e-2.

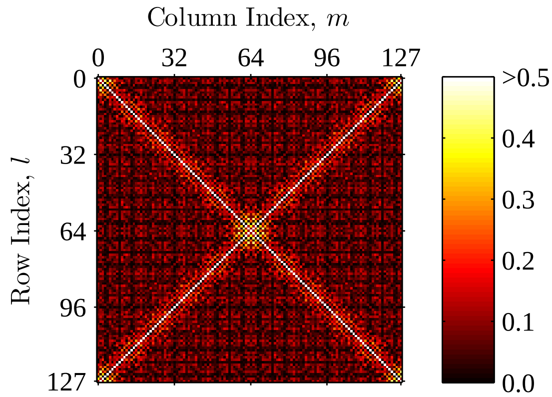


Maximal non-unity entry=0.424, $\sigma_g^2$=1.000,
$|\mathcal{A}_{\boldsymbol{d}}|$=1e+5, $\Delta$=6.3e-2, $\beta$=1.000.

(d) $\Delta$=6.3e-2.

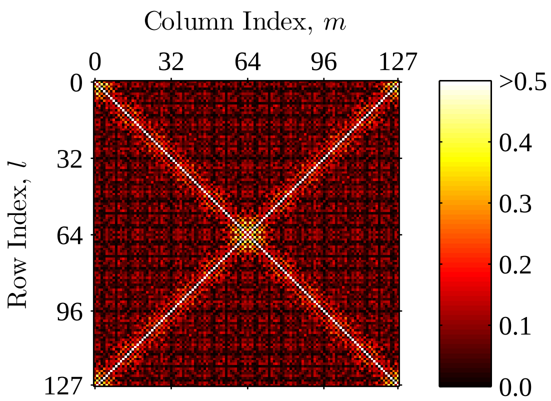


Maximal non-unity entry=0.424, $\sigma_g^2$=1.001,
$|\mathcal{A}_{\boldsymbol{d}}|$=1e+5, $\Delta$=9.5e-2, $\beta$=1.001.

(e) $\Delta$=9.5e-2.

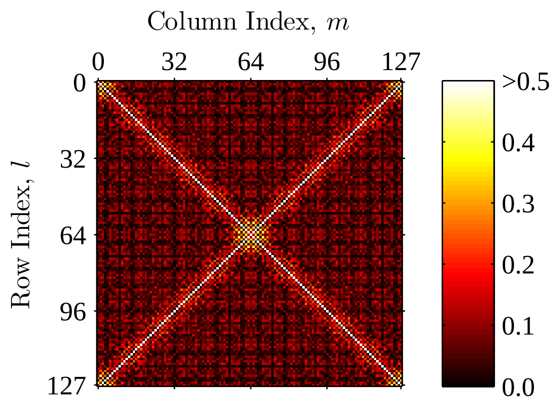


Maximal non-unity entry=0.421, $\sigma_g^2$=1.007,
$|\mathcal{A}_{\boldsymbol{d}}|$=1e+5, $\Delta$=3.2e-1, $\beta$=1.003.

(f) $\Delta$=3.2e-1.

OFDM Type 5.2: IEEE 802.11a, $N = 128, \mathcal{K}_{\mathrm{SZ}} = \{0{:}5,32,59{:}69,96,123{:}127\}$,
$\mathcal{K}_{\mathrm{SP}} = \{11, 25, 39, 53, 75, 89, 103, 117\}, \mathcal{A}_{\mathrm{SP}} = \mathcal{A}_{\mathrm{BPSK}}$,
$\mathcal{K}_{\mathrm{SD}} = \{6{:}10,12{:}24,26{:}31,33{:}38,40{:}52,54{:}58,70{:}74,76{:}88,90{:}95,97{:}102,104{:}116,118{:}122\}$,
$\mathcal{A}_{\mathrm{SD}} = \mathcal{A}_{\mathrm{BPSK}}, \mathcal{D}_{\mathrm{SP}} = \{+1, +1, +1, -1, -1, +1, +1, +1\}$.

Figure 5.35: ‘Monte Carlo’ magnitude $|\mathbf{CORR}(\boldsymbol{g})|$ of the correlation matrix of the quantizer output time-sample vector $\boldsymbol{g}$, OFDM Type = 5.2 (IEEE 802.11a, BPSK), quantization only, no clipping, for various quantizer step sizes $\Delta$ matching the $b = 6$ case in Figure 5.33.

### 5.4.3 'Monte Carlo' Correlation Matrix of the IDFT Output Time-Sample Real-Part Vector and the Quantizer Error Time-Sample Vector

Next, we examine the correlation matrix $\mathbf{CORR}(\boldsymbol{f}, \boldsymbol{q})$ of the IDFT output (quantizer input) time sample vector $\boldsymbol{f}$ and the quantizer error time-sample vector $\boldsymbol{q}$ for the cases shown in Table 5.4.

| Figure | OFDM Type | $b$ | Quantization | Clipping | $\kappa \in$ | $\Delta \in$ |
|---|---|---|---|---|---|---|
| 5.36 | 5.2 | 3 | Yes | Yes | {0.4,0.6,1,2,3,10} | {1.1e-1,1.7e-1,2.9e-1,5.7e-1,8.6e-1,2.9e+0} |
| 5.37 | 5.2 | - | No | Yes | {0.4,0.6,1,2,3,10} | {0} |
| 5.38 | 5.2 | - | Yes | No | - | {1.1e-1,1.7e-1,2.9e-1,5.7e-1,8.6e-1,2.9e+0} |
| 5.39 | 5.2 | 6 | Yes | Yes | {0.4,0.6,1,2,3,10} | {1.3e-2,1.9e-2,3.9e-2,6.3e-2,9.5e-2,3.2e-1} |
| 5.40 | 5.2 | - | No | Yes | {0.4,0.6,1,2,3,10} | {0} |
| 5.41 | 5.2 | - | Yes | No | - | {1.3e-2,1.9e-2,3.9e-2,6.3e-2,9.5e-2,3.2e-1} |

Table 5.4: Schedule for $\mathbf{CORR}(\boldsymbol{f}, \boldsymbol{q})$ results.

These particular cases match those already used for the correlation matrix $\mathbf{CORR}(\boldsymbol{g})$ of the quantizer output time-sample vector $\boldsymbol{g}$ as shown in Table 5.3 which were selected as exemplars to demonstrate the effects of combined quantization and clipping, clipping only, quantization only, and the number of quantizer bits on a typical OFDM system - IEEE 802.11a WLAN [1] with BPSK data.

$|\mathbf{CORR}(\boldsymbol{f}, \boldsymbol{q})|$ is of particular importance since it gives an indication of whether the quantizer error time samples $q_m, m \in \mathbb{Z}_N$ can be considered to be independent of the quantizer input (IDFT output) time samples $f_l, l \in \mathbb{Z}_N$. We note here, as elsewhere in this thesis, that a significantly non-zero value of $[|\mathbf{CORR}(\boldsymbol{f}, \boldsymbol{q})|]_{l,m}$ indicates a dependence between $f_l$ and $q_m$. However, a close-to-zero value of $[|\mathbf{CORR}(\boldsymbol{f}, \boldsymbol{q})|]_{l,m}$ does not necessarily indicate independence of $f_l$ and $q_m$.

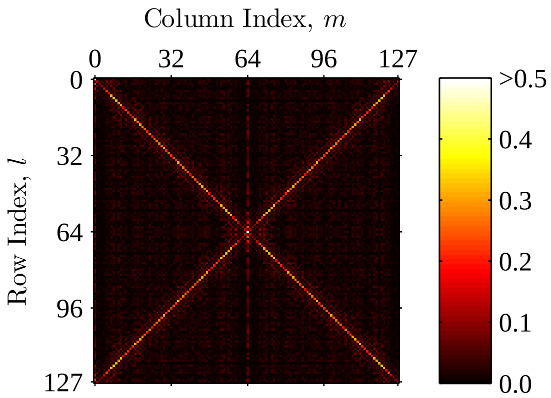


Maximal entry=0.676, corr$(f, q)$= -0.253,
$|\mathcal{A}_{\boldsymbol{d}}|$=1e+5, $\Delta$=1.1e-1, $\beta$=0.357.
(a) $\kappa = 0.4$ (severe clipping).

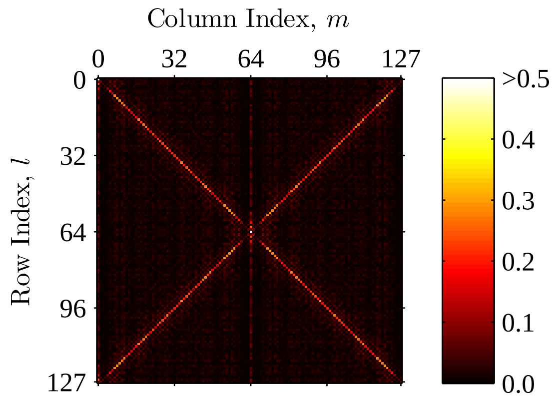


Maximal entry=0.687, corr$(f, q)$= -0.221,
$|\mathcal{A}_{\boldsymbol{d}}|$=1e+5, $\Delta$=1.7e-1, $\beta$=0.502.
(b) $\kappa = 0.6$.

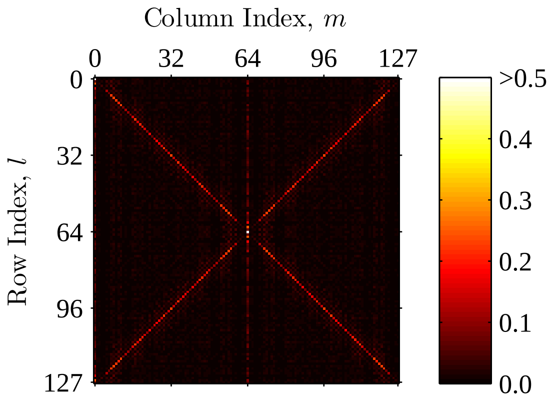


Maximal entry=0.696, corr$(f, q)$= -0.164,
$|\mathcal{A}_{\boldsymbol{d}}|$=1e+5, $\Delta$=2.9e-1, $\beta$=0.724.
(c) $\kappa = 1$.

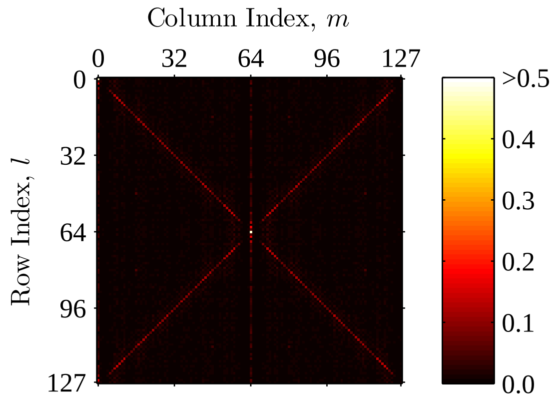


Maximal entry=0.473, corr$(f, q)$= -0.097,
$|\mathcal{A}_{\boldsymbol{d}}|$=1e+5, $\Delta$=5.7e-1, $\beta$=0.977.
(d) $\kappa = 2$.

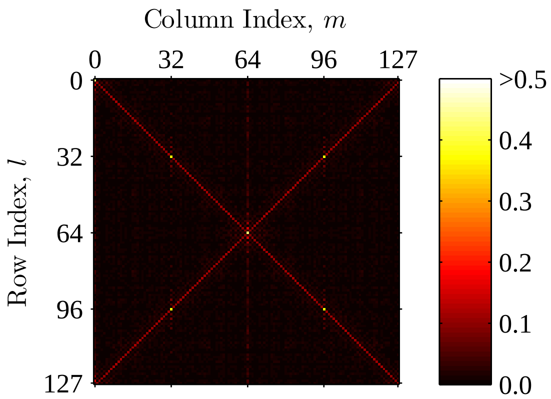


Maximal entry=0.424, corr$(f, q)$= -0.122,
$|\mathcal{A}_{\boldsymbol{d}}|$=1e+5, $\Delta$=8.6e-1, $\beta$=1.026.
(e) $\kappa = 3$.

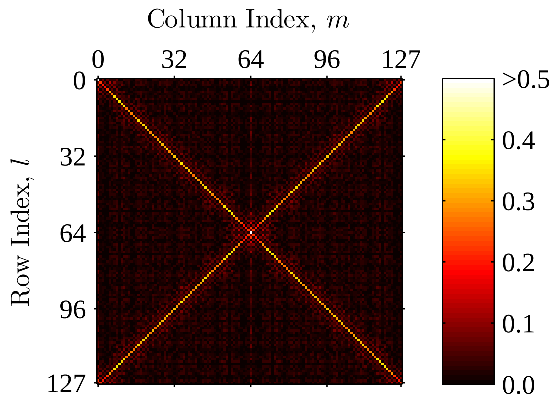


Maximal entry=0.626, corr$(f, q)$= -0.307,
$|\mathcal{A}_{\boldsymbol{d}}|$=1e+5, $\Delta$=2.9e+0, $\beta$=1.451.
(f) $\kappa = 10$ (no clipping).

OFDM Type 5.2: IEEE 802.11a, $N = 128, \mathcal{K}_{\mathrm{SZ}} = \{$0:5,32,59:69,96,123:127$\}$,
$\mathcal{K}_{\mathrm{SP}} = \{11, 25, 39, 53, 75, 89, 103, 117\}, \mathcal{A}_{\mathrm{SP}} = \mathcal{A}_{\mathrm{BPSK}}$,
$\mathcal{K}_{\mathrm{SD}} = \{$6:10,12:24,26:31,33:38,40:52,54:58,70:74,76:88,90:95,97:102,104:116,118:122$\}$,
$\mathcal{A}_{\mathrm{SD}} = \mathcal{A}_{\mathrm{BPSK}}, \mathcal{D}_{\mathrm{SP}} = \{+1, +1, +1, -1, -1, +1, +1, +1\}$.

Figure 5.36: 'Monte Carlo' magnitude $|\mathbf{CORR}(\boldsymbol{f}, \boldsymbol{q})|$ of the correlation matrix of the IDFT output time-sample vector $\boldsymbol{f}$ with the quantizer error vector $\boldsymbol{q}$, OFDM Type = 5.2 (IEEE 802.11a, BPSK), $b = 3$ bits, for various clipping-factors $\kappa$.

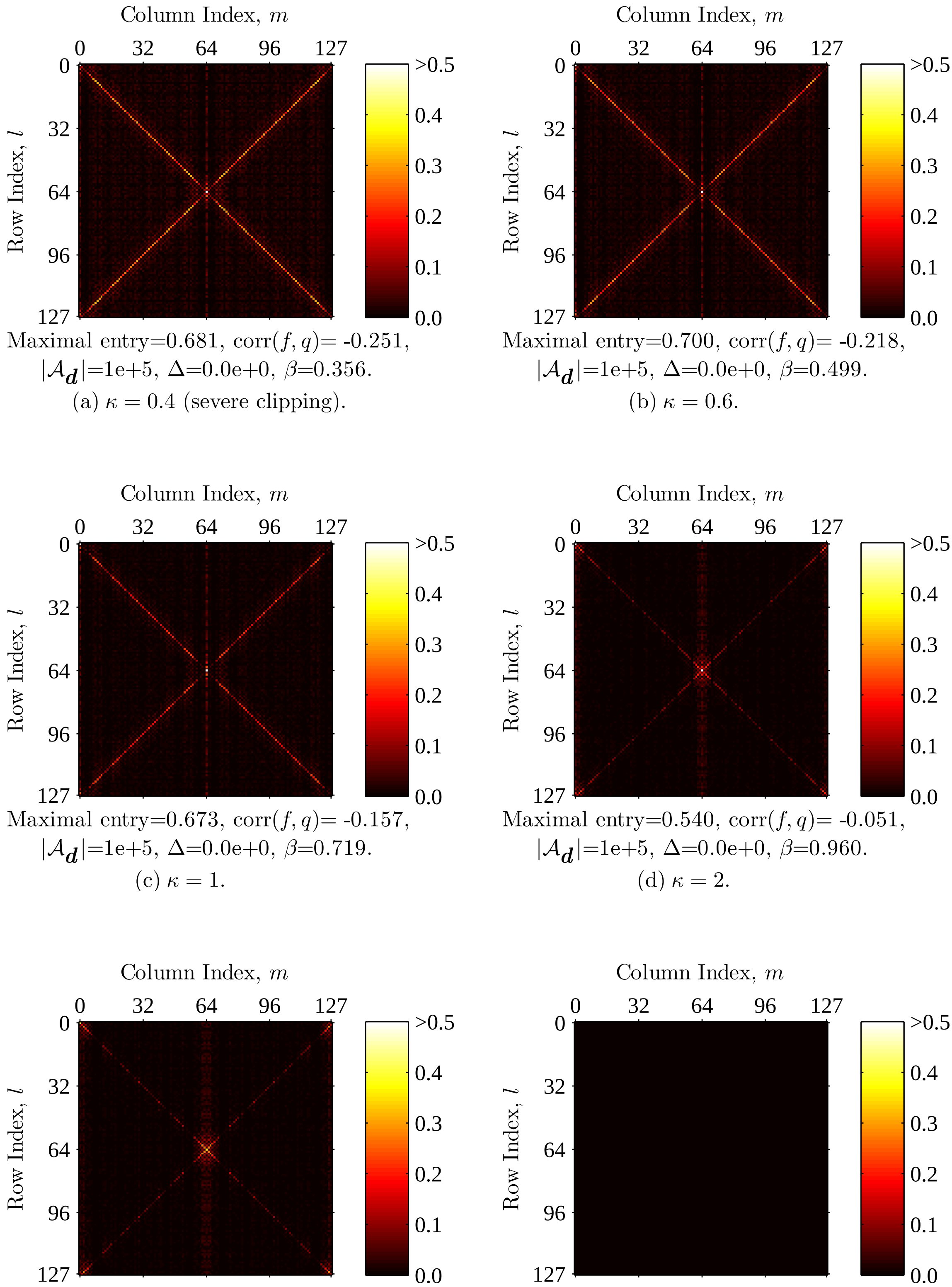


(a) $\kappa = 0.4$ (severe clipping).
(b) $\kappa = 0.6$.
(c) $\kappa = 1$.
(d) $\kappa = 2$.
(e) $\kappa = 3$.
(f) $\kappa = 10$ (no clipping).

| | |
|---|---|
| OFDM Type 5.2: | IEEE 802.11a, $N = 128, \mathcal{K}_{\mathrm{SZ}} = \{$0:5,32,59:69,96,123:127$\}$,<br>$\mathcal{K}_{\mathrm{SP}} = \{11, 25, 39, 53, 75, 89, 103, 117\}, \mathcal{A}_{\mathrm{SP}} = \mathcal{A}_{\mathrm{BPSK}}$,<br>$\mathcal{K}_{\mathrm{SD}} = \{$6:10,12:24,26:31,33:38,40:52,54:58,70:74,76:88,90:95,97:102,104:116,118:122$\}$,<br>$\mathcal{A}_{\mathrm{SD}} = \mathcal{A}_{\mathrm{BPSK}}, \mathcal{D}_{\mathrm{SP}} = \{+1, +1, +1, -1, -1, +1, +1, +1\}$. |

Figure 5.37: 'Monte Carlo' magnitude $|\mathbf{CORR}(\boldsymbol{f}, \boldsymbol{q})|$ of the correlation matrix of the IDFT output time-sample vector $\boldsymbol{f}$ with the quantizer error vector $\boldsymbol{q}$, OFDM Type $=$ 5.2 (IEEE 802.11a, BPSK), no quantization, clipping only , for various clipping-factors $\kappa$ matching the $b = 3$ case in Figure 5.36 .

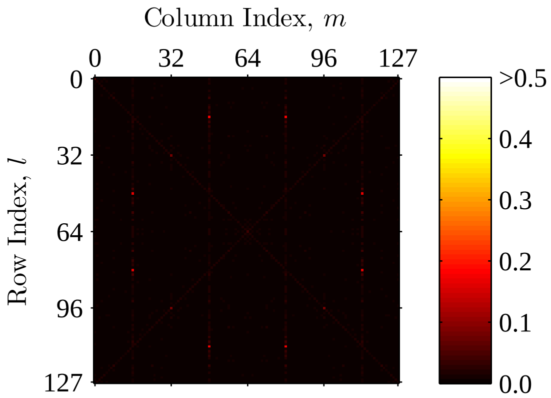


Maximal entry=0.173, corr($f, q$)= -0.017,
$|\mathcal{A}_{\boldsymbol{d}}|$=1e+5, $\Delta$=1.1e-1, $\beta$=1.001.
(a) $\Delta$=1.1e-1.

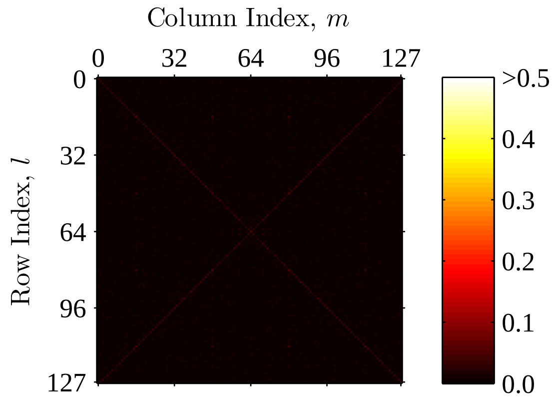


Maximal entry=0.046, corr($f, q$)= -0.025,
$|\mathcal{A}_{\boldsymbol{d}}|$=1e+5, $\Delta$=1.7e-1, $\beta$=1.001.
(b) $\Delta$=1.7e-1.

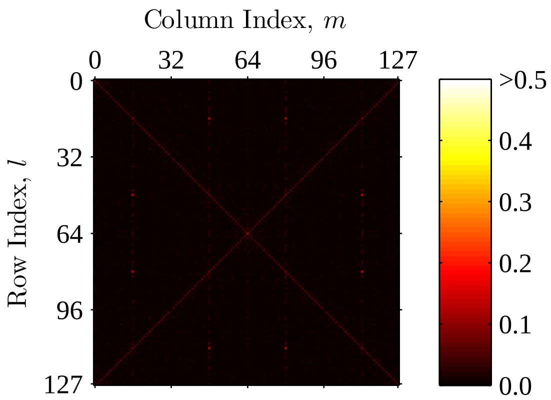


Maximal entry=0.111, corr($f, q$)= -0.041,
$|\mathcal{A}_{\boldsymbol{d}}|$=1e+5, $\Delta$=2.9e-1, $\beta$=1.003.
(c) $\Delta$=2.9e-1.

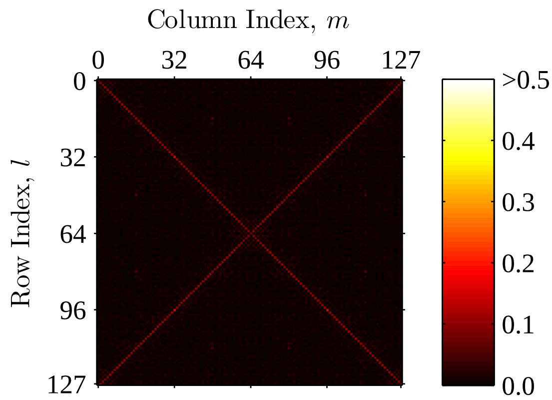


Maximal entry=0.141, corr($f, q$)= -0.082,
$|\mathcal{A}_{\boldsymbol{d}}|$=1e+5, $\Delta$=5.7e-1, $\beta$=1.015.
(d) $\Delta$=5.7e-1.

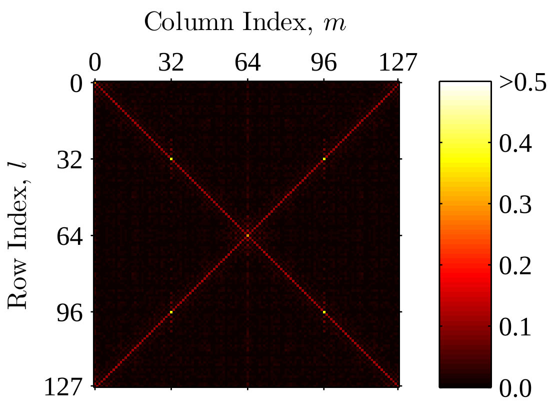


Maximal entry=0.371, corr($f, q$)= -0.121,
$|\mathcal{A}_{\boldsymbol{d}}|$=1e+5, $\Delta$=8.6e-1, $\beta$=1.028.
(e) $\Delta$=8.6e-1.

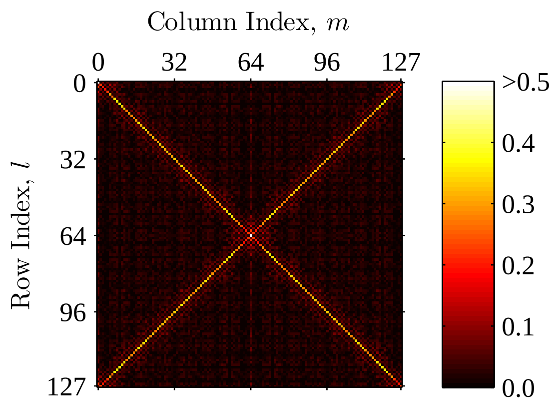


Maximal entry=0.626, corr($f, q$)= -0.307,
$|\mathcal{A}_{\boldsymbol{d}}|$=1e+5, $\Delta$=2.9e+0, $\beta$=1.451.
(f) $\Delta$=2.9e+0.

OFDM Type 5.2: IEEE 802.11a, $N = 128, \mathcal{K}_{\mathrm{SZ}} = \{$0:5,32,59:69,96,123:127$\}$,
$\mathcal{K}_{\mathrm{SP}} = \{11, 25, 39, 53, 75, 89, 103, 117\}, \mathcal{A}_{\mathrm{SP}} = \mathcal{A}_{\mathrm{BPSK}}$,
$\mathcal{K}_{\mathrm{SD}} = \{$6:10,12:24,26:31,33:38,40:52,54:58,70:74,76:88,90:95,97:102,104:116,118:122$\}$,
$\mathcal{A}_{\mathrm{SD}} = \mathcal{A}_{\mathrm{BPSK}}, \mathcal{D}_{\mathrm{SP}} = \{+1, +1, +1, -1, -1, +1, +1, +1\}$.

Figure 5.38: 'Monte Carlo' magnitude $|\mathbf{CORR}(\boldsymbol{f}, \boldsymbol{q})|$ of the correlation matrix of the IDFT output time-sample vector $\boldsymbol{f}$ with the quantizer error vector $\boldsymbol{q}$, OFDM Type = 5.2 (IEEE 802.11a, BPSK), quantization only, no clipping, for various quantizer step sizes $\Delta$ matching the $b = 3$ case in Figure 5.36 .

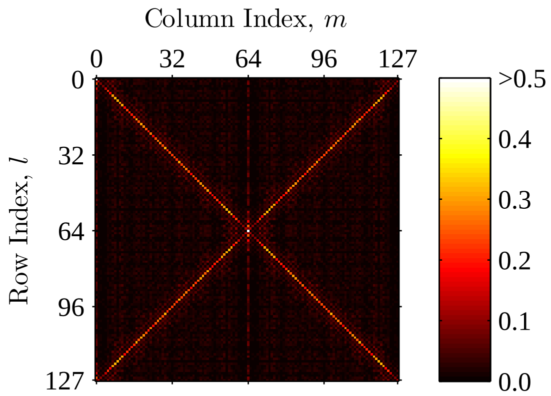


Maximal entry=0.684, corr($f,q$)= -0.251,
$|\mathcal{A}_{\boldsymbol{d}}|$=1e+5, $\Delta$=1.3e-2, $\beta$=0.356.
(a) $\kappa = 0.4$ (severe clipping).

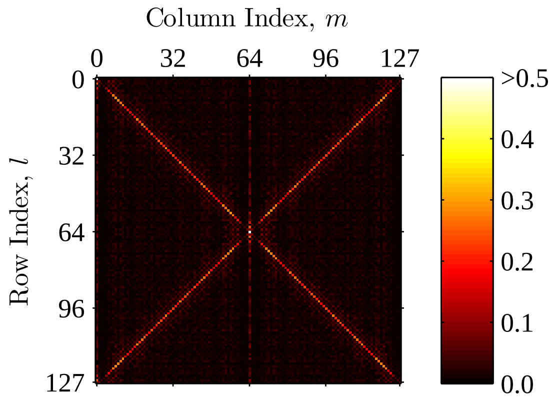


Maximal entry=0.701, corr($f,q$)= -0.218,
$|\mathcal{A}_{\boldsymbol{d}}|$=1e+5, $\Delta$=1.9e-2, $\beta$=0.499.
(b) $\kappa = 0.6$.

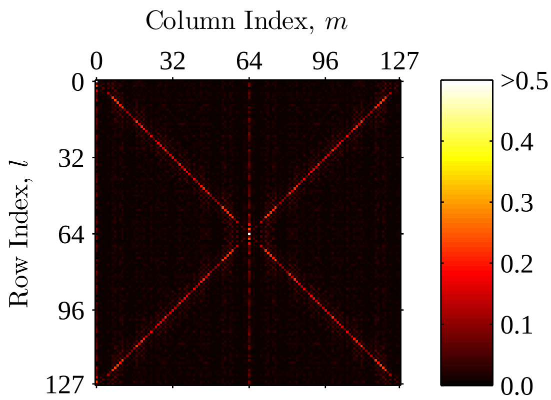


Maximal entry=0.675, corr($f,q$)= -0.157,
$|\mathcal{A}_{\boldsymbol{d}}|$=1e+5, $\Delta$=3.2e-2, $\beta$=0.719.
(c) $\kappa = 1$.

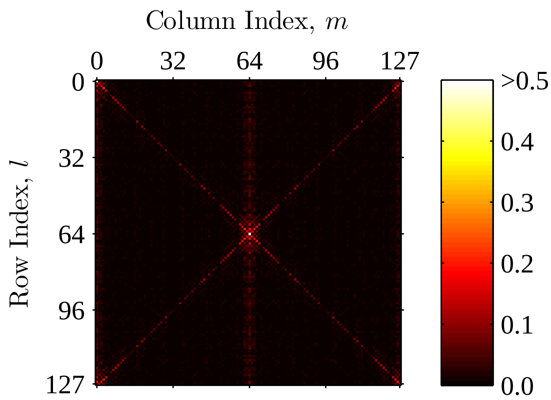


Maximal entry=0.550, corr($f,q$)= -0.051,
$|\mathcal{A}_{\boldsymbol{d}}|$=1e+5, $\Delta$=6.3e-2, $\beta$=0.960.
(d) $\kappa = 2$.

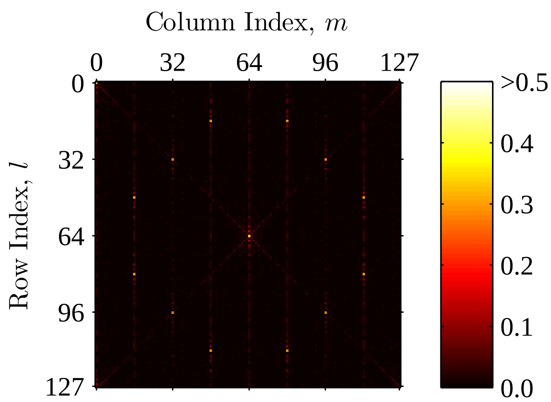


Maximal entry=0.333, corr($f,q$)= -0.018,
$|\mathcal{A}_{\boldsymbol{d}}|$=1e+5, $\Delta$=9.5e-2, $\beta$=0.998.
(e) $\kappa = 3$.

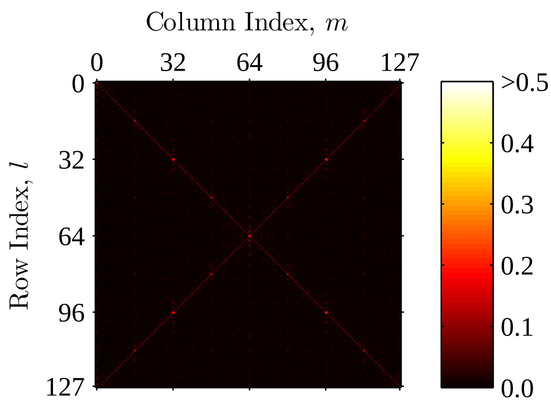


Maximal entry=0.178, corr($f,q$)= -0.046,
$|\mathcal{A}_{\boldsymbol{d}}|$=1e+5, $\Delta$=3.2e-1, $\beta$=1.003.
(f) $\kappa = 10$ (no clipping).

OFDM Type 5.2: IEEE 802.11a, $N = 128, \mathcal{K}_{\text{SZ}} = \{$0:5,32,59:69,96,123:127$\}$,
$\mathcal{K}_{\text{SP}} = \{11, 25, 39, 53, 75, 89, 103, 117\}, \mathcal{A}_{\text{SP}} = \mathcal{A}_{\text{BPSK}}$,
$\mathcal{K}_{\text{SD}} = \{$6:10,12:24,26:31,33:38,40:52,54:58,70:74,76:88,90:95,97:102,104:116,118:122$\}$,
$\mathcal{A}_{\text{SD}} = \mathcal{A}_{\text{BPSK}}, \mathcal{D}_{\text{SP}} = \{+1, +1, +1, -1, -1, +1, +1, +1\}$.

Figure 5.39: 'Monte Carlo' magnitude $|\mathbf{CORR}(\boldsymbol{f}, \boldsymbol{q})|$ of the correlation matrix of the IDFT output time-sample vector $\boldsymbol{f}$ with the quantizer error vector $\boldsymbol{q}$, OFDM Type = 5.2 (IEEE 802.11a, BPSK), $b = 6$ bits, for various clipping-factors $\kappa$.

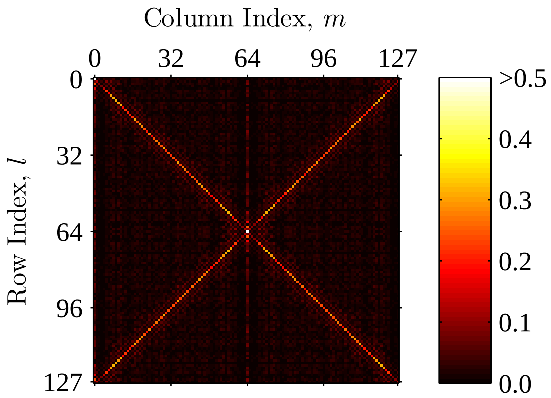


Maximal entry=0.681, corr($f, q$)= -0.251, $|\mathcal{A}_{\boldsymbol{d}}|$=1e+5, $\Delta$=0.0e+0, $\beta$=0.356.

(a) $\kappa = 0.4$ (severe clipping).

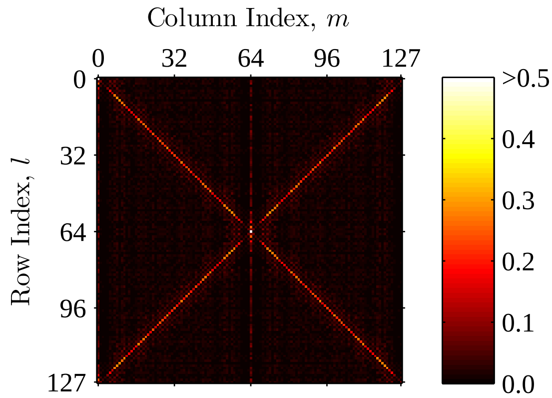


Maximal entry=0.700, corr($f, q$)= -0.218, $|\mathcal{A}_{\boldsymbol{d}}|$=1e+5, $\Delta$=0.0e+0, $\beta$=0.499.

(b) $\kappa = 0.6$.

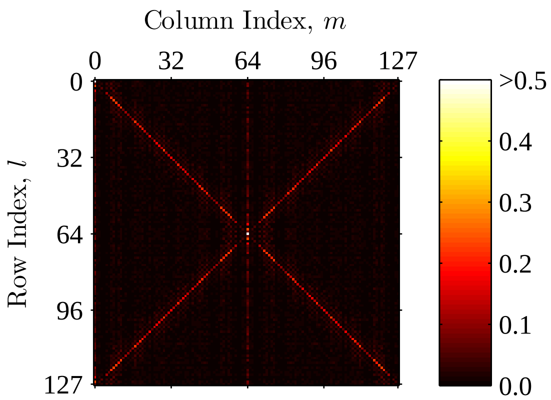


Maximal entry=0.673, corr($f, q$)= -0.157, $|\mathcal{A}_{\boldsymbol{d}}|$=1e+5, $\Delta$=0.0e+0, $\beta$=0.719.

(c) $\kappa = 1$.

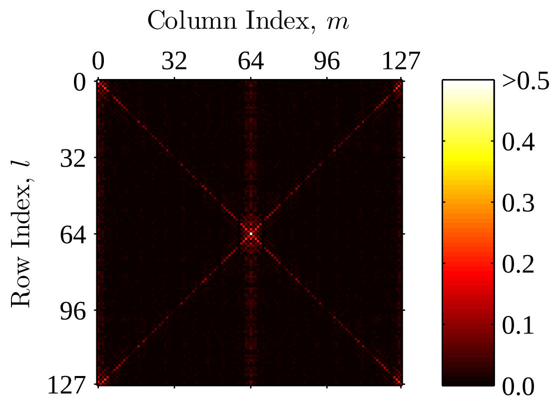


Maximal entry=0.540, corr($f, q$)= -0.051, $|\mathcal{A}_{\boldsymbol{d}}|$=1e+5, $\Delta$=0.0e+0, $\beta$=0.960.

(d) $\kappa = 2$.

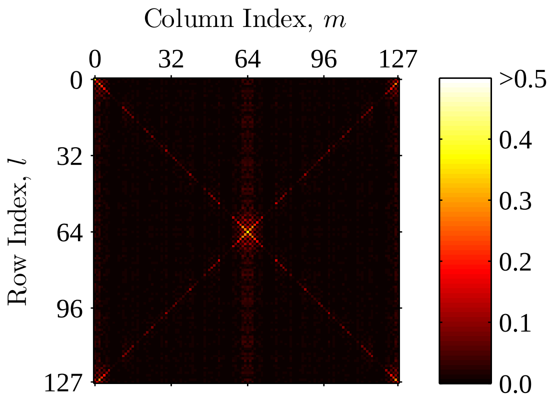


Maximal entry=0.352, corr($f, q$)= -0.011, $|\mathcal{A}_{\boldsymbol{d}}|$=1e+5, $\Delta$=0.0e+0, $\beta$=0.997.

(e) $\kappa = 3$.

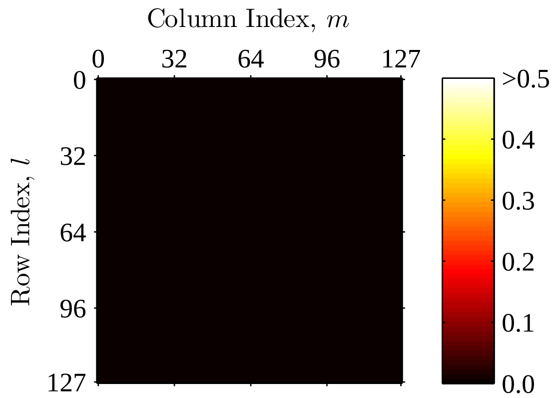


Maximal entry=NaN, corr($f, q$)= NaN, $|\mathcal{A}_{\boldsymbol{d}}|$=1e+5, $\Delta$=0.0e+0, $\beta$=1.000.

(f) $\kappa = 10$ (no clipping).

OFDM Type 5.2: IEEE 802.11a, $N = 128, \mathcal{K}_{\mathrm{SZ}} = \{0{:}5{,}32{,}59{:}69{,}96{,}123{:}127\}$,
$\mathcal{K}_{\mathrm{SP}} = \{11, 25, 39, 53, 75, 89, 103, 117\}, \mathcal{A}_{\mathrm{SP}} = \mathcal{A}_{\mathrm{BPSK}}$,
$\mathcal{K}_{\mathrm{SD}} = \{6{:}10{,}12{:}24{,}26{:}31{,}33{:}38{,}40{:}52{,}54{:}58{,}70{:}74{,}76{:}88{,}90{:}95{,}97{:}102{,}104{:}116{,}118{:}122\}$,
$\mathcal{A}_{\mathrm{SD}} = \mathcal{A}_{\mathrm{BPSK}}, \mathcal{D}_{\mathrm{SP}} = \{+1, +1, +1, -1, -1, +1, +1, +1\}$.

Figure 5.40: 'Monte Carlo' magnitude $|\mathbf{CORR}(\boldsymbol{f}, \boldsymbol{q})|$ of the correlation matrix of the IDFT output time-sample vector $\boldsymbol{f}$ with the quantizer error vector $\boldsymbol{q}$, OFDM Type = 5.2 (IEEE 802.11a, BPSK), no quantization, clipping only, for various clipping-factors matching the $b = 6$ case in Figure 5.39 .

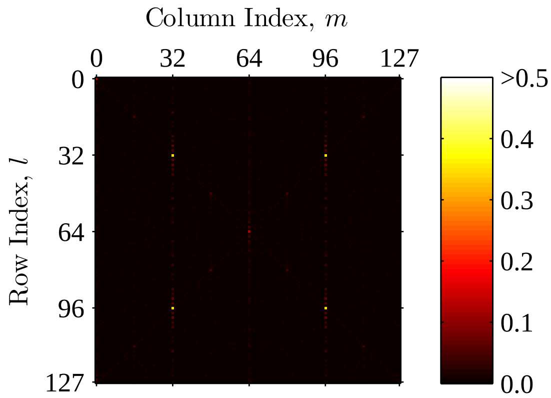


Maximal entry=0.347, corr($f, q$)= -0.002,
$|\mathcal{A}_{\boldsymbol{d}}|$=1e+5, $\Delta$=1.3e-2, $\beta$=1.000.
(a) $\Delta$=1.3e-2.

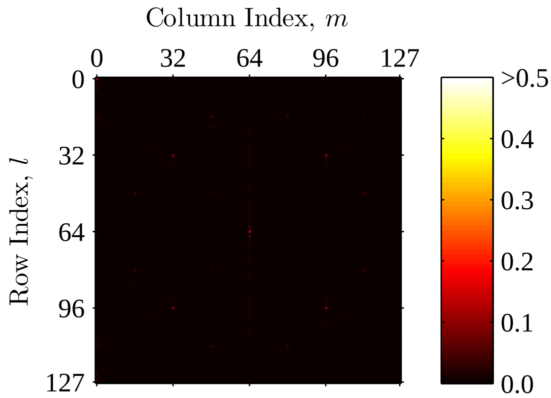


Maximal entry=0.129, corr($f, q$)= -0.003,
$|\mathcal{A}_{\boldsymbol{d}}|$=1e+5, $\Delta$=1.9e-2, $\beta$=1.000.
(b) $\Delta$=1.9e-2.

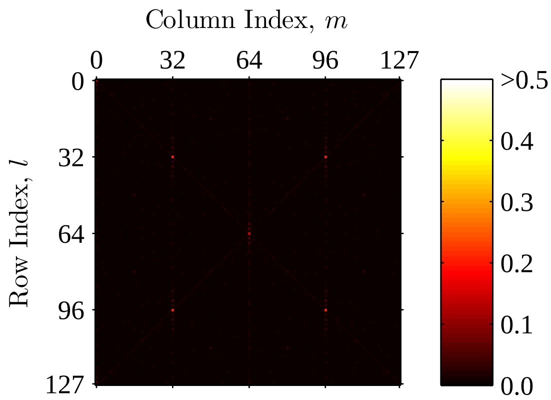


Maximal entry=0.200, corr($f, q$)= -0.005,
$|\mathcal{A}_{\boldsymbol{d}}|$=1e+5, $\Delta$=3.2e-2, $\beta$=1.000.
(c) $\Delta$=3.2e-2.

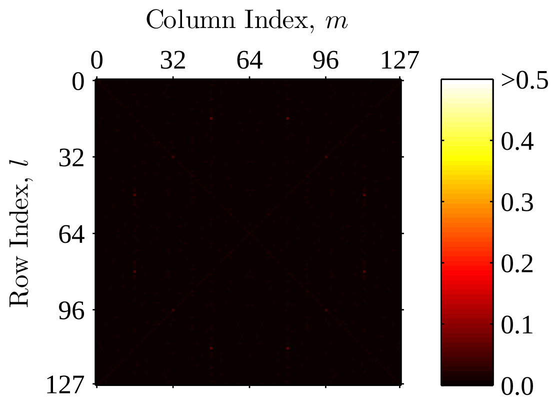


Maximal entry=0.065, corr($f, q$)= -0.009,
$|\mathcal{A}_{\boldsymbol{d}}|$=1e+5, $\Delta$=6.3e-2, $\beta$=1.000.
(d) $\Delta$=6.3e-2.

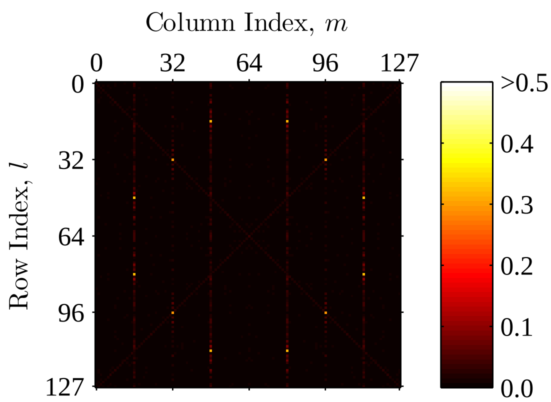


Maximal entry=0.323, corr($f, q$)= -0.014,
$|\mathcal{A}_{\boldsymbol{d}}|$=1e+5, $\Delta$=9.5e-2, $\beta$=1.001.
(e) $\Delta$=9.5e-2.

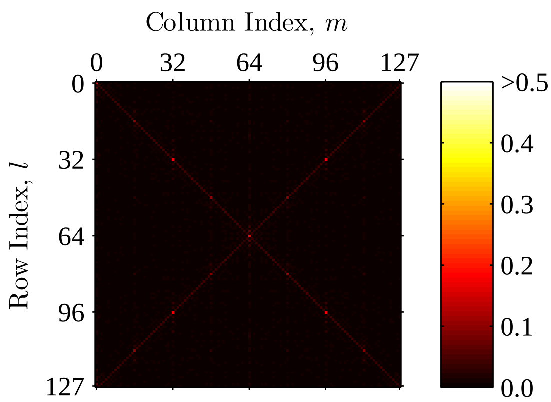


Maximal entry=0.179, corr($f, q$)= -0.046,
$|\mathcal{A}_{\boldsymbol{d}}|$=1e+5, $\Delta$=3.2e-1, $\beta$=1.003.
(f) $\Delta$=3.2e-1.

| | |
|---|---|
| OFDM Type 5.2: | IEEE 802.11a, $N = 128, \mathcal{K}_{\mathrm{SZ}} = \{0{:}5{,}32{,}59{:}69{,}96{,}123{:}127\}$,<br>$\mathcal{K}_{\mathrm{SP}} = \{11, 25, 39, 53, 75, 89, 103, 117\}, \mathcal{A}_{\mathrm{SP}} = \mathcal{A}_{\mathrm{BPSK}}$,<br>$\mathcal{K}_{\mathrm{SD}} = \{6{:}10{,}12{:}24{,}26{:}31{,}33{:}38{,}40{:}52{,}54{:}58{,}70{:}74{,}76{:}88{,}90{:}95{,}97{:}102{,}104{:}116{,}118{:}122\}$,<br>$\mathcal{A}_{\mathrm{SD}} = \mathcal{A}_{\mathrm{BPSK}}, \mathcal{D}_{\mathrm{SP}} = \{+1, +1, +1, -1, -1, +1, +1, +1\}$. |

Figure 5.41: 'Monte Carlo' magnitude $|\mathbf{CORR}(\boldsymbol{f}, \boldsymbol{q})|$ of the correlation matrix of the IDFT output time-sample vector $\boldsymbol{f}$ with the quantizer error vector $\boldsymbol{q}$, OFDM Type = 5.2 (IEEE 802.11a, BPSK), quantization only, no clipping, for various quantizer step sizes $\Delta$ matching the $b = 6$ case in Figure 5.39 .

#### 5.4.3.1 Predicted Results

Before evaluating the results of Figures 5.36 to 5.41, we will do a quick analysis in an attempt to obtain some insight into what we might expect to see in the results.

We start with the case of severe clipping. Referring back to the quantizer function in Figure 3.2, when clipping is occurring, the $m^{th}$ quantizer output time-sample $g_m$ is given, in terms of the $m^{th}$ quantizer input time-sample $f_m$, by

$$g_m = \begin{cases} -k & , f_m < -k \\ k & , f_m \geq k. \end{cases} \tag{5.83}$$

The $m^{th}$ quantizer error time-sample is given by

$$q_m = g_m - \beta f_m, \tag{5.84}$$

which, using (5.83), expands to

$$q_m = \begin{cases} -k - \beta f_m & , f_m < -k \\ k - \beta f_m & , f_m \geq k, \end{cases} \tag{5.85}$$

where $k = \kappa \cdot \sigma_g$ is the clipping level. Therefore, the covariance between the $l^{th}$ quantizer input time-sample $f_l$ (which we note is zero-mean so that $\mathrm{E}[f_l] = 0$) and the $m^{th}$ quantizer error $q_m$ may be expressed as

$$
\begin{aligned}
&[\mathbf{COV}(\boldsymbol{f}, \boldsymbol{q})]_{l,m} \\
= \quad & \mathrm{E}[f_l q_m] - \mathrm{E}[f_l]\mathrm{E}[q_m] \\
= \quad & \mathrm{E}[f_l q_m] \\
= \quad & \mathrm{P}(|f_l| < k) \cdot \mathrm{E}[f_l \cdot q_m| \, |f_l| < k] \\
& +\mathrm{P}(f_l < -k) \cdot \mathrm{E}[f_l \cdot q_m | f_l < -k] \\
& +\mathrm{P}(f_l \geq k) \cdot \mathrm{E}[f_l \cdot q_m | f_l \geq k] \\
= \quad & \mathrm{P}(|f_l| < k) \cdot \mathrm{E}[f_l \cdot q_m| \, |f_l| < k] \\
& +\mathrm{P}(f_l < -k) \cdot \mathrm{E}[f_l \cdot (-k - \beta f_m) | f_l < -k] \\
& +\mathrm{P}(f_l \geq k) \cdot \mathrm{E}[f_l \cdot (k - \beta f_m) | f_l \geq k] \\
= \quad & \mathrm{P}(|f_l| < k) \cdot \mathrm{E}[f_l \cdot q_m| \, |f_l| < k] \\
& +\mathrm{P}(f_l < -k) \cdot (-k\mathrm{E}[f_l | f_l < -k] - \beta \mathrm{E}[f_l f_m | f_l < -k]) \\
& +\mathrm{P}(f_l \geq k) \cdot (k\mathrm{E}[f_l | f_l \geq k] - \beta \mathrm{E}[f_l f_m | f_l \geq k]) \\
= \quad & \mathrm{P}(|f_l| < k) \cdot \mathrm{E}[f_l \cdot q_m| \, |f_l| < k] \\
& -\beta \mathrm{P}(f_l < -k) \cdot (\mathrm{E}[f_l f_m | f_l < -k]) \\
& -\beta \mathrm{P}(f_l \geq k) \cdot (\mathrm{E}[f_l f_m | f_l \geq k]) \\
= \quad & \mathrm{P}(|f_l| < k) \cdot \mathrm{E}[f_l \cdot q_m| \, |f_l| < k] \\
& -\beta \mathrm{P}(|f_l| \geq k) \cdot \mathrm{E}[f_l f_m | \, |f_l| \geq k],
\end{aligned} \tag{5.86}
$$

from which we obtain the limit of the covariance matrix as the clipping becomes more severe (i.e as $\kappa \to 0$) as

$$
\begin{aligned}
\lim_{\mathrm{P}(f_l \geq k) \to 1} [\mathbf{COV}(\boldsymbol{f}, \boldsymbol{q})]_{l,m} &= -\beta \mathrm{E}\left[f_l \cdot f_m\right] = -\beta [\mathbf{COV}(\boldsymbol{f})]_{l,m} \\
\Leftrightarrow \quad \lim_{\kappa \to 0} [\mathbf{COV}(\boldsymbol{f}, \boldsymbol{q})]_{l,m} &= -\beta [\mathbf{COV}(\boldsymbol{f})]_{l,m},
\end{aligned} \tag{5.87}
$$

and thence, by implication, the limit of the correlation matrix as the clipping becomes more severe (i.e as $\kappa \to 0$) is

$$\lim_{\kappa \to 0} [\mathbf{CORR}(\boldsymbol{f}, \boldsymbol{q})]_{l,m} = [\mathbf{CORR}(\boldsymbol{f})]_{l,m}. \tag{5.88}$$

Next, we will examine the case of a large quantizer step-size $\Delta$ and will find it to have many similarities to the case of severe clipping just examined. For quantizer input time-samples $f_m, m \in \mathbb{Z}_N$ occurring *inside* the least positive and negative quantizer cells, the $m^{th}$ quantizer output time-sample is given, in terms of the $m^{th}$ quantizer input time-sample $f_m$, by

$$g_m = \begin{cases} -\Delta/2 & , -\Delta \leq f_m < 0 \\ \Delta/2 & , \quad 0 \leq f_m < \Delta. \end{cases} \tag{5.89}$$

The $m^{th}$ quantizer error time-sample is given by

$$q_m = g_m - \beta f_m, \tag{5.90}$$

which, using (5.89), expands to

$$q_m = \begin{cases} -\Delta/2 - \beta f_m & , -\Delta \leq f_m < 0 \\ \Delta/2 - \beta f_m & , \quad 0 \leq f_m < \Delta. \end{cases} \tag{5.91}$$

Therefore, the covariance between the $l^{th}$ quantizer input time-sample $f_l$ (which we note is zero-mean so that $\mathrm{E}[f_l] = 0$) and the $m^{th}$ quantizer error $q_m$ may be expressed as

$$
\begin{aligned}
&[\mathbf{COV}(\boldsymbol{f},\boldsymbol{q})]_{l,m} \\
= \quad & \mathrm{E}[f_l q_m] - \mathrm{E}[f_l]\mathrm{E}[q_m] \\
= \quad & \mathrm{E}[f_l q_m] \\
= \quad & \mathrm{P}(|f_l| \geq \Delta) \cdot \mathrm{E}[f_l \cdot q_m \,|f_l| \geq \Delta] \\
& +\mathrm{P}(-\Delta \leq f_l < 0) \cdot \mathrm{E}[f_l \cdot q_m| - \Delta \leq f_l < 0] \\
& +\mathrm{P}(0 \leq f_l < \Delta) \cdot \mathrm{E}[f_l \cdot q_m|0 \leq f_l < \Delta] \\
= \quad & \mathrm{P}(|f_l| \geq \Delta) \cdot \mathrm{E}[f_l \cdot q_m| \,|f_l| \geq \Delta] \\
& +\mathrm{P}(-\Delta \leq f_l < 0) \cdot \mathrm{E}[f_l \cdot (-\Delta/2 - \beta f_m)| - \Delta \leq f_l < 0] \\
& +\mathrm{P}(0 \leq f_l < \Delta) \cdot \mathrm{E}[f_l \cdot (\Delta/2 - \beta f_m)|0 \leq f_l < \Delta] \\
= \quad & \mathrm{P}(|f_l| \geq \Delta) \cdot \mathrm{E}[f_l \cdot q_m| \,|f_l| \geq \Delta] \\
& +\mathrm{P}(-\Delta \leq f_l < 0) \cdot (-\Delta/2 \cdot \mathrm{E}[f_l|f_l < -\Delta \leq f_l < 0] - \beta \mathrm{E}[f_l f_m| - \Delta \leq f_l < 0]) \\
& +\mathrm{P}(0 \leq f_l < \Delta) \cdot (\Delta/2 \cdot \mathrm{E}[f_l] - \beta \mathrm{E}[f_l f_m|0 \leq f_l < \Delta]) \\
= \quad & \mathrm{P}(|f_l| \geq \Delta) \cdot \mathrm{E}[f_l \cdot q_m| \,|f_l| \geq \Delta] \\
& -\beta \mathrm{P}(-\Delta \leq f_l < 0) \cdot \mathrm{E}[f_l f_m|f_l < -\Delta \leq f_l < 0] \\
& -\beta \mathrm{P}(0 \leq f_l < \Delta) \cdot \mathrm{E}[f_l f_m|0 \leq f_l < \Delta] \\
= \quad & \mathrm{P}(|f_l| \geq \Delta) \cdot \mathrm{E}[f_l \cdot q_m| \,|f_l| \geq \Delta] \\
& -\beta \mathrm{P}(0 \leq |f_l| < \Delta) \cdot \mathrm{E}[f_l f_m|0 \leq |f_l| < \Delta], \qquad (5.92)
\end{aligned}
$$

from which we obtain the limit of the covariance matrix as the quantizer step-size becomes larger (i.e as $\Delta \to \infty$) as

$$
\begin{aligned}
& \lim_{\mathrm{P}(0 \leq |f_l| < \Delta) \to 1} [\mathbf{COV}(\boldsymbol{f},\boldsymbol{q})]_{l,m} = -\beta \mathrm{E}\left[f_l \cdot f_m\right] = -\beta [\mathbf{COV}(\boldsymbol{f})]_{l,m} \\
\Leftrightarrow \quad & \lim_{\Delta \to \infty} [\mathbf{COV}(\boldsymbol{f},\boldsymbol{q})]_{l,m} = -\beta [\mathbf{COV}(\boldsymbol{f})]_{l,m}. \qquad (5.93)
\end{aligned}
$$

Thence, by implication, the limit of the correlation matrix as the quantizer step-size becomes larger (i.e as $\Delta \to \infty$) is

$$
\lim_{\Delta \to \infty} [\mathbf{CORR}(\boldsymbol{f},\boldsymbol{q})]_{l,m} = [\mathbf{CORR}(\boldsymbol{f})]_{l,m}. \qquad (5.94)
$$

Now, we will comment on these quite surprising results.

For the severe-clipping case, we see from the last line of (5.86) that $[\mathbf{COV}(\boldsymbol{f}, \boldsymbol{q})]_{l,m}$ can be expressed as in terms of contributions from unclipped times-samples (first term) and clipped time-samples (second-term). Also, from (5.88), we deduce that, as the clipping-severity increases (i.e. as $\kappa \to 0$), the correlation matrix $\mathbf{CORR}(\boldsymbol{f}, \boldsymbol{q})$ of the quantizer input (IDFT output) time-sample vector $\boldsymbol{f}$ and the quantizer error time-sample vector $\boldsymbol{g}$ approaches a scaled version (with the scaling approaching 1 from 0) of the correlation matrix $\mathbf{CORR}(\boldsymbol{f})$ of the quantizer input (IDFT output) time-sample vector $\boldsymbol{f}$.

Surprisingly, a similar result applies for the large quantizer step-size (large-$\Delta$) case. From the last line of (5.92) we see that $[\mathbf{COV}(\boldsymbol{f}, \boldsymbol{q})]_{l,m}$ can be expressed as in terms of contributions from quantized times-samples occurring *outside* the least positive and negative quantizer cells (first term) and those time-samples occurring *inside* the least positive and negative quantizer cells (second-term). Also, from (5.94), we deduce that, as the quantizer step-size increases (i.e. as $\Delta \to \infty$), the correlation matrix $\mathbf{CORR}(\boldsymbol{f}, \boldsymbol{q})$ of the quantizer input (IDFT output) time-sample vector $\boldsymbol{f}$ and the quantizer error time-sample vector $\boldsymbol{g}$ approaches a scaled version (with the scaling approaching 1 from 0) of the correlation matrix $\mathbf{CORR}(\boldsymbol{f})$ of the quantizer input (IDFT output) time-sample vector $\boldsymbol{f}$.

To sum up, the correlation matrix $\mathbf{CORR}(\boldsymbol{f}, \boldsymbol{q})$ of the quantizer input (IDFT output) time-sample vector $\boldsymbol{f}$ and the quantizer error time-sample vector $\boldsymbol{g}$ approaches a scaled version of the correlation matrix $\mathbf{CORR}(\boldsymbol{f})$ of the quantizer input (IDFT output) time-sample vector $\boldsymbol{f}$ for both the quantizer severe-clipping and large step-size cases.

#### 5.4.3.2 Summary of Results

We now evaluate the results for the correlation matrix $\mathbf{CORR}(\boldsymbol{f}, \boldsymbol{q})$ of the quantizer input (IDFT output) time-sample vector $\boldsymbol{f}$ and the quantizer error time-sample vector $\boldsymbol{g}$ shown in Figures 5.36 to 5.41.

Firstly, looking at the 3-bit, no-quantization, clipping-only case in Figure 5.37(f), we see, when there is no clipping and no quantization, that the quantizer error time samples are all zero, and there is therefore no correlation between the quantizer input and quantizer error time samples (as evidenced by the all-black plot). This agrees with what we would expect from (5.86). As we reduce the clipping-factor from no clipping at $\kappa = 10$ to severe clipping at $\kappa = 0.4$, we transit from Figure 5.37(f) to (a) and observe increasing correlations mainly on the correlation matrix diagonals and offset-anti-diagonals. As the clipping factor $\kappa$ decreases, we begin to notice off-diagonal and off-offset-anti-diagonal non-zero entries appearing so that the correlation matrix $\mathbf{CORR}(\boldsymbol{f}, \boldsymbol{q})$ of the quantizer input (IDFT output) time-sample vector $\boldsymbol{f}$ and the quantizer error time-sample vector $\boldsymbol{g}$ resembles more and more a scaled version of the correlation matrix $\mathbf{CORR}(\boldsymbol{f})$ of the quantizer input (IDFT output) time-sample vector $\boldsymbol{f}$ which is shown in Figure 5.26. This is exactly as predicted in §5.4.3.1.

Now, looking at the 3-bit, quantization-only, no-clipping case in Figure 5.26(f), we see, for a large quantizer step-size $\Delta$ of $2.6 \times 10^0$, that the correlation matrix resembles a scaled version of the correlation matrix $\mathbf{CORR}(\boldsymbol{f})$ of the quantizer input (IDFT output) time-sample vector $\boldsymbol{f}$ shown in Figure 5.26. This phenomenom is the flip-side of the severe-clipping case already discussed and is also exactly as predicted in §5.4.3.1.

Transiting through Figures 5.36(f) to (a), we see that, as the quantizer step-size $\Delta$ decreases from $2.9 \times 10^0$ to $1.1 \times 10^{-1}$, most correlation entries values diminish to close to zero.

Next, we look at the 3-bit combined quantization and clipping case in Figure 5.36. We note, per the results schedule in Table 5.4, that the same values of the quantizer clipping-factor $\kappa$ are used as for the clipping-only case in Figure 5.37; and that these values of $\kappa$ cause the same values of the quantizer step-size $\Delta$ as for the quantization-only case in Figure 5.38. As expected, the results of the combined quantization and clipping case in Figure 5.36 combine the results of the clipping-only case in Figure 5.37 and the quantization-only case in Figure 5.38. That is, results for the case of severe quantizer clipping (small quantizer clipping-factor $\kappa$) with accompanying small quantizer step-size $\Delta$ in Figure5.36(a) are dominated by the clipping and so resemble the clipping-only case in Figure 5.37(a). Similarly, the results for the case of no quantizer clipping (large quantizer clipping-factor $\kappa$) with accompanying large quantizer step-size $\Delta$ in Figure 5.36(f) are dominated by quantization and so resemble the quantization-only case in Figure 5.37(f). In both cases, the results for $\mathbf{CORR}(\boldsymbol{f}, \boldsymbol{q})$ resemble closely a scaled version of $\mathbf{CORR}(\boldsymbol{f})$. Transiting, in Figures 5.36(a) to (f), from severe clipping to a large quantizer step-size, we see that the optimally smallest correlation entry magnitudes occur for the $\kappa = 2$ case in Figure 5.36(d).

Next, looking at the 6-bit case in Figures 5.39 to 5.41, we observe similar trends to the 3-bit case already discussed. The most noticeable difference from the 3-bit case is the reduction in the magnitudes of correlations due to quantization-only as evidenced by the mainly black (low-correlation magnitude) plots in the quantization-only case of Figure 5.41. This can be explained by the fact that, for the same clipping factor $\kappa$, the 6-bit case quantizer step-size $\Delta$ is reduced by a factor of $2^{6-3} = 8$ compared to the 3-bit case. Since the contribution to correlations from quantization versus clipping is reduced for the 6-bit case, the optimally smallest correlation entry magnitudes have changed from $\kappa = 2$ for the 3-bit case case in Figure 5.36(d) to $\kappa = 3$ for the 6-bit case in Figure 5.39(e).

For each of the correlation matrix plots of Figures 5.36 to 5.41, the correlation of all matching-index quantizer input and quantizer error time-samples

$$\mathrm{corr}(f, q) = \frac{1}{|\mathcal{A}_{\boldsymbol{d}}| \cdot N} \sum_{\boldsymbol{d} \in \mathcal{A}_{\boldsymbol{d}}} \sum_{n=0}^{N-1} f_n q_n, \tag{5.95}$$

is displayed at the bottom of the plot. From (5.95), we see that $\mathrm{corr}(f, q)$ is the average of the diagonal entries of $\mathbf{CORR}(\boldsymbol{f}, \boldsymbol{q})$. We note that $\mathrm{corr}(f, q)$ is useful since, as already mentioned, it represents a single-figure statistic describing correlations between all matching-index quantizer input and quantizer error time-samples. Its short-coming is that it doesn't incorporate any of the correlations between any of the non-matching-index entries (e.g. $f_l, q_m, m \neq l$) manifesting as the off-diagonal entries of $\mathbf{CORR}(\boldsymbol{f}, \boldsymbol{q})$.

Looking at the correlation matrix plots of Figures 5.36 to 5.41, we note that quite significant values of $\mathrm{corr}(f, q)$ are apparent for severe-clipping and large quantizer step-size cases.

Summing up, the results for the approximate 'Monte Carlo' magnitude $|\mathbf{CORR}(\boldsymbol{f}, \boldsymbol{q})|$ of the correlation matrix of the IDFT output time-sample vector $\boldsymbol{f}$ with the quantizer error vector $\boldsymbol{q}$ for OFDM Type = 5.2 (IEEE 802.11a, BPSK) 3-bit and 6-bit quantization cases shown in Figures 5.36 to 5.41 demonstrate that significant correlations exist between the quantizer input time-samples $f_l, l \in \mathbb{Z}_N$ and the quantizer error time-samples $q_m, m \in \mathbb{Z}_N$ for the cases of significant clipping or significantly large quantizer step-sizes.

### 5.4.4 'Monte Carlo' PDF and CDF of the Individual Quantizer Error Frequency-Sample Real-Parts

Next, we examine the PDF $f_{u_k}(u'_k)$ and CDF $F_{u_k}(u''_k)$ of the individual quantizer error frequency-sample real-parts obtained by the 'Monte Carlo' method. These PDFs and CDFs give important insight into the variability of the PDF and CDF with the particular frequency-sample observed as well as a surprising 'non-Gaussian-ness' of some of the frequency-samples. The author has not been able to find these kind of results, shown in Figures 5.42 to 5.45 , in any of the literature and, accordingly believes them to be an original contribution to the state-of-the-art.

Figure 5.42(a) shows the PDFs and CDFs for individual quantizer error frequency-samples for a small-complexity OFDM system with no Zero or Pilot sub-carriers. The PDFs and CDFs demonstrate striking departures from Gaussian distributions with quite noticeable 'clumpings' of diracs in the PDFs. $\mathcal{A}_{\boldsymbol{d}}$ indicates the number of IDFT input symbols $\boldsymbol{d}$ used in the Monte Carlo simulation, $\beta$ indicates the scaling factor due to quantization, $\beta D_s/2$ indicates the half-BPSK-symbol distance (shown by the vertical dotted blue lines on the plots), and $N_\delta$ indicates the number of discrete diracs found in the PDF

In Figure 5.43, we address a high-complexity real-world IEEE 802.11a WLAN

OFDM system. Figure 5.43(a) demonstrates that, curiously, only a small number of PDF diracs occur for the $k = 0$ sub-carrier. Insight into the reasons for this are given by the combinatoric analysis in §6.3. The other PDFs and CDFs of Figure 5.43 demonstrate the variability between the different quantizer error frequency-samples.

In Figure 5.44, the quantizer clipping-factor $\kappa$ has been increased from 2 to 3.5. As a result, we observe significant departures from Gaussian-ness in the PDFs and CDFs for multiple different quantizer error frequency-samples.

In Figure 5.45, the same phenomenom remains for a quantizer clipping-factor $\kappa$ of 4.

To summarize, non-Gaussian-ness is observed in the quantizer error frequency-samples. Also, variability between the PDFs and CDFs of the various frequency-samples is observed.

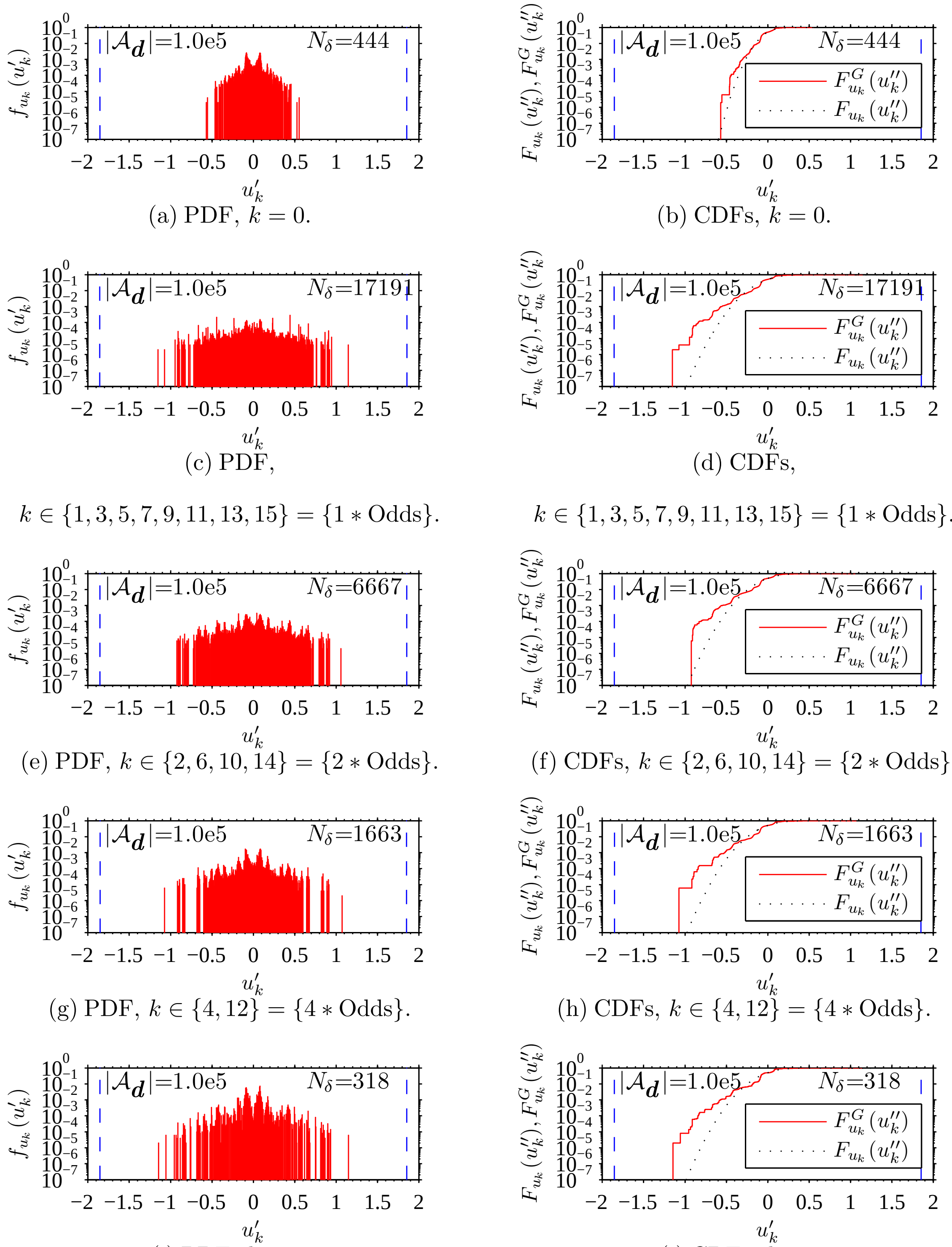


(a) PDF, $k = 0$.

(b) CDFs, $k = 0$.

(c) PDF, $k \in \{1, 3, 5, 7, 9, 11, 13, 15\} = \{1 * \text{Odds}\}$.

(d) CDFs, $k \in \{1, 3, 5, 7, 9, 11, 13, 15\} = \{1 * \text{Odds}\}$.

(e) PDF, $k \in \{2, 6, 10, 14\} = \{2 * \text{Odds}\}$.

(f) CDFs, $k \in \{2, 6, 10, 14\} = \{2 * \text{Odds}\}$.

(g) PDF, $k \in \{4, 12\} = \{4 * \text{Odds}\}$.

(h) CDFs, $k \in \{4, 12\} = \{4 * \text{Odds}\}$.

(i) PDF, $k = 8$.

(j) CDFs, $k = 8$.

OFDM Type 3.2: $N = 32, \mathcal{K}_{\text{SZ}} = \{\}, \mathcal{K}_{\text{SP}} = \{\}, \mathcal{K}_{\text{SD}} = \mathbb{Z}_N, \mathcal{A}_{\text{SD}} = \mathcal{A}_{\text{BPSK}}, \text{E}[f^2] = 1.$

Figure 5.42: 'Monte Carlo' PDFs $f_{u_k}(u'_k)$, CDFs $F_{u_k}(u''_k)$, and Gaussian approximation CDFs $F^G_{u_k}(u''_k)$ for individual quantizer error frequency-sample real-parts $u_k$, OFDM Type = 3.2, $b = 8, \kappa = 2$ (major clipping), for various frequency-sample indeces $k$.

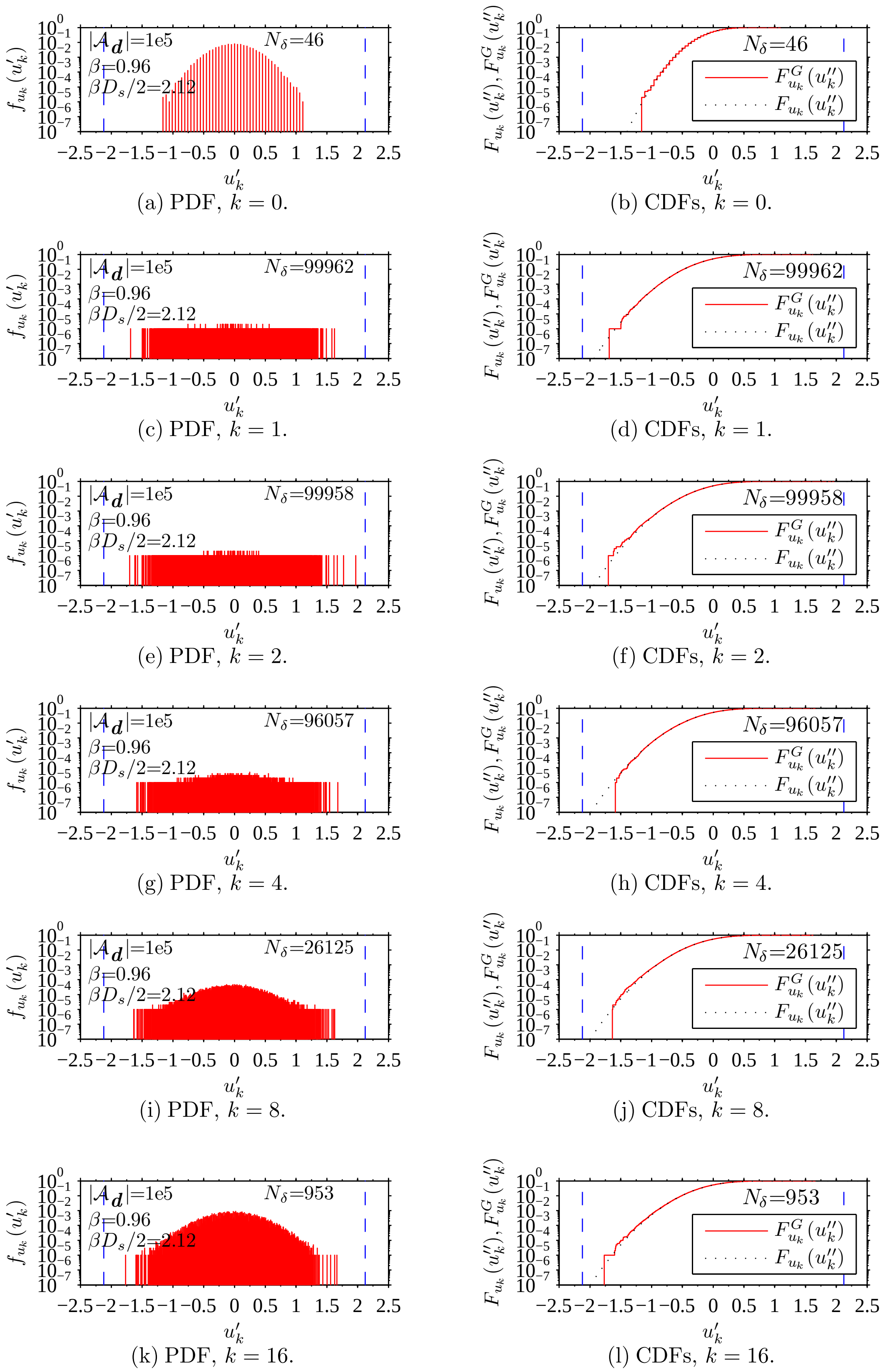


(a) PDF, $k = 0$. (b) CDFs, $k = 0$.

(c) PDF, $k = 1$. (d) CDFs, $k = 1$.

(e) PDF, $k = 2$. (f) CDFs, $k = 2$.

(g) PDF, $k = 4$. (h) CDFs, $k = 4$.

(i) PDF, $k = 8$. (j) CDFs, $k = 8$.

(k) PDF, $k = 16$. (l) CDFs, $k = 16$.

OFDM Type 5.2: IEEE 802.11a, $N = 128, \mathcal{K}_{\text{SZ}} = \{0{:}5,32,59{:}69,96,123{:}127\}$,
$\mathcal{K}_{\text{SP}} = \{11, 25, 39, 53, 75, 89, 103, 117\}, \mathcal{A}_{\text{SP}} = \mathcal{A}_{\text{BPSK}}$,
$\mathcal{K}_{\text{SD}} = \{6{:}10,12{:}24,26{:}31,33{:}38,40{:}52,54{:}58,70{:}74,76{:}88,90{:}95,97{:}102,104{:}116,118{:}122\}$,
$\mathcal{A}_{\text{SD}} = \mathcal{A}_{\text{BPSK}}, \mathcal{D}_{\text{SP}} = \{+1, +1, +1, -1, -1, +1, +1, +1\}$.

Figure 5.43: 'Monte Carlo' PDFs $f_{u_k}(u'_k)$, CDFs $F_{u_k}(u''_k)$, and Gaussian approximation CDFs $F^G_{u_k}(u''_k)$ for individual quantizer error frequency-sample real-parts $u_k$, OFDM Type = 5.2 (IEEE 802.11a, BPSK), $b = 3, \kappa = 2$, for various frequency-sample indeces $k$.

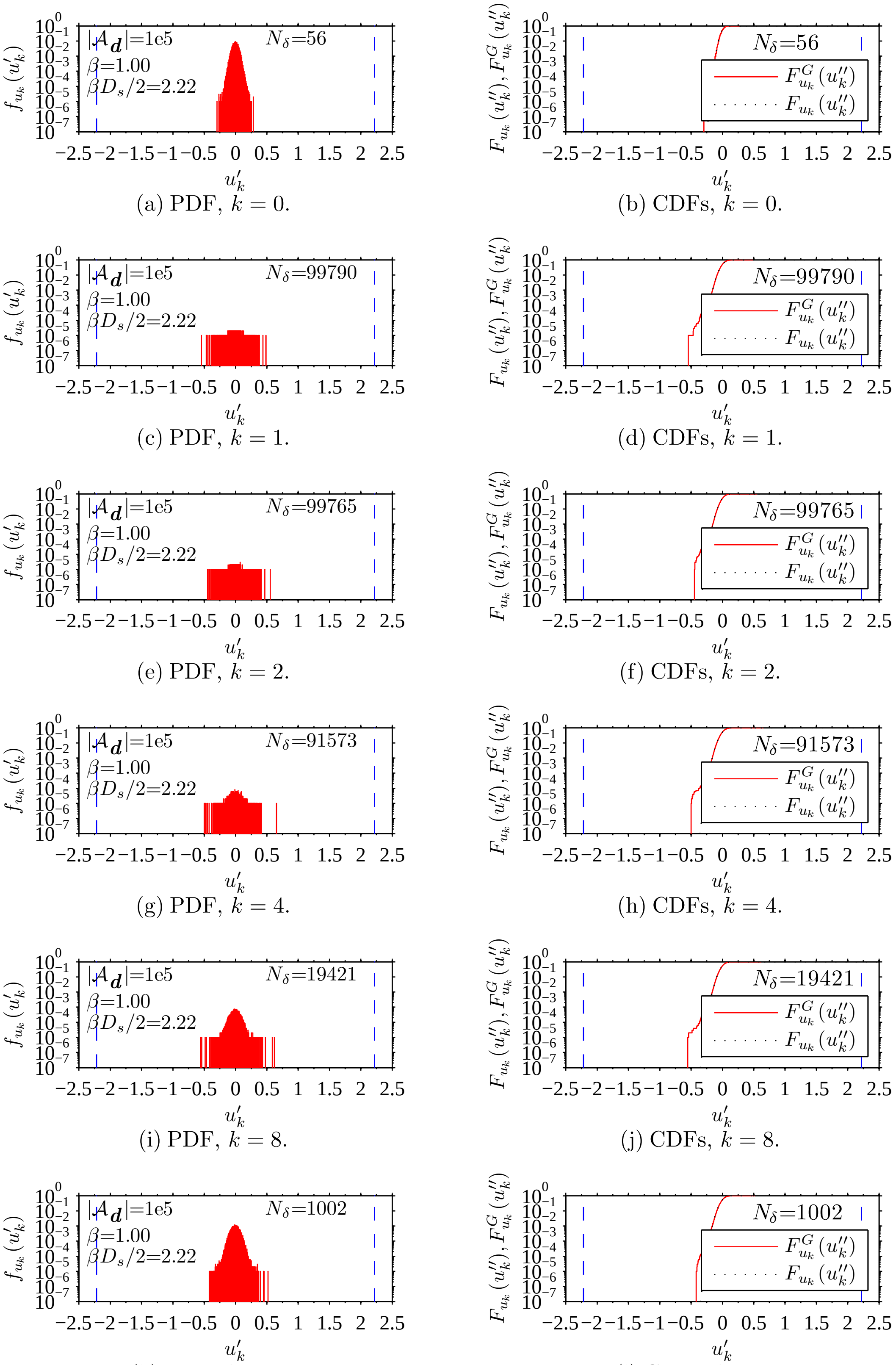


(a) PDF, $k = 0$. (b) CDFs, $k = 0$.

(c) PDF, $k = 1$. (d) CDFs, $k = 1$.

(e) PDF, $k = 2$. (f) CDFs, $k = 2$.

(g) PDF, $k = 4$. (h) CDFs, $k = 4$.

(i) PDF, $k = 8$. (j) CDFs, $k = 8$.

(k) PDF, $k = 16$. (l) CDFs, $k = 16$.

| | |
|---|---|
| OFDM Type 5.2: | IEEE 802.11a, $N = 128, \mathcal{K}_{\text{SZ}} = \{0{:}5,32,59{:}69,96,123{:}127\}$,<br>$\mathcal{K}_{\text{SP}} = \{11, 25, 39, 53, 75, 89, 103, 117\}, \mathcal{A}_{\text{SP}} = \mathcal{A}_{\text{BPSK}}$,<br>$\mathcal{K}_{\text{SD}} = \{6{:}10,12{:}24,26{:}31,33{:}38,40{:}52,54{:}58,70{:}74,76{:}88,90{:}95,97{:}102,104{:}116,118{:}122\}$,<br>$\mathcal{A}_{\text{SD}} = \mathcal{A}_{\text{BPSK}}, \mathcal{D}_{\text{SP}} = \{+1, +1, +1, -1, -1, +1, +1, +1\}$. |

Figure 5.44: 'Monte Carlo' PDFs $f_{u_k}(u'_k)$, CDFs $F_{u_k}(u''_k)$, and Gaussian approximation CDFs $F^G_{u_k}(u''_k)$ for individual quantizer error frequency-sample real-parts $u_k$, OFDM Type = 5.2 (IEEE 802.11a, BPSK), $b = 6, \kappa = 3.5$, for various frequency-sample indeces $k$.

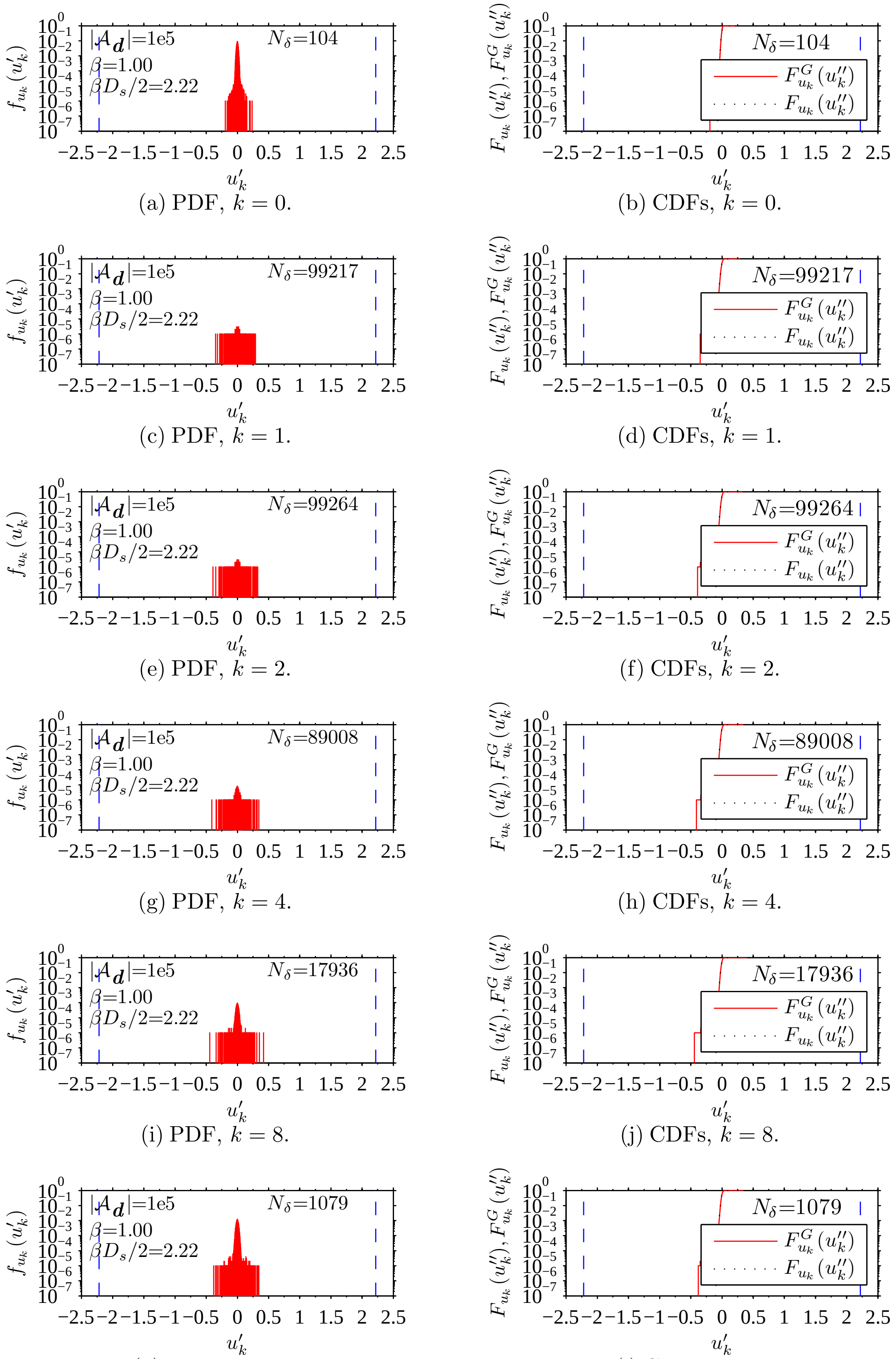


(a) PDF, $k = 0$. (b) CDFs, $k = 0$.

(c) PDF, $k = 1$. (d) CDFs, $k = 1$.

(e) PDF, $k = 2$. (f) CDFs, $k = 2$.

(g) PDF, $k = 4$. (h) CDFs, $k = 4$.

(i) PDF, $k = 8$. (j) CDFs, $k = 8$.

(k) PDF, $k = 16$. (l) CDFs, $k = 16$.

OFDM Type 5.2: IEEE 802.11a, $N = 128, \mathcal{K}_{\text{SZ}} = \{0{:}5{,}32{,}59{:}69{,}96{,}123{:}127\}$,
$\mathcal{K}_{\text{SP}} = \{11, 25, 39, 53, 75, 89, 103, 117\}, \mathcal{A}_{\text{SP}} = \mathcal{A}_{\text{BPSK}}$,
$\mathcal{K}_{\text{SD}} = \{6{:}10{,}12{:}24{,}26{:}31{,}33{:}38{,}40{:}52{,}54{:}58{,}70{:}74{,}76{:}88{,}90{:}95{,}97{:}102{,}104{:}116{,}118{:}122\}$,
$\mathcal{A}_{\text{SD}} = \mathcal{A}_{\text{BPSK}}, \mathcal{D}_{\text{SP}} = \{+1, +1, +1, -1, -1, +1, +1, +1\}$.

Figure 5.45: 'Monte Carlo' PDFs $f_{u_k}(u'_k)$, CDFs $F_{u_k}(u''_k)$, and Gaussian approximation CDFs $F^G_{u_k}(u''_k)$ for individual quantizer error frequency-sample real-parts $u_k$, OFDM Type = 5.2 (IEEE 802.11a, BPSK), $b = 8, \kappa = 4$, for various frequency-sample indeces $k$.

### 5.4.5 'Monte Carlo' PDF and CDF of All Quantizer Error Frequency-Sample Real-Parts

Next, we examine the PDF $f_u(u')$ and CDF $F_u(u'')$ of all of the quantizer error frequency-sample real-parts obtained by the 'Monte Carlo' method. These PDFs and CDFs are amongst the most important results of this thesis since they directly provide all of the necessary information to derive symbol error rates for the received OFDM symbols after quantization. Although, these results show PDFs and CDFs for the quantization noise only, other noise (e.g. LNA noise) can easily be incorporated by convolving each of the PDF diracs with the PDF of the additional noise. Also, importantly, with these results, the issue of independence of the quantization noise from the required QAM symbols is bypassed since the quantization noise PDFs are relative to nominal QAM points and a symbol error occurs whenever the noise PDF exceeds half the intersymbol distance (indicated by $\beta D_s/2$ and the vertical dotted lines).

The author has not been able to find these kind of results, shown in Figures 5.46 to 5.49, in any of the literature and, accordingly believes them to be an original contribution to the state-of-the-art.

Figure 5.46 shows the PDFs and CDFs for a BPSK 802.11a WLAN OFDM system using only 3 quantizer bits $b$. As the quantizer clipping factor $\kappa$ is varied, the optimal SQNR $\gamma_u$ is found to be 15.1dB for $\kappa = 2$. The PDFs and CDFs for this case appear to closely approximate Gaussian PDFs and CDFs.

In Figure 5.47, the number of quantizer bits $b$ has been increased to 6. As the quantizer clipping-factor $\kappa$ is varied, the optimal SQNR $\gamma_u$ is found to be 30.4dB for $\kappa = 3.5$. However, importantly, the quantizer error PDF at this point is not Gaussian.

In Figure 5.48, the number of quantizer bits $b$ has been increased to 8. As the quantizer clipping-factor $\kappa$ is varied, the optimal SQNR $\gamma_u$ is found to be 40.8dB for $\kappa = 4$. However, like the 6-bit case, the quantizer error PDF at this point is not Gaussian.

To summarize, the signal to quantization noise SQNR has been optimized for 3, 6, and 8 bit quantization by adjustment of the quantizer clipping-facto $\kappa$. However, for the 6 and 8 bit cases, the quantizer error noise PDFs and CDFs are not Gaussian in contradiction to much of the extant literature (refer §1.1).

## 5.5 Summary of Results of Numerical Methods

The 'Exhaustive' and 'Monte Carlo' methods have produced exact results for small-scale systems and approximate results for large-scale systems. The discrete nature of PDFs of the transmitter signal before and after quantization has been demonstrated and the curiously small number of discrete signal levels (compared to the IDFT input alphabet size) in both the time-domain and the frequency-domain has been noted. Also, the PDFs of the time-domain and frequency-domain signals have been observed to depart from Gaussian in many cases contrary to the assumptions of much of the literature. Finally, the time-domain cross-correlation matrix of the transmitter quantizer input and quantizer error has demonstrated significant correlations between the input and the error meaning that the quantizer noise cannot be modeled as independent and additive. Again, this is contrary to the assumptions of much of the literature.

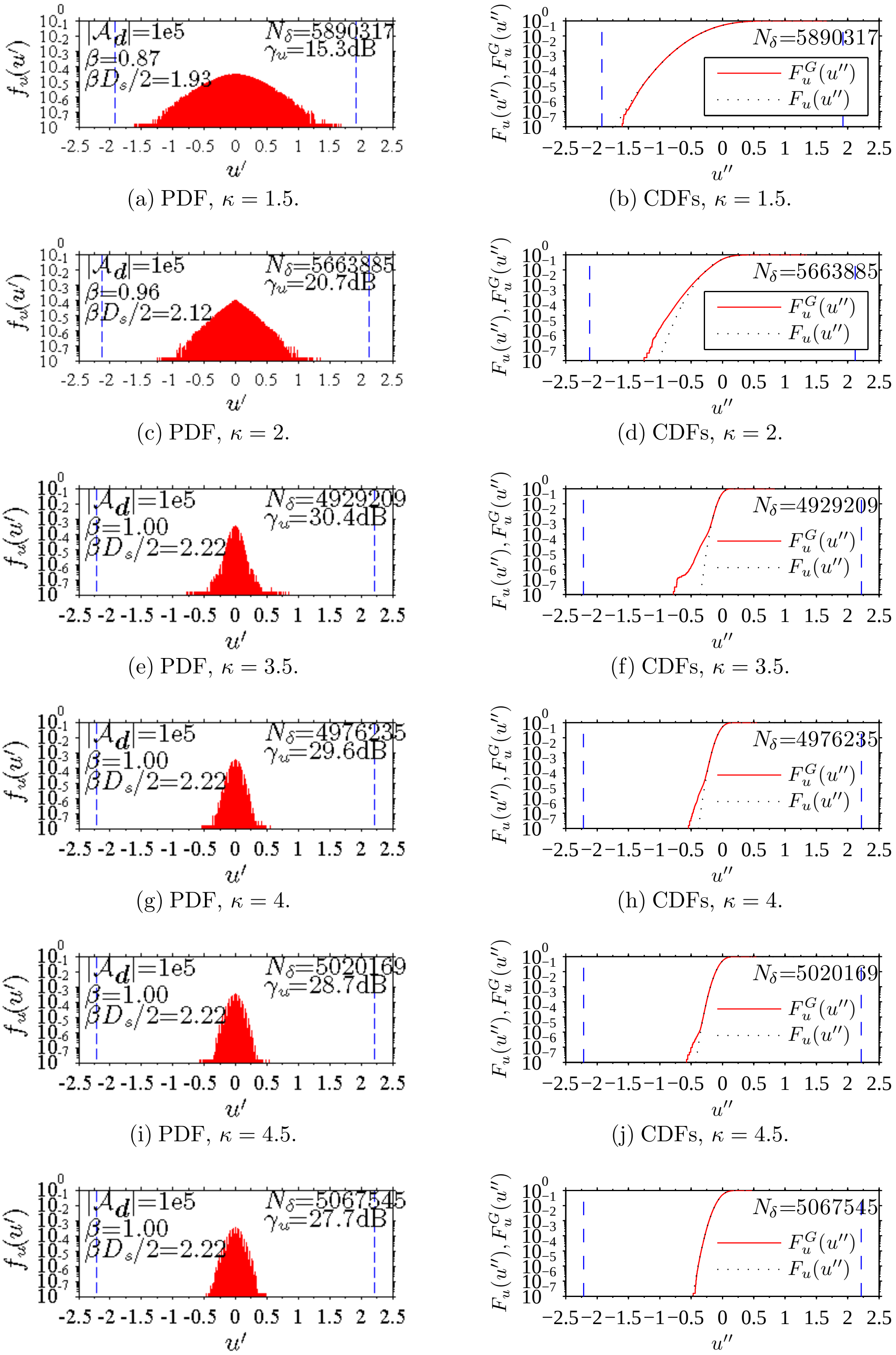


(a) PDF, $\kappa = 1.5$.

(b) CDFs, $\kappa = 1.5$.

(c) PDF, $\kappa = 2$.

(d) CDFs, $\kappa = 2$.

(e) PDF, $\kappa = 3.5$.

(f) CDFs, $\kappa = 3.5$.

(g) PDF, $\kappa = 4$.

(h) CDFs, $\kappa = 4$.

(i) PDF, $\kappa = 4.5$.

(j) CDFs, $\kappa = 4.5$.

(k) PDF, $\kappa = 5$.

(l) CDFs, $\kappa = 5$.

| | |
|---|---|
| OFDM Type 5.2: | IEEE 802.11a, $N = 128, \mathcal{K}_{\mathrm{SZ}} = \{0{:}5,32,59{:}69,96,123{:}127\}$,<br>$\mathcal{K}_{\mathrm{SP}} = \{11, 25, 39, 53, 75, 89, 103, 117\}, \mathcal{A}_{\mathrm{SP}} = \mathcal{A}_{\mathrm{BPSK}}$,<br>$\mathcal{K}_{\mathrm{SD}} = \{6{:}10,12{:}24,26{:}31,33{:}38,40{:}52,54{:}58,70{:}74,76{:}88,90{:}95,97{:}102,104{:}116,118{:}122\}$,<br>$\mathcal{A}_{\mathrm{SD}} = \mathcal{A}_{\mathrm{BPSK}}, \mathcal{D}_{\mathrm{SP}} = \{+1,+1,+1,-1,-1,+1,+1,+1\}$. |

Figure 5.47: 'Monte Carlo' PDFs $f_u(u')$, CDFs $F_u(u'')$, and Gaussian approximation CDFs $F_u^G(u'')$ for all quantizer error frequency-sample real-parts $u$, OFDM Type = 5.2 (IEEE 802.11a, BPSK), $b = 6$, for various clipping-factors $\kappa$.

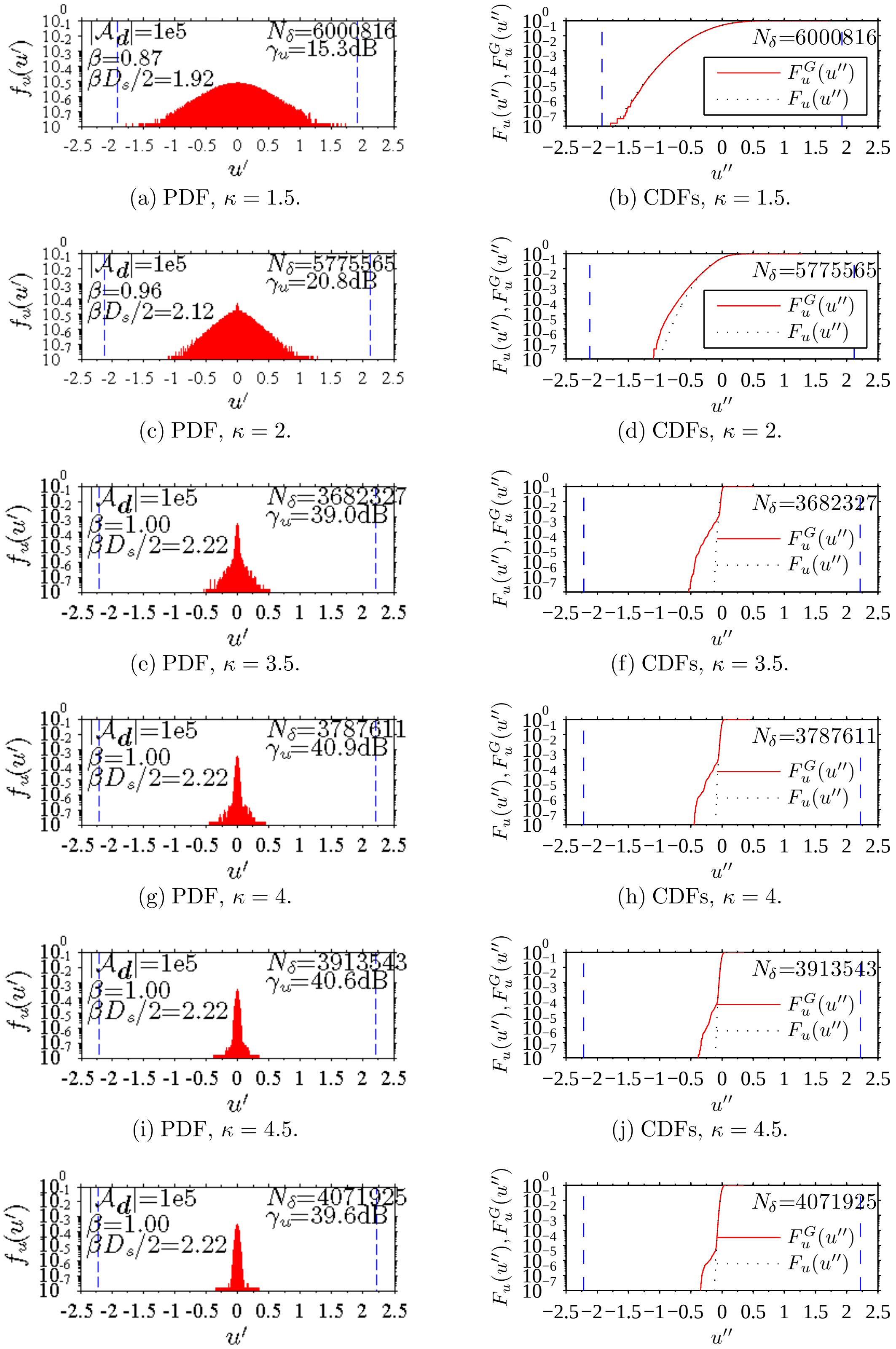


(a) PDF, $\kappa = 1.5$. (b) CDFs, $\kappa = 1.5$.

(c) PDF, $\kappa = 2$. (d) CDFs, $\kappa = 2$.

(e) PDF, $\kappa = 3.5$. (f) CDFs, $\kappa = 3.5$.

(g) PDF, $\kappa = 4$. (h) CDFs, $\kappa = 4$.

(i) PDF, $\kappa = 4.5$. (j) CDFs, $\kappa = 4.5$.

(k) PDF, $\kappa = 5$. (l) CDFs, $\kappa = 5$.

OFDM Type 5.2: IEEE 802.11a, $N = 128, \mathcal{K}_{\mathrm{SZ}} = \{0{:}5,32,59{:}69,96,123{:}127\}$,
$\mathcal{K}_{\mathrm{SP}} = \{11, 25, 39, 53, 75, 89, 103, 117\}, \mathcal{A}_{\mathrm{SP}} = \mathcal{A}_{\mathrm{BPSK}}$,
$\mathcal{K}_{\mathrm{SD}} = \{6{:}10,12{:}24,26{:}31,33{:}38,40{:}52,54{:}58,70{:}74,76{:}88,90{:}95,97{:}102,104{:}116,118{:}122\}$,
$\mathcal{A}_{\mathrm{SD}} = \mathcal{A}_{\mathrm{BPSK}}, \mathcal{D}_{\mathrm{SP}} = \{+1, +1, +1, -1, -1, +1, +1, +1\}$.

Figure 5.48: 'Monte Carlo' PDFs $f_u(u')$, CDFs $F_u(u'')$, and Gaussian approximation CDFs $F_u^G(u'')$ for all quantizer error frequency-sample real-parts $u$, OFDM Type = 5.2 (IEEE 802.11a, BPSK), $b = 8$, for various clipping-factors $\kappa$.

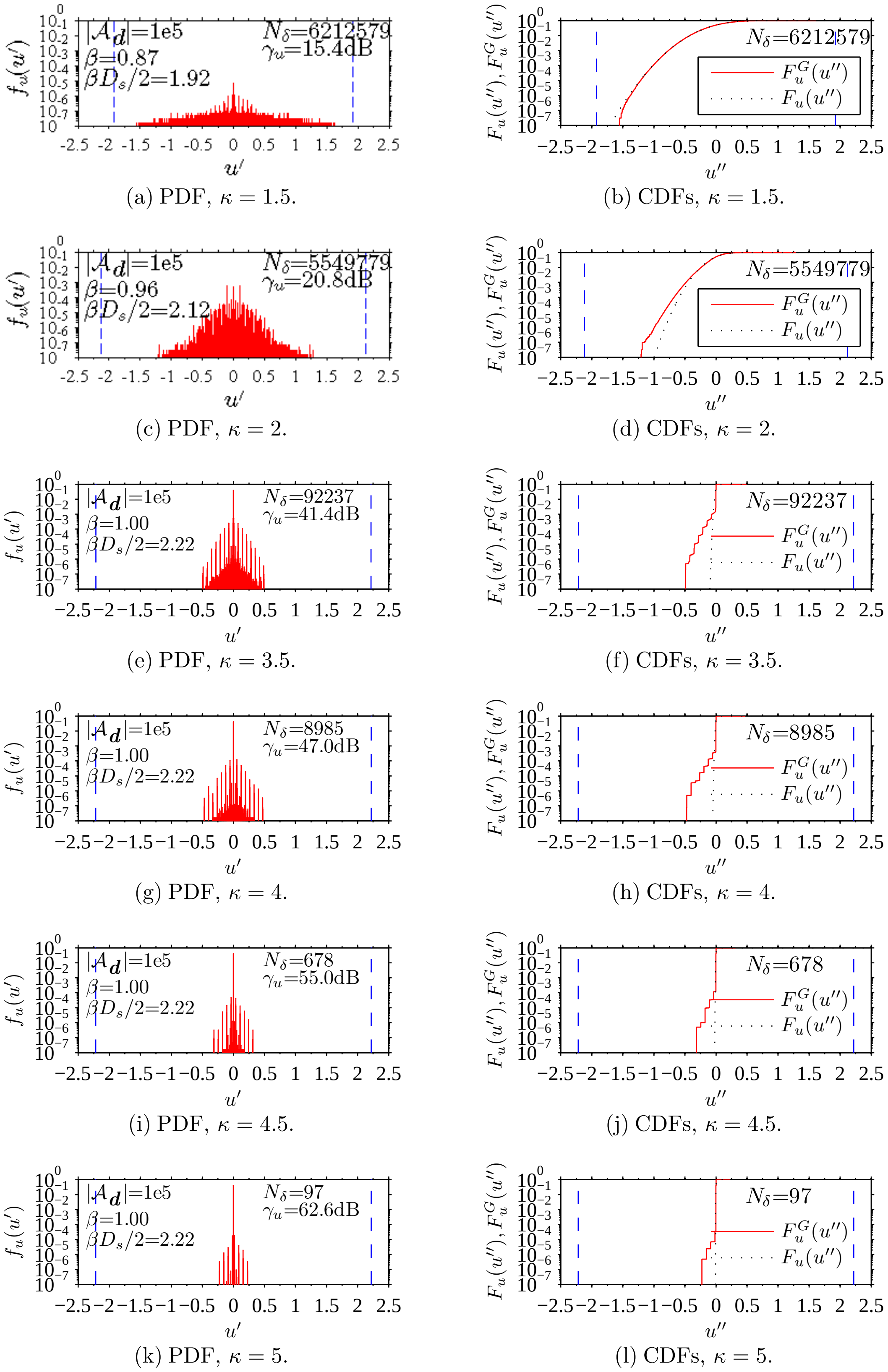


(a) PDF, $\kappa = 1.5$. (b) CDFs, $\kappa = 1.5$.

(c) PDF, $\kappa = 2$. (d) CDFs, $\kappa = 2$.

(e) PDF, $\kappa = 3.5$. (f) CDFs, $\kappa = 3.5$.

(g) PDF, $\kappa = 4$. (h) CDFs, $\kappa = 4$.

(i) PDF, $\kappa = 4.5$. (j) CDFs, $\kappa = 4.5$.

(k) PDF, $\kappa = 5$. (l) CDFs, $\kappa = 5$.

OFDM Type 5.2: IEEE 802.11a, $N = 128, \mathcal{K}_{\text{SZ}} = \{0{:}5, 32, 59{:}69, 96, 123{:}127\}$,
$\mathcal{K}_{\text{SP}} = \{11, 25, 39, 53, 75, 89, 103, 117\}, \mathcal{A}_{\text{SP}} = \mathcal{A}_{\text{BPSK}}$,
$\mathcal{K}_{\text{SD}} = \{6{:}10, 12{:}24, 26{:}31, 33{:}38, 40{:}52, 54{:}58, 70{:}74, 76{:}88, 90{:}95, 97{:}102, 104{:}116, 118{:}122\}$,
$\mathcal{A}_{\text{SD}} = \mathcal{A}_{\text{BPSK}}, \mathcal{D}_{\text{SP}} = \{+1, +1, +1, -1, -1, +1, +1, +1\}$.

Figure 5.49: 'Monte Carlo' PDFs $f_u(u')$, CDFs $F_u(u'')$, and Gaussian approximation CDFs $F_u^G(u'')$ for all quantizer error frequency-sample real-parts $u$, OFDM Type = 5.2 (IEEE 802.11a, BPSK), no quantization, clipping only, for various clipping-factors $\kappa$.

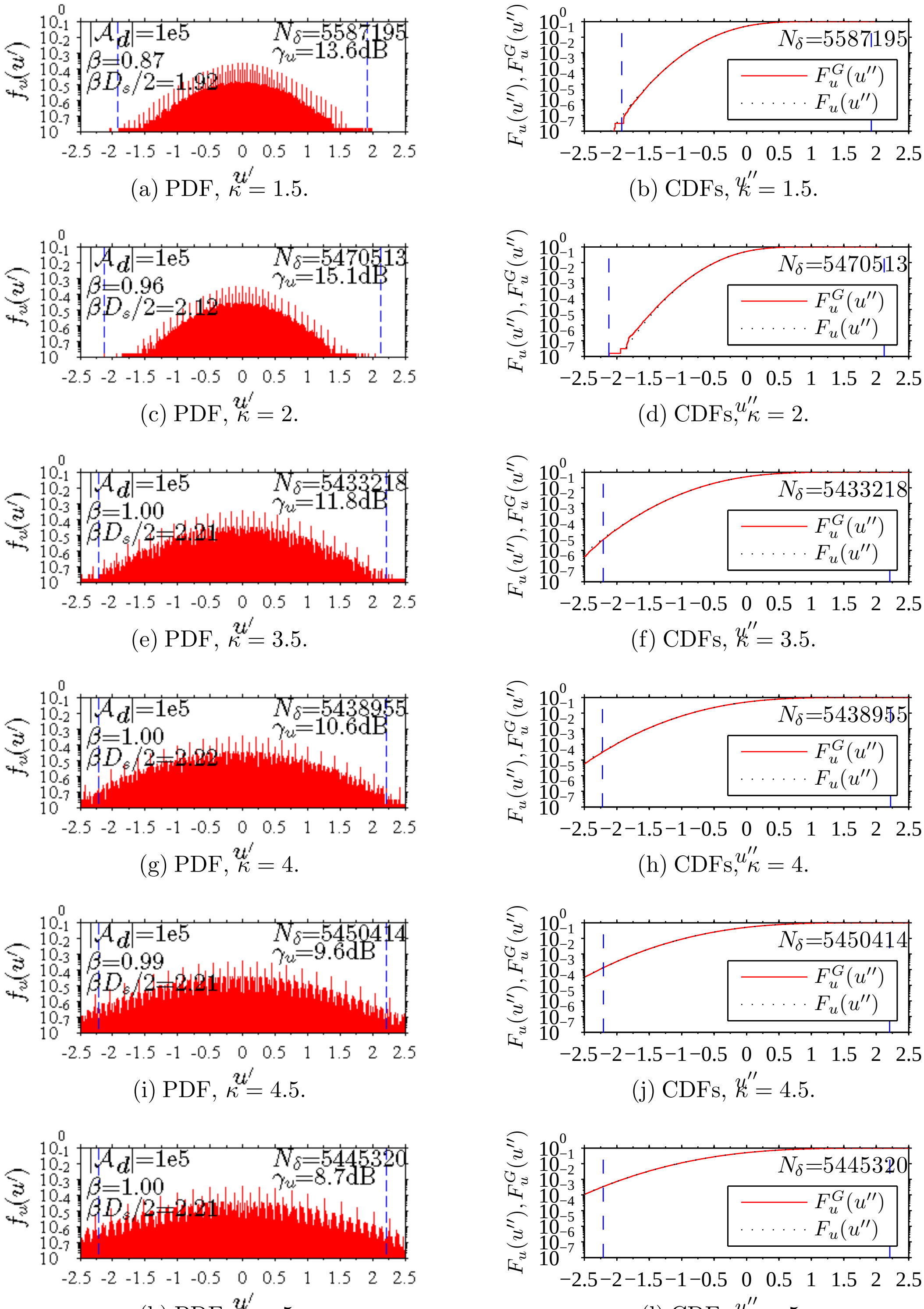


(a) PDF, $\kappa = 1.5$. (b) CDFs, $\kappa = 1.5$.

(c) PDF, $\kappa = 2$. (d) CDFs, $\kappa = 2$.

(e) PDF, $\kappa = 3.5$. (f) CDFs, $\kappa = 3.5$.

(g) PDF, $\kappa = 4$. (h) CDFs, $\kappa = 4$.

(i) PDF, $\kappa = 4.5$. (j) CDFs, $\kappa = 4.5$.

(k) PDF, $\kappa = 5$. (l) CDFs, $\kappa = 5$.

| | |
|---|---|
| OFDM Type 5.2: | IEEE 802.11a, $N = 128$, $\mathcal{K}_{SZ} = \{0{:}5,32,59{:}69,96,123{:}127\}$,<br>$\mathcal{K}_{SP} = \{11,25,39,53,75,89,103,117\}$, $\mathcal{A}_{SP} = \mathcal{A}_{BPSK}$,<br>$\mathcal{K}_{SD} = \{6{:}10,12{:}24,26{:}31,33{:}38,40{:}52,54{:}58,70{:}74,76{:}88,90{:}95,97{:}102,104{:}116,118{:}122\}$,<br>$\mathcal{A}_{SD} = \mathcal{A}_{BPSK}$, $\mathcal{D}_{SP} = \{+1,+1,+1,-1,-1,+1,+1,+1\}$. |

Figure 5.46: ‘Monte Carlo’ PDFs $f_u(u')$, CDFs $F_u(u'')$, and Gaussian approximation CDFs $F_u^G(u'')$ for all quantizer error frequency-sample real-parts $u$, OFDM Type = 5.2 (IEEE 802.11a, BPSK), $b = 3$, for various clipping-factors $\kappa$.

# Chapter 6

# Analytical Approaches

From the discussion of the Monte Carlo numerical simulations in §3 and §5.4, we gained some insight into quantization of OFDM systems.

We note, however, that Monte Carlo simulations have several short-comings. Firstly, accurate simulations require very long simulation times. Secondly, the reasons for specific particular numerical simulation results are not immediately apparent.

In order to gain further insight, we will now proceed to develop analytical models of quantization of OFDM at digital IF.

In §6.1, we develop the 'Matrix Transformation' method to obtain exact auto-correlation and cross-correlation matrices for various system signals. This is an original contribution to the state of the art. These correlation matrices give insight into the correlations between quantizer input signals and the quantizer noise at the quantizer output thus determining whether quantization noise can be modeled as independent of the input as is often the case in the literature (refer §1.1).

In §6.2, we develop the 'Convolution' method to obtain exact PDFs and CDFs for the transmitter digital IF OFDM signals at the IDFT output for arbitrary complexity OFDM systems. This is another original contribution to the state of the art. The PDFs obtained are of particular interest since we find that they challenge the notion common in the literature (refer §1.1) that quantization noise generated in the time-domain always becomes Gaussian when passed through an FFT into the frequency-domain. The CDFs are interesting in that they allow exact determination of error rates of the frequency-domain decision variables without resorting to the common, sometimes inappropriate, approximations and assumptions used in the literature (refer §1.1).

Finally, in §6.3, we develop the 'Combinatorics' method to obtain the preliminary steps to obtaining exact PDFs and CDFs of the transmitter quantizer output and quantizer error. Again, this is another original contribution to the state of the art.

## 6.1 The Exact 'Matrix Transformation' Method

### 6.1.1 'Matrix Transformation' Covariance Matrix of the OFDM Source Symbol Frequency-Samples at the Upconverter Output

The covariance matrix of the upconverted transmitter digital IF vector $\boldsymbol{d}$ is given by

$$\begin{aligned}
\mathbf{COV}(\boldsymbol{d}) &\equiv \mathbf{COV}[\boldsymbol{d},\boldsymbol{d}] \equiv \mathbf{COV}[\boldsymbol{d}] \equiv \mathbf{VAR}[\boldsymbol{d}] \\
&= \mathrm{E}[(\boldsymbol{d}-\mathrm{E}[\boldsymbol{d}])(\boldsymbol{d}-\mathrm{E}[\boldsymbol{d}])^{\mathrm{H}}] \\
&= \mathrm{E}[\boldsymbol{d}\boldsymbol{d}^{\mathrm{H}}-\mathrm{E}[\boldsymbol{d}]\boldsymbol{d}^{\mathrm{H}}-\boldsymbol{d}\mathrm{E}[\boldsymbol{d}]^{\mathrm{H}}+\mathrm{E}[\boldsymbol{d}]\mathrm{E}[\boldsymbol{d}]^{\mathrm{H}}] \\
&= \mathrm{E}[\boldsymbol{d}\boldsymbol{d}^{\mathrm{H}}]-\mathrm{E}[\boldsymbol{d}]\mathrm{E}[\boldsymbol{d}^{\mathrm{H}}]-\mathrm{E}[\boldsymbol{d}]\mathrm{E}[\boldsymbol{d}]^{\mathrm{H}}+\mathrm{E}[\boldsymbol{d}]\mathrm{E}[\boldsymbol{d}]^{\mathrm{H}} \\
&= \mathrm{E}[\boldsymbol{d}\boldsymbol{d}^{\mathrm{H}}]-\mathrm{E}[\boldsymbol{d}]\mathrm{E}[\boldsymbol{d}^{\mathrm{H}}] \\
&= ([\mathbf{COV}(\boldsymbol{d})]_{l,m}) \quad , \; l,m \in \mathbb{Z}_N,
\end{aligned} \tag{6.1}$$

where the $(l,m)^{\mathrm{th}}$ entry of $\mathbf{COV}(\boldsymbol{d})$ is

$$[\mathbf{COV}(\boldsymbol{d})]_{l,m} = \mathrm{cov}[d_l,d_m] = \mathrm{E}[d_l d_m^*] - \mathrm{E}[d_l]\mathrm{E}[d_m^*], \tag{6.2}$$

$\mathrm{cov}[\cdot,\cdot]$ indicates the bi-variate covariance operation, $\mathrm{E}[\cdot]$ indicates statistical expectation, $\{\cdot\}^{\mathrm{H}}$ indicates the matrix Hermitian operation which is the complex-conjugate of the transpose, and $\{\cdot\}^*$ indicates complex-conjugate.

We let all of the entries $b_k$ of the transmitter baseband source symbol vector $\boldsymbol{b}$ be MQAM, MPSK, or Zero symbols (which are all zero-mean). Via the "UPCON-

VERTER #2" mapping function of (4.23), these two conditions also apply to all of the entries $d_k$ of the upconverted transmitter digital IF vector $\boldsymbol{d}$ so that

$$b_k, d_k \in \mathcal{A}_{\mathrm{MQAM}} \cup \mathcal{A}_{\mathrm{MPSK}} \cup \mathcal{A}_{\mathrm{ZERO}}, \tag{6.3}$$

and

$$\mathrm{E}[b_k] = \mathrm{E}[d_k] = 0 \quad , \forall k. \tag{6.4}$$

Some minor manipulation of (4.23) also reveals the conjugate relationship between the entries of $d_k, k \in \mathbb{Z}_N$ of the IDFT input vector $\boldsymbol{d}$ as

$$d_k = \begin{cases} 0 & , k \in \{0, N/2\} \\ d^*_{N-k} & , \text{otherwise.} \end{cases} \tag{6.5}$$

Using (6.4) and (6.5), we expand the expression for the covariance matrix of the upconverted transmitter digital IF vector $\boldsymbol{d}$ already given in (6.2) for various relevant cases of $d_l$ and $d_m$ to obtain

$$[\mathbf{COV}(\boldsymbol{d})]_{l,m} = \begin{cases} \mathrm{E}[|d_l|^2] & , m = l & , l \notin \{0, N/2\} \\ \mathrm{E}[d_l^2] & , m = N - l & , l \notin \{0, N/2\} \\ \mathrm{E}[d_l d_m^*] & , d_l, d_m \text{ dependent} & , l, m \notin \{0, N/2\}. \\ 0 & , \text{ otherwise} & \end{cases} \tag{6.6}$$

We now divide the transmitter source baseband sub-carrier symbols $b_k$ (and, by implication, the non-precoded digital IF sub-carrier symbols $d_k$) into the three categories of Zero, Pilot, and Data symbols which are typical for OFDM [1, 2] so that

$$d_k \in \begin{cases} \mathcal{A}_{\mathrm{SZ}} & , k \in \mathcal{K}_{\mathrm{SZ}} \\ \mathcal{A}_{\mathrm{SP}} & , k \in \mathcal{K}_{\mathrm{SP}} \\ \mathcal{A}_{\mathrm{SD}} & , k \in \mathcal{K}_{\mathrm{SD}}, \end{cases} \tag{6.7}$$

where the symbols used in (6.7) and subsequent equations are already defined in §5.2. The Zero sub-carrier symbols are deterministic and, as the name implies, zero-valued so that

$$d_k \in \mathcal{A}_{SZ} = \{0\} \quad , k \in \mathcal{K}_{SZ}. \tag{6.8}$$

We let the Data digital IF sub-carrier symbols be independent, except for the conjugate cases in (6.5), random MQAM or MPSK symbols with zero-mean and unity average energy per symbol so that

$$d_k \in \mathcal{A}_{SD} \in (\mathcal{A}_{MQAM} \cup \mathcal{A}_{MPSK}) \quad , k \in \mathcal{K}_{SD}. \tag{6.9}$$

Finally, we let the Pilot sub-carrier symbols be a fixed unity average energy per symbol MQAM or MPSK symbol sequence $\mathcal{D}_{SP}$ randomly multiplied by $\pm 1$, per normal practice [2], so that

$$d_k \in \mathcal{A}_{SP} \in (\mathcal{A}_{MQAM} \cup \mathcal{A}_{MPSK}) \quad , k \in \mathcal{K}_{SP}. \tag{6.10}$$

Note that any two Pilot symbols are statistically dependent; but any Pilot symbol and any Data symbol are statistically independent. With the above conditions on the data symbols $d_k$, after some manipulation of (6.6), we obtain the numerical expression for the covariance matrix of the upconverted transmitter digital IF vector $\boldsymbol{d}$ as

$$\begin{aligned} [\mathbf{COV}(\boldsymbol{d})]_{l,m} &= \begin{cases} d_l d_m^* & , l,m \in \mathcal{K}_{\mathrm{SP}} \\ 1 & , l,m \in \mathcal{K}_{\mathrm{SD}} \quad , m = l \\ 1 & , l,m \in \mathcal{K}_{\mathrm{SD}} \quad , m = N-l \quad , \mathcal{A}_{\mathrm{SD}} = \mathcal{A}_{\mathrm{BPSK}} \\ 0 & , \text{otherwise}, \end{cases} \\ & , \mathcal{A}_{\mathrm{SP}}, \mathcal{A}_{\mathrm{SD}} \in \mathcal{A}_{\mathrm{MQAM}} \cup \mathcal{A}_{\mathrm{MPSK}}. \end{aligned} \tag{6.11}$$

Note, for the case of unity energy per symbol BPSK Pilot symbols, we have

$$d_k \in \mathcal{A}_{\mathrm{SP}} = \mathcal{A}_{\mathrm{BPSK}} = \{-1, +1\}, \;\; k \in \mathcal{K}_{\mathrm{SP}}, \tag{6.12}$$

and, therefore, $d_l d_m^*$ in (6.11) is given by

$$d_l d_m^* \in \{-1, +1\} \quad , l, m \in \mathcal{K}_{\mathrm{SP}}, \quad \mathcal{A}_{\mathrm{SP}} = \mathcal{A}_{\mathrm{BPSK}}. \tag{6.13}$$

#### 6.1.1.1 Case: OFDM Type 2.2, Zero, Pilot, and Data Sub-Carriers, No Pre-Coding, BPSK Data

For an example case of $N = 16$ digital IF sub-carriers, with Zero, Pilot, and BPSK Data sub-carriers all present, the covariance matrix of the real digital IF frequency-sample vector $\boldsymbol{d}$ at the upconverter output, calculated from (6.11), is shown in Figure 6.1.

$$\begin{bmatrix}
0 & 0 & 0 & 0 & 0 & 0 & 0 & 0 & 0 & 0 & 0 & 0 & 0 & 0 & 0 & 0 \\
0 & 1 & 0 & 0 & 0 & 0 & 0 & 0 & 0 & 0 & 0 & 0 & 0 & 0 & 0 & 1 \\
0 & 0 & 1 & 0 & -1 & 0 & -1 & 0 & 0 & 0 & -1 & 0 & -1 & 0 & 1 & 0 \\
0 & 0 & 0 & 1 & 0 & 0 & 0 & 0 & 0 & 0 & 0 & 0 & 0 & 1 & 0 & 0 \\
0 & 0 & -1 & 0 & 1 & 0 & 1 & 0 & 0 & 0 & 1 & 0 & 1 & 0 & -1 & 0 \\
0 & 0 & 0 & 0 & 0 & 1 & 0 & 0 & 0 & 0 & 0 & 1 & 0 & 0 & 0 & 0 \\
0 & 0 & -1 & 0 & 1 & 0 & 1 & 0 & 0 & 0 & 1 & 0 & 1 & 0 & -1 & 0 \\
0 & 0 & 0 & 0 & 0 & 0 & 0 & 0 & 0 & 0 & 0 & 0 & 0 & 0 & 0 & 0 \\
0 & 0 & 0 & 0 & 0 & 0 & 0 & 0 & 0 & 0 & 0 & 0 & 0 & 0 & 0 & 0 \\
0 & 0 & 0 & 0 & 0 & 0 & 0 & 0 & 0 & 0 & 0 & 0 & 0 & 0 & 0 & 0 \\
0 & 0 & -1 & 0 & 1 & 0 & 1 & 0 & 0 & 0 & 1 & 0 & 1 & 0 & -1 & 0 \\
0 & 0 & 0 & 0 & 0 & 1 & 0 & 0 & 0 & 0 & 0 & 1 & 0 & 0 & 0 & 0 \\
0 & 0 & -1 & 0 & 1 & 0 & 1 & 0 & 0 & 0 & 1 & 0 & 1 & 0 & -1 & 0 \\
0 & 0 & 0 & 1 & 0 & 0 & 0 & 0 & 0 & 0 & 0 & 0 & 0 & 1 & 0 & 0 \\
0 & 0 & 1 & 0 & -1 & 0 & -1 & 0 & 0 & 0 & -1 & 0 & -1 & 0 & 1 & 0 \\
0 & 1 & 0 & 0 & 0 & 0 & 0 & 0 & 0 & 0 & 0 & 0 & 0 & 0 & 0 & 1
\end{bmatrix}$$

| | |
|---|---|
| OFDM Type 2.2: | $N = 16, \mathcal{K}_{\text{SZ}} = \{0, 7, 8, 9\}, \mathcal{K}_{\text{SP}} = \{2, 4, 6, 10, 12, 14\}$, $\mathcal{K}_{\text{SD}} = \{1, 3, 5, 11, 13, 15\}, \mathcal{D}_{\text{SP}} = \{+1, -1, -1, -1, -1, +1\}$, $\mathcal{A}_{\text{SD}} = \mathcal{A}_{\text{BPSK}}$ . |

Figure 6.1: 'Matrix Transformation' covariance matrix $\mathbf{COV}(\boldsymbol{d})$ of the upconverted transmitter digital IF vector $\boldsymbol{d}$, $\text{OFDM Type} = 2.2$ .

We note, from (6.11), that the unity-valued diagonal elements are due to both BPSK Data sub-carriers and Pilot sub-carriers. The presence of unity-valued offset-anti-diagonal entries clearly indicate the dependencies due to the conjugate relationships between various non-zero entries of $\boldsymbol{d}$ as described in (6.5). As is the case for the diagonal entries, some of these unity-valued offset-anti-diagonal entries are due to the Pilot sub-carriers and others are due to the BPSK Data sub-carriers The remaining scattered $\pm$ unity-valued entries are due to the inter-dependencies of different Pilot sub-carriers.

#### 6.1.1.2 Case: OFDM Type 2.$M$, Zero, Pilot, and Data Sub-Carriers, No Pre-Coding, MQAM or MPSK Data (Excluding BPSK)

For an example case of $N = 16$ digital IF sub-carriers, with Zero, Pilot, and, this time, MQAM or MPSK (excluding BPSK) Data sub-carriers all present, the covariance matrix, calculated from (6.11), of the real digital IF frequency-sample vector $\boldsymbol{d}$ at the upconverter output is shown in Figure 6.2.

$$\begin{bmatrix}
0 & 0 & 0 & 0 & 0 & 0 & 0 & 0 & 0 & 0 & 0 & 0 & 0 & 0 & 0 & 0 \\
0 & 1 & 0 & 0 & 0 & 0 & 0 & 0 & 0 & 0 & 0 & 0 & 0 & 0 & 0 & 0 \\
0 & 0 & 1 & 0 & -1 & 0 & -1 & 0 & 0 & 0 & -1 & 0 & -1 & 0 & 1 & 0 \\
0 & 0 & 0 & 1 & 0 & 0 & 0 & 0 & 0 & 0 & 0 & 0 & 0 & 0 & 0 & 0 \\
0 & 0 & -1 & 0 & 1 & 0 & 1 & 0 & 0 & 0 & 1 & 0 & 1 & 0 & -1 & 0 \\
0 & 0 & 0 & 0 & 0 & 1 & 0 & 0 & 0 & 0 & 0 & 0 & 0 & 0 & 0 & 0 \\
0 & 0 & -1 & 0 & 1 & 0 & 1 & 0 & 0 & 0 & 1 & 0 & 1 & 0 & -1 & 0 \\
0 & 0 & 0 & 0 & 0 & 0 & 0 & 0 & 0 & 0 & 0 & 0 & 0 & 0 & 0 & 0 \\
0 & 0 & 0 & 0 & 0 & 0 & 0 & 0 & 0 & 0 & 0 & 0 & 0 & 0 & 0 & 0 \\
0 & 0 & 0 & 0 & 0 & 0 & 0 & 0 & 0 & 0 & 0 & 0 & 0 & 0 & 0 & 0 \\
0 & 0 & -1 & 0 & 1 & 0 & 1 & 0 & 0 & 0 & 1 & 0 & 1 & 0 & -1 & 0 \\
0 & 0 & 0 & 0 & 0 & 0 & 0 & 0 & 0 & 0 & 0 & 1 & 0 & 0 & 0 & 0 \\
0 & 0 & -1 & 0 & 1 & 0 & 1 & 0 & 0 & 0 & 1 & 0 & 1 & 0 & -1 & 0 \\
0 & 0 & 0 & 0 & 0 & 0 & 0 & 0 & 0 & 0 & 0 & 0 & 0 & 1 & 0 & 0 \\
0 & 0 & 1 & 0 & -1 & 0 & -1 & 0 & 0 & 0 & -1 & 0 & -1 & 0 & 1 & 0 \\
0 & 0 & 0 & 0 & 0 & 0 & 0 & 0 & 0 & 0 & 0 & 0 & 0 & 0 & 0 & 1
\end{bmatrix}$$

| | |
|---|---|
| OFDM Type 2.$M$: | $N = 16, \mathcal{K}_{\mathrm{SZ}} = \{0, 7, 8, 9\}, \mathcal{K}_{\mathrm{SP}} = \{2, 4, 6, 10, 12, 14\}$, $\mathcal{K}_{\mathrm{SD}} = \{1, 3, 5, 11, 13, 15\}, \mathcal{D}_{\mathrm{SP}} = \{+1, -1, -1, -1, -1, +1\}$, $\mathcal{A}_{\mathrm{SD}} \in \mathcal{A}_{\mathrm{MQAM}} \cup \mathcal{A}_{\mathrm{MPSK}} - \mathcal{A}_{\mathrm{BPSK}}$. |

Figure 6.2: 'Matrix Transformation' covariance matrix $\mathbf{COV}(\boldsymbol{d})$ of the upconverted transmitter digital IF vector $\boldsymbol{d}$, OFDM Type $= 2.M$.

Comparing the covariance matrix for the BPSK Data case in Figure 6.1 with that for the MQAM/MPSK (excluding BPSK) Data case in 6.2, we see that the offset-anti-diagonal covariance matrix entries associated with the Data sub-carriers have curiously changed from being unity-valued for the BPSK Data case to being zero-valued for the MQAM/MPSK (excluding BPSK) Data case despite the dependence of the conjugated entries of $\boldsymbol{d}$ as described in (6.5) still being in effect. This phenomenon demonstrates very clearly that a zero-valued covariance (or correlation) can exist even when there is direct dependence between two variables (in this case a conjugate dependence).

What, then, is the value of determining the covariances and correlations? The answer is subtle. A zero-correlation does not prove independence. However, a non-zero correlation does prove dependence; and finding the existence of dependence between the OFDM system signal variables is a key objective in this thesis.

### 6.1.2 'Matrix Transformation' Covariance Matrix of the OFDM Time-Samples at the IDFT Output

Our next goal is to determine the covariance matrix of the real digital IF time-samples contained in the entries of column-vector $\boldsymbol{f}$ at the the IDFT output.

The IDFT output vector is given by

$$\boldsymbol{f} = \boldsymbol{F}^{-1}\boldsymbol{P}\boldsymbol{d}. \tag{6.14}$$

We then obtain the covariance matrix of the IDFT output vector $\boldsymbol{f}$ in terms of the covariance matrix $\mathbf{COV}(\boldsymbol{d})$ of the non-precoded digital IF signal vector $\boldsymbol{d}$ as

$$\begin{aligned} \mathbf{COV}(\boldsymbol{f}) &= \mathbf{COV}\left(\boldsymbol{F}^{-1}\boldsymbol{P}\boldsymbol{d}\right) \\ &= \left(\boldsymbol{F}^{-1}\boldsymbol{P}\right)\mathbf{COV}(\boldsymbol{d})\left(\boldsymbol{F}^{-1}\boldsymbol{P}\right)^{\mathrm{H}}. \end{aligned} \tag{6.15}$$

In order to gain further insight, we now proceed to expand (6.15). We start with the $(l, m)^{\text{th}}$ entry of the expression $(\boldsymbol{F}^{-1}\boldsymbol{P})$ in (6.15) which is given by

$$\left[\boldsymbol{F}^{-1}\boldsymbol{P}\right]_{l,m} = \sum_{i\in\mathbb{Z}_N}\left[\boldsymbol{F}^{-1}\right]_{l,i}\cdot\left[\boldsymbol{P}\right]_{i,m}. \tag{6.16}$$

The $(l,i)^{\text{th}}$ entry of the inverse discrete fourier transform matrix $\boldsymbol{F}$ is given by

$$\left[\boldsymbol{F}^{-1}\right]_{l,i} = \frac{1}{\sqrt{N}}\, e^{j\frac{2\pi li}{N}}, \tag{6.17}$$

and the $(i,m)^{\text{th}}$ entry of the diagonal precoding matrix $\boldsymbol{P}$ is given by

$$[\boldsymbol{P}]_{i,m} = \begin{cases} p_{i,i} & , m = i \\ 0 & , \text{otherwise.} \end{cases}$$

Substituting (6.17) and (6.18) into (6.16), we then obtain

$$\left[\boldsymbol{F}^{-1}\boldsymbol{P}\right]_{l,m} = \frac{1}{\sqrt{N}}\, e^{j\frac{2\pi lm}{N}} p_{m,m}. \tag{6.18}$$

Next, using (6.18), we evaluate the $(l,m)^{\text{th}}$ entry of the expression $\left(\boldsymbol{F}^{-1}\boldsymbol{P}\right)^{\text{H}}$ in (6.15) as

$$\left[\left(\boldsymbol{F}^{-1}\boldsymbol{P}\right)^{\text{H}}\right]_{l,m} = \left[\boldsymbol{F}^{-1}\boldsymbol{P}\right]^{*}_{m,l} = \frac{1}{\sqrt{N}}\, e^{-j\frac{2\pi lm}{N}} p_{l,l}. \tag{6.19}$$

Proceeding on, using (6.11) and (6.19), we evaluate the $(l,m)^{\text{th}}$ entry of the expression $\mathbf{COV}(\boldsymbol{d})\left(\boldsymbol{F}^{-1}\boldsymbol{P}\right)^{\text{H}}$ in (6.15) as

$$\begin{aligned} &\left[\mathbf{COV}(\boldsymbol{d})\left(\boldsymbol{F}^{-1}\boldsymbol{P}\right)^{\text{H}}\right]_{l,m} \\ &\quad = \sum_{i\in\mathbb{Z}_N}\left[\mathbf{COV}(\boldsymbol{d})\right]_{l,i}\cdot\left[\left(\boldsymbol{F}^{-1}\boldsymbol{P}\right)^{\text{H}}\right]_{i,m} \\ &\quad = \begin{cases} \frac{1}{\sqrt{N}} e^{-j\frac{2\pi lm}{N}}\cdot p^{*}_{l,l} & , l\in\mathcal{K}_{\text{SD}} \quad , \mathcal{A}_{\text{SD}} \neq \mathcal{A}_{\text{BPSK}} \\ \frac{1}{\sqrt{N}}\left[e^{-j\frac{2\pi lm}{N}}\cdot p^{*}_{l,l} + e^{j\frac{2\pi lm}{N}}\cdot p^{*}_{N-l,N-l}\right] & , l\in\mathcal{K}_{\text{SD}} \quad , \mathcal{A}_{\text{SD}} = \mathcal{A}_{\text{BPSK}} \\ \frac{1}{\sqrt{N}}\sum_{i\in\mathcal{K}_{SP}} d_l d_i^{*} e^{-j\frac{2\pi im}{N}}\cdot p^{*}_{i,i} & , l\in\mathcal{K}_{\text{SP}} \\ 0 & , \text{otherwise,} \end{cases} \\ &\qquad , \mathcal{A}_{\text{SP}}, \mathcal{A}_{\text{SD}} \in \mathcal{A}_{\text{MQAM}} \cup \mathcal{A}_{\text{MPSK}}. \end{aligned} \tag{6.20}$$

Finally, using (6.16) and (6.20), we obtain our required result for the $(l,m)^{\text{th}}$ entry of the covariance matrix $\mathbf{COV}(\boldsymbol{f})$ of the real digital IF time-sample vector $\boldsymbol{f}$ at the

the IDFT output as

$$
\begin{aligned}
[\mathbf{COV}(\boldsymbol{f})]_{l,m} &= \left[\left(\boldsymbol{F}^{-1}\boldsymbol{P}\right)\mathbf{COV}(\boldsymbol{d})\left(\boldsymbol{F}^{-1}\boldsymbol{P}\right)^{\mathrm{H}}\right]_{l,m} \\
&= \sum_{r\in\mathbb{Z}_N}\left[\boldsymbol{F}^{-1}\boldsymbol{P}\right]_{l,r}\cdot\left[\mathbf{COV}(\boldsymbol{d})\left(\boldsymbol{F}^{-1}\boldsymbol{P}\right)^{\mathrm{H}}\right]_{r,m} \\
&= \frac{1}{N}\sum_{r\in\mathcal{K}_{\mathrm{SD}}} e^{j\frac{2\pi r(l-m)}{N}}\cdot|p_{r,r}|^2 \\
&\quad +\frac{1}{N}\sum_{\substack{r\in\mathcal{K}_{\mathrm{SD}},\\ \mathcal{A}_{\mathrm{SD}}=\mathcal{A}_{\mathrm{BPSK}}}} e^{j\frac{2\pi r(l+m)}{N}}\cdot p_{r,r}\cdot p^*_{N-r,N-r} \\
&\quad +\frac{1}{N}\sum_{r\in\mathcal{K}_{\mathrm{SP}}}\sum_{i\in\mathcal{K}_{\mathrm{SP}}} e^{j\frac{2\pi(rl-im)}{N}}\cdot p_{r,r}\cdot p^*_{i,i} \\
&\quad ,\mathcal{A}_{\mathrm{SP}},\mathcal{A}_{\mathrm{SD}}\in\mathcal{A}_{\mathrm{MQAM}}\cup\mathcal{A}_{\mathrm{MPSK}}.
\end{aligned}
\tag{6.21}
$$

Referring to the last equation line of (6.21), we see that $[\mathbf{COV}(\boldsymbol{f})]_{l,m}$ consists of a summation of three terms. The first 'Data sub-carrier' term is the contribution from all of the Data sub-carriers. The second 'BPSK Data sub-carrier' term is an extra contribution which only occurs when the Data sub-carriers are modulated with BPSK (a.k.a. 2PSK, 2QAM). The third 'Pilot sub-carrier' term is the contribution from all of the Pilot sub-carriers. We have now attained our goal of gaining insight into the covariance matrix $\mathbf{COV}(\boldsymbol{f})$ of the real digital IF time-samples contained in the entries of column-vector $\boldsymbol{f}$ at the the IDFT output.

#### 6.1.2.1 Case: OFDM Type 2.2, Zero, Pilot, and Data Sub-Carriers, No Pre-Coding, BPSK Data

For the example case, already used for the determination of $\mathbf{COV}(\boldsymbol{d})$ in §6.1.1.1, of Zero, Pilot, and BPSK Data sub-carriers all present, $N = 16$ digital IF sub-carriers and no pre-coding, using (6.21), the numerical result for the covariance matrix $\mathbf{COV}(\boldsymbol{f})$ of the real digital IF time-sample vector $\boldsymbol{f}$ at the the IDFT output exactly matches the result already independently obtained using the 'Exhaustive' method shown in Figure 5.1. Thus, in this case, the 'Exhaustive' method validates the 'Matrix

Transformation' method.

Referring to Figure 5.1, we note that all of the non-diagonal entries of the the covariance matrix $\mathbf{COV}(\boldsymbol{f})$ of the real digital IF time-sample vector $\boldsymbol{f}$ at the the IDFT output are non-zero; and therefore, in this case, all of the digital IF time-samples $f_n, n \in \mathbb{Z}_N$ are correlated (and dependent). This is not unexpected since every one of the time-sample entries $f_n, n \in \mathbb{Z}_N$ of the IDFT output vector $\boldsymbol{f}$ is comprised of a weighted sum (the IDFT equation) of the frequency-sample entries $d_k, k \in \mathbb{Z}_N$ of the IDFT input vector $\boldsymbol{d}$. Accordingly, any two IDFT output time-samples, say $f_n$ and $f_n'$ will be comprised of common terms which in most cases will lead to a correlation between the two IDFT output time-samples.

#### 6.1.2.2 Case: OFDM Type 2.$M$, Zero, Pilot, and Data Sub-Carriers, No Pre-Coding, MQAM or MPSK Data (Excluding BPSK)

For the example case, already used for the determination of $\mathbf{COV}(\boldsymbol{d})$ in §6.1.1.2, of Zero, Pilot, and MQAM or MPSK (excluding BPSK) Data sub-carriers all present, $N = 16$ digital IF sub-carriers and no pre-coding, using (6.21), the numerical result for the covariance matrix $\mathbf{COV}(\boldsymbol{f})$ of the real digital IF time-sample vector $\boldsymbol{f}$ at the the IDFT output exactly matches the result already independently obtained using the 'Exhaustive' method shown in Figure 5.2.

Referring to Figure 5.2, we note that all of the non-diagonal entries of the covariance matrix $\mathbf{COV}(\boldsymbol{f})$ of the real digital IF time-sample vector $\boldsymbol{f}$ at the the IDFT output are non-zero; and therefore, in this case, as for the previously discussed BPSK data sub-carrier case, all of the digital IF time-samples $f_n, n \in \mathbb{Z}_N$ are correlated (and dependent).

### 6.1.3 'Matrix Transformation' Correlation Matrix of the OFDM Time-Samples at the IDFT Output

As already described in §5.3.5, the $(l, m)^{\text{th}}$ entry of the correlation matrix of the real part $\boldsymbol{f}$ of the IDFT output time-sample vector is the Pearson's correlation coefficient between the $l^{\text{th}}$ and $m^{\text{th}}$ entries of $\boldsymbol{f}$ and, in terms of the entries of its covariance matrix $\mathbf{COV}(\boldsymbol{f})$, is given by

$$\begin{aligned}
[\mathbf{CORR}(\boldsymbol{f})]_{l,m} &= \frac{\operatorname{cov}(f_l, f_m)}{\sqrt{\operatorname{cov}(f_l, f_l)} \cdot \sqrt{\operatorname{cov}(f_m, f_m)}} \\
&= \frac{[\mathbf{COV}(\boldsymbol{f})]_{l,m}}{\sqrt{[\mathbf{COV}(\boldsymbol{f})]_{l,l}} \cdot \sqrt{[\mathbf{COV}(\boldsymbol{f})]_{m,m}}}.
\end{aligned} \tag{6.22}$$

The corresponding matrix formulation is

$$\mathbf{CORR}(\boldsymbol{f}) = \left(\mathbf{DIAG}[\mathbf{COV}(\boldsymbol{f})]\right)^{-1/2} \ \mathbf{COV}(\boldsymbol{f}) \ \left(\mathbf{DIAG}[\mathbf{COV}(\boldsymbol{f})]\right)^{-1/2}. \tag{6.23}$$

In order to gain insight into the correlations between the digital IF time-samples $f_n, n \in \mathbb{Z}_N$, using (6.22) and (6.23), we will now proceed, in the following sub-sections, to give numerical results for the correlation matrix $\mathbf{CORR}(\boldsymbol{f})$ for the example cases already covered in §6.1.1 and §6.1.2.

#### 6.1.3.1 Case: OFDM Type 2.2, Zero, Pilot, and Data Sub-Carriers, No Pre-Coding, BPSK Data

For the example case, already used for the determination of $\mathbf{COV}(\boldsymbol{f})$ in §6.1.2.1 , of Zero, Pilot, and BPSK Data sub-carriers all present, $N = 16$ digital IF sub-carriers and no pre-coding, using (6.23), the numerical result for the correlation matrix $\mathbf{CORR}(\boldsymbol{f})$ of the real digital IF time-sample vector $\boldsymbol{f}$ at the the IDFT output exactly matches the result already independently obtained using the 'Exhaustive' method shown in Figure 5.3.

Referring to Figure 5.3, we note that all of the non-diagonal entries of the correlation matrix $\mathbf{CORR}(\boldsymbol{f})$ of the real digital IF time-sample vector $\boldsymbol{f}$ at the the IDFT output are non-zero; and therefore, in this case, all of the digital IF time-samples $f_n, n \in \mathbb{Z}_N$ are correlated (and dependent).

We note also that many of the correlation magnitudes are quite large with the maximal non-diagonal and non-offset-anti-diagonal correlation magnitude being

$|\,[\mathbf{CORR}(\boldsymbol{f})]_{4,7}| = 0.797$.

#### 6.1.3.2 Case: OFDM Type 2.$M$, Zero, Pilot, and Data Sub-Carriers, No Pre-Coding, MQAM or MPSK Data (Excluding BPSK)

For the example case, already used for the determination of $\mathbf{COV}(\boldsymbol{f})$ in §6.1.2.2 , of Zero, Pilot, and MQAM or MPSK Data (Excluding BPSK) Data sub-carriers all present, $N = 16$ digital IF sub-carriers and no pre-coding, using (6.23), the numerical result for the correlation matrix $\mathbf{CORR}(\boldsymbol{f})$ of the real digital IF time-sample vector $\boldsymbol{f}$ at the the IDFT output exactly matches the result already independently obtained using the 'Exhaustive' method shown in Figure 5.4.

Referring to Figure 5.4, we note that all of the non-diagonal entries of the the correlation matrix $\mathbf{CORR}(\boldsymbol{f})$ of the real digital IF time-sample vector $\boldsymbol{f}$ at the the IDFT output are non-zero; and therefore, in this case, all of the digital IF time-samples $f_n, n \in \mathbb{Z}_N$ are correlated (and therefore dependent).

Like the BPSK case already discussed in §6.1.3.1, we note for this case that many of the correlation magnitudes are quite large with the maximal non-diagonal and non-offset-anti-diagonal correlation magnitude being $|\,[\mathbf{CORR}(\boldsymbol{f})]_{3,13}| = 0.672$.

#### 6.1.3.3 Case: OFDM Type 5.2, IEEE 802.11a WLAN, BPSK Data

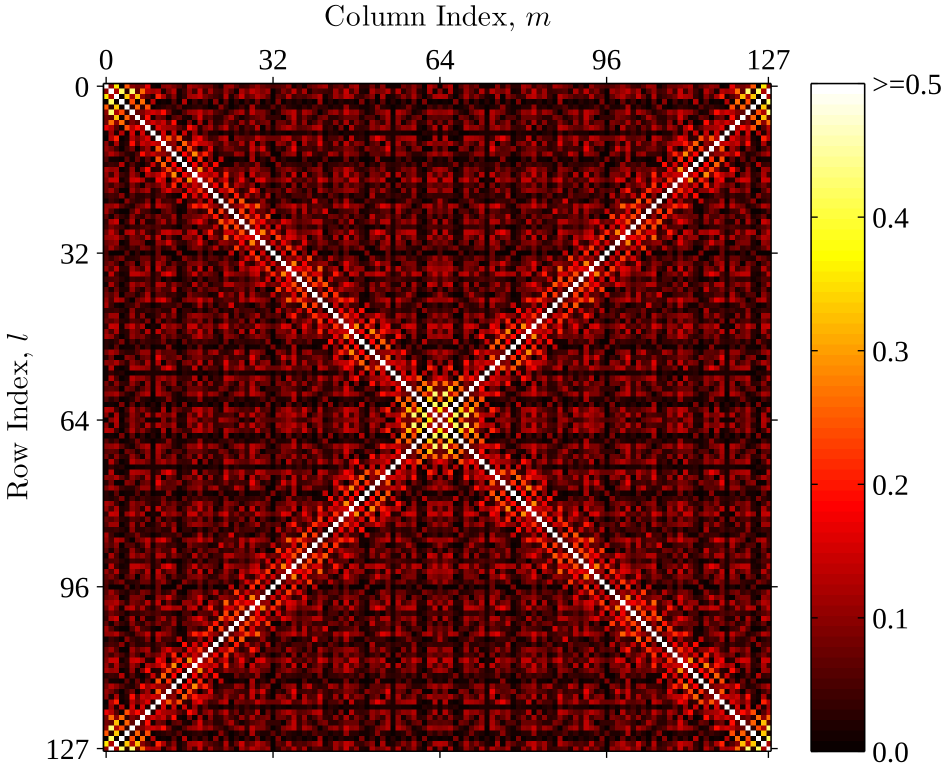


$\max(|\mathbf{CORR}(\boldsymbol{f})|) = 0.424$, excluding $|\mathbf{CORR}(\boldsymbol{f})| = 1$.

| | |
|---|---|
| OFDM Type 5.2: | IEEE 802.11a, $N = 128, \mathcal{K}_{\mathrm{SZ}} = \{0{:}5,32,59{:}69,96,123{:}127\}$,<br>$\mathcal{K}_{\mathrm{SP}} = \{11, 25, 39, 53, 75, 89, 103, 117\}, \mathcal{A}_{\mathrm{SP}} = \mathcal{A}_{\mathrm{BPSK}}$,<br>$\mathcal{K}_{\mathrm{SD}} = \{6{:}10,12{:}24,26{:}31,33{:}38,40{:}52,54{:}58,70{:}74,76{:}88,90{:}95,97{:}102,104{:}116,118{:}122\}$,<br>$\mathcal{A}_{\mathrm{SD}} = \mathcal{A}_{\mathrm{BPSK}}, \mathcal{D}_{\mathrm{SP}} = \{+1, +1, +1, -1, -1, +1, +1, +1\}, \mathrm{E}[f^2] = 1$. |

Figure 6.3: 'Matrix Transformation' magnitude $|\mathbf{CORR}(\boldsymbol{f})|$ of the correlation matrix of the real digital IF time-sample vector $\boldsymbol{f}$ at the IDFT output, OFDM Type = 5.2 (IEEE 802.11a, BPSK).

This exact 'Matrix Transformation' result for $|\mathbf{COV}(\boldsymbol{f})|$ is verified by a close match with the independently derived approximate 'Monte Carlo' result for the same case as shown in Figure 5.26.

#### 6.1.3.4 Case: OFDM Type 5.$M$, IEEE 802.11a WLAN, MQAM or MPSK Data (Excluding BPSK)

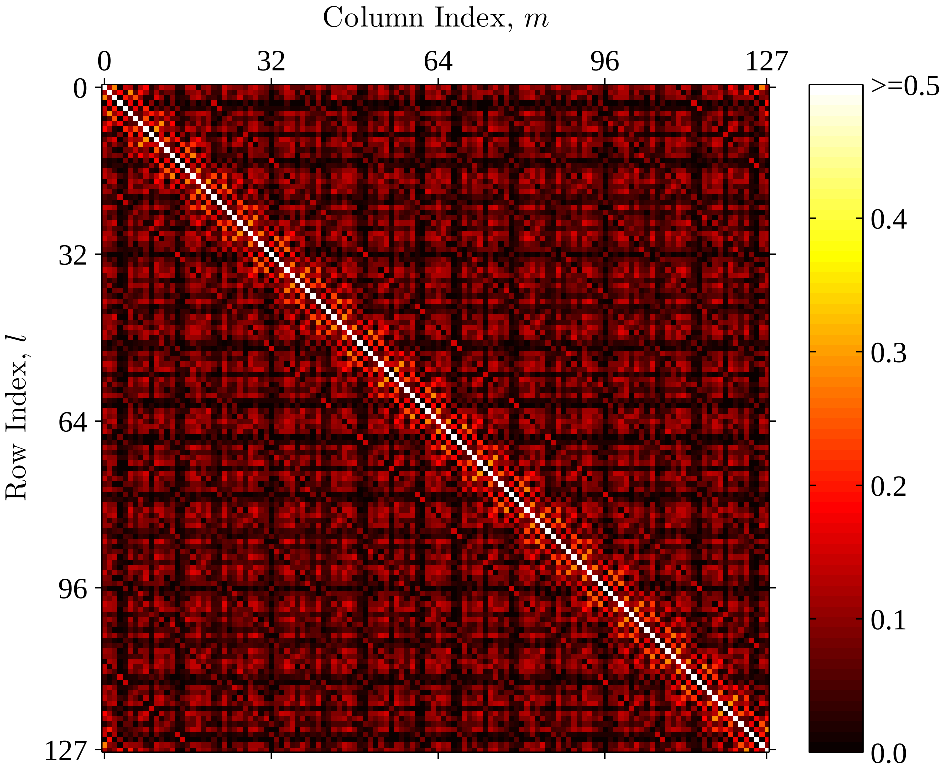


max(|$\mathbf{CORR}(\boldsymbol{f})$|) = 0.290, excluding |$\mathbf{CORR}(\boldsymbol{f})$| = 1.

| | |
|---|---|
| OFDM Type 5.$M$: | IEEE 802.11a, $N = 128, \mathcal{K}_{\text{SZ}} = \{0{:}5,32,59{:}69,96,123{:}127\}$, $\mathcal{K}_{\text{SP}} = \{11, 25, 39, 53, 75, 89, 103, 117\}, \mathcal{A}_{\text{SP}} = \mathcal{A}_{\text{BPSK}}$, $\mathcal{K}_{\text{SD}} = \{6{:}10,12{:}24,26{:}31,33{:}38,40{:}52,54{:}58,70{:}74,76{:}88,90{:}95,97{:}102,104{:}116,118{:}122\}$, $\mathcal{A}_{\text{SD}} \in \mathcal{A}_{\text{MQAM}} \cup \mathcal{A}_{\text{MPSK}} - \mathcal{A}_{\text{BPSK}}, \mathcal{D}_{\text{SP}} = \{+1, +1, +1, -1, -1, +1, +1, +1\}$. |

Figure 6.4: 'Matrix Transformation' magnitude $|\mathbf{CORR}(\boldsymbol{f})|$ of the correlation matrix of the real digital IF time-sample vector $\boldsymbol{f}$ at the IDFT output, OFDM Type = 5.$M$ (IEEE 802.11a, $M$QAM or $M$PSK, excluding BPSK).

This exact 'Matrix Transformation' result for $|\mathbf{COV}(\boldsymbol{f})|$ is verified by a close match with the independently derived approximate 'Monte Carlo' result for the same case as shown in Figures 5.27 to 5.29.

#### 6.1.3.5 Summary

The various cases of the correlation matrix $\mathbf{CORR}(\boldsymbol{f})$ of the real digital IF time-sample vector $\boldsymbol{f}$, examined in §6.1.3.1 to §6.1.3.4 above, demonstrate that significant correlations exist between the real digital IF time-samples $f_n, n \in \mathbb{Z}_N$ due to the presence of Zero and Pilot sub-carriers, and, therefore, the time-samples cannot be considered to be independent.

## 6.2 The Finite Resolution 'Convolution' Method

We now proceed to develop a novel method, which we shall call the 'convolution method', to obtain the exact (to any arbitrary finite resolution) PDFs and CDFs of the entries $f_n$ of the IDFT output $\boldsymbol{f}$ which is the digital IF signal. Such PDFs and CDFs give insight into the variability between the different IDFT output time-samples $f_n, n \in \mathbb{Z}_N$ and also the variability due to different modulation schemes. Also, the range of the PDFs gives insight into the effect of the clipping-factor $\kappa$.

The author has not seen such exact PDFs elsewhere in the literature and so believes this to be a novel contribution.

Referring to the system diagram in Figure 4.2, we see that the IDFT output is given by

$$\boldsymbol{f} = \Re\{\boldsymbol{F}^{-1}\boldsymbol{y}\} = \Re\{\boldsymbol{F}^{-1}\boldsymbol{X}\boldsymbol{c}\}. \tag{6.24}$$

To simplify this analysis, we will assume no precoding so that the precoding matrix $\boldsymbol{X}$ is set to the identity matrix $\mathbf{I}$ and (6.24) becomes

$$\boldsymbol{f} = \Re\{\boldsymbol{F}^{-1}\boldsymbol{c}\} \quad , \boldsymbol{X} = \mathbf{I}. \tag{6.25}$$

The $n^{th}$ entry of the IDFT output vector $\boldsymbol{f}$ is then given by

$$\begin{aligned}
f_n &= \Re\left\{\frac{1}{\sqrt{N}}\sum_{k=0}^{N-1} c_k e^{j\frac{2\pi kn}{N}}\right\} \\
&= \Re\left\{\frac{1}{\sqrt{N}}\sum_{k=0}^{N-1}(c_{k,\Re}+jc_{k,\Im})\left(\cos\left(\frac{2\pi kn}{N}\right)+j\sin\left(\frac{2\pi kn}{N}\right)\right)\right\} \\
&= \frac{1}{\sqrt{N}}\sum_{k=0}^{N-1} c_{k,\Re}\cos\left(\frac{2\pi kn}{N}\right) - c_{k,\Im}\sin\left(\frac{2\pi kn}{N}\right) \\
&= \frac{1}{\sqrt{N}}\sum_{k=0}^{N-1} \alpha_{k,n}+\gamma_{k,n} \\
&= \frac{1}{\sqrt{N}}\sum_{k=0}^{N-1} \xi_{k,n}, \\
&= \frac{1}{\sqrt{N}}\lambda_n
\end{aligned} \tag{6.26}$$

where $c_{k,\Re}$ is the real part of the $k^{th}$ entry $c_k$ of the IDFT input vector $\boldsymbol{c}$, $c_{k,\Im}$ is the imaginary part of the $k^{th}$ entry $c_k$ of the IDFT input vector $\boldsymbol{c}$,

$$\alpha_{k,n} \triangleq c_{k,\Re}\cos\left(\frac{2\pi kn}{N}\right), \tag{6.27}$$

$$\gamma_{k,n} \triangleq -c_{k,\Im} \in \left(\frac{2\pi kn}{N}\right), \tag{6.28}$$

$$\xi_{k,n} \triangleq \alpha_{k,n}+\gamma_{k,n}, \tag{6.29}$$

and

$$\lambda_n \triangleq \sum_{k=0}^{N-1}\xi_{k,n}. \tag{6.30}$$

We denote the PDF of $c_{k,\Re}$ as $f_{c_{k,\Re}}(c'_{k,\Re})$ and the PDF of $c_{k,\Im}$ as $f_{c_{k,\Im}}(c'_{k,\Im})$ and note that both of these PDFs are known from the particular modulation (MQAM, MPSK, Zero, etc) assigned to the particular IDFT input entry (a.k.a sub-carrier) $c_k$. We also note that $c_{k,\Re}$ and $c_{k,\Im}$ are independent. Using (6.27), the PDF of $\alpha_{k,n}$ is then

$$f_{\alpha_{k,n}}(\alpha'_{k,n}) = f_{c_{k,\Re}}\left(\alpha'_{k,n}/\cos\left(\frac{2\pi kn}{N}\right)\right). \tag{6.31}$$

Similarly, using (6.28), the PDF of $\gamma_{k,n}$ is

$$f_{\gamma_{k,n}}(\gamma'_{k,n}) = f_{c_{k,\Im}}\left(-\gamma'_{k,n}/\sin\left(\frac{2\pi kn}{N}\right)\right). \tag{6.32}$$

We note that $c_{k,\Re}$ and $c_{k,\Im}$ are independent, so that the PDF of $\xi_{k,n}$ may be obtained from the convolution of the PDF $f_{\alpha_{k,n}}(\alpha'_{k,n})$ of $\alpha_{k,n}$ and the PDF $f_{\gamma_{k,n}}(\gamma'_{k,n})$ of $\gamma_{k,n}$ as

$$f_{\xi_{k,n}}(\xi'_{k,n}) = [f_{\alpha_{k,n}} \star f_{\gamma_{k,n}}](\xi'_{k,n}). \tag{6.33}$$

Next, referring to (6.30), we note that all of the terms $\xi_{k,n}$ are independent so that PDF of $\lambda_n$ may be formed by the $N$-fold convolution of the PDFs $f_{\xi_{k,n}}(\xi'_{k,n})$ of each $\xi_{k,n}$ to obtain

$$f_{\lambda_n}(\lambda'_n) = [f_{\xi_{0,n}} \star f_{\xi_{1,n}} \star \cdots \star f_{\xi_{N-1,n}}](\lambda'_n). \tag{6.34}$$

Finally, using the last line of (6.26), we obtain our objective, the PDF of individual IDFT output time-samples $f_n$, as

$$f_{f_n}(f'_n) = f_{\lambda_n}(N \cdot f'_n). \tag{6.35}$$

Using (6.35), we then obtain the average PDF of all IDFT output time-samples $f_n$ as

$$f_f(f') = \sum_{0}^{N-1} f_{\lambda_n}(N \cdot f'_n). \tag{6.36}$$

The CDF of individual IDFT output time-samples $f_n$ is then given by

$$F_{f_n}(f''_n) = \int_{-\infty}^{f''_n} f_{f_n}(f'_n) \quad df'_n, \tag{6.37}$$

and, similarly, the CDF of all IDFT output time-samples $f$ is then given by

$$F_f(f'') = \int_{-\infty}^{f''} f_f(f') \quad df'. \tag{6.38}$$

For our purposes, the convolutions and integrations of (6.27) to (6.38) are performed in the Matlab simulation programme as discrete convolutions and integrations necessitating the use of a finite discrete numerical grid. The spacing of that finite numerical grid is hereafter referred to as the 'resolution'. The resolution is chosen to be as small as possible whilst allowing reasonable Matlab simulation times. In all of the presented results, the resolution is fine enough as to be unnoticeable.

Equations (6.27) to (6.38) will now be used to generate plots of PDFs and CDFs of individual IDFT output time-samples $f_n$ and the average of all IDFT output time-samples in the following sections §6.2.1 and §6.2.2.

### 6.2.1 Exact 'Convolution' PDF and CDF of Individual IDFT Output Time-Sample Real-Parts

Next, we examine the PDF $f_{f_n}(f_n')$ and CDF $F_{f_n}(f_n'')$ of Individual IDFT Output Time-Sample Real-Parts $f_n$ obtained by the convolution 'method'. These PDF and CDF results give important insight into the variability of the PDF and CDF with the particular time-sample observed as well as a surprising 'non-Gaussian-ness' of some of the time-samples. The author has not been able to find these kind of results, shown Figures 6.5 to 6.10, in any of the literature and, accordingly believes them to be an original contribution to the state-of-the-art.

In Figure 6.5, we see PDFs and CDFs for a small complexity OFDM system with no Pilots and Zeros. The results exactly match those obtained by the 'exhaustive' method in §5.3, thus verifying the 'convolution' method. Figure 6.5(a) strikingly shows only 17 diracs in the PDF for the $N \in \{0, 16\}$ time-samples. This is despite the size $|\mathcal{A}_{\boldsymbol{d}|}$ of the alphabet $\mathcal{A}_{\boldsymbol{d}}$ all possible IDFT input symbols $\boldsymbol{d}$ being 65,536 ($= 2^{16}$). This immediately alerts us to the fact that the structure of the OFDM signal cause the IDFT output values to recur again and again as we traverse all of the possible IDFT input symbols $\boldsymbol{d} \in \mathcal{A}_{\boldsymbol{d}}$. This phenomenom occurs for the other time-samples as well. We examine the reasons for this with the study of combinatorics in §6.3. The other noteworthy result in Figure 6.5 is the variability of the PDF and CDF with the particular time-sample - which is at odds with assumptions and assertions in some of the literature (refer §1.1).

Figure 6.6 shows the results for a small-complexity OFDM system which does include Pilot and Zero sub-carriers. Again, these results exactly match those obtained by the 'exhaustive' method in §5.3, thus verifying the 'convolution' method.

Figure 6.7 shows the results for an high-complexity, real-world IEEE 802.11a WLAN system [1] using BPSK data. Figures 6.7(a)-(d) demonstrate that, despite the repeated invocation of the Central Limit Theorem in the literature (refer §1.1), the PDF and CDF for the $n \in \{0, 64\}$ time-samples is not Gaussian and, in fact, the PDF has a remarkably small number of diracs. As mentioned earlier, this is explained by combinatorics in §6.3. Also, again, we see significant variability in the PDFs and CDFs between individual time-samples.

In Figures 6.8 to 6.10, we address IEEE 802.11a with QPSK, 16QAM, and 64QAM modulations. The PDF and CDF variability with time-sample and the small number of diracs for some time-samples is evident in these cases also.

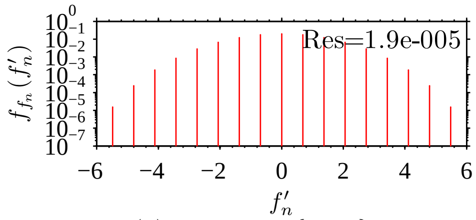


(a) PDF, $n \in \{0, 16\}$.

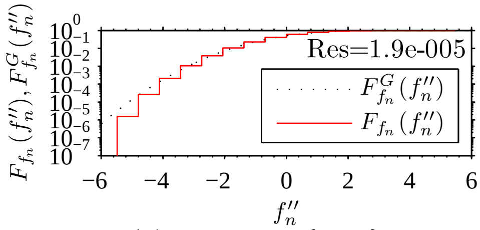


(b) CDFs, $n \in \{0, 16\}$.

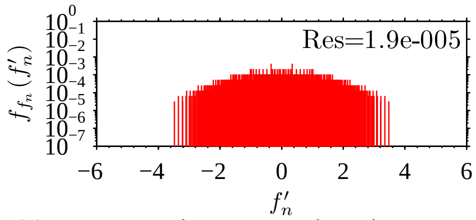


(c) PDF, $n \in \{1, 3, \cdots, 31\} = \{1 * \text{Odds}\}$.

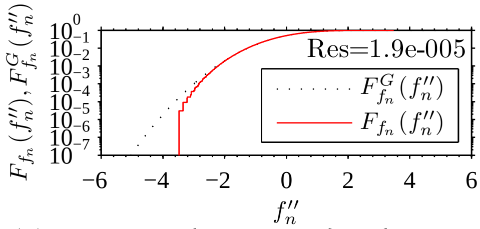


(d) CDFs, $n \in \{1, 3, \cdots, 31\} = \{1 * \text{Odds}\}$.

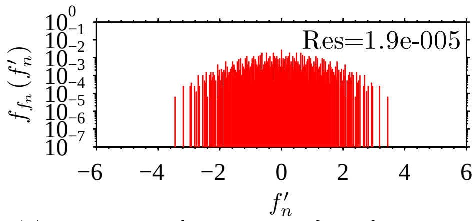


(e) PDF, $n \in \{2, 6, \cdots, 30\} = \{2 * \text{Odds}\}$.

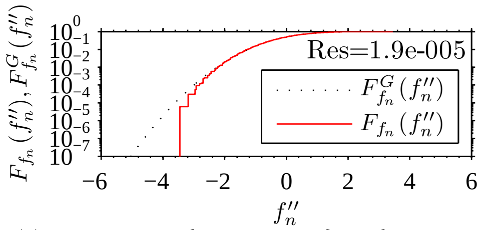


(f) CDFs, $n \in \{2, 6, \cdots, 30\} = \{2 * \text{Odds}\}$.

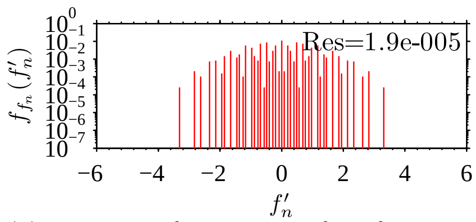


(g) PDF, $n \in \{4, 12, \cdots, 28\} = \{4 * \text{Odds}\}$.

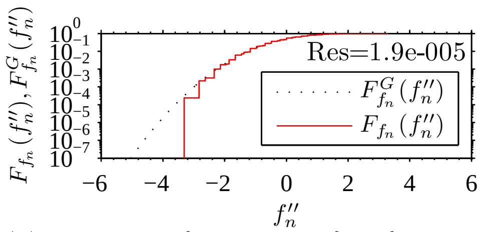


(h) CDFs, $n \in \{4, 12, \cdots, 28\} = \{4 * \text{Odds}\}$.

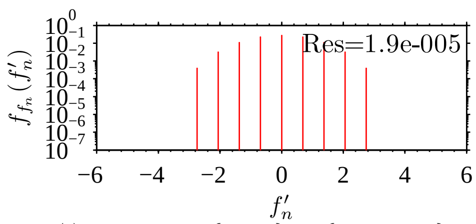


(i) PDF, $n \in \{8, 24\} = \{8 * \text{Odds}\}$.

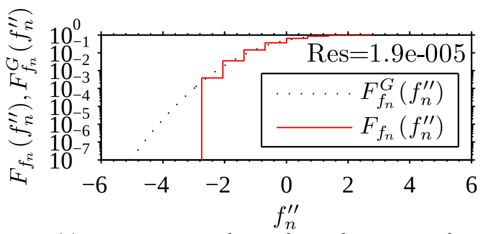


(j) CDFs, $n \in \{8, 24\} = \{8 * \text{Odds}\}$.

OFDM Type 3.2: $N = 32, \mathcal{K}_{\text{SZ}} = \{\}, \mathcal{K}_{\text{SP}} = \{\}, \mathcal{K}_{\text{SD}} = \mathbb{Z}_N, \mathcal{A}_{\text{SD}} = \mathcal{A}_{\text{BPSK}}, \text{E}[f^2] = 1.$

Figure 6.5: 'Convolution' PDFs $f_{f_n}(f'_n)$, CDFs $F_{f_n}(f''_n)$, and Gaussian approximation CDFs $F^G_{f_n}(f''_n)$ of individual IDFT output time-sample real-parts, OFDM Type = 3.2, accuracy = $10^{-4}$, for each time-sample index $n$.

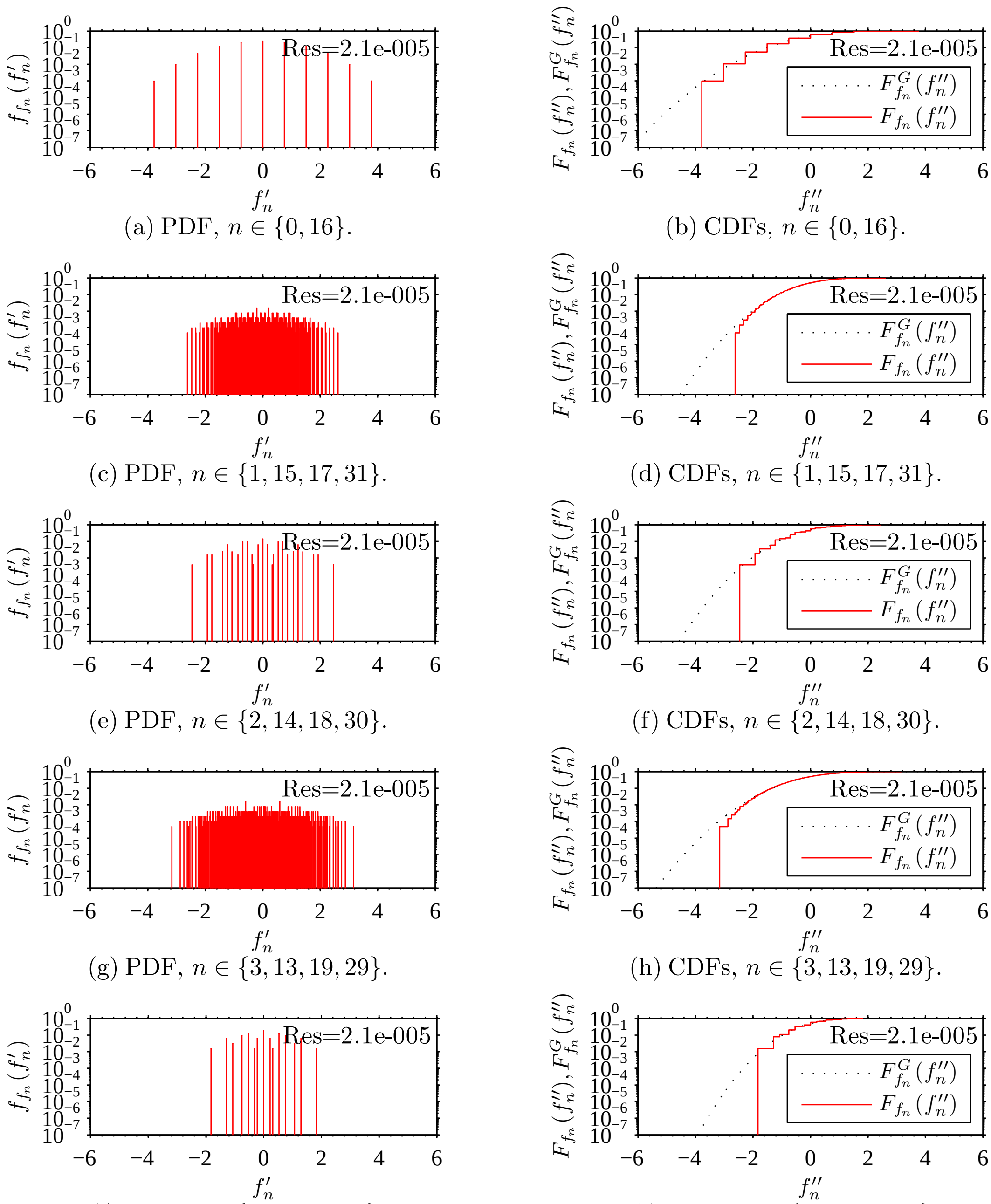


(a) PDF, $n \in \{0, 16\}$.
(b) CDFs, $n \in \{0, 16\}$.
(c) PDF, $n \in \{1, 15, 17, 31\}$.
(d) CDFs, $n \in \{1, 15, 17, 31\}$.
(e) PDF, $n \in \{2, 14, 18, 30\}$.
(f) CDFs, $n \in \{2, 14, 18, 30\}$.
(g) PDF, $n \in \{3, 13, 19, 29\}$.
(h) CDFs, $n \in \{3, 13, 19, 29\}$.
(i) PDF, $n \in \{4, 12, 20, 28\}$.
(j) CDFs, $n \in \{4, 12, 20, 28\}$.

OFDM Type 4.2: $N = 32$, $\mathcal{K}_{\mathrm{SZ}} = \{0, 8, 16, 24\}$, $\mathcal{K}_{\mathrm{SP}} = \{3, 5, 11, 13, 19, 21, 27, 29\}$, $\mathcal{A}_{\mathrm{SP}} = \mathcal{A}_{\mathrm{BPSK}}$, $\mathcal{K}_{\mathrm{SD}} = \{1, 2, 4, 6, 7, 9, 10, 12, 14, 15, 17, 18, 20, 22, 23, 25, 28, 30, 31\}$, $\mathcal{A}_{\mathrm{SD}} = \mathcal{A}_{\mathrm{BPSK}}$, $\mathcal{D}_{\mathrm{SP}} = \{-1, +1, -1, +1, +1, -1, +1, -1\}$, $\mathrm{E}[f^2] = 1$.

Figure 6.6: 'Convolution' PDFs $f_{f_n}(f'_n)$, CDFs $F_{f_n}(f''_n)$, and Gaussian approximation CDFs $F^G_{f_n}(f''_n)$ of individual IDFT output time-sample real-parts, OFDM Type 4.2, accuracy $= 10^{-4}$, for each time-sample index $n$.

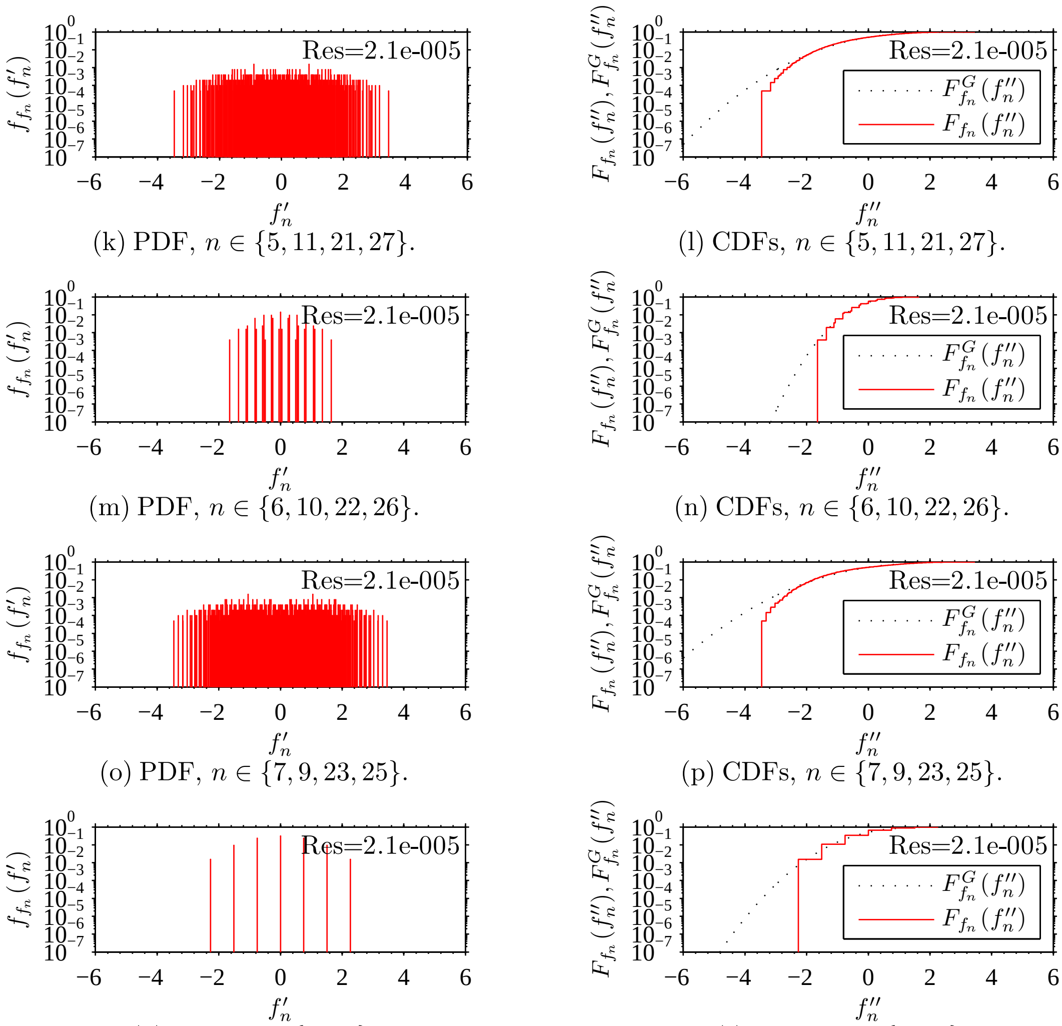


(k) PDF, $n \in \{5, 11, 21, 27\}$. (l) CDFs, $n \in \{5, 11, 21, 27\}$.

(m) PDF, $n \in \{6, 10, 22, 26\}$. (n) CDFs, $n \in \{6, 10, 22, 26\}$.

(o) PDF, $n \in \{7, 9, 23, 25\}$. (p) CDFs, $n \in \{7, 9, 23, 25\}$.

(q) PDF, $n \in \{8, 24\}$. (r) CDFs, $n \in \{8, 24\}$.

OFDM Type 4.2: $N = 32, \mathcal{K}_{\text{SZ}} = \{0, 8, 16, 24\}, \mathcal{K}_{\text{SP}} = \{3, 5, 11, 13, 19, 21, 27, 29\}, \mathcal{A}_{\text{SP}} = \mathcal{A}_{\text{BPSK}}$, $\mathcal{K}_{\text{SD}} = \{1, 2, 4, 6, 7, 9, 10, 12, 14, 15, 17, 18, 20, 22, 23, 25, 28, 30, 31\}, \mathcal{A}_{\text{SD}} = \mathcal{A}_{\text{BPSK}}$, $\mathcal{D}_{\text{SP}} = \{-1, +1, -1, +1, +1, -1, +1, -1\}, \text{E}[f^2] = 1$.

Figure 6.6: (Cont'd) 'Convolution' PDFs $f_{f_n}(f'_n)$, CDFs $F_{f_n}(f''_n)$, and Gaussian approximation CDFs $F^G_{f_n}(f''_n)$ of individual IDFT output time-sample real-parts, OFDM Type 4.2, accuracy $= 10^{-4}$, for each time-sample index $n$.

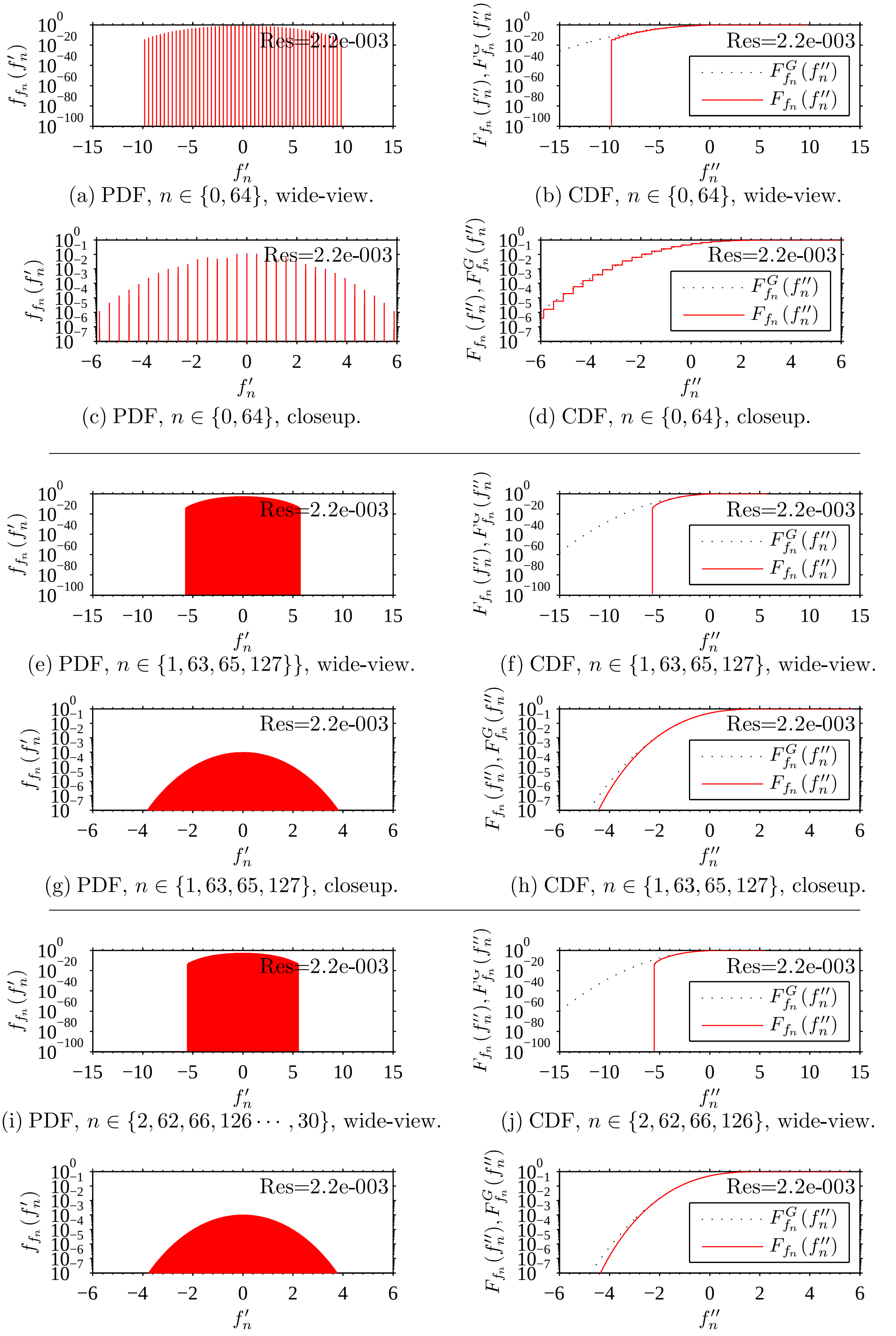


(a) PDF, $n \in \{0, 64\}$, wide-view.

(b) CDF, $n \in \{0, 64\}$, wide-view.

(c) PDF, $n \in \{0, 64\}$, closeup.

(d) CDF, $n \in \{0, 64\}$, closeup.

(e) PDF, $n \in \{1, 63, 65, 127\}\}$, wide-view.

(f) CDF, $n \in \{1, 63, 65, 127\}$, wide-view.

(g) PDF, $n \in \{1, 63, 65, 127\}$, closeup.

(h) CDF, $n \in \{1, 63, 65, 127\}$, closeup.

(i) PDF, $n \in \{2, 62, 66, 126 \cdots, 30\}$, wide-view.

(j) CDF, $n \in \{2, 62, 66, 126\}$, wide-view.

(k) PDF, $n \in \{2, 62, 66, 126 \cdots, 30\}$, closeup.

(l) CDF, $n \in \{2, 62, 66, 126 \cdots, 30\}$, closeup.

OFDM Type 5.2: IEEE 802.11a, $N = 128, \mathcal{K}_{\text{SZ}} = \{0{:}5{,}32{,}59{:}69{,}96{,}123{:}127\}$,
$\mathcal{K}_{\text{SP}} = \{11, 25, 39, 53, 75, 89, 103, 117\}, \mathcal{A}_{\text{SP}} = \mathcal{A}_{\text{BPSK}}$,
$\mathcal{K}_{\text{SD}} = \{6{:}10{,}12{:}24{,}26{:}31{,}33{:}38{,}40{:}52{,}54{:}58{,}70{:}74{,}76{:}88{,}90{:}95{,}97{:}102{,}104{:}116{,}118{:}122\}$,
$\mathcal{A}_{\text{SD}} = \mathcal{A}_{\text{BPSK}}, \mathcal{D}_{\text{SP}} = \{+1, +1, +1, -1, -1, +1, +1, +1\}, \text{E}[f^2] = 1$.

Figure 6.7: ‘Convolution’ PDFs $f_{f_n}(f'_n)$, CDFs $F_{f_n}(f''_n)$, and Gaussian approximation CDFs $F^G_{f_n}(f''_n)$ of individual IDFT output time-sample real-parts, OFDM Type 5.2 (IEEE 802.11a, BPSK data), accuracy $= 10^{-4}$, for selected time-sample indeces $n$.

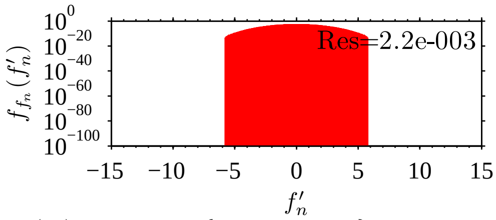


(m) PDF, $n \in \{4, 60, 68, 124\}$, wide-view.

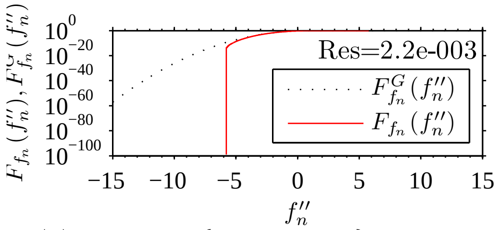


(n) CDF, $n \in \{4, 60, 68, 124\}$, wide-view.

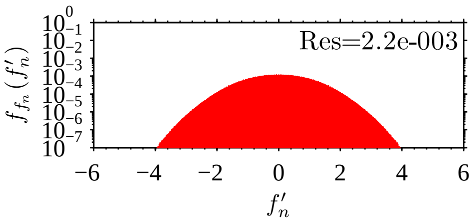


(o) PDF, $n \in \{4, 60, 68, 124\}$, closeup.

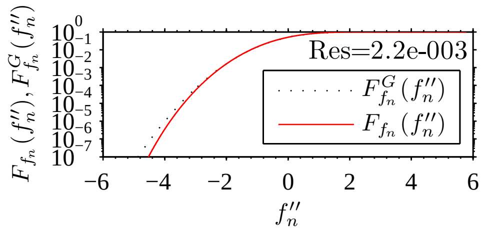


(p) CDF, $n \in \{4, 60, 68, 124\}$, closeup.

---

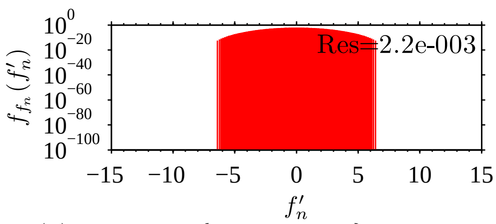


(q) PDF, $n \in \{8, 56, 72, 120\}$, wide-view.

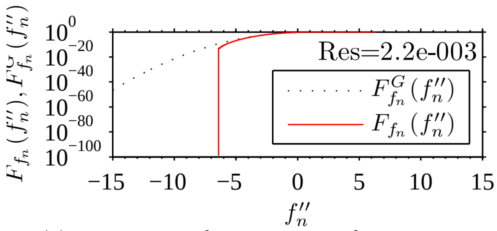


(r) CDF, $n \in \{8, 56, 72, 120\}$, wide-view.

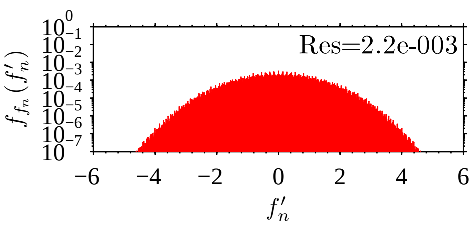


(s) PDF, $n \in \{8, 56, 72, 120\}$, closeup.

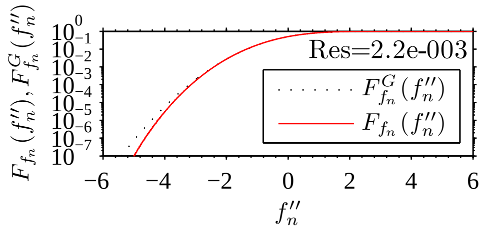


(t) CDF, $n \in \{8, 56, 72, 120\}$, closeup.

---

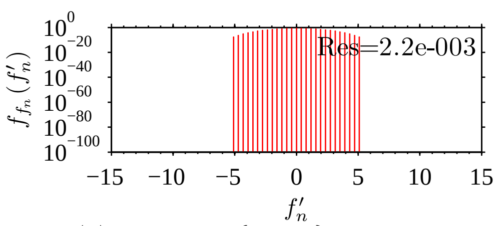


(q) PDF, $n \in \{32, 96\}$, wide-view.

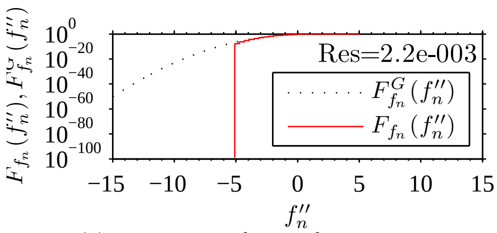


(r) CDF, $n \in \{32, 96\}$, wide-view.

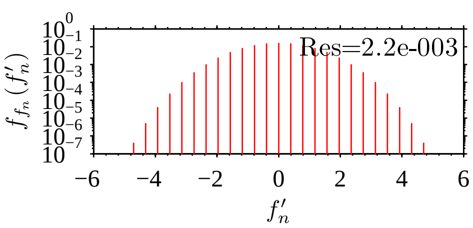


(s) PDF, $n \in \{32, 96\}$, closeup.

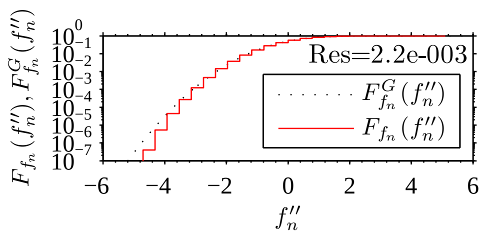


(t) CDF, $n \in \{32, 96\}$, closeup.

OFDM Type 5.2: IEEE 802.11a, $N = 128, \mathcal{K}_{\text{SZ}} = \{0{:}5{,}32{,}59{:}69{,}96{,}123{:}127\}$,
$\mathcal{K}_{\text{SP}} = \{11, 25, 39, 53, 75, 89, 103, 117\}, \mathcal{A}_{\text{SP}} = \mathcal{A}_{\text{BPSK}}$,
$\mathcal{K}_{\text{SD}} = \{6{:}10{,}12{:}24{,}26{:}31{,}33{:}38{,}40{:}52{,}54{:}58{,}70{:}74{,}76{:}88{,}90{:}95{,}97{:}102{,}104{:}116{,}118{:}122\}$,
$\mathcal{A}_{\text{SD}} = \mathcal{A}_{\text{BPSK}}, \mathcal{D}_{\text{SP}} = \{+1, +1, +1, -1, -1, +1, +1, +1\}, \mathrm{E}[f^2] = 1$.

Figure 6.7: (Cont'd) 'Convolution' PDFs $f_{f_n}(f'_n)$, CDFs $F_{f_n}(f''_n)$, and Gaussian approximation CDFs $F^G_{f_n}(f''_n)$ of individual IDFT output time-sample real-parts, OFDM Type 5.2 (IEEE 802.11a, BPSK data), accuracy $= 10^{-4}$, for selected time-sample indeces $n$.

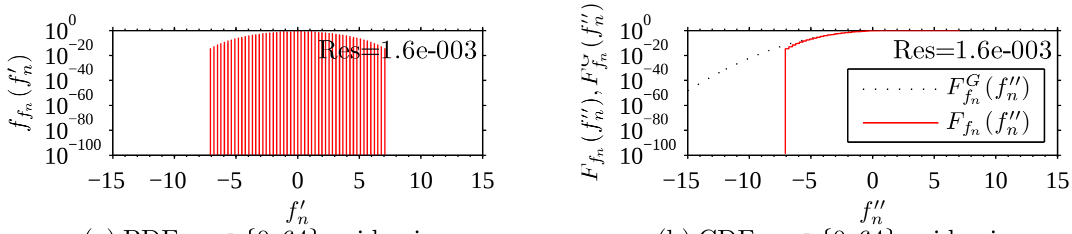


(a) PDF, $n \in \{0, 64\}$, wide-view.

(b) CDF, $n \in \{0, 64\}$, wide-view.

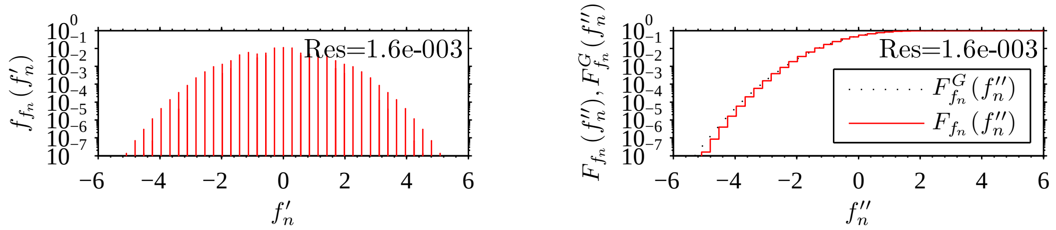


(c) PDF, $n \in \{0, 64\}$, closeup.

(d) CDF, $n \in \{0, 64\}$, closeup.

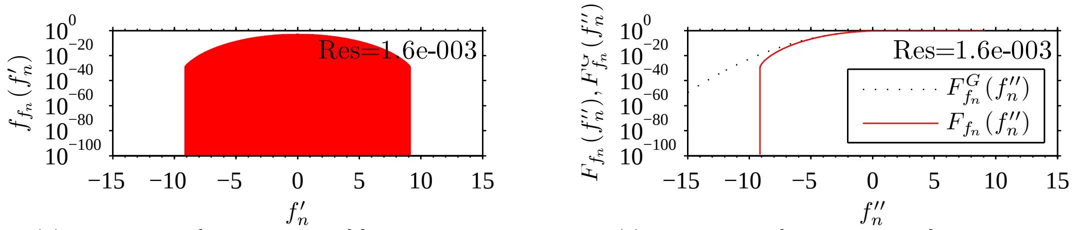


(e) PDF, $n \in \{1, 63, 65, 127\}\}$, wide-view.

(f) CDF, $n \in \{1, 63, 65, 127\}$, wide-view.

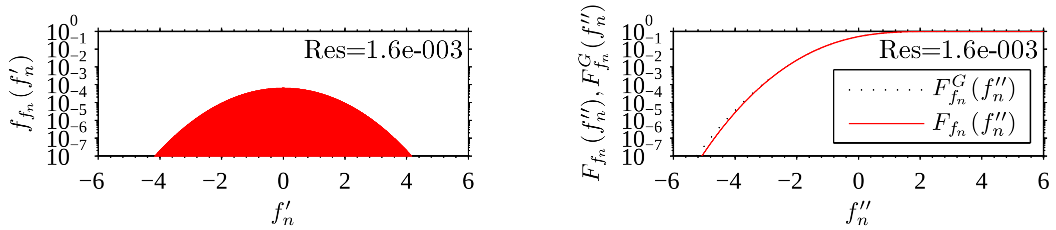


(g) PDF, $n \in \{1, 63, 65, 127\}$, closeup.

(h) CDF, $n \in \{1, 63, 65, 127\}$, closeup.

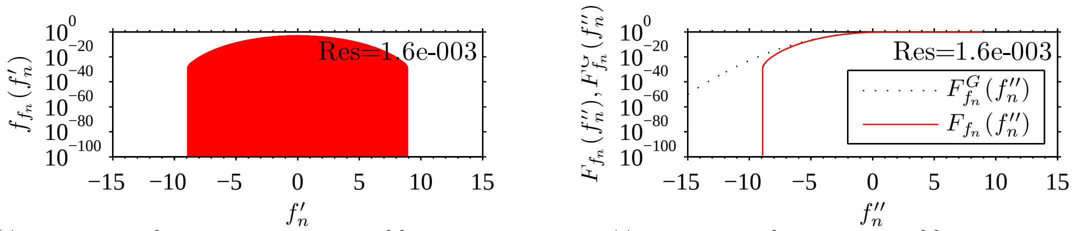


(i) PDF, $n \in \{2, 62, 66, 126 \cdots, 30\}\}$, wide-view.

(j) CDF, $n \in \{2, 62, 66, 126\}\}$, wide-view.

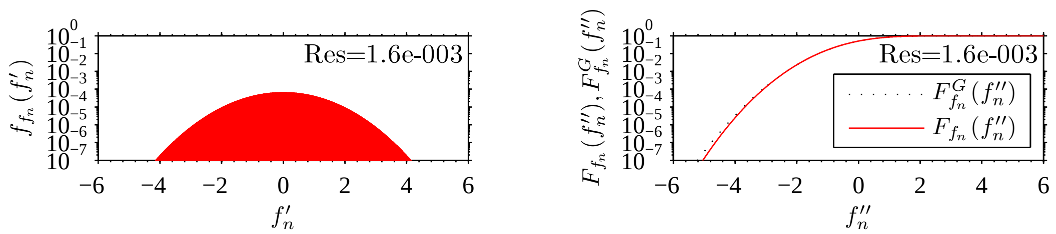


(k) PDF, $n \in \{2, 62, 66, 126 \cdots, 30\}$, closeup.

(l) CDF, $n \in \{2, 62, 66, 126 \cdots, 30\}$, closeup.

| | |
|---|---|
| OFDM Type 5.4: | IEEE 802.11a, $N = 128, \mathcal{K}_{\text{SZ}} = \{0{:}5{,}32{:}59{:}69{,}96{,}123{:}127\}$, |
| | $\mathcal{K}_{\text{SP}} = \{11, 25, 39, 53, 75, 89, 103, 117\}, \mathcal{A}_{\text{SP}} = \mathcal{A}_{\text{BPSK}}$, |
| | $\mathcal{K}_{\text{SD}} = \{6{:}10{,}12{:}24{,}26{:}31{,}33{:}38{,}40{:}52{,}54{:}58{,}70{:}74{,}76{:}88{,}90{:}95{,}97{:}102{,}104{:}116{,}118{:}122\}$, |
| | $\mathcal{A}_{\text{SD}} = \mathcal{A}_{\text{QPSK}}, \mathcal{D}_{\text{SP}} = \{+1, +1, +1, -1, -1, +1, +1, +1\}, \text{E}[f^2] = 1$. |

Figure 6.8: ‘Convolution’ PDFs $f_{f_n}(f'_n)$, CDFs $F_{f_n}(f''_n)$, and Gaussian approximation CDFs $F^G_{f_n}(f''_n)$ of individual IDFT output time-sample real-parts, OFDM Type 5.4 (IEEE 802.11a, QPSK data), accuracy $= 10^{-3}$, for selected time-sample indeces $n$.

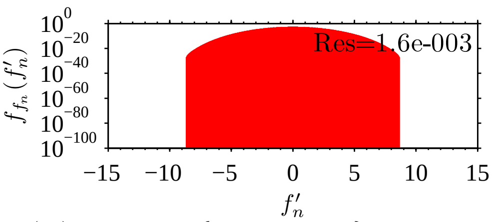


(m) PDF, $n \in \{4, 60, 68, 124\}$, wide-view.

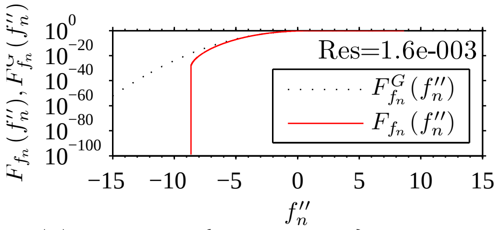


(n) CDF, $n \in \{4, 60, 68, 124\}$, wide-view.

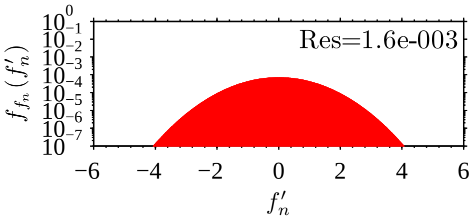


(o) PDF, $n \in \{4, 60, 68, 124\}$, closeup.

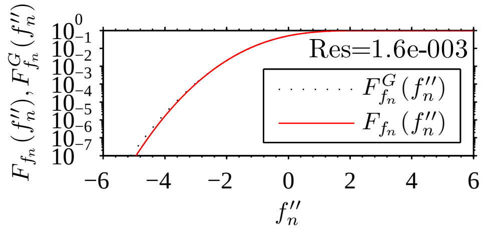


(p) CDF, $n \in \{4, 60, 68, 124\}$, closeup.

---

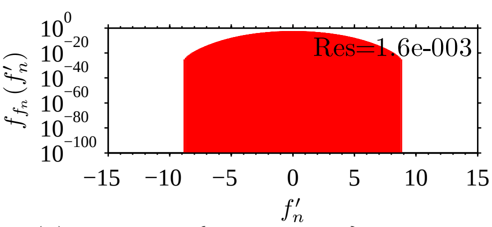


(q) PDF, $n \in \{8, 56, 72, 120\}$, wide-view.

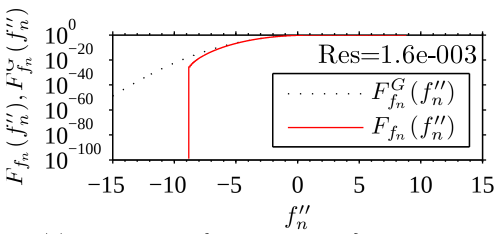


(r) CDF, $n \in \{8, 56, 72, 120\}$, wide-view.

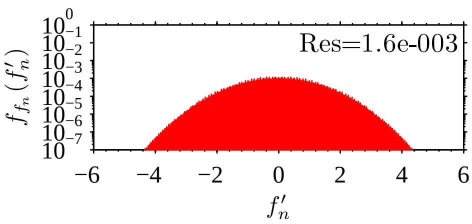


(s) PDF, $n \in \{8, 56, 72, 120\}$, closeup.

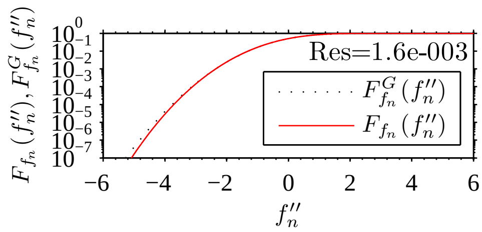


(t) CDF, $n \in \{8, 56, 72, 120\}$, closeup.

---

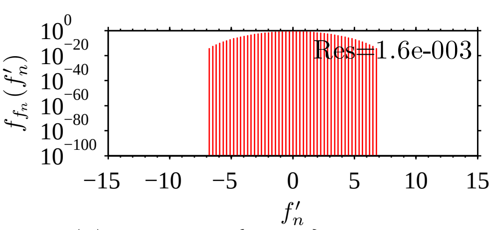


(u) PDF, $n \in \{32, 96\}$, wide-view.

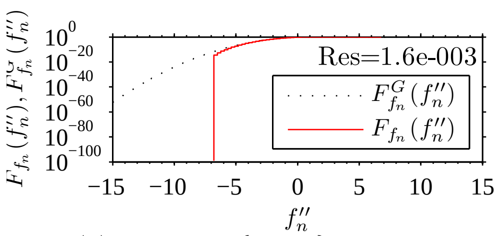


(v) CDF, $n \in \{32, 96\}$, wide-view.

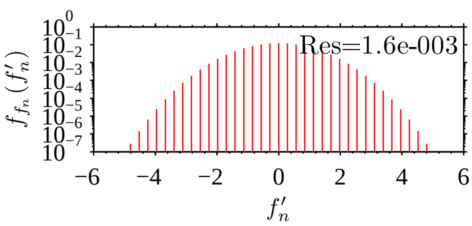


(w) PDF, $n \in \{32, 96\}$, closeup.

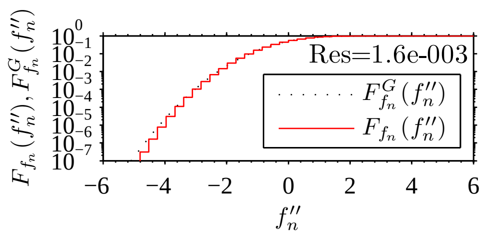


(x) CDF, $n \in \{32, 96\}$, closeup.

OFDM Type 5.4: IEEE 802.11a, $N = 128, \mathcal{K}_{\text{SZ}} = \{0{:}5,32,59{:}69,96,123{:}127\}$,
$\mathcal{K}_{\text{SP}} = \{11, 25, 39, 53, 75, 89, 103, 117\}, \mathcal{A}_{\text{SP}} = \mathcal{A}_{\text{BPSK}}$,
$\mathcal{K}_{\text{SD}} = \{6{:}10,12{:}24,26{:}31,33{:}38,40{:}52,54{:}58,70{:}74,76{:}88,90{:}95,97{:}102,104{:}116,118{:}122\}$,
$\mathcal{A}_{\text{SD}} = \mathcal{A}_{\text{BPSK}}, \mathcal{D}_{\text{SP}} = \{+1, +1, +1, -1, -1, +1, +1, +1\}, \text{E}[f^2] = 1.$

Figure 6.8: (Cont'd) 'Convolution' PDFs $f_{f_n}(f'_n)$, CDFs $F_{f_n}(f''_n)$, and Gaussian approximation CDFs $F^G_{f_n}(f''_n)$ of individual IDFT output time-sample real-parts, OFDM Type 5.4 (IEEE 802.11a, QPSK data), accuracy $= 10^{-3}$, for selected time-sample indeces $n$.

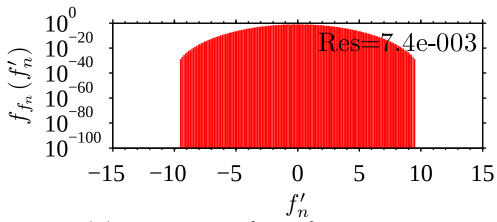


(a) PDF, $n \in \{0, 64\}$, wide-view.

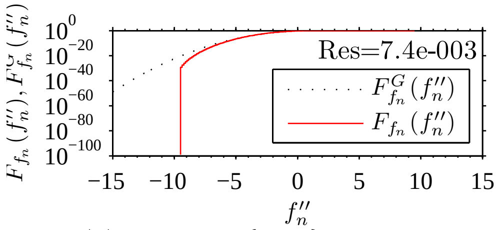


(b) CDF, $n \in \{0, 64\}$, wide-view.

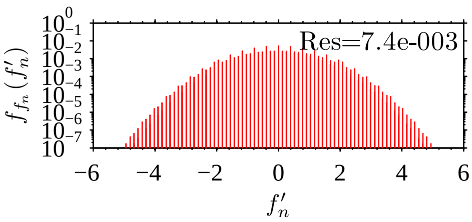


(c) PDF, $n \in \{0, 64\}$, closeup.

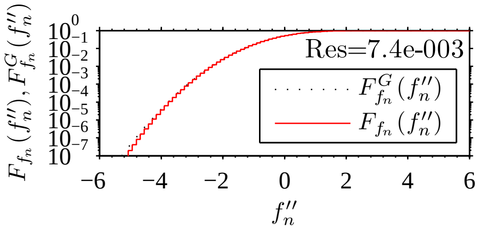


(d) CDF, $n \in \{0, 64\}$, closeup.

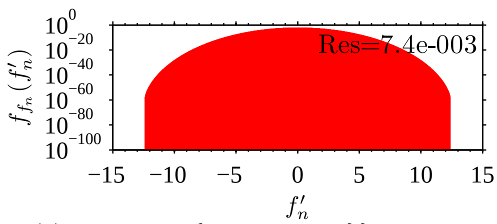


(e) PDF, $n \in \{1, 63, 65, 127\}\}$, wide-view.

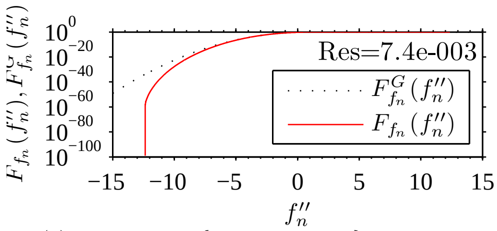


(f) CDF, $n \in \{1, 63, 65, 127\}$, wide-view.

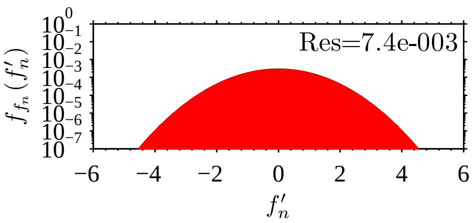


(g) PDF, $n \in \{1, 63, 65, 127\}$, closeup.

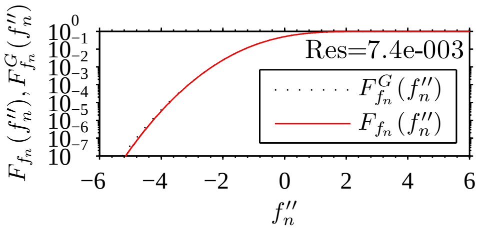


(h) CDF, $n \in \{1, 63, 65, 127\}$, closeup.

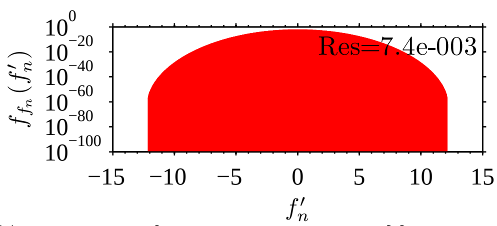


(i) PDF, $n \in \{2, 62, 66, 126 \cdots, 30\}\}$, wide-view.

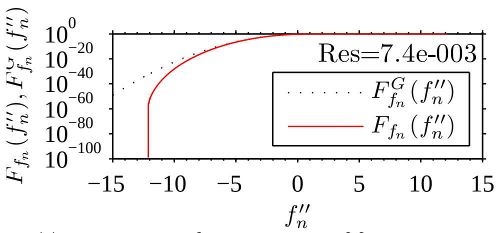


(j) CDF, $n \in \{2, 62, 66, 126\}\}$, wide-view.

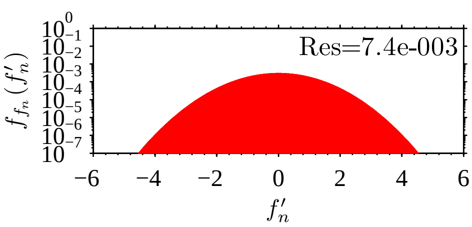


(k) PDF, $n \in \{2, 62, 66, 126 \cdots, 30\}$, closeup.

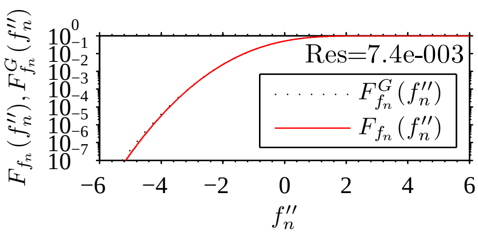


(l) CDF, $n \in \{2, 62, 66, 126 \cdots, 30\}$, closeup.

OFDM Type 5.16: IEEE 802.11a, $N = 128, \mathcal{K}_{\text{SZ}} = \{0{:}5{,}32{,}59{:}69{,}96{,}123{:}127\}$,
$\mathcal{K}_{\text{SP}} = \{11, 25, 39, 53, 75, 89, 103, 117\}, \mathcal{A}_{\text{SP}} = \mathcal{A}_{\text{BPSK}}$,
$\mathcal{K}_{\text{SD}} = \{6{:}10{,}12{:}24{,}26{:}31{,}33{:}38{,}40{:}52{,}54{:}58{,}70{:}74{,}76{:}88{,}90{:}95{,}97{:}102{,}104{:}116{,}118{:}122\}$,
$\mathcal{A}_{\text{SD}} = \mathcal{A}_{\text{16QAM}}, \mathcal{D}_{\text{SP}} = \{+1, +1, +1, -1, -1, +1, +1, +1\}, \text{E}[f^2] = 1$.

Figure 6.9: 'Convolution' PDFs $f_{f_n}(f'_n)$, CDFs $F_{f_n}(f''_n)$, and Gaussian approximation CDFs $F^G_{f_n}(f''_n)$ of individual IDFT output time-sample real-parts, OFDM Type 5.16 (IEEE 802.11a, 16QAM data), accuracy $= 10^{-3}$, for selected time-sample indeces $n$.

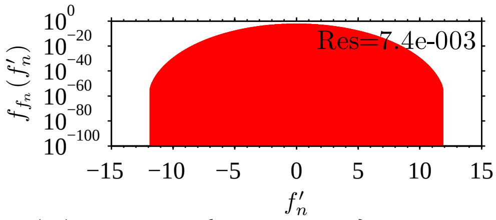


(m) PDF, $n \in \{4, 60, 68, 124\}$, wide-view.

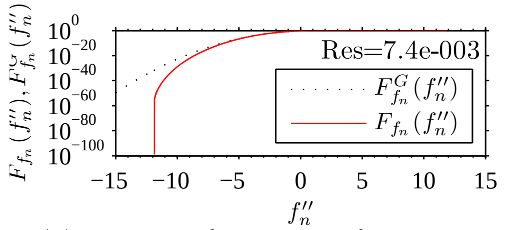


(n) CDF, $n \in \{4, 60, 68, 124\}$, wide-view.

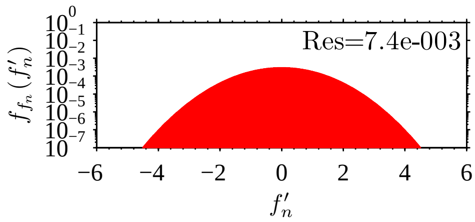


(o) PDF, $n \in \{4, 60, 68, 124\}$, closeup.

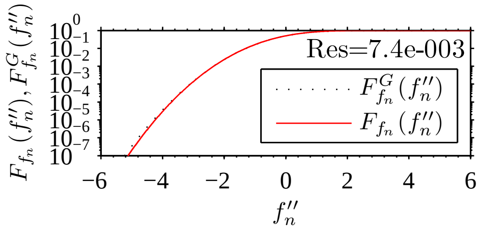


(p) CDF, $n \in \{4, 60, 68, 124\}$, closeup.

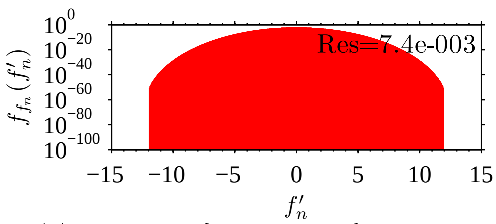


(q) PDF, $n \in \{8, 56, 72, 120\}$, wide-view.

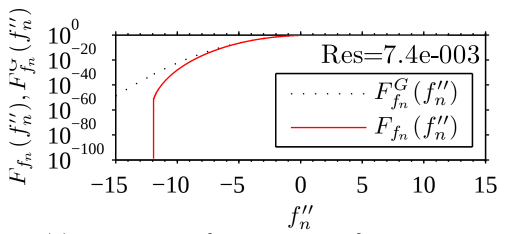


(r) CDF, $n \in \{8, 56, 72, 120\}$, wide-view.

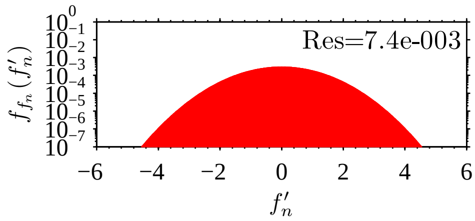


(s) PDF, $n \in \{8, 56, 72, 120\}$, closeup.

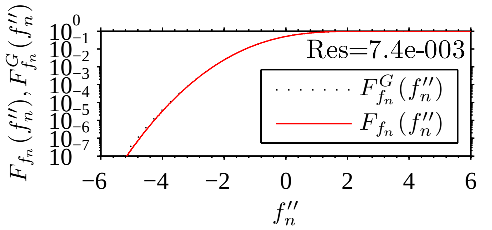


(t) CDF, $n \in \{8, 56, 72, 120\}$, closeup.

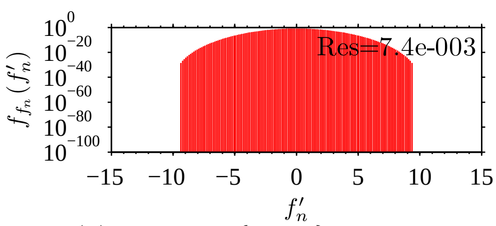


(u) PDF, $n \in \{32, 96\}$, wide-view.

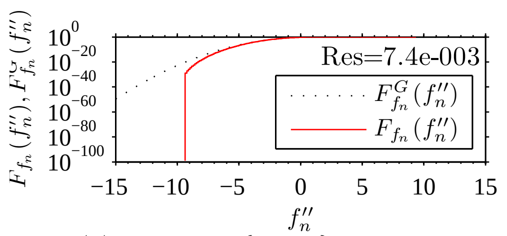


(v) CDF, $n \in \{32, 96\}$, wide-view.

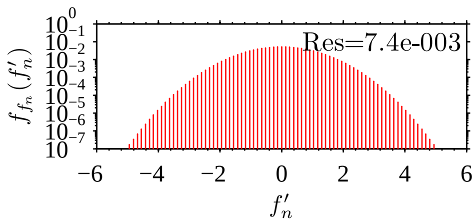


(w) PDF, $n \in \{32, 96\}$, closeup.

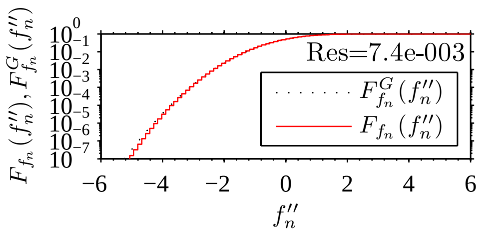


(x) CDF, $n \in \{32, 96\}$, closeup.

OFDM Type 5.16: IEEE 802.11a, $N = 128, \mathcal{K}_{\mathrm{SZ}} = \{0{:}5, 32, 59{:}69, 96, 123{:}127\}$,
$\mathcal{K}_{\mathrm{SP}} = \{11, 25, 39, 53, 75, 89, 103, 117\}, \mathcal{A}_{\mathrm{SP}} = \mathcal{A}_{\mathrm{BPSK}}$,
$\mathcal{K}_{\mathrm{SD}} = \{6{:}10, 12{:}24, 26{:}31, 33{:}38, 40{:}52, 54{:}58, 70{:}74, 76{:}88, 90{:}95, 97{:}102, 104{:}116, 118{:}122\}$,
$\mathcal{A}_{\mathrm{SD}} = \mathcal{A}_{\mathrm{16QAM}}, \mathcal{D}_{\mathrm{SP}} = \{+1, +1, +1, -1, -1, +1, +1, +1\}, \mathrm{E}[f^2] = 1$.

Figure 6.9: (Cont'd) 'Convolution' PDFs $f_{f_n}(f'_n)$, CDFs $F_{f_n}(f''_n)$, and Gaussian approximation CDFs $F^G_{f_n}(f''_n)$ of individual IDFT output time-sample real-parts, OFDM Type 5.16 (IEEE 802.11a, 16QAM data), accuracy $= 10^{-3}$, for selected time-sample indeces $n$.

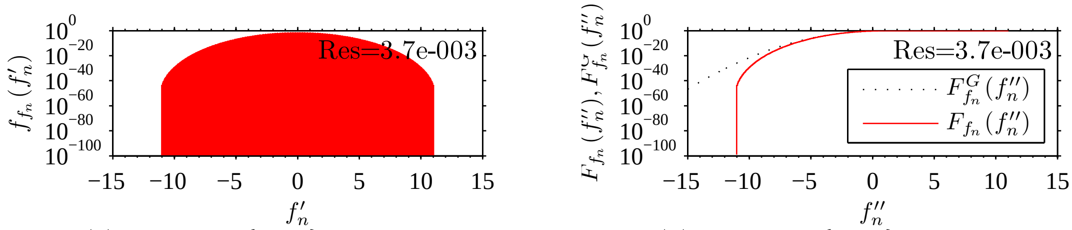


(a) PDF, $n \in \{0, 64\}$, wide-view. (b) CDF, $n \in \{0, 64\}$, wide-view.

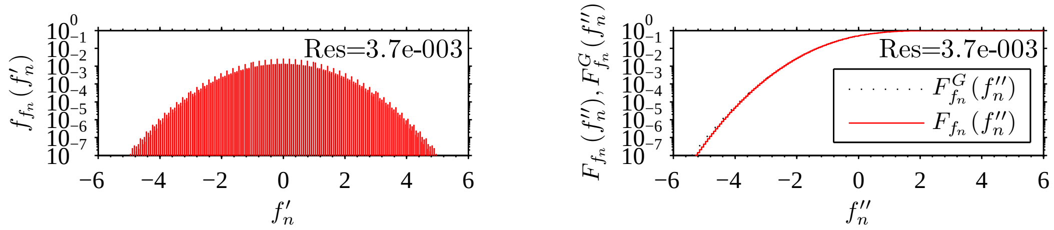


(c) PDF, $n \in \{0, 64\}$, closeup. (d) CDF, $n \in \{0, 64\}$, closeup.

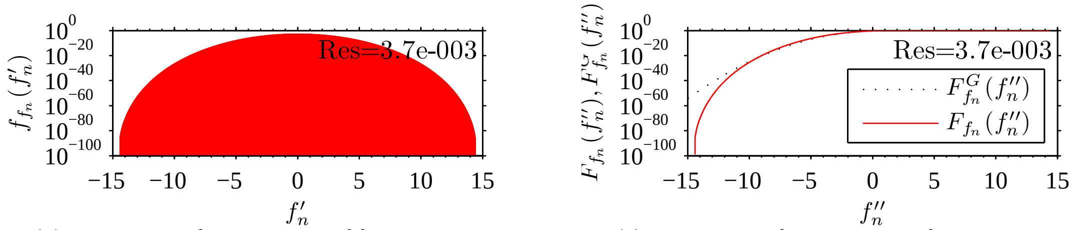


(e) PDF, $n \in \{1, 63, 65, 127\}\}$, wide-view. (f) CDF, $n \in \{1, 63, 65, 127\}$, wide-view.

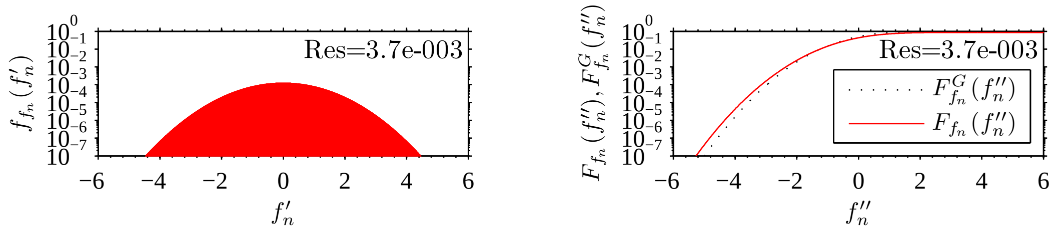


(g) PDF, $n \in \{1, 63, 65, 127\}$, closeup. (h) CDF, $n \in \{1, 63, 65, 127\}$, closeup.

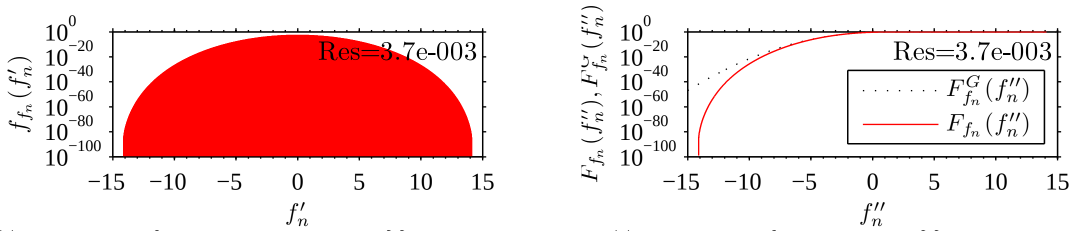


(i) PDF, $n \in \{2, 62, 66, 126 \cdots, 30\}\}$, wide-view. (j) CDF, $n \in \{2, 62, 66, 126\}\}$, wide-view.

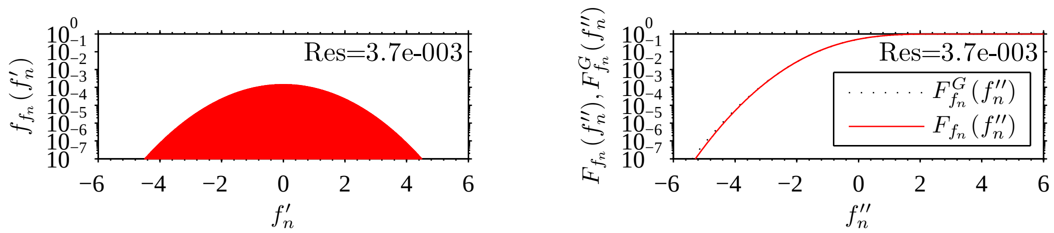


(k) PDF, $n \in \{2, 62, 66, 126 \cdots, 30\}$, closeup. (l) CDF, $n \in \{2, 62, 66, 126 \cdots, 30\}$, closeup.

OFDM Type 5.64: IEEE 802.11a, $N = 128, \mathcal{K}_{\text{SZ}} = \{$0:5,32,59:69,96,123:127$\}$,
$\mathcal{K}_{\text{SP}} = \{11, 25, 39, 53, 75, 89, 103, 117\}, \mathcal{A}_{\text{SP}} = \mathcal{A}_{\text{BPSK}}$,
$\mathcal{K}_{\text{SD}} = \{$6:10,12:24,26:31,33:38,40:52,54:58,70:74,76:88,90:95,97:102,104:116,118:122$\}$,
$\mathcal{A}_{\text{SD}} = \mathcal{A}_{\text{64QAM}}, \mathcal{D}_{\text{SP}} = \{+1, +1, +1, -1, -1, +1, +1, +1\}, \text{E}[f^2] = 1$.

Figure 6.10: 'Convolution' PDFs $f_{f_n}(f'_n)$, CDFs $F_{f_n}(f''_n)$, and Gaussian approximation CDFs $F^G_{f_n}(f''_n)$ of individual IDFT output time-sample real-parts, OFDM Type 5.64 (IEEE 802.11a, 64QAM data), accuracy $= 10^{-2}$, for selected time-sample indeces $n$.

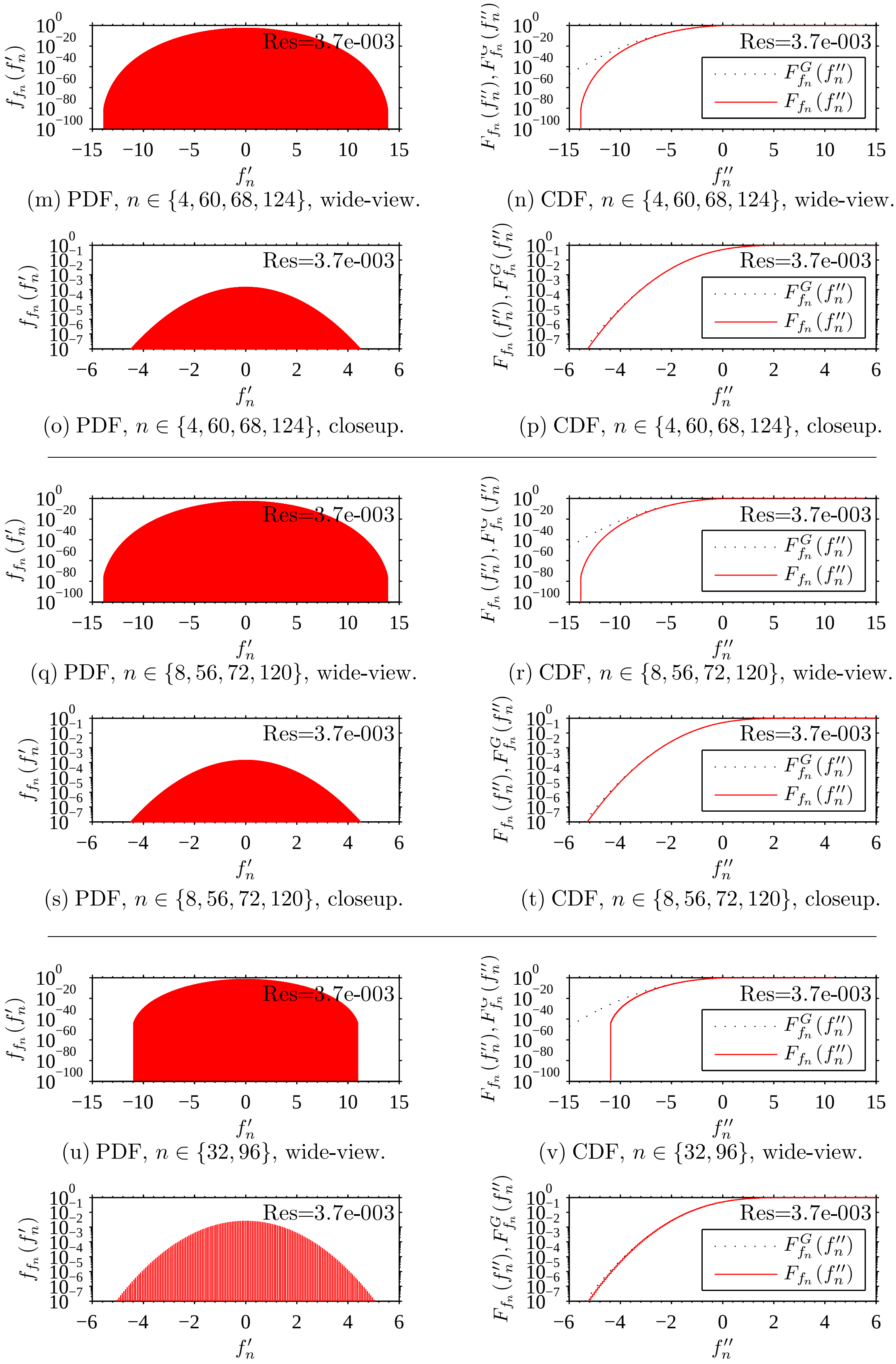


(m) PDF, $n \in \{4, 60, 68, 124\}$, wide-view. (n) CDF, $n \in \{4, 60, 68, 124\}$, wide-view.

(o) PDF, $n \in \{4, 60, 68, 124\}$, closeup. (p) CDF, $n \in \{4, 60, 68, 124\}$, closeup.

(q) PDF, $n \in \{8, 56, 72, 120\}$, wide-view. (r) CDF, $n \in \{8, 56, 72, 120\}$, wide-view.

(s) PDF, $n \in \{8, 56, 72, 120\}$, closeup. (t) CDF, $n \in \{8, 56, 72, 120\}$, closeup.

(u) PDF, $n \in \{32, 96\}$, wide-view. (v) CDF, $n \in \{32, 96\}$, wide-view.

(w) PDF, $n \in \{32, 96\}$, closeup. (x) CDF, $n \in \{32, 96\}$, closeup.

OFDM Type 5.64: IEEE 802.11a, $N = 128, \mathcal{K}_{\text{SZ}} = \{0{:}5, 32, 59{:}69, 96, 123{:}127\}$,
$\mathcal{K}_{\text{SP}} = \{11, 25, 39, 53, 75, 89, 103, 117\}, \mathcal{A}_{\text{SP}} = \mathcal{A}_{\text{BPSK}}$,
$\mathcal{K}_{\text{SD}} = \{6{:}10, 12{:}24, 26{:}31, 33{:}38, 40{:}52, 54{:}58, 70{:}74, 76{:}88, 90{:}95, 97{:}102, 104{:}116, 118{:}122\}$,
$\mathcal{A}_{\text{SD}} = \mathcal{A}_{\text{64QAM}}, \mathcal{D}_{\text{SP}} = \{+1, +1, +1, -1, -1, +1, +1, +1\}, \text{E}[f^2] = 1$.

Figure 6.10: (Cont'd) 'Convolution' PDFs $f_{f_n}(f'_n)$, CDFs $F_{f_n}(f''_n)$, and Gaussian approximation CDFs $F^G_{f_n}(f''_n)$ of individual IDFT output time-sample real-parts, OFDM Type 5.16 (IEEE 802.11a, 64QAM data), accuracy $= 10^{-2}$, for selected time-sample indeces $n$.

### 6.2.2 Finite Resolution 'Convolution' PDF and CDF of All IDFT Output Time-Sample Real-Parts

Next, we examine the PDF $f_f(f')$ and CDF $F_f(f'')$ of all IDFT Output Time-Sample Real-Parts $f$ obtained by the 'convolution' method. Like the PDFs and CDFs for individual time-samples already discussed, these PDF and CDF results give important insight into the variability of the PDF and CDF with the particular time-sample observed as well as a surprising 'non-Gaussian-ness' of some of the time-samples. The author has not been able to find these kind of results, shown Figures 6.5 to 6.10, in any of the literature and, accordingly believes them to be an original contribution to the state-of-the-art.

#### 6.2.2.1 Results for Small-Scale OFDM Types

The results for the 'Convolution' PDFs $f_f(f')$ and CDFs $F_f(f'')$ of all IDFT output time-sample real-parts for example small-scale OFDM Types 1.2, 1.4, 2.2, 2.4, 3.2, and 4.2 exactly match the results already independently obtained using the 'Exhaustive' method shown in Figure 5.11. Thus, in these cases, the 'Exhaustive' method validates the 'Convolution' method.

#### 6.2.2.2 Results for Large-Scale OFDM Types

The results for the 'Convolution' PDFs $f_f(f')$ and CDFs $F_f(f'')$ of all IDFT output time-sample real-parts for example large-scale OFDM Types 5.2, 5.4, 5.16, and 5.64 using the 'Exhaustive' method are shown in Figure 6.11. To the best of the author's knowledge, such results have not been published elsewhere in the literature and this is an original contribution to the state of the art.

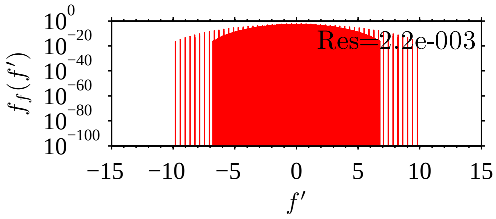


(m) PDF, OFDM Type 5.2, wide-view.

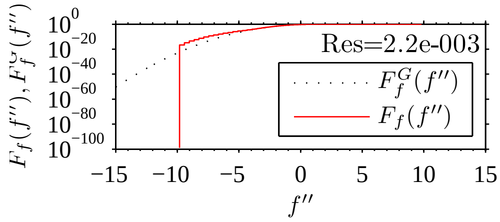


(n) CDF, OFDM Type 5.2, wide-view.

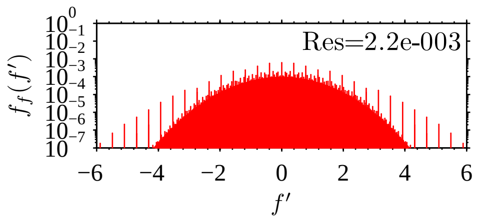


(o) PDF, OFDM Type 5.2, closeup.

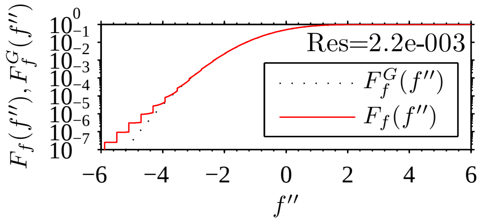


(p) CDF, OFDM Type 5.2, closeup.

OFDM Type 5.2 : IEEE 802.11a, $N = 128, \mathcal{K}_{\text{SZ}} = \{0{:}5{,}32{,}59{:}69{,}96{,}123{:}127\}$,
$\mathcal{K}_{\text{SP}} = \{11, 25, 39, 53, 75, 89, 103, 117\}, \mathcal{A}_{\text{SP}} = \mathcal{A}_{\text{BPSK}}$,
$\mathcal{K}_{\text{SD}} = \{6{:}10{,}12{:}24{,}26{:}31{,}33{:}38{,}40{:}52{,}54{:}58{,}70{:}74{,}76{:}88{,}90{:}95{,}97{:}102{,}104{:}116{,}118{:}122\}$,
$\mathcal{A}_{\text{SD}} = \mathcal{A}_{\text{BPSK}}, \mathcal{D}_{\text{SP}} = \{+1, +1, +1, -1, -1, +1, +1, +1\}, \text{E}[f^2] = 1$.

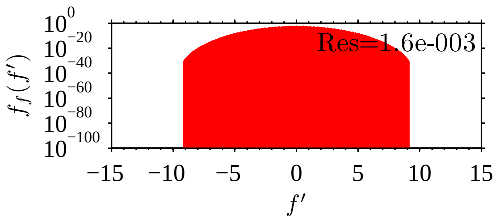


(q) PDF, OFDM Type 5.4, wide-view.

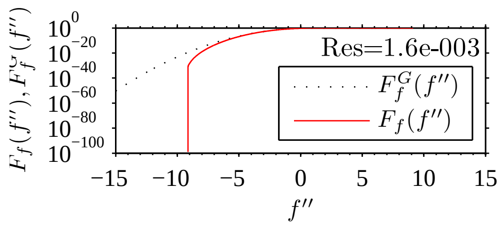


(r) CDF, OFDM Type 5.4, wide-view.

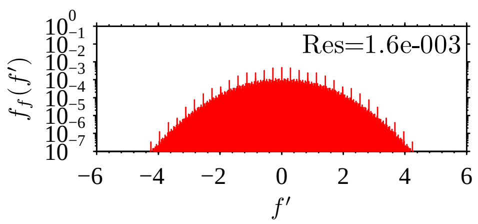


(s) PDF, OFDM Type 5.4, closeup.

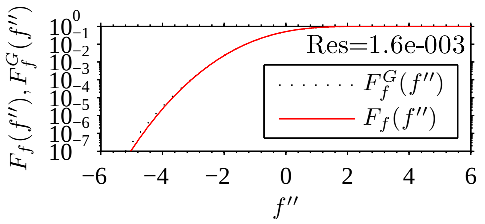


(t) CDF, OFDM Type 5.4, closeup.

OFDM Type 5.4 : IEEE 802.11a, $N = 128, \mathcal{K}_{\text{SZ}} = \{0{:}5{,}32{,}59{:}69{,}96{,}123{:}127\}$,
$\mathcal{K}_{\text{SP}} = \{11, 25, 39, 53, 75, 89, 103, 117\}, \mathcal{A}_{\text{SP}} = \mathcal{A}_{\text{BPSK}}$,
$\mathcal{K}_{\text{SD}} = \{6{:}10{,}12{:}24{,}26{:}31{,}33{:}38{,}40{:}52{,}54{:}58{,}70{:}74{,}76{:}88{,}90{:}95{,}97{:}102{,}104{:}116{,}118{:}122\}$,
$\mathcal{A}_{\text{SD}} = \mathcal{A}_{\text{QPSK}}, \mathcal{D}_{\text{SP}} = \{+1, +1, +1, -1, -1, +1, +1, +1\}, \text{E}[f^2] = 1$.

Figure 6.11: (Cont'd) 'Convolution' PDFs $f_f(f')$, CDFs $F_f(f'')$, and Gaussian approximation CDFs $F_f^G(f'')$ of all IDFT output time-sample real-parts, for various OFDM types.

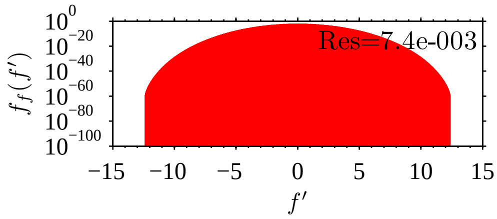


(u) PDF, OFDM Type 5.16, wide-view.

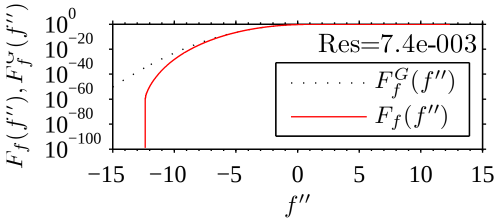


(v) CDF, OFDM Type 5.16, wide-view.

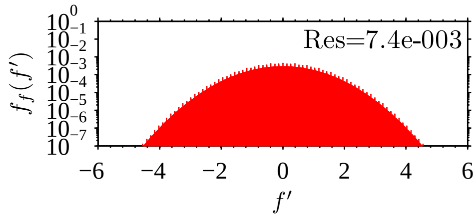


(w) PDF, OFDM Type 5.16, closeup.

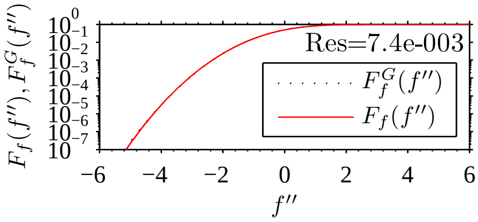


(x) CDF, OFDM Type 5.16, closeup.

| | |
|---|---|
| OFDM Type 5.16 : | IEEE 802.11a, $N = 128, \mathcal{K}_{\text{SZ}} = \{0{:}5{,}32{,}59{:}69{,}96{,}123{:}127\}$, $\mathcal{K}_{\text{SP}} = \{11, 25, 39, 53, 75, 89, 103, 117\}, \mathcal{A}_{\text{SP}} = \mathcal{A}_{\text{BPSK}}$, $\mathcal{K}_{\text{SD}} = \{6{:}10{,}12{:}24{,}26{:}31{,}33{:}38{,}40{:}52{,}54{:}58{,}70{:}74{,}76{:}88{,}90{:}95{,}97{:}102{,}104{:}116{,}118{:}122\}$, $\mathcal{A}_{\text{SD}} = \mathcal{A}_{\text{16QAM}}, \mathcal{D}_{\text{SP}} = \{+1, +1, +1, -1, -1, +1, +1, +1\}, \text{E}[f^2] = 1.$ |

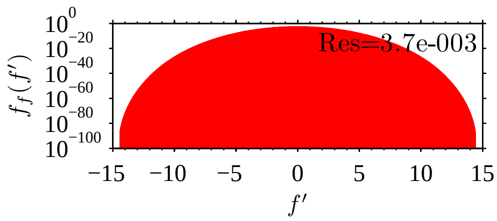


(y1) PDF, OFDM Type 5.64, wide-view.

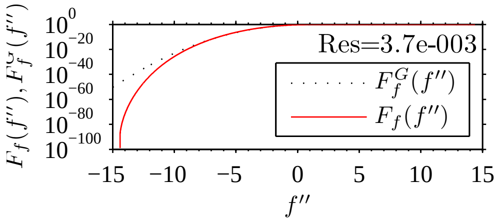


(y2) CDF, OFDM Type 5.64, wide-view.

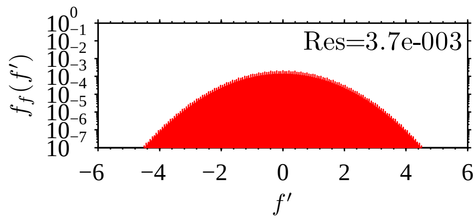


(z1) PDF, OFDM Type 5.64, closeup.

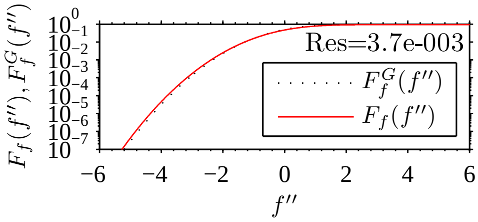


(z2) CDF, OFDM Type 5.64, closeup.

| | |
|---|---|
| OFDM Type 5.64 : | IEEE 802.11a, $N = 128, \mathcal{K}_{\text{SZ}} = \{0{:}5{,}32{,}59{:}69{,}96{,}123{:}127\}$, $\mathcal{K}_{\text{SP}} = \{11, 25, 39, 53, 75, 89, 103, 117\}, \mathcal{A}_{\text{SP}} = \mathcal{A}_{\text{BPSK}}$, $\mathcal{K}_{\text{SD}} = \{6{:}10{,}12{:}24{,}26{:}31{,}33{:}38{,}40{:}52{,}54{:}58{,}70{:}74{,}76{:}88{,}90{:}95{,}97{:}102{,}104{:}116{,}118{:}122\}$, $\mathcal{A}_{\text{SD}} = \mathcal{A}_{\text{64QAM}}, \mathcal{D}_{\text{SP}} = \{+1, +1, +1, -1, -1, +1, +1, +1\}, \text{E}[f^2] = 1.$ |

Figure 6.11: (Cont'd) 'Convolution' PDFs $f_f(f')$, CDFs $F_f(f'')$, and Gaussian approximation CDFs $F_f^G(f'')$ of all IDFT output time-sample real-parts, for various OFDM types.

# 6.3 The Exact 'Combinatorics' Method

To this point, we have obtained approximate PDFs for the frequency-domain quantizer noise using the 'Monte Carlo' method of §5.4 and we have obtained exact PDFs using the 'Exhaustive' method of §5.3. However, the 'exhaustive' method has only been able to obtain exact PDFs for low-complexity OFDM systems. Real-world ODFM systems such as IEEE 802.11a [1] or IEEE 802.11n [2], are beyond the ability of the 'exhaustive' method and an alternative is desirable. We now proceed to begin developing a method, which we shall designate the 'combinatorics' method, as a possible solution for obtaining exact PDFs and CDFs for such systems.

Regarding a definition of combinatorics, one source [44] says, '$\cdots$ combinatorics is a branch of mathematics concerning the study of finite or countable discrete structures $\cdots$ combinatorial problems arise in many areas of pure mathematics, notably in $\cdots$ probability theory $\cdots$'.

Another source [14] says, ' $\cdots$ branch of mathematics concerned with the selection, arrangement, and combination of objects chosen from a finite set $\cdots$ See also permutations and combinations $\cdots$'.

In the following sections, we develop the beginnings of an approach for the 'Combinatorics method'.

## 6.3.1 'Combinatorics' PDFs and CDFs of the Transmitter Quantization Error Frequency-Samples

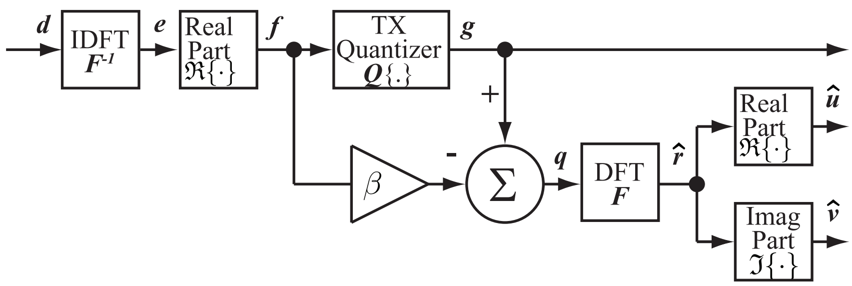


Figure 6.12: Calculation of the frequency-domain quantizer error $\hat{\boldsymbol{r}}$.

A method to calculate the frequency-domain quantizer error $\hat{\boldsymbol{r}}$ is depicted in block diagram form in Figure (6.12), with:

real DFT input vector

$\boldsymbol{q} = [q_0, q_1, \cdots, q_n, \cdots, q_{N-1}]^{\mathrm{T}} \in \mathcal{A}_{\boldsymbol{q}} = \{\boldsymbol{q_j}\}_{j=1}^{N_{\boldsymbol{q}}}$,

N-point DFT matrix

$\boldsymbol{F} = (\frac{1}{\sqrt{N}} e^{-j\frac{2\pi\hat{k}n}{N}}), \quad \hat{k}, n \in \mathbb{Z}_N$,

complex DFT output vector

$\hat{\boldsymbol{r}} = [\hat{r}_0, \hat{r}_1, \cdots, \hat{r}_{\hat{k}}, \cdots, \hat{r}_{N-1}]^{\mathrm{T}} \in \mathcal{A}_{\hat{\boldsymbol{r}}} = \{\hat{\boldsymbol{r}}_{\boldsymbol{j}}\}_{j=1}^{N_{\hat{\boldsymbol{r}}}}$, and

real part of complex DFT output vector

$\hat{\boldsymbol{u}} = [\hat{u}_0, \hat{u}_1, \cdots, \hat{u}_{\hat{k}}, \cdots, \hat{u}_{N-1}]^{\mathrm{T}} \in \mathcal{A}_{\hat{\boldsymbol{u}}} = \{\hat{\boldsymbol{u}}_{\boldsymbol{j}}\}_{j=1}^{N_{\hat{\boldsymbol{u}}}}$,

such that $\hat{\boldsymbol{r}} = \boldsymbol{F}\boldsymbol{q}$ and $\hat{\boldsymbol{u}} = \Re\{\hat{\boldsymbol{r}}\}$.

We will now find the PDF of the $\hat{k}^{\text{th}}$ entry $\hat{u}_{\hat{k}}$ of the frequency-domain DFT output vector $\hat{\boldsymbol{u}}$ over all time-domain DFT input vectors $\boldsymbol{q} \in \mathcal{A}_{\boldsymbol{q}}$.

The $\hat{k}^{\text{th}}$ DFT output vector entry is given by

$$\hat{r}_{\hat{k}} = \frac{1}{\sqrt{N}} \sum_{n=0}^{N-1} q_n e^{-j\frac{2\pi\hat{k}n}{N}} \quad, \hat{k} \in \mathbb{Z}_N. \tag{6.39}$$

Now, remembering that $q_n$ is real, the real part of the $k^{\text{th}}$ DFT output vector entry is given by

$$\hat{u}_{\hat{k}} = \Re\{\hat{r}_{\hat{k}}\} = \frac{1}{\sqrt{N}} \sum_{n=0}^{N-1} q_n \cos\left(\frac{2\pi\hat{k}n}{N}\right) = \frac{1}{\sqrt{N}} \sum_{n=0}^{N-1} q_n c_{\hat{k},n} \quad, \hat{k} \in \mathbb{Z}_N, \tag{6.40}$$

where the factor $\cos\left(\frac{2\pi\hat{k}n}{N}\right)$ is short-handed with

$$c_{\hat{k},n} \triangleq \cos\left(\frac{2\pi\hat{k}n}{N}\right). \tag{6.41}$$

We note that the various $c_{\hat{k},n}$ may not be unique, so that there may exist one or more cases where $c_{\hat{k},n} = c_{\hat{k}',n}$, when $\hat{k} \neq \hat{k}'$.

So

$$c_{\hat{k},n} \in \mathcal{A}_{c_{\hat{k}}} = \{c_{\hat{k},\hat{l}}\}_{\hat{l}=0}^{N_{c_{\hat{k}}}-1} \quad , \tag{6.42}$$

where $\mathcal{A}_{c_{\hat{k}}}$ is the alphabet of distinct letters (or instances) of $c_{\hat{k},n}$, $c_{\hat{k},\hat{l}}$ is the $\hat{l}^{\text{th}}$ letter of $\mathcal{A}_{c_{\hat{k}}}$, and $N_{c_{\hat{k}}}$ is the total number of letters in $\mathcal{A}_{c_{\hat{k}}}$. We also define the number of occurrences of each $c_{\hat{k},\hat{l}}$ to be $N_{c_{\hat{k},\hat{l}}}$.

We define the set of time-indeces $n$ of the DFT input vector entries $q_n$ for which $c_{\hat{k},n} = c_{\hat{k},\hat{l}}$ to be

$$\mathcal{N}_{c_{\hat{k},\hat{l}}} \triangleq \left\{ n : c_{\hat{k},n} = c_{\hat{k},\hat{l}} \right\}, \tag{6.43}$$

and note that, since, from (6.43), each $n \in \mathcal{N}_{c_{\hat{k},\hat{l}}}$ yields an occurrence of $c_{\hat{k},\hat{l}}$, the size of the set $\mathcal{N}_{c_{\hat{k},\hat{l}}}$ is the same as the number of occurrences of $c_{\hat{k},\hat{l}}$ so that

$$|\mathcal{N}_{c_{\hat{k},\hat{l}}}| = N_{c_{\hat{k},\hat{l}}}. \tag{6.44}$$

We also define the set of DFT input vector entries $q_n$ for which $c_{\hat{k},n} = c_{\hat{k},\hat{l}}$ to be

$$\mathcal{Q}_{c_{\hat{k},\hat{l}}} \triangleq \left\{ q_n : c_{\hat{k},n} = c_{\hat{k},\hat{l}} \right\} = \left\{ q_n : n \in \mathcal{N}_{c_{\hat{k},\hat{l}}} \right\}, \tag{6.45}$$

and note that, since, from (6.45), each $q_n \in \mathcal{Q}_{c_{\hat{k},\hat{l}}}$ corresponds uniquely to a particular $n \in \mathcal{N}_{c_{\hat{k},\hat{l}}}$ which, from (6.43), yields an occurrence of $c_{\hat{k},\hat{l}}$, the size of the set $\mathcal{Q}_{c_{\hat{k},\hat{l}}}$ is the same as the number of occurrences of $c_{\hat{k},\hat{l}}$ so that

$$|\mathcal{Q}_{c_{\hat{k},\hat{l}}}| = N_{c_{\hat{k},\hat{l}}}. \tag{6.46}$$

Using (6.42) and (6.45), (6.40) may be rewritten

$$\begin{aligned} \hat{u}_{\hat{k}} &= \frac{1}{\sqrt{N}} \sum_{l=0}^{N_{c_{\hat{k}}}-1} c_{\hat{k},\hat{l}} \sum_{q_n \in \mathcal{Q}_{c_{\hat{k},\hat{l}}}} q_n & (6.47) \\ &= \frac{1}{\sqrt{N}} \sum_{l=0}^{N_{c_{\hat{k}}}-1} c_{\hat{k},\hat{l}} \cdot s_{c_{\hat{k},\hat{l}}} \quad , & (6.48) \end{aligned}$$

where

$$s_{c_{\hat{k},\hat{l}}} \triangleq \sum_{q_n \in \mathcal{Q}_{c_{\hat{k},\hat{l}}}} q_n. \tag{6.49}$$

Referring back to (6.45), we note that, because $q_n \in \boldsymbol{q} \in \mathcal{A}_{\boldsymbol{q}}$, a finite number of distinct instances of the set $\mathcal{Q}_{c_{\hat{k},\hat{l}}}$ exists so that

$$\mathcal{Q}_{c_{\hat{k},\hat{l}}} \in \mathcal{A}_{\mathcal{Q}_{c_{\hat{k},\hat{l}}}} = \{\mathcal{Q}_{c_{\hat{k},\hat{l},j}}\}_{j=1}^{N_{\mathcal{Q}_{c_{\hat{k},\hat{l}}}}} \quad , \tag{6.50}$$

where $\mathcal{A}_{\mathcal{Q}_{c_{\hat{k},\hat{l}}}}$ is the alphabet of $\mathcal{Q}_{c_{\hat{k},\hat{l}}}$, $\mathcal{Q}_{c_{\hat{k},\hat{l},j}}$ is the $j^{\text{th}}$ instance or 'letter' of $\mathcal{A}_{\mathcal{Q}_{c_{\hat{k},\hat{l}}}}$, and $N_{\mathcal{Q}_{c_{\hat{k},\hat{l}}}}$ is the total number of letters in $\mathcal{A}_{\mathcal{Q}_{c_{\hat{k},\hat{l}}}}$. We also define the number of occurrences of the $j^{\text{th}}$ set $\mathcal{Q}_{c_{\hat{k},\hat{l},j}}$, over all DFT input vector letters $\boldsymbol{q} \in \mathcal{A}_{\boldsymbol{q}}$, to be $N_{\mathcal{Q}_{c_{\hat{k},\hat{l},j}}}$.

We also note that multiple DFT input vector letters, e.g. $\boldsymbol{q_i}, \boldsymbol{q_j}, \boldsymbol{q_k}$, of $\boldsymbol{q} \in \mathcal{A}_{\boldsymbol{q}}$, may map to the same $\mathcal{Q}_{c_{\hat{k},\hat{l}}} \in \mathcal{A}_{\mathcal{Q}_{c_{\hat{k},\hat{l}}}}$ because $q_n \in \mathcal{Q}_{c_{\hat{k},\hat{l}}}$ is only a subset of $q_n \in \boldsymbol{q}$ and, also, because the elements of $\mathcal{Q}_{c_{\hat{k},\hat{l}}} \in \mathcal{A}_{\mathcal{Q}_{c_{\hat{k},\hat{l}}}}$ are unordered per the definition of a set. Therefore, $N_{\mathcal{Q}_{c_{\hat{k},\hat{l}}}} \leq N_{\boldsymbol{q}}$.

Next, referring back to (6.49), we note that each distinct letter $\mathcal{Q}_{c_{\hat{k},\hat{l},p}}$ of alphabet $\mathcal{A}_{\mathcal{Q}_{c_{\hat{k},\hat{l}}}}$ maps uniquely to a distinct value of $s_{c_{\hat{k},\hat{l}}}$ so that

$$s_{c_{\hat{k},\hat{l}}} \in \mathcal{A}_{s_{c_{\hat{k},\hat{l}}}} = \{s_{c_{\hat{k},\hat{l},p}}\}_{p=1}^{N_{s_{c_{\hat{k},\hat{l}}}}} \tag{6.51}$$

where $\mathcal{A}_{s_{c_{\hat{k},\hat{l}}}}$ is the alphabet of $s_{c_{\hat{k},\hat{l}}}$, $s_{c_{\hat{k},\hat{l},p}}$ is the $p^{\text{th}}$ letter of $\mathcal{A}_{s_{c_{\hat{k},\hat{l}}}}$, and $N_{s_{c_{\hat{k},\hat{l}}}}$ is the total number of letters in $\mathcal{A}_{s_{c_{\hat{k},\hat{l}}}}$. We also define the number of occurrences of $s_{c_{\hat{k},\hat{l},p}}$, over $\boldsymbol{q} \in \mathcal{A}_{\boldsymbol{q}}$, to be $N_{s_{c_{\hat{k},\hat{l},p}}}$ $(= N_{\mathcal{Q}_{c_{\hat{k},\hat{l},p}}})$.

Now, (6.48) may be expanded as

$$\hat{u}_{\hat{k}} = \frac{1}{\sqrt{N}} \left[ c_{\hat{k},1} \cdot s_{c_{\hat{k},1}} + c_{\hat{k},2} \cdot s_{c_{\hat{k},2}} + \cdots + c_{\hat{k},\hat{l}} \cdot s_{c_{\hat{k},\hat{l}}} + \cdots + c_{\hat{k},N_{c_{\hat{k}}}} \cdot s_{c_{\hat{k},N_{c_{\hat{k}}}}} \right]. \tag{6.52}$$

Next, we use the $p_{\hat{l}}^{\text{th}}$ letter $s_{c_{\hat{k},\hat{l},p_{\hat{l}}}}$ of the alphabet $\mathcal{A}_{s_{c_{\hat{k},\hat{l}}}}$ of each summation $s_{c_{\hat{k},\hat{l}}}$ to get the corresponding DFT output letter

$$\hat{u}_{\hat{k}}(\boldsymbol{p}) = \frac{1}{\sqrt{N}} \left[ c_{\hat{k},1} \cdot s_{c_{\hat{k},1,p_1}} + c_{\hat{k},2} \cdot s_{c_{\hat{k},2,p_2}} + \cdots + c_{\hat{k},\hat{l}} \cdot s_{c_{\hat{k},\hat{l},p_{\hat{l}}}} + \cdots c_{\hat{k},N_{c_{\hat{k}}}} \cdot s_{c_{\hat{k},N_{c_{\hat{k}}},p_{N_{c_{\hat{k}}}}}} \right], \tag{6.53}$$

where

$$\boldsymbol{p} \triangleq \left[ p_1, p_2, \cdots, p_{\hat{l}}, \cdots p_{N_{c_{\hat{k}}}} \right]. \tag{6.54}$$

Now,

$$p_{\hat{l}} \in \mathcal{A}_{p_{\hat{l}}} = \left\{ p_{\hat{l},j} \right\}_{j=1}^{N_{p_{\hat{l}}}}, \tag{6.55}$$

where $\mathcal{A}_{p_{\hat{l}}}$ is the alphabet of $p_{\hat{l}}$, $p_{\hat{l},j}$ is the $j^{\text{th}}$ letter of $\mathcal{A}_{p_{\hat{l}}}$, and $N_{p_{\hat{l}}}$ is the total number of letters in $\mathcal{A}_{p_{\hat{l}}}$.

It then follows that

$$\begin{aligned} \boldsymbol{p} \in \mathcal{A}_{\boldsymbol{p}} &= \mathcal{A}_{p_1} \times \mathcal{A}_{p_2} \times \cdots \times \mathcal{A}_{p_{\hat{l}}} \times \cdots \times \mathcal{A}_{p_{N_{c_{\hat{k}}}}} & (6.56) \\ &= \{\boldsymbol{p_j}\}_{j=1}^{N_{\boldsymbol{p}}}, & (6.57) \end{aligned}$$

where $\mathcal{A}_{\boldsymbol{p}}$ is the alphabet of $\boldsymbol{p}$, $\times$ is the Cartesian product operator, $\boldsymbol{p}_j$ is the $j^{\text{th}}$ letter of $\mathcal{A}_{\boldsymbol{p}}$, and $N_{\boldsymbol{p}} = \Pi_{l=1}^{N_{c_{\hat{k}}}} N_{p_{\hat{l}}}$ is the total number of letters in $\mathcal{A}_{\boldsymbol{p}}$. We also define the number of occurrences of $\boldsymbol{p_j}$, over $\boldsymbol{q} \in \mathcal{A}_{\boldsymbol{q}}$, to be $N_{\boldsymbol{p_j}}$.

Then, from (6.53) and (6.57), again it follows

$$\hat{u}_{\hat{k}} \in \mathcal{A}_{\hat{u}_{\hat{k}}} = \{\hat{u}_{\hat{k},j}\}_{j=1}^{N_{\hat{u}_{\hat{k}}}}, \tag{6.58}$$

where $\mathcal{A}_{\hat{u}_{\hat{k}}}$ is the alphabet of $\hat{u}_{\hat{k}}$, $\hat{u}_{k,j} = \hat{u}_{\hat{k}}(\boldsymbol{p_j})$ is the $j^{\text{th}}$ letter of $\mathcal{A}_{\hat{u}_{\hat{k}}}$, and $N_{\hat{u}_{\hat{k}}}$ is the total number of letters in $\mathcal{A}_{\hat{u}_{\hat{k}}}$. We also define the number of occurrences of $\hat{u}_{\hat{k},j}$, over $\boldsymbol{q} \in \mathcal{A}_{\boldsymbol{q}}$, to be $N_{\hat{u}_{\hat{k},j}}$ $(= N_{\boldsymbol{p_j}})$.

The probability of $\hat{u}_{\hat{k},j}$, over $\boldsymbol{q} \in \mathcal{A}_{\boldsymbol{q}}$, is then

$$\mathrm{P}(\hat{u}_{\hat{k},j}) = \frac{N_{\hat{u}_{\hat{k},j}}}{\sum_{j=1}^{N_{\hat{u}_{\hat{k}}}} N_{\hat{u}_{\hat{k},j}}}. \tag{6.59}$$

Finally, the PDF of $\hat{u}_{\hat{k}}$, over $\boldsymbol{q} \in \mathcal{A}_{\boldsymbol{q}}$, is given by

$$f_{\hat{u}_{\hat{k}}}(u'_{\hat{k}}) = \sum_{j=1}^{N_{\hat{u}_{\hat{k}}}} \mathrm{P}(\hat{u}_{\hat{k},j}) \cdot \delta(u'_{\hat{k}} - \hat{u}_{\hat{k},j}). \tag{6.60}$$

Now, we proceed to obtain analytic formulations of the above-mentioned parameters $N_{c_{\hat{k}}}, c_{\hat{k},\hat{l}}, \mathcal{A}_{c_{\hat{k}}}$, and $N_{c_{\hat{k},\hat{l}}}$ which are needed to determine the the PDF of $\hat{u}_{\hat{k}}$, over $\boldsymbol{q} \in \mathcal{A}_{\boldsymbol{q}}$ per (6.60).

We start by attempting to gain some insight by observing the components terms $e^{-j\frac{2\pi \hat{k} n}{N}}$ of a simple example $N = 8$ point DFT for various specially selected values of the DFT output vector indeces $k$ with all values of the DFT input vector indeces $n$ as shown in Figure 6.13.

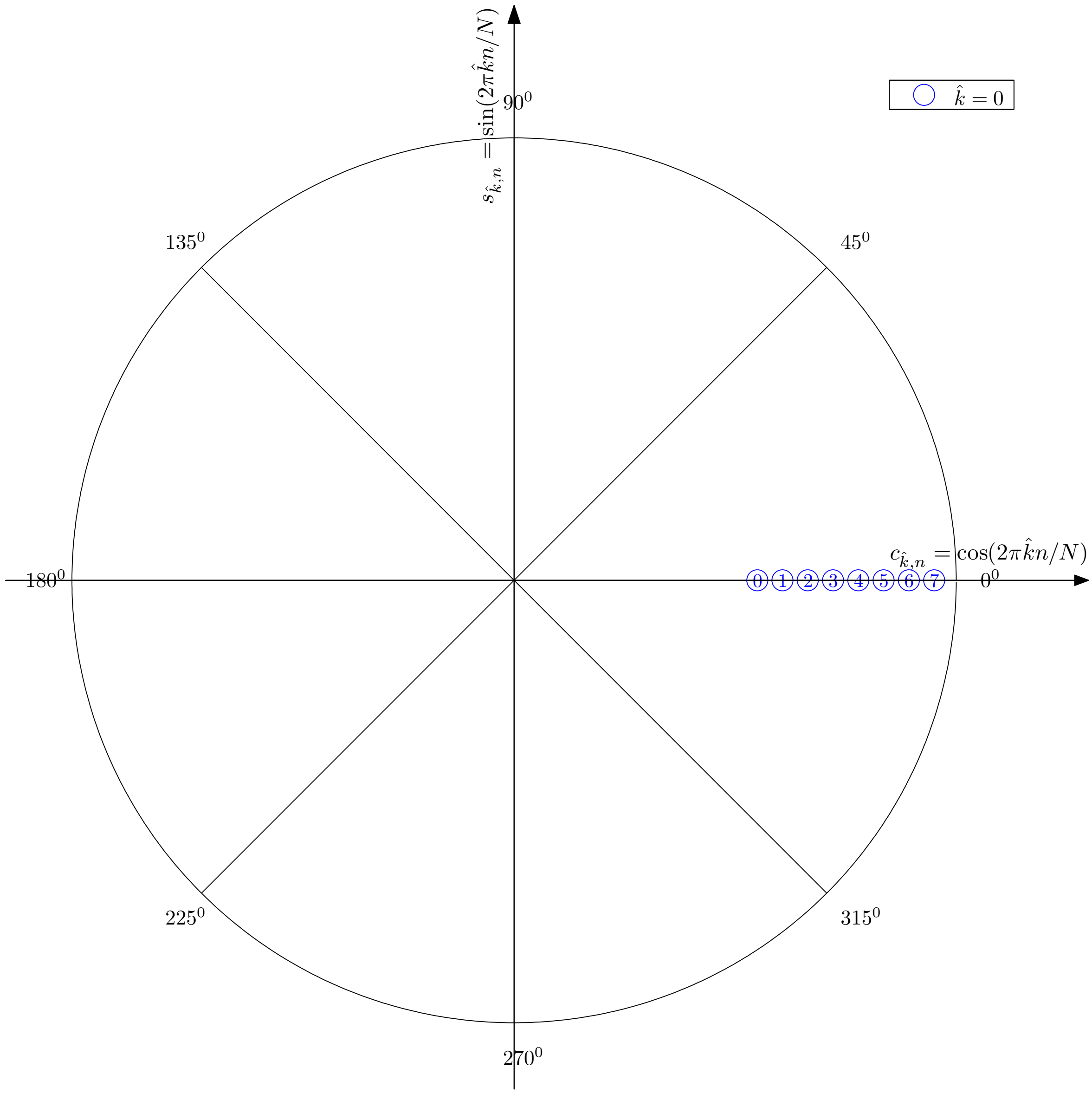


(a) $\hat{k} = 0$.

Figure 6.13: $e^{-j\frac{2\pi\hat{k}n}{N}}$ on the complex plane for $N = 8, n \in \mathbb{Z}_N$, various $\hat{k}$.

NOTES:

(1) $|e^{-j\frac{2\pi\hat{k}n}{N}}| = 1$ always but, for the sake of clarity, is not shown to scale in the figure.

(2) $\hat{k}$ is indicated by the colour and marker shape, and $n$ is indicated by the numbers inside the markers.

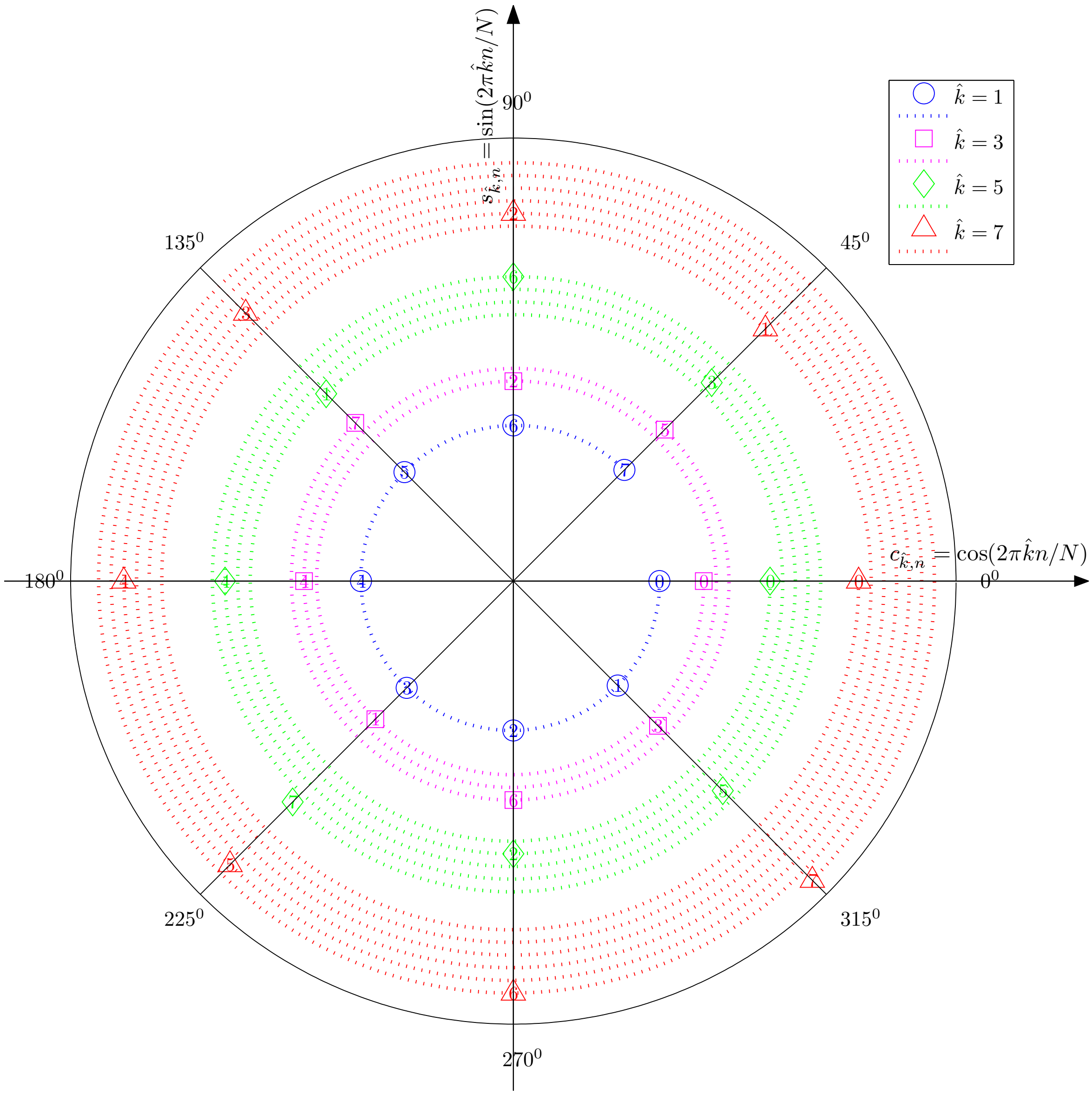


(b) $\hat{k} \in \hat{\mathcal{K}}_0 = \{1, 3, 5, 7\}$.

Figure 6.13: $e^{-j\frac{2\pi\hat{k}n}{N}}$ on the complex plane for $N = 8, n \in \mathbb{Z}_N$, various $\hat{k}$.

NOTES:

(1) $|e^{-j\frac{2\pi\hat{k}n}{N}}| = 1$ always but, for the sake of clarity, is not shown to scale in the figure.

(2) $\hat{k}$ is indicated by the colour and marker shape, and $n$ is indicated by the numbers inside the markers.

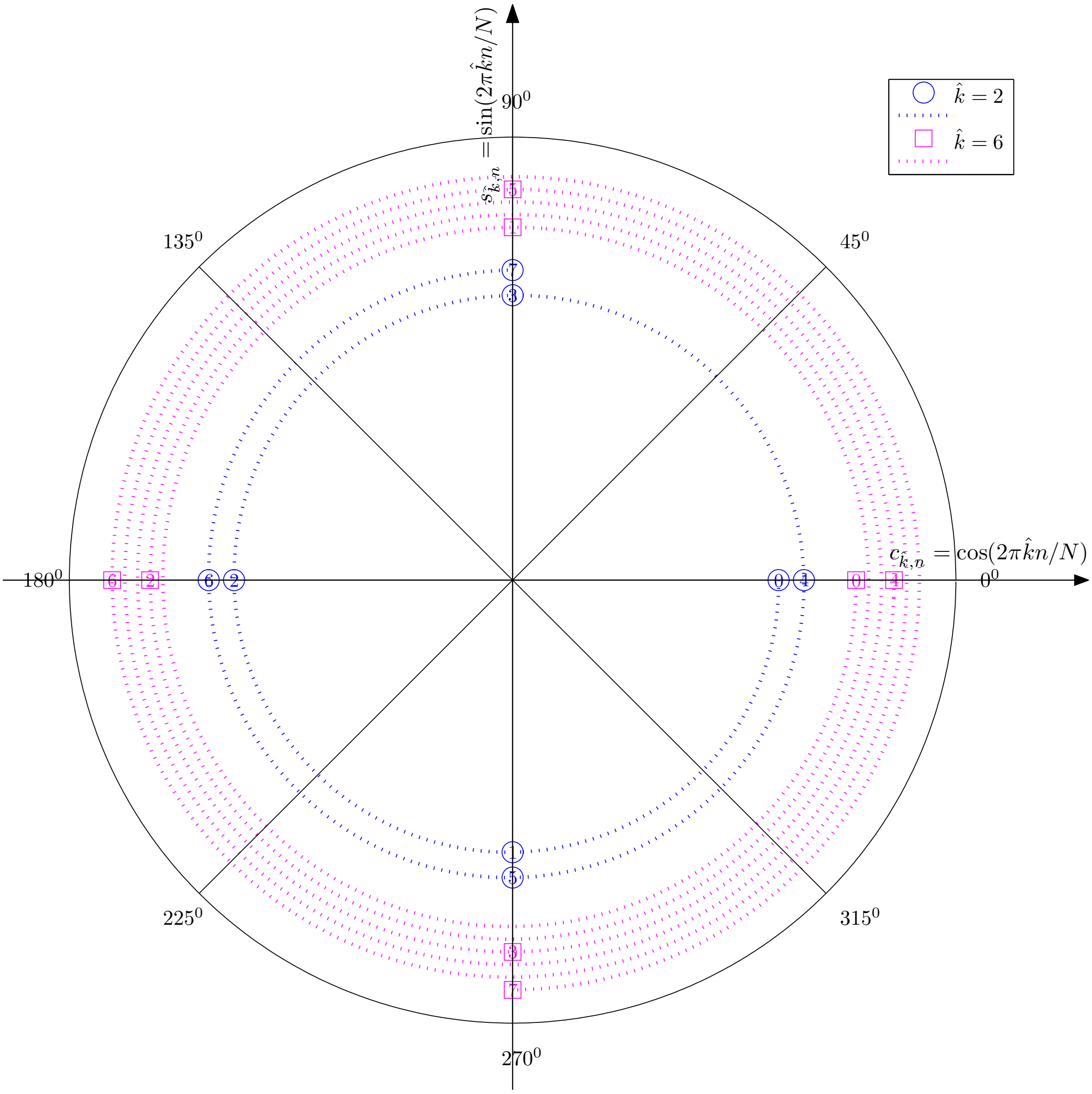


(c) $\hat{k} \in \hat{\mathcal{K}}_1 = \{2, 6\}$.

Figure 6.13: $e^{-j\frac{2\pi\hat{k}n}{N}}$ on the complex plane for $N = 8, n \in \mathbb{Z}_N$, various $\hat{k}$.

NOTES:

(1) $|e^{-j\frac{2\pi\hat{k}n}{N}}| = 1$ always but, for the sake of clarity, is not shown to scale in the figure.

(2) $\hat{k}$ is indicated by the colour and marker shape, and $n$ is indicated by the numbers inside the markers.

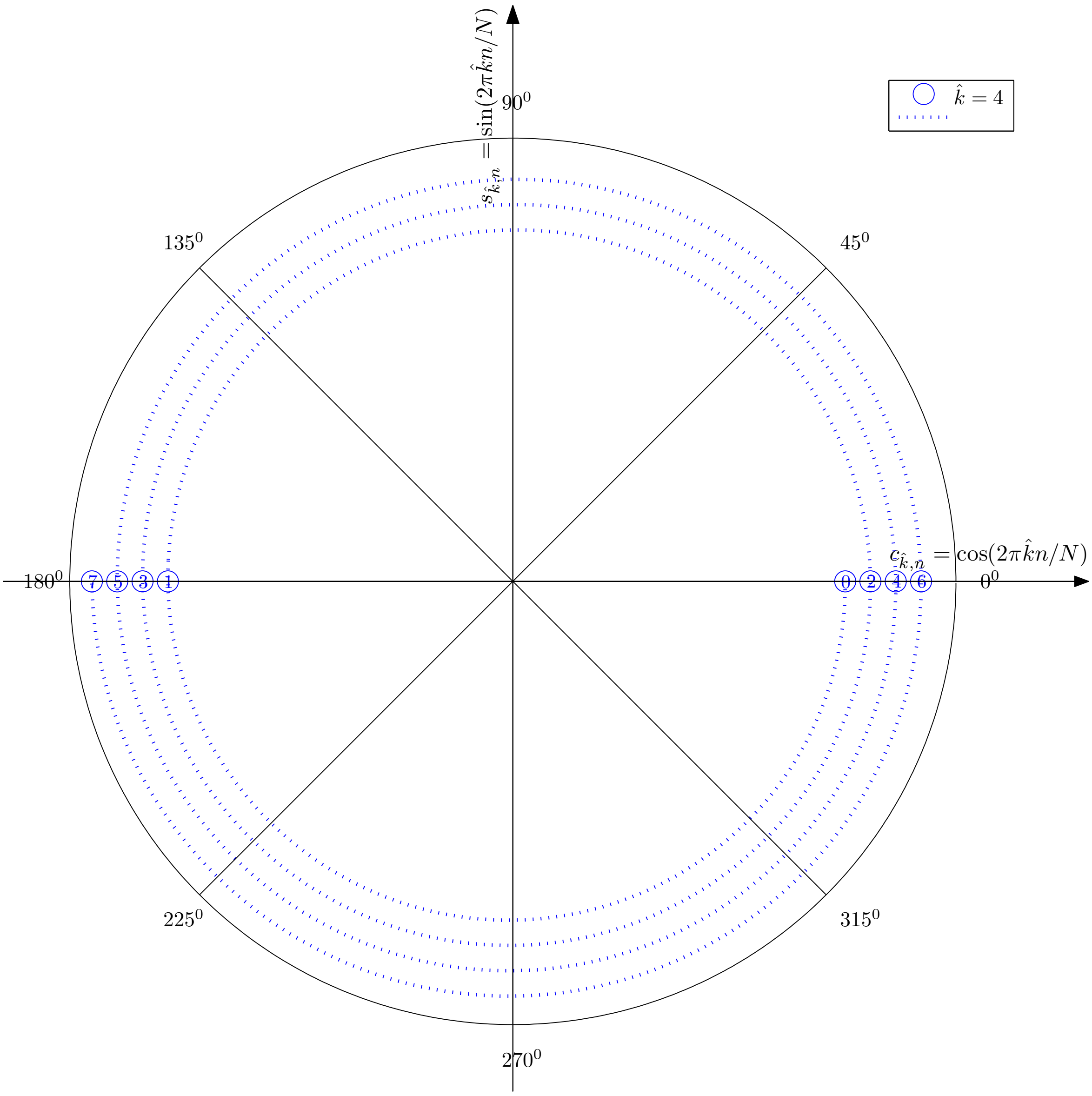


(d) $\hat{k} \in \hat{\mathcal{K}}_2 = \{4\}$.

Figure 6.13: $e^{-j\frac{2\pi\hat{k}n}{N}}$ on the complex plane for $N = 8, n \in \mathbb{Z}_N$, various $\hat{k}$.

NOTES:

(1) $|e^{-j\frac{2\pi\hat{k}n}{N}}| = 1$ always but, for the sake of clarity, is not shown to scale in the figure.

(2) $\hat{k}$ is indicated by the colour and marker shape, and $n$ is indicated by the numbers inside the markers.

In Figure 6.13a, we see that, for $\hat{k} = 0$, $e^{-j\frac{2\pi\hat{k}n}{N}} = 1$ and $c_{\hat{k},n} = 1$ for all possible values of $n$. This is true for all N and yields the following values for the required parameters:

$$\begin{aligned} N_{c_{\hat{k}}} &= 1, \quad \hat{k} = 0 && (6.61) \\ c_{\hat{k},\hat{l}} &= 1, \quad \hat{k} = 0, \hat{l} = 0 && (6.62) \\ N_{c_{\hat{k},\hat{l}}} &= N, \quad \hat{k} = 0, \hat{l} = 0 && (6.63) \\ \mathcal{N}_{c_{\hat{k},\hat{l}}} &= \mathbb{Z}_N, \quad \hat{k} = 0, \hat{l} = 0. && (6.64) \end{aligned}$$

In Figure 6.13b, we see that, for $\hat{k}$ having odd values multiplied by $2^0 = 1$ (i.e. for $\hat{k} \in \hat{\mathcal{K}}_0$, $e^{-j\frac{2\pi\hat{k}n}{N}}$ takes on $N$ different values equi-spaced with angle increments of $2\pi/N$ radians around the unit circle. As a result, $c_{\hat{k},n}$ takes on $N/2+1$ distinct values. This is true for all N.

In Figure 6.13c, we see that, for $\hat{k}$ having odd values multiplied by $2^1 = 2$ (i.e. for $\hat{k} \in \hat{\mathcal{K}}_1$), $e^{-j\frac{2\pi\hat{k}n}{N}}$ takes on $N/2$ different values equi-spaced with angle increments of $2 \cdot 2\pi/N$ radians around the unit circle. As a result, $c_{\hat{k},n}$ takes on $N/4+1$ distinct values. This is true for all N.

Lastly, in Figure 6.13d, we see that, for $\hat{k}$ having odd values multiplied by $2^2 = 4$ (i.e. for $\hat{k} \in \hat{\mathcal{K}}_2$, $e^{-j\frac{2\pi\hat{k}n}{N}}$ takes on $N/4$ different values equi-spaced with angle increments of $4 \cdot 2\pi/N$ radians around the unit circle. As a result, $c_{\hat{k},n}$ takes on $N/8+1$ distinct values. This is true for all N.

We now generalize the results of Figure 6.13b to Figure 6.13d for any DFT size $N$ to obtain

$$\begin{aligned} N_{c_{\hat{k}}} &= N/2^{\gamma+1}+1, && \hat{k} \in \hat{\mathcal{K}}_\gamma, \gamma \in \mathbb{Z}_{\log_2(N/2)+1} && (6.65) \\ c_{\hat{k},\hat{l}} &= \cos(2\pi \cdot 2^\gamma \hat{l}/N), && \hat{k} \in \hat{\mathcal{K}}_\gamma, \gamma \in \mathbb{Z}_{\log_2(N/2)+1} && (6.66) \\ N_{c_{\hat{k},\hat{l}}} &= \left\{ \begin{array}{ll} 2^\gamma, & \hat{l} = 0 \\ 2^\gamma, & \hat{l} = N/2^{\gamma+1} \\ 2^{\gamma+1}, & \text{otherwise} \end{array} \right\}, && \hat{k} \in \hat{\mathcal{K}}_\gamma, \gamma \in \mathbb{Z}_{\log_2(N/2)+1}. && (6.67) \end{aligned}$$

where $\hat{\mathcal{K}}_\gamma$ is the set of DFT output indeces $\hat{k}$ having odd values multiplied by $2^\gamma$ formally defined as

$$\hat{\mathcal{K}}_\gamma \triangleq \{\hat{k} : \hat{k} = 2^\gamma \cdot z, \quad z \text{ is odd}, \quad 0 < z < N/2^\gamma\}. \tag{6.68}$$

Now, we will find, for $\hat{k} \in \hat{\mathcal{K}}\gamma$, the set $\mathcal{N}_{c_{\hat{k},\hat{l}}}$ of time-indeces $n$ of the DFT input vector entries $q_n$ for which $\cos\left(\frac{2\pi\hat{k}n}{N}\right) = c_{\hat{k},\hat{l}}$.

First, we define the set of all indeces of the entries $\hat{u}_{\hat{k}}$ of the real part of complex $N$-point DFT output vector $\hat{\boldsymbol{u}}$ to be

$$\hat{\mathcal{K}} \;\triangleq\; \mathbb{Z}_N. \tag{6.69}$$

We then compose the set of indeces $\hat{\mathcal{K}}$ as the union of the single-element zero-set $\{0\}$ and multiple sets of odd numbers multiplied by powers of 2 as follows

$$\begin{aligned}
\hat{\mathcal{K}} &= \{0\} \;\cup\; \{\hat{k} : \hat{k} = 2^0 \cdot z, \quad z \text{ is odd}, \quad 0 < 2^0 \cdot z < N\} \\
&\qquad\quad\; \cup\; \{\hat{k} : \hat{k} = 2^1 \cdot z, \quad z \text{ is odd}, \quad 0 < 2^1 \cdot z < N\} \\
&\qquad\quad\; \cup\; \{\hat{k} : \hat{k} = 2^2 \cdot z, \quad z \text{ is odd}, \quad 0 < 2^2 \cdot z < N\} \\
&\qquad\quad\; \vdots \\
&\qquad\quad\; \cup\; \{\hat{k} : \hat{k} = 2^{\log_2(N/2)} \cdot z, \quad z \text{ is odd}, \quad 0 < 2^{\log_2(N/2)} \cdot z < N\} \\
&= \{0\} \;\cup\; \bigcup_{\gamma=0}^{\log_2(N/2)} \{\hat{k} : \hat{k} = 2^\gamma \cdot z, \quad z \text{ is odd}, \quad 0 < z < N/2^\gamma\} \\
&= \{0\} \;\cup\; \bigcup_{\gamma=0}^{\log_2(N/2)} \hat{\mathcal{K}}_\gamma.
\end{aligned} \tag{6.70}$$

Next, we will obtain the set $\mathcal{N}_{c_{\hat{k},\hat{l}}}$, already defined in (6.43), of IDFT input time indeces $n$ which result in $c_{\hat{k},n} = c_{\hat{k},\hat{l}}$. For $\hat{k} \in \hat{\mathcal{K}}_\gamma$, (6.43) becomes

$$\begin{aligned}
\mathcal{N}_{c_{\hat{k},\hat{l}}} &= \Big\{ n : \cos\left(\tfrac{2\pi\hat{k}n}{N}\right) &&= \cos\left(\tfrac{2\pi 2^\gamma \cdot \hat{l}}{N}\right), && n \in \mathbb{Z}_N, \hat{l} \in \mathbb{Z}_{N_{c_{\hat{k}}}} \Big\}, && \hat{k} \in \hat{\mathcal{K}}_\gamma \\
&= \Big\{ n : \hat{k}n \pmod N &&\equiv \pm 2^\gamma \cdot \hat{l}, && n \in \mathbb{Z}_N, \hat{l} \in \mathbb{Z}_{N_{c_{\hat{k}}}} \Big\}, && \hat{k} \in \hat{\mathcal{K}}_\gamma \\
&= \Big\{ n : \hat{k}n &&= \pm 2^\gamma \cdot \hat{l} + pN, && n \in \mathbb{Z}_N, \hat{l} \in \mathbb{Z}_{N_{c_{\hat{k}}}}, p \in \mathbb{N}_0 \Big\}, && \hat{k} \in \hat{\mathcal{K}}_\gamma \\
&= \Big\{ n : n &&= \tfrac{\pm 2^\gamma \cdot \hat{l} + pN}{k}, && n \in \mathbb{Z}_N, \hat{l} \in \mathbb{Z}_{N_{c_{\hat{k}}}}, p \in \mathbb{N}_0 \Big\}, && \hat{k} \in \hat{\mathcal{K}}_\gamma.
\end{aligned} \tag{6.71}$$

The $\pm$ in (6.71) implies that there are two solution sets for $\mathcal{N}_{c_{\hat{k},\hat{l}}}$. The first solution set is

$$\begin{aligned}
\mathcal{N}^{(1)}_{c_{\hat{k},\hat{l}}} &= \Big\{ n : n = \tfrac{+2^\gamma \cdot \hat{l} + pN}{\hat{k}}, \quad n \in \mathbb{Z}_N, \hat{l} \in \mathbb{Z}_{N_{c_{\hat{k}}}}, p \in \mathbb{N}_0 \Big\}, && \hat{k} \in \hat{\mathcal{K}}_\gamma \\
&= \Big\{ n : n = \tfrac{+2^\gamma \cdot \hat{l} + pN}{\hat{k}}, \quad n \in \mathbb{Z}_N, \hat{l} \in \mathbb{Z}_{N_{c_{\hat{k}}}}, p \in \mathbb{Z}_{\lfloor (N-1-2^\gamma \cdot \hat{l})/N \rfloor + 1} \Big\}, && \hat{k} \in \hat{\mathcal{K}}_\gamma,
\end{aligned} \tag{6.72}$$

where $\lfloor \cdot \rfloor$ indicates the floor (round down to nearest integer) operation. The second solution set is

$$\begin{aligned}
\mathcal{N}^{(2)}_{c_{\hat{k},\hat{l}}} &= \Big\{ n : n = \tfrac{-2^\gamma \cdot \hat{l} + pN}{k}, \quad n \in \mathbb{Z}_N, \hat{l} \in \mathbb{Z}_{N_{c_{\hat{k}}}}, p \in \mathbb{N}_0 \Big\}, && \hat{k} \in \hat{\mathcal{K}}_\gamma \\
&= \left\{ \begin{array}{ll} n : n = \tfrac{-2^\gamma \cdot \hat{l} + pN}{k}, & n \in \mathbb{Z}_N, \hat{l} \in \mathbb{Z}_{N_{c_{\hat{k}}}}, \\ & p \in \{ \lceil (2^\gamma \cdot \hat{l})/N \rceil, \cdots, \lfloor (N - 1 + 2^\gamma \cdot \hat{l})/N \rfloor \} \end{array} \right\}, && \hat{k} \in \hat{\mathcal{K}}_\gamma,
\end{aligned} \tag{6.73}$$

where $\lceil \cdot \rceil$ indicates the ceil (round up to nearest integer) operation. Combining (6.72) and (6.73), we get

$$\begin{aligned}
\mathcal{N}_{c_{\hat{k},\hat{l}}} &= \mathcal{N}^{(1)}_{c_{\hat{k},\hat{l}}} \cup \mathcal{N}^{(2)}_{c_{\hat{k},\hat{l}}}, && \hat{k} \in \hat{\mathcal{K}}_\gamma \\
&= \begin{array}{l} \Big\{ n : n = \tfrac{+2^\gamma \cdot \hat{l} + pN}{\hat{k}}, \quad n \in \mathbb{Z}_N, \hat{l} \in \mathbb{Z}_{N_{c_{\hat{k}}}}, p \in \mathbb{Z}_{\lfloor (N-1-2^\gamma \cdot \hat{l})/N \rfloor + 1} \Big\} \\ \bigcup \left\{ \begin{array}{ll} n : n = \tfrac{-2^\gamma \cdot \hat{l} + pN}{\hat{k}}, & n \in \mathbb{Z}_N, \hat{l} \in \mathbb{Z}_{N_{c_{\hat{k}}}}, \\ & p \in \{ \lceil (2^\gamma \cdot \hat{l})/N \rceil, \cdots, \lfloor (N - 1 + 2^\gamma \cdot \hat{l})/N \rfloor \} \end{array} \right\}, \end{array} && \hat{k} \in \hat{\mathcal{K}}_\gamma.
\end{aligned} \tag{6.74}$$

Combining all of the above results for $\hat{k} = 0$ and $\hat{k} \in \hat{\mathcal{K}}_\gamma$, we get complete versions of the required equations

$$N_{c_{\hat{k}}} = \begin{cases} 1, & \hat{k} = 0 \\ N/2^{\gamma+1} + 1, & \hat{k} \in \hat{\mathcal{K}}_\gamma, \gamma \in \mathbb{Z}_{\log_2(N/2)+1} \end{cases} \tag{6.75}$$

$$c_{\hat{k},\hat{l}} = \begin{cases} 1, & \hat{k} = 0 \\ \cos(2\pi \cdot 2^\gamma l/N), & \hat{k} \in \hat{\mathcal{K}}_\gamma, \gamma \in \mathbb{Z}_{\log_2(N/2)+1} \end{cases} \tag{6.76}$$

$$N_{c_{\hat{k},\hat{l}}} = \begin{cases} N, & \hat{k} = 0 \\ \left\{ \begin{array}{ll} 2^\gamma, & \hat{l} = 0 \\ 2^\gamma, & \hat{l} = N/2^{\gamma+1} \\ 2^{\gamma+1}, & \text{otherwise} \end{array} \right\}, & \hat{k} \in \hat{\mathcal{K}}_\gamma, \gamma \in \mathbb{Z}_{\log_2(N/2)+1} \end{cases} \tag{6.77}$$

$$\mathcal{N}_{c_{\hat{k},\hat{l}}} = \begin{cases} \mathbb{Z}_N, & \hat{k} = 0, \hat{l} = 0 \\ \left\{ \begin{array}{l} \left\{ n : n = \frac{+2^\gamma \cdot \hat{l} + pN}{\hat{k}}, \quad n \in \mathbb{Z}_N, \hat{l} \in \mathbb{Z}_{N_{c_{\hat{k}}}}, p \in \mathbb{Z}_{\lfloor (N-1-2^\gamma \cdot \hat{l})/N \rfloor + 1} \right\} \\ \bigcup \left\{ \begin{array}{ll} n : n = \frac{-2^\gamma \cdot \hat{l} + pN}{\hat{k}}, & n \in \mathbb{Z}_N, \hat{l} \in \mathbb{Z}_{N_{c_{\hat{k}}}}, \\ & p \in \{ \lceil (2^\gamma \cdot l)/N \rceil, \cdots, \lfloor (N - 1 + 2^\gamma \cdot \hat{l})/N \rfloor \} \end{array} \right\} \end{array} \right\}, & \begin{array}{l} k \in \hat{\mathcal{K}}_\gamma, \\ \gamma \in \mathbb{Z}_{\log_2(N/2)+1}. \end{array} \end{cases} \tag{6.78}$$

Applying (6.76) to (6.78) to the previously used $N = 8$ point DFT example, we get the results of Table 6.1. These results match those shown graphically in Figure 6.13 thus validating (6.76) to (6.78).

| $\gamma$ | $N_{c_{\hat{k}}}$ | $\hat{k}$ | $\hat{l}$ | $c_{\hat{k},\hat{l}}$ | $N_{c_{\hat{k},\hat{l}}}$ | $\mathcal{N}_{c_{\hat{k},\hat{l}}}$ | | | | | | | |
|---|---|---|---|---|---|---|---|---|---|---|---|---|---|
| - | 1 | 0 | 0 | 1.0000 | 8 | 0 | 1 | 2 | 3 | 4 | 5 | 6 | 7 |
| 0 | 5 | 1 | 0 | 1.0000 | 1 | 0 | - | - | - | - | - | - | - |
| | | | 1 | 0.7071 | 2 | - | 1 | - | - | - | - | - | 7 |
| | | | 2 | 0.0000 | 2 | - | - | 2 | - | - | - | 6 | - |
| | | | 3 | -0.7071 | 2 | - | - | - | 3 | - | 5 | - | - |
| | | | 4 | -1.0000 | 1 | - | - | - | - | 4 | - | - | - |
| | | 3 | 0 | 1.0000 | 1 | 0 | - | - | - | - | - | - | - |
| | | | 1 | 0.7071 | 2 | - | - | - | 3 | - | 5 | - | - |
| | | | 2 | 0.0000 | 2 | - | - | 2 | - | - | - | 6 | - |
| | | | 3 | -0.7071 | 2 | - | 1 | - | - | - | - | - | 7 |
| | | | 4 | -1.0000 | 1 | - | - | - | - | 4 | - | - | - |
| | | 5 | 0 | 1.0000 | 1 | 0 | - | - | - | - | - | - | - |
| | | | 1 | 0.7071 | 2 | - | - | - | 3 | - | 5 | - | - |
| | | | 2 | 0.0000 | 2 | - | - | 2 | - | - | - | 6 | - |
| | | | 3 | -0.7071 | 2 | - | 1 | - | - | - | - | - | 7 |
| | | | 4 | -1.0000 | 1 | - | - | - | - | 4 | - | - | - |
| | | 7 | 0 | 1.0000 | 1 | 0 | - | - | - | - | - | - | - |
| | | | 1 | 0.7071 | 2 | - | 1 | - | - | - | - | - | 7 |
| | | | 2 | 0.0000 | 2 | - | - | 2 | - | - | - | 6 | - |
| | | | 3 | -0.7071 | 2 | - | - | - | 3 | - | 5 | - | - |
| | | | 4 | -1.0000 | 1 | - | - | - | - | 4 | - | - | - |
| 1 | 3 | 2 | 0 | 1.0000 | 2 | 0 | - | - | - | 4 | - | - | - |
| | | | 1 | 0.0000 | 4 | - | 1 | - | 3 | - | 5 | - | 7 |
| | | | 2 | -1.0000 | 2 | - | - | 2 | - | - | - | 6 | - |
| | | 6 | 0 | 1.0000 | 2 | 0 | - | - | - | 4 | - | - | - |
| | | | 1 | 0.0000 | 4 | - | 1 | - | 3 | - | 5 | - | 7 |
| | | | 2 | -1.0000 | 2 | - | - | 2 | - | - | - | 6 | - |
| 2 | 2 | 4 | 0 | 1.0000 | 4 | 0 | - | 2 | - | 4 | - | 6 | - |
| | | | 1 | -1.0000 | 4 | - | 1 | - | 3 | - | 5 | - | 7 |

Table 6.1: DFT parameters for $N = 8$ point DFT example.

Next, we proceed to gain insight into the conditions under which the sets of time-sample values can be permuted.

Referring back to Fig(6.12), we see that the entries of the complex IDFT output vector $\boldsymbol{e}$ are given by

$$\begin{aligned} e_n &= \frac{1}{\sqrt{N}} \sum_{k=0}^{N-1} d_k \cdot e^{j\frac{2\pi kn}{N}} \\ &= \frac{1}{\sqrt{N}} \sum_{k=0}^{N-1} \left[ d_{\Re,k} + j d_{\Im,k} \right] \cdot \left[ \cos\left(\frac{2\pi kn}{N}\right) + j \sin\left(\frac{2\pi kn}{N}\right) \right] \\ &= \frac{1}{\sqrt{N}} \sum_{k=0}^{N-1} \quad \left[ d_{\Re,k} \cdot \cos\left(\frac{2\pi kn}{N}\right) - d_{\Im,k} \cdot \sin\left(\frac{2\pi kn}{N}\right) \right] + \\ &\qquad\qquad j \left[ d_{\Im,k} \cdot \cos\left(\frac{2\pi kn}{N}\right) + d_{\Re,k} \cdot \sin\left(\frac{2\pi kn}{N}\right) \right]. \end{aligned} \tag{6.79}$$

Next, we define the short-hand notations

$$c_{k,n} \triangleq \cos\left(\frac{2\pi kn}{N}\right), \quad k, n \in \mathbb{Z}_N \tag{6.80}$$

and

$$s_{k,n} \triangleq \sin\left(\frac{2\pi kn}{N}\right), \quad k, n \in \mathbb{Z}_N \tag{6.81}$$

which allows (6.79) to be simplified to

$$e_n = \frac{1}{\sqrt{N}} \sum_{k=0}^{N-1} \left[ d_{\Re,k} \cdot c_{k,n} - d_{\Im,k} \cdot s_{k,n} \right] + j \left[ d_{\Im,k} \cdot c_{k,n} + d_{\Re,k} \cdot s_{k,n} \right]. \tag{6.82}$$

Taking the real part of the complex IDFT output vector $\boldsymbol{e}$ yields real vector $\boldsymbol{f}$ whose entries are then given by

$$f_n = \Re\{e_n\} = \frac{1}{\sqrt{N}} \sum_{k=0}^{N-1} \left[ d_{\Re,k} \cdot c_{k,n} - d_{\Im,k} \cdot s_{k,n} \right]. \tag{6.83}$$

The alphabet of all possible unique magnitudes $|c_{k,n}|$ of $c_{k,n}$ is

$$\mathcal{A}_{|c_{k,n}|} = \{c_{l,1}\}_{l=0}^{N/4-1}, \tag{6.84}$$

which allows (6.80) to be re-expressed as

$$c_{k,n} = \sum_{l=0}^{N/4-1} \chi_{\Re,l,k,n} \cdot c_{l,1}, \quad k,n \in \mathbb{Z}_N, \tag{6.85}$$

where

$$\chi_{\Re,l,k,n} \triangleq \begin{cases} c_{k,n}/c_{l,1}, & |c_{k,n}| = c_{l,1} \\ 0, & \text{otherwise,} \end{cases} \tag{6.86}$$

which implies

$$\chi_{\Re,l,k,n} \in \{-1, 0, +1\}. \tag{6.87}$$

Similarly, the alphabet of all possible unique magnitudes $|s_{k,n}|$ of $s_{k,n}$ is

$$\mathcal{A}_{|s_{k,n}|} = \{s_{l,1}\}_{l=0}^{N/4-1}, \tag{6.88}$$

which we note is the same as the alphabet of all possible unique magnitudes $|c_{k,n}|$ of $c_{k,n}$ in (6.84) above so that

$$\mathcal{A}_{|s_{k,n}|} = \mathcal{A}_{|c_{k,n}|}, \tag{6.89}$$

which allows (6.81) to be re-expressed as

$$s_{k,n} = \sum_{l=0}^{N/4-1} \chi_{\Im,l,k,n} \cdot c_{l,1}, \quad k,n \in \mathbb{Z}_N, \tag{6.90}$$

where

$$\chi_{\Im,l,k,n} \triangleq \begin{cases} s_{k,n}/c_{l,1}, & |s_{k,n}| = c_{l,1} \\ 0, & \text{otherwise,} \end{cases} \tag{6.91}$$

which implies

$$\chi_{\Im,l,k,n} \in \{-1, 0, +1\}. \tag{6.92}$$

Substituting (6.85) and (6.90) into (6.83), we obtain the $n^{\text{th}}$ entry of the real part of the IDFT output (i.e. the time-domain digital IF) as

$$\begin{aligned}
f_n &= \frac{1}{\sqrt{N}} \sum_{k=0}^{N-1} \left[ d_{\Re,k} \sum_{l=0}^{N/4-1} \chi_{\Re,l,k,n} \cdot c_{l,1} - d_{\Im,k} \sum_{l=0}^{N/4-1} \chi_{\Im,l,k,n} \cdot c_{l,1} \right] \\
&= \frac{1}{\sqrt{N}} \sum_{k=0}^{N-1} \sum_{l=0}^{N/4-1} \left[ d_{\Re,k} \cdot \chi_{\Re,l,k,n} - d_{\Im,k} \cdot \chi_{\Im,l,k,n} \right] \cdot c_{l,1} \\
&= \frac{1}{\sqrt{N}} \sum_{l=0}^{N/4-1} c_{l,1} \sum_{k=0}^{N-1} \left[ d_{\Re,k} \cdot \chi_{\Re,l,k,n} - d_{\Im,k} \cdot \chi_{\Im,l,k,n} \right]. \qquad (6.93)
\end{aligned}$$

Next, we note that the IDFT input vector $\boldsymbol{d}$ may take on many distinct values (letters) so that

$$\boldsymbol{d} \in \mathcal{A}_{\boldsymbol{d}} = \{\boldsymbol{d_j}\}_{j=0}^{N_{\boldsymbol{d}}-1}, \qquad (6.94)$$

where $\mathcal{A}_{\boldsymbol{d}}$ is the alphabet of $\boldsymbol{d}$, $\boldsymbol{d_j}$ is the $j^{\text{th}}$ letter of $\mathcal{A}_{\boldsymbol{d}}$, and $N_{\boldsymbol{d}}$ is the size of (number of letters in) $\mathcal{A}_{\boldsymbol{d}}$. The $k^{\text{th}}$ entry of the vector $\boldsymbol{d_j}$ is denoted $d_{j,k}$ and the $k^{\text{th}}$ entry of the real part of the vector $\boldsymbol{d_j}$ is denoted $d_{j,\Re,k}$.

Similarly, the real part $\boldsymbol{f}$ of the IDFT output vector $\boldsymbol{e}$ may take on many distinct values (letters) so that

$$\boldsymbol{f} \in \mathcal{A}_{\boldsymbol{f}} = \{\boldsymbol{f_j}\}_{j=0}^{N_{\boldsymbol{f}}-1}, \qquad (6.95)$$

where $\mathcal{A}_{\boldsymbol{f}}$ is the alphabet of $\boldsymbol{f}$, $\boldsymbol{f_j}$ is the $j^{\text{th}}$ letter of $\mathcal{A}_{\boldsymbol{f}}$, and $N_{\boldsymbol{f}}$ is the size of (number of letters in) $\mathcal{A}_{\boldsymbol{f}}$. The $n^{\text{th}}$ entry of the $j^{\text{th}}$ letter $\boldsymbol{f_j}$ of $\mathcal{A}_{\boldsymbol{f}}$ is denoted $f_{j,n}$ and, using (6.93), is given by

$$f_{j,n} = \frac{1}{\sqrt{N}} \sum_{l=0}^{N/4-1} c_{l,1} \sum_{k=0}^{N-1} \left[ d_{j,\Re,k} \cdot \chi_{\Re,l,k,n} - d_{j,\Im,k} \cdot \chi_{\Im,l,k,n} \right]. \qquad (6.96)$$

Next, we proceed to determine a general condition for recurrences of various time-samples values in various entries $f_{j,n}$ of the real part $\boldsymbol{f}$ of the IDFT output over all possible letters $\boldsymbol{f_j} \in \mathcal{A}_{\boldsymbol{f}}$ of the IDFT output. More formally, we wish to obtain that the general condition for the $n'^{\text{th}}$ entry of the $j'^{\text{th}}$ letter of $\mathcal{A}_{\boldsymbol{f}}$ equalling the $n''^{\text{th}}$ entry of the $j''^{\text{th}}$ letter of $\mathcal{A}_{\boldsymbol{f}}$.

The general condition for the $n'^{\text{th}}$ entry of the $j'^{\text{th}}$ letter of $\mathcal{A}_{\boldsymbol{f}}$ equalling the $n''^{\text{th}}$

entry of the $j''^{\text{th}}$ letter of $\mathcal{A}_{\boldsymbol{f}}$ is

$$
\begin{aligned}
& f_{j',n'} = f_{j'',n''} \text{ when } \cdots \\
& \frac{1}{\sqrt{N}} \sum_{l=0}^{N/4-1} c_{l,1} \sum_{k=0}^{N-1} \left[ d_{j',\Re,k} \cdot \chi_{\Re,l,k,n'} - d_{j',\Im,k} \cdot \chi_{\Im,l,k,n'} \right] \\
= \; & \frac{1}{\sqrt{N}} \sum_{l=0}^{N/4-1} c_{l,1} \sum_{k=0}^{N-1} \left[ d_{j'',\Re,k} \cdot \chi_{\Re,l,k,n''} - d_{j'',\Im,k} \cdot \chi_{\Im,l,k,n''} \right] \\
\Leftrightarrow \; & \sum_{l=0}^{N/4-1} c_{l,1} \sum_{k=0}^{N-1} [ \quad d_{j',\Re,k} \cdot \chi_{\Re,l,k,n'} - d_{j',\Im,k} \cdot \chi_{\Im,l,k,n'} \\
& \qquad - d_{j'',\Re,k} \cdot \chi_{\Re,l,k,n''} + d_{j'',\Im,k} \cdot \chi_{\Im,l,k,n''} ] = 0 \\
\Leftrightarrow \; & \sum_{l=0}^{N/4-1} c_{l,1} \cdot D_{l,j',n',j'',n''} = 0,
\end{aligned}
\tag{6.97}
$$

where

$$
D_{l,j',n',j'',n''} \triangleq \sum_{k=0}^{N-1} [d_{j',\Re,k} \cdot \chi_{\Re,l,k,n'} - d_{j',\Im,k} \cdot \chi_{\Im,l,k,n'} - d_{j'',\Re,k} \cdot \chi_{\Re,l,k,n''} + d_{j'',\Im,k} \cdot \chi_{\Im,l,k,n''}]. \tag{6.98}
$$

Now, let us analyse (6.98) further. First, we note that, for $d_{j,\Re,k}$ and $d_{j,\Im,k}$ being the real part and imaginary part respectively of QAM signals, we obtain

$$
d_{j,\Re,k}, \quad d_{j,\Im,k} \quad \in \{\text{odd integers}\} \in \mathbb{Z}, \quad \forall j, k, \tag{6.99}
$$

where $\mathbb{Z}$ is the set of integers. Note that, if the $d_{j,\Re,k}$ and $d_{j,\Im,k}$ of (6.99) were both multiplied by a constant, say for power setting of the OFDM digital IF signal, it would have no effect on (6.97); so the constant is omitted here and elsewhere for added clarity.

Next, we note from (6.87) and (6.92) that

$$
\chi_{\Re,l,k,n}, \quad \chi_{\Im,l,k,n} \quad \in \mathbb{Z}, \quad \forall l, k, n. \tag{6.100}
$$

Therefore, using (6.99), (6.100), and the property of $\mathbb{Z}$ being closed under the operations of addition and multiplication, we obtain

$$D_{l,j',n',j'',n''} \in \mathbb{Z}, \quad \forall l, j', n', j'', n''. \tag{6.101}$$

Next, we note [9] that the only rational values of $\cos(\theta), \theta < \pi/2$ are

$$\cos(\theta) = \begin{cases} 1, & \theta = 0 \\ 1/2, & \theta = \pi/6, \end{cases} \tag{6.102}$$

and, therefore, the values of $c_{l,1}$ in (6.97) are described by

$$c_{l,1} = \cos(2\pi l/N) \in \left\{ \begin{array}{ll} \mathbb{Q}, & l = 0 \\ \mathbb{Q}^C, & l \in \{1, \cdots, N/4-1\} \end{array} \right\}, N \in \{\text{power of } 2\}, \tag{6.103}$$

where $\mathbb{Q}$ is the set of rational numbers, $\mathbb{Q}^C$ is the set of irrational numbers, and the condition $N \in \{\text{power of } 2\}$ is imposed for all IDFT operations realized by an IFFT (Inverse Fast Fourier Transform) which corresponds to all of our cases under consideration. In summary, (6.103) states that $c_{l,1}$ is only rational when $l = 0$ and is irrational when $l \neq 0$.

Applying (6.101) and (6.103) to (6.97), (6.97) we then ascertain that the general condition for the $n'^{\text{th}}$ entry of the $j'^{\text{th}}$ letter of $\mathcal{A}_{\boldsymbol{f}}$ equalling the $n''^{\text{th}}$ entry of the $j''^{\text{th}}$ letter of $\mathcal{A}_{\boldsymbol{f}}$ is simplified to

$$\begin{aligned} f_{j',n'} &= f_{j'',n''} \text{ when} \cdots \\ D_{l,j',n',j'',n''} &= 0, \quad \forall l, \end{aligned} \tag{6.104}$$

which, by substituting (6.98) into (6.104), is expanded to

$$\begin{aligned}
& f_{j',n'} = f_{j'',n''} \text{ when} \cdots \\
& \sum_{k=0}^{N-1} [\quad d_{j',\Re,k} \cdot \chi_{\Re,l,k,n'} - d_{j',\Im,k} \cdot \chi_{\Im,l,k,n'} \\
& \qquad - d_{j'',\Re,k} \cdot \chi_{\Re,l,k,n''} + d_{j'',\Im,k} \cdot \chi_{\Im,l,k,n''}] = 0, \quad \forall l
\end{aligned} \tag{6.105}$$

$$\begin{aligned}
\Leftrightarrow \quad & \sum_{k=0}^{N-1} [d_{j',\Re,k} \cdot \chi_{\Re,l,k,n'} - d_{j',\Im,k} \cdot \chi_{\Im,l,k,n'}] \\
= & \sum_{k=0}^{N-1} [d_{j'',\Re,k} \cdot \chi_{\Re,l,k,n''} - d_{j'',\Im,k} \cdot \chi_{\Im,l,k,n''}], \quad \forall l
\end{aligned} \tag{6.106}$$

$$\begin{aligned}
\Leftrightarrow \quad & \sum_{k=0}^{N-1} [\mathrm{sgn}(\chi_{\Re,l,k,n'}) \cdot d_{j',\Re,k} \cdot |\chi_{\Re,l,k,n'}| - \mathrm{sgn}(\chi_{\Im,l,k,n'}) \cdot d_{j',\Im,k} \cdot |\chi_{\Im,l,k,n'}|\,] \\
= & \sum_{k=0}^{N-1} [\mathrm{sgn}(\chi_{\Re,l,k,n''}) \cdot d_{j'',\Re,k} \cdot |\chi_{\Re,l,k,n''}| - \mathrm{sgn}(\chi_{\Im,l,k,n''}) \cdot d_{j'',\Im,k} \cdot |\chi_{\Im,l,k,n''}|\,], \quad \forall l.
\end{aligned} \tag{6.107}$$

$$\begin{aligned}
\Leftrightarrow \quad & \sum_{k=0}^{N-1} [\tilde{d}_{j',\Re,k} \cdot |\chi_{\Re,l,k,n'}| + \tilde{d}_{j',\Im,k} \cdot |\chi_{\Im,l,k,n'}|\,] \\
= & \sum_{k=0}^{N-1} [\tilde{d}_{j'',\Re,k} \cdot |\chi_{\Re,l,k,n''}| + \tilde{d}_{j'',\Im,k} \cdot |\chi_{\Im,l,k,n''}|\,], \quad \forall l,
\end{aligned} \tag{6.108}$$

where,

$$\tilde{d}_{j,\Re,k} \triangleq \mathrm{sgn}(\chi_{\Re,l,k,n}) \cdot d_{j,\Re,k} \tag{6.109}$$

and

$$\tilde{d}_{j,\Im,k} \triangleq -\mathrm{sgn}(\chi_{\Im,l,k,n}) \cdot d_{j,\Im,k}. \tag{6.110}$$

Now,

$$d_{j,\Re,k} \in \begin{cases} \mathcal{A}_{\sqrt{\mathrm{M}}\mathrm{PAM}}, & \text{MQAM modulations} \\ \mathcal{A}_{\mathrm{MPAM}}, & \text{MPAM modulations,} \end{cases} \tag{6.111}$$

and

$$d_{j,\Im,k} \begin{cases} \in \mathcal{A}_{\sqrt{\mathrm{M}}\mathrm{PAM}}, & \text{MQAM modulations} \\ = 0, & \text{MPAM modulations,} \end{cases} \tag{6.112}$$

where $\mathcal{A}_{\sqrt{\mathrm{M}}\text{-PAM}} \in \{\text{odd integers}\}$ is the $\sqrt{\mathrm{M}}$-PAM modulation symbol alphabet and $\mathcal{A}_{\mathrm{MPAM}} \in \{\text{odd integers}\}$ is the MPAM modulation symbol alphabet.

We note that, from (6.112), for MPAM (including BPSK) modulations, $d_{j,\Im,k} = 0$ so that (6.108) simplifies to

$$\begin{aligned} & f_{j',n'} = f_{j'',n''} \text{ when} \cdots \\ & \sum_{k=0}^{N-1} \left[ \tilde{d}_{j',\Re,k} \cdot |\chi_{\Re,l,k,n'}| \right] = \sum_{k=0}^{N-1} \left[ \tilde{d}_{j'',\Re,k} \cdot |\chi_{\Re,l,k,n''}| \right], \quad \forall l, \text{ MPAM modulation.} \end{aligned} \tag{6.113}$$

Now, since the elements of both $\mathcal{A}_{\sqrt{\mathrm{M}}\mathrm{PAM}}$ and $\mathcal{A}_{\mathrm{MPAM}}$ are symmetric about zero, it then follows that the transformations of (6.109) and (6.110) result in

$$\tilde{d}_{j,\Re,k} \begin{cases} \in \mathcal{A}_{\sqrt{\mathrm{M}}\mathrm{PAM}}, & \text{MQAM modulation,} \quad \mathrm{sgn}(\chi_{\Re,l,k,n}) = \pm 1 \\ \in \mathcal{A}_{\mathrm{MPAM}}, & \text{MPAM modulation,} \quad \mathrm{sgn}(\chi_{\Re,l,k,n}) = \pm 1, \\ = 0, & \mathrm{sgn}(\chi_{\Re,l,k,n}) \neq \pm 1, \end{cases} \tag{6.114}$$

and

$$\tilde{d}_{j,\Im,k} \begin{cases} \in \mathcal{A}_{\sqrt{\mathrm{M}}\mathrm{PAM}}, & \text{MQAM modulation,} \quad \mathrm{sgn}(\chi_{\Im,l,k,n}) = \pm 1 \\ = 0, & \text{MPAM modulation} \\ = 0, & \mathrm{sgn}(\chi_{\Im,l,k,n}) \neq \pm 1. \end{cases} \tag{6.115}$$

Using (6.87), we obtain

$$|\chi_{\Re,l,k,n}| \in \{0, +1\}, \tag{6.116}$$

and, using (6.92), we obtain

$$|\chi_{\Im,l,k,n}| \in \{0, +1\}. \tag{6.117}$$

Next, we define

$$S_{l,n} \triangleq \begin{cases} \displaystyle\sum_{k=0}^{N-1} |\chi_{\Re,l,k,n}| + |\chi_{\Im,l,k,n}|, & \text{MQAM modulation} \\ \displaystyle\sum_{k=0}^{N-1} |\chi_{\Re,l,k,n}|, & \text{MPAM modulation,} \end{cases} \tag{6.118}$$

and

$$\delta_p \in \begin{cases} \mathcal{A}_{\sqrt{\text{M}}\text{PAM}} \in \{\text{odd numbers}\}, & \text{MQAM modulation} \\ \mathcal{A}_{\text{MPAM}} \in \{\text{odd numbers}\}, & \text{MPAM modulation.} \end{cases} \tag{6.119}$$

For MQAM modulations, from (6.114) and (6.115), we see that $\tilde{d}_{j,\Re,k}$ and $\tilde{d}_{j,\Im,k}$ both are random variables which take on values from the same alphabet $\mathcal{A}_{\sqrt{\text{M}}\text{PAM}}$ and, for our current immediate purposes, may both be replaced in (6.108) by the single random variable $\delta_p$ already defined above.

For MPAM modulations, from (6.114) and (6.115), we see that $\tilde{d}_{j,\Re,k} \in \mathcal{A}_{\text{MPAM}}$; so that $\tilde{d}_{j,\Re,k}$ may be replaced by $\delta_p$; and $\tilde{d}_{j,\Im,k} = 0$.

Now, the negative form of (6.108) is

$$\begin{aligned} & f_{j',n'} \neq f_{j'',n''} \text{ when} \cdots \\ & \sum_{k=0}^{N-1} [\tilde{d}_{j',\Re,k} \cdot |\chi_{\Re,l,k,n'}| + \tilde{d}_{j',\Im,k} \cdot |\chi_{\Im,l,k,n'}|] \\ \neq & \sum_{k=0}^{N-1} [\tilde{d}_{j'',\Re,k} \cdot |\chi_{\Re,l,k,n''}| + \tilde{d}_{j'',\Im,k} \cdot |\chi_{\Im,l,k,n''}|], \quad \forall l. \end{aligned} \tag{6.120}$$

Using (6.116), (6.117), (6.118) and (6.119), we now re-express (6.120) as

$$\begin{aligned} f_{j',n'} &\neq f_{j'',n''} \text{ when} \cdots \\ \sum_{p'=1}^{S_{l,n'}} \delta_{p'} &\neq \sum_{p''=1}^{S_{l,n''}} \delta_{p''}, \quad \forall l, \quad \text{MQAM or MPAM modulations.} \end{aligned} \tag{6.121}$$

Now, since $\delta_p \in \{\text{odd numbers}\}$, it may be re-expressed as

$$\delta_p = 2\phi_p + 1, \quad \phi_p \in \mathbb{Z}, \tag{6.122}$$

so that (6.121) then becomes

$$\begin{aligned}
& f_{j',n'} \neq f_{j'',n''} \text{ when} \cdots \\
& \sum_{p'=1}^{S_{l,n'}} [2\phi_{p'} + 1] \neq \sum_{p''=1}^{S_{l,n''}} [2\phi_{p''} + 1], \quad \forall l, \quad \phi_{p'}, \phi_{p''} \in \mathbb{Z} \\
\Leftrightarrow \quad & 2\sum_{p'=1}^{S_{l,n'}} \phi_{p'} + S_{l,n'} \neq 2\sum_{p''=1}^{S_{l,n''}} \phi_{p''} + S_{l,n''}, \quad \forall l, \quad \phi_{p'}, \phi_{p''} \in \mathbb{Z} \\
\Leftrightarrow \quad & \text{Parity}\left(2\sum_{p'=1}^{S_{l,n'}} \phi_{p'} + S_{l,n'}\right) \neq \text{Parity}\left(2\sum_{p''=1}^{S_{l,n''}} \phi_{p''} + S_{l,n''}\right), \quad \forall l, \quad \phi_{p'}, \phi_{p''} \in \mathbb{Z} \\
\Leftrightarrow \quad & \text{Parity}\left(S_{l,n'}\right) \neq \text{Parity}\left(S_{l,n''}\right), \quad \forall l \\
\Leftrightarrow \quad & P_{l,n'} \neq P_{l,n''}, \quad \forall l,
\end{aligned} \tag{6.123}$$

where

$$P_{l,n} \triangleq \text{Parity}(S_{l,n}) = \begin{cases} \text{Parity}\left(\displaystyle\sum_{k=0}^{N-1} [\,|\chi_{\Re,l,k,n}| + |\chi_{\Im,l,k,n}|\,]\right), & \text{MQAM modulation} \\ \text{Parity}\left(\displaystyle\sum_{k=0}^{N-1} |\chi_{\Re,l,k,n}|\right), & \text{MPAM modulation.} \end{cases} \tag{6.124}$$

In summary, (6.123) describes a sufficient condition for the $n'^{\text{th}}$ entry of the $j'^{\text{th}}$ letter of $\mathcal{A}_{\boldsymbol{f}}$ not equalling the $n''^{\text{th}}$ entry of the $j''^{\text{th}}$ letter of $\mathcal{A}_{\boldsymbol{f}}$ and may be used to knock out a significant portion of the ineligible candidates for $f_{j',n'} = f_{j'',n''}$.

### 6.3.2 Conclusions

The discussion of the 'Combinatorics' method has provided valuable insights into the reasons for the small number of discrete states in the PDF of the transmitter quantizer output and error.

We have now carried this analysis to a point where we have laid solid groundwork and provided insight into a methodology for obtaining the exact PDF of the quantizer error. The author recommends that this groundwork be used as a basis for future work in fully developing the 'Combinatorics' method to its full potential.

# Chapter 7

# Applying Quantization to MIMO

Here, we divert slightly from the main thrust of this thesis and consider applying quantization to a non-OFDM baseband MIMO (Multiple Input Multiple Output) system. MIMO wireless systems exploit the spatial domain to provide high capacities without bandwidth expansion [41, 45]. The practical effects of quantization and automatic gain control (AGC) have been largely ignored to date and optimal quantization of MIMO systems is still an open question. A literature search reveals no relevant papers on this topic apart from the author's [35, 36]. Also, an extensive patent search revealed only two relevant patents which were heuristically based (not mathematically-based). A preliminary investigation into MIMO quantization then seems a worthy goal.

## 7.1 Simulation Case-Study: AGC and Quantization Effects in a Zero-Forcing MIMO Wireless System

We now undertake a numerical simulation case-study which considers automatic gain control (AGC) and quantization for multiple-input multiple-output (MIMO) wireless systems. We will examine the effect of clipping and quantization on capacity and bit error rate (BER), finding that even quite low resolution quantizers can perform close to the capacity of ideal unquantized systems. Results will be presented for BPSK and

$M$-ary QAM, and for 2×2, 3×3, and 4×4 MIMO configurations. We will find that, in each case, less than 6 quantizer bits are required to achieve 98% of unquantized capacity for SNRs above 15dB.

We start by proposing an AGC algorithm which assumes perfect channel state information (CSI), then use a numerical simulation approach to calculate the capacity and uncoded BER for a range of quantizer resolutions (quantizer bits). The simulations show that surprisingly low resolution quantizers can achieve close to the capacity of an unquantized system. Lastly, we examine the sensitivity to the assumption of perfect CSI.

### 7.1.1 System Description

We consider a typical MIMO system with a zero-forcing (ZF) detector (see e.g. [8, 20, 26, 30, 33]) as shown in Figure 7.1. The complex output vector $\boldsymbol{z} = [z_1, \cdots, z_{N_t}]^T$ is given by

$$\begin{aligned} \boldsymbol{z} &= \boldsymbol{W}(\boldsymbol{G}(\boldsymbol{H}\boldsymbol{x} + \boldsymbol{n}) + \boldsymbol{q}) \\ &= \boldsymbol{x} + \boldsymbol{W}(\boldsymbol{G}\boldsymbol{n} + \boldsymbol{q}), \end{aligned} \tag{7.1}$$

where

$$\boldsymbol{W} = \left((\boldsymbol{G}\boldsymbol{H})^{\mathrm{H}}\boldsymbol{G}\boldsymbol{H}\right)^{-1}(\boldsymbol{G}\boldsymbol{H})^{\mathrm{H}}, \tag{7.2}$$

and where $\boldsymbol{x} = [x_1, \cdots, x_{N_t}]^T$ is the complex transmitted symbol vector (containing BPSK or M-ary QAM symbols) with covariance matrix $\mathrm{E}[\boldsymbol{x}\boldsymbol{x}^H] = \frac{E_S}{N_t}\boldsymbol{I}_{N_t}$, $\boldsymbol{n} = [n_1, \cdots, n_{N_r}]^T$ is the i.i.d. zero-mean complex circular Gaussian noise vector with covariance matrix $\mathrm{E}[\boldsymbol{n}\boldsymbol{n}^H] = N_0\boldsymbol{I}_{N_r}$, and $\boldsymbol{q} = [q_1, \cdots, q_{N_r}]^T$ is the quantization noise vector. Also, $\boldsymbol{H} = (h_{r,t}), r \in \{1, \cdots N_r\}, t \in \{1, \cdots N_t\}$ is the flat-fading Rayleigh channel matrix with i.i.d. zero-mean unit-variance complex circular Gaussian entries $h_{r,t}$ representing the channel gain to the $r^{\text{th}}$ receiver from the $t^{\text{th}}$ transmitter, $\boldsymbol{G}$ is the diagonal AGC gain matrix whose $(r,r)^{\text{th}}$ entry $g_{r,r}$ indicates the AGC gain of the $r^{\text{th}}$ receiver, and $(\cdot)^{\mathrm{H}}$ indicates Hermitian transpose. The average signal-to-noise ratio per receive antenna is $\text{SNR} = \frac{E_S}{N_0}$.

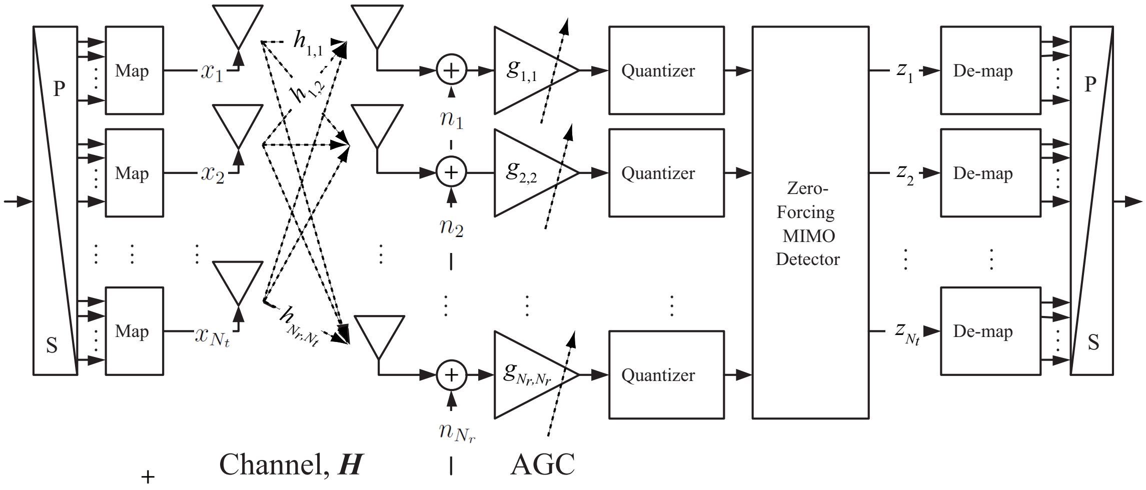


Figure 7.1: MIMO system with AGC, quantization, and zero-forcing.

### 7.1.2 AGC Description

The purpose of the AGC is to set the receiver gains $g_{r,r}, r \in \{1, \cdots, N_r\}$ to adjust the signal levels into the quantizers in order to balance between clipping errors, which result when the quantizer input levels are too high, and quantization errors which increase when the quantizer input signal levels are too low.

We start by assuming that $\boldsymbol{H}$ is known perfectly at the receiver (perfect CSI), and consider a straightforward AGC algorithm where the AGC gain $g_{r,r}$ for the $r^{\text{th}}$ receive antenna is scaled so that the magnitude of the largest received-constellation point is equal to $1/k$, where $k$ is the normalized clip level of the AGC. This choice of AGC algorithm ensures that, for $k \geq 1$, all of the received-constellation points at the AGC output will be within the normalized range $\pm 1$ regardless of the channel rotation. This is achieved by setting

$$g_{r,r} = \frac{1/k}{\max\limits_{\boldsymbol{x} \in \mathcal{A}_{\boldsymbol{x}}} \| \sum\limits_{t=1}^{N_t} h_{r,t} \cdot x_t \|} \quad , \tag{7.3}$$

where $\mathcal{A}_{\boldsymbol{x}}$ is the the transmit symbol alphabet (and also the receive symbol alphabet after zero-forcing detection). Other AGC algorithms are possible, however the purpose of this simulation case-study is to examine the effect of quantization rather than to optimize the AGC algorithm.

### 7.1.3 Quantizer Description

For each of the quantizer blocks shown in Figure 7.1, the real and imaginary components of the signal are each sampled with a finite resolution scalar uniform symmetric mid-riser quantizer [18]. The quantizer input thresholds are given by

$$u_\ell = \begin{cases} -\infty\ , & \ell = 1 \\ (\frac{-L}{2} - 1 + \ell)\Delta\ , & \ell \in \{2, \cdots, L\} \\ +\infty\ , & \ell = L+1 \end{cases} \tag{7.4}$$

where $\Delta$ is the quantizer step-size (set the same for the real and imaginary dimensions) and $L = 2^b$ is the number of quantizer levels for $b$ quantizer bits (set the same for all the quantizers). The quantizer output levels are given by

$$v_\ell = \left(\frac{-L}{2} - \frac{1}{2} + \ell\right)\Delta\ ,\ \ell \in \{1, \cdots, L\}. \tag{7.5}$$

The quantizer output clip level is the same for both real and imaginary dimensions and is given by

$$c = -v_1 = v_L = \left(\frac{L-1}{2}\right)\Delta. \tag{7.6}$$

We set $c = 1$ by setting $\Delta = \frac{2}{L-1}$. For a quantizer input $a$ and a quantizer output $q$, the quantizer function is then given by

$$q = v_\ell \quad , u_\ell \le a < u_{\ell+1} \quad , \ell \in \{1, \cdots, L\} \tag{7.7}$$

which is depicted in Figure 7.2.

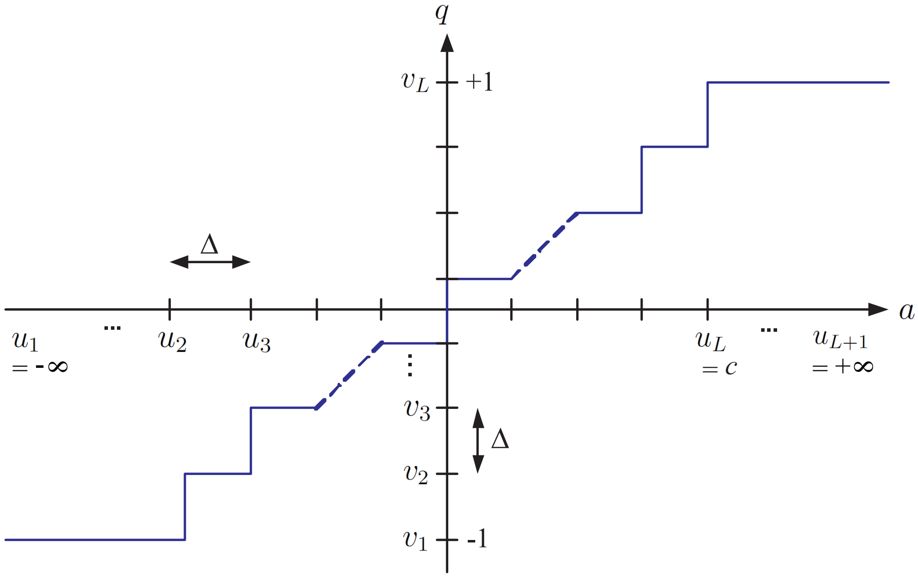


Figure 7.2: Quantizer function.

### 7.1.4 Quantized Receiver Performance

We consider performance in terms of both average input-constrained mutual information (hereafter referred to simply as capacity) and uncoded BER. The mutual information for each MIMO channel realization is given by [11]

$$\begin{aligned} \mathrm{I}(\boldsymbol{x};\boldsymbol{y}) &= \mathrm{H}(\boldsymbol{y}) - \mathrm{H}(\boldsymbol{y}|\boldsymbol{x}) \\ &= -\sum_{\boldsymbol{y}\in\mathcal{A}_{\boldsymbol{x}}} \mathrm{P}(\boldsymbol{y}) \log_2 \mathrm{P}(\boldsymbol{y}) \\ &\quad - \sum_{\boldsymbol{x}\in\mathcal{A}_{\boldsymbol{x}}} \sum_{\boldsymbol{y}\in\mathcal{A}_{\boldsymbol{x}}} \mathrm{P}(\boldsymbol{x},\boldsymbol{y}) \log_2 \mathrm{P}(\boldsymbol{y}|\boldsymbol{x}) \text{ bits/channel use,} \end{aligned} \tag{7.8}$$

where $\mathrm{H}(\cdot)$ indicates entropy, and $\mathrm{P}(\cdot)$ indicates probability. The probabilities are approximated numerically during simulations using a large number of randomly selected transmit symbols.

The ergodic capacity is given by

$$C = \mathrm{E}_{\boldsymbol{H}}\left[\mathrm{I}(\boldsymbol{x}; \boldsymbol{y})\right], \tag{7.9}$$

where $\mathrm{E}_{\boldsymbol{H}}[\cdot]$ indicates expectation over the MIMO channel $\boldsymbol{H}$ which is approximated numerically during simulations by averaging over a large number of randomly selected channel realizations.

### 7.1.5 Sensitivity to Number of Quantizer Bits

Figure 7.3 shows simulation results for the effect of the number of quantizer bits $b$ on capacity for a $2 \times 2$ MIMO system using BPSK modulation. Throughout this section we choose the normalized clip level $k = 1$ as a baseline. Later, in Section 7.1.6, we will see this is a good choice. As $b$ increases, the quantization noise $\boldsymbol{q}$ decreases due to the decreasing quantizer step-size $\Delta$ at each receiver and the capacity is dominated by the Gaussian noise $\boldsymbol{n}$ leading to a flattening of the curves. At all SNRs, the capacity reaches within 98% of its limit for $b \geq 3$ bits. Figure 7.4 shows simulation results for the effect of the number of bits $b$ on BER for the same $2 \times 2$ MIMO system using BPSK modulation. Like the capacity curves, the BER curves flatten when the BER performance is dominated by the Gaussian noise. At all SNRs, BER $< 10^{-2}$ is achieved for $b \geq 3$ bits.

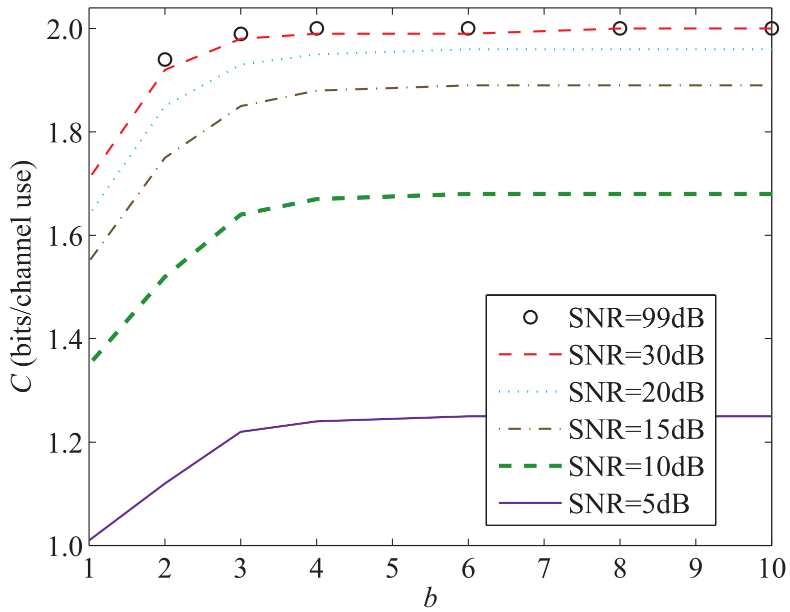


Figure 7.3: Sensitivity of capacity $C$ to number of quantizer bits $b$ for BPSK, 2x2, $k = 1$.

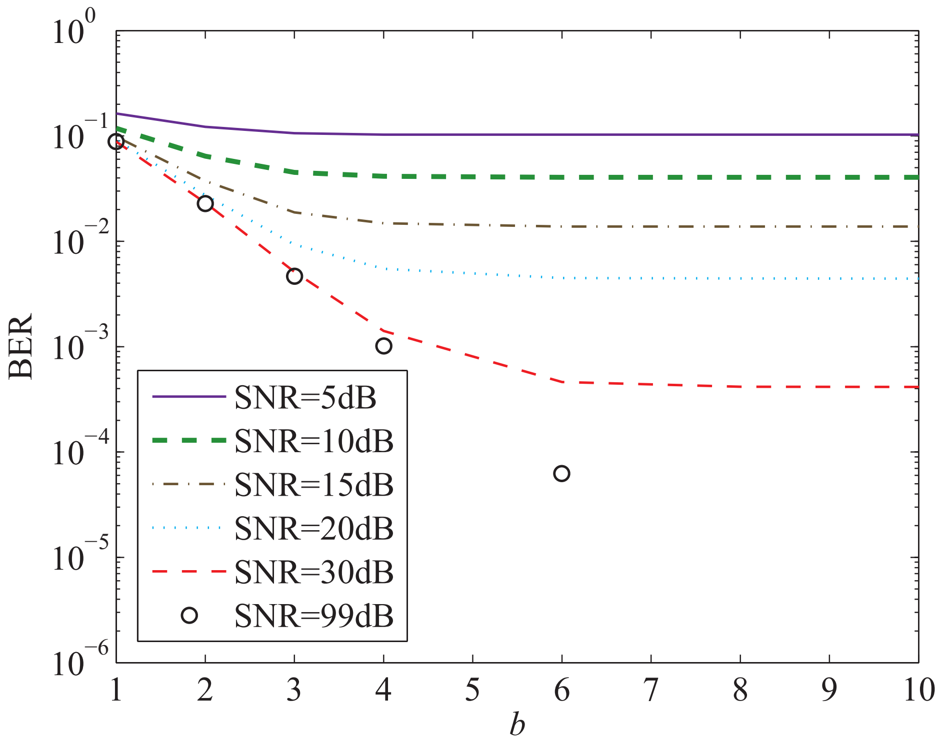


Figure 7.4: Sensitivity of uncoded BER to number of quantizer bits $b$ for BPSK, 2x2, $k = 1$.

Additional simulations were done for a range of modulation formats, antenna configurations, and SNRs. The results summarized in Table 7.1 show that a surprisingly small number of quantizer bits are required to achieve a quantized capacity within 98% of unquantized capacity. For example, consider the 4QAM $4 \times 4$ case. Note that there are 256 points in the received constellation per antenna, however we see that only 32 quantizer levels ($b = 5$) are required to achieve 98% of unquantized capacity.

| SNR (dB) | Modulation | | | | | | |
|---|---|---|---|---|---|---|---|
| | BPSK | | | 4QAM | | | 16QAM |
| | Configuration | | | Configuration | | | Configuration |
| | 2×2 | 3×3 | 4×4 | 2×2 | 3×3 | 4×4 | 2×2 |
| 15 | 3 | 4 | 4 | 4 | 4 | 5 | 5 |
| 20 | 3 | 4 | 4 | 4 | 4 | 5 | 5 |
| 25 | 3 | 4 | 4 | 4 | 4 | 5 | 5 |
| 30 | 3 | 4 | 4 | 4 | 4 | 5 | 5 |
| 35 | 3 | 4 | 4 | 3 | 4 | 4 | 5 |
| 99 | 3 | 3 | 4 | 3 | 4 | 4 | 4 |

Table 7.1: Minimum number of quantizer bits $b$ required to achieve within 98% of the unquantized system capacity (for $k$=1)

Table 7.2 shows the minimum number of quantizer bits required to achieve a target BER $< 10^{-2}$ (uncoded). Again, the numbers are surprisingly low. An X indicates that the target BER cannot be achieved with any $b$. This occurs when the BER performance is dominated by the Gaussian noise $\boldsymbol{n}$.

| SNR (dB) | Modulation | | | | | | |
|---|---|---|---|---|---|---|---|
| | BPSK | | | 4QAM | | | 16QAM |
| | Configuration | | | Configuration | | | Configuration |
| | 2×2 | 3×3 | 4×4 | 2×2 | 3×3 | 4×4 | 2×2 |
| 20 | 3 | 4 | 6 | 6 | X | X | X |
| 25 | 3 | 4 | 4 | 4 | 4 | 6 | X |
| 30 | 3 | 4 | 4 | 4 | 4 | 5 | 5 |
| 35 | 3 | 4 | 4 | 4 | 4 | 5 | 5 |
| 99 | 3 | 4 | 4 | 4 | 4 | 5 | 5 |

Table 7.2: Minimum number of quantizer bits $b$ required to achieve uncoded BER $< 10^{-2}$ for $k$=1.

### 7.1.6 Sensitivity to Imperfect CSI

Clearly, from (7.3), imperfect CSI yields incorrect AGC scaling. In this paper we investigate this effect by incorporating the channel estimation error into the normalized clip level $k$, and plotting performance as a function of $k$. Of course, since the quantizer has a fixed range (between the limits $\pm 1$), there will be an optimal value of $k$ for each $b$, however when there are channel estimation errors (imperfect CSI), this optimal value will not be known at the receiver.

Figure 7.5 shows the simulation results for capacity as a function of $k$ for various $b$ at a large SNR.

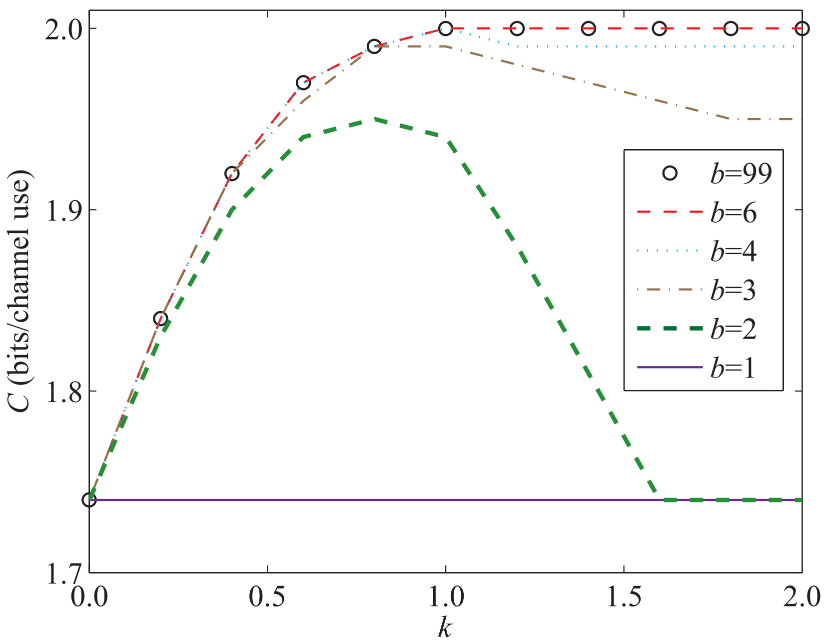


Figure 7.5: Sensitivity of capacity $C$ to quantizer normalized clip level $k$ for BPSK, 2x2, SNR=99dB.

Note that for each value of $b$, the corresponding optimal capacity is close to the capacity for $k = 1$. Also, for $k$ less than the optimal, capacity degrades quickly due to excessive clipping noise (even for large $b$). For $k$ greater than the optimal, the capacity degrades due to increasing quantization noise. Interestingly, for $b \geq 3$ the loss from choosing $k$ too large, is not as great as when $k$ is chosen too small. These trends also apply for lower SNRs, for example, as in Figure 7.6 for SNR = 10dB. A similar result occurs for the effect of $k$ on BER as shown in Figs. 7.7 and 7.8.

The conclusion therefore is that in practical MIMO systems with imperfect CSI, $k$ should be set to a value greater than one.

### 7.1.7 Conclusions

This numerical simulation study has examined the performance of practical MIMO implementations. It shows that by using a straight-forward AGC algorithm with less

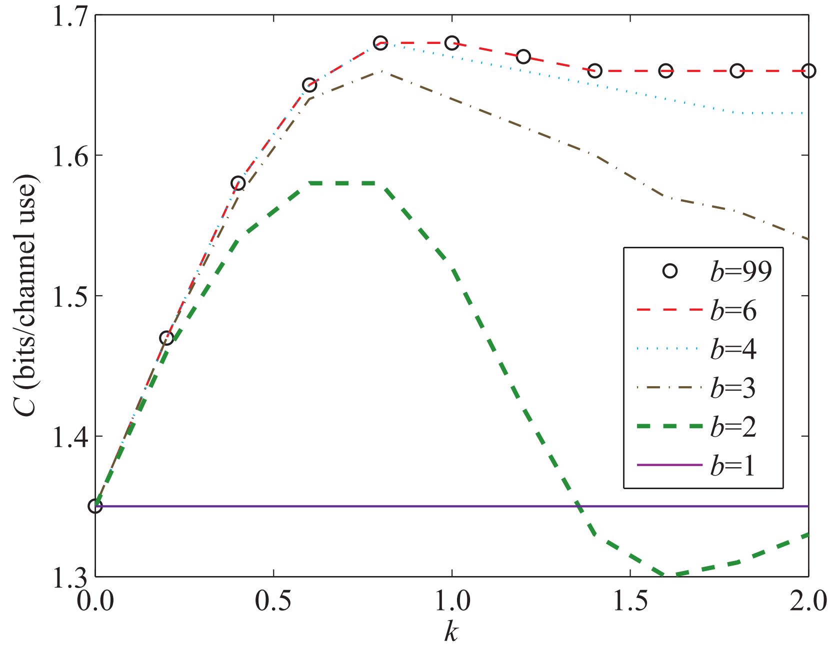


Figure 7.6: Sensitivity of capacity $C$ to quantizer normalized clip level $k$ for BPSK, 2x2, SNR=10dB.

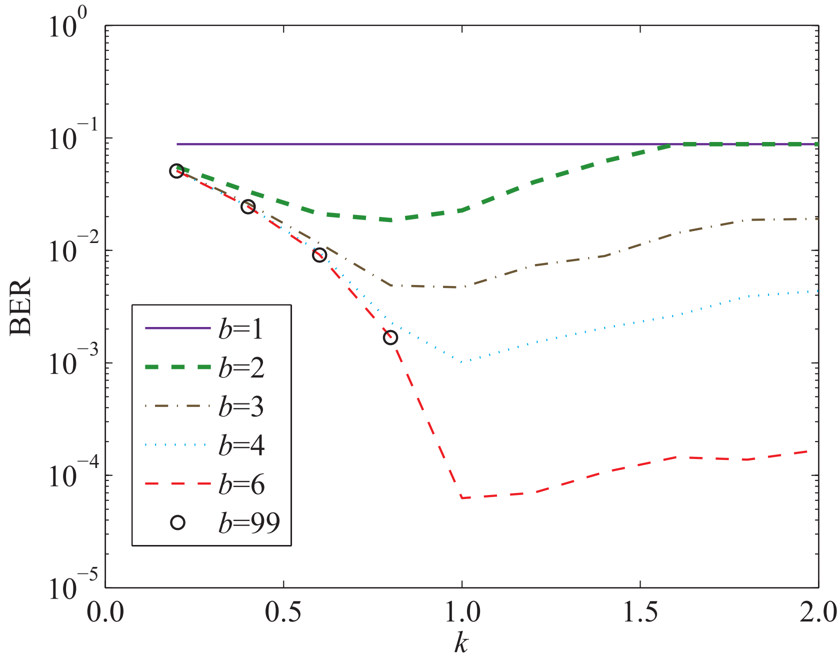


Figure 7.7: Sensitivity of uncoded BER to quantizer normalized clip level $k$ for BPSK, 2x2, SNR=99dB.

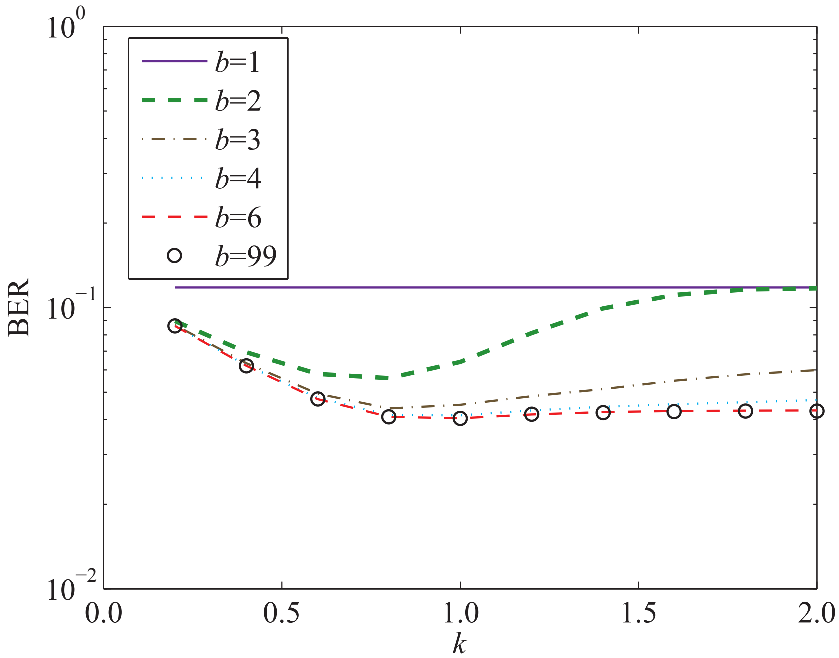


Figure 7.8: Sensitivity of uncoded BER to quantizer normalized clip level $k$ for BPSK, 2x2, SNR=10dB.

than 6 quantization bits, performance can be achieved close to unquantized capacity and at practical BER targets, for a range of MIMO configurations. It has also demonstrated that the AGC normalized clip level parameter $k$ should be increased beyond unity when the CSI is not known perfectly.

## 7.2 Simulation Case-Study: Maximizing the Cutoff Rate in a Quantized MIMO Wireless System with AGC

We now proceed to another simulation case-study where we will investigate the effects of quantization and AGC (Automatic Gain Control) in MIMO (Multiple Input Multiple Output) wireless systems. We will derive the cutoff rate equations for a deterministic MIMO channel with quantization at the receiver inputs and demonstrate by numerical simulation the dependence of the cutoff rate on the receiver AGC settings. Then we will propose a fast AGC algorithm to maximize the cutoff rate for each channel realization and use it in numerical simulations to evaluate the quantized MIMO system performance in a Rayleigh channel. We will find that even quite low resolution quantizers yield cutoff rates very close to those of equivalent unquantized systems when the fast AGC algorithm is applied. Simulation results will be presented for BPSK and QPSK modulations for a 2×2 MIMO configuration in deterministic and Rayleigh channels.

### 7.2.1 Introduction

It is now well known [45], [41] that MIMO wireless systems can be used to achieve high bandwidth efficiencies by using spatial multiplexing to transmit multiple data streams simultaneously within the same frequency spectrum. The cutoff rate [32] is an important tool for evaluating the effect of the modulator/demodulator sub-system on the error performance of coded communication systems. Practical wireless systems use quantizers to convert received analog signals into digital signals for subsequent processing and AGC to minimize the effect of quantization errors. Various studies [21], [22], [23] have evaluated the cutoff rate in unquantized MIMO systems but not in quantized systems. Other studies [32], [4] have optimized the cutoff rate in quantized SISO (Single Input Single Output) systems but not in MIMO systems. The practical effects of quantization and AGC in MIMO systems have been largely ignored to date. Here, we extend the previous work to use AGC to maximize the cutoff rate of a quantized MIMO system.

We start by deriving the equations for the cutoff rate of a general quantized MIMO system assuming perfect channel state information (CSI) at the receiver. These equations are used to determine the effect of varying the quantizer step size at each receiver on the cutoff rate for a deterministic channel. This is done for a range of quantizer resolutions (quantizer bits). A fast (sub-optimal) AGC algorithm is proposed and then applied to each realization of a MIMO Rayleigh channel. We show that surprisingly low resolution quantizers can achieve close to the cutoff rate of an unquantized system.

### 7.2.2 System Description

Consider the quantized MIMO system as shown in Figure 7.9. This leads to the system equation

$$\boldsymbol{q} = \mathcal{Q}\{\boldsymbol{y}\} = \mathcal{Q}\{\boldsymbol{w} + \boldsymbol{n}\} = \mathcal{Q}\{\boldsymbol{H}\boldsymbol{x} + \boldsymbol{n}\}, \tag{7.10}$$

where

$\boldsymbol{q} = [q_1, \cdots, q_{N_r}]^T$ is the complex quantized output symbol vector,

$\mathcal{Q}\{\cdot\}$ indicates the quantization operation,

$\boldsymbol{y} = [y_1, \cdots, y_{N_r}]^T$ is the complex unquantized output vector (with noise),

$\boldsymbol{w} = [w_1, \cdots, w_{N_r}]^T$ is the complex unquantized output vector at the receiver antennas (before noise),

$\boldsymbol{n} = [n_1, \cdots, n_{N_r}]^T$ is the i.i.d. zero-mean complex circular Gaussian noise vector with covariance matrix $\mathrm{E}[\boldsymbol{n}\boldsymbol{n}^{\mathrm{H}}] = \frac{1}{\gamma}\boldsymbol{I}_{N_r}$,

$\{\cdot\}^{\mathrm{H}}$ indicates Hermitian transpose,

$\gamma$ indicates the signal-to-noise ratio (SNR),

$\boldsymbol{H} = (h_{r,t}), r \in \{1, \cdots N_r\}, t \in \{1, \cdots, N_t\}$ is the complex channel matrix,

$h_{r,t}$ is the complex channel gain to the $r^{\text{th}}$ receiver from the $t^{\text{th}}$ transmitter,

$\boldsymbol{x} = [x_1, \cdots, x_{N_t}]^T$ is the complex transmitted symbol vector (containing BPSK or QPSK symbols) with covariance matrix $\mathrm{E}[\boldsymbol{x}\boldsymbol{x}^{\mathrm{H}}] = \frac{1}{N_t}\boldsymbol{I}_{N_t}$,

$N_r$ is the number of MIMO receivers, and

$N_t$ is the number of MIMO transmitters.

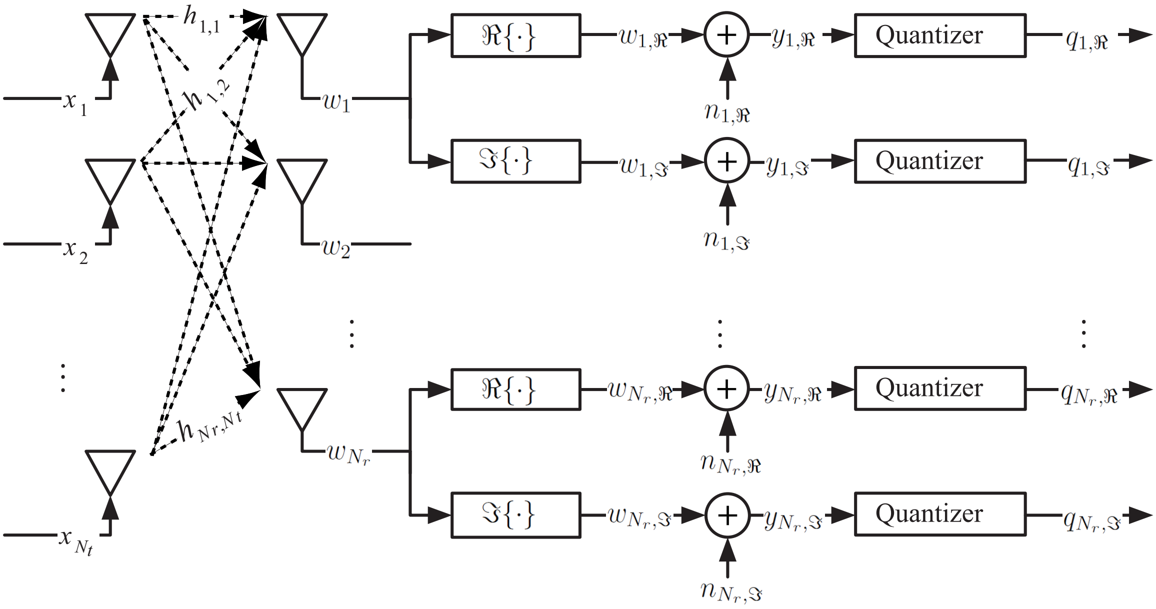


Figure 7.9: MIMO system with quantization

### 7.2.3 Quantizer Description

As shown in Figure 7.9, the real and imaginary components of the signal are each sampled with a finite resolution scalar quantizer which we choose to be a uniform symmetric mid-riser type [18]. The quantizer for complex dimension $c \in \{\Re, \Im\}$, where $\Re$ indicates real and $\Im$ indicates imaginary, of receiver $r$ will now be described. The quantizer cell boundaries are given by

$$u_{r,c,\ell_{r,c}} = \begin{cases} -\infty\ , & \ell_{r,c} = 1 \\ (\frac{-L}{2} - 1 + \ell_{r,c})\Delta_r\ , & \ell_{r,c} \in \{2, \cdots, L\} \\ +\infty\ , & \ell_{r,c} = L+1 \end{cases} \tag{7.11}$$

where $\Delta_r$ is the quantizer step-size (set the same for the real and imaginary dimensions) and $L = 2^b$ is the number of quantizer levels for $b$ quantizer bits (set the same for all the quantizers). The quantizer input clip level is the same for both real and imaginary dimensions and is given by

$$k_r = -u_{r,c,2} = u_{r,c,L} = (\frac{L}{2} - 1)\Delta_r\ , c \in \{\Re, \Im\}. \tag{7.12}$$

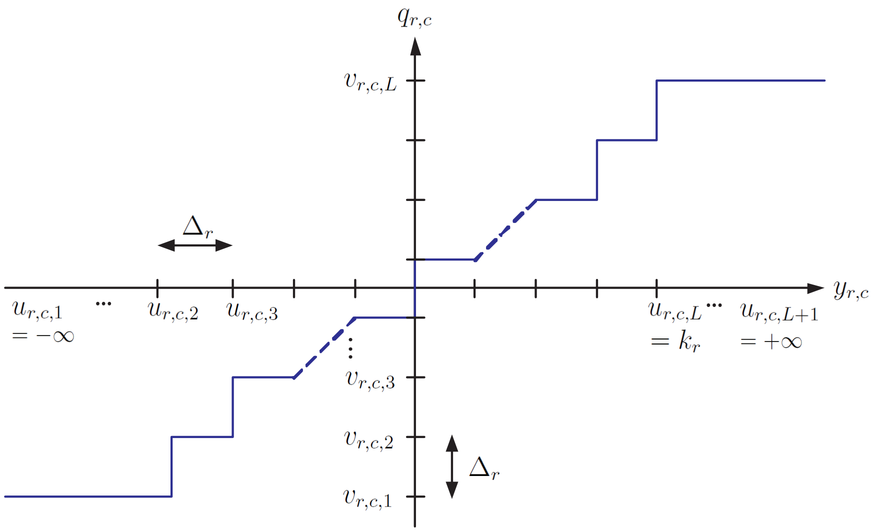


Figure 7.10: Quantizer function for receiver $r$, complex dimension $c$

The quantizer output levels are given by

$$v_{r,c,\ell_{r,c}} = (\frac{-L}{2} - \frac{1}{2} + \ell_{r,c})\Delta_r \ , \ \ell_{r,c} \in \{1, \cdots, L\}. \tag{7.13}$$

The quantizer function is then given by

$$\begin{aligned} q_{r,c} = v_{r,c,\ell_{r,c}} \quad &, \ u_{r,c,\ell_{r,c}} \leq y_{r,c} < u_{r,c,\ell_{r,c}+1} \\ &, \ \ell_{r,c} \in \{1, \cdots, L\} \end{aligned} \tag{7.14}$$

which is depicted in Figure 7.10.

### 7.2.4 MIMO Cutoff Rate

The cutoff rate $R_0$ can be used for practical finite length block codes in discrete memoryless channels to upper-bound codeword error rates after maximum likelihood decoding according to [32]

$$P_e \leq 2^{-N(R_0-R)}\ ,\ \ R < R_0 \tag{7.15}$$

where $N$ is the block length and $R = \frac{k}{n}\log_2(Z)$ is the binary code rate for a $(n,k)_Z$ block code which is defined to have $n$ information bits per block, $k$ coded bits per block and $\log_2(Z)$ code bits per channel symbol (letter) yielding a channel symbol alphabet of size $Z$. The cutoff rate is a function of the modem implementation which should be designed to maximize it. By rearranging (7.15), the cutoff rate can be used to set the operating code rate according to

$$R \leq R_0 + \frac{1}{N}\log_2([P_e]_{\text{desired}}) < R_0 \tag{7.16}$$

or to set the code block length according to

$$N \geq \frac{\log_2([\mathrm{P}_e]_{\text{desired}})}{R - R_0}\ ,\ \ R < R_0. \tag{7.17}$$

We assume a discrete memoryless channel so that the cutoff rate evaluated at the quantized output $\boldsymbol{q}$ of the system shown in Figure 7.1 is given from [32] as

$$R_0 = -\log_2 \sum_{\boldsymbol{q}\in\mathcal{A}_{\boldsymbol{q}}} \left( \sum_{\boldsymbol{x}\in\mathcal{A}_{\boldsymbol{x}}} \mathrm{P}(\boldsymbol{x})\sqrt{\mathrm{P}(\boldsymbol{q}|\boldsymbol{x})} \right)^2 \tag{7.18}$$

where $\mathcal{A}_{\boldsymbol{q}} = \{\boldsymbol{q}_1, \cdots, \boldsymbol{q}_Z\}$ is the (quantized) receive vector alphabet, $\mathcal{A}_{\boldsymbol{x}} = \{\boldsymbol{x}_1, \cdots, \boldsymbol{x}_T\}$ is the source vector alphabet, $\mathrm{P}(\boldsymbol{x})$ is the a priori probability of source symbol $\boldsymbol{x}$, and $\mathrm{P}(\boldsymbol{q}|\boldsymbol{x})$ is the probability of the quantized received symbol $\boldsymbol{q}$ conditioned on the source symbol $\boldsymbol{x}$. We assume each entry $x_j$ (corresponding to transmitter $j$) of a source symbol $\boldsymbol{x}$ is drawn from the same discrete BPSK or QPSK modulation alphabet $\mathcal{A}_x$, with

$|\mathcal{A}_x| = M$, so that the source vector alphabet $\mathcal{A}_{\boldsymbol{x}} = \mathcal{A}_x \times \mathcal{A}_x \times \cdots \times \mathcal{A}_x = (\mathcal{A}_x)^{N_t}$ is the $N_t$-factor Cartesian product of each transmitter's source alphabet; and

$$|\mathcal{A}_{\boldsymbol{x}}| = T = M^{N_t}. \tag{7.19}$$

Also, we assume the source symbols are equi-probable so that $\mathrm{P}(\boldsymbol{x}) = \frac{1}{T}$. From (7.13), the quantized receive alphabet for the quantizer at receiver $r$, complex dimension $c$ is $\mathcal{A}_{q_{r,c}} = \{v_{r,c,1}, \ \cdots \ , v_{r,c,L}\}$ and $|\mathcal{A}_{q_{r,c}}| = L$. The quantized receive vector alphabet $\mathcal{A}_{\boldsymbol{q}} = \mathcal{A}_{q_{1,\Re}} \times \mathcal{A}_{q_{1,\Im}} \times \mathcal{A}_{q_{2,\Re}} \times \mathcal{A}_{q_{2,\Im}} \times \cdots \times \mathcal{A}_{q_{N_r,\Re}} \times \mathcal{A}_{q_{N_r,\Im}}$ is the $2N_r$-factor Cartesian product of each quantizer's receive alphabet; and $|\mathcal{A}_{\boldsymbol{q}}| = Z = L^{2N_r}$. With some algebraic manipulation and using results from [27], (7.18) can be re-written as

$$R_0 = -\log_2(T) - \log_2\left(1 + \frac{2}{T}\sum_{t=1}^{T-1}\sum_{t'=t+1}^{T} S(t,t')\right) \tag{7.20}$$

where we define

$$S(t,t') \triangleq \sum_{z=1}^{Z} \sqrt{\mathrm{P}(\boldsymbol{q}_z|\boldsymbol{x}_t)\mathrm{P}(\boldsymbol{q}_z|\boldsymbol{x}_{t'})} \tag{7.21}$$

as the similarity measure for transmitted symbols $\boldsymbol{x}_t$ and $\boldsymbol{x}'_t$. Because all of the real and imaginary components of the receiver noise $\boldsymbol{n}$ are statistically independent, we can express each of the conditional probabilities of (7.21) as the product of the conditional probabilities on each receiver dimension

$$\mathrm{P}(\boldsymbol{q}|\boldsymbol{x}) = \prod_{r=1}^{N_r}\prod_{c\in\{\Re,\Im\}} \mathrm{P}(q_{r,c}|\boldsymbol{x}), \tag{7.22}$$

and (7.21) can then be rewritten as

$$S(t,t') = \sum_{\ell_{1,\Re}=1}^{L}\sum_{\ell_{1,\Im}=1}^{L}\cdots\sum_{\ell_{N_r,\Re}=1}^{L}\sum_{\ell_{N_r,\Im}=1}^{L}\prod_{r=1}^{N_r}\prod_{c\in\{\Re,\Im\}}\sqrt{\mathrm{P}(v_{r,c,\ell_{r,c}}|\boldsymbol{x}_t)\mathrm{P}(v_{r,c,\ell_{r,c}}|\boldsymbol{x}'_t)}, \tag{7.23}$$

where the probability of the ${\ell_{r,c}}^{\text{th}}$ quantizer output level of receiver $r$, complex dimension $c$ conditioned on source symbol $\boldsymbol{x}$ is

$$\mathrm{P}(v_{r,c,\ell_{r,c}}|\boldsymbol{x}) = \mathrm{Q}\left(\frac{u_{r,c,\ell_{r,c}} - [\boldsymbol{H}\boldsymbol{x}]_{r,c}}{\sigma_{r,c}}\right) - \mathrm{Q}\left(\frac{u_{r,c,\ell_{r,c}+1} - [\boldsymbol{H}\boldsymbol{x}]_{r,c}}{\sigma_{r,c}}\right), \tag{7.24}$$

where $\mathrm{Q}(x) = \int_x^\infty e^{\frac{-t^2}{2}} dt$ is the complementary cumulative distribution function and

$$\sigma_{r,c} = \frac{1}{\sqrt{2\gamma}} \tag{7.25}$$

is the standard deviation of the noise at each quantizer input. The cutoff rate $R_0$ of the quantized system can now be evaluated by substituting (7.11), (7.12), (7.19), (7.23), (7.24), and (7.25) into (7.20). We note in particular that $R_0$ is a function of the modulation alphabet at each transmitter $\mathcal{A}_x$, the vector of quantizer step-sizes at each receiver $\boldsymbol{\Delta} = [\Delta_1, \cdots \Delta_{N_r}]^T$, the number of quantizer bits $b$, the channel $\boldsymbol{H}$, and the SNR $\gamma$.

For comparison, the cutoff rate of an unquantized (infinite resolution) system is [27]

$$R_0 = -\log_2(T) - \log_2\left(1 + \frac{2}{T}\sum_{t=1}^{T-1}\sum_{t'=t+1}^{T} \exp\left(-\frac{||\boldsymbol{H}\boldsymbol{x}_t - \boldsymbol{H}\boldsymbol{x}'_t||^2}{4\sigma_n^2}\right)\right) \tag{7.26}$$

where $\sigma_n = \frac{1}{\sqrt{\gamma}}$ is the standard deviation of the noise at each receiver.

### 7.2.5 Cutoff Rate Example for a Fixed MIMO Channel

We use AGC to maximize the cutoff rate $R_0$ for each channel $\boldsymbol{H}$ in order to minimize the upper bound on the codeword error rate according to (7.15). We define the normalized quantizer clip level at receiver $r$ to be

$$\kappa_r = \frac{k_r}{\max(\max\limits_{\boldsymbol{x}\in\mathcal{A}_{\boldsymbol{x}}}([\boldsymbol{H}\boldsymbol{x}]_{r,\Re}), \max\limits_{\boldsymbol{x}\in\mathcal{A}_{\boldsymbol{x}}}([\boldsymbol{H}\boldsymbol{x}]_{r,\Im}))}. \tag{7.27}$$

That is, $\kappa_r$ is the quantizer clip level $k_r$ normalized to the maximum of the real and imaginary components of all the received constellation points at receiver $r$. The

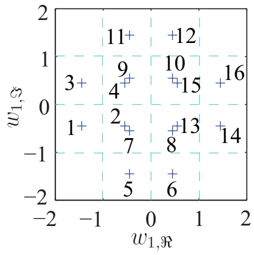


(a) Constellation at receiver 1.

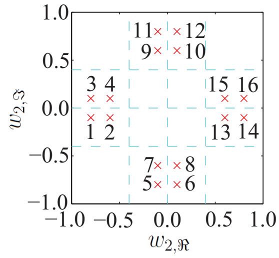


(b) Constellation at receiver 2.

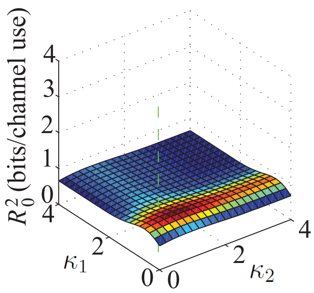


(c) $R_0^2$ vs $\kappa_1 \& \kappa_2, \gamma = 0$dB.

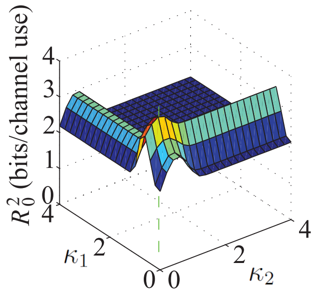


(d) $R_0^2$ vs $\kappa_1 \& \kappa_2, \gamma = 15$dB.

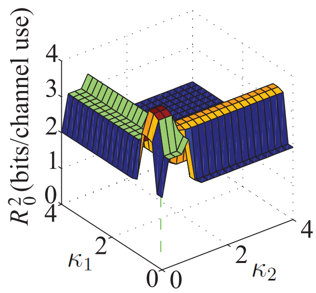


(e) $R_0^2$ vs $\kappa_1 \& \kappa_2, \gamma = 30$dB.

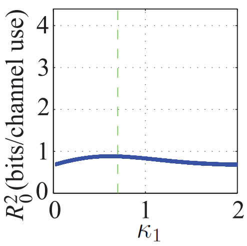


(f) $R_0^2$ vs $\kappa_1, \kappa_2 \in [0, 4], \gamma = 0$dB.

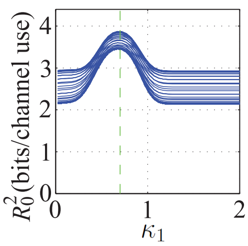


(g) $R_0^2$ vs $\kappa_1, \kappa_2 \in [0, 4], \gamma = 15$dB.

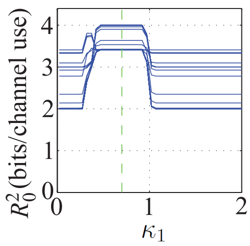


(h) $R_0^2$ vs $\kappa_1, \kappa_2 \in [0, 4], \gamma = 30$dB.

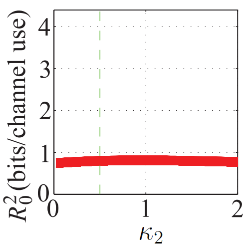


(i) $R_0^2$ vs $\kappa_2, \kappa_1 \in [0, 4], \gamma = 0$dB.

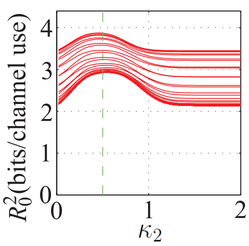


(j) $R_0^2$ vs $\kappa_2, \kappa_1 \in [0, 4], \gamma = 15$dB.

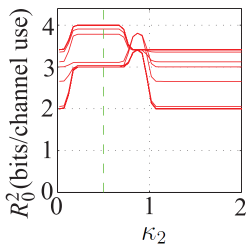


(k) $R_0^2$ vs $\kappa_2, \kappa_1 \in [0, 4], \gamma = 30$dB.

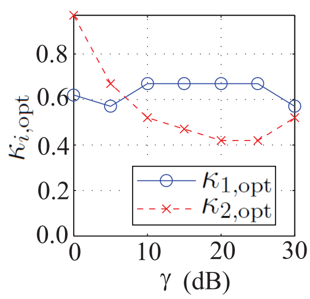


(l) Optimal normalized clip levels

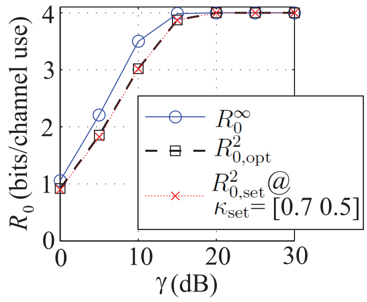


(m) Cutoff rates

Figure 7.11: Simulation results for $N_t = 2$, $N_r = 2$, $M = 4$ (QPSK), $b = 2$, and $\boldsymbol{H} = [1.0 + 1.0\text{i},\ 0.0 + 0.9\text{i}; 0.7 + 0.7\text{i},\ 0.0 + 0.2\text{i}]$.

AGC function is implemented by setting the vector of normalized quantizer clip levels $\boldsymbol{\kappa} = [\kappa_1, \cdots, \kappa_{Nr}]$ to achieve maximal cutoff rate $R_0$. Note that $\boldsymbol{\kappa}$ is related to the vector of quantizer step-sizes $\Delta$ through (7.27) and (7.12).

Figure 7.11 shows simulation results for a $2 \times 2$ QPSK MIMO system with 2 quantization bits and a fixed channel $\boldsymbol{H}$. Note that $R_0^b$ indicates the cutoff rate when all quantizers use $b$ bits and $R_0^\infty$ indicates the cutoff rate for an unquantized (infinite resolution) system. The received signal constellations (before noise) are shown in Figure 7.11(a) and (b). The dependence of the cutoff rate $R_0^2$ on the normalized clip levels $\boldsymbol{\kappa}$ is shown in Figure 7.11(c) to (k). For low SNRs ($\gamma$ = 0dB), $R_0^2$ is quite tolerant to variations in $\boldsymbol{\kappa}$ as seen in Figure 7.11(c), (f), and (i). For intermediate SNRs ($\gamma$ = 15dB), a clear optimum occurs as seen in Figure 7.11(d), (g), and (j). For high SNRs ($\gamma$ = 30dB), $R_0^2$ is again quite tolerant to variations in $\boldsymbol{\kappa}$ about the optimum as seen in Figure 7.11(e), (h), and (k). At each simulated SNR, the vector of optimal normalized clip levels $\boldsymbol{\kappa}_{\text{opt}} = [\kappa_{1,\text{opt}}\ \kappa_{2,\text{opt}}]$ was found by a rigorous search and is shown in Figure 7.11(l). The corresponding optimal cutoff rate $R_{0,\text{opt}}^2$ is shown in Figure 7.11(m) together with the cutoff rate $R_0^\infty$ for infinite resolution quantization and the cutoff rate $R_{0,\text{set}}^2$ for a fixed setting of the normalized clip levels $\boldsymbol{\kappa}_{\text{set}} = [0.7\ 0.5]$. $\boldsymbol{\kappa}_{\text{set}}$ was chosen to optimize $R_0^2$ at $\gamma$ =15dB which yields very close to optimal cutoff rates over the entire range of $\gamma$ as evidenced by the close overlap of the $R_{0,\text{opt}}$ and $R_{0,\text{set}}^2$ curves in Figure 7.11(l). $\boldsymbol{\kappa}_{\text{set}}$ is indicated by dotted lines in Figure 7.11(c) to (k) and the quantizer cell boundaries corresponding to $\boldsymbol{\kappa}_{\text{set}}$ are indicated by dotted lines in Figure 7.11(a) and (b). The results shown in Figure 7.11 were for a particular channel $\boldsymbol{H}$ which was chosen to demonstrate a cutoff rate which is highly sensitive to $\boldsymbol{\kappa}$. Generally, each different combination of the modulation order $M$, quantizer bits $b$, and the channel $\boldsymbol{H}$ yields different results for which, in most cases, $R_0$ is not as sensitive to $\boldsymbol{\kappa}$ as in Figure 7.11.

### 7.2.6 Fast AGC Algorithm

The simulations of Figure 7.11 required a 2-dimensional search over $\kappa_1$ and $\kappa_2$ to find the optimal $R_0$ for every SNR. Additional simulations showed that a fast AGC algorithm yielded close to optimal cutoff rate over the entire SNR range for numerous simulated Rayleigh channel realizations. The fast AGC algorithm consists of two 1-dimensional searches and is described as follows. a) Set $\gamma = 15$dB, b) set $\kappa_1 = 1$, c) search for optimal (maximal) $R_0$ while varying $\kappa_2$ over range 0 to 4, d) set $\kappa_2$ to its optimum value, e) search for optimal (maximal) $R_0$ while varying $\kappa_1$ over range 0 to 4, f) set $\boldsymbol{\kappa}_{set}$ with the optimal values of $\kappa_1$ and $\kappa_2$, and g) use $\boldsymbol{\kappa}_{set}$ to calculate $R_0$ at all SNRs. This fast AGC algorithm assumes perfect CSI at the receiver which is used in the calculations to optimize the cutoff rate $R_0$ for each channel $\boldsymbol{H}$.

### 7.2.7 Quantized Receiver Performance with AGC in a Rayleigh Channel

We now evaluate the performance of the quantized system with AGC in a flat-fading Rayleigh channel $\boldsymbol{H}$ with i.i.d. zero-mean unit variance complex circular Gaussian elements. We assume block-fading where each channel realization is independent of all other realizations. For each channel realization, the fast AGC algorithm described above is applied to select the AGC to achieve close to the optimal cutoff rate. The cutoff rate for the quantized system with AGC in the Rayleigh channel is formulated by using the expectation of the similarity measure over the Rayleigh channel [22] and is given by

$$R_0 = -\log_2(T) - \log_2\left(1 + \frac{2}{T}\sum_{t=1}^{T-1}\sum_{t'=t+1}^{T} \mathrm{E}_{\boldsymbol{H}}\{S(t,t')\}\right) \tag{7.28}$$

where $\mathrm{E}_{\boldsymbol{H}}\{\cdot\}$ indicates the expectation over the channel $\boldsymbol{H}$ and $S(t,t')$ is evaluated for each channel realization after applying the fast AGC algorithm. We note that $R_0$ is a function of the modulation alphabet at each transmitter $\mathcal{A}_x$ (also described by the modulation order $M$), the number of quantizer bits $b$, and the SNR $\gamma$. In our simulations, $\mathrm{E}_{\boldsymbol{H}}\{S(t,t')\}$ is numerically approximated by averaging $S(t,t')$ over a sufficiently large number of randomly selected Rayleigh channel realizations. The cutoff rate simulation results are shown in Figure 7.12. The quantization loss under the cutoff rate criterion for $b$ bits is

$$\Gamma(R) = \frac{\gamma_{|R_0^\infty = R}}{\gamma_{|R_0^b = R}}. \tag{7.29}$$

The simulation results of Figure 7.13 show that quantization losses of less than 0.6dB can be achieved over a large range of cutoff rates for only $b = 3$ quantizer bits for both BPSK ($M = 2$) and QPSK ($M = 4$) modulations. For $b = 2$ quantizer bits, the quantization loss is higher at around 1dB for low cutoff rates and rises quicker than for $b = 3$ as the cutoff rate rises for both BPSK and QPSK.

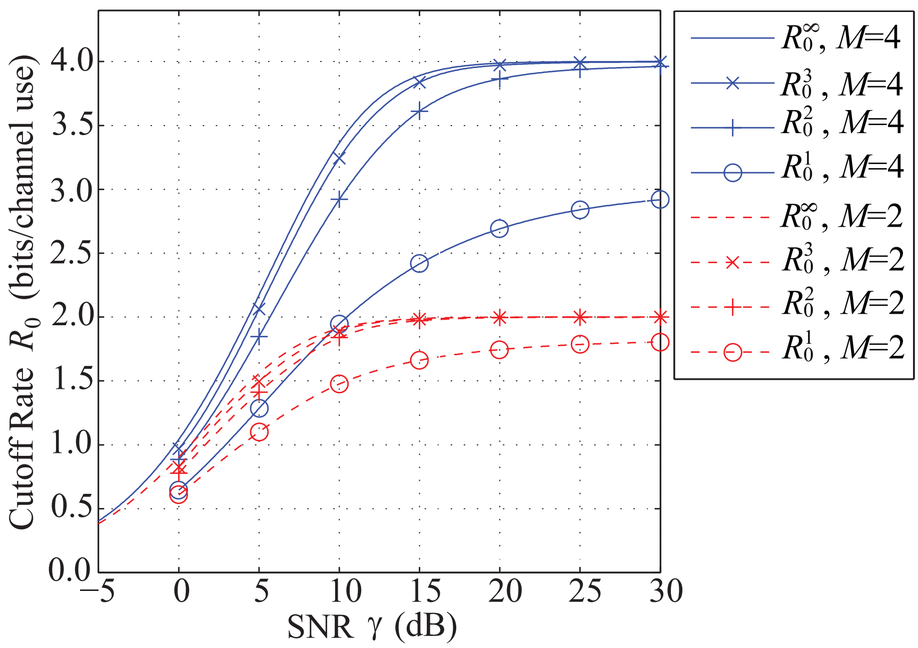


Figure 7.12: Cutoff rates in a Rayleigh $2 \times 2$ MIMO channel with AGC for BPSK ($M = 2$) and QPSK ($M = 4$) and quantizer bits $b \in \{1, 2, 3, \infty\}$.

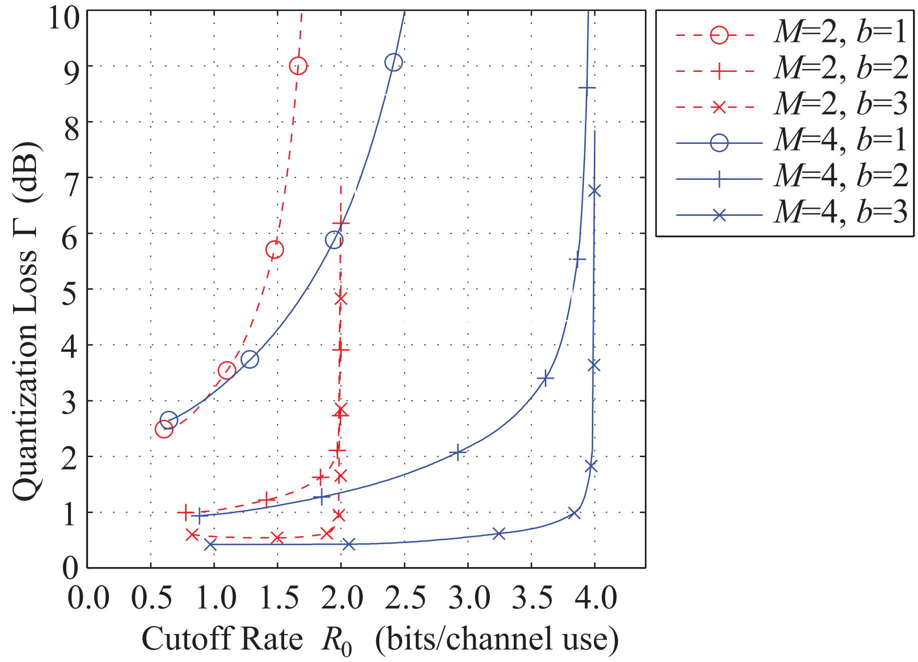


Figure 7.13: Quantization loss in a Rayleigh $2 \times 2$ MIMO channel with AGC for BPSK ($M = 2$) and QPSK ($M = 4$) and quantizer bits $b \in \{1, 2, 3\}$.

### 7.2.8 Conclusions

This simulation-study has examined the performance of practical MIMO implementations with quantization and AGC. Assuming perfect CSI at the receiver, we have derived the cutoff rate for the quantized system and used simulations to show the dependence of the cutoff rate on the normalized clip levels of the quantizers. Also, we have shown that, by using a straight-forward fast AGC algorithm, quantization losses of less than 0.6dB under the cutoff rate criterion can be achieved using only 3 quantizer bits for BPSK and QPSK modulations with a $2 \times 2$ MIMO configuration in a Rayleigh channel.

# Chapter 8

# Conclusions

## 8.1 Challenging of the Unjustified Assumptions Often Made in OFDM Quantization Analyses

In this thesis, we found that many assumptions often made in the literature regarding OFDM quantization analyses are unjustified and can lead to incorrect conclusions. We have exposed and correcting such incorrect assumptions in order to advance the state of knowledge in this important topic is a key research objective for this thesis.

The key assumptions sucessfully challenged in this thesis are as follows.

'The PDF of OFDM signals is Gaussian'. Numerous simulations have shown that in many cases the ODFM signal PDF is not Gaussian. This is most evident for small-complexity (low IDFT size) systems. However, it is still evident even for some time-samples of high-complexity OFDM systems.

'The quantization noise is Gaussian'. This has been shown to be incorrect. Even in high-complexity OFDM systems, the quantization noise can be non-Gaussian for certain combinations of number of quantization bits and clipping-factor.

'The quantization noise is independent from the quantizer input signal'. This has been shown to be incorrect. The correlation matrix simulations show that the quantization noise is correlated to the quantizer input in the cases of severe clipping and large quantizer step-size. For the case of the frequency-domain quantizer noise, the issue of correlation of the quantizer noise to the quantizer input is irrelevant since

PDFs and CDFs of the the quantizer noise have been provided and the probability of symbol errors can be directly surmised from those PDFs and CDFs.

## 8.2 The Inclusion of Clipping in OFDM Quantization Analysis

As discussed in §1.1, the inclusion of clipping is only evident in a few publications in the literature. This thesis includes clipping in its analysis and, in some cases, separates out the effects of clipping and quantization.

## 8.3 The Generation of Exact Correlation, PDF, and CDF Results, Where Possible

A large majority of the relevant literature relies on simplifying assumptions to obtain results pertaining to OFDM quantization. This thesis provides much exact analysis. This includes

- exact PDFs and CDFs for the OFDM signals before and after the quantizer for low complexity OFDM systems,

- exact PDFs and CDFs for the OFDM signals before quantizer (at the IDFT output for arbitrary-complexity OFDM systems,

- exact covariance and correlation matrices after quantizer for low-complexity OFDM systems, and

- exact covariance and correlation matrices before and after the IDFT for arbitrary-complexity OFDM systems.

## 8.4 The Provision of Reference Data for OFDM Quantization Optimization

Much of the literature does not pertain to real-world OFDM systems. This thesis provides a prodigious amount of reference data for PDFs, CDFs, covariance matrices, and correlation matrices for both small-complexity systems and larger-scale real-world OFDM systems (IEEE 802.11a). The reference data provides a benchmark against which the various claims in the literature are be tested. The reference data also provide data (in the form of PDFs and of the frequency-domain quantizer errors) from which OFDM system performance metrics (such as BER) can be derived.

## 8.5 Effect of Quantization on OFDM System BER

BER (bit error ratio or bit error rate) is an important metric of the performance of any digital communication system which indicates the ratio of errored received bits to total received bits. Figures 5.46 to 5.49 show PDFs and CDFs of the transmitter quantizer error in the receiver frequency-domain (i.e. after the receiver DFT). The author has not been able to find these kind of results elsewhere in the literature and, accordingly believes them to be an original contribution to the state-of-the-art. The significance of these results is that the receiver frequency-domain is the *decision* domain for received data and, because of this, PDFs/CDFs of received signal errors due to quantization noise and thermal noise in this domain can be used directly to obtain symbol error rates (and thence bit error rates).

Referring to, for example, Figure 5.47, we can see significant deviations from Gaussian in the receiver frequency-domain quantization error CDFs $F_u(u'')$ for the various normalized clipping factors $\kappa$. Received symbol errors would occur for any section of the PDF which exceeds the range set by the half-symbol spacing $\beta D_S/2$ as indicated by the dotted vertical blue lines on the PDF and CDF plots. The probability of a symbol error would be indicated by the value at which the CDF curve crosses the half-symbol spacing. Close examination shows that, in none of the cases shown, does the transmitter quantization error alone error cause a symbol error (because the half-symbol spacing is never exceeded). However, receiver front-end thermal noise in addition to the already discussed quantization error noise can cause symbol errors.

The addition of receiver front-end thermal noise is achieved by replacing each of the PDF diracs with a normal distribution with variance given by the thermal noise variance scaled by the probability of the original dirac. The summation of all of these normal distributions then gives the overall PDF of the combined quantization noise and thermal noise. Integration of the combined PDF yields the corresponding CDF from which symbol error rates (and thence bit error rates) can be determined from the crossing of the half-symbol distance.

Using the above technique, symbol error rates (and bit error rates) could be determined for combined quantization noise and thermal noise cases. Just as for the quantization noise-only case discussed in this thesis, the effect of a Gaussian noise approximation of the transmitter quantization noise could be determined for the combined quantization noise and thermal noise case for various OFDM types, numbers of quantization bits, thermal signal to noise ratios, etc. This is considered outside of the scope of this thesis but is recommended for future work.

## 8.6 Future Work

We have laid significant groundwork in the 'combinatorics' method in §6.3 for attempting to obtain exact PDFs and CDFs of the quantizer error frequency-sample PDFs and CDFs for arbitrary-complexity OFDM systems. Such exact PDFs and CDFs can be used to obtain exact symbol error rates which can be used in the optimization of quantization of OFDM systems.

We recommend that the 'combinatorics' method be pursued in future work.

# Bibliography

[1] IEEE standard for information technology - telecommunications and information exchange between systems - local and metropolitan area networks - specific requirements - part 11: Wireless LAN medium access control (MAC) and physical layer (PHY) specifications: High-speed physical layer in the 5 GHz band. *IEEE Std 802.11-1999*, Jan. 1999.

[2] IEEE standard for information technology - telecommunications and information exchange between systems - local and metropolitan area networks - specific requirements - part 11: Wireless LAN medium access control (MAC) and physical layer (PHY): Enhancements for higher throughput. *IEEE Std 802.11n/D1.08*, Dec. 2007.

[3] T. Araujo and R. Dinis. Performance evaluation of quantization effects on multicarrier modulated signals. *Vehicular Technology, IEEE Transactions on*, 56(5):2922 –2930, Sep. 2007.

[4] S. Baggen, S. Egner, and B. Vandewiele. Using $R_0$ for determining the quantization of the input of a viterbi decoder on fading channels. Technical report, Philips Research Laboratories, Prof. Holstlaan 4, 5656 AA Eindhoven, The Netherlands, May. 2003.

[5] Ahmad R.S. Bahai, Burton R. Salzberg, and Mustafa Ergen. *Multi-Carrier Digital Communications: Theory and Applications of OFDM.* Springer, New York, USA, 2004.

[6] Sergio Benedetto, Ezio Biglieri, and Valentino Castellani. *Digital Transmission Theory*. Prentice-Hall, Inc., Upper Saddle River, NJ, USA, 1988.

[7] J. J. Bussgang. Crosscorrelation functions of amplitude-distorted gaussian signals. Technical report, Research Laboratory of Electronics, Massachusetts Institute of Technology, Mar. 1952.

[8] M. Butler and I. B. Collings. A zero-forcing approximate log-likelihood receiver for MIMO bit-interleaved coded modulation. *IEEE Commun. Lett.*, 8(2):105–107, Feb. 2004.

[9] L. Carlitz and J. M. Thomas. Rational tabulated values of trigonometric functions. *The American Mathematical Monthly*, 69(8):789–793, Oct. 1962.

[10] Chris Cloninger and Analog Devices. Converters for 3G are optimized for cost, size and power, 2007. Online: http://www.planetanalog.com/showArticle.jhtml?articleID=184429169.

[11] T. M. Cover and J. A. Thomas. *Elements of Information Theory*. John Wiley & Sons, Inc., 1991.

[12] D. Dardari. Exact analysis of joint clipping and quantization effects in high speed WLAN receivers. In *Communications, 2003. ICC '03. IEEE International Conference on*, volume 5, pages 3487 – 3492 vol.5, May. 2003.

[13] D. Dardari. Joint clip and quantization effects characterization in OFDM receivers. *IEEE Transactions on Circuits and Systems I: Regular Papers*, 53:1741–1748, August 2006.

[14] The Free Dictionary. Combinatorics, 2012. Online: http://encyclopedia2.thefreedictionary.com/Combinatorics.

[15] A. Doufexi, S. Armour, M. Butler, A. Nix, D. Bull, J. McGeehan, and P. Karlsson. A comparison of the HIPERLAN/2 and IEEE 802.11a wireless LAN standards. *IEEE Communications Magazine*, 40:172–180, 2002.

[16] H. Ehm, S. Winter, and R. Weigel. Analytic quantization modeling of ofdm signals using normal gaussian distribution. In *Microwave Conference, 2006. APMC 2006. Asia-Pacific*, pages 847 –850, Dec. 2006.

[17] H. Ekström, A. Furuskär, J. Karlsson, M. Meyer, S. Parkvall, J. Torsner, and M. Wahlqvist. Technical solutions for the 3G Long-Term Evolution. *IEEE Communications Magazine*, 44:38–45, 2006.

[18] A. Gersho and R. M. Gray. *Vector Quantization and Signal Compression*. Kluwer Academic Publishers, 1992.

[19] A. Ghosh, D.R. Wolter, J.G. Andrews, and R. Chen. Broadband wireless access with WiMax/802.16: current performance benchmarks and future potential. *IEEE Communications Magazine*, 43:129–136, 2005.

[20] D. Gore, R. Heath, and A. Paulraj. Transmit selection in spatial multiplexing systems. *IEEE Commun. Lett.*, 6(11):491–493, 2002.

[21] A. O. Hero and T. L. Marzetta. On computational cut-off rate for space-time coding. Technical report, Bell Laboratories, Lucent Technologies, Murray Hill, NJ, 1999.

[22] A. O. Hero and T. L. Marzetta. Optimal signal constellations for space-time Rayleigh channels. Technical report, Bell Laboratories, Lucent Technologies, Murray Hill, NJ, 1999.

[23] M. T. Ivrlac, W. Utschick, and J.A. Nossek. Fading correlations in wireless MIMO communication systems. *IEEE J. Select. Areas Commun.*, 21(5):819–828, Jun. 2003.

[24] P.B. Kenington and L. Astier. Power consumption of A/D converters for software radio applications. *Vehicular Technology, IEEE Transactions on*, 49(2):643 –650, Mar. 2000.

[25] Walt Kester and Analog Devices. MT-010: The importance of data converter static specifications - don't lose sight of the basics!, 2005. Online: http://www.analog.com/static/imported-files/tutorials/MT-010.pdf.

[26] M. Kiessling and J. Speidel. Analytical performance of MIMO zero-forcing receivers in correlated Rayleigh fading environments. In *Proc. IEEE Workshop Signal Process. Adv. Wireless Commun.*, pages 383–387, Rome, Italy, 2003.

[27] T. Kurpjuhn and M. Ivrlac. Information theoretic measures for MIMO-channels. Technical Report TUM-LNS-TR-01-01, Lehrstuhl für Netzwertheorie und Signalvararbeitung, Munich, Germany, Technische Univ. München, 2001.

[28] B. Le. Analog-to-digital converters. In *IEEE Signal Processing Magazine*, pages 69–77, Nov. 2005.

[29] C.-L. Liu. Impacts of I/Q imbalance on QPSK-OFDM-QAM detection. In *Proc. Int. Conf. Consumer Electronics*, page 122, Feb. 1999.

[30] H. Liu. Error performance of MIMO systems in frequency-selective Rayleigh fading channels. In *Proc. IEEE Global Telecommun. Conf.*, volume 4, pages 2104–2108, San Francisco, CA, 2003.

[31] M. Liyanage and I. Sasase. Statistical analysis of quantization noise in an end-to-end ofdm link. In *Communications (ICC), 2010 IEEE International Conference on*, pages 1 –6, May. 2010.

[32] J. L. Massey. Coding and modulation in digital communications. Mar. 1974. presented at the Int. Zurich Seminar, Sindelfingen, Germany.

[33] M. R. McKay and I. B. Collings. Capacity and performance of MIMO-BICM with zero-forcing receivers. *IEEE Trans. Commun.*, 53(1):74–83, 2005.

[34] A. Moschitta and D. Petri. Wideband communication system sensitivity to quantization noise. In *Instrumentation and Measurement Technology Conference,*

*2002. IMTC/2002. Proceedings of the 19th IEEE*, volume 2, pages 1071 – 1075 vol.2, 2002.

[35] B. M. Murray and I. B. Collings. AGC and quantization effects in a zero-forcing MIMO wireless system. In *Vehicular Technology Conference, 2006. VTC 2006-Spring. IEEE 63rd*, volume 4, pages 1802 –1806, May. 2006.

[36] B. M. Murray and S. Reisenfeld. Maximizing the cutoff rate in a quantized MIMO wireless system with AGC. In *1'st Australian Conference on Wireless Broadband and Ultra Wideband Communications (AusWireless'06)*, Mar. 2006.

[37] B. M. Murray, H. Suzuki, and S. Reisenfeld. Optimal quantization of OFDM at digital IF. In *TENCON 2008 - 2008 IEEE Region 10 Conference*, pages 1 –5, Nov. 2008.

[38] National Instruments. Sources of error in IQ based RF signal generation, 2007. Online: http://zone.ni.com/devzone/cda/tut/p/id/5657.

[39] Ramjee Prasad. *OFDM for Wireless Communications Systems.* Artech House Publishers, Norwood, MA, USA, 2004.

[40] H. Suzuki, B. Murray, A. Grancea, R. Shaw, J. Pathikulangara, and I.B. Collings. Real-time wideband mimo demonstrator. In *Communications and Information Technologies, 2007. ISCIT '07. International Symposium on*, pages 284 –289, Oct. 2007.

[41] I. E. Telatar. Capacity of multi-antenna Gaussian channels. *Europ. Trans. Commun.*, Nov.-Dec. 1999.

[42] B. Widrow and I. Kollar. *Quantization Noise: Round Off Error in Digital Computation, Signal Processing, Control and Communications.* Cambridge University Press, 2008.

[43] B. Widrow, I. Kollar, and Ming-Chang Liu. Statistical theory of quantization. *Instrumentation and Measurement, IEEE Transactions on*, 45(2):353 –361, Apr. 1996.

[44] Wikipedia. Combinatorics, 2012. Online: http://en.wikipedia.org/wiki/Combinatorics.

[45] J. H. Winters. On the capacity of radio communication systems with diversity in a Rayleigh fading environment. *IEEE J. Select. Areas Commun.*, SAC-5(5):871–878, Jun. 1987.